

12-1-2015

Characterization of Gold and Related Mineralization at the North Bullion Carlin System, Railroad Project, a Nevada Carlin-type Gold Prospect

Melanie Nicole Newton
University of Nevada, Las Vegas

Follow this and additional works at: <https://digitalscholarship.unlv.edu/thesesdissertations>

 Part of the [Geochemistry Commons](#), and the [Geology Commons](#)

Repository Citation

Newton, Melanie Nicole, "Characterization of Gold and Related Mineralization at the North Bullion Carlin System, Railroad Project, a Nevada Carlin-type Gold Prospect" (2015). *UNLV Theses, Dissertations, Professional Papers, and Capstones*. 2567.
<http://dx.doi.org/10.34917/8220147>

This Thesis is protected by copyright and/or related rights. It has been brought to you by Digital Scholarship@UNLV with permission from the rights-holder(s). You are free to use this Thesis in any way that is permitted by the copyright and related rights legislation that applies to your use. For other uses you need to obtain permission from the rights-holder(s) directly, unless additional rights are indicated by a Creative Commons license in the record and/or on the work itself.

This Thesis has been accepted for inclusion in UNLV Theses, Dissertations, Professional Papers, and Capstones by an authorized administrator of Digital Scholarship@UNLV. For more information, please contact digitalscholarship@unlv.edu.

CHARACTERIZATION OF GOLD AND RELATED MINERALIZATION AT THE
NORTH BULLION CARLIN SYSTEM, RAILROAD PROJECT,
A NEVADA CARLIN-TYPE GOLD PROSPECT

By

Melanie Nicole Newton

Bachelor of Science in Geology

Western Kentucky University

2011

A thesis submitted in partial fulfillment
of the requirements for the

Master of Science - Geosciences

Department of Geoscience

College of Sciences

The Graduate College

University of Nevada, Las Vegas

December 2015

Copyright by Melanie N. Newton, 2015

All Rights Reserved



Thesis Approval

The Graduate College
The University of Nevada, Las Vegas

September 17, 2015

This thesis prepared by

Melanie Nicole Newton

entitled

Characterization of Gold and Related Mineralization at the North Bullion Carlin System,
Railroad Project, A Nevada Carlin-type Gold Prospect

is approved in partial fulfillment of the requirements for the degree of

Master of Science – Geoscience
Department of Geosciences

Jean S. Cline, Ph.D.
Examination Committee Chair

Kathryn Hausbeck Korgan, Ph.D.
Graduate College Interim Dean

Rodney V. Metcalf, Ph.D.
Examination Committee Member

John L. Mutean, Ph.D.
Examination Committee Member

Barbara Luke, Ph.D.
Graduate College Faculty Representative

ABSTRACT

Characterization of Gold and Related Mineralization at the North Bullion Carlin System, Railroad Project, a Nevada Carlin-type Gold Prospect

by

Melanie N. Newton

Dr. Jean S. Cline, Examination Committee Chair

Professor

University of Nevada, Las Vegas

A study of the North Bullion Carlin system, a Nevada Carlin-type gold prospect located on trend with the large Carlin-type gold deposits (CTGD) of the Carlin Trend, identified characteristics of ore and alteration mineralization, mineral paragenesis, and pyrite and whole rock geochemistry that are similar to characteristics that typify Carlin-type gold deposits. The North Bullion Carlin system is hosted in Devonian shelf carbonates and the Mississippian overlap assemblage, host rocks that are different from typical CTGD shelf-slope carbonate assemblage host rocks. The mineralogy and ore-stage gold-bearing pyrite rims at North Bullion are not as well developed as they are in typical CTGD, and alteration and geochemical relationships are subtle. Yet the North Bullion Carlin system exhibits many of the features observed in large deposits.

Observations demonstrate that North Bullion Carlin system is a CTGD, potentially on the periphery of a larger system. Gold mineralization at the North Bullion Carlin system is controlled by structures, which include the North Bullion Fault Zone and the Massif Fault, and stratigraphic controls, which include the lithologic contacts between

the Devonian Devils Gate Collapse Breccia, Mississippian Webb Formation, and Mississippian Chainman Formation. The uppermost horizon of gold mineralization is located at a lithological contact between limestone and mudstone within the Webb Formation, and grade decreases away from this contact in the mudstone. The lowermost horizon of gold mineralization is located within the Devonian Devil's Gate collapse breccia and the multi-lithic tectonic breccia along the North Bullion Fault Zone and Massif fault. Gold mineralization does not extend above the uppermost dacite dikes and sills within the Mississippian Chainman Formation, suggesting the dacite dikes and sills provided a local seal to the deposit.

Cross-cutting relationships, textures, and geochemistry indicated the presence of four generations of pyrite. Pre-ore stage (POS) pyrites formed during diagenesis of the Devonian Devil's Gate Formation, Mississippian Webb Formation, and Mississippian Chainman Formation. Pre-ore stage pyrites contain Fe, S, Co, Ni, Pb, Ag, and Sn, with variable Bi, Ti, and Zn. Ore-stage 1 (OS 1) pyrites are Au-bearing hydrothermal pyrites within the 38.2 Ma Tertiary porphyritic dacite dikes. Electron probe microanalyzer and LA-ICP-MS quantified Fe, S, Co, and Pb, with variable Bi and Ti, and Au in OS 1 pyrites, but did not detect significant As, Tl, Hg, or Sb. Ore-stage 2 (OS 2) pyrites are more typical Carlin-type Au-bearing pyrites that form partial sub-micrometer rims on POS and OS 1 pyrites and OS 2 microcrystals. Based on electron probe microanalyzer and LA-ICP-MS analyses, OS 2 pyrites contain Au and variable As, Cu, Hg, Sb, and Tl. Late-ore-stage (LOS) pyrites cross-cut sedimentary host rock minerals and late-ore-stage drusy quartz. Late-ore-stage pyrites contain Fe, S, Pb, and Ag, with variable Bi, Sn, and Zn, and locally contain Au, As and Sb.

Ore-stage 1 pyrites within Tertiary porphyritic dacite dikes are associated with quartz, illite, and kaolinite. Ore-stage 2 pyrites that rim POS pyrites in sedimentary host rocks are associated with jasperoid, illite, and carbon; OS 2 pyrites that rim OS 1 pyrites in dacite dikes are associated with quartz, illite, and kaolinite.

Late-ore-stage minerals within sedimentary host rocks include secondary quartz, late-ore-stage pyrite, realgar, and calcite. Post-ore-stage minerals within sedimentary host rocks include barite, stephanite, kaolinite, halloysite, and oxide minerals. High-grade silver intervals at North Bullion Carlin system ($\leq \sim 20$ oz/t) result from the presence of the mineral stephanite (Ag_5SbS_4) that precipitated after Carlin-type gold mineralization, is unrelated to Carlin-type mineralization, and is likely related to one of the post-dacite igneous intrusive events.

A compilation of statistical analyses including classification support vector machine, non-metric multi-dimensional scaling model, Spearman rank correlation matrix, and Mann-Whitney U-Test on whole rock geochemistry on 5' drill core samples reveal the key elements related to gold and deposit scale trends. These statistical analyses and models illustrate that in samples with a low gold grade (0.1 ppm Au) the elements that best correlate with Au, with decreasing correlation, are Hg, Sb, Tl, and/or As. In samples with a moderate gold grade (1.0 ppm Au) the elements that best correlate with Au, with decreasing correlation, are Tl, Hg, and As. Gold correlates positively with Fe, S, Pb, Co, Ni, Cu, Al, and K identifying these elements as good indicators predicting the presence of gold. Gold correlates negatively with elements in carbonate host rocks (Ba, Ca, Mg, Mn, and Sr), and these elements indicate of the absence of gold. Silver, Mo, and Zn do not correlate with Au.

At the deposit scale the North Bullion Carlin system exhibits characteristics of ore, alteration, and mineral paragenesis that are typical of Carlin-type gold deposits, but the mineralization is subtle and not as well developed as in large, high-grade deposits. At the micro-scale the ore pyrites, and whole rock geochemistry are similar to typical Carlin-type gold deposits. The Carlin-type pathfinder trace elements, As, Hg, Sb, and Tl, best correlate with gold in ore-stage mineralization. Statistical analyses of whole rock geochemistry indicate that Ba, Mn, Al, P, Cr, and V are the elements that provide the best vector to ore and could identify the periphery of gold mineralization.

ACKNOWLEDGEMENTS

I would like to thank Dr. Jean Cline, my committee chair, for always being available to answer questions, discuss my ideas, advise me, and provide direction in every aspect. Thank you to Dr. John Muntean and Dr. Rod Metcalf for being actively involved committee members and providing significant insight into my research, and to Dr. Barbara Luke, the graduate college representative. I want to thank my family and friends for emotional support, encouragement, guidance, and for enriching my life.

I am also grateful to Gold Standard Ventures Corporation for funding this project and for providing a summer internship. A special thanks goes to Dave Mathewson, Steve Koehler, Mac Jackson, Mike Harp, Rob Edie, Neil Whitmer, and Chrisstan Betancourt for all of the time dedicated to assisting me in so many aspects of this project, including sample collection, compiling background information, and suggestions on the presentation of data. Thank you to Dave Mathewson for originally getting this project started. Thank you to Steve Koehler for handling the financial logistics, to Mac Jackson, Mike Harp, and Rob Edie who dedicated so much of their time, and for making this project possible.

I would also like to acknowledge the Society of Economic Geologists (SEG), University of Nevada, Las Vegas (UNLV) Graduate and Professional Student Association, and the UNLV Geosciences Department for the grants and scholarships that I was awarded throughout my graduate studies. I am grateful to Barrick Gold and ExxonMobil for providing a summer internship opportunities.

Additionally, special thanks to everyone who helped me collect data and the hours of discussion that came along with it, including Minghua Ren at the UNLV Electron

Microanalysis & Imaging Laboratory, Mandy White for help and discussions on geochemical statistics, Alan Koenig at the United States Geological Survey Denver LA-ICP- MS lab, Oliver Tschauner at the UNLV XRD lab, Paul Bowen for running my samples on the TerraSpec, Andreas Beinlich at the University of British Columbia Mineral Deposit Research Unit for sample analysis, Debra Soukup and Tracy Cail for discussions on the methodology in clay identification for XRD analyses, and Paul Dobak at the Barrick Gold Elko Exploration Office for allowing me time on their petrographic microscope during my summer internship with Gold Standard Ventures Corporation.

TABLE OF CONTENTS

ABSTRACT	iii
ACKNOWLEDGEMENTS	vii
LIST OF TABLES	xii
LIST OF FIGURES	xiii
CHAPTER 1 INTRODUCTION.....	1
CHAPTER 2 BACKGROUND GEOLOGY.....	3
Carlin Trend Gold Deposits Geology.....	3
North Bullion Carlin System	9
CHAPTER 3 METHODS.....	15
Sample collection	15
Optical petrography	16
Scanning electron microscopy	16
Electron probe microanalysis	17
Laser ablation, inductively-coupled plasma, mass spectrometry.....	18
X-Ray Diffraction	19
TerraSpec Analysis	20
Multi-element geochemical analysis	20
Geostatistical Analysis	21
Off Axis - Integrated Output Cavity Spectroscopy	23
CHAPTER 4 PRE-ORE STAGE.....	25
Host Rocks.....	25
Secondary Pre-ore-stage Minerals	29
Interpretation	30
Discussion	31
Pre-ore-stage Pyrite.....	32
Discussion of Pre-ore-stage pyrite	43
Mineral Paragenesis Discussion.....	43
CHAPTER 5 ORE STAGE.....	45
Ore-stage 1 Pyrite	45
Ore-stage 2 Pyrite	50
Interpretation of Ore-stage 2 Pyrites.....	56
Illite and Jasperoid.....	57
Sample Transects	58
Interpretation	61
Discussion.....	61
Mineral Paragenesis Discussion	62

CHAPTER 6	LATE- TO POST-ORE STAGE.....	63
	Quartz	63
	Interpretation.....	64
	Late-ore-stage Pyrite	64
	Realgar	68
	Calcite	68
	Post-ore-stage Minerals.....	69
	Mineral Paragenesis Discussion	70
CHAPTER 7	BRECCIATION.....	72
	Interpretation.....	73
CHAPTER 8	WHOLE ROCK GEOCHEMISTRY.....	75
	Classification Support Vector Machine	75
	Interpretation.....	76
	Non-metric Multi-Dimensional Scaling Model	77
	Interpretation.....	78
	Spearman Rank Correlation Matrix	79
	Interpretation.....	79
	Mann-Whitney U-Test	80
	Interpretation.....	84
	Discussion.....	85
CHAPTER 9	CONCLUSIONS.....	88
APPENDIX A	TABLES	91
APPENDIX B	FIGURES	133
APPENDIX C	SAMPLES COLLECTED	202
APPENDIX D	DOCUMENTED MINERAL LOCATIONS FOR POLISHED SECTIONS.....	215
APPENDIX E	SEM DATA.....	223
APPENDIX F	EPMA DATA.....	235
APPENDIX G	LA-ICP-MS DATA.....	282
APPENDIX H	XRD DATA.....	294
APPENDIX I	TERRASPEC DATA.....	325
APPENDIX J	OFF AXIS - INTEGRATED OUTPUT CAVITY SPECTROSCOPY DATA.....	329

REFERENCES.....	341
CURRICULUM VITAE.....	348

LIST OF TABLES

Table 1	List of Acronyms.....	92
Table 2	Probe Conditions.....	93
Table 3	X-ray line, spectrometer, peak data, and minimum detection limit for the suite of elements used for EMPA analysis at the North Bullion Fault Zone.....	94
Table 4	LA-ICP-MS conditions.....	96
Table 5	X-Ray Diffraction Settings.....	97
Table 6	Multi-element Geochemical Laboratory Analysis Techniques....	98
Table 7	Principal Components Analysis Procedure.....	99
Table 8	EPMA analysis points of all pyrite types.....	100
Table 9	Pre-ore-stage pyrite classification.....	104
Table 10	Principal Components Analysis of all EPMA pyrite data.....	105
Table 11	Principal Components Analysis of Pre-ore-stage pyrite data.....	107
Table 12	Composition of Components of all EPMA pyrite data and Pre- ore-stage pyrites.....	108
Table 13	Spearman Rank Correlation Matrix of all EPMA data.....	109
Table 14	Mann-Whitney U-Test of EPMA data to identify elements in pyrites and Au-bearing rims.....	111
Table 15	Ore-stage 1 pyrite classification.....	113
Table 16	Principal Components Analysis of Ore-stage 1 pyrite data.....	114
Table 17	Composition of Components of Ore-stage 1, Ore-stage 2, and Late-ore-stage pyrite data.....	115
Table 18	Ore-stage 2 pyrite classification.....	116
Table 19	Principal Components Analysis of Ore-stage 2 pyrite data.....	117
Table 20	Late-ore-stage pyrite classification.....	118
Table 21	Principal Components Analysis of Late-ore-stage pyrite data....	119
Table 22	Classification Support Vector Machine (C-SVM) for 0.1 ppm Au classification.....	120
Table 23	Classification Support Machine (C-SVM) for 1.0 ppm Au classification.....	121
Table 24	Whole rock Spearman Rank Correlation Matrix of 36 elements...	122
Table 25	Non-metric Multi-dimensional Scaling Model Axis 1 and 2 R, and R ² values for 0.1 ppm and 1.0 ppm gold classifications for whole rock assay data.....	127
Table 26	Mann-Whitney U-Test for 0.004, 0.1, 0.3, 1.0, 2.0, 3.0, 6.0 ppm Au classifications.....	128

LIST OF FIGURES

Figure 1	Nevada State map showing the location of the GSV Railroad Project in relation to the Carlin trend.....	134
Figure 2	Location of North Bullion Carlin system on Railroad Project.....	135
Figure 3	Rain Mine Stratigraphic Section.....	136
Figure 4	Tectono-stratigraphic history of Nevada.....	137
Figure 5	Generalized east-west cross section of northern Nevada and Utah....	138
Figure 6	Generalized long section of the Carlin trend, Nevada, looking southwest.....	139
Figure 7	Mineral paragenesis for the Getchell CTGD.....	140
Figure 8	Idealized E-W cross section of the North Bullion Carlin system.....	141
Figure 9	Idealized N-S cross section of the North Bullion Carlin system.....	142
Figure 10	Timing of igneous activity and related mineralization at the Railroad property.....	143
Figure 11	North Bullion Carlin system drill holes at the Railroad Project.....	144
Figure 12	EPMA peak overlap relationships.....	145
Figure 13	EPMA transect method across pyrite.....	147
Figure 14	Devonian Devil's Gate Formation.....	149
Figure 15	North Bullion Carlin system Mineral Paragenesis.....	151
Figure 16	Mississippian Webb Formation.....	152
Figure 17	Mississippian Chainman Formation.....	153
Figure 18	Tertiary porphyry dacite dike.....	155
Figure 19	EPMA element maps of OS 1 pyrite, sphalerite, and rutile in Tertiary porphyry dacite dike.....	157
Figure 20	Pre-ore-stage pyrite, rutile, and sphalerite within multi-lithic breccias.....	159
Figure 21	Pre-ore stage (POS) pyrites.....	160
Figure 22	X-Y graphs of Fe versus analyzed elements in POS pyrite.....	162
Figure 23	Mann-Whitney U-Test bar graphs of EPMA pyrite data for Fe, S, Co, Ni, and Pb.....	163
Figure 24	Mann-Whitney U-Test bar graphs of EPMA pyrite data for Al, Si, Ag, and Ca.....	164
Figure 25	X-Y graphs of Fe versus analyzed elements in OS 1 pyrite.....	165
Figure 26	Trace element chemistry of OS 2 pyrite rims and microcrystals in Mississippian Webb mudstone.....	166
Figure 27	Trace element chemistry of OS 2 pyrite in Mississippian Chainman sandstone.....	167
Figure 28	Trace element chemistry of OS 2 pyrite on POS framboidal pyrite in Mississippian Webb mudstone.....	168
Figure 29	Trace element chemistry of OS 2 pyrite in Multi-lithic Breccia.....	169
Figure 30	Spatial distribution of Au and Carlin-type pathfinder elements.....	171
Figure 31	X-Y graphs of Fe versus analyzed elements in OS 2 pyrite.....	173
Figure 32	X-Y graphs of Au versus analyzed elements in OS 2 pyrite.....	174
Figure 33	Mann-Whitney U-Test bar plots of EPMA pyrite data for Au, As, Hg, Cu, Sb, and Tl.....	175

Figure 34	Cartoon of OS 2 pyrite on POS pyrite.....	176
Figure 35	Devonian Devil's Gate Formation sample transect.....	177
Figure 36	Mississippian Webb Formation micrite samples.....	179
Figure 37	Mississippian Webb Formation mudstone samples.....	181
Figure 38	Mississippian Chainman Formations sandstone transect.....	182
Figure 39	Late-ore-stage alteration minerals: quartz.....	184
Figure 40	Late-ore-stage and Post-ore-stage alteration minerals: realgar, coarsely crystalline calcite, and barite cross-cutting relationships.....	186
Figure 41	Late-ore-stage pyrite textures.....	188
Figure 42	Late-ore-stage vein pyrite.....	190
Figure 43	X-Y graphs of Fe versus analytical elements in LOS pyrite.....	192
Figure 44	Post-ore-stage barite and stephanite.....	193
Figure 45	Non-metric multidimensional scaling model with 0.1 Au classification.....	195
Figure 46	Non-metric multidimensional scaling model with 1.0 Au classification.....	196
Figure 47	Mann-Whitney U-Test bar graphs of whole rock geochemistry data for Au, As, Hg, Sb, and Tl.....	197
Figure 48	Mann-Whitney U-Test bar graphs of whole rock geochemistry data for Ag, Mo, and Zn.....	198
Figure 49	Mann-Whitney U-Test bar graphs of whole rock geochemistry data for Fe, S, Pb, Cu, Ni, and Co.....	199
Figure 50	Mann-Whitney U-Test bar graphs of whole rock geochemistry data for Al, K, Cr, P, and V.....	200
Figure 51	Mann-Whitney U-Test bar graphs of whole rock geochemistry data for Ba, Ca, Mn, Mg, Na, and Sr.....	201

CHAPTER 1

INTRODUCTION

The North Bullion Carlin system is located on the Railroad property, eight kilometers south of the Rain deposit and Emigrant mine that mark the southern-most extent of the Carlin trend (Figs. 1, 2). Nevada is the type locality for Carlin-type gold deposits (CTGD), which are estimated to have contained more than 200 million ounces of gold before mining began (Cline et al., 2005; Sillitoe, 2008). Carlin-type gold deposits contain one of the largest concentrations of gold in the world, and are the second leading gold producing region in the world, with more than 76 million ounces of gold produced from the Carlin trend alone by the end of 2010 (Nevada Bureau of Mines and Geology, 2010; Muntean et al., 2011). Due to their large gold endowments, several of the large deposits have been studied in great detail. Typical host rocks in most CTGD are early Paleozoic miogeoclinal carbonate shelf-slope rocks containing thin-bedded pyritic and carbonaceous, silty dolomitic limestone and marl with primary porosity in turbidite sequences that commonly contain abundant fossils (Cline et al., 2005).

Research continues on deposits that are atypical, such as the North Bullion Carlin system. The mineralized system contains two distinct zones of gold mineralization hosted in mixed siliciclastic-carbonate rocks that formed within the Mississippian foreland basin overlap sequence and Devonian shelf carbonates, which are different from host rocks in most CTGD (Fig. 3). Although these host rocks have a high siliciclastic component, the North Bullion Carlin system exhibits ore and alteration minerals, mineralization style, pyrite geochemistry, and a mineral paragenesis that are similar to typical CTGD, but

which are subtle and not as well developed as in most economic Carlin-type deposits.

The North Bullion Carlin system may represent the periphery of a larger deposit.

This project characterizes Carlin-type mineralization in Mississippian siliciclastic rocks by characterizing ore and alteration minerals, identifying alteration features most closely related to gold, determining the extent and intensity of the alteration, determining the mineral paragenesis, identifying pyrite populations and quantifying pyrite geochemistry, characterizing whole rock geochemistry using statistical analyses, and identifying what features were the best vectors to ore to use for exploration. Due to the presence of subtle alteration at the North Bullion Carlin system, which does not provide a useful vector to ore mineralization, analysis of whole rock geochemical data provides the best indicator of proximity to ore. Project results can be applied in the exploration for CTGD beyond typical Carlin host rocks that occur beyond the Carlin trend.

CHAPTER 2

BACKGROUND GEOLOGY

Carlin-type Gold Deposit Geology

During the Late Proterozoic through the early Paleozoic, rifting of the western continental margin of Laurentia, present day western North America, led to the development of a westward thickening passive margin miogeoclinal sequence of carbonates and siliciclastic rocks (Fig. 4) (Saleeby et al. 1987; Poole 1992). Late Proterozoic rifting of the Laurentia continental margin caused the formation of deep NNW oriented fault structures (Fig. 5) (Tosdal et al., 2000; Crafford and Grauch, 2002). The Carlin trend and Battle Mountain - Eureka trend are interpreted to be crustal scale fault zones that formed during continental break-up and accommodated thinning of the transitional Laurentian continental crust (Tosdal et al., 2000; Grauch, Rodriguez and Wooden, 2003). The Getchell trend and Jerriitt Canyon trend were interpreted as paleo-transform faults along the paleo-continental margin (Tosdal et al., 2000). These deep rift structures likely became fluid pathways that focused ore fluids along regional scale linear trends. This allowed gold-bearing fluids to access and react with reactive sedimentary rocks, porous carbonate rocks underlying impermeable siliciclastic rocks, which led to precipitation of gold-bearing pyrite and/or marcasite as ore fluids sulfidized iron-bearing host rocks (Hofstra et al., 1991; Tosdal et al., 2000; Crawford and Grauch, 2002; Cline et al., 2005).

Most CTGD are contained within a carbonate shelf-slope facies, part of the westward thickening passive margin miogeoclinal sequence of carbonates and shales. This miogeoclinal carbonate sequence contains thin-bedded, pyritic and carbonaceous,

silty dolomitic limestone and marl, which are ideal host rocks in most CTGD (Cline et al., 2005). The reactive host rocks have primary porosity due to the presence of fossiliferous turbidite sequences (Poole et al. 1992).

Compressional events beginning with the Antler Orogeny (385-345 Ma), led to the development of multiple easterly converging thrust faults (Fig. 4). The Antler Orogeny during the Devonian-Early Mississippian caused deep-water siliciclastic sedimentary rocks of the deep basin to be thrust over shallow water shelf-slope carbonate facies rocks, creating the Roberts Mountain thrust (Figs. 5, 6) (Roberts, 1958; Burchfiel and Royden, 1991). Episodic compressional deformation generally continued along the western margin of North America, although there were periods of extension related to the Humboldt orogeny during the late Pennsylvanian and during the Eocene (Fig. 4) (Roberts, 1958; Burchfield and Royden, 1991; Dickinson, 2004). Delamination at the base of the North American plate and/or decoupling of the subducting Farallon plate from the North American plate allowed upwelling of asthenosphere, and is interpreted to have triggered a transition from compression to tension, which reopened preexisting structures (Seedorff, 1991; Humphreys, 1995; Sonder and Jones, 1999). Extension reopened Neoproterozoic rift-related basement faults in the Great Basin province that had a general trend of north-northwest and west-northwest (Cline et al., 2005). Carlin-type fluids used high-angle rift-related basement faults as conduits below low-angle thrust faults, like the Roberts Mountain Thrust (Cline et al., 2005). The Roberts Mountain thrust fault provided a regional aquitard forcing fluids to disperse laterally through reactive carbonates of the lower plate (Cline et al., 2005).

Igneous Rocks

Magmatism along the Carlin trend occurred in four distinct pulses at ~158, 112, 40 to 36, and ~15 Ma based on $^{40}\text{Ar}/^{39}\text{Ar}$ dating on plagioclase, hornblende, biotite, sericite, and U-Pb dating on zircon and titanite (Ressel and Henry, 2006). The close spatial and temporal association between the gold deposits and Eocene plutons of the Carlin trend led to the interpretation that the plutons were a primary heat source for large hydrothermal systems and gold deposition (Ressel and Henry, 2006). The 40 to 36 Ma magmatic pulse of high K calc-alkaline magma centers and porphyritic rhyolite, porphyritic dacite, aphyric rhyolite, and basaltic andesite dikes (Ressel and Henry, 2006) swept from north to south, and was likely triggered by the foundering of the Farallon plate (Humphreys, 1995; du Bray, 2007; Humphreys, 2009).

Carlin-type Gold Mineralization and Alteration

Hydrothermal processes related to CTGD produced subtle alteration and ore mineralization patterns, which are generally similar in all CTGD, but which exhibit differences due to different host rocks and structural complexities. Paragenetic sequences for several deposits (Groff et al., 1997; Cline, 2001; Almeida et al., 2010; Clark, 2012) identified the temporal relationships of the pre-ore, syn-ore, and late-ore stages related to mineralization (Fig. 7) that are present in the unoxidized regions of most deposits. Ore fluids in CTGD decarbonatized, argillized, and locally silicified host wall rocks, (Hofstra and Cline, 2000; Cline et al., 2005). Decarbonatization is the removal of carbonate material. Decarbonatization characteristically produced vugs in rock, that are generally hard to discern in the field, but which are visible in core and polished section. Collapse brecciation in CTGD is related to decarbonatization and dissolution of carbonate host

rocks; however, tectonic breccias also are present. Silicification is characterized by the jasperoid replacement of limestone, drusy quartz rimming or infilling voids from brecciation and/or pores in rocks from decarbonatization; quartz veins are generally absent. Argillization is characterized by the formation of clay minerals including illite, interlayered illite/smectite, and kaolinite and/or dickite. Sulfidation of iron in the wall rock by reduced sulfur in ore fluid caused the precipitation of trace element-rich and gold bearing pyrite and/or marcasite (Hofstra et al., 1991). Gold and related trace elements substitute for iron and sulfur in the pyrite structure (Cline et al., 2005). Late-stage minerals may include orpiment, realgar, stibnite, calcite, and barite (Cline, 2001; Cline et al., 2005).

Stratigraphy of the Southern Carlin trend

Rain deposit and Emigrant mine are examples of deposits that do not contain typical CTGD host rocks (Figs. 3, 6). Gold mineralization at these deposits is hosted in collapse breccias that formed along the contact between the Devonian Devil's Gate Formation and the overlying Mississippian Webb Formation (Fig. 3) (Longo et al., 2002), similar to host rocks and gold mineralization at the North Bullion Carlin system eight kilometers to the south (GSV, 2014).

At the Rain deposit, the Devonian Nevada group, an unmineralized part of the section, lies below the Devonian Devil's Gate Formation. The Devonian Nevada group contains the lower Devonian Nevada group (Dnl), correlative with the Beacon Peak Formation, the middle Devonian Nevada group (Dnm), correlative with the Oxyoke Canyon Formation, and the upper Devonian Nevada group (Dnu), correlative with the Telegraph Canyon Formation. These formations are present at both the Rain deposit and

North Bullion Carlin system. The Telegraph Canyon Formation is ~152-183 meters thick reaching up to 354 meters thick and is a light-medium grey dolomite, generally thick to massive bedded with < 1mm crystals (Carlisle et al., 1957; Longo et al., 2002; GSV, 2014). Interbedded calcareous sandstone and dolomite mark the lower transitional contact with the Oxyoke Canyon Formation. Zebra dolomite marks upper contact with the overlying Devil's Gate Formation (Longo et al., 2002; GSV, 2014).

The Devonian Devil's Gate Formation (Ddg) is approximately 60 - 152 meters thick, contains thin to thick beds, medium to dark gray limestone with calcarenite units greater than calcisiltite, micrite, and bioclastic limestone units, and can locally be fossiliferous (Carlisle et al., 1957; Longo et al., 2002; GSV, 2014). Unaltered Devil's Gate is a clean pure limestone (Carlisle et al. 1957; Jackson, 2014). This unit was deposited prior to the onset of the Antler Orogeny and has an unconformable contact with the overlying Mississippian Webb Formation (Smith and Ketner, 1975), which formed in response to the orogeny.

The overlying Mississippian Webb Formation is the dominant mineralized host rock at the Rain deposit where it exhibits pervasive silicification. The Webb Formation was deposited from sediments that were shed off the Antler highland, which prograded westward during deposition of the Mississippian Chainman Formation, as evident from the coarsening upward sequence (Longo et al., 2002). The Mississippian Webb Formation consists of thin- to medium-bedded, calcareous, carbonaceous mudstone and silty mudstone with approximately 10 percent discontinuous lenses of sandstone and local silty limestone units (Fig. 3) (Smith and Ketner, 1975; Mathewson, 1993; 1994; Longo et al., 2002). Silty limestone units can be present at the top and base of the

Mississippian Webb Formation (Smith and Ketner, 1975). The Mississippian Webb Formation is a part of a coarsening upward sequence and a lateral facies transition into the Mississippian Chainman Formation.

The Mississippian Chainman Formation represents a widespread fluvial environment and is derived from source rock related to the erosion of the Antler highland (Sadlick, 1995). At the Rain deposit, the Mississippian Chainman Formation has been described as having two facies, a lower transitional facies of fine clastics and an upper coarse clastic facies (Fig. 3). The lower transitional facies consists of mudstones, siltstones, arkosic sandstones, and pebble conglomerates (Longo et al., 2002). The upper coarse clastic facies consists of poorly sorted coarse conglomerates and quartz sandstones (Longo et al., 2002). Silty mudstone in the lower transitional facies is dark grey to black, thin planar mudstone with interbedded medium grey, laminated-to thin-bedded siltstone, interpreted as fining upward sequences. Sandstone in the lower transitional and upper coarse clastic facies is light to medium grey, thick bedded, and contains angular rounded clasts of quartz, chert, and mudstone. Conglomerate in the lower transitional and upper coarse clastic facies is multi-colored thick bedded, and contains angular rounded pebble clasts, and grey-green chert, black mudstone, grey siltstone, and minor greenstone clasts. The grey-green chert of the Chainman sandstone units is what distinguishes it from the sandstone lenses within the Mississippian Webb Formation (Sadlick, 1995; Longo et al., 2002; GSV, 2014). Above the Chainman Formation at the Rain deposit is the Devonian Woodruff Formation. This contact between the Chainman and Woodruff Formations represents the Robert's Mountain Thrust.

North Bullion Carlin System

The North Bullion Carlin system is a 1.6 square kilometer target within the 35.4 square kilometer Railroad property, located within the Pinon Range, eight kilometers south of the Rain deposit and Emigrant Mine (Fig. 1 and 2). The North Bullion Carlin system shares a stratigraphy similar to that described for the Rain deposit, with local differences related to lateral facies changes and structural complexities. The North Bullion Carlin system contains two distinct zones of gold mineralization. The upper gold zone is hosted within flysch facies sandstone, silty mudstone, mudstone, micrite, and multi-lithic breccia along the faulted contacts between the Mississippian Webb and Chainman Formations. The lower gold zone is within Devonian Devil's Gate limestone collapse breccia and the multi-lithic tectonic breccia along the North Bullion Fault Zone and Massif fault (Gold Standard Ventures Corp., 2013) (Figs. 3, 8, and 9).

Stratigraphy of North Bullion Carlin System

The Devonian Devil's Gate Formation (Ddg) is one of the three units that hosts significant gold mineralization at the North Bullion Carlin system, and the lower gold zone that contains low- to high-grade gold ore (GSV, 2014) occurs in the Devil's Gate limestone collapse breccia. The unit has variable thickness and has been thinned by faulting and dissolution along the upper contact. Locally at North Bullion, the Devil's Gate limestone is a thick-bedded, grey, dissolution collapse breccia. Dolomite alteration and brecciation in the Devil's Gate intensify towards the North Bullion Fault zone, suggesting hydrothermal fluids coming up these faults were responsible for the alteration and brecciation (Jackson, 2014), but the timing of these fluids is unknown.

The Mississippian Webb Formation, which is also mineralized at North Bullion Carlin system, consists mostly of thin- to medium-bedded, non-calcareous, carbonaceous, mudstone and siltstone with some discontinuous lenses of sandstone, and two horizons of silty limestone present at the top and base of the Mississippian Webb Formation that contain gold. The base of the Webb Formation (Fig. 3) is referred to as the lower limestone 2, a grey, thin-bedded calcarenite, and calcisiltite with lesser micrite (GSV, 2014). The upper limestone 1 at the top of the formation is a medium grey to black, thin-bedded, carbonaceous micrite (GSV, 2014). The Webb Formation is present in the eastern portion of the North Bullion Carlin system, but was faulted and removed from the western portion of North Bullion Carlin system by low angle faults (Fig. 8).

The Mississippian Chainman Formation is comprised of sandstone and silty mudstone with lesser conglomerate (Jackson, 2014) (Fig. 3). In the west part of the North Bullion Carlin system (Fig. 8), the Mississippian Chainman Formation has been thickened, by faulting, and lies above the Devonian Devil's Gate Formation and multi-lithic breccia, the Webb Formation has been removed by faulting (Fig. 3). In this western part of the section, (Fig. 8) the Chainman Formation 'basal' unit above the Devil's Gate reaches 122 meters in thickness and is composed of 60 % sandstone, 30 % mudstone, and 10 % conglomerate. In the east part of this section (Fig. 8) the 'basal' Chainman present to the west is absent and multi-lithic breccias and Mississippian Webb Formation are present and between the Devil's Gate and Chainman Formations (Figs. 3, 8).

Above the 'basal' unit of the Chainman in the west portion and above the Webb Formation of the east portion of the North Bullion Carlin system (Fig. 8), the Mississippian Chainman is 18-34 meters thick and comprised of 50 % sandstone and 50

% silty mudstone (Fig. 3) (Longo et al., 2002; GSV, 2014). Above the Chainman – Webb contact, the Chainman commonly is cross cut by Tertiary porphyry dacite sills (Fig. 8). Above this section, the Mississippian Chainman Formation transitions to the coarser clastic facies (300-350 ft.) of 45 % sandstone, 45 % silty mudstone, and 5-10 % conglomerate (Fig. 3) (Longo et al., 2002; GSV, 2014). The contacts between Devonian Devil's Gate, Mississippian Webb, and Mississippian Chainman Formations have strong penetrative shear features and small-scale folds are present in these units. The variation in the thickness of the Chainman Formation from east to west across the section (Fig. 8) is dominantly a result of low angle faulting that repeats the section (GSV, 2014).

Multi-lithic breccias are located in the eastern portion of the section between the Devil's Gate and Webb Formation and present in the western portion of the section along the contact between the Devil's Gate and the 'basal' Chainman unit (Fig. 8). Multi-lithic breccia, which is up to 122 meters thick, consists of medium to dark grey angular clasts of mudstone, siltstone, sandstone, micrite and limestone derived from the Devonian Devil's Gate, Mississippian Webb, and Mississippian Chainman Formations (GSV, 2014). Brecciation intensifies towards the North Bullion Fault zone, suggesting hydrothermal fluids came up these faults and were the source (Jackson, 2014).

Breccias at the North Bullion Carlin system include tectonic breccias related to mechanical movement along faults, and collapse breccias related to the chemical dissolution of Devil's Gate carbonate rocks during hydrothermal fluid/rock reaction and/or volume reduction of carbonates due to dolomitization (GSV, 2014). Multi-lithic breccia units in the eastern portion of the east-west cross section (Fig. 8) are interpreted as also having a tectonic component, and are related to movement along the North

Bullion and Massif faults (GSV, 2014). The Devil's Gate and the "tectonic" multi-lithic breccia contact, on the east side of the east-west cross section (Fig. 8), has a geometry consistent with collapse by dissolution on the north-south cross section (Fig. 9), and has also been interpreted as both a collapse and tectonic breccia. Breccias within the Devonian Devil's Gate Formation are interpreted as collapse breccias (Fig. 8) (GSV, 2014). Multi-lithic breccias along the contact between the Devil's Gate and the 'basal' Chainman unit on the west side of the east-west cross section (Fig. 8) are interpreted as both collapse and tectonic in origin (GSV, 2014).

The Tertiary Elko Formation (Te) unconformably overlies the Chainman Formation at the North Bullion Carlin system, which is different from geology of the Rain deposit. The Elko Formation is interpreted as a lacustrine facies, up to 91 meters thick, that consists of mudstone, sandstone, micrite, and conglomerate (Solomon, McKee, and Andersen, 1979; Longo et al., 2002; GSV, 2014). The mudstones are black, laminated to thick bedded, and carbonaceous. The sandstones are grey, thin to thick bedded, calcareous, and comprised of quartz and chert grains. The micrites are grey to black and thin to thick bedded. The conglomerates are grey to multi-colored, medium to thick bedded, containing lithic grains of multiple lithologies (GSV, 2014).

Igneous Rocks

Henry (2014) dated at least five intrusive episodes between 38.9 and 37.5 Ma on the Railroad property (Fig. 10). Analyses indicate that dacite porphyry dikes and sills that cross cut the Devonian Devil's Gate, the Mississippian Webb, and Chainman Formations, and the multi-lithic breccias in the NBFZ of the Railroad property range from 38.4 to 38.9 Ma (Figs. 8, 10) based on U/Pb dates obtained on zircon and $^{40}\text{Ar}/^{39}\text{Ar}$ dates

obtained on biotite, hornblende, and plagioclase (Henry, 2014). The contacts between the dikes and the sedimentary units are commonly sheared. Where unaltered porphyry dacite sills and dikes are light grey to white, with 15-25 vol. % 2-4 mm plagioclase feldspar phenocrysts, up to 5 vol. % each of biotite and hornblende, with variable amounts of quartz phenocrysts (Henry, 2014). Where these dacite sills and dikes are highly altered; the matrix has been altered to quartz-sericite-pyrite and feldspar phenocrysts have been argillized (Henry, 2014; Harp, 2014). The dikes and sills commonly occur along fault zones and at contacts between lithologic units. They are spatially associated with the North Bullion Fault zone (Figs. 3, 8 and 9), and occur as sills above the mineralized zone, and formed a cap to the system as shown by hydrothermal alteration immediately below them (Jackson, 2014). The porphyritic dacite dikes formed prior to Carlin mineralization as they contain up to 1.5 ppm Au, but they are not major host rocks for gold mineralization (GSV, 2014).

The Tertiary Indian Wells Formation ash-flow tuffs (Tiw) (0 - < 305 meters thick) unconformably overlie the Tertiary Elko Formation. The Indian Wells Formation is a crystal tuff with 15-40 vol. % phenocrysts and is divided into two units. The lower unit is grey to light green with phenocrysts of feldspar > biotite and hornblende > quartz. The upper unit is pink and has a similar phenocryst assemblage. The $^{40}\text{Ar}/^{39}\text{Ar}$ dates obtained on sanidine from Indian Wells Formation tuffs, rhyolite from a lava dome, and quartz porphyry indicate ages of ~37.8 – 37.9 Ma (Henry, 2014). The granodiorite stock, Pine Mountain rhyolite dikes, and late rhyolites (Fig. 10) are located within the Railroad property, but were not identified at the North Bullion Carlin system, and are not related to this study.

Structure

Previous research in the Pinon Range near the Rain deposit (Tosdal et al., 2001) describes regional structures as including “northwest-trending folds and reverse faults are localized along inverted Early Mississippian normal faults that disrupted the north-striking Antler fold and thrust belt prior to the deposition of late Mississippian post-orogenic strata... [that are] in part the result of inversion of the north-northwest- and west-northwest-striking basement and Paleozoic normal faults” (Cline et al., 2005, p. 458). Important structures at the North Bullion Carlin system include, the North Bullion Fault Zone and the Massif fault (Fig. 8) (Jackson, 2014). The North Bullion Fault Zone is a normal fault, north striking, with a 70° dip to the east, and is approximately 10 km long (Jackson, 2014). Total displacement on the North Bullion Fault Zone is unknown, though the current estimation of the offset is a minimum of 500 meters (Jackson, 2014). The Massif Fault strikes N12W and dips 75° to the east and is a splay fault on the main North Bullion Fault Zone (Jackson, 2014). The Massif Fault does not propagate to surface, but terminates against low angle fault structures at the base of the Webb limestone 1 unit. Small low angle fault structures along contacts between the Devil’s Gate, Webb, and Chainman Formations are evident in penetrative bedding shear zones, and are also present in Webb Formation where bedding planes slipped along mudstone and carbon-rich layers (Jackson, 2014). Small-scale structures, such as recumbent folds, are identified within drill core within the Webb Formation.

CHAPTER 3

METHODS

Sample collection

Samples were collected from drill core from the North Bullion Carlin system within the Railroad Project (Fig. 11), along an east-west cross section (Fig. 8), and an intersecting north-south cross section (Fig. 9). Selected drill holes intersect low- to high-grade mineralization and geologic features potentially responsible for the presence of gold including faults, lithologic contacts, breccia zones, cross-cutting igneous rocks, and intersections of these features.

The two selected cross sections maximize drill core for this study by intersecting thirteen drill holes (Fig. 11), with the east-west cross section intersecting 7 drill holes, and the north-south cross section intersects 8 drill holes. These sections were chosen because the east-west cross section (Fig. 8) cross cuts gold mineralization and the North Bullion Fault and the north-south cross section parallels the strike of gold mineralization (Fig. 9).

Samples were collected along short transects from high- to low-grade mineralization from each of the different lithologies that host gold and also from different locations across the North Bullion Carlin system to examine spatial distribution as well as lithologic control of mineralization. Short transects from within a single rock type are preferred as they reduce lithological variability and facilitate identifying mineral and textural changes related to ore-forming processes. Ideal transects were difficult to collect because of the lack of continuity of lithology and gold grade across the large distances between drill holes, and because of lateral changes in lithology and drill spacing. Sample

transects were collected within a single drill hole or from multiple drill holes from the same host rock contacts. Four hundred and forty-six samples were collected from drill core, and of those, 86 samples were selected for polished section preparation and various analyses (Appendix C).

Optical petrography

A total of 86 polished 30 µm thick sections were prepared from core samples that were stabilized with blue epoxy. Of the 86 core samples chosen, 46 were from the 8 drill holes from the north - south transect, and 50 were from the 7 drill holes from the east - west transect. Locations of samples selected for polished section are illustrated on Figures 8 and 9. Transmitted and reflected light petrography were used to identify pre-, syn-, and late-stage minerals, determine cross-cutting and textural relationships, and establish a mineral paragenesis (Appendix D). Microscopic examination of polished sections assisted in identifying samples for additional analyses.

Scanning electron microscopy

Nineteen samples were examined using a JEOL-5600 scanning electron microscope (SEM) and semi-quantitative electron dispersive spectroscopy (EDS) analyses were collected using Link ISIS 3.2 software-INCA at the Electron Microanalysis and Imaging Laboratory at UNLV. Polished sections were carbon coated before analysis. The carbon coating contributed 13 wt. % Carbon, determined by analyzing quartz a non-carbon bearing mineral. Samples of altered and mineralized to unaltered and unmineralized rocks were analyzed to identify clay, carbonate, and unknown minerals, various generations of pyrite, and examine textural and spatial relationships of pyrite generations to alteration minerals. Analytical results are compiled in Appendix E.

Electron probe microanalysis

A JEOL-8900 Electron Probe Microanalyzer (EPMA) at UNLV Electron Microanalysis and Imaging Laboratory was used to quantify trace element concentrations in pyrites, stephanite, sphalerite, rutile, and clay minerals. Selection of samples was based on gold grade and the presence of various pyrite types. Fifteen polished sections containing low to high gold grade were analyzed to identify gold-bearing pyrite, quantify gold content, and quantify the trace-element chemistry of texturally diverse pyrite types. Table 2 provides the probe conditions used for analysis, and Table 3 provides the suite of elements quantified and standards used. Figure 12 provides the peak overlap relationships between Fe and Mo, and Au and Zn (Ren, 2014), and analyzed data were collected for these overlaps. All samples selected for EPMA were carbon coated prior to analysis.

Petrography and SEM analyses did not identify Carlin-type gold-bearing rims, so did not reveal whether or not the pyrites were gold-bearing. Instead, EPMA WDS elemental maps of Au, As, Hg, Tl, Sb, and/or Si were created to identify pyrites that contain gold, though the maps did not quantify the concentrations of those elements. Selected sample areas were then quantitatively analyzed using an EPMA line transect method, with analytical spot distances of ~5 to 20 μm , to quantify Au and other trace elements in pyrite. Electron probe microanalysis lines started in host rock and traversed across the host rock/pyrite crystal boundary, across a gold-bearing rim if present, and across pre-ore-stage pyrite, ending in host rock (Fig. 13). Many analyses analyzed a combination of pyrite and adjacent host minerals, and the percent of Fe in the analysis gives an indication as to the relative percent of pyrite and host rocks analyzed. All raw data collected are presented in Appendix F.10. This method produced datasets with

analytical totals commonly below 98%. Such totals are a result of the following: 1) EPMA is optimized on flat polished surfaces; slopes within the samples, owing to poor polish or crystal boundaries, especially between minerals with significant hardness differences, scatter the signal and reduce analytical totals, 2) elements present in the sample are not included in analysis, and 3) analyzing an impure phase, such as mixed minerals or mineral with inclusions, can result in loss of counts and low totals (Ren, 2014). Figure 13 shows that in these analyses, Fe and S exhibit a generally constant ratio for pyrite. Low Fe and S totals occur in analyses in which Si and Al are abundant, reflecting analyses on the boundary of pyrite and a host rock mineral or, because of the presence of an uneven surface, possibly at the contact between two minerals, which yields low totals.

Laser ablation, inductively-coupled plasma, mass spectrometry

Trace element concentrations of pyrites were quantified by using laser ablation inductively-coupled plasma mass spectrometry (LA-ICP-MS) at the United States Geological Survey laboratory in Denver, Colorado. LA-ICP-MS uses a Photon Machines Analyte G2 LA system (193 nm, 4 ns Excimer laser) coupled to a PerkinElmer DRC-e Inductively Coupled Plasma Mass Spectrometer. Typical LA-ICP-MS operating conditions are listed in Table 4. To observe relative changes in trace-element concentrations along a single line or within an area, line scans and maps were generated, respectively, across pyrite rims and into pyrite cores. Pyrites were analyzed by creating 13 μm line scans and maps. Methods for mapping pyrites are similar to those reported in Koenig et al. (2009). The standard reference material (MASS-1) was analyzed 5 times at

the beginning and end of each analytical session to correct for spectra drift that can occur during the analytical session. All raw data are presented in Appendix G.

X-Ray Diffraction

A PANalytical X'PERT Pro X-ray Diffraction Spectrometer at the UNLV XRD/XRF laboratory was used to identify clay and carbonate minerals and to determine semi-quantitative abundances of quartz and carbonate minerals. Forty-five samples from altered and mineralized to unaltered and unmineralized rocks of different lithologies were analyzed to identify alteration minerals and their approximate abundances relative to gold grade. Each sample was crushed to a fine powder using a tungsten carbide shatter box and sieved at 250-mesh to insure sufficient homogeneity. An internal standard of 5 wt. % 250-mesh pure silica was added to each sample to obtain semi-quantitative results. XRD settings are reported in Table 5.

The first diagnostic diffraction peaks of most minerals present in CTGD occur near or above $6^\circ 2\theta$ (14.5 \AA); therefore, prepared whole rock samples were analyzed from 5° - $75^\circ 2\theta$ (Cail and Cline, 2001). X'Pert Highscore Plus and Crystal Sleuth software were used to interpret the raw XRD patterns which utilize ICD Database and American Mineralogist Crystal Structure Database to generate peak pattern mineral matches used to identify minerals for each X-ray diffraction pattern. Additional mineral patterns were manually suggested in Crystal Sleuth until all background, peak positions (2θ), and intensities achieved a best fit, and the known 5 wt. % silica internal standard was accurately quantified. PowderCell 24 was used to calculate semi-quantitative relative mineral abundances of quartz and carbonate minerals by peak areas and standard intensity ratios, and was compared to the internal silicon standard. Intensity ratios used to

calculate mineral abundances are listed in Appendix H. See Cail and Cline (2001) for sample preparation and analytical methods.

TerraSpec Analysis

Nineteen samples were analyzed using TerraSpec 4 Hi-Res Mineral Spectrometer in order to identify vein minerals, clay minerals present in altered, mineralized rock and unaltered, unmineralized rock, and to determine changes in clay mineralogy and abundance with increasing gold grade. SpectaExplorer was used to identify clay minerals.

This analytical technique identifies minerals based on the reflectivity of the mineral analyzed; minerals absorb short wave infrared energy at different wavelengths. Carlin-type gold deposit ore is commonly dark grey to black owing to the presence of carbon, causing problems with this technique, as the analytical peaks can be poorly developed due to the low reflectivity of dark rock or to weakly crystalline clays. This technique did obtain matches and was useful for identifying clays, but it is possible that not all clays present were identified (Bowen, 2013). Results are listed in Appendix I.

Multi-element geochemical analysis

All drill core was analyzed at drill core intervals of approximately 5 feet for major trace elements. The geochemical analyses were completed by ALS Geochemistry Laboratories. Analyses, methods, elements analyzed, and detection limits are summarized in Table 6. Analysis (ME-ICP41) used an aqua regia digestion, and Inductively Coupled Plasma atomic emission spectrometry (ICP AES) to quantify Ag, Al, As, B, Ba, Be, Bi, Ca, Cd, Co, Cr, Cu, Fe, Ga, Hg, K, La, Mg, Mn, Mo, Na Ni, P, Pb, S, Sb, Sc, Sr, Th, Ti, Tl, U, V, W, Zn. All samples containing > 100 ppm Ag were reanalyzed (Ag-OG46)

using an aqua regia digestion, ICP AES, and/or atomic absorption spectroscopy (AAS) finish to quantify higher Ag concentrations. Analysis (Au-AA23) used the fire assay method and AAS finish to quantify Au in the sample. All samples containing > 10 ppm Au, were reanalyzed (Au-GRA21) using the fire assay method and gravimetric finish to quantify higher Au concentrations.

Geostatistical Analysis

Classification support vector machine, non-metric multi-dimensional scaling model, Spearman rank correlation matrix, Mann-Whitney U-Test, and principal components analyses were used to analyze and transform geochemical data.

Classification support vector machine and non-metric multi-dimensional scaling model data sets were generated from a randomized 1/3 of the bulk rock geochemistry data from all drill holes sampled. Spearman rank correlation matrix and Mann-Whitney U-Test were conducted on all whole rock geochemistry data from samples from all drill holes intersected on the two cross sections. Non-metric multi-dimensional scaling model, Spearman rank correlation matrix, Mann-Whitney U-Test, and principal components analysis were applied to all EPMA pyrite data.

Classification support vector machine is a classification tool that compares chemical elements in two sets of data, one above and one below a specified gold grade, compares the concentrations of each analyzed element to the concentration of gold, and determines the degree, given as a percentage, to which the evaluated element is correlated with gold. The percentage assigned to an element that shows no correlation with gold is referred to as the “accuracy floor.” The two classes evaluated in this study include gold is present and above a specified value (0.1, 1.0 ppm), and gold is present and below a

specified value (0.1, 1.0 ppm). Though the accuracy percentage results indicate the degree to which each element predicts gold, it does not indicate whether the element is positively or negatively predicting gold.

The non-metric multi-dimensional scaling model uses a two-dimension ordination method to reduce a data set with multiple variables to be viewed with the least number of ordination axes possible; each variable and data point are plotted based on their R and R^2 values relative to each ordination axis (McCune et al., 2002).

Whole rock trace element geochemistry data collected on drill core and EPMA data collected on pyrites were evaluated using a Spearman rank correlation matrix. Each value within the matrix describes the strength of the relationship between two elements and indicates whether that relationship is positive or negative. Matrix values greater than 0.4 are considered to have a statistically significant positive correlation, and matrix values less than -0.4 are considered to have a statistically significant negative correlation (Pallent, 2007).

The Mann-Whitney U-Test determines median concentrations of analyzed elements in two groups of data that are separated by gold classification (grade) and determines if the median values of the two groups are significantly different. This analysis identifies elements that are significantly, positively or negatively, correlated with gold at various gold concentrations. One group includes data for an element in samples in which the gold concentration was less than the gold classification value. The second group includes data for that same element for samples in which the gold concentration was equal to or greater than the gold classification value. Both groups represent data for a single element that has been split into two groups based on the gold classification value.

Median concentrations of each element in each group are determined and compared in a table for each gold classification.

EMPA data collected on all iron sulfide minerals were evaluated using principal components analysis. This is a statistical method used to “condense a large set of variables or scale items to a smaller more manageable number of dimensions or factors...by summarizing the underlying patterns of correlation and looking for ‘clumps’ or groups of closely related items” (Pallent, 2007). The parameters for the analysis are summarized in Table 7 (Pallent, 2007).

Off Axis - Integrated Output Cavity Spectroscopy

Carbon and oxygen isotopic ratios were measured in carbonate minerals in 98 samples using Off Axis-Integrated Output Cavity Spectroscopy at the University of British Columbia in Vancouver, Canada, to identify potential isotopic halos related to gold mineralization. Samples were selected from sample transects of low- to high-grade gold in carbonate rocks. Micro-samples were prepared using a small drill to collect ~35-100 mg from vein or wall rock. The hardness of some samples made sample collection difficult using the standard drill. Where samples appeared homogeneous, a tungsten carbide shatter box was used to powder the sample. See Barker et al. (2012) for all Off Axis-Integrated Output Cavity Spectroscopy method techniques and standards. Sample powders were acidified using 85% phosphoric acid at 70° C for one hour to release CO₂ gas from carbonate minerals, which is introduced into the Off Axis-Integrated Output Cavity Spectroscopy instrument. The standard (85 % phosphoric acid) was analyzed before and after every 7 sample runs during the analytical session to correct the mass spectra for drift that can occur during the analytical session. The concentration and

isotopic composition of CO₂ is measured using infrared laser spectroscopy. Generation of H₂S gas due to acidification of unstable sulfide minerals will contaminate and alter results and samples that generated H₂S were not analyzed. When H₂S was released during sample run, the monitor showed a peak, notifying the operator to discard that analysis. Results are reported in Appendix J.

CHAPTER 4

PRE-ORE STAGE

The following definitions are used to describe the various stages related to ore. Samples defined as non-ore contain < 5 ppb gold as determined by drill core assay. Samples defined as ore samples contain > 5 ppb gold, and are assumed to have been mineralized by Carlin-type gold ore fluids. The ore stage is defined as the time period during which Carlin-type gold ore fluids were mineralizing and altering the host rocks at the North Bullion Carlin system.

The pre-ore stage is defined as the time before Carlin-type gold ore fluids were introduced to the North Bullion Carlin system. Samples of unmineralized and unaltered host rock could not be collected at North Bullion as drilling did not penetrate rock outside of the alteration zone. Samples that were least altered and mineralized (gold < 0.010 ppm) were examined to identify and characterize least-altered pre-ore stage minerals and textures. The post-ore stage is defined as the time period after Carlin-type mineralization formed.

Host Rocks

The Devonian Devil's Gate Formation, is a dolomitized limestone; the Mississippian Webb Formation composed of micrites, silty mudstones, and mudstones; and the Mississippian Chainman Formation composed of sandstones, conglomerates, and silty mudstones, are the primary host rocks whose pre-ore mineralogy are described in this section. Pre-ore minerals within the Devonian Devil's Gate Formation, the Mississippian Webb Formation, and the Mississippian Chainman Formation predominantly include calcite, dolomite, detrital quartz grains, illite, montmorillonite, and

pyrite. One sample of a Tertiary dacite porphyry dike that cross cut host rocks, but which is pre-ore stage, was also examined. Pre-ore minerals within the dacite dike include quartz, illite, kaolinite, apatite, pyrite, sphalerite, and rutile.

Devonian Devil's Gate Formation

All Devonian Devil's Gate Formation samples examined in this study are brecciated dolomitized limestone. The rock is comprised primarily of carbonate minerals (~90—100 wt. %), with minor silt- to sand-sized (3 - 250 μm) jasperoid, illite, and carbonaceous material (~0—10 wt. %) (Fig. 14 A-E) that form a crackle breccia matrix. Other trace pre-ore minerals include pyrite, sphalerite, and rutile; sphalerite is not associated with the deposition of the host rock and is most likely hydrothermal. Calcite, locally with barite, fills late-ore-stage veins that cross cut the breccia texture (Fig. 14 A, D).

The dominant carbonate mineral is dolomite and trace calcite and/or ankerite are present (Fig. 14 A, B, and D); crystals vary in size from sand to gravel (250 μm - 8 mm). SEM analyses of dolomite indicate that the Devil's Gate Ca:Mg ratio (Fig. 14 G; Appendix E), is variable with Mg ranging from 3-20 wt. %, giving evidence of dolomitization of Devil's Gate limestone.

Jasperoid, illite, and carbon occur within fractures and between dolomite crystals and comprise a crackle breccia matrix between Devonian Devil's Gate clasts (Fig. 14 A-E). As shown in Figure 14 C and E, illite appears dark brown to black when analyzed in polished section, owing to the presence of carbon (Fig. 14 F).

Interpretation

Devonian Devil's Gate Formation at the North Bullion Carlin system has been altered to dolomite and brecciated (Fig. 15). Within the Devonian Devil's Gate Formation most primary calcite has been altered to dolomite, such that calcite present within samples is remnant calcite or late-ore-stage calcite veins. The timing of formation of the crackle breccia is unknown, but could be 1) hydrothermal and related to a pre-Carlin hydrothermal event, or 2) hydrothermal and related to the Carlin mineralizing event. As unaltered Devonian Devil's Gate is a clean pure limestone (Carlisle et al., 1957), the illite and jasperoid that form the breccia matrix are not primary or diagenetic minerals. They are secondary alteration minerals related to the Carlin hydrothermal fluids or another event. Brecciation and dolomitization intensify towards the North Bullion Fault zone (Fig. 8), suggesting that this structure contributed to alteration and brecciation (Jackson, 2014).

Mississippian Webb Formation

Mississippian Webb Formation at North Bullion, as described by Gold Standard Venture geologists, is comprised of limestone 2, a calcarenite/calcsiltite, which is at the base of the Webb Formation. Calcareous mudstones and siltstones that comprise the bulk of the Webb Formation overlie limestone 2. Above the calcareous mudstones and siltstones is limestone 1, a micrite, which forms the top of the Webb Formation (Fig. 3).

Altered samples described as calcarenite, calcsiltite, or micrite in limestone 1 and 2 (Jackson, 2014) and examined in this study have no apparent differences at the microscopic scale. Limestone 1 and 2 are comprised of silt- to sand-sized detrital calcite and/or dolomite cemented within fine-grained calcite and/or dolomite, illite,

montmorillonite, and carbon matrix, based on petrography and SEM analyses (Fig. 16 A-C). Rock described as altered calcareous mudstones and siltstones that make up the bulk of the Webb Formation are comprised of silt- to sand-sized detrital quartz cemented within fine-grained quartz, illite, montmorillonite, and carbon matrix (Fig. 16 D, E). Other trace pre-ore minerals include pyrite, sphalerite, and rutile.

Mississippian Chainman Formation

The Mississippian Chainman Formation sandstone is comprised of well-rounded sand-to-gravel-sized detrital quartz grains (95%), apatite and green chert (0-5 %), with minor illite and montmorillonite (0-5%) along grain boundaries (Fig. 17). Other trace pre-ore minerals include pyrite, sphalerite, apatite, and rutile. The Mississippian Chainman Formation also contains minor conglomerates and silty mudstones, not examined in this study.

Tertiary Porphyritic Dacite Dikes

Tertiary dacite porphyry dikes contain up to 1.5 ppm gold, demonstrating that dike intrusion at 38.4 to 38.9 Ma (Henry, 2014) is part of the pre-ore stage. The altered Tertiary porphyry dacite dike, RR12-05 1408.5, examined in this study contains ore-stage pyrite plus sphalerite, rutile, quartz, and apatite phenocrysts (0-5 %) within a quartz, illite, and kaolinite matrix (~ 95 %) (Fig. 18). All primary plagioclase phenocrysts (Henry, 2014) were altered to illite, kaolinite, and pyrite (Fig. 18 D, E). Primary biotite and hornblende phenocrysts (Henry, 2014) were altered to illite and rutile (Fig. 19 B, C). Late-ore-stage calcite and realgar and post-ore-stage barite occur in vugs.

Interpretation

Henry (2014) described all primary plagioclase phenocrysts as altered to sericite and calcite, but in dacite examined in this study, plagioclase has been altered to illite and kaolinite. Primary biotite and hornblende phenocrysts were not identified in this study, but, if originally present, are interpreted to have altered to illite and rutile. Henry (2014) concluded that the alteration in the dikes is related to Carlin gold mineralization and therefore, the gold event is younger than 38.4 Ma.

Apatite identified in this study is most likely relict primary apatite that formed within the dacite dike. Other minerals identified in the dacite dike in this study including quartz, illite, kaolinite, pyrite, rutile, and sphalerite are alteration minerals related to Carlin gold mineralization as interpreted by Henry (2014), or during an earlier hydrothermal event (Fig. 15). Realgar, calcite, and barite, which occur in vugs, are likely related to late- or post-ore-stage mineralization.

Secondary Pre-ore-stage Minerals

Rutile and sphalerite are minor secondary pre-ore-stage minerals. These minerals are not associated with the deposition of the host rocks, and the timing of their formation with respect to the host rocks is unclear.

Rutile

Rutile crystals are most common in the Tertiary porphyritic dacite dike, but also occur in sedimentary rocks. In altered dacite, rutile occurs as single crystals within illite, kaolinite, and quartz and as inclusions intergrown along the edges of and enclosed within OS 1 pyrites (Fig. 19 B-E). Rutile crystals also occur within the matrix of the Devonian Devil's Gate collapse breccia and multi-lithic breccias, and within host rock matrix in the

Mississippian Webb, and Chainman Formations (Fig. 20 D). Rutile was commonly detected in EPMA analysis (Appendix F.1, F.10) within host rock minerals along the POS pyrite - host rock mineral grain boundaries.

Sphalerite

Single crystals or clusters of anhedral sphalerite crystals occur in the Tertiary porphyritic dacite dike and also multi-lithic breccia. Sphalerite in the dike occurs within the quartz, illite, and kaolinite matrix (Fig. 19 G, I, and J) and as inclusions intergrown with OS 1 pyrites (Fig. 19 H, K). Sphalerite and euhedral quartz shown in Figure 19 H and K are overgrown by OS 1 pyrites, which have an outermost rim in which sphalerite and euhedral quartz are absent.

Sphalerite also occurs within the matrix of multi-lithic breccia with POS pyrite (Fig. 20). Sphalerite crystals within multi-lithic breccia are anhedral, and do not appear to be conforming to other minerals (Fig. 20). Zinc in sphalerite was commonly detected in EPMA analysis (Appendix F.2 and F.10) within the host rock minerals along the POS pyrite - host rock mineral boundary.

Interpretation

Sphalerite and rutile are present in host rocks and dacite dikes and are not related to Carlin-type hydrothermal fluids based on spatial relationships with OS 1 pyrite; this interpretation is supported by EPMA data showing that Ti in rutile and Zn in sphalerite are negatively correlated with Au. The alteration of primary biotite and hornblende in the dacite dikes would release Ti that could have contributed to rutile within the dike, and also produced available Fe for OS 1 pyrite to form. Subsequently, rutile and pyrite were engulfed by illite, kaolinite and quartz during the ore stage where permitted by available

porosity and permeability. Rutile crystals appear to have formed prior to OS 1 pyrites in the dacite dike as they were overgrown by OS 1 pyrites. Rutile crystals do not show textural relationships with pre-ore-stage minerals in Devil's Gate, Webb, or Chainman Formations that indicate relative timing. The rutile crystals appear to be part of the sedimentary rock package, and are likely relict rutile from prior rocks that contributed to the formation of the Devil's Gate, Webb, or Chainman Formations.

Likewise, the alteration of primary biotite and hornblende in the dacite dikes could have released Zn that contributed to the formation of sphalerite within the dike (Blaxland, 1971). Sphalerite crystals formed prior to and were overgrown by OS 1 pyrites within the dike. Sphalerite within multi-lithic breccia is anhedral, and does not conform to other surrounding minerals, and does not show textural relationships that indicate relative timing of formation in Devil's Gate, Webb, or Chainman Formations. There have been several documented events that produced Zn mineralization in northern Nevada related to sedimentary exhalative deposits (Fig. 4) (Emsbo, 1999). Sphalerite in all formations formed prior to Carlin-style mineralization, potentially during the Devonian (Emsbo, 1999). Sphalerite crystals could have been eroded from some prior source and deposited during the formation of the Devil's Gate, Webb, or Chainman Formations.

Discussion

Drill holes have not penetrated fresh unaltered and unmineralized samples of the formations that host gold mineralization at North Bullion. This has made it difficult to characterize the mineralogy of these formations prior to the gold mineralizing event. The Devil's Gate Formation encountered within the least mineralized hole, RR 11-04, is part of a collapse breccia. Without knowledge of the mineralogy and textures of the Devil's

Gate Formation prior to the Carlin-type mineralization, it is unclear whether illite and jasperoid present within the collapse breccia matrix are hydrothermal and related to some pre-Carlin hydrothermal event, or related to Carlin-type hydrothermal fluids.

Unmineralized Mississippian Webb Formation has not been encountered by drilling. Mississippian Webb samples with low gold grades were collected from shallower intervals in drill core that are higher in the stratigraphic section than the high-grade gold samples. Thus distinguishing primary minerals from alteration minerals remains difficult. Illite and quartz are the main alteration minerals that characterize CTGDs, but they may also be primary minerals in the sedimentary formations. Thus, it is unclear whether these minerals were present prior to the Carlin mineralizing event or whether they formed as part of the Carlin gold mineralization event.

The mineralogy of the Tertiary porphyritic dacite dikes was described by Henry (2014), who concluded that “Carlin-type Au mineralization at North Bullion is no older than ~38.4 Ma.” This is based on his interpretation that hydrothermal fluids related to Carlin mineralization altered and mineralized the dacite dikes after they formed at ~38.4 Ma. Quartz, illite, kaolinite, and pyrite are secondary alteration minerals, and it is reasonable that these minerals are related to the Carlin hydrothermal fluids (Henry, 2014); however, this has not been confirmed.

Pre-ore-stage Pyrite

Pre-ore-stage (POS) pyrites were identified in least altered Devonian Devil’s Gate, Mississippian Webb, and Mississippian Chainman Formations and characterized using petrography. Pre-ore-stage pyrites comprise the vast majority of pyrites present and analyzed in the host rocks and are commonly associated with quartz, illite,

montmorillonite, calcite, and/or dolomite. The pyrites exhibit a range of morphologies including euhedral to anhedral pyrites, framboidal pyrite, (Fig. 21 A-C), or micron-sized crystals. Framboids are both isolated and clustered (Fig. 21 B-E) as “clouds” of sub micrometer framboids and microcrystals. Fine microcrystals are located in dissolution zones containing clay and carbon (Fig. 21 F). All of these pyrites are variably concentrated along and within sedimentary beds (Fig. 21 G-H). The POS pyrites range in size from 1 μ m to 1mm. Euhedral and anhedral pyrites are found in all formations, whereas framboids and pyrite microcrystals are found in Mississippian Webb and Chainman Formations, and in multi-lithic breccias. Pre-ore stage pyrite descriptions, associated minerals, and chemistry are summarized in Table 9.

Pre-ore-stage Pyrite Geochemistry

Pre-ore stage pyrites identified by petrography were confirmed by EPMA, which show all pyrite morphologies in all formations have similar geochemistry. Analyses that detected gold from OS 2 rims are not included in the POS pyrite data set and not shown in Figure 22. Analyses with elevated concentrations of CTGD pathfinder elements and which possibly analyzed ore-stage rims in which gold was not detected are included in Figure 22 that illustrates POS data; as there was no unbiased method in which analyses of possible ore-stage rims, in which Au was either not detected or below detection, could be separated from POS pyrite data. The relative amounts of Fe and S versus Al, Si, and Ca in host rocks indicate the approximate ratio of pyrite to host rock analyzed, and by examining analyses that contain high Fe and S, trace elements present in pyrite can be inferred.

The X-Y graphs (Fig. 22) of Fe versus all elements analyzed using EPMA show the variability of trace elements within POS pyrites (Table 9) as well as components in host rocks analyzed at the beginning and end of analytical transects across pyrite. The plot of Fe versus S (Fig. 22) shows a positive linear pattern, approximately reflecting the 46:54 Fe:S ratio that characterizes pure pyrite. There are two sub-parallel trends, one at intermediate Fe (~15-45 wt. % Fe) and low S (15-30 wt. % S), and one at high Fe (45-53 wt. % Fe) and high S (35-45 wt. % S). The Fe-Si, Fe-Al, and Fe-Ca plots indicate that most Si, some Al, and lesser Ca decrease with increasing Fe. The Fe-Co, Fe-Ni, and Fe-Pb plots exhibit two trends: most data exhibit a low positive correlation with Fe; however, some data points indicate elevated Co, Ni, and Pb between ~35 - 46 wt. % Fe. These points analyzed primarily pyrite, and, therefore, these analyses inform which elements are present in pyrite. In such analyses of pyrite, where Co, Ni, and Pb are elevated, Co varies from 0.1 to 0.4 wt. %, Ni varies from 0.15 to 1.25 wt. %, and Pb varies from 0.25 to 1.0 wt. %. Elements typically associated with Au in Carlin-type deposits including As, Cu, Hg, Sb, and Tl exhibit more than one trend. Most As, Cu, Hg, Sb, and Tl data do not correlate with Fe and values for most analyses of these elements are low; however, some analyses identified elevated As (to 12.5 wt. %), Hg (to 0.3 wt. %), and Tl (to 0.3 wt. %) between ~18 – 45.5 wt. % Fe and elevated Cu (to 1 wt. %) and Sb (to 2.5 wt. %) between ~30 – 46.22 wt. % Fe. Silver, Se, Sn, Te, and Zn do not correlate with Fe and values for these elements are typically low; however some analyses identified elevated Ag (to 4000 ppm), Se (0.075 wt. %), Te (to 0.075 wt. %), and Zn (to 0.3 wt. %) between ~30 – 46.6 wt. % Fe, and elevated Sn (to 0.075 wt. %) between 43.9 – 46.2 wt. % Fe. Bismuth and Ti have a range of low values for all Fe concentration,

though the majority of analyses are at or close to zero. The majority of W data points are below detection, though a few points above detection reach ~0.03 wt. % W between 43.9 - 46.6 wt. % Fe. Table 9 (points 1-5, 88-93, and 1154-1161) provides example of analyses of three POS pyrites: points 1-5 show POS pyrite without elevated Co, Ni, and Pb, points 88-93 show POS pyrite with elevated Co and Ni, and points 154-1161 show POS pyrite with elevated Pb.

Interpretation

Analytical results indicate the relative amounts of pre-ore stage pyrite and other minerals incorporated in individual analyses; those analyses that contain ~35 to 52 wt. % Fe inform about the trace element chemistry of pre-ore stage pyrites. Analyses with abundant Si, Al, and Ca and low Fe and S represent analyses at the beginning and end of the analytical transects that primarily analyzed host rock minerals including quartz, illite, montmorillonite, dolomite and calcite, and inform about host rock rather than pyrite. Analyses with abundant Fe and S and low to no Si, Al, and Ca, represent analytical points that primarily or only analyzed POS pyrite. The inverse relationship of the Fe-S plot with the Fe-Si, Fe-Al, and Fe-Ca plots reflects a coincident increase in host rock mineral analysis points with a corresponding decrease in pyrite and vice versa. The positive linear correlation between Fe and S from low to high concentrations of Fe indicates a near constant ratio of these elements, consistent with analyses of pyrite. Low Fe and S analyses result from analyses of host rock minerals, a mix of host rock minerals and pyrite, or analyses where the polished section has a poor polish or uneven surface such as at mineral boundaries. Focusing on analyses with ~36 to 52 wt. % Fe, results indicate that POS pyrite trace element chemistry is variable, but Fe exhibits a weak positive

correlation with Pb, Co and Ni. Locations with elevated Pb, Co, and Ni cannot be distinguished morphologically by petrography or SEM back scatter electron imaging as pyrite zones representing a different POS pyrite generation. Elevated Pb, Co, and Ni are most likely related to the depositional environment of POS pyrites, as elements can be heterogeneously elevated and selectively incorporated in the POS pyrite structure as it was forming such that those elements were somewhat more concentrated in parts of the pyrite and in trace amounts in other parts of a pyrite (Large et al., 2014). Silver, Se, Sn, Te, W, and Zn are also variably elevated within POS pyrite, but generally show no correlation to POS pyrites in a majority of analyses.

Principal Components Analysis of POS pyrite

Principal components analysis of all EPMA pyrite data and POS pyrite and the contributing elements to each component for each analysis are listed in Tables 10, 11, and 12. For all analyzed data, the requirements related to the Kaiser Meyer-Olkin Measure of Sampling Adequacy and the Barlett's Test of Sphericity (Pallent, 2007) were met. The Kaisers Criterion or eigenvalue rule method was used to determine the number of components to retain in the table, but can retain too many components. The Catell's Scree Test is the second method to determine the number of components to retain, and was used to determine the number of components to discuss. The Catell's Scree Test involves plotting each of the initial eigenvalues ('Total ^d') of the components and recommends retaining components above the point where the slope of the curve changes, because these components "contribute the most to the explanation of the variance in the data set" (Pallent, 2007). All Catell's Scree Tests for all Principal components analyses are listed in Appendix F.

Principal components analysis of all EPMA pyrite data identified 8 components that account for 65.742 % cumulative variance of the data (Table 10). Using the Catell's Scree Test (Appendix F.3) components 1 and 2 are above the change in slope, and contribute 33.54 % cumulative variance of the data. Component 1 includes Fe, S, Pb, Co, Ni (Si, Al, and Ti) with a total eigenvalue of 4.604, and a variance of 20.92 %. Component 2 includes Hg, Tl, As, Sb and Cu with a total eigenvalue of 2.766, and a variance of 12.61 %. Components 3-8 are below the change in slope and are not discussed, but are included in Table 10 and Appendix F.3.

Principal components analysis of POS pyrites has 7 components that account for 63.414 % cumulative variance of the data. Using the Catell's Scree Test (Appendix F.4) components 1 and 2 are above the change in slope, and contribute 34.86 % cumulative variance of the data. Component 1 includes Fe, S, Pb, Co, Ni (Si, Al, and Ti), with a total eigenvalue of 4.571, and a variance of 21.76 %. Component 2 includes Hg, Tl, As, and Sb with a total eigenvalue of 2.751, and a variance of 13.09 %. Components 3-7 are below the change in slope and are not discussed, but are included in Table 11 and Appendix F.4. Results (Table 12) show that principal components analysis for all EPMA pyrite data and POS pyrites are similar for components 1- 4, but show minor differences for other components.

Interpretation

Principal components analysis for all pyrites and for POS pyrites are similar with small differences for each of the components. This is because the great majority of analyses conducted on POS pyrites dominates the data set. Principal components analysis of POS pyrite component 1 identified the inverse relationship between POS pyrite

elements Fe, S, Pb, Co, and Ni with Si, Al, and Ti, related to the EPMA transect method of analysis. Component 2 of the POS pyrite analysis clusters Hg, Tl, As, and Sb, which are Carlin-type pathfinder elements probably occurring in OS 2 rims that were analyzed along on the host rock/POS pyrite grain boundaries, but which did not contain detectable gold.

Spearman Rank Correlation Matrix of Pyrite EPMA data

Electron probe microanalyses were evaluated using a Spearman rank correlation matrix (Table 13), which identified elements that have the strongest positive and negative correlations with Fe and S in pyrites. Strong positive or negative correlations are indicated by values greater than 0.4 or less than - 0.4, respectively (Pallent, 2007).

Correlations illustrate the relationships of elements within POS pyrite. Iron correlates positively with Pb (0.723), Co (0.571), and S (0.944) and correlates negatively with Si (-0.926) and Al (-0.560). Lead correlates positively with Fe (0.723), Co (0.473), and S (0.669) and correlates negatively with Si (-0.663), and Al (-0.454). Cobalt correlates positively with Pb (0.473), Ni (0.724), Fe (0.571) and S (0.561) and correlates negatively with Si (-0.568).

Interpretation

Pre-ore-stage pyrite trace element chemistry is variable (Fig. 22), but EPMA quantified elevated Pb, Co, and Ni in some POS pyrites, and this relationship was confirmed by the Spearman rank correlation matrix, which shows that Fe, S, Pb, and Co all share strong positive correlations and have strong negative correlations with Si and Al. Co is the only element that shares a strong positive correlation with Ni. Iron's negative

correlation with Si and Al confirms their inverse relationship in single analyses that included both host rock and pyrite.

Mann-Whitney U-Test EPMA pyrite data

The Mann-Whitney U-Test searches for differences in trace and major element chemistry between two groups of data that are separated based on a value or “classification,” within the data set. In this analysis, this test compares two groups of data separated by three classification values that equal three different concentrations of gold. One of the two groups in each analysis includes concentrations of a selected element in all samples that contain gold in concentrations less than the classification value and is called the “low gold class.” The second group, the “high gold class,” includes concentrations of the selected element in all samples with gold concentrations equal to or greater than the gold classification value. Three gold classifications, 0.0001, 0.0144, and 0.0500 wt. % Au, were selected to evaluate all pyrite EPMA data. The Mann-Whitney U-Test methodology and figures and tables showing analysis results for elements related to POS pyrites are described here.

Evaluated elements relevant to pyrites and the adjacent host rocks include Fe, S, Co, Ni, Pb, Al, Si, Ag, and Ca; median values for each element in each of the low and high gold classes for each classification value were determined and are listed in Table 14. The low gold class median values for each element are listed in the columns labeled ‘Median < 0.0001, 0.0144, and 0.0500.’ The high gold class median values for each element are listed in the columns labeled ‘Median >= 0.0001, 0.0144, and 0.0500.’ The high and low median values for all gold classifications are also presented on bar graphs (Figs. 23, 24), allowing comparison of high and low median values for all elements.

Median values for the low gold class of each element in pyrites and adjacent host rocks are represented by the blue bars and median values for the high gold class of each element are represented by the orange bars in the bar graphs (Figs. 23, 24).

The Mann-Whitney U-Test calculates asymptotic significance (2-tailed) values that indicate whether or not differences in median values for an element in the low and high gold classes are significant. Values indicating that the median values in the low and high gold class are significantly different and < 0.005 , and are highlighted in blue in Table 14. For those elements for which the median values are not significantly different, the asymptotic significance is > 0.005 , and they are highlighted in white in Table 14. Note that in general, median values are significantly different for most elements based on a gold classification of 0.0001 wt. % gold; however, median values are not significantly different for most elements based on a gold classification of 0.0500 wt. % gold (Table 14). Bar graphs (Figs. 23, 24) show gold classification values in wt. % gold on the X axis and element median values in wt. % on the Y axis. Gold classifications with median values that are significantly different lack the symbol “*”.

Elements associated with pyrites include Fe, S, Pb, Co, and Ni, all of which show similar patterns by having higher median values in the low gold class (blue) than in the high gold class (orange) (Fig. 23). In addition, the median values of each element in the low gold class exhibit a small decrease, with increasing gold classification (Fig. 23). The median values for the high gold class (orange) also decrease with increasing gold classification, except Ni, which increases slightly from the classification of 0.0001 to 0.0144 (Fig. 23). In general, the median concentrations of the high gold class for Fe, S, Co, and Pb decrease from the 0.0001 to the 0.05 gold classifications with the greatest

change between the 0.0144 and 0.05 classifications (Fig. 23). The Mann-Whitney U-Test determined that the median values for the high and low gold classes for Fe in all gold classifications were not significantly different (Table 15, Fig. 23). The median values for the high and low gold classes for S and Co were determined to be significantly different for all gold classifications, and for Pb and Ni for the 0.0001 and 0.0144 classifications (Table 15, Fig. 23).

The low and high gold class median values for Al and Si, elements that are commonly in siliciclastic host rocks (Fig. 24), have asymptotic significant values > 0.005 for all gold classifications, indicating that the differences in median values are not significant (Table 14). Median values of Al and Si are the highest in high gold class analyses (orange) (Fig. 24) owing to EPMA on the edges of pyrite that include host rock.

Median values for Ca, present in carbonate host rocks, are highest in the low gold class, and decrease with increasing gold classification (Fig. 24). The median values for the high and low gold classes for Ca were determined to be significantly different for the 0.0001 and 0.0144 classifications, but median values are at low concentrations (Table 14, Fig. 24).

Median values of Ag are the highest in the high gold class (Fig. 24). The Ag median values for the low gold class (blue) increase, but very little with increasing gold classification (Fig. 24). The median values for the high and low gold classes for Ag were determined to be significantly different for the 0.0001 and 0.0144 classifications, but median values are at low concentrations (Table 14, Fig. 24).

Asymptotic significant values for Fe, As, Tl, Bi, Sn, Zn, and Ti are > 0.005 in all gold classifications, indicating there are no significant differences between median values in all gold classifications (Table 14). Selenium, Sn, Te, W, and Zn have a median values of zero in all classes (Table 14), indicating that these elements are rare in these rocks and that there are no differences in the concentrations of these elements in all gold classifications; they are not plotted on bar graphs.

Interpretation

Elements, for which median values of the low and high gold classes of a gold classification have significant differences, provide information about the gold concentrations and, therefore, may have applications for gold exploration. Focusing here on the pre-ore stage, the Mann-Whitney U-Test shows that low and high gold class median values for S, Pb, Co, and Ni, elements that are commonly in POS pyrites, have significantly different median values for some or all gold classifications, and these values can provide information about gold grade associated with these elements. These relationships indicate that these elements are consistently present in POS pyrites and are unrelated to gold. The median values are not significantly different for any gold classifications for Al and Si and that the concentrations of Ca and Ag are so low in all medians that they are not of practical importance in terms of providing information about gold in the rocks. They do, however, indicate that Ca and Ag are not important with respect to ore-stage pyrites.

The median values of the low and high gold classes for Fe, Si, Al, As, Tl, Bi, Sn, Zn, and Ti show no significant difference in all gold classifications, indicating that these elements have similar concentrations no matter the gold classification, and are not

informative about variations in gold. Selenium, Sn, Te, W, and Zn have median values of 0 in all classes, demonstrating that these elements are unimportant in the host rocks and not related to hydrothermal mineralization.

Discussion of Pre-ore-stage pyrite

Petrography in conjunction with X-Y plots of EPMA data, Spearman rank correlation matrix, Mann-Whitney U-Test, and principal components analysis of EPMA data contributed to identifying the characteristics and geochemical similarities of POS pyrites, and do not distinguish multiple POS pyrite types (Table 9). All POS pyrites are interpreted as diagenetic; POS pyrites have different pyrite morphologies, but all POS pyrites have similar geochemistry, and are not intergrown with sphalerite. Statistical analyses of the EPMA data did, however, recognize as non-typical the presence of As, Cu, Hg, Sb, and Tl that are related to the ore stage.

Mineral Paragenesis Discussion

The three mineralized formations include the Devonian Devil's Gate, the Mississippian Webb, and the Mississippian Chainman Formations. The Devonian Devil's Gate Formation, originally comprised of primary diagenetic calcite, was recrystallized and altered to dolomite (Fig. 15). Gold Standard Venture geologists have interpreted dolomitization to be pre-ore stage, but exact timing is unknown. The Mississippian Webb and Mississippian Chainman Formation are comprised of diagenetic quartz, calcite, illite, montmorillonite and apatite. Pre-ore stage pyrites (Fe, S, Pb, Co, and Ni) are dominated by syngenetic to diagenetic pyrite that are present in the Devonian Devil's Gate, Mississippian Webb, and the Mississippian Chainman Formations (Fig. 15).

Porphyritic dacite dikes that formed ~ 38.4 - 38.9 Ma, represent the earliest igneous intrusive event at the North Bullion Carlin system, and cross cut all sedimentary host rocks (Henry, 2014). Primary minerals in dacite include plagioclase, biotite, hornblende, quartz, and apatite (Henry, 2014). These primary minerals were variably altered to quartz, illite, kaolinite, rutile, and possibly sphalerite (Fig. 15). Both petrography and statistical analyses show that sphalerite is a secondary pre-ore-stage mineral that formed prior to ore-stage mineralization.

CHAPTER 5

ORE STAGE

The ore stage is defined as the time during which Carlin-type gold ore fluids were introduced to and mineralized the North Bullion Carlin system. Ore-stage mineralogy and alteration were identified by examining variations in mineralogy and textural relationships from unmineralized to mineralized samples along sample transects. Ore-stage mineralogy includes ore-stage 1 (OS 1) pyrites and ore-stage 2 (OS 2) pyrites. Ore-stage 1 pyrites occur in the highly altered Tertiary dacite dike and contain detectable Au throughout the pyrite. Observed ore-stage alteration within the dacite dike includes quartz and illite. Ore-stage 2 pyrites form irregular, sub-micrometer pyrite rims on POS and OS 1 pyrites, or occur as OS 2 microcrystals. Ore-stage alteration in sedimentary rocks includes jasperoid, illite, and variably concentrated residual carbon, all commonly spatially associated with OS 2 pyrite rims or microcrystals. Increased porosity that is commonly associated with increasing grade in other Carlin-type gold deposits (Clark, 2012) does not correlate with increasing grade at North Bullion Carlin system.

Ore-stage 1 pyrite

Ore-stage 1 pyrites, identified as containing Au up to 450 ppm by using EPMA analyses (Table 8; Appendix F.5 and F.10), are euhedral to anhedral pyrites in dacite, which cross cuts sedimentary rock that contains POS pyrites. These pyrites are brassy, with bright reflectivity (Fig. 18 B, E), range in size from 20 μm to 1 mm, and are associated with quartz and illite (Fig. 18). Ore-stage 1 pyrites variably enclose euhedral quartz (Fig. 19 H, K), rutile (Fig. 19 B, E), sphalerite (Fig. 19 H, K), and apatite (Fig. 19 B, F).

EPMA element maps illustrate the presence of arsenic-rich rims around OS 1 pyrites (Fig. 19 G, J). These arsenic-rich rims with elevated gold and/or Carlin pathfinder elements are ore stage 2 (OS 2) pyrites, and are found rimming both POS and OS 1 pyrites. This relationship of OS 2 pyrites rimming OS 1 pyrites (Fig. 19 G, J) shows that OS 2 rims formed after OS 1 pyrites, and after the dacite dikes.

Interpretation

Ore-stage 1 pyrites are interpreted to be a part of the Carlin-type mineralizing event related to mineralization and alteration of the porphyry dacite dike. Ore-stage 1 pyrites were not identified by morphology, but instead by quantifying Au within OS 1 pyrite using EPMA. Sphalerite formed after the dike, yet is encompassed by OS 1 pyrite, indicating that it probably formed before the Carlin mineralizing event, and further indicating that pyrite is a secondary mineral in the dike. Given the lack of the Carlin trace element suite in OS 1 pyrites, their relationship to the Carlin mineralizing event is uncertain. Euhedral quartz phenocrysts, rutile, sphalerite, and apatite occur as inclusions in OS 1 pyrite and are likely related to hydrothermal alteration of the dike. Textures indicate that the dacite dike with euhedral quartz phenocrysts and apatite formed initially, followed by precipitation of rutile and sphalerite, subsequent Au-bearing OS 1 pyrite, and later OS 2 pyrite rims. The Tertiary porphyry dacite dike was emplaced ~38.9 – 38.4 Ma, thus OS 1 pyrites were formed after 38.4 Ma, and OS 2 pyrites after OS 1 pyrites.

Ore-stage 1 Pyrite Geochemistry

Graphs (Fig. 25) of Fe versus all elements analyzed using EPMA show the variability of trace elements within OS 1 pyrites (Table 15) and in host rocks analyzed at the beginning and end of analytical transects across pyrite. Though ore-stage 1 pyrites

contain detectable Au throughout the pyrite, they are generally not elevated in other Carlin pathfinder elements (Table 8 points 2460-2473) and, thus, are distinct from POS pyrites and OS 2 rims. Rims with elevated arsenic are detected on OS 1 pyrite (Fig. 19 B, D, G and J).

Iron and S (Fig. 25) correlate positively, approaching the 46:54 Fe:S ratio that characterizes pure pyrite. About 70% of the analyzed points contain 46 - 53 wt. % Fe, reflecting that the pyrites may be partially oxidized. Silicon, which reaches 25 wt. %, and Al, which reaches 17.5 wt. %, exhibit an inverse trend and decrease with increasing Fe, reflecting inclusion of varying amounts of host rock in analyses. Calcium is generally below 1 wt. %, and few analyses reach 6.5 wt. % Ca. Gold is generally below 100 ppm, but reaches 450 ppm in analyses dominated by pyrite that contain 50 - 53 wt. % Fe. Most Co data cluster between 0.04 to 0.08 wt. % and most Pb data cluster between 0.25 - 0.35 wt. % where Fe varies from 37- 53 wt. %. Arsenic, Hg, Sb, and Tl plots exhibit two trends: most data indicate low concentrations of these elements that do not correlate with Fe; however, a smaller number of analyses indicated elevated As, Hg, Sb and Tl where Fe varied from ~20 - 52.64 wt. % Fe. In these analyses As reaches 3 wt. %, Hg reaches 0.006 wt. %, Sb reaches 0.35 wt. %, and Tl reaches 0.05 wt. %. Bismuth, Cu, and Ti are generally low, but exhibit a range of concentrations between 40 - 53 wt. % Fe in analyses dominated by pyrite. Silver, Se, Sn, Te, and Zn exhibit two trends: most data do not correlate with Fe and analyses are close to zero for most concentrations of Fe; other data for analyses dominantly of pyrite with ~35 - 53 wt. % Fe, points indicate elevated Ag, Se, Sn, Te, and Zn. In these analyses Ag reaches 125 ppm, Se reaches 0.0175 wt. %, Sn reaches 0.005 wt. %, Te reaches 0.015 wt. %, and Zn reaches 0.6 wt. %.

Interpretation

Analytical results reveal the relative amounts of OS 1 pyrite and host rocks evaluated by individual analytical points, and indicate that pyrites contain low Bi, Pb, Co, Ni, Ag, Se, Sn, Te, and Zn relative to POS pyrites. Analyses further show that though the OS 1 pyrites contain Au, they do not contain elevated As, Sb, Hg or Tl. This calls into question whether or not these pyrites are related to the Carlin mineralizing event. It is possible that the Au-bearing pyrite is alternatively related to a late, low-temperature hydrothermal event directly related to intrusion and cooling of the dacite dike. However, as no other Au event has been identified, and because the pyrites in the dikes are secondary, Au in these pyrites is interpreted as being related to the Carlin mineralizing event. Ore-stage 2 pyrites form rims that are generally elevated in Au, As, Hg, Sb, and/or Tl, and these As-rich rims detected on OS 1 pyrites are interpreted to be OS 2 pyrite rims. The presence of OS 2 As-rich pyrite rims on OS 1 pyrites indicates that OS 1 pyrites formed prior to, and are older than the rims.

Analyses that identified Au in addition to high concentrations of Fe and S and low to no Si or Al, primarily or only analyzed OS 1 pyrite. The positive linear correlation between Fe and S at relatively high Fe is consistent with analysis of pyrite. However a Fe:S ratio of 52:46 for some analyses, indicates low S compared to a normal 46:52 ratio, suggesting that these pyrites may be partially oxidized. Some S is being replaced by O, which explains the change in Fe:S ratio. Analyses that identified abundant Si or Al and low Fe and S primarily analyzed host rock minerals including quartz, illite, and kaolinite at the beginning or end of analytical transects. Ore-stage 1 pyrites exhibit weak positive correlations between Fe with Pb > ~0.25 wt. % and with Co > ~0.04 wt. %. Bismuth, Cu,

and Ti are variable within OS 1 pyrites. In plots of Fe vs Au, As, Hg, Sb, and Tl, the CTGD pathfinder elements are at low concentrations for values of Fe between 52.64 - 53.12 wt. % , illustrating that OS 1 pyrite contain Au, but are not elevated in CTGD pathfinder elements. In plots of Fe vs As, Hg, Sb, and Tl, the CTGD pathfinder elements are elevated for values of Fe between 20 - 52.64 wt. % Fe, illustrating that OS 2 pyrite rims, located at the boundary between host rock and OS 1 pyrite, were included in these analyses.

Principal Components Analysis of Ore-stage 1 Pyrites

Principal components analysis of OS 1 pyrite (Tables 16, 17) identified 7 components that account for 83.771 % cumulative variance of the data. For this data set, the Bartlett's Test of Sphericity is 0.000, and the KMO is 0.536, a value that indicates that this data set is not suited for principal components analysis. Using the Catell's Scree Test (Appendix F.5) components 1 and 2 are above the change in slope, and contribute 44.669 % cumulative variance of the data. Component 1 includes S, Fe, Pb, Co, Bi, Cu (Si, Al, Ni, and Sn) with a total eigenvalue of 6.756, and a variance of 32.173 %. Component 2 includes Tl, Ca, Hg, Te, Ti, (Cu, As, Zn, Bi, and Sb) with a total eigenvalue of 2.624, and a variance of 12.496 %. Components 3-7 are below the change in slope (Table 16; Appendix F.5) and are not discussed.

Interpretation

This data set is likely unsuitable for Principal components analysis due to small sample size; however, geochemical patterns identified could still be informative. Component 1 of OS 1 pyrite identified two groups of elements that are inversely related: Fe, S, Pb, Co, Bi, and Cu are positively correlated and correlate negatively with Si, Al,

Ni, and Sn. These results probably reflect the EPMA transect method that analyzed both pyrite and host rocks; however, both components 1 and 2 are difficult to fully interpret.

Ore-stage 2 Pyrite

Ore-stage 2 pyrite, identified as containing Au by using EPMA and LA-ICP-MS, occurs most commonly as discontinuous sub-micrometer rims or as ore-stage microcrystals. In all of these figures (Figs. 26-30), the color on the Fe maps reflects the size of the pyrite crystals, with red to green indicating the presence of the largest pyrites (~ 0.1 – 0.7 mm), and blue indicating the presence of less concentrated small pyrites (< 0.1 mm). This is a result of the LA-ICP-MS spot size (Table 4), as analyses of smaller pyrites include adjacent illite, jasperoid, and/or quartz. Gold maps (Figs. 26-30), show OS 2 pyrites rimming earlier pyrites. Gold associated with small pyrites (< 0.1 mm) is either in small rims or in OS 2 pyrite microcrystals. These maps further show that though the Carlin pathfinder elements, As, Hg, Sb, and Tl are present, they do not perfectly mirror the location of Au.

Ore-stage 2 pyrites occur as rims on, or within fractures and pores of euhedral to anhedral POS pyrite within the Devonian Devil's Gate, Mississippian Webb (Fig. 26), and Mississippian Chainman Formations (Fig. 27) and as rims on OS 1 pyrite in Tertiary porphyry dacite dikes (Fig. 19 G, J). The OS 2 pyrites also formed rims on and within interstitial spaces of framboidal POS pyrites (Fig. 28), and occur as "clouds" of concentrated fine disseminated OS 2 pyrite microcrystals (Figs. 26, 29) within the Mississippian Webb Formation and multi-lithic breccias. These OS 2 pyrites cannot be distinguished from other pyrite generations using optical petrography or SEM analyses

only, and are identified by the presence of Au and Carlin trace metals using EPMA and LA-ICP-MS.

Ore-stage 2 pyrites are consistently spatially associated with jasperoid, illite, and variable carbon. Illite and carbon form a matrix cementing Chainman quartz sandstone grains and contain POS euhedral and anhedral pyrites with OS 2 pyrite rims and OS 2 pyrite microcrystals (Fig. 27). Webb mudstone and multi-lithic breccia (Figs. 26, 29), contain OS 2 pyrite rimming POS pyrite within an illite and carbon plus lesser jasperoid quartz matrix. Devil's gate limestone also contains OS 2 pyrite rimming POS pyrite within a jasperoid, illite, and carbon matrix.

Carlin pathfinder elements As and Tl correlate with Au extremely well in some samples (Figs. 26, 29, and 30); however, in other samples As, Sb, and Tl are present in OS 2 rims around POS pyrite, but Au is below detection or absent (Fig. 30 B). Ore-stage 2 pyrites are summarized in Table 18.

Interpretation

Laser ablation ICP-MS maps of OS 2 pyrites demonstrate that the spatial correlation of Au and the Carlin-type pathfinder elements in pyrite is variable. In samples in which both pathfinder elements and gold are present in pyrite, the coincidence of all elements in all analyses is imperfect, but the CTGD pathfinder elements are generally present in analyses quite close to analysis points that detected Au. Results show that the presence of As, Sb, Tl, and Hg in pyrite extends beyond areas containing detectable Au.

Regions of laser ablation ICP-MS maps that appear to show low Fe (Fig. 26) are in part a result of analysis points that are larger than the size of the analyzed pyrites, resulting in an analysis that is a mixture of POS pyrite and host rock. The gold detected in

these maps (Table 8 points 790-803, and Fig. 26) is either in OS 2 pyrite microcrystals or OS 2 pyrite rims on POS pyrite microcrystals.

Ore-stage 2 Pyrite Geochemistry

The X-Y graphs (Fig. 31) of Fe versus all elements quantified using EPMA show the variability of trace elements within OS 2 pyrites (Table 18); however because of the line transect method used to collect EPMA, data points also analyzed POS pyrite and host rocks that were adjacent to OS 2 pyrites, and which contribute to the analysis totals. Iron exhibits an (Fig. 31) inverse relationship with Si and some Al, present in host rocks and Si and Al decrease with increasing Fe, though Al is low in many analyses. Alternatively, Fe and S in pyrite exhibit a strong positive correlation though a sub-parallel trend is present below the major trend (Fig. 31). Low Co and Pb also correlate positively with Fe. Iron and Au are not correlated. Elements typically associated with Au in pyrite in Carlin-type deposits, including As, Cu, Hg, Sb, and Tl exhibit more than one trend. Most As, Cu, Hg, Sb, and Tl data do not correlate with Fe and values for these elements are typically low; however, some analyses quantified elevated As (to 5 wt. %) and Hg (to 0.15 wt. %) between ~13 – 47 wt. % Fe, elevated Cu (to 0.15 wt. %) between ~17 – 47 wt. % Fe, elevated Sb (to 1.25 wt.%) between ~33 – 47 wt. % Fe, and elevated Tl (to 0.25 wt. %) between ~15 – 51 wt. % Fe. These data exhibit weak positive correlations with Fe and likely best represent analyses of ore-stage 2 pyrites with minimal host rock or POS pyrite. Silver, Bi, Ca, Ni, Se, Sn, Ti, and Zn have low values for all Fe concentrations, and the majority of analyses of these elements are at or close to zero.

The X-Y graphs (Fig. 32) of Au versus all elements analyzed using EPMA show the variability of trace elements within OS 2 pyrites with detectable gold. Gold, which

varies from detection to ~800 ppm (Fig. 32), does not correlate with any element. Gold was detected in analyses in which Fe varied from 0 – 53 wt. %, and high Au, between 500 – 800 ppm, was detected in analyses in which Fe varied from 7 – 53 wt. %. The Carlin pathfinder elements vary widely in analyses that detected Au, however As, Hg, Tl, Cu, and Sb are not detected in many of these analyses (Fig. 32, Table 8 points 412-418, and 790-803). In analyses with Au > 600 ppm, the Carlin pathfinder elements vary from detection to higher values. Analyses that quantified high As, Cu, Hg, and Tl (Fig. 32) are dominated by teal data points (yellow box) representing 17.51 to 39.59 wt. % Fe, and 0-700 ppm Au. These data points analyzed varying amounts of OS 2 pyrite, host rock, and POS pyrite adjacent to the OS 2 pyrite.

This relationship is also indicated by EPMA points 412- 418 and 790-803 (Table 8), where point 412 analyzed an OS 2 pyrite rim with detectable Au and elevated As, points 413 - 417 analyzed POS pyrite with no Au, and point 418 analyzed an OS 2 rim with elevated As, but without detectable gold. Analyses 792-802 (Table 8; Fig. 26) also detected Au within a mixed phase of OS 2 pyrite microcrystals, POS pyrite, and host rock. Laser ablation ICP-MS maps of OS 2 pyrite microcrystals (Fig. 26) show Au is detected where Fe is low, indicating analysis of a rim at the edge of a pyrite or the pyrite size was smaller than the LA-ICP-MS spot size.

Interpretation

Electron probe microanalyses included in the ore stage quantified Au above the detection limit. Inspection of all analyses shows that some analyses of OS 2 pyrite rims, that quantified Carlin pathfinder elements, did not detect Au and, as Au is absent, these

analyses are grouped with POS pyrite data because there was no unbiased method in which these analyses could be separated from POS data.

Principal Components Analysis of Ore-stage 2 Pyrite

Principal components analysis of EPMA data for OS 2 pyrite (Tables 17, 19) identified 7 components that accounts for 69.599% of the data. The KMO value and Bartlett's Test of Sphericity indicate that these analyses produced acceptable results. Using the Catell's Scree Test (Appendix F.6) components 1 and 2 are above the change in slope, and contribute 40.278 % cumulative variance of the data. Component 1 includes Fe, S, Pb, Co, Bi, W, (Si, Al, Hg, Tl, Cu, and As) with a total eigenvalue of 5.153 and a variance of 23.425 %. Component 2 includes As, Tl, Hg, Cu, Co, S, Fe, W, (Si, and Al) with a total eigenvalue of 3.708, and a variance of 16.854 %. Components 3-7 (Table 19; Appendix F.6) are below the change in slope and are not discussed.

Interpretation

Principal components analysis component 1 identified the inverse relationship between POS pyrite elements Fe, S, Pb, Co, Bi, and W with Si, Al, Hg, Tl, Cu, and As that are present in analyses of OS 2 pyrite and adjacent host rocks. Component 2 identified the inverse relationship between elements within OS 2 pyrite including As, Tl, Hg, Cu, Co, S, and Fe with Si and Bi that are present in host rocks. These analyses identified inverse relationships between Carlin pathfinder elements with both host rock elements and POS pyrite elements.

Spearman Rank Correlation Matrix for EPMA data

Electron probe microanalyses were evaluated using a Spearman rank correlation matrix (Table 13). Gold does not exhibit a significant positive or negative correlation

with any element. The Carlin-type pathfinder elements (As, Sb, Hg, Tl, and Cu) that typically correlate with Au in other CTGDs correlate strongly with each other (Table 13). Arsenic correlates positively with Hg (0.597), Tl (0.585), and Sb (0.448). Antimony also correlates positively with Hg (0.425) and Tl (0.351), and Hg also correlates positively with Tl (0.814).

Interpretation

Because of the variable detection of Au in many analyses of ore-stage pyrite, the Spearman's correlation matrix indicates a poor correlation between Au with Hg, Sb, Tl, and As, though these pathfinder elements share strong positive correlations with each other. As the Au concentration in most samples is low, Au may be present but below detection in analyses in which pathfinders were quantified. Laser ablation ICP-MS maps of some pyrites support this interpretation as they confirm the presence of Au coincident with Carlin-type pathfinder elements.

Mann-Whitney U-Test EPMA pyrite data

Gold and the Carlin pathfinder elements were examined using the Mann-Whitney U-Test, previously described for analysis of POS pyrites. These elements show similar patterns of median values in the high gold class (orange) increasing with increasing gold classification (Fig. 33). As indicated by the lack of the symbol “*” (Fig. 33), the difference in median values of Au in the low and high gold classes for all gold classifications is significant; however, the difference in median values for As and Tl are not significant for any of the gold classifications. Median values are significantly different for Cu and Hg in the lowest gold classification, and for Sb in the low and intermediate classification. In addition, median values of each element in the low gold

class (blue) decrease or remain constant with increasing gold classification (Fig. 33). The gold median values in the high gold class, increase significantly from 0.0146 wt. % Au in the lowest gold classification to 0.0616 wt. % Au in the highest gold classification (Fig. 33 A); however, gold's median concentrations in the low gold class remain constant at 0.000 wt. % Au. Arsenic, Cu, Hg, Sb, and Tl median concentrations in the high gold class increase from the low to high gold classification (Fig. 33 B-F). Alternatively, As, Cu, Hg, Sb and Tl's median concentrations in the low gold class decrease or remain approximately constant from low to high gold classification.

Interpretation

These relationships show that As, Cu, Hg, Sb, and Tl increase with Au, consistent with the association of these elements with Au in OS 2 pyrites. Results (Table 14; Fig. 33) indicating significantly different median values for Cu and Hg in the low gold classification, and for Sb in the low and intermediate gold classifications indicate that these elements are indicators of the presence of gold in pyrite in low-grade rocks. These results confirm the role of pathfinder elements and determine the value of each element as a pathfinder at various concentrations of Au.

Interpretation of Ore-stage 2 Pyrites

Ore-stage 2 pyrites have discontinuous sub-micrometer rims on POS pyrite cores and in fractures and vugs in POS and OS 1 euhedral and anhedral pyrite. Ore-stage 2 pyrites also form rims and fill interstitial voids of POS framboids and occur as disseminated pyrite microcrystals (Fig. 34). Although Au concentrations are low in ore-stage pyrites, and are likely below EPMA detection limits in many analyses, LA-ICP-MS maps show that the Carlin-type pathfinder elements have a strong positive correlation

with Au. These observations are confirmed by these analyses and partially confirmed by the Mann-Whitney U-Test that indicates that the pathfinder elements increase with increasing gold classification, and that the median values of the low to medium gold classifications of Cu, Hg, and Sb are significantly different.

Illite and Jasperoid

Ore-stage 2 pyrite rims and OS 2 microcrystals are more closely spatially associated with illite in all formations, than with other alteration minerals (Figs. 26-29). Both illite and montmorillonite were identified by SEM analysis, (Figs. 28, 29), but montmorillonite was less commonly identified and significantly less abundant (Fig. 28 C) in ore. Graphs of Fe versus other analyzed elements (Fig. 31) that show the inverse relationship of Si and Al with Fe and S reflect the presence of quartz and clay minerals proximal to POS pyrites and OS 2 rims.

Ore-stage 2 pyrites with the highest gold concentrations are commonly encompassed by illite in carbon-rich dissolution veins or vugs (Fig. 29) that contain concentrated insoluble material including jasperoid, quartz, illite, carbon, and POS pyrites, some of which have OS 2 rims, and/or OS 2 microcrystals (Fig. 29 C). Dissolution veins and vugs are generally within quartz, and/or jasperoid, and probably formed by dissolution of primary calcite during replacement and formation of jasperoid. Illite is significantly more abundant within dissolution veins and vugs and brecciated matrix compared to primary unaltered host rock.

Examination of transects of samples from low to high grade, show that jasperoid formed as quartz replaced carbonate minerals, and replacement is identified by presence of small inclusions of highly birefringent calcite within quartz. In Devonian Devil's Gate

carbonate host rocks and in multi-lithic breccias with carbonate clasts, jasperoid is spatially associated with OS 2 pyrites and occurs within dissolution veins and vugs that host OS 2 pyrites (Fig. 29 A, B). The jasperoid alteration process is illustrated by the presence of relict carbonate clasts within illite, jasperoid, and relict carbon in matrix and also trace porosity within the matrix indicated by blue epoxy (Figs. 35 D, F, and 36 H). Porosity is locally created by decarbonatization (Fig. 35 D, F), but porosity is not always present in decarbonatized host rocks, which suggests that pore spaces were variably filled with jasperoid and illite.

Sample Transects

Devonian Devil's Gate Formation

A sample transect through dolomitized breccia in the Devonian Devil's Gate Formation (Fig. 35 A, C, and E) illustrates changes in rock textures and abundances of dolomite, jasperoid, illite, carbon material, and POS pyrite with increasing gold grade. An increase in gold grade from 0.017 to 0.585 ppm correlates with an increase in fractures, porosity, and darker material within the breccia. In the low-grade sample (Fig. 35 A, B) the crystal size of the dolomite is 0.1-0.9 mm, and illite, jasperoid, and carbon are confined to fractures between brecciated dolomite clasts. With increasing grade (Fig. 35 C, D), dolomite crystals decrease in size (0.05-0.2 mm) and illite, jasperoid, carbon, and pyrite are more abundant. An increase in gold grade from 0.585 to 4.7 ppm (Fig. 35 F) correlates with an increase in abundance of sulfides within fractures and porosity. Dolomite crystals remain small (0.05-0.2 mm), and illite, jasperoid, carbon, and porosity are present. Jasperoid and pyrite have increased in abundance and size of the dolomite crystals and the abundance of carbonate minerals have decreased along the transect from

low to high grade, showing increased decarbonatization of the Devonian Devil's Gate with increasing grade.

Mississippian Webb Formation

Due to drill hole spacing continuous transects of unmineralized to high-grade Mississippian Webb micrites and mudstones were not available for collection; however, comparisons were made between available samples of unmineralized and mineralized rocks. In Mississippian Webb Formation micrites, jasperoid is spatially associated with OS 2 pyrites and occurs within dissolution veins and vugs that host OS 2 pyrites (Fig. 29 A, B). With increasing grade, Mississippian Webb Formation micrites (Fig. 36 A, B, E, and F) exhibit changes in rock textures and abundances of calcite, dolomite, jasperoid, illite, carbonaceous material, and pyrite. In low-grade samples (Fig. 36 A-D) calcite crystals (0.02-0.22 mm) and POS pyrites occur within a calcite/dolomite, illite, and carbon matrix. With increasing grade (Fig. 36 E, F, G, and H) illite, jasperoid, carbon, and pyrite increase relative to carbonate minerals. Dissolution veins (Fig. 36 A, E) in which insolubles are concentrated are increasingly common.

High-grade mineralized Mississippian Webb micrite samples that have been decarbonatized either show a decrease in carbonate minerals with an increase in jasperoid, illite, and carbon (Fig. 36 C, G), or a decrease in carbonate minerals, with an increase in jasperoid and porosity (Fig. 36 D, H). Non-porous decarbonatized Mississippian Webb micrites (Fig. 36 G) contain increased jasperoid, illite, and carbon, which replaced previous carbonate minerals. Overall, porosity of mineralized Webb micrites varies (Fig. 36 E, F), and porosity is unrelated to gold concentration.

Mississippian Webb Formation mudstones (Fig. 37 A, C, and E) exhibit changes in mineral abundances and rock textures with increasing gold grade. Low-grade Webb mudstone samples (Fig. 37 A, B) are composed of quartz crystals and POS pyrite within in a quartz, illite, carbon, and minor montmorillonite matrix. With increasing grade (Fig. 37 C, D) there is an increase in quartz within the matrix. Quartz is more commonly microcrystalline quartz with illite and carbon impurities (Fig. 37 D), and less commonly euhedral quartz crystals as observed in Figure 37 B. In addition, with increasing grade the color of the Webb mudstone changes to a darker shade of brown due to increase in carbon (Fig. 37). Changes exhibited by Webb from low grade mineralization to high grade mineralization (Fig. 37 E, F) include an increase in microcrystalline quartz in the matrix and veins, the matrix becomes darker due to an increase in carbon and an increase in dissolution veins that concentrate insolubles.

Mississippian Chainman Formation

A sample transect through Mississippian Chainman Formation (Fig. 38 A, D, and F) illustrates changes in mineral abundances and rock textures with increasing gold grade. All samples are composed mainly of sand-to gravel sized detrital quartz grains and have varying minor abundances of green chert, apatite, illite, montmorillonite, carbon, POS pyrite, and rutile. An increase in gold grade from 0.18 to 1.44 ppm (Fig. 38 A-F) correlates with an increase in fractures filled by quartz and late-ore-stage minerals barite and calcite, an increase in dark clasts composed of POS pyrite, illite, and carbonaceous material, and secondary microcrystalline quartz is present. Ore-stage 2 rims on POS pyrites and OS 2 microcrystals within illite-rich areas between quartz grains (Fig. 27) are present within moderate grade samples (Fig. 38 D). An increase in gold grade from 1.44

to 2.98 ppm (Fig. 38 D-I) is accompanied by a small increase in percentage of dark clasts composed of POS pyrite, illite, and concentrated residual carbon. Fractures filled by secondary quartz and LOS pyrite are still present.

Interpretation

Petrography shows that minerals commonly associated with OS 2 pyrite rims include illite, +/- carbon in siliciclastic rocks and jasperoid, illite, +/- carbon and porosity in carbonate rocks, suggesting that these are the alteration minerals associated with ore deposition. However, illite also occurs in weakly altered and weakly mineralized host rock units examined, and there are no clear optical differences in primary versus secondary illite.

An increase in decarbonatization with increasing grade and alteration intensity at North Bullion is indicated by the removal of carbonate minerals. At other deposits, porosity increases with decarbonatization. However, increasing porosity does not necessarily correlate with increasing decarbonatization and gold grade at North Bullion, perhaps because silicification or clay alteration occurred simultaneously with or after decarbonatization. The formation of jasperoid and, illite may have prohibited an increase in porosity.

Discussion

It is difficult to determine if the illite associated with OS 2 pyrite is primary illite or an alteration phase related to mineralization. Samples of weakly altered and mineralized Devonian Devil's Gate, Mississippian Webb, and Mississippian Chainman Formation contain some illite. However, unmineralized and unaltered samples of Devonian Devil's Gate and Mississippian Webb were not available for study. Thus it is

unclear whether or not illite in weakly altered and mineralized samples is related to hydrothermal alteration or a primary component of the sedimentary host rocks.

Unaltered Devonian Devil's Gate Formation has been described as a clean limestone (Carlisle et al., 1957) and should not contain clays or jasperoid. However, it is not known whether or not Devonian Devil's Gate was altered by the Carlin event or some other event prior to Carlin mineralization.

Mineral Paragenesis Discussion

Gold-bearing (Fig. 15) OS 2 pyrite that typically contains Au and variable As, Hg, Sb, Tl +/- Cu formed discontinuous sub-micrometer rims primarily on POS pyrites and OS 1 pyrites or formed OS 2 microcrystals. These pyrites are spatially associated with illite, jasperoid, and carbon. Ore-stage 1 pyrites within a Tertiary dacite dike are interpreted to be a part of the Carlin-stage hydrothermal alteration of the porphyry dacite dike, and the As-rich rims OS2 pyrite on OS 1 pyrites indicate formation of OS 1 pyrite prior to OS 2 pyrite.

CHAPTER 6

LATE- TO POST-ORE STAGE

Late-ore-stage minerals precipitated after ore-stage gold-bearing pyrite and are associated with cooling down of the ore system; post-ore stage minerals formed at a later time, with some minerals forming after uplift and erosion, and during weathering of the ore system. Late-ore-stage minerals include quartz, pyrite, realgar, and calcite.

Stephanite, which is interpreted to be related to a post-Carlin intrusive event, and spatially associated barite along with kaolinite and halloysite clays that are concentrated in fractures within host rock, are interpreted as post-ore-stage minerals. Trace oxide minerals located at grain boundaries are interpreted as post-ore-stage minerals related to oxidation and weathering.

Quartz

Late-ore-stage secondary quartz is present in quartz veins as euhedral drusy quartz and/or as microcrystalline quartz (Fig. 39), and occurs in Mississippian Webb and Chainman Formations and in multi-lithic breccias. Drusy quartz conforms to host rock minerals along fractures or vugs and growing perpendicular from wall rock into open space. Microcrystalline quartz commonly forms a matrix between brecciated rock clasts (Fig. 39 A, B, C, and E), and replaces host rock minerals (Fig. 39 B, D, E, F, H, and I). These types of late-ore-stage secondary quartz are not spatially associated with OS 2 pyrite.

Euhedral drusy quartz veins and microcrystalline quartz are commonly spatially associated and appear to have formed at the same time, with drusy quartz precipitating in open space and microcrystalline quartz replacing host rock minerals (Fig. 39 C, D, E, F,

G, and I). Drusy quartz was subsequently enveloped by LOS pyrite, realgar, and/or calcite, and post-ore barite. Less commonly, small fragmented realgar occurs as inclusions within euhedral drusy quartz crystals in veins (Fig. 40 D) or realgar rims host rock clasts and drusy quartz conforms to realgar (Fig. 40 C). Microcrystalline quartz precipitated both prior to and coincident with LOS pyrite and realgar (Fig. 41 E, F, G, and H). Late-ore-stage pyrite and realgar occur within a microcrystalline quartz matrix in a collapse feature (Fig. 41 E, F, G, and H). Less commonly, microcrystalline quartz precipitated both prior to and coincident with post-ore-stage stephanite (Fig. 44 F, G, H, and I). Both secondary quartz types can show variable undulatory extinction.

Interpretation

Secondary hydrothermal quartz is interpreted to be late- to post-ore stage. Drusy quartz and microcrystalline quartz are interpreted as late- to post-ore stage owing to a lack of spatial association with Au-bearing pyrite and a close temporal and spatial relationship with LOS pyrite, late-ore-stage realgar, and post-ore-stage stephanite. All quartz associated with OS 2 pyrite is interpreted as primary diagenetic quartz or ore-stage jasperoid, and not late-ore-stage microcrystalline and drusy quartz. Observations indicate that drusy and microcrystalline hydrothermal quartz are part of the late- to post-ore stages. In addition, late-ore-stage drusy and microcrystalline quartz encapsulate breccia clasts in many of the multi-lithic and collapse breccias (Fig. 39 A, B), which contain moderate gold grades and ore-stage jasperoid quartz.

Late-ore-stage Pyrite

Late-ore-stage (LOS) pyrite occurs in veins, and anhedral pyrite crystals that are individual crystals of pyrite or masses of pyrite crystals. Late-ore-stage pyrite veins

(~0.1 mm) occur in all formations and overgrew late-ore-stage euhedral drusy quartz (Fig. 42 A, B) in veins that cross-cut host rock (Fig. 42 C, D, and E). Late-ore-stage masses of pyrite crystal (~ 20 μ m to 3 mm) in sulfidized breccia overgrew POS pyrite, OS 2 rims, and late-ore-stage quartz, and is encompassed by post-ore-stage barite (Fig. 41 B). Late-ore-stage anhedral pyrites (0.1 to 1 mm) and late-ore-stage anhedral realgar occur within a microcrystalline quartz matrix in a collapse feature in a multi-lithic breccia (Fig. 41 E, F, G, and H).

Late-ore-stage Pyrite Geochemistry

Late-ore-stage pyrites identified by petrography were confirmed by EPMA, which shows that LOS pyrites contain Fe, S, Pb, and Ag, with variable Bi, Sn, and Zn, and do not contain typical concentrations of Carlin-type pathfinder elements, but locally contain elevated As and Sb and low concentrations of gold (Figs. 42 D, E and 43; Table 8). Other trace elements (Co, Ni, Se, Sn, Ti, and Zn) are depleted relative to previously described pyrite types (Fig. 43; Table 8, 20). Late-ore-stage massive pyrite exhibits compositionally varied Au- and As-bearing bands that crystallized in open space (Fig. 41 B, C, and D). Gold concentrations range from 0 to 230 ppm (Table 8 points 2261-2266) in these As-rich bands, with most gold values below detection.

The graph of Fe versus S (Fig. 43) shows a positive linear correlation, approximately reflecting the 46:54 Fe:S ratio that characterizes pure pyrite. Late-ore-stage pyrites Fe varied from 45.15 - 46.77 wt. %. Iron exhibits an (Fig. 43) inverse relationship with Si and Al that are present in host rocks, though Al is low in many analyses. Gold varied from a detection limit of 144 to 350 ppm between 44 and 46.77 Fe wt. %. Carlin pathfinder elements are generally lower than concentrations than in OS 2

pyrite. Arsenic varies from 0 to 5 wt.%, Cu varies from 0 to 0.050 excepting one point at 0.125 wt. %, Hg varies from 0 to 0.125 wt. %, Sb varies from 0 to 1.25 wt. %, and Tl varies from a detection limit of 169 ppm to 0.1 wt. %. Silver varies from 0 to 1250 ppm, and Pb varies from 0.12 to 0.30 wt. %. Most of the elevated concentrations of these elements are at Fe concentrations > ~43 wt. %. Other trace elements (Co, Bi, Se, Sn, Ti, Zn, and Ni) are low and are listed in (Table 20).

Interpretation

Late-ore-stage pyrite is spatially related to late-ore-stage quartz and realgar, indicating it is not related to main ore-stage mineralization. Gold was detected as high as 350 ppm, between 44 and 46.77 Fe wt. %, and Carlin pathfinder elements are present, but at concentrations below those generally quantified in OS 2 pyrite rims. Concentrations of Ag, Bi, and Pb in LOS pyrite are similar to concentrations in POS pyrites, but Co, Ni, Se, Sn, Ti, and Zn are lower than concentrations in POS pyrites. Generally, LOS pyrites are depleted in trace elements relative to earlier-formed pyrite types. Low concentrations of Au, As, and Sb in LOS pyrite indicate that these elements were still present in a hydrothermal fluid when LOS pyrite formed, but the late-ore-stage did not contribute significantly to deposit mineralization.

A comparison of gold concentrations determined for OS 1, OS 2, and LOS pyrites (Appendix F.7) shows that ranges of gold concentrations vary from 0-450 ppm Au and 50-53 wt. % Fe and 0-350 ppm for 45-47 wt. % Fe for OS1 and LOS pyrites, respectively. Alternatively, the range of Au concentrations determined for OS 2 pyrite is larger, and ranges from 0-800 ppm Au and 0-52 wt. % Fe. Ore-stage 1 and LOS pyrite data points cluster for narrow ranges of Fe, and trace elements are less variable, whereas

OS 2 data points have more variable trace element geochemistry. These differences support the interpretations of three distinct pyrite types that are not a part of a single ore-stage event. The preferred interpretation that LOS pyrite is a separate generation of pyrite that formed after POS, OS 1, and OS 2 pyrites is supported by both spatial and temporal relationships with late-ore-stage quartz and realgar, and subtle geochemical differences.

Principal Components Analysis of Late-ore-stage Pyrite

Principal components analysis of LOS pyrite (Tables 17 and 21) identified seven components that account for 75.733% of the data. The KMO value and Bartlett's Test of Sphericity indicate that these results are acceptable. Using the Catell's Scree Test (Appendix F.8) components 1 and 2 are above the change in slope and contribute 40.64 % cumulative variance of the data. Component 1 includes Fe, S, Co, Pb, (Si, Al, Ti, and Ca) with a total eigenvalue of 5.433, and a variance of 25.87 %. Component 2 includes Hg, Sb, Tl, As, Sn, Ag, Cu, and Se with a total eigenvalue of 3.101 and a variance of 14.76 %. Components 3-7 are below the change in slope and are not discussed (Appendix F.8).

Interpretation

Component 1 for LOS pyrites identified an inverse relationship between the LOS pyrite elements Fe, S, Co, and Pb, with Si, Al, Ti, and Ca in host rocks reflecting analyses of pyrite plus host rock minerals. Component 2 for LOS pyrite identified a positive correlation between Carlin-type pathfinder elements Hg, Sb, Tl, As, and Cu together with Sn, Ag, and Se, which, though of low abundance, may vary similarly within LOS pyrite.

Realgar

Realgar veins cross-cut Webb Formation and fill vugs in Devil's Gate, Webb, and Chainman Formations. Realgar fills open spaces and conforms to euhedral crystals of quartz in veins and vugs (Fig. 40 A, B), and hair-line veins of realgar cross-cut quartz veins. Realgar is most commonly overgrown by later calcite and occasionally barite that infill veins and vugs (Fig. 40 A, B). Realgar crystals occur as small inclusions in calcite and/or barite veins, indicating realgar crystallized first and was later encapsulated by these minerals. Less common relationships include the presence of small fragments of realgar as inclusions within euhedral drusy quartz crystals in veins (Fig. 40 D) or realgar crystals rimming host rock clasts with drusy quartz conforming to realgar (Fig. 40 C). Anhedral realgar and LOS anhedral pyrite occur within a collapse breccia cemented by a microcrystalline quartz matrix (Fig. 41 F, G, and H). These textures indicate that realgar most commonly precipitated after late-ore-stage drusy quartz, but late-ore-stage quartz and realgar precipitation did overlap.

Calcite

Coarsely crystalline calcite filled vugs or formed veins that cross-cut all host rocks, and all previous vein types. Coarsely crystalline calcite veins cross-cut Devil's Gate, Webb, and Chainman Formations and fills vugs in Devil's Gate, Webb, and Chainman Formations, and Tertiary porphyry dacite dike. Coarsely crystalline calcite conforms to euhedral quartz in veins or vugs, or to realgar that rims vugs in host rock (Fig. 40 A). Less commonly, post-ore-stage barite conforms to coarsely crystalline calcite.

Post-ore-stage Minerals

Barite

Post-ore-stage barite primarily occurs as vug fillings and veins. Barite veins cross cut Devil's Gate, Webb, and Chainman Formations. Barite fills vugs in Devil's Gate, Webb, and Chainman Formations, and in Tertiary porphyry dacite dikes. Barite conforms to pre-, ore-, and late-ore-stage euhedral quartz, late-ore-stage realgar (Fig. 40 B, E), and late-ore-stage coarsely crystalline calcite that rims veins or vugs. Barite also cross cuts LOS pyrite, and conforms to massive sulfidized breccia clasts (Fig. 41 B).

Post-ore-stage barite occurs within mineralized Mississippian Webb mudstone/sandstone breccia sample 12-01A 1226.5 as veins that cross-cut brecciated host rock or as brecciated fragments (Fig. 44 A). Barite conforms to host rock minerals, quartz, +/- illite, and carbon. Barite veins are cross-cut by dissolution veins (Fig. 44 A-C) that contain quartz, jasperoid, illite, carbonaceous material, and pyrite +/- ore-stage 2 rims, +/- stephanite (Fig. 44 D, E) that do not appear to have precipitated within fracture, but were transported mechanically as clasts by fluids.

Stephanite

Stephanite (Ag_5SbS_4) occurs as deep red to black anhedral crystals within mineralized Mississippian Webb mudstone/sandstone breccia sample 12-01A 1226.5. The composition was confirmed by EPMA, which also determined that this mineral lacks gold (Appendix F.9). Stephanite conforms to post-ore-stage barite and host rock quartz, illite, and carbon (Fig. 44 F, I), infills vugs in brecciated host rock (Fig. 44 I), and appears as fragments within a dissolution vein (Fig. 44 C). Stephanite also occurs as

inclusions within late- to post-ore-stage quartz, (Fig. 44 G, H), and within growth zones of post-ore-stage barite (Fig. 44 F, I).

Interpretation

Stephanite occurs in vugs in Mississippian Webb breccia, conforming to and forming as inclusions within late- to post-ore-stage quartz and post-ore-stage barite. This consistent relationship suggests that stephanite formed concurrent with and after post-ore-stage barite mineralization. Cross cutting relationships that indicate that stephanite precipitation is associated with formation of post-ore-stage barite indicates that Ag mineralization is part of the post-ore stage (Fig. 44).

Minor Post ore-stage Minerals

White clays including well-ordered, crystalline kaolinite and poorly-ordered halloysite, identified through XRD and Terra-spec analyses, occur along fractures that cross cut calcite veins in unmineralized and mineralized samples in all formations. These clays are related to weathering. Trace amounts of goethite and hematite occur along quartz crystal boundaries within Mississippian Webb and Chainman Formations.

Mineral Paragenesis Discussion

The mineral paragenesis of the North Bullion Carlin system (Fig. 15) includes late-ore-stage quartz, LOS pyrite, realgar, and calcite, and post-ore-stage barite, stephanite, kaolinite, halloysite, goethite, and hematite. Late-ore-stage pyrite and realgar formed after ore-stage mineralization and alteration, but prior to late-ore-stage calcite and post-ore-stage barite. The common paragenetic sequence for veins and vugs from early to late is drusy euhedral quartz, realgar, and calcite, followed by barite and locally stephanite. However, in some samples quartz precipitated after realgar and LOS pyrite

and concurrent with post-ore-stage stephanite. These observations are consistent with silicification coincident with realgar, LOS pyrite, and stephanite, but not with calcite and barite. Stephanite crystals conform to and are inclusions within post-ore-stage barite crystals, indicating stephanite also precipitated during the post-ore stage. Coarsely crystalline calcite mineralization extends to the post-ore stage, as it cross-cuts all host rocks and all other vein types. Kaolinite, halloysite, goethite, and hematite are the latest secondary minerals to form and are related to supergene oxidation and weathering.

CHAPTER 7

BRECCIATION

Samples of both collapse and tectonic breccias were examined to identify the timing of mineralization relative to the timing of brecciation. Two types of breccias, a collapse breccia consisting of Devonian Devil's Gate Formation and a tectonic breccia located between the North Bullion and Massif faults (Figs. 8, 9), have been identified at the North Bullion Carlin system. There are no petrographic textures that identify them as either collapse or tectonic breccias, but are distinguishable by their geometries. Within the cross sections, samples are identified as collapse or tectonic breccia based on their location (Figs. 8, 9); however, there are areas where breccias are formed by both collapse and tectonic processes.

Collapse brecciation is associated with dissolution of the Devonian Devil's Gate Formation, which shows textures that indicate collapse brecciation was concurrent with ore-stage mineralization. All Devil's Gate samples of breccia examined in this study are collapse breccias (Fig. 8). Collapse brecciation in the Devil's Gate increases in intensity with proximity to the North Bullion Fault Zone (Figs. 8, 9, and 35). These samples also become more fractured and show increasing porosity, decarbonatization, and abundance of jasperoid, illite, and carbonaceous material with increasing gold grade (Fig. 35). Pre-ore-stage pyrites with OS 2 pyrite rims occur in collapse breccias within both matrix and clasts, but predominate in clay-rich matrix.

Tectonic breccias are related to movement along the North Bullion and Massif faults and textural relationships between the breccias and ore- and late-ore-stage minerals indicate tectonic brecciation occurred prior to, concurrent with, and post-date ore-stage

mineralization. Pre-ore-stage pyrites with OS 2 pyrite rims occur in tectonic breccias within both matrix and clasts, but predominantly in clay-rich matrix, and indicate that the timing of tectonic brecciation is prior to, and/or coincident with ore-stage mineralization. Late-ore-stage secondary hydrothermal quartz encompasses breccia clasts (Fig. 39 A, B), indicating that brecciation occurred prior to late-ore-stage quartz. Late-ore-stage pyrite that encompasses POS pyrite, jasperoid, and late-ore-stage quartz, is brecciated and forms clasts that are encompassed by post-ore-stage barite (Fig. 41 A, B), indicating brecciation after LOS pyrite formed, but prior to post-ore-stage barite. Within the multi-lithic tectonic breccia zone (Figs. 8, 9), the breccia textures are cross cut by post-ore-stage barite veins (Fig. 44), indicating that brecciation occurred prior to post-ore-stage barite.

Interpretation

Petrographic studies demonstrate that collapse breccias formed prior to and/or coincident with the ore stage, and tectonic breccias within the area formed prior to, coincident with, and following the ore stage (Fig. 15). If OS 2 pyrite was restricted to breccia clasts it would suggest mineralization occurred prior to brecciation, and if OS 2 pyrites were restricted to the matrix it would suggest mineralization occurred coincident with or after brecciation. With OS 2 pyrite occurring in both clasts and matrix it may indicate that the timing of collapse brecciation is closely associated with ore-stage mineralization or, occurred after mineralization.

Fault movement and multi-stage brecciation occurred prior to, with, and following gold mineralization, suggesting that the porosity and permeability of the host rocks was varied and that multiple faulting events and extensive brecciation likely caused hydrothermal ore fluid pathways to have evolved through time. The lack of robust OS 2

pyrite rims on any POS pyrites may have resulted from silicification that sealed fluid pathways, and along with structure, contributed to varied host rock permeability through time.

CHAPTER 8

WHOLE ROCK GEOCHEMISTRY

Whole rock trace and major element geochemical data collected on approximately five-foot intervals from 14 drill holes were reduced to a smaller sample set using a randomized selection of 1/3 of the data. The final data set was analyzed using several statistical calculations and models to determine patterns in the whole rock geochemical data related to gold mineralization.

Classification Support Vector Machine

The classification support vector machine statistical method was applied to the whole rock data using Au classifications of 0.1 and 1.0 ppm. This method separates all data into two data sets; one contains samples with Au less than the Au classification, and the second data set contains samples with Au greater than the gold classification. Within each of those two sets of data, the method compares Au to each other analyte (each of the 36 elements analyzed separately) to determine the degree to which the analyte predicts the presence or absence of Au at the specified Au classification (0.1 or 1.0 ppm Au) (Miller-Coleman et al., 2012). For those elements that have a high percentage of predicting the presence or absence of gold (Tables 22 and 23), inspection of the Spearman rank correlation matrix (Table 24) indicates whether the elements (Tables 22 and 23) is positively or negatively correlated to Au. For example, As has a 73.35 % ability to predict gold for 0.1 ppm classification (Table 22). The Spearman rank correlation matrix value is 0.489 (Table 24), thus As predicts the presence of Au. The accuracy floor value (Tables 22 and 23) is a percentage value determined for non-predicting elements (i.e. an element that has no correlation to gold). For example, U, an

element that has no correlation to gold, has a 65.38 % ability to predict both the presence and absence of gold for 0.1 ppm classification (Table 22), which by definition is the accuracy floor for U.

Using a gold classification of 0.1, the CTGD pathfinder elements (Table 22), have the following accuracy at predicting either the presence or absence of gold: Hg (84.01%), Sb (81.67%), Tl (79.27%), and As (72.40%). As these are known pathfinder elements these elements predict the presence of Au. Other indicator elements include V (76.45%), P (75.46%), Mg (73.55%), Al (73.35%), Mn (73.34%), Ca (72.91%), and Cd (72.75%). The value of the accuracy floor for this calculation is 65.38 %. Analysis of a gold classification of 1.0 ppm gold classification (Table 23) shows that the pathfinder elements have the following accuracy at predicting the presence or absence of gold: Tl (93.91 %), Hg (92.93 %), As (92.80 %), and Sr (92.34 %). The accuracy floor for this analysis is 92.19 %.

Interpretation

Classification support vector machine analysis and the Spearman rank correlation matrix determined that Hg, Sb, Tl, Cd, and As, listed in decreasing order, are the elements that best predict the presence of gold at the 0.1 ppm classification (Table 22). Elements V, P, Mg, Al, Mn, and Ca, listed in decreasing order, are the elements that best predict the absence of gold at the 0.1 ppm classification. Thallium, Hg, and As, listed in decreasing order, are the elements that best predict the presence of gold at the 1.0 ppm gold classification (Table 23). Strontium best predict the absence of gold at the 1.0 ppm classification. The classification support vector machine and Spearman rank correlation matrix demonstrate that Hg and Sb can best predict the presence of gold in low-grade

rock (0.1 ppm gold) and Tl and Hg can best predict the presence of gold in high-grade rock (1.0 ppm Au).

Non-metric Multi-Dimensional Scaling Model

The non-metric multi-dimensional scaling model reduces a data set with multiple variables so that it can be viewed with the least number of ordination axes possible, and on an X-Y plot. Each variable and data point are plotted based on R and R^2 values relative to each ordination axis. R values measure of the linear correlation between two variables (Axis 1 or 2 and an element (X)); +1 indicates a 100% positive correlation, -1 indicates a 100% negative correlation, 0 indicates no correlation, and values in between indicate correlations that are less than 100 % positive or negative. R^2 values equal the square of the R value. The lengths of the line for the variables (elements) and the positions of the variables on the graph indicate the degree to which the variables (elements) correlate with the axis, and a longer line indicates a stronger correlation (Figs. 45, 46). Lines that cluster or group indicate variables (elements) that have similar behavior.

A non-metric multi-dimensional scaling model calculation using a 0.100 ppm gold classification (Fig. 45) illustrates that samples with $Au > 0.100$ ppm, shown as pink triangles, cluster in the bottom right corner and extend to the right, and the top right corner of the image. The lengths of the element lines and their positions on the graph (Fig. 45) show that the samples largely fall into four groups. These groups include group1: Ca, Mg, Ba, Sr, and Na; group 2: K, Al, Fe, Cu, Ni, P, V, Co, Cr, S, Pb, Mo, and Zn; group 3: Be and Sc; and group 4: Au, Sb, and Hg. This model (Fig. 45) illustrates that As is located between groups 2 and 4. Elements included in the Table 25 that are not

significant and would have a short line length are not plotted in Figures 45 and 46.

Thallium and Ag are not significant and do not appear in Figures 45 and 46. However, numerical results (Table 25) show that Tl would plot at (0.193, -0.256), where it would cluster with Hg, Sb, and Au in group 4. Numerical results for Ag (Table 25) show that it would plot at (0.101, -0.409), where it would cluster with Mo and Zn in group 2.

The non-metric multi-dimensional scaling model calculation using a 1.00 ppm gold classification (Fig. 46) illustrates that samples with Au > 1.00 ppm shown by pink triangles, cluster in the southeast quadrant of the figure. The element groups are the same as those described for the 0.1 ppm classification. This gold classification highlights how higher-grade samples plot relative to Axis 1 and Axis 2.

Interpretation

The non-metric multi-dimensional scaling model element shows that the samples largely fall in four classes: 1) Ca, Mg, Ba, Sr, and Na, which are dominantly in carbonate rocks, 2) K, Al, Fe, Cu, Ni, P, V, Co, Cr, S, Pb, Mo, and Zn, which are dominantly in siliciclastic rocks, POS pyrite, and/or base metal minerals, 3) Au, Hg, and Sb, which are Carlin hydrothermal elements, and 4) Be and Sc. The model also illustrates that Au and the CTGD pathfinder elements plot roughly half way between the elements that represent the two rock types, but closer to the siliciclastic group. This positioning indicates that Au and pathfinder elements are associated with both siliciclastic and carbonate rocks at North Bullion, but are more closely associated with the siliciclastic rocks as indicated by the cluster of pink data points in the lower right hand quadrant (Fig. 45, 46). Elements Be and Sc plot opposite Au and, thus, are negatively correlated with Au. Silver, which would plot near Mo and Zn, is unrelated to Au. The scaling models illustrate that the majority of

samples containing Au > 0.1 and > 1.0 ppm cluster in bottom right quadrant and fewer samples in top right quadrant, which is consistent with siliciclastic rocks in the upper gold zone comprising the majority of mineralized samples (Fig. 3) and a minority of samples that contain Au > 1 ppm are found in the Lower Gold Zone (Fig. 3) dissolution collapse breccia in carbonate rocks.

Spearman Rank Correlation Matrix

A Spearman rank correlation matrix of all whole rock geochemistry is illustrated in Table 24. Gold exhibits a strong positive correlation (≥ 0.4) with Hg (0.696), Sb (0.694), Tl (0.559), and As (0.489) and a strong negative correlation (≤ -0.4) with Be (-0.419). Iron exhibits a strong positive correlation with Cu (0.841), Ni (0.831), V (0.826), K (0.815), Al (0.814), Co (0.796), P (0.787), Sc (0.787), S (0.722), Cr (0.695), Pb (0.629), Mo (0.592), Zn (0.569), Tl (0.559), As (0.555), Be (0.502), and Ag (0.466), and a strong negative correlation with Ba (-0.677), Ca (-0.674), Mg (-0.620), Na (-0.452), and Sr (-0.467).

Interpretation

The Spearman rank correlation matrix determined that Au has a strong positive correlation with the Carlin-pathfinder elements, Hg, Sb, Tl, and As. This analysis identified positive correlations between Fe and elements related to siliciclastic rocks (Al, K, P, V, Cr, Sc, plus Be), to pyrite (S, Co, Pb, Ni, plus Cu), to base metal mineralization (Mo, Zn, plus Ag). Iron has a strong negative correlation to elements that are related to the carbonate rocks including Ba, Ca, Mg, Na, plus Sr.

Mann-Whitney U-Test

The Mann-Whitney U-Test, previously described for POS and ore-stage pyrites, was applied to seven gold classifications of 0.004, 0.1, 0.3, 1.0, 2.0, 3.0, and 6.0 ppm Au in order to examine the distribution of various elements in relation to gold in whole rock geochemical data (Table 26; Figs. 47-51). The calculated “asymptotic significant values”, if <0.005 , indicate that the difference in the median values for a gold class is significant, and these values are highlighted in blue (Table 26). Significant differences of median values are further identified on bar graphs by the lack of the symbol * (Figs. 47-51).

Results show that there is no significant difference between the median values of Bi and W in all gold classifications (Table 26). Median values determined for B, Be, Cd, Ga, La, Th, and U are constant for all gold classifications, and results for some gold classifications indicate no significant difference between the two median values (Table 26); medians for these element were not plotted. Median values for Sc and Ti were also not plotted as they show little change (Table 26).

Gold and the Carlin pathfinder elements As, Hg, Sb, and Tl all have significant differences for all or some median values (Table 26) and show similar patterns of higher median values in the high gold class (orange) (Fig. 47), and these median values increase with increasing gold classification with the exception of Sb. Median values are significantly lower in low gold class samples (blue) for these elements, with the exception of Tl, which has median values that do not vary for the low and high gold class for the 0.004 and 0.1 ppm gold classification. Gold’s median concentrations in the high gold class (orange) increase significantly from 0.48 ppm Au in the 0.004 ppm gold classification to 10.55 ppm in the 6 ppm gold classification. The As median

concentrations in the high gold class (orange) increase significantly from 69 ppm As in the 0.004 ppm gold classification to 1560 ppm in the 6 ppm gold classification. The Hg median concentrations in the high gold class (orange) increase significantly from 1 ppm Hg in the 0.004 ppm gold classification to 35 ppm in the 6 ppm gold classification. Alternatively, the range of As and Hg concentrations in the low gold class (blue) are significantly lower and increase very little from the 0.004 ppm to the 6 ppm gold classification. The Tl median concentrations in the high gold class (orange) increase significantly from 9 ppm Tl in the 0.004 ppm gold classification to 50 ppm in the 6 ppm gold classification; however, thallium's median concentrations in the low gold class (blue) remain constant at 9 ppm. The Sb median concentrations in the high gold class (orange) increase significantly from 6 ppm Sb in the 0.004 ppm gold classification to 34 ppm in the 2 ppm gold classification, and then decrease to 12 ppm in the 6 ppm gold classification. Alternatively, Sb median concentrations in the low gold class (blue) increase very little from the 0.004 ppm to the 6 ppm gold classification.

The base metals elements Ag, Mo, and Zn show patterns similar to one another in which the median values for the lower gold classes are the same or similar, but high gold classifications medians vary (Table 26; Fig. 48). Patterns further show an increase in median values for the high gold class (orange) from low to intermediate gold classifications followed by a decrease from intermediate to high gold classifications (Fig. 48). Silver, Mo, and Zn median values for the low gold class (blue) are generally less than or equal to the high gold class median values (orange) (Fig. 48).

Median values for Fe, S, Pb, Co, Ni, and Cu, elements that are commonly present in POS pyrites, exhibit generally similar patterns for both the low and high gold classes

(Fig. 49), and the differences in median values for the low and high gold classes are usually significant, though exceptions occur for the low gold classifications for Fe, Cu, Ni, and Co (Table 26). The median values for the high gold class (orange) for Fe, S, Pb, Cu, Ni, and Co increase with increasing gold classification (Fig. 49). Median values for Fe, S, Pb, Cu, Ni, and Co typically have lower median values in the low gold class samples (blue), with the exception of Fe, Cu, Ni, and Co, which have median values that are higher for the low gold class (blue) in the 0.004 ppm gold classification and for Cu and Co for the 0.1 ppm gold classification (Fig. 49). Iron's median concentrations in the high gold class increases significantly from 1.5 wt. % Fe in the 0.004 ppm gold classification to 2.81 wt. % in the 6 ppm gold classification. Sulfur's median concentrations in the high gold class increases significantly from 0.78 wt. % S in the 0.004 ppm gold classification to 3.09 wt. % in the 6 ppm gold classification. Lead's median concentrations in the high gold class increases very little from 9 ppm Pb in the 0.004 ppm gold classification to 17 ppm in the 6 ppm gold classification. Copper's median concentrations in the high gold class increases significantly from 11 ppm Cu in the 0.004 ppm gold classification to 35.5 ppm in the 6 ppm gold classification. Nickel's median concentrations in the high gold class increases significantly from 14 ppm Ni in the 0.004 ppm gold classification to 29 ppm in the 6 ppm gold classification. Cobalt's median concentrations in the high gold class increases very little from 3 ppm Co in the 0.004 ppm gold classification to 9 ppm in the 6 ppm gold classification. Median concentrations in the low gold class for Fe, S, Pb, Cu, Ni, and Co changed very little from the 0.004 ppm to the 6 ppm gold classification.

The median values for low to high classifications for Al, K, Cr, P, and V, elements that are commonly in siliciclastic host rocks, are variably significant (Table 26; Fig. 50); however, all values are significantly different for all gold classes for Al and K. The median values for the high gold class (orange) for Al and K increase with increasing gold classification; these values increase at low classifications for Cr, P, V, but decrease for the 6.0 ppm gold classification (Fig. 50). Median values of low gold class samples (blue) generally exhibit an inverse relationship in which the lowest gold class has the highest median value, with median values decreasing, generally irregularly with high gold classifications (Fig. 50). Aluminum, K and Cr exhibit very small changes in medium concentrations in both the low and high gold classifications. Even though the median values for Cr, P, and V are significant; the bar graphs show that they are not distinctive and are not useful in determining the presence or absence of gold.

The low and high gold class median values for Ba, Ca, Mg, Mn, Sr, and Na, elements that are commonly present in carbonate host rocks, are all significantly different with the exception of the low gold class for Ca (Table 26; Fig. 51). The median values for the high gold class (orange) for Ca, Mn, Mg, Sr, and Ba) show a significant decrease from the low to high gold classifications, and values are significantly lower at classifications of 0.3 and higher compared to classifications of 0.004 and 0.1 (Fig. 51). The median values for the low gold class (blue), the change in concentrations is less dramatic and the higher concentrations occur at intermediate gold classifications (Fig. 51). The median values in the low gold class are higher than the high gold class with the exception of Ca and Mg for the 0.004 ppm gold classification (Fig. 51). Even though the

median values for Na are significant; the values are low and may not be useful in determining the presence or absence of gold.

Interpretation

The Mann-Whitney U-Test has identified the following trends. The median values for gold and CTGD pathfinder elements are higher in the high gold class and increase with increasing gold grade, because they were added by gold-bearing hydrothermal fluids, but not elevated in the low gold class. Antimony median values increase, peak at the 2.0 ppm gold classification, then decrease with increasing gold grade, indicating Sb is an indicator element at low to moderate gold grade but not necessarily high grade. The CTGD pathfinder elements (As, Hg, and Sb) median values have significant differences between gold classes at moderate to high Au grade (> 0.3 ppm Au), indicating these would be useful indicators in predicting the presence of Au. Thallium median values have significant differences between gold classes at high Au grade (> 2.0 ppm Au), indicating these would be useful indicators in predicting the presence of high grade Au.

Median values for base metals Ag, Mo, and Zn behave differently from Au and Carlin pathfinder elements, are elevated in the high gold class at intermediate gold classifications, and are likely related to a different non-Au hydrothermal event. Median values for Fe, S, Pb, Co, Ni, Cu, Al, and K are elevated in the high gold class and increase with increasing gold classification, because these elements are in the siliciclastic rocks and may indicate an increase in pyrite and illite with increasing Au. Iron, S, Pb, Co, Ni, Cu, Al, and K median values have significant differences between gold classes at moderate to high Au grade (> 1.0 ppm Au), indicating these would be useful indicators in predicting the presence of Au. Median values for Ba, Ca, Mg, Mn, and Sr are reduced in

high gold class because of decarbonatization, and higher concentrations in the low grade class and median values are largely unchanged because there was no decarbonatization. Barium, Ca, Mg, Mn, and Sr median values have significant differences between gold classes at moderate to high Au grade (> 0.3 ppm Au), indicating these would be useful indicators in predicting the absence of Au.

Discussion

Multiple statistical calculations including the classification support vector machine, Spearman's rank correlation matrix, non-metric multi-dimensional scaling model and Mann-Whitney U-Test of whole rock geochemical data identified several geochemical relationships similar to relationships identified at the micro scale of the pyrite geochemical analyses. At the pyrite scale, Spearman rank correlation matrix showed Au does not have a strong correlation with any other element, but that the CTGD pathfinder elements do have strong correlations with each other. The Mann-Whitney U-Test of pyrite data showed Co and S do have significantly different medians for the low and high gold classes for all gold classifications; Co and S are elevated in the low gold class and may be an indicator element for the absence of Au. The Mann-Whitney U-Test of pyrite data shows that Al, Si, Fe, As, Tl, Bi, Sn, Ti, Zn do not have significantly different medians for the low and high gold classes, indicating their concentrations are not related to gold concentration.

Each of the statistical calculations of whole rock geochemical data favor different elements in terms of their ability to predict the presence or absence of gold. The NMS model of whole rock data identified four element groups (group 1: Ca, Mg, Ba, Sr, and Na; group 2: K, Al, Fe, Cu, Ni, P, V, Co, Cr, S, Pb, Mo, and Zn; group 3: Be and Sc; and

group 4: Au, Sb, and Hg) related to the geology of the samples; however, only group 4 includes elements directly related to the presence of gold. The C-SVM method, with a 0.1 gold classification interpreted with the Spearman rank correlation matrix, shows that the best predictors of the presence of Au are As, Hg, Tl and Sb, good predictors are Cd, Pb, and S, and weak predictors are Ag, Mo, and Zn. Arsenic, Hg, and Tl are the only elements that best predict gold for the 1.0 gold classification. The C-SVM method, with a 0.1 gold classification interpreted with the Spearman rank correlation matrix, shows that the elements that best predict the absence of gold are Ba, Mn, and Sc, good predictors are Al, K, P, and V, and weak predictors are Ca, Co, Cr, Cu, Fe, Mg, Ni, and Sr. Strontium is the only element that weakly predicts the absence of gold for the 1.0 gold classification. The Mann-Whitney U-Test determined that As, Hg, Sb, and Tl have significantly different medians for the low and high gold classes for moderate to high gold classifications; As, Hg, Sb, and Tl are higher in the high gold class and are the best indicator elements for the presence of Au. The test further determined that Fe, S, Pb, Cu, Ni, Co, Al, and K have significantly different medians for the low and high gold classes for moderate to high gold classifications; Fe, S, Pb, Cu, Ni, Co, Al, and K have higher concentrations in the high gold class and could be good indicator elements for the presence of Au. Barium, Ca, Mg, Mn, and Sr also have significantly different medians for the low and high gold classes for moderate to high gold classifications; Ba, Ca, Mg, Mn, and Sr have higher concentrations in the low gold class and may be good indicator elements for the absence of Au.

During exploration drilling, Ba, Mn, Al, P, Cr, and V are elements could indicate proximity to gold mineralization. These have high median concentrations in the low gold

class at the 0.004 ppm Au classification, and significantly lower median concentrations in the high gold class. These elements could provide significant information about proximity to a hydrothermal system, indicating the presence of a halo that may contain a deposit.

CHAPTER 9

CONCLUSIONS

North Bullion gold mineralization is hosted in Devonian shelf carbonates, and Mississippian foreland basin flysch, in coarsening upward assemblages. These host rocks are atypical for Carlin deposits. However, the style of mineralization and alteration present at the North Bullion Carlin system is similar to other large-scale CTGD in the region. Carlin-type mineralization at North Bullion, and at the nearby Rain and Emigrant deposits indicates the potential for the discovery of CTGD in other underexplored areas in Northern Nevada.

- Deposit-scale controls of gold deposition include structures, the North Bullion and Massif Faults, and lithologic contacts between the Devonian Devil's Gate, Mississippian Webb and Mississippian Chainman Formations. Intersections of two or more of these features created permeable pathways along which host rocks reacted with hydrothermal ore fluids and were preferentially mineralized.
- Gold mineralization does not extend above the dacite dikes and sills within the Mississippian Chainman Formation, consistent with the possibility that the dacite dikes provided a local seal to mineralizing ore fluids.
- The uppermost horizon of mineralization occurs within the Webb Formation at a lithological contact between limestone and mudstone, with preferentially higher grade in the mudstone host rock; grade decreases away from this contact in the mudstone.

- The lowermost horizon of gold mineralization occurs within the Devonian Devil's Gate limestone collapse breccia and the multi-lithic tectonic breccia along the North Bullion Fault Zone and Massif fault.
- Collapse breccias formed coincident with gold mineralization and tectonic breccias formed prior to, coincident with, and following mineralization. Multi-stage tectonic brecciation was related to multiple episodes of movement and long-lived hydrothermal activity along the Bullion Fault corridor and other related structures in the area.
- Four generations of pyrite identified at North Bullion include diagenetic POS pyrite, present within sedimentary host rocks, and which locally contains elevated Pb, Co, and Ni. Gold-bearing OS 1 pyrites occur within Tertiary porphyritic dacite dikes, and contain Au, Pb, Co, and variable Bi and Ti. Carlin-type OS 2 pyrites that contain Au and variably elevated As, Cu, Hg, Sb, and Tl formed partial sub-micrometer rims on POS and OS 1 pyrites, and also formed OS 2 microcrystals. Ore-stage 2 pyrites at North Bullion may be representative of ore-stage pyrites in low-grade zones in large, high-grade deposits that are less commonly studied. Late-ore stage pyrites contain elevated Ag and Pb, with variable Bi, Sn, and Zn, and they locally contain As and Sb, and low, variable Au.
- At the deposit scale North Bullion host rocks have been decarbonatized, argillized, and silicified, exhibiting alteration similar to known CTGD, though alteration is subtle and not as well developed as in higher-grade CTGD. Alteration minerals adjacent to OS 1 pyrite include quartz, illite, and kaolinite,

and alteration minerals adjacent to OS 2 pyrite include jasperoid, illite, and concentrated carbon.

- High silver grades ($\leq \sim 20$ oz/t) are related to the presence of stephanite (Ag_5SbS_4), which precipitated during the post-ore stage, probably related to one of the later intrusive events.
- Statistical analyses of whole rock geochemistry indicate that exploration at North Bullion would benefit by evaluation of elements in addition to Carlin-type pathfinder elements. Carlin-type pathfinder elements correlate best with gold, and elevated Hg and Sb are strong indicators of gold in low- to moderate-grade samples, and Tl, Hg, and As are strong indicators of gold in moderate- to high-grade samples. Statistical analyses also determined that Fe, S, Pb, Co, Ni, Cu, Al, and K predict the presence of gold in moderate- to high-grade gold samples, and that Ba, Ca, Mg, Mn, and Sr predict the absence of gold in moderate- to high-grade samples. Barium, Mn, Al, P, Cr, and V have high median concentrations at low gold grade samples peripheral to ore, and median concentrations decrease significantly with increasing grade; thus, significantly they could indicate the periphery of gold mineralization.

APPENDIX A

TABLES

Table 1. List of acronyms

CTGD	Carlin Type Gold Deposit
GSV	Gold Standard Ventures Corporation
Dtc	Devonian Telegraph Canyon Formation
Ddg	Devonian Devil's Gate Formation
Mw	Mississippian Webb Formation
Mc	Mississippian Chainman Formation
Te	Tertiary Elko Formation
Tiw	Tertiary Indian Well Formation
NBFZ	North Bullion Fault Zone
UNLV	University of Nevada, Las Vegas
EMiL	Electron Microanalysis and Imaging Laboratory
SEM	Scanning Electron Microscope
EMPA	Electron Probe Microanalyzer
LA-ICP-MS	Laser Ablation - Inductively Coupled Plasma - Mass Spectrometry
XRD	X-ray Diffraction
USGS	United States Geological Survey
C-SVM	Classification Support Vector Machine
NMS	Non-metric Multi-dimensional Scaling model
OA-IOCS	Off Axis – Integrated Output Cavity Spectroscopy
MDL	Method Detection Limit
POS	Pre-ore-stage Pyrite
OS 1	Ore-stage 1 Pyrite
OS 2	Ore-stage 2 Pyrite
LOS	Late-ore-stage Pyrite

Table 2. Probe Conditions

20 kV, 100nA, 1-2 μ m			
TRACE	1	2	3
	TAP	PETH	LIF
	Se	Ag	Tl
	Al	Hg	Au
	Zn	Pb	Bi
	As	W	Cu
	Si	Te	Ni
		Sb	Co
		Sn	Ti
		Mo	Fe
		Ca	
		S	
Run Time (sec)	140	390	590
Instrument: JEOL-8900 Electron Probe Microanalyzer.			

Table 3. X-ray line, spectrometer, peak data, and minimum detection limit for the suite of elements used for EMPA analysis at the North Bullion Fault Zone

Element	X-ray	Spectrometer	Crystal	Peak (mm)	Back [H+I] (mm)	Back [L-I] (mm)	Peak (sec)	Back (sec)	MDL (ppm)	Standard
Ag	L β	SP2	PETH	133.285	2	2.5	30	15	30	CM1- Ag
Al	K α	SP1	TAP	90.697	5.5	5	20	10	22	SMH- Plagioclase
As	L α	SP1	TAP	105.145	5	5	30	15	32	MAC- Arsenic
Au	L α	SP3	LIF	88.741	4	2.8	200	30	144	GLR- Au
Bi	L α	SP3	LIF	79.461	5	5	120	30	220	CM1- Bi
Ca	K α	SP2	PETH	108.1	2.8	2.8	30	15	15	MAC- Wollastonite
Co	K α	SP3	LIF	124.506	5	5	30	15	43	GLR- CO
Cu	K α	SP3	LIF	107.174	2.8	2.8	30	15	59	MAC-Chalcocopyrite
Fe	K α	SP3	LIF	134.709	4	2	30	15	47	MAC- FeS2
Hg	M α	SP2	PETH	180.983	2.4	2.4	120	30	38	CM2- HgS
Mo	L β	SP2	PETH	165.869	5	5	30	15	40	GLR- Mo
Ni	K α	SP3	LIF	115.308	4.5	4.5	30	15	44	GLR- Ni
Pb	M α	SP2	PETH	169.465	5.5	3	30	15	64	MAC- PbS

Table 3. Continued

Element	X-ray	Spectrometer	Crystal	Peak (mm)	Back [H+] (mm)	Back [L-] (mm)	Peak (sec)	Back (sec)	MDL (ppm)	Standard
S	K α	SP2	PETH	172.089	5	5.5	30	15	12	MAC- FeS ₂
Sb	L β	SP2	PETH	110.634	4	4	30	15	42	CM1- Sb
Se	L α	SP1	TAP	97.705	2.75	5	30	15	33	CM1- Se
Si	K α	SP1	TAP	77.435	2.25	2.25	30	15	22	SMH- Plagioclase
Sn	L β	SP2	PETH	115.669	1.5	1.5	30	15	33	CM1- Sn
Te	L β	SP2	PETH	105.058	3.75	3.75	30	15	55	CM2- PbTe
Ti	K α	SP3	LIF	191.192	1.5	1.5	30	15	57	SMH-Ilmenite
Tl	L α	SP3	LIF	83.921	1.2	0.98	120	30	169	CM2- TlBr
W	M α	SP2	PETH	223.57	3	3	30	15	279	CM1- W
Zn	L α	SP1	TAP	133.266	5	5	30	15	52	MAC- ZnS

Instrument: JEOL-8900 Electron Probe Microanalyzer.

Abbreviations: K α = K alpha-line x ray; L α = L alpha-line x ray; L β = L alpha-line x ray; M α = M alpha-line x ray; SP = spectrometer; TAP = Thallium acid phthalate; PETH = High pentaerythritol; LIF = Lithium fluoride; Back[H+] = high background; Back[L-] = low background; MDL = Method detection limit; MAC, SMH, GLR, CM1, CM2 = standard blocks.

Table 4. LA-ICP-MS conditions

Laser System		ICP-MS	
Wavelength	193 nm	rF Power	1300 W
Spot Size	12 μm	Carrier Gas (He)	0.8/min
Pulse Frequency	20 (Hz (lines/maps))	Makup Gas (Ar)	0.6 l/min
Scan Speed	2 $\mu\text{m}/\text{sec}$		
Energy Density	$\sim 5 \text{ J}/\text{cm}^2$		

Instrument information: Photon Machines Analyte G2 LA system (193 nm, 4 ns Excimer laser) coupled to a PerkinElmer DRC-e Inductively Coupled Plasma Mass Spectrometer.

Table 5. X-Ray Diffraction Settings

Configuration	Sample Spinner
Scan Axis	Gonio Th/ 2Th
Scan Mode	Lock Coupled
Start Angle	5.00
End Angle	76.0040
Step Size	0.003931779
Time per step	17.780 0.17
Scan Speed	0.029842
Number of Steps	18059
Sample disk diameter	27 mm
Total Time	56 minutes

Instrument information: Bruker AXS D8 Advance with 1D LynxEye detector Cu K alpha
1- xray frequency wavelength, PANalytical X'PERT Pro X-ray Diffraction Spectrometer

Table 6. Multi-element Geochemical Laboratory Analysis Techniques

ALS Geochemistry Laboratories Assay Techniques			
ALS Method	Digestion Methods	Elements Analyzed	Detection Range
ME-ICP41	Aqua Regia	Ag, Al, As, B, Ba, Be, Bi, Ca, Cd, Co Cr, Cu, Fe, Ga, Hg K, La, Mg, Mn, Mo Na Ni, P, Pb, S Sb, Sc, Sr, Th, Ti Tl, U, V, W, Zn	
Au-AA23	Fire Assay AAS finish	Au	> 10 ppm
Au- GRA21	Fire Assay Gravimetric finish	Au	< 10 ppm
Ag-OG46	Aqua Regia ICP-AES AAS finish	Ag	>100 ppm

Table 7. Principal Components Analysis Procedure

Statistics Output	Correlations Matrix Coefficients
KMO	> 0.600
Bartlett's test of sphericity	< 0.005
Extraction	Principal Components Analyze – Correlation Matrix
Display	Screeplot Unrotated Factor Solution
Eigenvalues	> 1.0
Rotation	Direct Oblimin
Missing Values	Exclude case pairwise
Coefficient Display Format	Sorted by size Suppress absolute values <0.3

SPSS 22 software and instruction manual (Pallent, 2007) was used to operate a Principals Component Analysis for all pyrites analyzed by EPMA.

Table 8. EPMA analysis points of all pyrite types

No.	NOTE	Figure	Fe	S	Pb	Co	Ni	Au
1	POS		42.942	48.014	0.260	0.052	0.002	0.000
2	POS		45.261	50.582	0.249	0.069	0.009	0.000
3	POS		45.001	50.433	0.287	0.049	0.025	0.000
4	POS		44.893	50.051	0.268	0.061	0.000	0.000
5	POS		46.527	51.410	0.261	0.065	0.000	0.000
88	POSw/HR		4.229	7.065	0.045	0.008	0.016	0.000
89	POSw/CoNi		38.760	46.226	0.256	0.407	1.053	0.000
90	POSw/CoNi		42.621	49.453	0.247	0.306	0.875	0.000
91	POSw/CoNi		41.519	48.752	0.262	0.406	1.111	0.000
92	POSw/CoNi		42.465	48.823	0.252	0.378	1.269	0.000
93	POS		41.300	44.269	0.228	0.199	0.427	0.000
1154	POS		11.450	17.630	0.254	0.036	0.025	0.000
1155	POS		45.811	50.667	0.230	0.103	0.023	0.000
1156	POSw/Pb		44.151	47.273	0.444	0.142	0.100	0.000
1157	POS		46.274	50.398	0.251	0.111	0.026	0.000
1158	POS		42.386	46.160	0.269	0.141	0.070	0.000
1159	POSw/Pb		43.365	48.280	0.452	0.197	0.553	0.000
1160	POS		45.289	49.291	0.237	0.132	0.029	0.000
1161	POSw/Pb		43.568	45.745	0.630	0.127	0.187	0.000
2460	OSlpy		19.530	23.330	0.140	0.018	0.000	0.000
2461	OSlpy		36.740	42.780	0.244	0.054	0.000	0.010
2462	OSlpy		28.449	33.436	0.225	0.050	0.004	0.017
2463	OSlpy		36.907	43.332	0.310	0.259	0.045	0.009
2464	OSlpy		36.196	42.357	0.268	0.081	0.006	0.042
2471	OSlpy		40.256	46.769	0.263	0.058	0.000	0.000
2472	OSlpy		44.675	51.452	0.302	0.060	0.000	0.021
2473	OSlpy		39.509	44.014	0.277	0.038	0.000	0.000
412	OS2pyRim		6.902	12.857	0.080	0.016	0.000	0.065
413	POS		40.632	46.353	0.223	0.092	0.046	0.000
417	POS		44.731	50.591	0.261	0.081	0.030	0.000
418	OS2pyRim-noAu		36.537	41.916	0.290	0.055	0.036	0.000
790	POSw/HR	26	3.860	5.411	0.016	0.004	0.019	0.000
791	POSw/HR	26	12.107	15.794	0.023	0.023	0.000	0.000
792	OS2pymcs-w/HR	26	20.784	25.575	0.071	0.042	0.000	0.026
793	OS2pymcs-w/HR	26	31.654	36.485	0.069	0.033	0.001	0.065
799	OS2pymcs-w/HR	26	31.270	36.006	0.095	0.057	0.000	0.064
800	OS2pymcs-w/HR	26	30.721	35.852	0.097	0.051	0.005	0.036
801	OS2pymcs-w/HR	26	29.325	34.552	0.090	0.056	0.000	0.027
802	OS2pymcs-w/HR	26	31.832	37.921	0.122	0.052	0.000	0.003
803	POSw/HR	26	28.002	32.937	0.126	0.054	0.011	0.000
2261	LOSw/AuAs	41	45.305	51.419	0.185	0.061	0.000	0.023
2262	LOSw/AuAs	41	46.277	52.401	0.221	0.063	0.003	0.014
2263	LOS-w/As	41	46.197	52.161	0.257	0.061	0.000	0.001
2264	LOS-w/As	41	45.406	51.588	0.170	0.060	0.000	0.000
2265	LOS-w/As	41	45.483	51.019	0.200	0.071	0.008	0.000
2266	LOS	41	46.115	52.537	0.209	0.067	0.000	0.000
1133	LOSvnPy	42	46.165	51.956	0.253	0.062	0.000	0.000
1134	LOSvnPy	42	45.350	52.787	0.260	0.071	0.000	0.000
1135	LOSvnPy	42	44.899	50.039	0.303	0.077	0.015	0.000
2134	LOS	41	46.136	52.867	0.217	0.079	0.028	0.000
2135	LOS	41	46.277	52.911	0.230	0.056	0.000	0.000
2136	LOS	41	45.857	52.571	0.260	0.067	0.000	0.000

No.	As	Hg	Tl	Sb	Cu	Si	Al	Ca	Ag
1	0.020	0.000	0.004	0.000	0.016	3.084	0.076	0.004	0.003
2	0.071	0.000	0.000	0.000	0.018	0.148	0.014	0.005	0.006
3	0.000	0.000	0.010	0.000	0.017	0.576	0.027	0.005	0.006
4	0.000	0.000	0.000	0.000	0.005	0.233	0.027	0.005	0.000
5	0.000	0.000	0.000	0.000	0.011	0.112	0.005	0.000	0.000
88	0.034	0.000	0.012	0.017	0.000	32.146	4.871	0.436	0.000
89	0.157	0.000	0.000	0.000	0.000	0.077	0.004	0.077	0.007
90	0.120	0.002	0.003	0.000	0.000	0.061	0.001	0.055	0.004
91	0.163	0.001	0.000	0.000	0.000	0.018	0.000	0.037	0.004
92	0.147	0.003	0.000	0.000	0.000	0.027	0.000	0.034	0.005
93	0.121	0.000	0.000	0.000	0.008	0.118	0.005	0.054	0.000
1154	0.928	0.004	0.073	0.108	0.016	25.950	0.287	0.000	0.034
1155	0.155	0.000	0.000	0.011	0.009	0.006	0.000	0.000	0.015
1156	1.474	0.011	0.000	0.196	0.063	0.033	0.008	0.000	0.090
1157	0.116	0.000	0.000	0.009	0.000	0.003	0.001	0.000	0.028
1158	0.450	0.002	0.012	0.058	0.004	0.056	1.332	0.185	0.024
1159	2.050	0.013	0.021	0.191	0.108	0.281	0.209	0.000	0.082
1160	0.137	0.000	0.028	0.009	0.000	0.015	0.001	0.056	0.009
1161	2.623	0.027	0.042	0.407	0.096	0.419	0.363	0.025	0.184
2460	0.723	0.000	0.000	0.241	0.000	13.114	13.035	0.000	0.000
2461	0.013	0.000	0.004	0.019	0.000	0.081	0.067	0.006	0.000
2462	0.041	0.000	0.004	0.036	0.000	0.283	0.936	0.009	0.004
2463	0.062	0.000	0.015	0.010	0.007	0.064	0.423	0.012	0.006
2464	0.029	0.000	0.015	0.008	0.007	0.093	0.495	0.009	0.000
2471	0.002	0.000	0.000	0.009	0.005	0.051	0.344	0.006	0.004
2472	0.000	0.000	0.000	0.010	0.005	0.028	0.052	0.004	0.000
2473	1.154	0.002	0.048	0.000	0.000	1.175	0.136	1.996	0.001
412	0.819	0.047	0.015	0.076	0.009	31.977	0.346	0.006	0.000
413	0.027	0.000	0.004	0.006	0.000	5.201	0.068	0.005	0.004
417	0.043	0.000	0.015	0.002	0.068	0.827	0.041	0.000	0.000
418	1.140	0.035	0.063	0.116	0.042	5.695	0.038	0.000	0.007
790	0.397	0.023	0.000	0.043	0.022	34.369	5.399	0.012	0.006
791	1.251	0.058	0.006	0.041	0.035	27.245	6.028	0.014	0.000
792	2.322	0.095	0.097	0.053	0.080	19.000	6.156	0.004	0.000
793	3.705	0.137	0.231	0.075	0.125	7.881	4.888	0.000	0.000
799	3.849	0.124	0.264	0.096	0.125	7.211	4.171	0.000	0.007
800	3.568	0.119	0.227	0.111	0.121	8.833	3.999	0.000	0.014
801	2.818	0.105	0.159	0.119	0.086	8.471	4.532	0.000	0.003
802	1.937	0.073	0.137	0.083	0.057	6.712	4.457	0.000	0.005
803	1.746	0.071	0.151	0.082	0.063	8.715	6.411	0.000	0.009
2261	1.813	0.000	0.000	0.133	0.000	0.020	0.000	0.000	0.001
2262	0.507	0.003	0.000	0.004	0.006	0.004	0.000	0.000	0.000
2263	0.725	0.000	0.000	0.037	0.000	0.009	0.002	0.000	0.001
2264	1.619	0.043	0.090	0.618	0.000	0.000	0.000	0.000	0.012
2265	1.428	0.021	0.010	0.288	0.000	0.011	0.000	0.000	0.009
2266	0.486	0.009	0.000	0.085	0.005	0.006	0.000	0.000	0.005
1133	0.162	0.006	0.027	0.016	0.003	0.045	0.000	0.000	0.003
1134	0.182	0.006	0.028	0.055	0.000	0.113	0.033	0.000	0.030
1135	0.193	0.000	0.003	0.040	0.004	0.364	0.128	0.000	0.044
2134	0.004	0.000	0.022	0.000	0.007	0.077	0.000	0.000	0.002
2135	0.000	0.000	0.003	0.000	0.000	0.020	0.000	0.000	0.002
2136	0.000	0.000	0.000	0.000	0.000	0.115	0.065	0.000	0.000

No.	Zn	Ti	Bi	Sn	Te	Se	W	Total
1	0.023	0.360	0.000	0.000	0.000	0.000	0.000	95.554
2	0.022	1.103	0.000	0.005	0.000	0.000	0.000	98.305
3	0.000	0.945	0.069	0.005	0.000	0.000	0.000	98.177
4	0.000	1.986	0.000	0.000	0.000	0.009	0.000	98.270
5	0.000	0.417	0.053	0.000	0.000	0.000	0.000	99.616
88	0.000	0.093	0.033	0.000	0.000	0.000	0.000	49.118
89	0.000	0.014	0.053	0.000	0.006	0.012	0.000	87.795
90	0.000	0.000	0.079	0.000	0.000	0.000	0.001	94.576
91	0.004	0.002	0.040	0.000	0.017	0.000	0.000	93.082
92	0.000	0.000	0.013	0.002	0.000	0.008	0.000	94.175
93	0.000	0.015	0.012	0.004	0.000	0.003	0.000	87.424
1154	0.000	0.000	0.071	0.000	0.000	0.000	0.000	57.145
1155	0.000	0.000	0.011	0.000	0.000	0.002	0.000	97.790
1156	0.001	0.005	0.045	0.000	0.000	0.000	0.000	94.751
1157	0.006	0.000	0.099	0.004	0.000	0.000	0.000	98.084
1158	0.086	0.000	0.000	0.000	0.000	0.000	0.000	91.908
1159	0.000	0.000	0.029	0.000	0.000	0.005	0.000	96.549
1160	0.005	0.001	0.074	0.000	0.000	0.000	0.002	96.060
1161	0.018	0.011	0.028	0.010	0.000	0.022	0.000	95.211
2460	0.001	0.183	0.054	0.003	0.000	0.000	0.000	70.683
2461	0.009	10.010	0.010	0.002	0.000	0.003	0.000	90.603
2462	0.006	19.076	0.045	0.000	0.000	0.000	0.000	83.043
2463	0.000	9.424	0.013	0.000	0.000	0.001	0.013	91.465
2464	0.000	10.308	0.045	0.000	0.000	0.002	0.000	90.503
2471	0.000	6.235	0.086	0.000	0.000	0.000	0.000	94.671
2472	0.000	1.213	0.075	0.000	0.000	0.000	0.017	98.574
2473	0.001	0.891	0.090	0.000	0.000	0.005	0.000	89.901
412	0.000	0.003	0.000	0.000	0.000	0.000	0.000	53.414
413	0.009	0.000	0.074	0.000	0.000	0.000	0.000	93.441
417	0.023	0.000	0.018	0.000	0.000	0.002	0.000	97.486
418	0.003	0.013	0.054	0.000	0.000	0.000	0.000	86.664
790	0.003	0.084	0.000	0.002	0.000	0.000	0.000	49.734
791	0.000	0.055	0.016	0.000	0.000	0.000	0.000	62.914
792	0.000	0.049	0.059	0.000	0.000	0.002	0.000	74.777
793	0.000	0.040	0.000	0.008	0.000	0.015	0.000	85.914
799	0.002	0.059	0.000	0.000	0.000	0.005	0.000	83.909
800	0.012	0.049	0.000	0.007	0.000	0.000	0.000	84.319
801	0.002	0.043	0.030	0.000	0.000	0.000	0.000	80.907
802	0.000	0.019	0.028	0.003	0.000	0.007	0.000	84.001
803	0.008	0.013	0.000	0.002	0.000	0.000	0.000	78.876
2261	0.000	0.000	0.028	0.002	0.000	0.000	0.000	99.747
2262	0.001	0.000	0.062	0.000	0.000	0.004	0.014	100.348
2263	0.000	0.000	0.000	0.000	0.000	0.000	0.000	100.228
2264	0.000	0.011	0.045	0.000	0.000	0.013	0.013	100.432
2265	0.000	0.004	0.045	0.008	0.000	0.000	0.000	99.369
2266	0.001	0.000	0.025	0.000	0.002	0.000	0.000	100.315
1133	0.000	0.008	0.021	0.000	0.000	0.004	0.000	99.493
1134	0.000	0.001	0.068	0.000	0.000	0.000	0.000	99.762
1135	0.026	0.008	0.101	0.000	0.000	0.001	0.000	96.978
2134	0.008	0.000	0.015	0.000	0.000	0.005	0.000	100.242
2135	0.003	0.000	0.026	0.000	0.000	0.002	0.010	100.329
2136	0.021	0.000	0.032	0.000	0.000	0.000	0.000	99.757

Numbers in left column indicate the analysis number in the raw data set, which is presented in Appendix F.10. Molybdenum was not included in this table due to the peak overlap relationships between Fe and Mo. POS = Pre-ore-stage pyrite, POS w/CoNi = Pre-ore-stage pyrite with elevated cobalt and nickel, POS w/HR = Pre-ore-stage with host rock, POS w/Pb = Pre-ore stage-pyrite with elevated lead, OS1py = Ore-stage 1 pyrite, OS2pyRim = Ore-stage 2 pyrite rim with detectable gold and Carlin pathfinder elements, OS2pyRim-noAU= Ore-stage 2 pyrite rim without detectable Au, but with detectable Carlin pathfinder elements, OS2pymcs-w/HR= Ore-stage 2 pyrite microcrystals with host rock, LOS = Late-ore-stage pyrite, LOS-w/As = Late-ore-stage pyrite with elevated arsenic, LOSw/AuAs = Late-ore-stage pyrite with elevated gold and arsenic, LOSvnPy = Late-ore-stage vein pyrite.

Table 9. Pre-ore-stage pyrite classification

Pyrite Type	Appearance in reflected light microscopy	Chemistry (Probe data)	Spatially Associated Minerals	Initial Process of Formation
POS	<p>1 μm to 1mm; Euhedral to anhedral</p> <p>Framboidal pyrite (types include singular and clustered framboids, clouds of fine framboids, nodules)</p> <p>Fine microcrystals</p>	<p>Fe = ~38 – 52 wt. %</p> <p>S = ~20-55 wt. %</p> <p>Au is absent</p> <p>Ag < 1,100 ppm</p> <p>some points reaching to ~4,500 ppm</p> <p>As 0 - 6 wt. % & some points approaching 12.5 wt. %,</p> <p>Bi < 0.125 wt. %</p> <p>Co = 0.05 - 0.4 wt. %</p> <p>Cu < 1 wt. %</p> <p>Hg < 0.3 wt. %</p> <p>Ni < 1.25 wt. %</p> <p>Pb < 1.0 wt. %</p> <p>Sb < 1 wt. % & some points reaching 2.5 wt. %</p> <p>Se < 0.075 wt. %</p> <p>Sn < 0.075 wt. %</p> <p>Te < 0.025</p> <p>Ti < 1 wt. %</p> <p>Tl < 0.3 wt. %</p>	Quartz, illite, montmorillonite, calcite, and/ or dolomite	Syngenetic to diagenetic

Table 10. Principal Components Analysis of all EPMA pyrite data

Component Matrix ^a									Communalities Extraction
	Component								
	1	2	3	4	5	6	7	8	
Fe	.933								.952
S	.904								.918
Si	-.869								.863
Pb	.790								.692
Co	.711		.493						.817
Al	-.642								.574
Hg		.851							.831
Tl		.819							.794
As		.774							.682
Sb		.558	-.307	.413					.627
Ni	.308		.790						.814
Se									.425
Ag				.593		-.315	.359		.649
Cu		.310		-.373			.338	-.345	.579
Ca					-.742		.346		.734
Ti	-.304					.386		-.398	.607
Au					.435	-.456			.532
Zn						.608	.454		.701
Sn							-.544		.479
Te			.349	-.304				.401	.438
Bi								.397	.508
W									.247
Total ^d	4.604	2.776	1.647	1.224	1.100	1.075	1.024	1.012	
% of Variance ^d	20.927	12.617	7.487	5.563	5.002	4.888	4.655	4.602	
Cumulative % ^d	20.927	33.544	41.031	46.595	51.597	56.485	61.140	65.742	
Extraction Method: Principal Component Analysis.									
a. 8 components extracted.									
b. Kaiser-Meyer-Olkin Measure of Sampling Adequacy =0.722									
c. Bartlett's Test of Sphericity sig. = 0.000									
d. Initial Eigenvalues									

For all analyzed data, requirements related to the set to be suitable for principal components analysis, Kaiser Meyer-Olkin Measure of Sampling Adequacy (KMO) value

must be > 0.6 , listed in b. of each table (Pallent, 2007) and the Barlett's Test of Sphericity value must be $p < 0.05$, listed in c. of each table (Pallent, 2007).

The 'Total ^d' are the initial eigenvalue for each component. The eigenvalue ' % of Variance ^d' of a component represents the amount of the total variance explained by that component and 'Cumulative % ^d' of a component represents the cumulative amount of total variance of each additional component (Pallent, 2007).

The Kaisers Criterion or Eigenvalue rule was used to determine the number of components to retain in each table. The Kaisers Criterion or Eigenvalue rule, only factors with the eigenvalue of 1.0 or more are retained for further investigation; these are listed in each principal components analysis table for each analysis as 'Total ^d'. The number of components extracted (a.) is determined by the initial eigenvalues total, which must be greater than 1.0, listed in 'Total ^d' of each table (Pallent, 2007).

Table 11. Principal Components Analysis of Pre-ore-stage pyrite

Component Matrix ^a								Communalities Extraction
	Component							
	1	2	3	4	5	6	7	
Fe	.934							.946
S	.900							.904
Si	-.863							.822
Pb	.775							.682
Co	.685		.541					.828
Al	-.652							.559
Hg		.844						.817
Tl		.822						.781
As		.779						.677
Sb		.615		.368				.610
Ni	.323		.809					.849
Se								.407
W								.172
Ag				.605		-.407	.308	.642
Te			.327	-.412				.389
Ca					-.776			.729
Ti	-.329				.441			.430
Bi					.337			.298
Sn						.545		.395
Cu				-.406		-.491		.595
Zn						.367	.793	.784
Total ^d	4.571	2.751	1.635	1.196	1.110	1.032	1.022	
Variance ^d	21.768	13.098	7.788	5.698	5.284	4.914	4.864	
Cumulative % ^d	21.768	34.866	42.654	48.351	53.636	58.550	63.414	
Extraction Method: Principal Component Analysis.								
a. 7 components extracted.								
b. Kaiser-Meyer-Olkin Measure of Sampling Adequacy =0.707								
c. Bartlett's Test of Sphericity sig. = 0.000								
d. Initial Eigenvalues								

Table 12. Composition of Components of all EPMA pyrite data and Pre-ore-stage pyrites

Factor Analysis for All Pyrites		Total Variance	Factor Analysis for POS pyrite		Total Variance
1	Fe, S, Pb, Co, Ni (Si, Al, Ti)	4.604	1	Fe, S, Pb, Co, Ni (Si, Al, Ti)	4.571
2	Hg, Tl, As, Sb, Cu	2.776	2	Hg, Tl, As, Sb	2.751
3	Co, Ni, Te, (Sb)	1.647	3	Ni, Co, Te	1.635
4	Sb, Ag, (Cu, Te)	1.224	4	Ag, Sb, (Te, Cu)	1.196
5	Au, (Ca)	1.100	5	Ti, Bi, (Ca)	1.110
6	Ti, Zn, (Ag, Au)	1.075	6	Sn, Zn, (Cu, Ag)	1.032
7	Ag, Cu, Ca, Zn, (Sn)	1.024	7	Zn, Ag	1.022
8	Te, Bi, (Ti, Cu)	1.012			
Elements within each component will be listed in order of highest to lowest positive, and highest to lowest negative in parenthesis ().					

Table 13. Spearman Rank Correlation Matrix of all EPMA data

[illegible]

Table 14. Mann Whitney U-Test of EPMA data to identify elements in pyrites and Au-bearing rims

Mann-Whitney U-Test	Asymp. Sig. (2-tailed)	Median < 0.0001	Median > = 0.0001	Asymp. Sig. (2-tailed)	Median < 0.0144	Median > = 0.0144	Asymp. Sig. (2-tailed)	Median < 0.0500	Median > = 0.0500
Ag	0.0004	0.0002	0.0012	0.0025	0.0003	0.0015	0.4011	0.0003	0.0009
Al	0.3886	0.1079	0.1587	0.2902	0.1088	0.1728	0.1247	0.1121	0.2767
As	0.0176	0.2234	0.1122	0.4369	0.2157	0.1361	0.1075	0.2131	0.5132
Au	0.0000	0.0000	0.0146	0.0000	0.0000	0.0255	0.0000	0.0000	0.0616
Bi	0.1980	0.0308	0.0338	0.4733	0.0309	0.0348	0.1390	0.0312	0.0336
Ca	0.0000	0.0168	0.0042	0.0000	0.0159	0.0019	0.2241	0.0143	0.0082
Co	0.0000	0.0649	0.0534	0.0000	0.0646	0.0514	0.0008	0.0641	0.0451
Cu	0.0000	0.0112	0.0042	0.0855	0.0105	0.0056	0.3795	0.0102	0.0114
Fe	0.0549	43.2170	39.2472	0.0809	43.2117	36.3592	0.0143	43.1989	29.5515
Hg	0.0001	0.0067	0.0025	0.0715	0.0062	0.0026	0.4744	0.0060	0.0051
Ni	0.0000	0.0120	0.0012	0.0000	0.0115	0.0013	0.0204	0.0108	0.0007
Pb	0.0000	0.2243	0.1931	0.0000	0.2219	0.1883	0.0052	0.2203	0.1274
S	0.0000	48.3641	42.7755	0.0000	48.2742	38.5649	0.0006	47.9820	34.2142
Sb	0.0012	0.0095	0.0258	0.0018	0.0100	0.0315	0.0490	0.0106	0.0749
Se	0.0000	0.0000	0.0000	0.0004	0.0000	0.0000	0.5136	0.0000	0.0000
Si	0.0192	0.6636	1.3474	0.0371	0.6636	2.3621	0.0591	0.6776	7.2631
Sn	0.8849	0.0000	0.0000	0.6222	0.0000	0.0000	0.8523	0.0000	0.0000
Te	0.0000	0.0000	0.0000	0.0002	0.0000	0.0000	0.1090	0.0000	0.0000
Ti	0.7469	0.0075	0.0077	0.0341	0.0074	0.0103	0.6657	0.0075	0.0129
Tl	0.1737	0.0163	0.0094	0.2991	0.0159	0.0179	0.0177	0.0159	0.0363
W	0.0011	0.0000	0.0000	0.0116	0.0000	0.0000	0.6477	0.0000	0.0000
Zn	0.0068	0.0000	0.0000	0.0883	0.0000	0.0000	0.9444	0.0000	0.0000

Asymptotic significance (2-tailed) values for each element for each gold classification. Element values highlighted in blue have asymptotic significance (2-tailed) values < 0.005 , indicating that the median values in the low and high gold classes are significantly different from each other. Element values highlighted in white have asymptotic significance (2-tailed) values > 0.005 , such that the median values in the low and high gold classes are not significantly different. Median values are in wt. %.

Table 15. Ore-stage 1 pyrite classification

Pyrite Type	Appearance in reflected light microscopy	Chemistry (Probe data)	Spatially Associated Minerals	Initial Process of Formation
OS 1 pyrite in Tertiary porphyry dacite dikes	1 μ m to 1mm; Euhedral to anhedral pyrites with bright white reflectivity	Fe = ~38 – 53 wt. % S = ~35-50 wt. % Ag < 125 ppm As < 3 wt. % Au < 450 ppm Bi < 0.150 wt. % Co = 0.035 - 0.08 wt. % Cu < 0.0175 wt. % Hg < 0.006 wt. % Pb = 0.25 - 0.35 wt. % Sb < 0.35 wt. % Se < 0.0175 wt. % Sn < 0.005 wt. % Te = ~ 0.0150 wt. % Ti < 1 wt. % Tl < 0.04 wt. % Zn < 0.5 wt. %	Illite, quartz, and kaolinite	Hydrothermal alteration of Tertiary porphyry dacite dike

Table 16. Principal Components Analysis of Ore-stage 1 pyrite

Component Matrix ^a								Communalities Extraction
	Component							
	1	2	3	4	5	6	7	
S	.987							.987
Fe	.986							.988
Si	-.981							.984
Al	-.976							.982
Pb	.968							.978
Co	.963							.954
Ni	-.568					.490	-.316	.689
Cu	.314	-.656					-.447	.789
As		-.617	.571					.897
Tl		.540	.495					.707
Zn		-.471			.436			.589
Bi	.375	-.459	.387		.383			.793
Ti		.359	.775					.804
Hg		.447	.751					.902
Te		.372	-.315	.834				.948
Ca		.526		.805				.958
W				-.466	.497			.724
Se			.460		-.484		-.343	.652
Sn	-.410					-.666		.753
Ag				-.315		.659		.668
Sb		-.327			-.557		.632	.846
Total ^d	6.756	2.624	2.333	1.942	1.463	1.438	1.035	
Variance ^d	32.173	12.496	11.110	9.247	6.965	6.850	4.931	
Cumulative % ^d	32.173	44.669	55.779	65.026	71.991	78.841	83.771	
Extraction Method: Principal Component Analysis.								
a. 7 components extracted.								
b. Kaiser-Meyer-Olkin Measure of Sampling Adequacy=0.536								
c. Bartlett's Test of Sphericity sig. = 0.000								
d. Initial Eigenvalues								

Table 17. Composition of Components of Ore-stage 1, Ore-stage 2, and Late-ore-stage pyrite data

Factor Analysis for OS 1 pyrites		Total	Factor Analysis for OS 2 pyrites		Total
		Variance			Variance
1	S, Fe, Pb, Co, Bi, Cu, (Si, Al, Ni, Sn)	6.756	1	Fe, S, Pb, Co, Bi, W (Si, Al, Hg, Tl, Cu, As)	5.153
2	Tl, Ca, Hg, Te, Ti, (Cu, As, Zn, Bi, Sb)	2.624	2	As, Tl, Hg, Cu, Co, S, Fe, W, (Si, Al)	3.708
3	Ti, Hg, As, Tl, Se, Bi, (Te)	2.333	3	Ag, Sb, Ti, Sn	1.732
4	Te, Ca, (W, Ag)	1.942	4	Ca, Te, Ni	1.335
5	W, Bi, Zn, (Sb, Se)	1.463	5	W, (Ni, Se)	1.229
6	Ag, Ni, (Sn)	1.438	6	Sn, Bi, (Ni)	1.120
7	Sb, (Cu, Se, Ni)	1.035	7	Zn, Ni, Ti, (Se, Ag)	1.034
		Total			
Factor Analysis for LOS pyrites		Variance			
1	Fe, S, Co, Pb, (Si, Al, Ti, Ca)	5.433			
2	Hg, Sb, Tl, As, Sn, Ag, Se, Cu	3.101			
3	Cu, Pb, Ag, As, Ca, Se, (Sb, Hg, Tl)	2.324			
4	Ca, Cu, Zn, (Ag, Ni, Pb)	1.467			
5	Te, W, As, (Ni, Zn)	1.276			
6	W, Zn, Se, (Bi)	1.218			
7	Se, Bi, Ni, (Sn, Zn)	1.084			
Elements within each component will be listed in order of highest to lowest positive, and highest to lowest negative in parenthesis ().					

Table 18. Ore-stage 2 pyrite classification

Pyrite Type	Appearance in reflected light microscopy	Chemistry (Probe data)	Spatially Associated Minerals	Initial Process of Formation
OS 2	Sub-micrometer discontinuous rims on POS, and OS 1 pyrite Sub-micrometer ore-stage microcrystals	Au = 0-800 ppm Ag < 550 ppm As < 4 wt.% Bi < 0.120 wt.% Co < 0.1 wt.% Cu < 0.15 wt.% Fe = 0 – 53 wt.% Hg < 0.14 wt.% Ni < 0.15 wt.% Pb < 0.3 wt.% S = 0-54 wt.% Sb < 0.5 wt.% Se < 0.025 wt.% Sn < 0.130 wt.% Te = ~ 0.015 wt.% Ti < 1 wt.% Tl < 0.25 wt.% Zn < 0.05 wt.%	Illite, jasperoid	Ore-stage Carlin-type hydrothermal fluids

Table 19. Principal Components Analysis of Ore-stage 2 pyrite

Component Matrix ^a								Communalities Extraction
	Component							
	1	2	3	4	5	6	7	
Fe	.854	.471						.960
S	.821	.524						.953
Pb	.814							.714
Co	.774	.535						.935
Si	-.759	-.551						.913
Al	-.648							.556
Bi	.424	-.313				.316		.451
As	-.428	.769						.816
Tl	-.529	.768						.897
Hg	-.548	.765						.896
Cu	-.447	.751						.773
Ag			.762				-.305	.709
Sb			.749					.745
Ti			.458				.344	.515
Sn			.338					.337
Ca				.767				.644
Te				.713				.653
Ni				.308	-.610	-.375	.368	.793
Se					-.500		-.349	.488
W	.404				.467			.481
Au								.273
Zn						.605	.627	.810
Total	5.153	3.708	1.732	1.335	1.229	1.120	1.034	
Variance	23.425	16.854	7.874	6.069	5.588	5.090	4.700	
Cumulative %	23.425	40.278	48.152	54.221	59.809	64.899	69.599	
Extraction Method: Principal Component Analysis.								
a. 7 components extracted.								
b. Kaiser-Meyer-Olkin Measure of Sampling Adequacy =0.764								
c. Bartlett's Test of Sphericity sig. = 0.000								
d. Initial Eigenvalues								

Table 20. Late-ore-stage pyrite classification

Pyrite Type	Appearance in reflected light microscopy	Chemistry (Probe data)	Spatially Associated Minerals	Initial Process of Formation
LOS	Anhedral vein pyrite (~ 0.1 mm) or anhedral pyrite (20- 120 μ m) in massive pyrite (~ 20 μ m to 3 mm) in sulfidized breccias	Fe = ~38 – 47 wt.% S = ~40 - 52 wt.% Ag < 1,250 ppm As < 2 wt.% & some points reaching 4 wt.% Au < 300 ppm Bi < 0.15 wt.% Co = 0.05 to 0.08 wt.% Cu < 0.05wt.% Hg < 0.125 wt.% Ni < 0.05 wt.% Pb = 0.12 to 0.3 wt.% Sb < 1.25 wt.% Se < 0.015 wt.% Sn < 0.01 wt.% Ti < 0.025 wt.% Tl < 0.1 wt.% Zn < 0.04 wt.%	Drusy quartz, realgar	Late-ore stage Carlin-type hydrothermal fluids

Table 21. Principal Components Analysis of Late-ore-stage pyrite

Component Matrix ^a								Communalities Extraction
	Component							
	1	2	3	4	5	6	7	
Fe	.950							.944
S	.941							.916
Si	-.919							.895
Co	.866							.814
Al	-.802							.743
Ti	-.761							.686
Pb	.657		.555	-.340				.887
Hg		.806	-.427					.899
Sb		.773	-.483					.911
Tl		.722	-.342					.715
As		.630	.448		.342			.792
Sn		.520					-.474	.625
Cu		.314	.611	.507				.798
Ag		.500	.538	-.425				.845
Ca	-.348		.435	.618				.783
Zn				.411	-.338	.358	-.334	.602
Ni				-.399	-.378		.381	.577
Te					.678			.560
W					.518	.598		.694
Bi						-.487	.384	.579
Se		.319	.413			.304	.478	.640
Total ^d	5.433	3.101	2.324	1.467	1.276	1.218	1.084	
Variance ^d	25.872	14.769	11.069	6.986	6.076	5.802	5.160	
Cumulative % ^d	25.872	40.641	51.709	58.695	64.771	70.572	75.733	
Extraction Method: Principal Component Analysis.								
a. 7 components extracted.								
b. Kaiser-Meyer-Olkin Measure of Sampling Adequacy =0.699								
c. Bartlett's Test of Sphericity sig. = 0.000								
d. Initial Eigenvalues								

Table 22. Classification Support Vector Machine results (C-SVM) for 0.1 ppm Au classification

Analyte	Au	Ag	Al	As	B	Ba	Be	Bi	Ca
Accuracy	0.9997	0.6792	0.7335	0.7240	0.6538	0.7208	0.6538	0.6538	0.7291

Analyte	Cd	Co	Cr	Cu	Fe	Ga	Hg	K	La
Accuracy	0.7275	0.6732	0.6837	0.6973	0.6611	0.6538	0.8401	0.7188	0.6538

Analyte	Mg	Mn	Mo	Na	Ni	P	Pb	S	Sb
Accuracy	0.7355	0.7334	0.6777	0.6538	0.7052	0.7546	0.7084	0.6838	0.8167

Analyte	Sc	Sr	Th	Ti	Tl	U	V	W	Zn
Accuracy	0.7165	0.6802	0.6538	0.6538	0.7927	0.6538	0.7645	0.6538	0.6803

Accuracy Floor: 0.6538

The Spearman rank correlation matrix (Table 24) indicates if the elements percentage of ability to predict gold (Table 22 and 23) is positive (R value > 0.4) and is predicting the presence of gold highlighted in red, or negative (R value < -0.4) and is predicting the absence) of gold highlighted in blue. Values highlighted in white are those elements whose percentage is equal to the accuracy floor, thus is a non-predicting element for gold.

Table 23. Classification Support Vector Machine results (C-SVM) for 1.0 ppm Au classification

Analyte	Au	Ag	Al	As	B	Ba	Be	Bi	Ca
Accuracy	0.9986	0.9219	0.9219	0.9280	0.9219	0.9219	0.9219	0.9219	0.9219

Analyte	Cd	Co	Cr	Cu	Fe	Ga	Hg	K	La
Accuracy	0.9219	0.9219	0.9219	0.9219	0.9219	0.9219	0.9293	0.9219	0.9219

Analyte	Mg	Mn	Mo	Na	Ni	P	Pb	S	Sb
Accuracy	0.9219	0.9219	0.9219	0.9219	0.9219	0.9219	0.9219	0.9219	0.9219

Analyte	Sc	Sr	Th	Ti	Tl	U	V	W	Zn
Accuracy	0.9219	0.9234	0.9219	0.9219	0.9391	0.9219	0.9219	0.9219	0.9219

Accuracy Floor: 0.921894

The Spearman rank correlation matrix (Table 24) indicates if the elements percentage of ability to predict gold (Table 22 and 23) is positive (R value > 0.4) and is predicting the presence of gold highlighted in red, or negative (R value < -0.4) and is predicting the absence) of gold highlighted in blue. Values highlighted in white are those elements whose percentage is equal to the accuracy floor, thus is a non-predicting element for gold.

Table 24. Whole rock Spearman rank correlation matrix of 36 elements

Au	1.000							
Ag	.147**	1.000						
Al	-.216**	.348**	1.000					
As	.489**	.392**	.370**	1.000				
B	-.144**	.071**	.503**	.100**	1.000			
Ba	-.367**	-.417**	-.490**	-.777**	-.161**	1.000		
Be	-.419**	.144**	.658**	-.089**	.376**	-.034*	1.000	
Bi	.024	-.093**	-.076**	-.067**	-.038**	.057**	-.003	1.000
Ca	-.118**	-.462**	-.594**	-.469**	-.250**	.576**	-.264**	.075**
Cd	.338**	.262**	-.005	.362**	-.067**	-.351**	-.094**	-.050**
Co	-.176**	.369**	.880**	.383**	.420**	-.509**	.575**	-.050**
Cr	-.152**	.413**	.724**	.345**	.433**	-.445**	.371**	-.148**
Cu	-.124**	.437**	.874**	.462**	.427**	-.561**	.602**	-.080**
Fe	-.025	.466**	.814**	.555**	.371**	-.677**	.502**	-.064**
Ga	-.133**	-.065**	.150**	-.137**	-.039**	.070**	.183**	.049**
Hg	.696**	.249**	.049**	.703**	-.032*	-.613**	-.309**	-.007
K	-.216**	.352**	.981**	.376**	.497**	-.493**	.675**	-.075**
La	-.114**	-.195**	.020	-.193**	-.067**	.151**	.062**	.068**
Mg	-.117**	-.423**	-.542**	-.569**	-.230**	.638**	-.161**	.076**
Mn	-.344**	-.112**	-.015	-.350**	.000	.369**	.251**	.045**
Mo	.128**	.469**	.513**	.482**	.238**	-.511**	.263**	-.036*
Na	-.153**	-.344**	-.290**	-.493**	-.109**	.518**	-.028	.019
Ni	-.126**	.436**	.852**	.468**	.431**	-.575**	.539**	-.114**
P	-.222**	.413**	.891**	.390**	.421**	-.499**	.554**	-.099**
Pb	.308**	.458**	.462**	.558**	.151**	-.604**	.179**	-.070**
S	.352**	.442**	.529**	.856**	.203**	-.868**	.042**	-.104**
Sb	.694**	.276**	-.057**	.720**	-.095**	-.572**	-.380**	.019
Sc	-.325**	.249**	.791**	.295**	.366**	-.333**	.636**	-.040**
Sr	-.185**	-.349**	-.354**	-.438**	-.161**	.478**	-.013	.068**
Th	-.042**	-.034*	.050**	-.046**	-.013	.035*	.058**	-.010
Ti	-.187**	-.081**	.205**	-.169**	-.032*	.088**	.248**	.053**
Tl	.559**	.205**	.137**	.593**	.016	-.511**	-.132**	.007
U	-.024	-.102**	-.125**	-.083**	.003	.108**	-.090**	-.012
V	-.222**	.390**	.934**	.406**	.452**	-.482**	.642**	-.074**
W	-.024	.125**	.031*	-.021	.017	.023	.051**	-.002
Zn	.127**	.369**	.404**	.382**	.123**	-.406**	.341**	-.031*
	Au	Ag	Al	As	B	Ba	Be	Bi

Table 24. Continued

Au								
Ag								
Al								
As								
B								
Ba								
Be								
Bi								
Ca	1.000							
Cd	-.190**	1.000						
Co	-.650**	-.015	1.000					
Cr	-.757**	.069**	.753**	1.000				
Cu	-.666**	.089**	.897**	.753**	1.000			
Fe	-.674**	.247**	.796**	.695**	.841**	1.000		
Ga	-.057**	-.025	.017	-.048**	-.037*	.056**	1.000	
Hg	-.325**	.457**	.074**	.097**	.125**	.273**	-.060**	1.000
K	-.598**	.001	.887**	.717**	.894**	.815**	.119**	.050**
La	.111**	-.114**	-.080**	-.136**	-.195**	-.123**	.332**	-.136**
Mg	.826**	-.214**	-.585**	-.644**	-.623**	-.620**	-.042**	-.393**
Mn	.565**	-.153	-.107**	-.268**	-.117**	-.055**	.081**	-.422**
Mo	-.521**	.294**	.512**	.517**	.546**	.592**	-.070**	.313**
Na	.545**	-.235**	-.369**	-.433**	-.452**	-.452**	.149**	-.330**
Ni	-.649**	.085**	.895**	.786**	.921**	.831**	-.102**	.153**
P	-.644**	.037*	.848**	.775**	.869**	.787**	.047**	.053**
Pb	-.486**	.439**	.431**	.398**	.510**	.629**	-.011	.469**
S	-.561**	.331**	.545**	.470**	.598**	.722**	-.137**	.605**
Sb	-.230**	.432**	-.056**	-.007	.021	.178**	-.114**	.776**
Sc	-.276**	-.009	.712**	.515**	.739**	.697**	.117**	-.069**
Sr	.784**	-.097**	-.478**	-.629**	-.503**	-.467**	.101**	-.335**
Th	-.030*	-.015	.009	-.016	-.015	.024	.219**	-.015
Ti	-.077**	-.055**	.058**	-.007	-.009	.086**	.735**	-.096**
Tl	-.390**	.339**	.160**	.139**	.213**	.336**	-.042**	.651**
U	.283**	-.071**	-.152**	-.210**	-.161**	-.184**	-.026	-.062**
V	-.568**	.064**	.843**	.730**	.880**	.826**	.123**	.063**
W	.000	-.012	.013	.018	.077**	.031*	.018	-.021
Zn	-.390**	.636**	.370**	.350**	.485**	.569**	.043**	.314**
	Ca	Cd	Co	Cr	Cu	Fe	Ga	Hg

Table 24. Continued

Au								
Ag								
Al								
As								
B								
Ba								
Be								
Bi								
Ca								
Cd								
Co								
Cr								
Cu								
Fe								
Ga								
Hg								
K	1.000							
La	-.014	1.000						
Mg	-.569**	.168**	1.000					
Mn	-.034*	.099**	.544**	1.000				
Mo	.502**	-.092**	-.437**	-.158**	1.000			
Na	-.333**	.269**	.679**	.362**	-.318**	1.000		
Ni	.866**	-.150**	-.610**	-.151**	.589**	-.450**	1.000	
P	.880**	-.094**	-.593**	-.102**	.550**	-.396**	.862**	1.000
Pb	.464**	-.064**	-.458**	-.216**	.506**	-.356**	.518**	.452**
S	.535**	-.199**	-.630**	-.356**	.514**	-.530**	.622**	.540**
Sb	-.066**	-.158**	-.302**	-.371**	.310**	-.333**	.035*	-.015
Sc	.791**	-.023	-.276**	.313**	.373**	-.189**	.689**	.728**
Sr	-.359**	.245**	.648**	.568**	-.364**	.521**	-.505**	-.457**
Th	.037*	.108**	-.016	.011	-.027	.050**	-.037*	.020
Ti	.162**	.377**	-.068**	.112**	-.069**	.175**	-.079**	.064**
Tl	.149**	-.125**	-.401**	-.401**	.307**	-.278**	.195**	.092**
U	-.119**	-.043**	.154**	.155**	-.147**	.144**	-.176**	-.131**
V	.921**	-.067**	-.517**	.057**	.538**	-.333**	.856**	.893**
W	.028	.016	.020	.052**	.028	.057**	.043**	.016
Zn	.432**	-.134**	-.416**	-.047**	.427**	-.410**	.453**	.421**
	K	La	Mg	Mn	Mo	Na	Ni	P

Table 24. Continued

Au								
Ag								
Al								
As								
B								
Ba								
Be								
Bi								
Ca								
Cd								
Co								
Cr								
Cu								
Fe								
Ga								
Hg								
K								
La								
Mg								
Mn								
Mo								
Na								
Ni								
P								
Pb	1.000							
S	.625**	1.000						
Sb	.425**	.585**	1.000					
Sc	.351**	.379**	-.113**	1.000				
Sr	-.333**	-.481**	-.263**	-.120**	1.000			
Th	.005	-.043**	-.040**	.048**	.023	1.000		
Ti	-.020	-.173**	-.163**	.164**	.121**	.238**	1.000	
Tl	.387**	.504**	.532**	-.028	-.358**	-.014	-.055**	1.000
U	-.147**	-.119**	-.066**	-.064**	.220**	-.008	-.033*	-.082**
V	.458**	.516**	-.014	.850**	-.349**	.045**	.173**	.118**
W	-.008	-.019	-.028	.037*	.001	-.002	.053**	-.018
Zn	.579**	.403**	.263**	.380**	-.182**	.011	.039**	.251**
	Pb	S	Sb	Sc	Sr	Th	Ti	Tl

Table 24. Continued

Au				
Ag				
Al				
As				
B				
Ba				
Be				
Bi				
Ca				
Cd				
Co				
Cr				
Cu				
Fe				
Ga				
Hg				
K				
La				
Mg				
Mn				
Mo				
Na				
Ni				
P				
Pb				
S				
Sb				
Sc				
Sr				
Th				
Ti				
Tl				
U	1.000			
V	-.134**	1.000		
W	-.022	.028	1.000	
Zn	-.157**	.469**	.014	1.000
	U	V	W	Zn

Data is from whole rock assay geochemistry data from 14 drill holes.

** Correlation value has asymptotic significance (2-tailed distribution) value at the 0.01 level. * Correlation value has asymptotic significance (2-tailed distribution) value at the 0.05 level. Correlation values without ** or * have asymptotic significance > 0.05 indicating values are not statistically significant.

Correlation value (R value) > 0.4 indicate strong positive correlations and are highlighted in pink and correlation value (R value) < -0.4 indicate strong negative correlations and are highlighted in blue.

Table 25. Non-metric Multi-dimensional Scaling Model Axis 1 and 2 R, and R2 values for 0.1 ppm and 1.0 ppm gold classifications for whole rock assay data

		Au	Ag	Al	As	B	Ba	Be	Bi	Ca	Cd
Axis 1	r	0.558	0.101	-0.299	0.355	-0.18	-0.283	-0.47	0.02	-0.041	0.345
	r ²	0.311	0.01	0.089	0.126	0.032	0.08	0.221	0	0.002	0.119
Axis 2	r	-0.163	-0.409	-0.857	-0.672	-0.24	0.779	-0.317	0.128	0.787	-0.16
	r ²	0.027	0.168	0.734	0.451	0.058	0.607	0.1	0.016	0.619	0.026
		Co	Cr	Cu	Fe	Ga	Hg	K	La	Mg	Mn
Axis 1	r	-0.357	-0.254	-0.244	-0.079	-0.093	0.516	-0.307	-0.171	-0.116	-0.281
	r ²	0.128	0.065	0.059	0.006	0.009	0.266	0.095	0.029	0.013	0.079
Axis 2	r	-0.829	-0.8	-0.903	-0.932	-0.03	-0.422	-0.88	-0.003	0.758	0.386
	r ²	0.687	0.64	0.816	0.869	0.001	0.178	0.774	0	0.574	0.149
		Mo	Na	Ni	P	Pb	S	Sb	Sc	Sr	Th
Axis 1	r	0.079	-0.123	-0.188	-0.289	0.095	0.221	0.603	-0.495	-0.091	0.005
	r ²	0.006	0.015	0.035	0.083	0.009	0.049	0.364	0.245	0.008	0
Axis 2	r	-0.487	0.562	-0.9	-0.876	-0.674	-0.763	-0.33	-0.524	0.563	-0.017
	r ²	0.238	0.316	0.811	0.767	0.455	0.582	0.109	0.275	0.318	0
		Ti	Tl	U	V	W	Zn				
Axis 1	r	-0.078	0.193	-0.048	-0.241	-0.058	0.063				
	r ²	0.006	0.037	0.002	0.058	0.003	0.004				
Axis 2	r	-0.037	-0.256	0.05	-0.845	-0.031	-0.515				
	r ²	0.001	0.066	0.003	0.714	0.001	0.265				

Table 26. Mann Whitney U-Test for 0.004, 0.1, 0.3, 1.0, 2.0, 3.0, and 6.0 ppm Au classifications

Mann-Whitney U-Test	Unit	Asymp. Sig. (2-tailed)	Median <0.004	Median >= 0.004	Asymp. Sig. (2-tailed)	Median Au <0.1	Median Au >=0.1
Au	ppm	.000	.004	.048	0.000	0.0130	0.3130
Ag	ppm	.000	.200	.200	.000	0.2000	0.3000
Al	wt. %	.000	.340	.170	.000	0.2200	0.1600
As	ppm	.000	17.000	69.000	.000	27.0000	198.0000
B	ppm	.217	9.000	9.000	.000	9.0000	9.0000
Ba	ppm	.000	190.000	100.000	.000	180.0000	40.0000
Be	ppm	.000	.400	.400	.000	0.4000	0.4000
Bi	ppm	.617	1.000	1.000	.141	1.0000	1.0000
Ca	wt. %	.167	2.500	3.305	.000	3.2900	2.3400
Cd	ppm	.000	.400	.400	.000	0.4000	0.4000
Co	ppm	.001	5.000	3.000	.006	4.0000	3.0000
Cr	ppm	.000	12.000	9.000	.613	10.0000	9.0000
Cu	ppm	.700	17.500	11.000	.319	13.0000	12.0000
Fe	wt. %	.052	2.015	1.500	.000	1.4100	1.6200
Ga	ppm	.000	9.000	9.000	.000	9.0000	9.0000
Hg	ppm	.000	.900	1.000	0.000	0.9000	4.0000
K	wt. %	.000	.155	.080	.000	0.1100	0.0800
La	ppm	.000	9.000	9.000	.000	9.0000	9.0000
Mg	wt. %	.000	.680	.960	.000	0.9700	0.5200
Mn	ppm	.000	255.000	217.000	.000	244.0000	103.0000
Mo	ppm	.000	1.000	1.000	.000	1.0000	1.0000
Na	wt. %	.000	.020	.020	.000	0.0200	0.0100
Ni	ppm	.110	19.000	14.000	.784	14.0000	14.0000
P	ppm	.000	720.000	240.000	.000	510.0000	230.0000
Pb	ppm	.000	6.000	9.000	.000	8.0000	12.0000
S	wt. %	.000	.330	.780	.000	0.4200	1.6500
Sb	ppm	.000	1.000	6.000	0.000	3.0000	20.0000
Sc	ppm	.000	3.000	1.000	.000	2.0000	1.0000
Sr	ppm	.000	40.000	40.000	.000	45.0000	29.0000
Th	ppm	.000	10.000	10.000	.140	10.0000	10.0000
Ti	ppm	.000	.009	.009	.000	0.0090	0.0090
Tl	ppm	.000	9.000	9.000	.000	9.0000	9.0000
U	ppm	.301	9.000	9.000	.000	9.0000	9.0000
V	ppm	.000	25.000	11.000	.000	15.0000	11.0000
W	ppm	.374	9.000	9.000	.402	9.0000	9.0000
Zn	ppm	.001	35.000	39.000	.000	28.0000	60.0000

Table 26. Continued

Mann-Whitney U-Test	Unit	Asymp. Sig. (2-tailed)	Median Au <0.3	Median Au >=0.3	Asymp. Sig. (2-tailed)	Median Au < 1.0	Median Au >= 1.0
Au	ppm	0.000	0.0210	0.8255	.000	0.03	2.13
Ag	ppm	.000	0.2000	0.3000	.000	0.20	0.30
Al	wt. %	.000	0.1700	0.2100	.000	0.17	0.26
As	ppm	.000	39.0000	330.5000	.000	51.00	582.00
B	ppm	.043	9.0000	9.0000	.000	9.00	9.00
Ba	ppm	.000	150.0000	30.0000	.000	120.00	30.00
Be	ppm	.000	0.4000	0.4000	.000	0.40	0.40
Bi	ppm	.791	1.0000	1.0000	.426	1.00	1.00
Ca	wt. %	.000	4.1850	0.7150	.000	3.78	0.44
Cd	ppm	.000	0.4000	0.4000	.000	0.40	0.40
Co	ppm	.000	3.0000	5.0000	.000	3.00	6.00
Cr	ppm	.000	8.0000	10.0000	.000	9.00	10.00
Cu	ppm	.000	7.0000	19.0000	.000	9.00	26.00
Fe	wt. %	.000	1.2200	1.9200	.000	1.38	2.23
Ga	ppm	.005	9.0000	9.0000	.050	9.00	9.00
Hg	ppm	0.000	1.0000	7.0000	.000	1.00	10.50
K	wt. %	.000	0.0800	0.1000	.000	0.08	0.13
La	ppm	.000	9.0000	9.0000	.000	9.00	9.00
Mg	wt. %	.000	1.0300	0.0800	.000	1.01	0.04
Mn	ppm	.000	237.0000	55.0000	.000	229.00	51.00
Mo	ppm	.000	1.0000	2.0000	.000	1.00	2.00
Na	wt. %	.000	0.0200	0.0100	.000	0.02	0.01
Ni	ppm	.000	10.0000	20.0000	.000	11.00	25.00
P	ppm	.029	220.0000	320.0000	.000	240.00	420.00
Pb	ppm	.000	8.0000	14.0000	.000	8.00	15.00
S	wt. %	.000	0.5100	1.9950	.000	0.62	2.35
Sb	ppm	.000	4.0000	28.0000	.000	5.00	32.50
Sc	ppm	.000	1.0000	1.0000	.003	1.00	1.00
Sr	ppm	.000	44.0000	19.0000	.000	42.00	12.00
Th	ppm	.346	10.0000	10.0000	.564	10.00	10.00
Ti	ppm	.000	0.0090	0.0090	.014	0.01	0.01
Tl	ppm	0.000	9.0000	10.0000	0.000	9.00	10.00
U	ppm	.000	9.0000	9.0000	.001	9.00	9.00
V	ppm	.071	11.0000	13.0000	.001	12.00	15.00
W	ppm	.583	9.0000	9.0000	.710	9.00	9.00
Zn	ppm	.000	31.0000	81.0000	.000	36.00	84.00

Table 26. Continued

Mann-Whitney U-Test	Unit	Asymp. Sig. (2-tailed)	Median < 2.0	Median >= 2.0	Asymp. Sig. (2-tailed)	Median Au < 3.0	Median Au >= 3.0
Au	ppm	.000	0.03	3.73	.000	0.03	5.40
Ag	ppm	.198	0.20	0.20	.547	0.20	0.20
Al	wt. %	.000	0.17	0.28	.000	0.18	0.30
As	ppm	.000	57.00	739.00	.000	59.00	1000.00
B	ppm	.000	9.00	9.00	.000	9.00	9.00
Ba	ppm	.000	110.00	30.00	.000	110.00	20.00
Be	ppm	.000	0.40	0.40	.000	0.40	0.40
Bi	ppm	.297	1.00	1.00	.490	1.00	1.00
Ca	wt. %	.000	3.50	0.47	.000	3.30	0.60
Cd	ppm	.000	0.40	0.40	.000	0.40	0.40
Co	ppm	.000	3.00	7.00	.000	3.00	7.00
Cr	ppm	.000	9.00	10.00	.001	9.00	10.00
Cu	ppm	.000	10.00	29.00	.000	10.00	33.00
Fe	wt. %	.000	1.45	2.38	.000	1.50	2.53
Ga	ppm	.157	9.00	9.00	.254	9.00	9.00
Hg	ppm	.000	1.00	14.00	.000	1.00	18.00
K	wt. %	.000	0.09	0.15	.000	0.09	0.17
La	ppm	.000	9.00	9.00	.001	9.00	9.00
Mg	wt. %	.000	0.98	0.04	.000	0.96	0.04
Mn	ppm	.000	226.00	55.00	.000	224.00	60.00
Mo	ppm	.000	1.00	2.00	.024	1.00	1.00
Na	wt. %	.000	0.02	0.01	.000	0.02	0.01
Ni	ppm	.000	12.00	25.00	.000	13.00	26.00
P	ppm	.002	270.00	410.00	.008	270.00	410.00
Pb	ppm	.000	8.00	16.00	.000	9.00	16.00
S	wt. %	.000	0.67	2.52	.000	0.69	2.78
Sb	ppm	.000	5.00	34.00	.000	6.00	25.00
Sc	ppm	.044	1.00	1.00	.992	1.00	1.00
Sr	ppm	.000	41.00	10.00	.000	41.00	10.00
Th	ppm	.678	10.00	10.00	.738	10.00	10.00
Ti	ppm	.078	0.01	0.01	.155	0.01	0.01
Tl	ppm	.000	9.00	20.00	.000	9.00	30.00
U	ppm	.010	9.00	9.00	.020	9.00	9.00
V	ppm	.003	12.00	16.00	.002	12.00	17.00
W	ppm	.773	9.00	9.00	.893	9.00	9.00
Zn	ppm	.000	37.00	76.00	.002	38.00	57.00

Table 26. Continued

Mann-Whitney U-Test	Unit	Asymp. Sig. (2-tailed)	Median Au < 6.0	Median Au >= 6.0
Au	ppm	.000	0.04	10.55
Ag	ppm	.855	0.20	0.20
Al	wt. %	.000	0.18	0.31
As	ppm	.000	61.00	1560.00
B	ppm	.001	9.00	9.00
Ba	ppm	.000	110.00	20.00
Be	ppm	.002	0.40	0.40
Bi	ppm	.031	1.00	1.00
Ca	wt. %	.000	3.19	0.48
Cd	ppm	.720	0.40	0.40
Co	ppm	.000	3.00	9.00
Cr	ppm	.085	9.00	9.00
Cu	ppm	.000	11.00	35.50
Fe	wt. %	.000	1.54	2.81
Ga	ppm	.456	9.00	9.00
Hg	ppm	.000	1.00	35.00
K	wt. %	.000	0.09	0.19
La	ppm	.032	9.00	9.00
Mg	wt. %	.000	0.94	0.04
Mn	ppm	.000	222.00	59.00
Mo	ppm	.136	1.00	1.00
Na	wt. %	.000	0.02	0.01
Ni	ppm	.000	13.00	29.00
P	ppm	.225	280.00	335.00
Pb	ppm	.000	9.00	17.00
S	wt. %	.000	0.73	3.09
Sb	ppm	.000	6.00	12.00
Sc	ppm	.928	1.00	1.00
Sr	ppm	.000	40.00	9.00
Th	ppm	.827	10.00	10.00
Ti	ppm	.353	0.01	0.01
Tl	ppm	.000	9.00	50.00
U	ppm	.047	9.00	9.00
V	ppm	.123	12.00	13.50
W	ppm	.311	9.00	9.00
Zn	ppm	.276	38.00	38.00

Asymptotic significance (2-tailed) values for each element for each gold classification. The values highlighted in blue are asymptotic significance (2-tailed) values < 0.005 , such that the median values in the low and high gold class are significantly different from each other. The values highlighted in white are asymptotic significance (2-tailed) values > 0.005 , such that the median values in the low and high gold class are not significantly different.

APPENDIX B

FIGURES

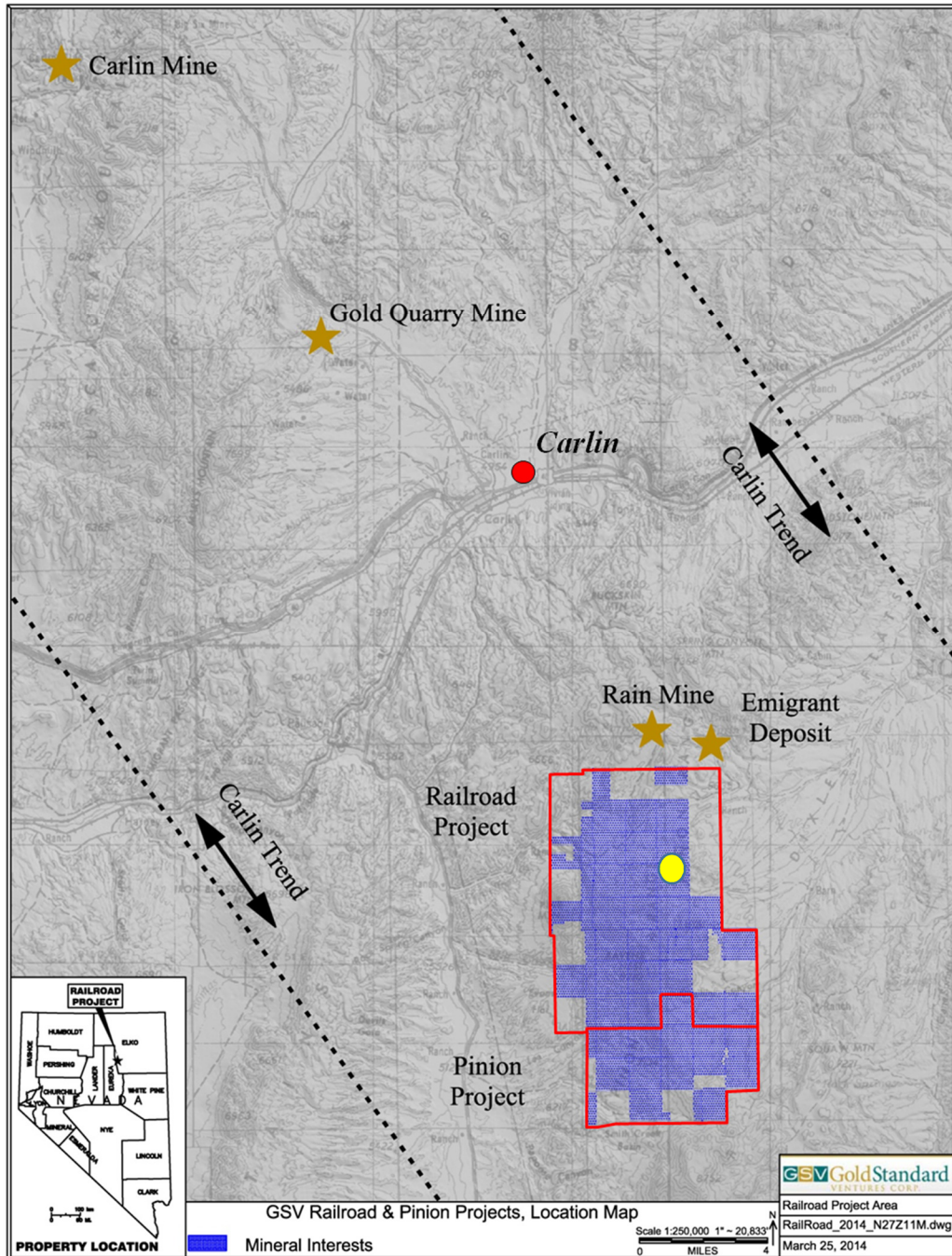


Figure 1. Nevada State map showing the location of the GSV Railroad Project in relation to the Carlin trend. The North Bullion Carlin system, marked by yellow dot, is a 3.2 square kilometer exploration target within the 35.4 square kilometers GSV Railroad Project located 8 kilometers south of the Rain Mine and Emigrant Deposit (from Gold Standard Ventures Corporation, 2014).

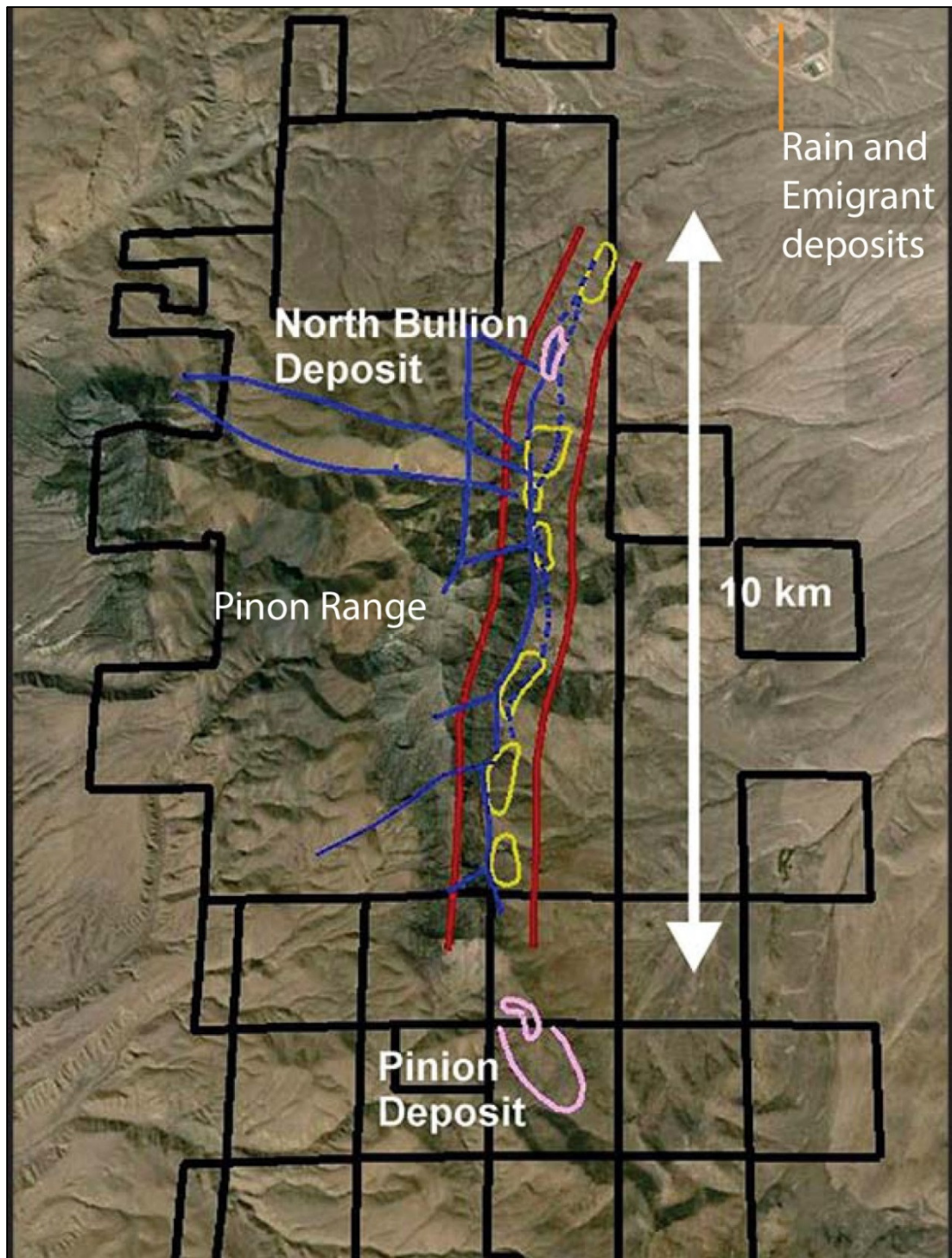


Figure 2. Location of North Bullion Carlin system on Railroad Project. Railroad Project area outlined in black, and shown in relation to CTGD in the area. Closest deposits are the Rain and Emigrant deposits (indicated by orange line) to the north, now considered the southern end of the Carlin trend. Blue lines are known faults, red lines outline the North Bullion Fault Corridor, yellow areas are GSV targets, and pink areas are the North Bullion (i.e. North Bullion Carlin system) and Pinion deposits within the property (from Gold Standard Ventures Corporation, 2012).

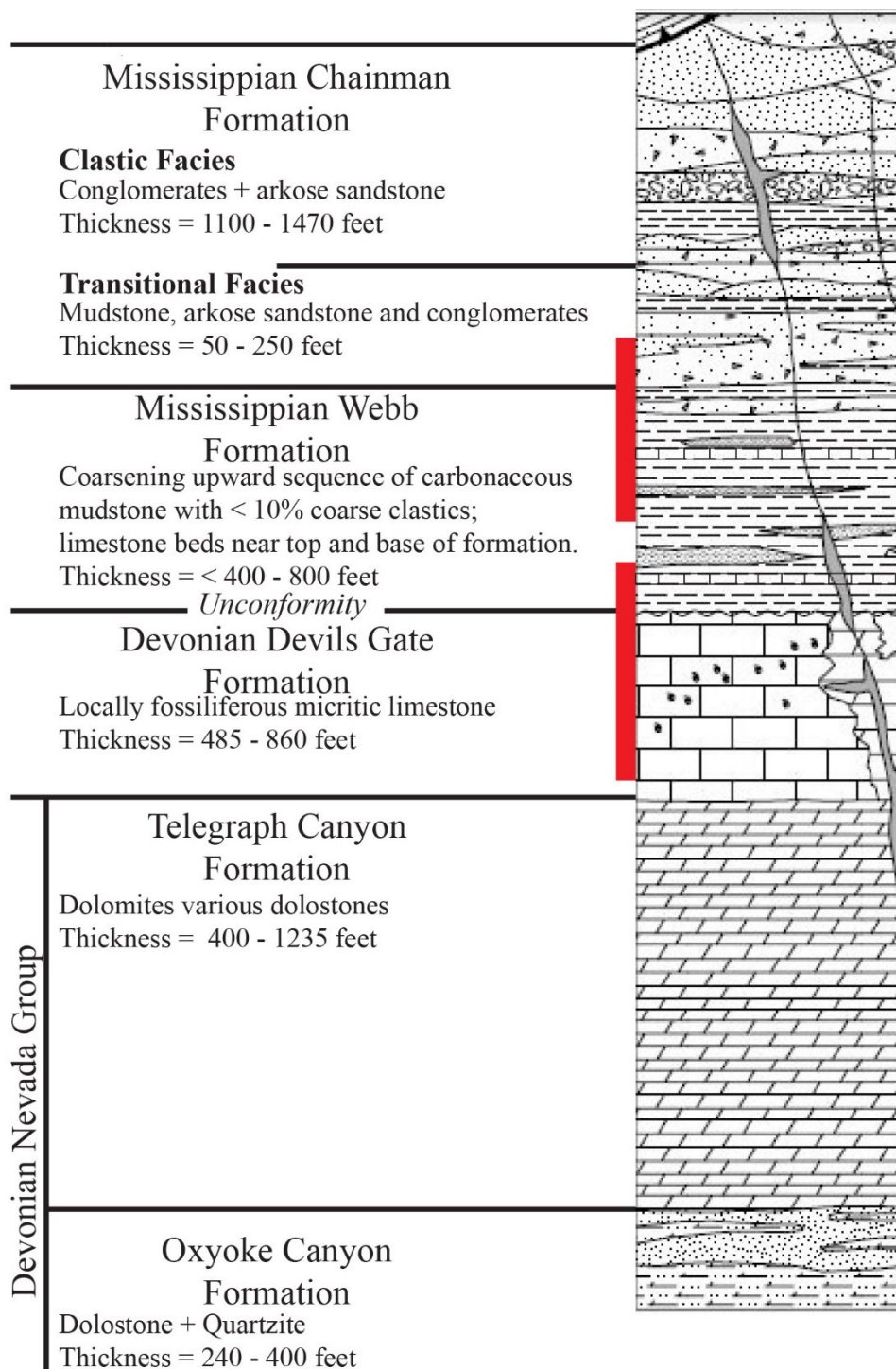


Figure 3. Rain Mine Stratigraphic Section. Location of North Bullion gold ore zones shown by red bars (Smith and Ketner, 1978; image modified from Longo et al., 2002).

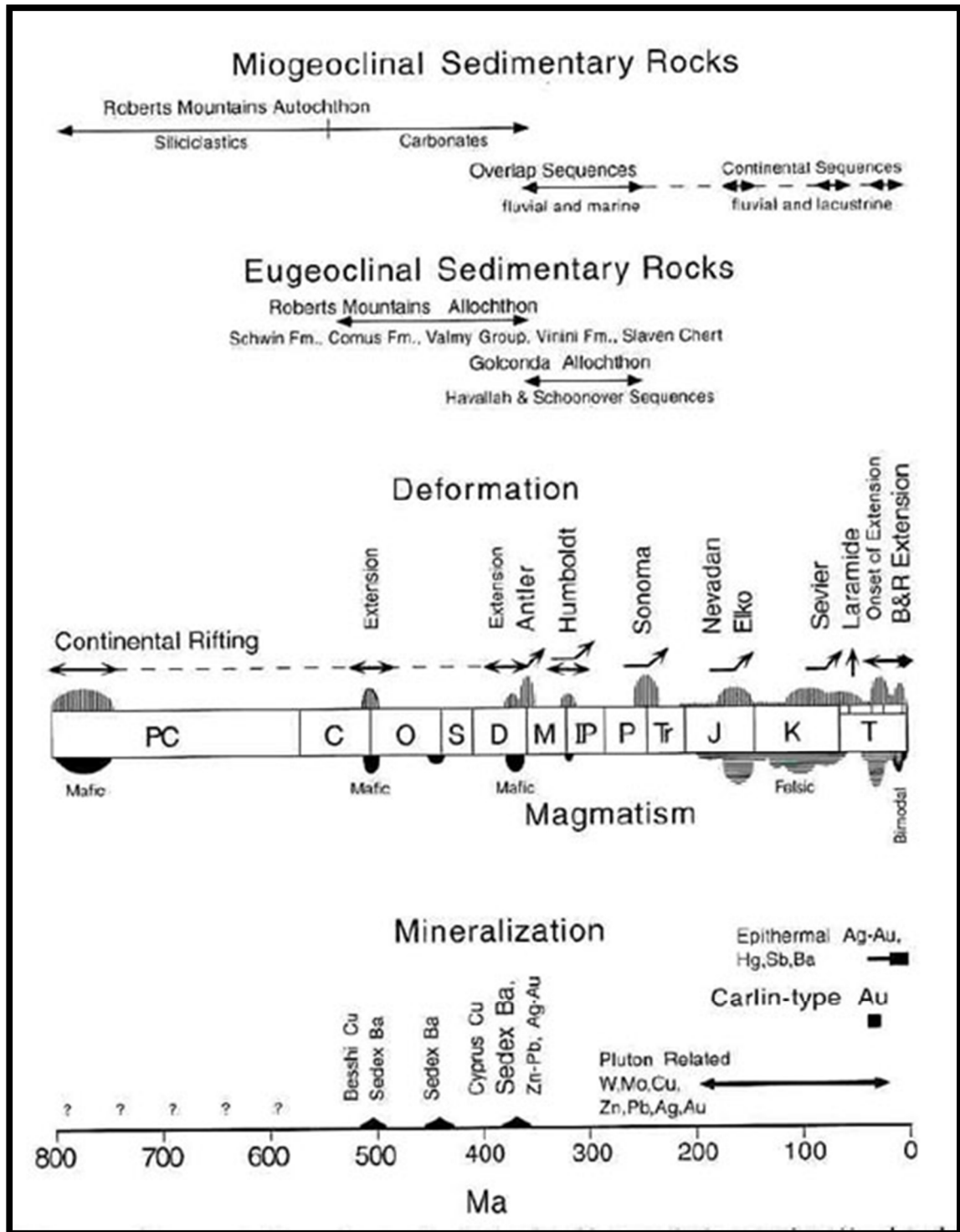


Figure 4. Tectono-stratigraphic history of Nevada. This figure shows the deformation and mineralization history of the area (from Hofstra and Cline, 2000; Cline et al., 2005).

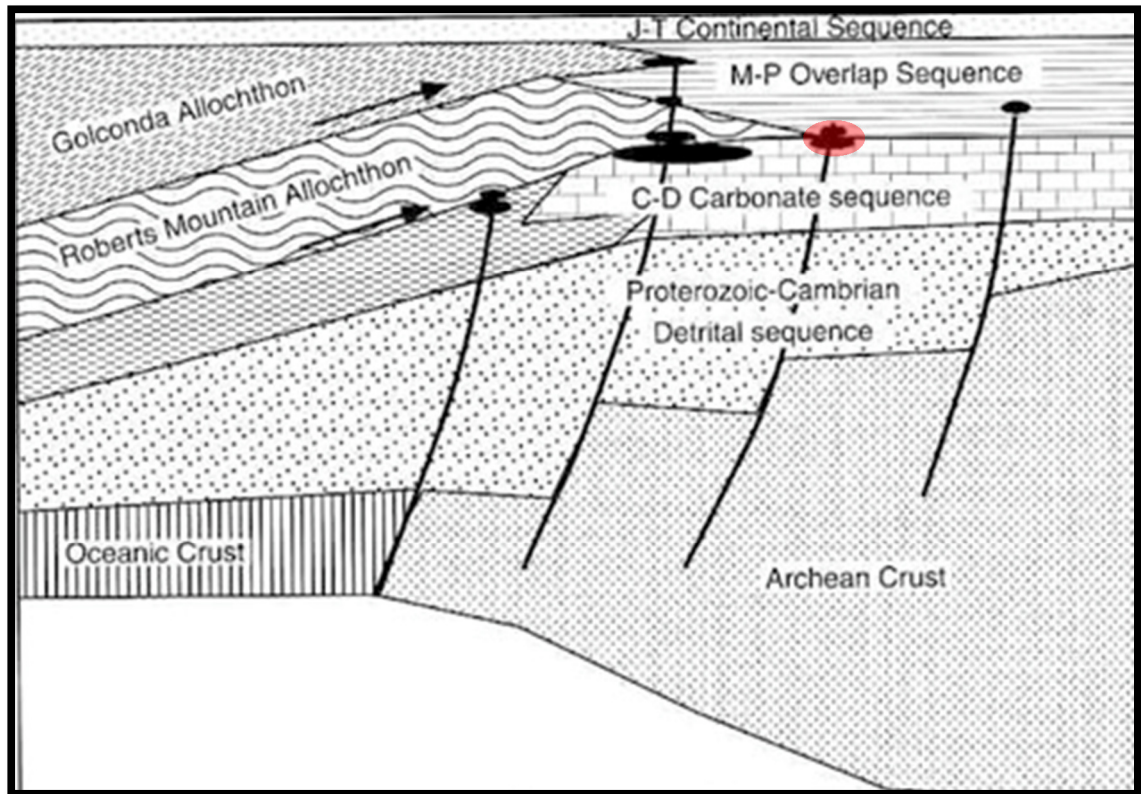


Figure 5. Generalized east-west cross section of northern Nevada and Utah. This figure shows miogeoclinal, eugeoclinal, allochthonous units and the location of Carlin type gold deposits (filled black ovals) in relation to the intersection of lithologic contacts and structures. The approximate setting of the North Bullion Carlin system is highlighted pink. The position of the North Bullion Carlin system is similar to some CTGD (modified from Cook and Corboy, 2004).

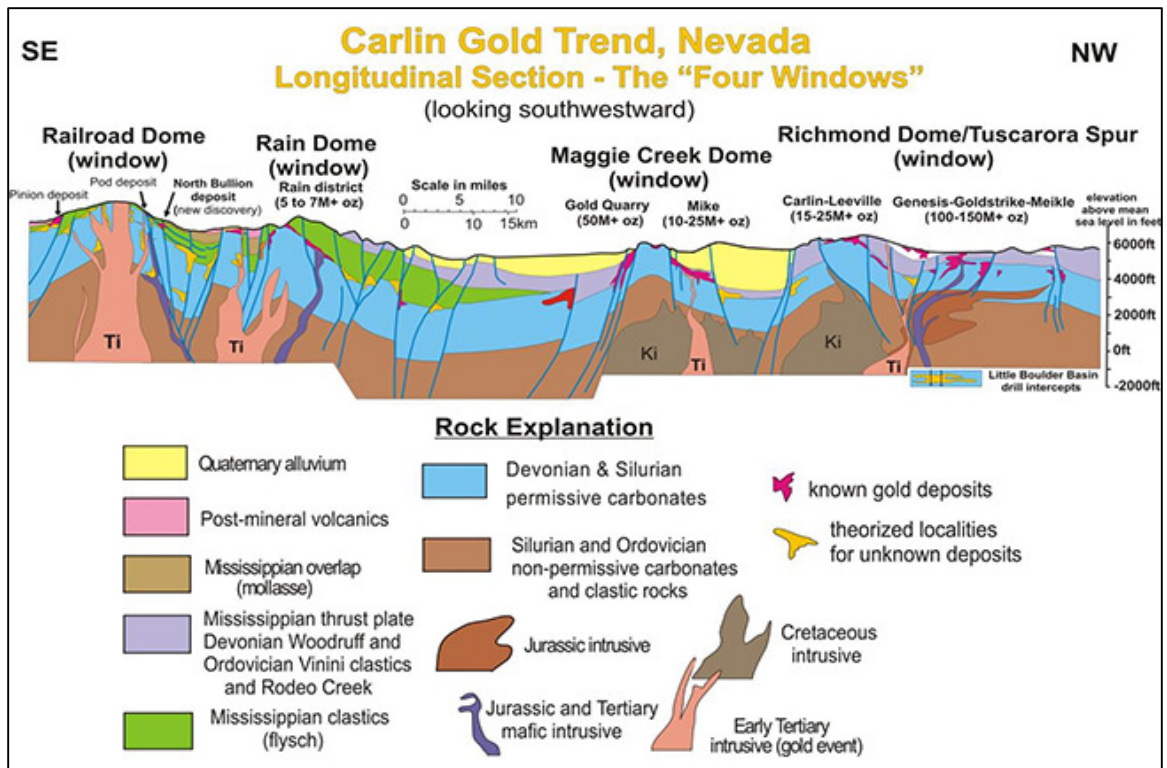


Figure 6. Generalized long section of the Carlin trend, Nevada, looking southwest. Note that each area with known gold deposits is centered on a dome and mineralization is localized along carbonate and siliciclastic lithological contacts (from Gold Standard Ventures Corporation, 2013).

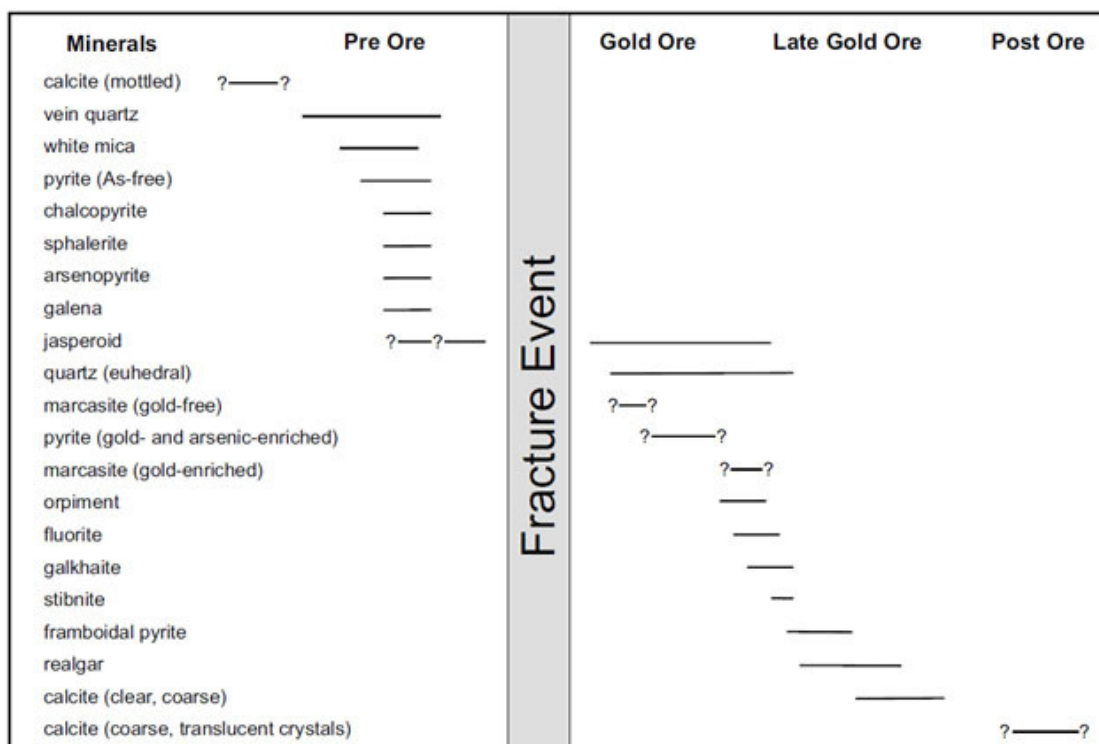


Figure 7. Mineral paragenesis for the Getchell CTGD (from Cline, 2001).

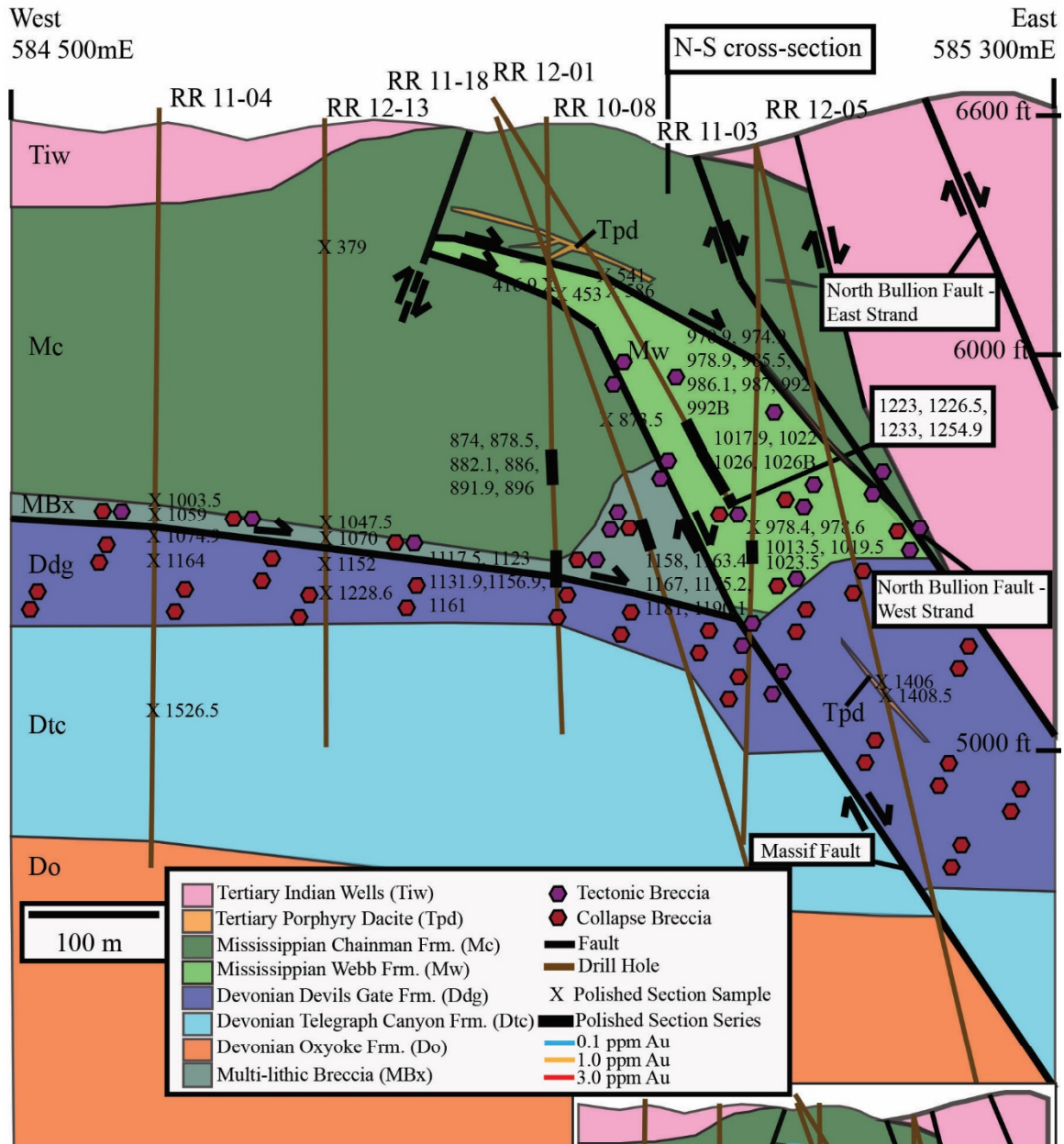
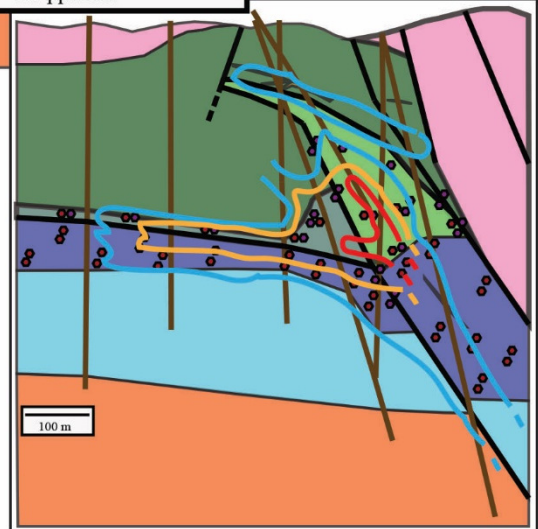


Figure 8. Idealized E-W cross section of the North Bullion Carlin system. Cross section at 4 488 700 N looking northward on the Railroad Project, Carlin trend, NV. Note that the sequence stratigraphy changes from east to west, and on the west side of the cross section the Mississippian Webb is absent and Chainman Formation has thickened as a result of low angle faults (modified from GSV, 2013).



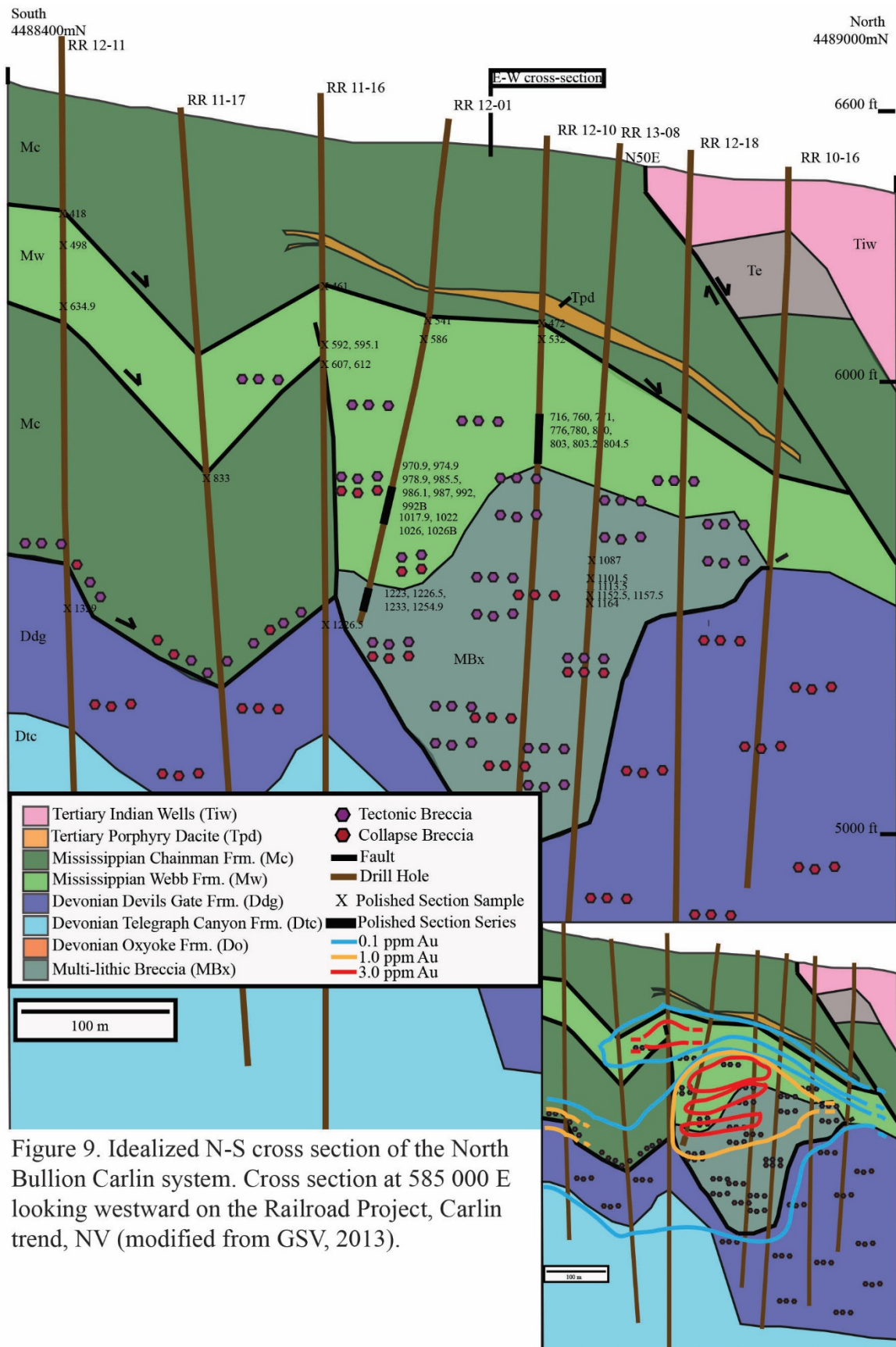


Figure 9. Idealized N-S cross section of the North Bullion Carlin system. Cross section at 585 000 E looking westward on the Railroad Project, Carlin trend, NV (modified from GSV, 2013).

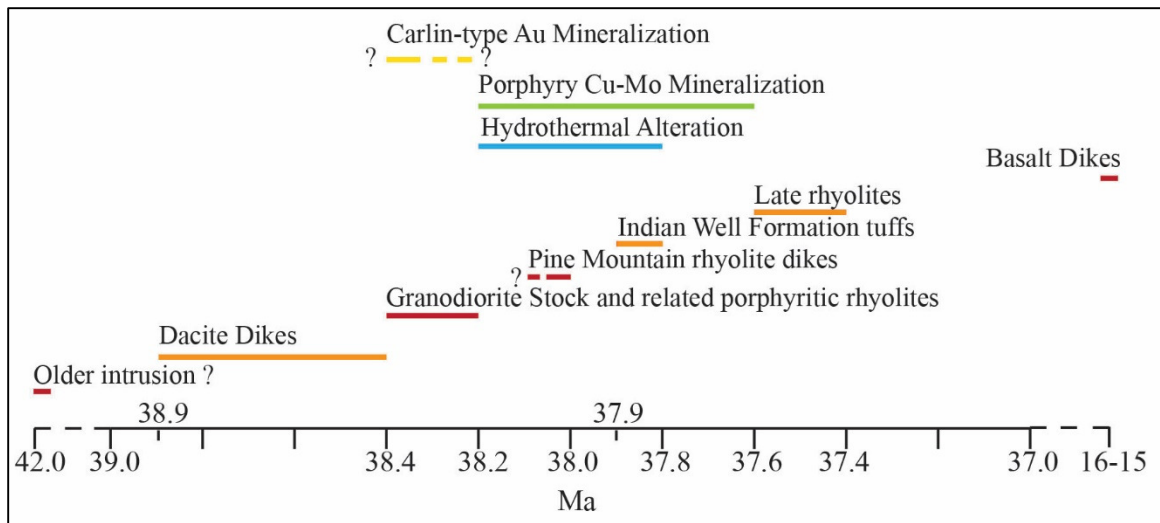


Figure 10. Timing of igneous activity and related mineralization at the Railroad property (Henry, 2014). Orange lines indicate igneous activity related to the North Bullion Carlin System, and red lines indicate igneous activity related to other areas within the Railroad property. Yellow lines indicate timing of Carlin-type Au mineralization related to the North Bullion Carlin system. Green, and blue lines indicate timing of porphyry Cu-Mo mineralization, and hydrothermal alteration related to other areas within the Railroad property. Line of dates show the initial ages of igneous activity at the Railroad property.

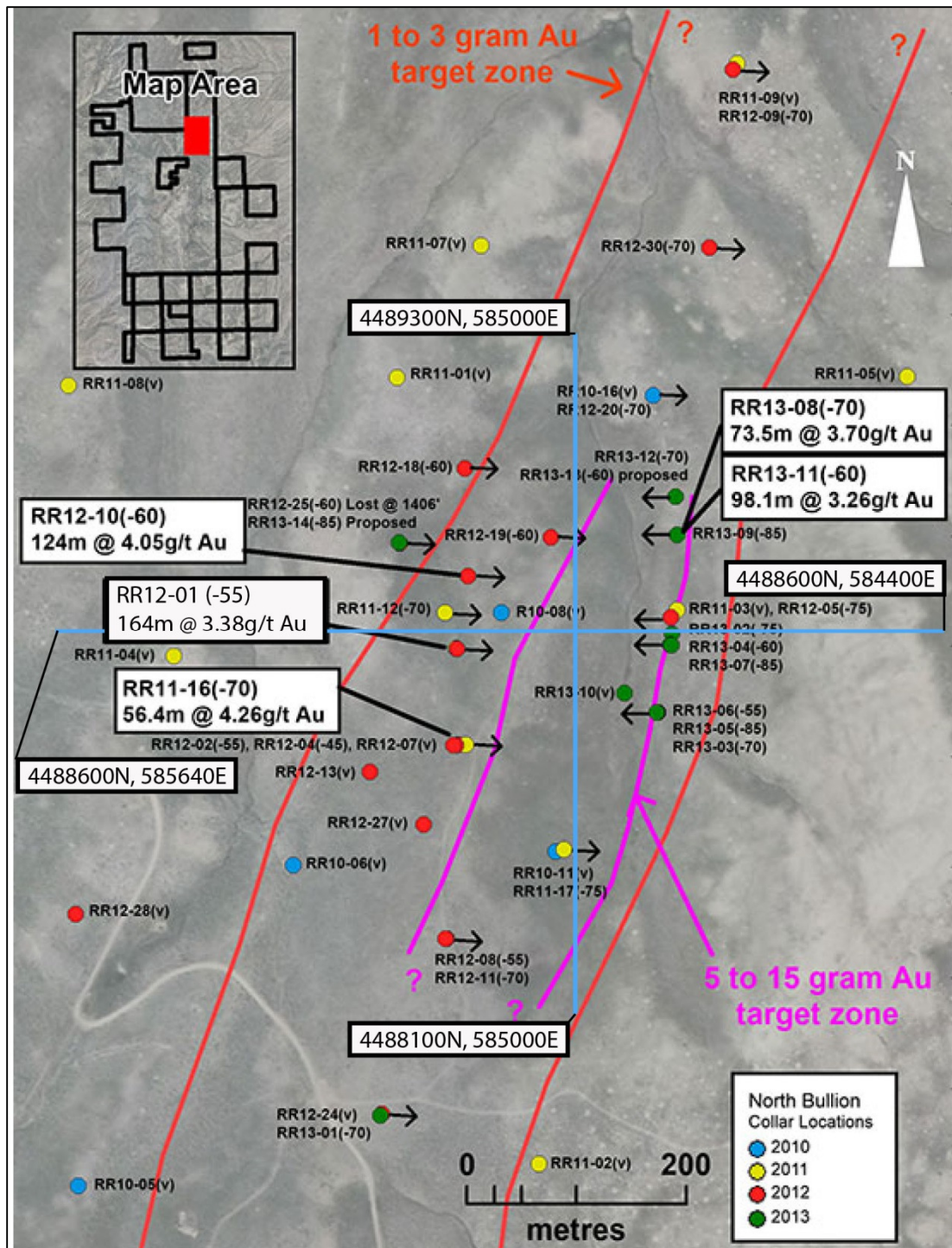
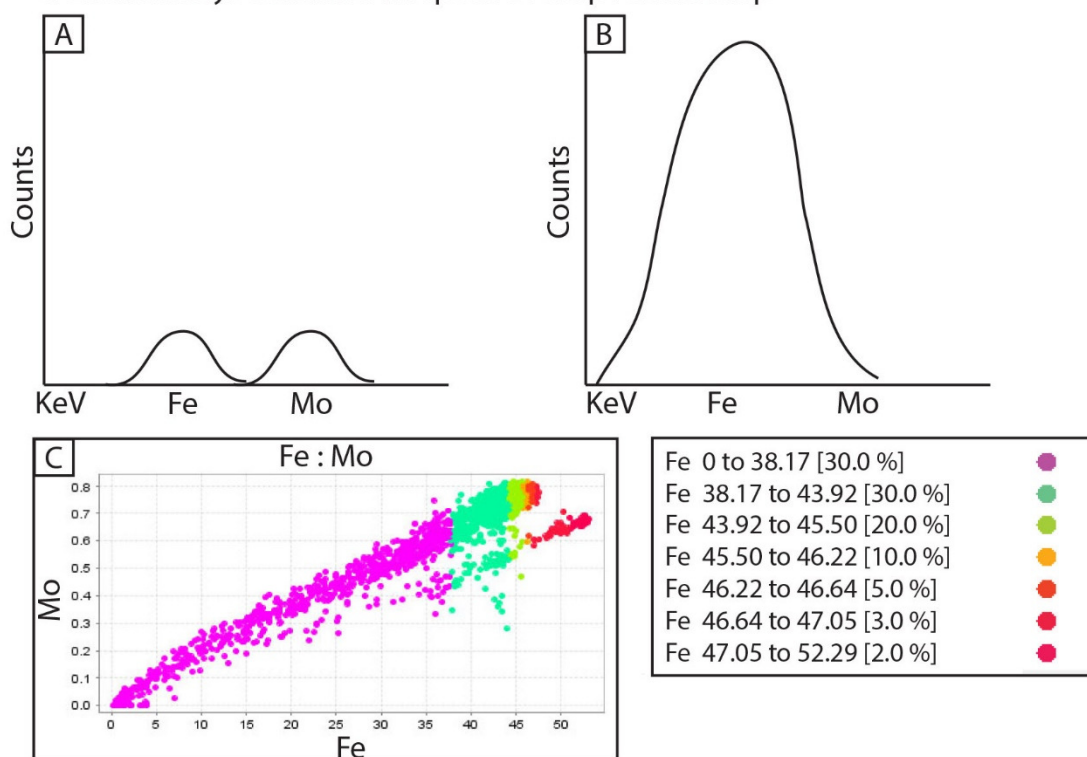


Figure 11. North Bullion Carlin system drill holes at the Railroad Project. Image shows gold target zones from drill core assays projected to surface, including 5-15 g/t outlined by pink lines, 1-3 g/t outlined by red lines, with blue lines showing E-W, and N-S oriented cross sections. Black arrows show the orientation and direction of dip of the drill hole (from Gold Standard Ventures Corporation, 2012).

Iron and Molybdenum EPMA peak overlap relationship



Zinc and Gold EPMA peak overlap relationship

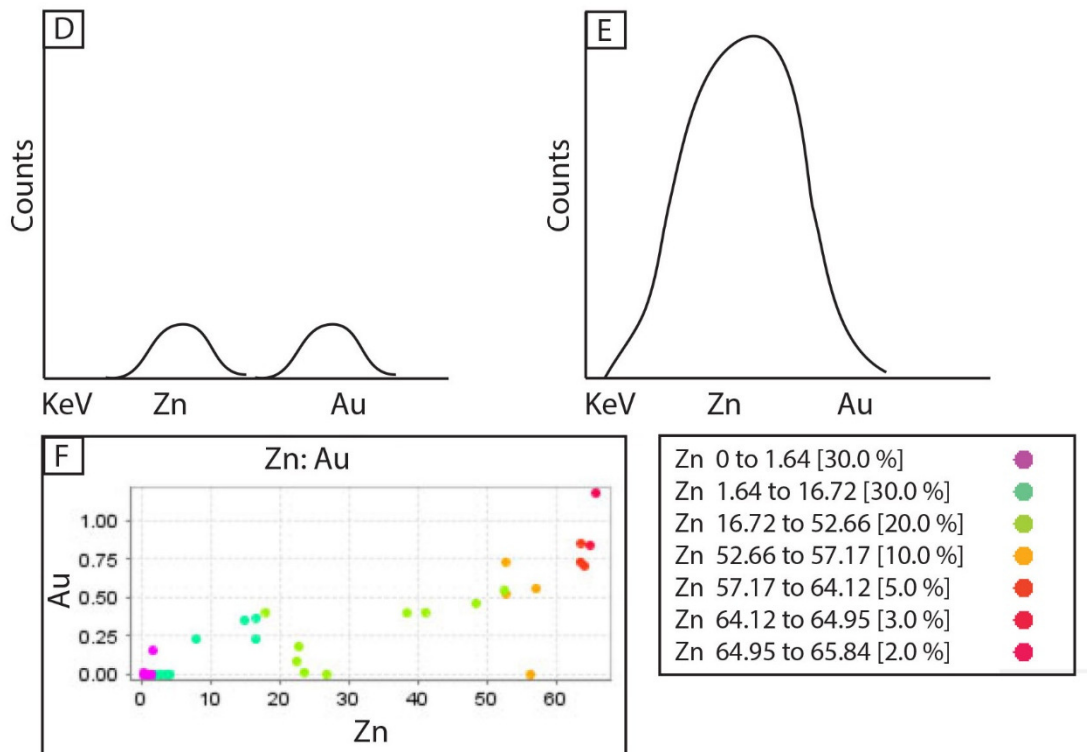


Figure 12. EPMA peak overlap relationships. A) For Mo, we choose the Mo $L\beta$ x-ray, with a λ 5.18, which is close to the third order Fe $K\beta$ x-ray (λ 5.23). If a mineral contains both Fe and Mo in trace amounts, the interference of peak overlap is not obvious or significant. The X-axis is energy (KeV) and the Y-axis is counts. B) If however, the analyzed point (pyrite or Fe-oxide) has a high Fe content, the tail of the Fe peak will generate false counts for Mo. The X-axis is energy (KeV). C) The positive correlation between Fe and Mo indicates the presence of false counts of Mo in Fe minerals. Iron can generate about 2% of Fe equivalent false Mo contents. Purple dots represent data that contain < 36 wt. % Fe, and are analytical points on Fe phases mixed with other phase (Si or C phases). Teal dots represent data that contain 36-45 wt. % Fe, and are analytical points on pyrite rims or arsenopyrite. Grass-green to red-orange dots (45-47 wt. % Fe) are analytical points on pyrite. Red dots are data that contain > 47 wt. % Fe, and are analytical points on Fe oxides. Percentages in '[30.0 %]' in the color key indicate the percentage of data analyzed that are within various ranges of Fe weight percent for each color. D) For Au, we choose the Au $L\alpha$ peak to quantify Au in each analysis. The λ of Au $L\alpha$ is 1.276, and is close to the λ of Zn $K\beta$ (λ 1.295). The X-axis is energy (KeV) and the Y-axis is in counts. E) For analytical points high in Zn, the tail of the Zn $K\beta$ peak will generate false counts for Au. F) The positive correlation between Zn and Au illustrates that these false counts of Au in high-Zn minerals. Zinc can generate about 1% of Zn equivalent false Au counts. Where Zn is present in trace concentrations, as in pyrite, the influence of Zn on Au is small and can be omitted. If the Zn content in a mineral is high, as in sphalerite, the Au content generated by EPMA need to be corrected based on the Zn content. Purple and teal dots represent data points that contain < 16 wt. % Zn, and are analytical points on a phase that contains Zn mixed with another phase (Si or Al phase). Grass green dots represent data points that contain 16-52 wt. % Zn, and are analytical points on sphalerite \sim /= another phase (Si or Al phase). Orange to red dots represent data points that quantified > 52 wt. % Zn, and are analytical points on dominantly sphalerite. Percentages in '[30.0 %]' in the color key indicate the percentage of data analyzed that are within various concentrations of Zn for that color. In addition, the W $L\beta$ wavelength is at 1.281; if analyzed points contain high W, the analysis will generate a false count of Au, but high counts of W were not detected during analysis.

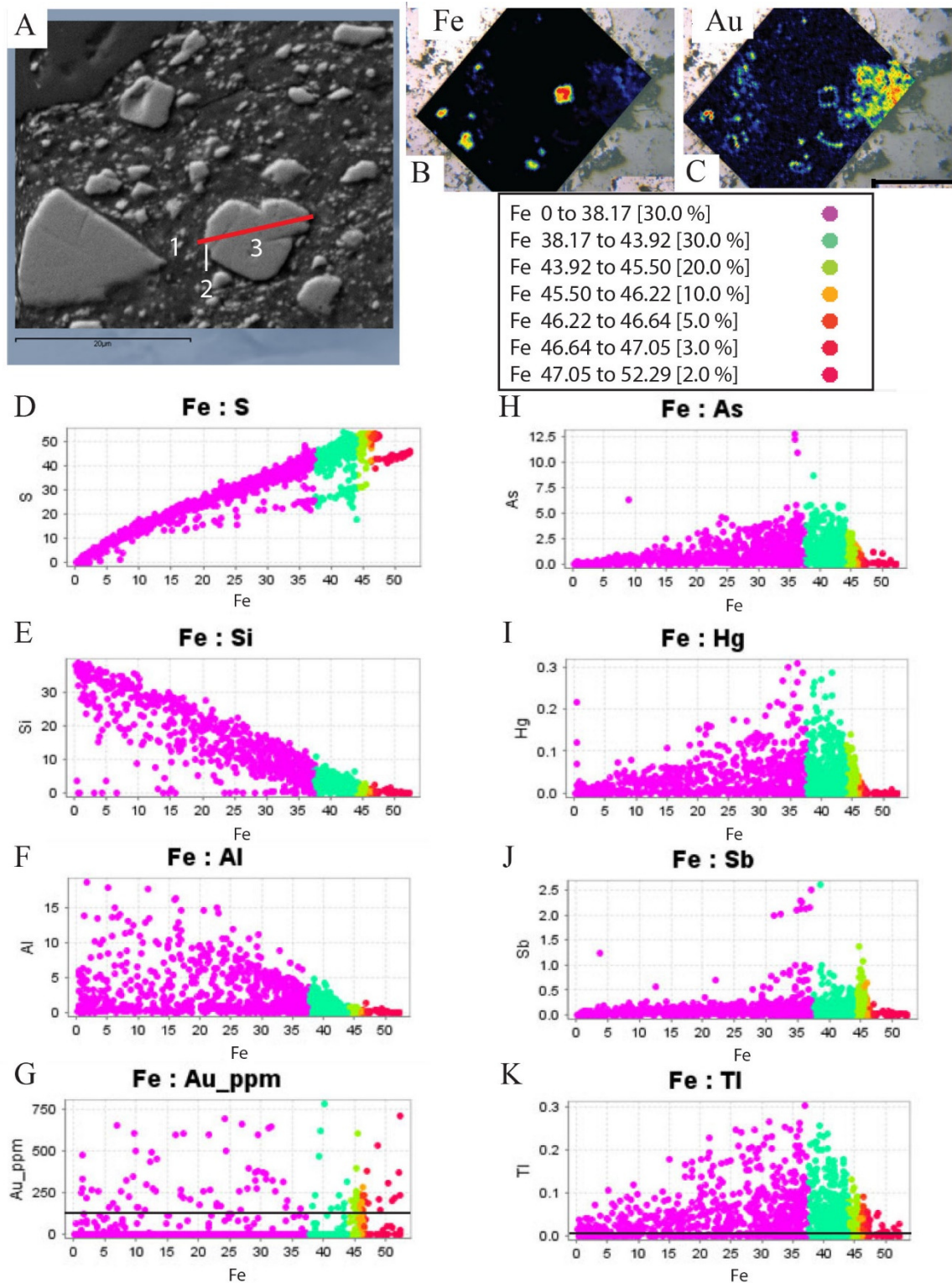


Figure 13. EPMA transect analytical method for pyrite. A) EPMA started in host rock minerals (1), crossed the host rock/ pyrite boundary +/- ore-stage gold-bearing rim (2), crossed the pyrite (3), possibly crossed another ore-stage rim, and ended in host rock. B) LA-ICP-MS map of Fe indicates the presence of pyrite crystals within the sample. C)

LA-ICP-MS map of Au in the same location indicates the presence of ore-stage rims on pre-ore stage pyrites and of ore-stage microcrystals. The EPMA analysis technique used to locate and quantify the chemistry of ore-stage rims, typically produced totals < 98 wt. %. However, because rims are very narrow, typically < 1-2 μm wide, many analyses include pyrite and host rock. Graphs D to K include all EPMA data for pyrites. In each graph, various elements are plotted against Fe, which reflects the percent of pyrite in each analysis. Purple dots represent data (< 38.17 wt. % Fe) from analyses on pyrite plus other minerals. Teal dots represent data (38.17 - 43.92 wt. % Fe) from analyses on pyrite rims or arsenopyrite. Grass-green (43.92 - 45.50 wt. % Fe), orange (45.50 – 46.22 wt. % Fe), red-orange (46.22 - 46.64 wt. % Fe), represent analyses on pyrite. Red and pink dots represent data (> 46.64 wt. % Fe) analyses on Fe oxide minerals. Percentages in the color key indicate the percent data in each range. D) Fe and S in the majority of analyses have a linear relationship, representing the 46:54 Fe: S ratio in pyrite, though some analyses have low S. E and F) Fe:Si and Fe:Al graphs show that analyses with low Fe represent analyses that included quartz and clays. Where Fe is between ~ 35- 55 wt. %, the analyzed mineral was pyrite and/or Fe oxides. G to K) Gold and the CTGD pathfinder elements are elevated at Fe concentrations between 10 – 45 Fe wt. %, consistent with the presence of ore stage rims between host rock minerals and pyrite. Analyses with low totals, reported in Appendix F, were not removed, in order to not remove the majority of analyses that quantified Au. The analysis technique, in which single analytical points bridged gangue mineral-gold-bearing pyrite rim boundaries resulted in low totals, particularly of analyses of gold-bearing rims.

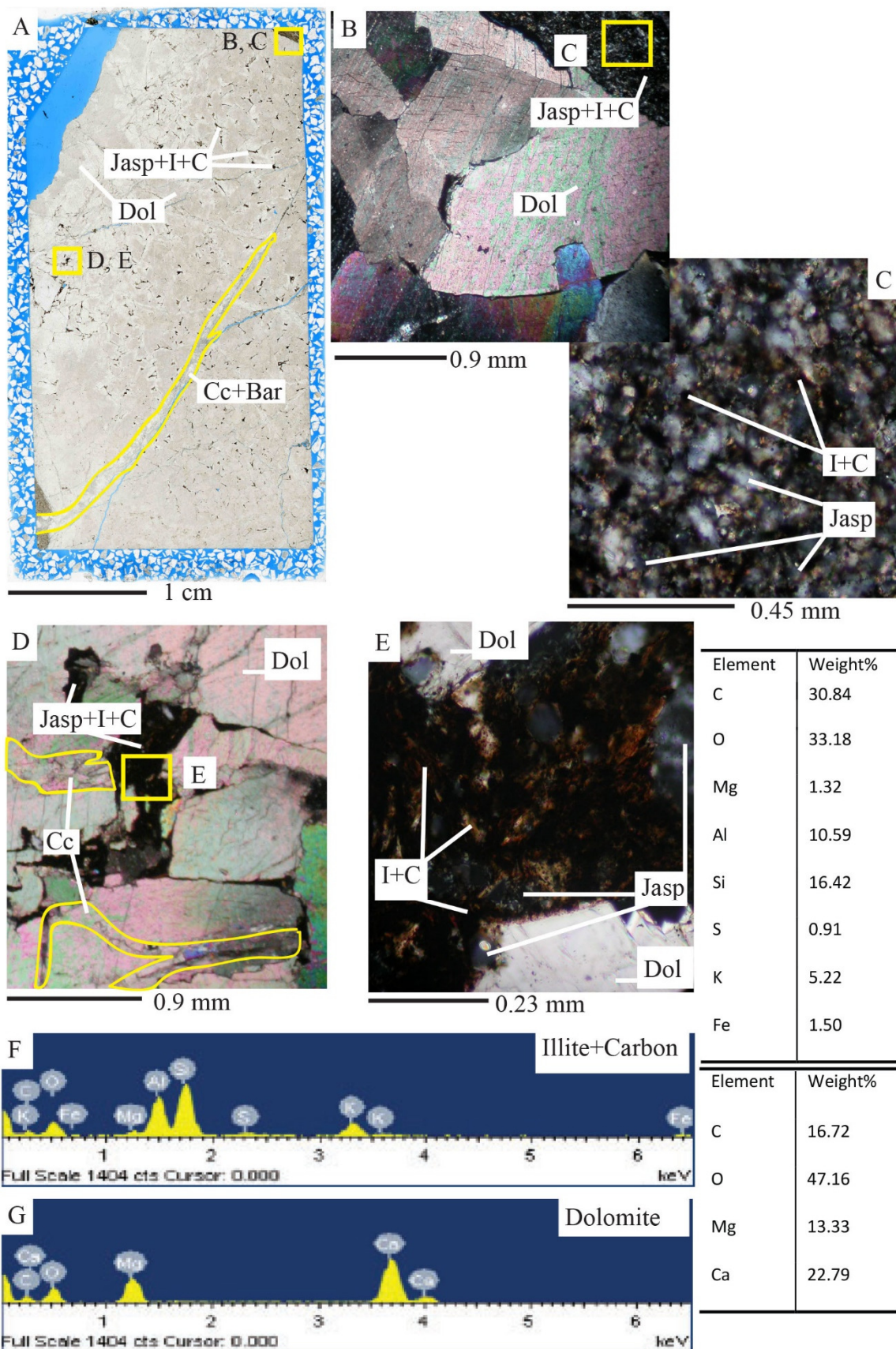


Figure 14. Devonian Devil's Gate Formation. A) Devonian Devil's Gate Formation, polished section 11-04 1074.9 (0.017 ppm Au). This sample is cross-cut by late-ore-stage calcite and barite. B-E) Photomicrographs showing Devonian Devil's Gate host rock is comprised of mostly dolomite with jasperoid, illite, and carbon filling fractures (TCPL). F- G) SEM analyses identified illite plus carbon and dolomite. Abbreviations: Bar = Barite, C = Carbon, Cc = Calcite, Dol = Dolomite, Jasp = Jasperoid, I = Illite, TCPL = Transmitted Crossed Polarized Light

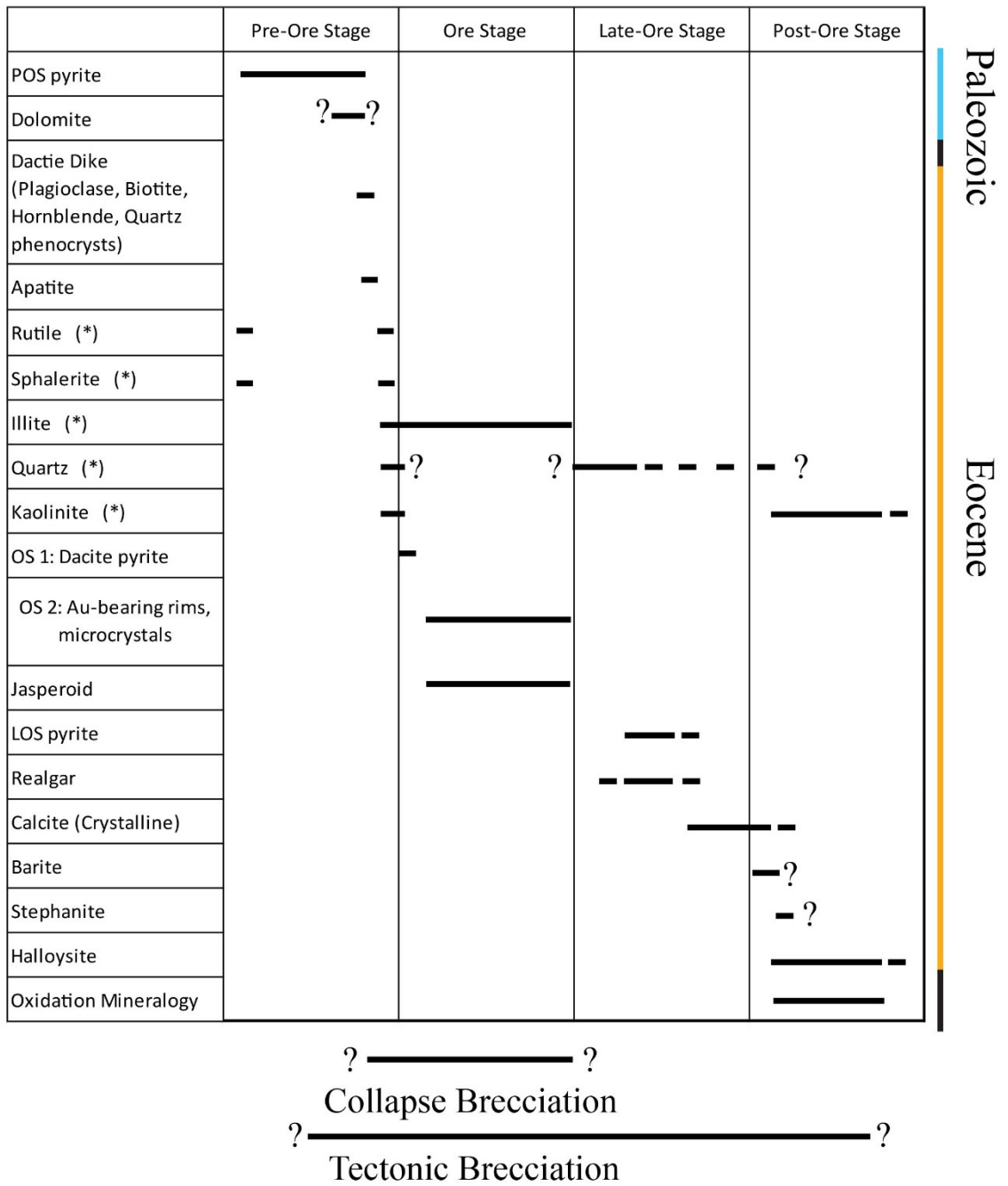


Figure 15. North Bullion Carlin system Mineral Paragenesis. Minerals (*) are found both in the altered dacite dike and the sedimentary host rocks.

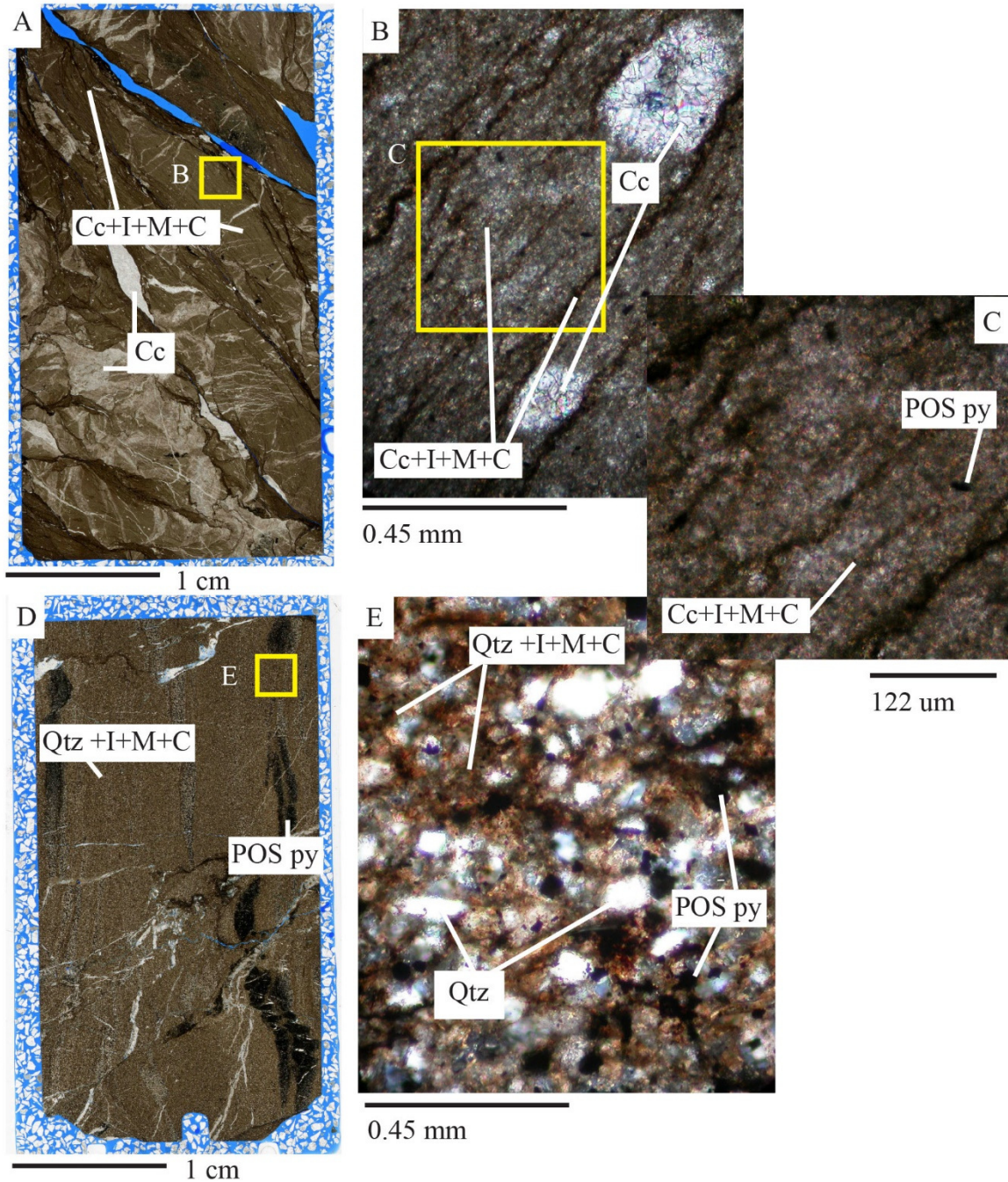


Figure 16. Mississippian Webb Formation. A) Polished section of micrite, 12-11 418 (0.004 ppm Au). B) Photomicrograph of micrite, showing silt-to-sand sized calcite crystals within a calcite, illite, montmorillonite, and carbon matrix (TCPL), but the darker bands have the same composition just more carbon. C) Photomicrograph of calcite, illite, montmorillonite, and carbon matrix (TCPL). D) Silty mudstone breccia polished thin section 12-10 476 (0.016 ppm Au). E) Photomicrograph of silty mudstone, showing silt-to-sand sized quartz crystals within finer quartz, illite, montmorillonite, and carbon matrix. Abbreviations: C = Carbon, Cc = Calcite, I = Illite, M = Montmorillonite, POS py = Pre-ore-stage pyrite, Qtz = Quartz, TCPL = Transmitted Crossed Polarized Light.

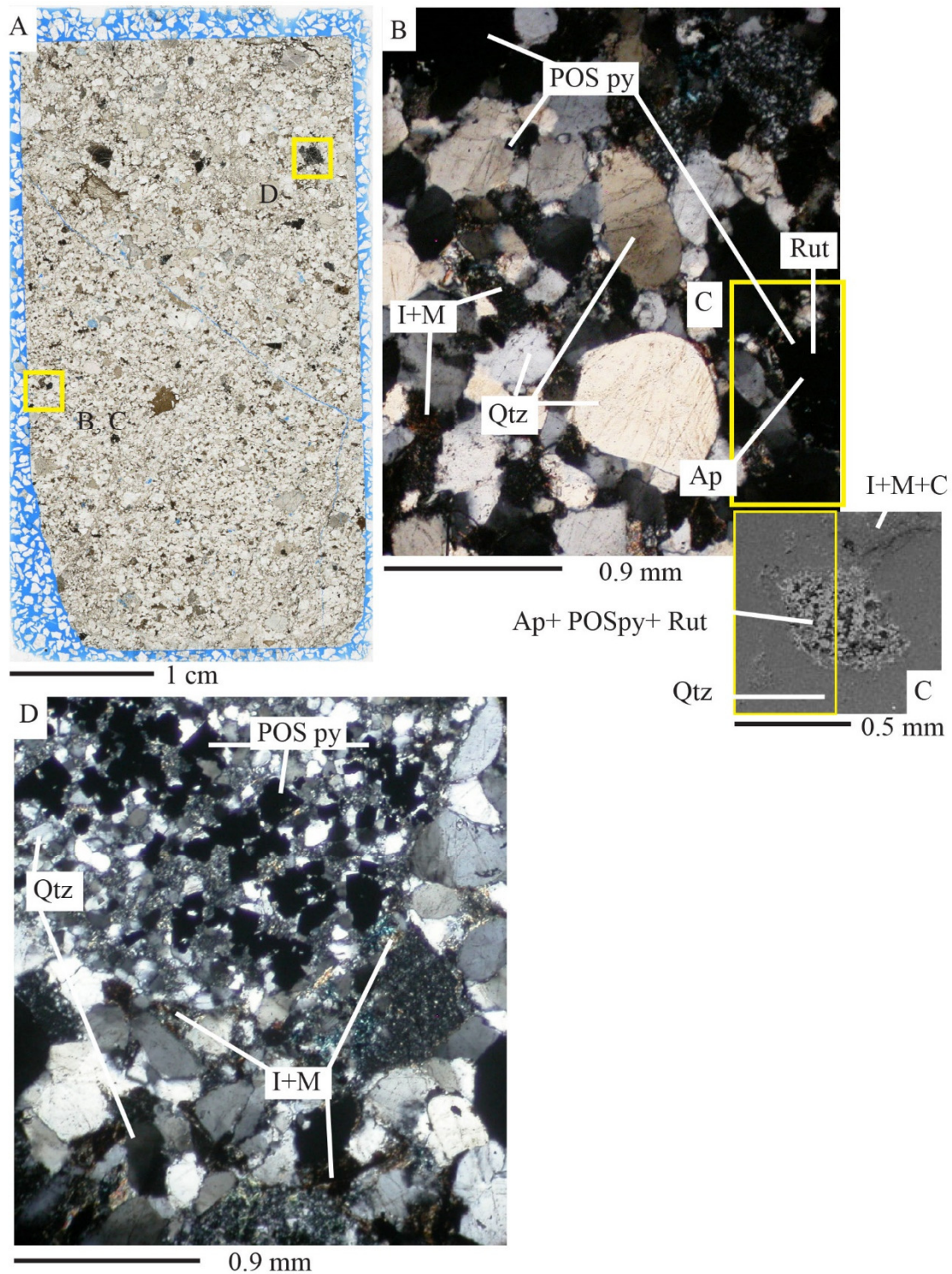


Figure 17. Mississippian Chainman Formation. A) Polished section of sandstone, 10-08 874 (0.180 ppm Au). B) Photomicrograph showing host rock is primarily comprised of sand-to-gravel sized quartz, with minor amounts of pre-ore-stage pyrite, apatite and rutile; illite, montmorillonite, and carbon are present in fractures (TCPL). C) SEM image of clast composed of apatite, pre-ore-stage pyrite, and rutile within sandstone. D)

Photomicrograph showing host rock is primarily comprised of sand- to gravel-sized quartz, with minor amounts of pre-ore stage pyrite; illite, montmorillonite, and carbon are present in fractures (TCPL). B and D show the variability of crystal sizes within sandstone sample. Abbreviations: Ap = Apatite, C = Carbon, I = Illite, M = Montmorillonite, POSpy = Pre-ore-stage pyrite, Qtz = Quartz, Rut = rutile, TCPL = Transmitted Crossed Polarized Light.

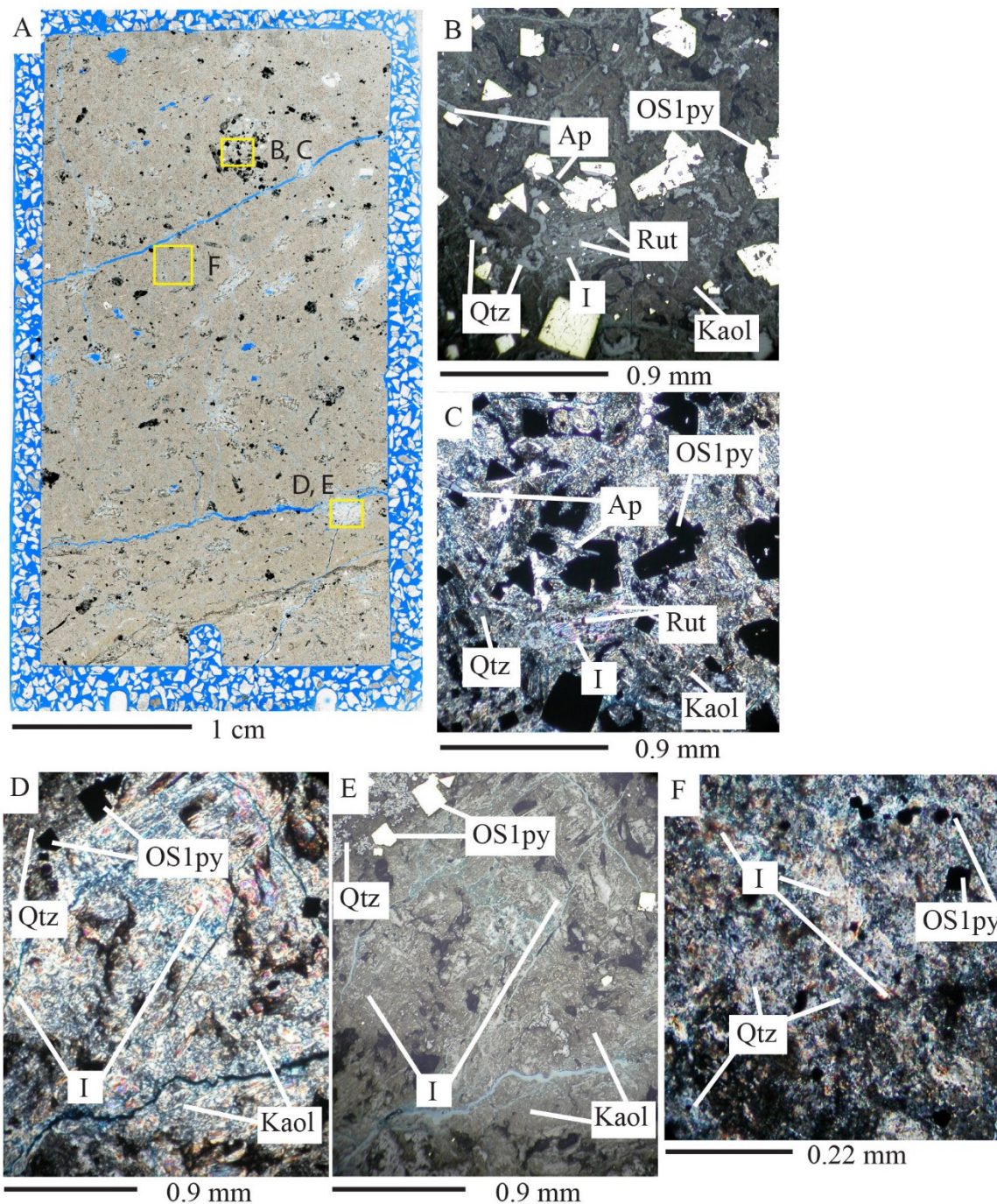


Figure 18. Tertiary porphyritic dacite dike. A) Altered Tertiary dacite dike that cross-cuts host rocks; polished section, 12-05 1408.5 (1.005 ppm Au). B-F) (B, E (RPPL); C, D, F (TPPL)) Photomicrographs showing altered dacite dike is composed of quartz, illite, and kaolinite matrix with ore-stage 1 (OS 1) pyrite, sphalerite, rutile, and apatite phenocrysts. B-C) Paired images showing OS 1 pyrite, rutile, and apatite in kaolinite, illite, and quartz matrix. D, E) Paired images showing alteration of primary plagioclase to illite, kaolinite, and OS 1 pyrite, appear as white patches in A. F) Dacite matrix composed of quartz, illite, and kaolinite. Abbreviations: Ap = Apatite, I = Illite, Kaol = Kaolinite, M =

Montmorillonite, OS1py = Ore-stage 1 pyrite, Qtz = Quartz, Rut = rutile, RPPL = Reflected Plane Polarized Light, TCPL = Transmitted Crossed Polarized Light.

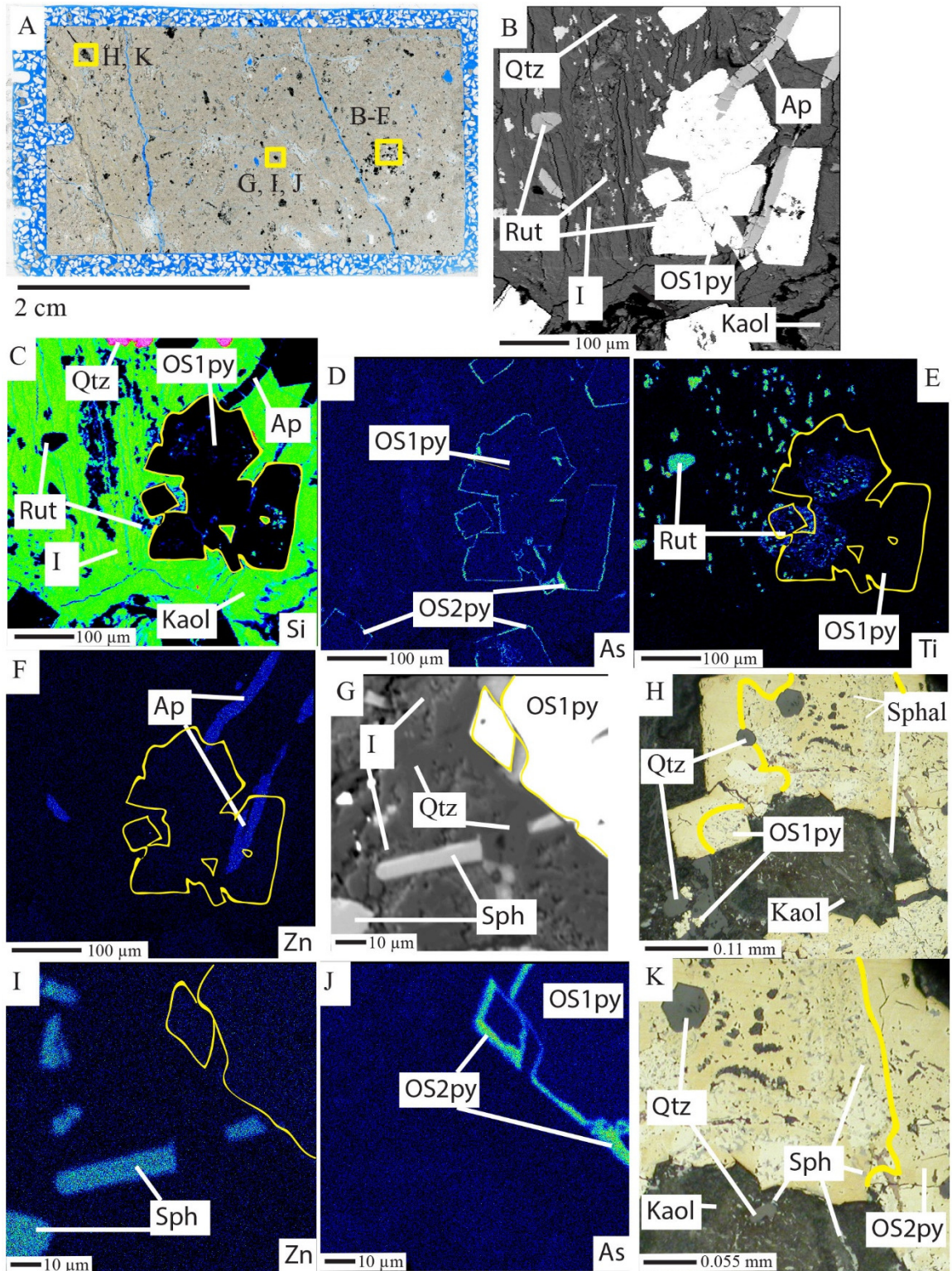


Figure 19. EPMA element maps of OS 1 pyrite, sphalerite, and rutile in Tertiary porphyry dacite dike. A) Sample 12-05 1408 (1.005 ppm Au) polished section of Tertiary porphyritic dacite. B-F) Photomicrograph and elemental maps of OS 1 pyrite overgrowing apatite and rutile within kaolinite, illite, and quartz. Rutile and apatite

inclusions within OS 1 pyrite show rutile and apatite formed prior to OS 1 pyrite. Image showing alteration of primary biotite to illite and rutile that is overgrown later by OS 1 pyrite. (B- BSE image, C-F are EPMA element maps of Si, As, Ti, and Zn, respectively, of image B). The As map (D) shows As, evidence of OS 2 rims on OS 1 pyrites. The Ti map (E) shows locations of rutile in image B, and that OS 1 pyrite overgrew rutile. The Zn map (F) shows location of apatite, which may be enriched in Zn or has sphalerite inclusions within apatite. G, I-J) Paired images of pyrite and sphalerite in quartz and illite (G- BSE image, I-J are EPMA element maps of Zn and As, respectively, of image G). The As map (J) shows As ore-stage 2 rims on OS 1 pyrites. OS 1 pyrite and sphalerite are within a quartz and kaolinite matrix. H and K) Sphalerite and euhedral quartz inclusions within OS 1 pyrite showing sphalerite and quartz formed prior to OS 1 pyrite (RPPL). Ore stage 1 pyrite with sphalerite, and quartz inclusions is overgrown by a later OS 1 pyrite generation without inclusions, indicated by yellow line. Abbreviations: Ap = Apatite, I = Illite, Kaol = Kaolinite, OS1py = Ore-stage 1 pyrite, OS2py = Ore-stage 2 pyrite rims, Qtz = Quartz, Rut = Rutile, Sph = Sphalerite, TCPL = Transmitted Crossed Polarized Light, RPPL = Reflected Plane Polarized Light

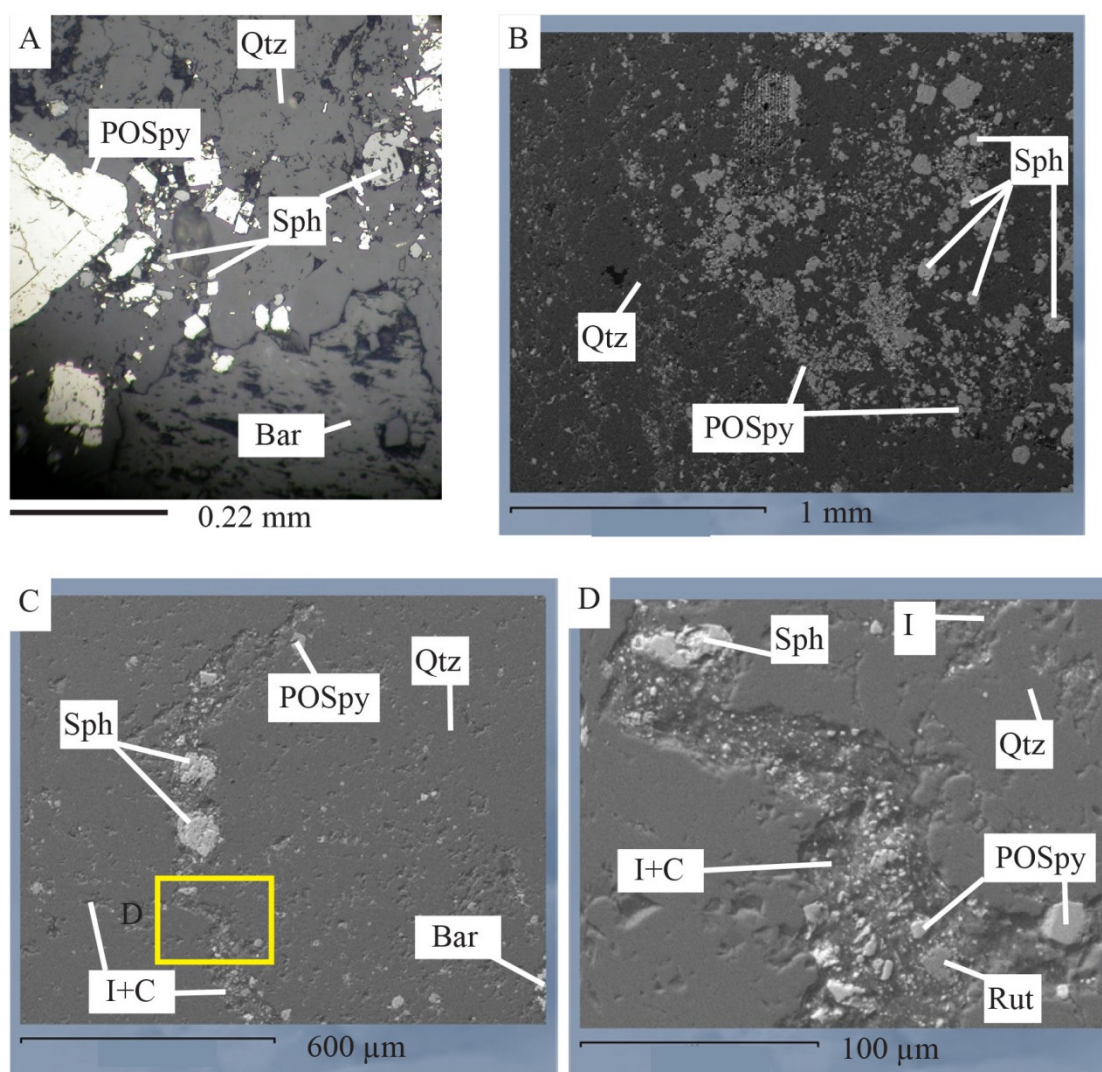


Figure 20. Pre-ore-stage pyrite, rutile, and sphalerite within multi-lithic breccias. A) Sample 13-08 1164 (14.5 ppm Au), photomicrograph of pyrite and anhedral sphalerite within multi-lithic breccia (RPPL). B) Sample 13-08 1164 (14.5 ppm Au), SEM BSE image of pyrite and anhedral sphalerite within multi-lithic breccia. C) Sample 11-18 1163.4 (1.345 ppm Au), SEM BSE image of pyrite and sphalerite within a multi-lithic breccia matrix. D) SEM BSE image of (C), showing illite, carbon-rich dissolution vein with POS pyrite, sphalerite, and rutile. Abbreviations: Bar = Barite, C = Carbon, I = Illite, Jasp = Jasperoid, POSpy = Pre-ore-stage pyrite, Qtz = Quartz, RPPL = Reflected Plane Polarized Light, Rut = Rutile, Sph = Sphalerite.

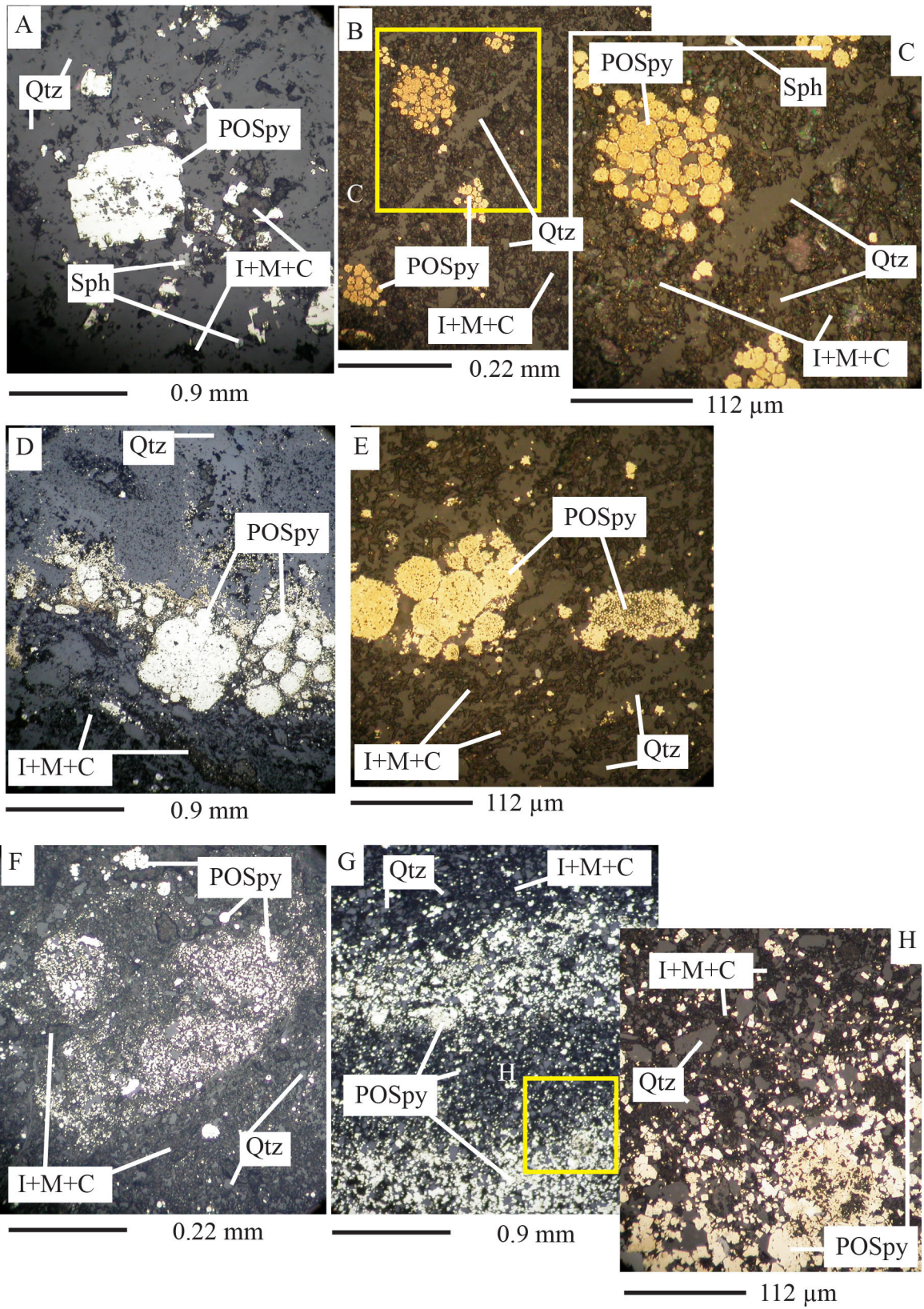


Figure 21. Pre-ore-stage (POS) pyrites. A) Sample 13-08 1113.5 (Mississippian Webb Formation, 13.9 ppm Au), photomicrograph of euhedral and anhedral POS pyrite, within a multi-lithic breccia (RPPL). B) Sample 12-01 1026 (Mississippian Webb Formation, 15.65 ppm Au), photomicrograph of framboids in a mudstone (RPPL). C) Photomicrograph of framboid texture (RPPL). D) Sample 12-13 379 (Mississippian Chainman Formation, 1.365 ppm Au), photomicrograph of clustered framboid POS pyrite within a multi-lithic breccia (RPPL). E) Sample 12-01A 986.1 (Mississippian Webb Formation, 20.82 ppm Au), photomicrograph of clustered framboid POS pyrite within a mudstone (RPPL). F) Sample 12-01A 987 (Mississippian Webb Formation, 20.82 ppm Au), photomicrograph of POS pyrite microcrystals in mudstone (RPPL). G) Sample 12-10 472 (Mississippian Chainman Formation, 0.016 ppm Au), photomicrograph of euhedral, anhedral, and framboidal POS pyrite concentrated in horizontal layers within sedimentary silty mudstone (RPPL). H) Photomicrograph of pyrite textures within sedimentary silty mudstone (RPPL). Abbreviations: C = Carbon, I = Illite, M = Montmorillonite, POSpy = Pre-ore-stage pyrite, Qtz = Quartz, Rut = Rutile, Sph = Sphalerite, RPPL = Reflected Plane Polarized Light.

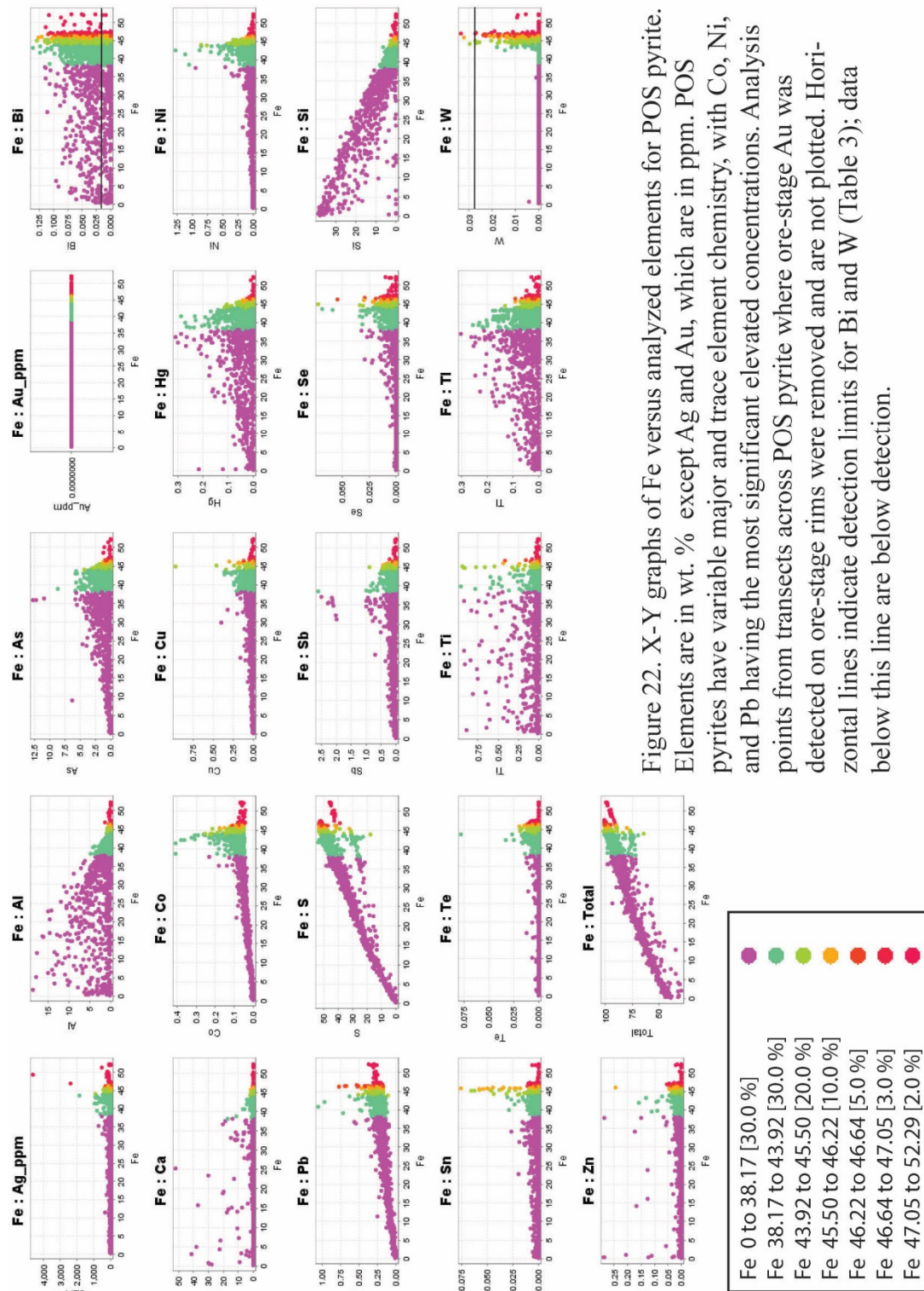


Figure 22. X-Y graphs of Fe versus analyzed elements for POS pyrite. Elements are in wt. % except Ag and Au, which are in ppm. POS pyrites have variable major and trace element chemistry, with Co, Ni, and Pb having the most significant elevated concentrations. Analysis points from transects across POS pyrite where ore-stage Au was detected on ore-stage rims were removed and are not plotted. Horizontal lines indicate detection limits for Bi and W (Table 3); data below this line are below detection.

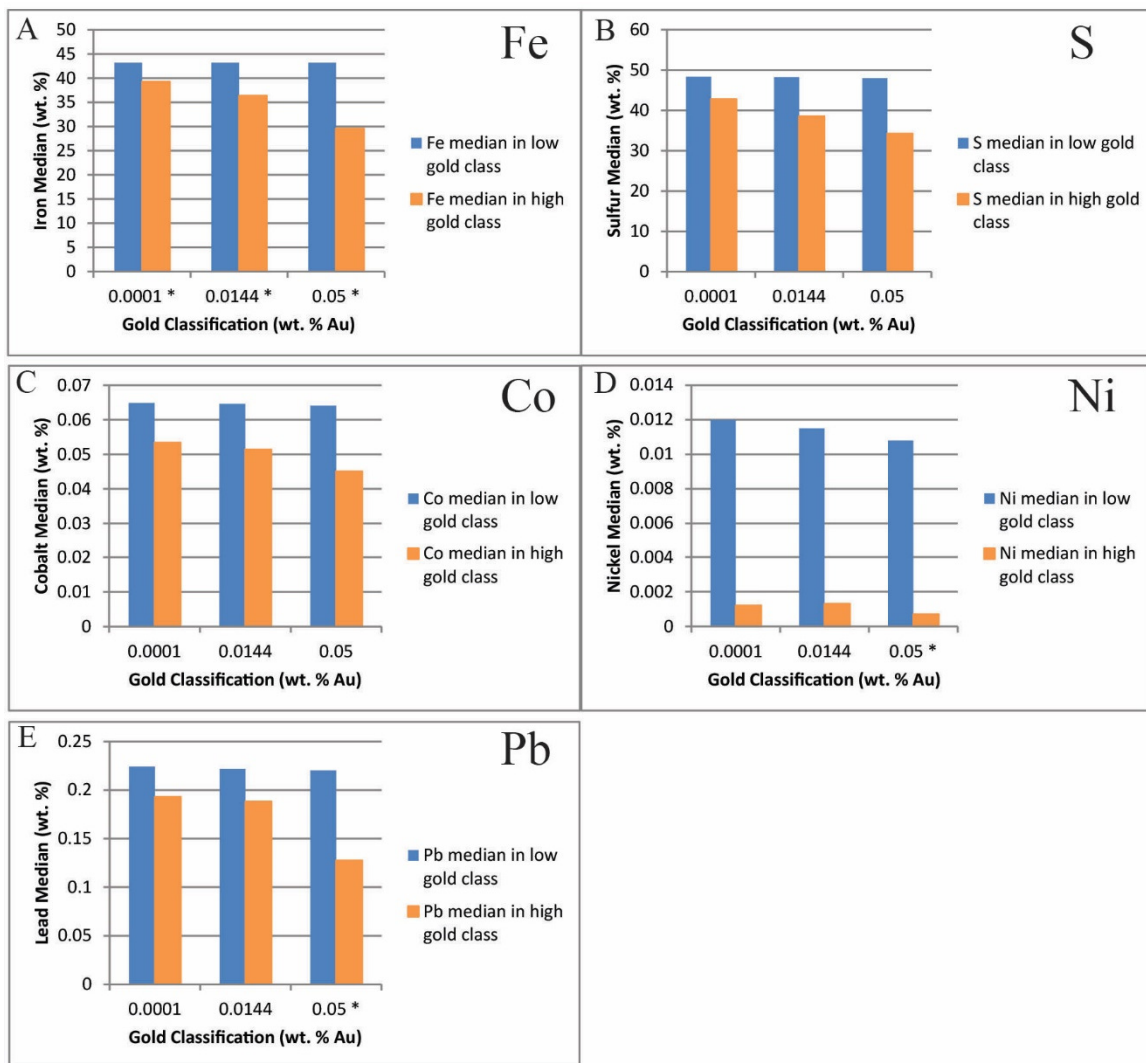


Figure 23. Mann-Whitney U-Test bar graphs of EPMA pyrite data for Fe, S, Co, Ni, and Pb. Bar graphs show progression of median values with increasing gold classification for A) Fe, B) S, C) Co, D) Ni, and E) Pb, elements that have variable concentrations in POS pyrite for each gold classification. The (*) on the X-axis identifies gold classifications for which the median values of the low and high gold classes are not significantly different, as determined by an asymptotic significant (2-tailed) value > 0.005 ; these values are not highlighted on Table 14. Median values of the low and high gold classes identified as significantly different are highlighted in blue in Table 14.

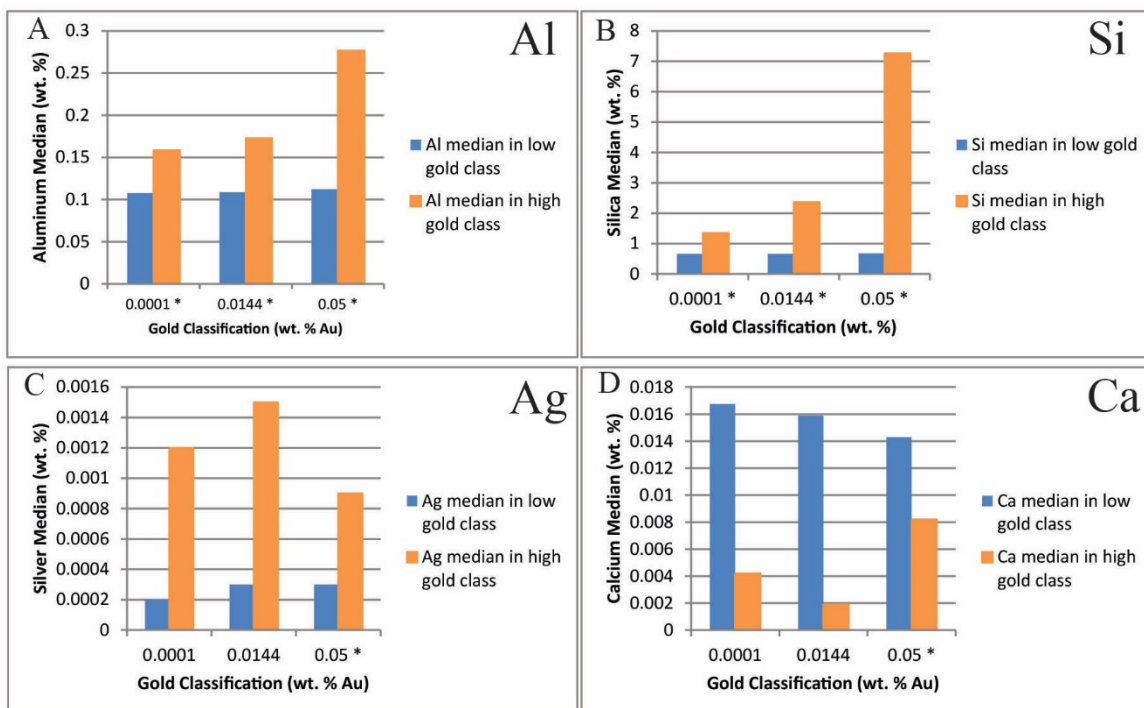
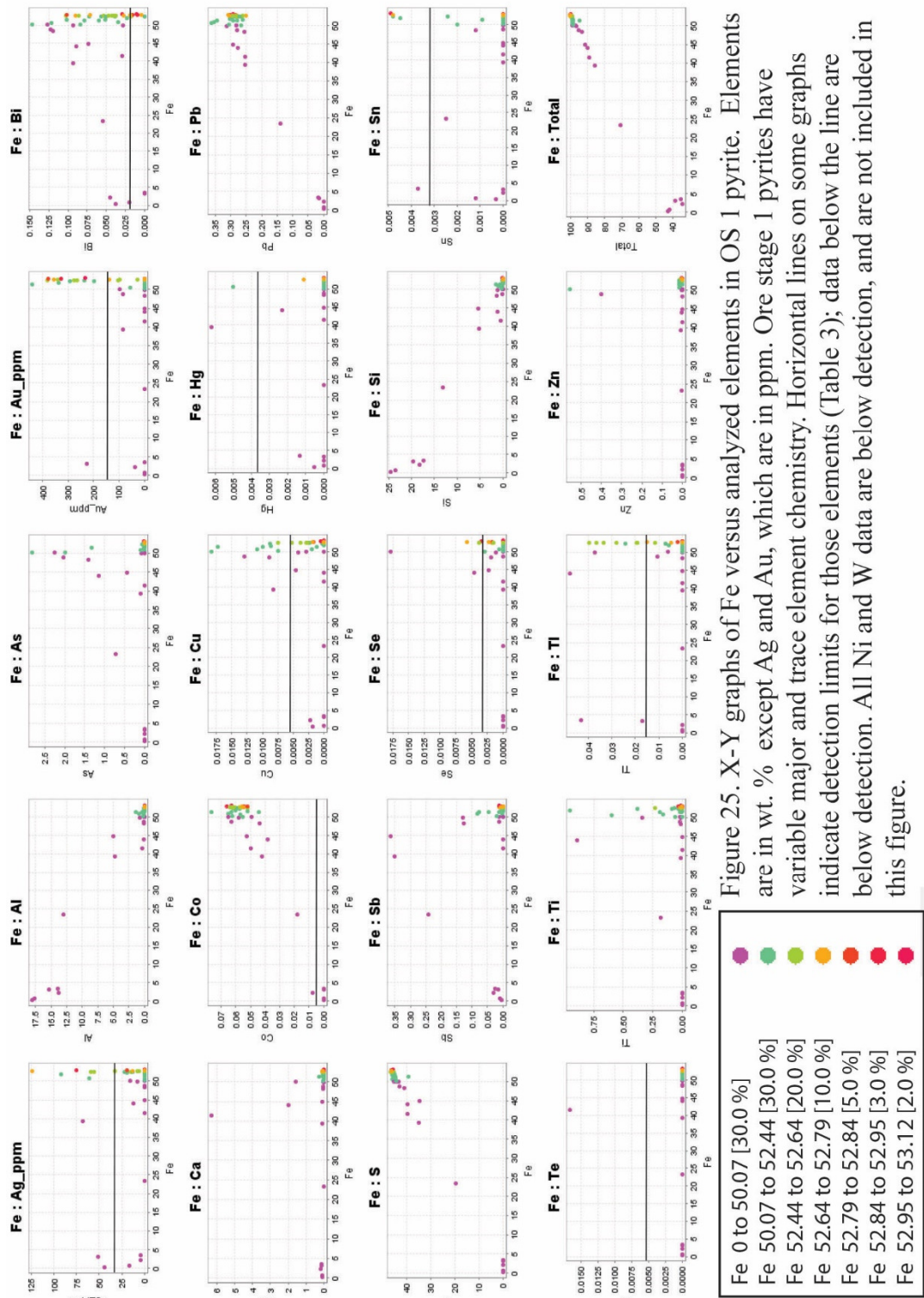


Figure 24. Mann-Whitney U-Test bar graphs of EPMA pyrite data for Al, Si, Ag, and Ca. Bar graphs show progression of median values with increasing gold classification for A) Al, B) Si, C) Ag, and D) Ca, elements that have commonly vary in host rocks or base metals for each gold classification. The (*) on the X-axis identifies gold classifications for which the median values of the low and high gold classes are not significantly different, as determined by an asymptotic significant (2-tailed) value > 0.005 ; these values are not highlighted on Table 14. Median values of the low and high gold classes identified as significantly different are highlighted in blue in Table 14.



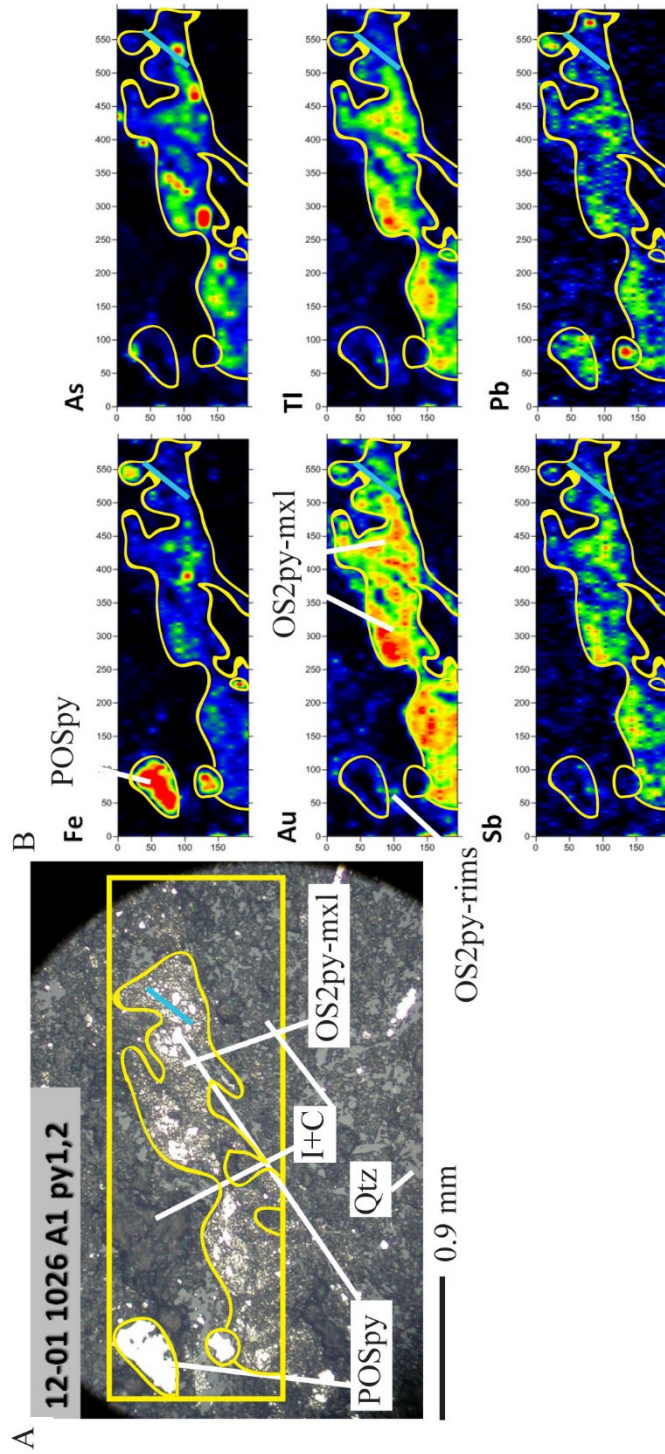


Figure 26. Trace element chemistry of OS 2 pyrite rims and microcrystals in Mississippian Webb mudstone. A) Sample 12-01 1026 (Webb silty mudstone, 15.65 ppm Au) photomicrograph of POS anhedra (outlined in yellow), OS 2 pyrite rims and OS 2 pyrite microcrystals, within an illite, quartz, and carbon matrix (RPPL). EPMA transect of POS pyrites, OS 2 microcrystals, and host rock (points 790-803 in Table #) indicated by light blue line. B) Iron (Fe) map shows the distribution of POS pyrite (red), blue in map is where pyrite is present but is mixed with illite and carbon and gives a weaker Fe signal. Gold (Au) map shows the distribution of OS 2 pyrite rims which rim POS pyrites (red), and OS 2 pyrite microcrystals, where Au is high (green to red) and Fe is low (blue). Carlin pathfinder elements As, Sb, and TI maps imperfectly reflect the distribution of Au and OS 2 pyrite. Lead is coincident with POS pyrites. Abbreviations: C = Carbon, I = Illite, OS2py-mxl = Ore-stage 2 pyrite microcrystals, OS2py-rims = Ore-stage 2 pyrite rims, POSpy = Pre-ore-stage pyrite, Qtz = Quartz, RPPL = Reflected Plane Polarized Light.

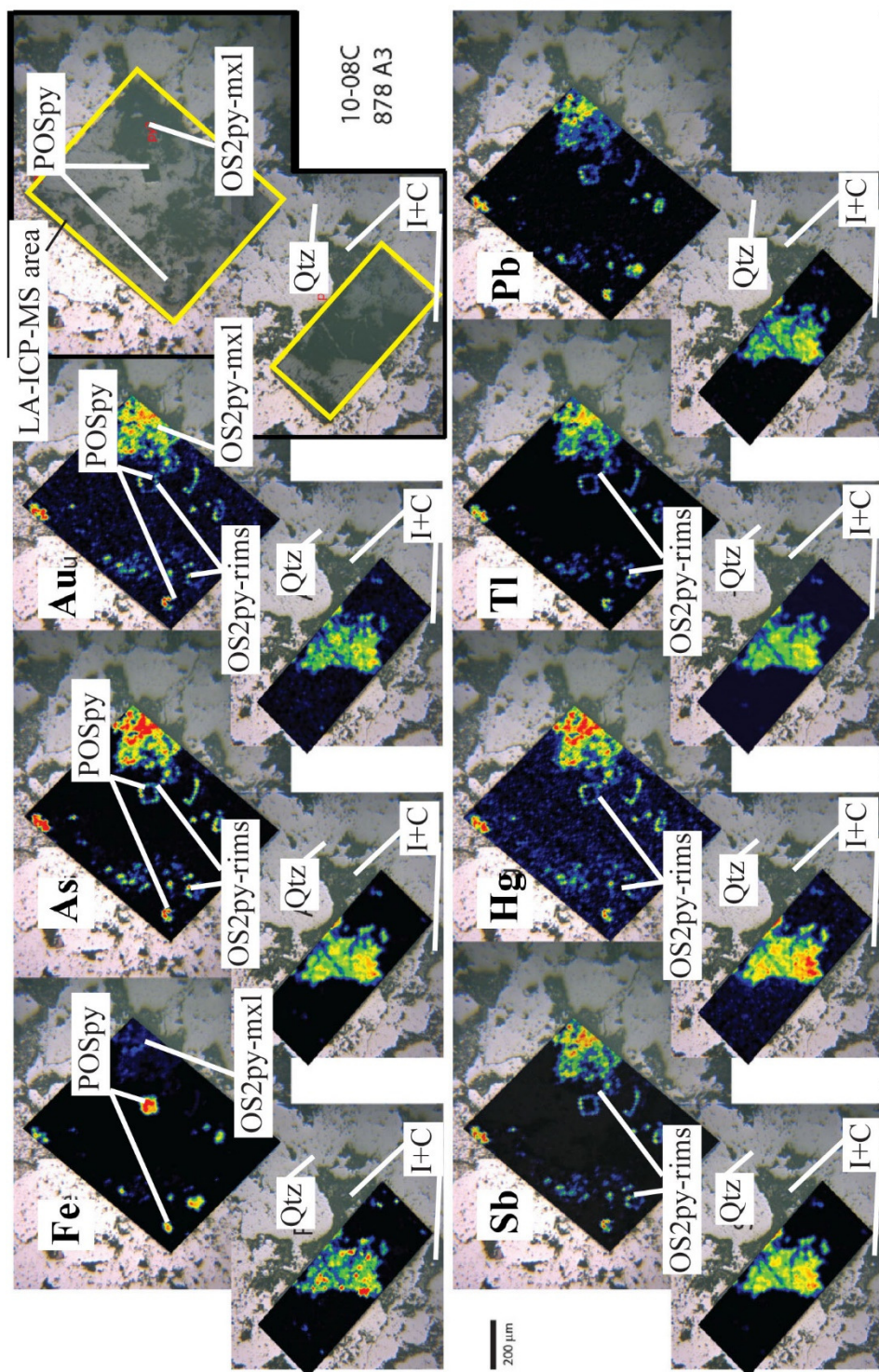


Figure 27: Trace element chemistry (RPPL) of area analyzed in yellow boxes, that correspond with the LA-ICP-MS element map areas. Maps show that POS euhebral and anhedral pyrites, identified on Fe map, have OS 2 pyrite rims, and OS 2 pyrite microcrystals, identified on Au map. Alteration minerals spatially associated with Au-bearing pyrites include illite and carbon (dark gray with poor polish in images) (RPPL). Abbreviations: C = Carbon, I = Illite, OS2py-mxl = Ore-stage 2 microcrystals, OS2py-rims = Ore-stage 2 pyrite rims, Qtz = Quartz POSpy = Pre-ore-stage pyrite, RPPL=Reflected Plane Polarized Light.

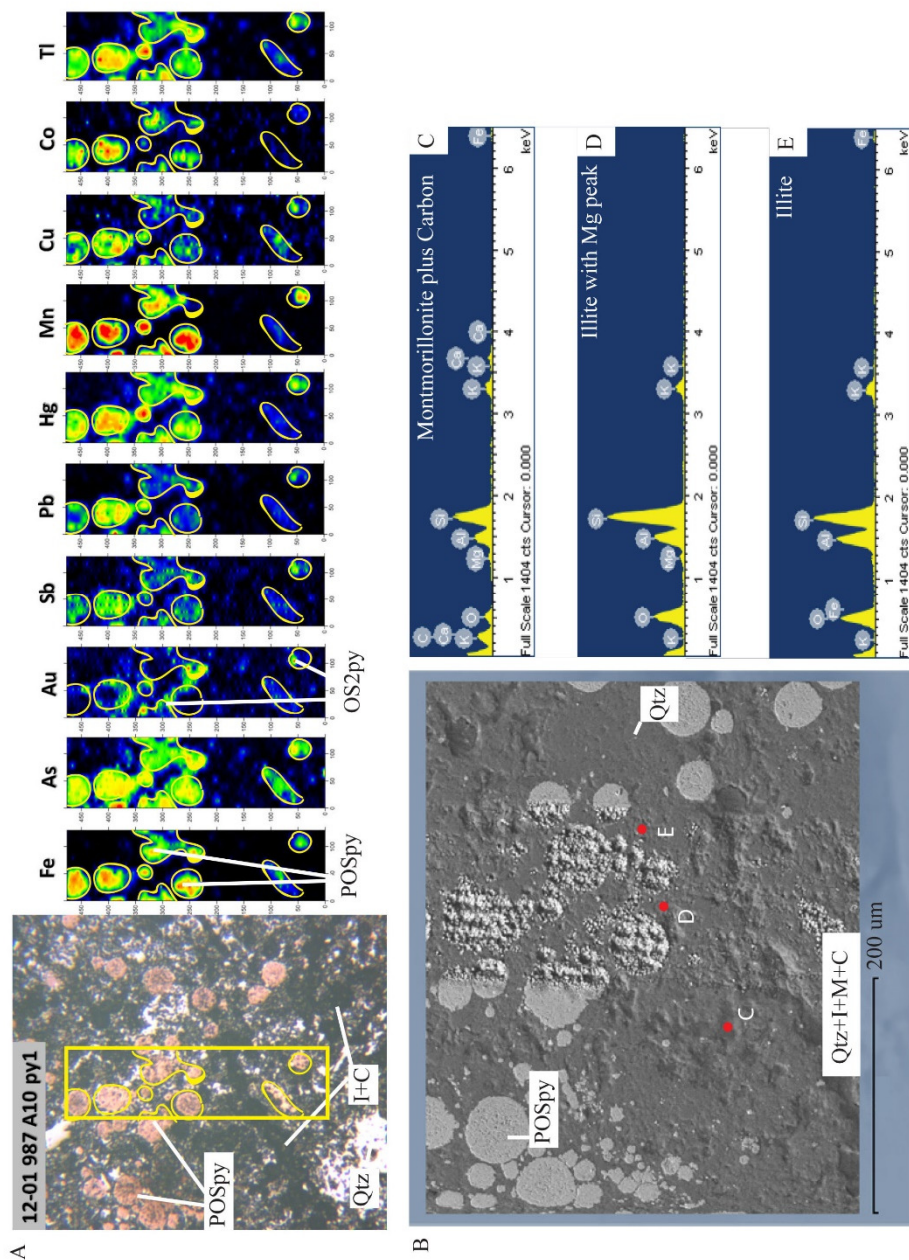


Figure 28. Trace metal chemistry of OS 2 pyrite on POS framboidal pyrite in Mississippi Webb mudstone. A) Photomicrograph and LA-ICP-MS maps of 12-01 987 (Webb mudstone, 20.8 ppm Au) show POS framboidal pyrite (outlined in yellow) in a quartz, illite, montmorillonite, and carbon matrix. Quartz appears white and illite, montmorillonite plus carbon are light to dark grey (RPPL). B) SEM BSE image of framboidal pyrite. Gold-bearing rims on framboidal pyrites and the CTGD pathfinder elements are present, but do not directly correlating with gold and are more widely distributed than Au. Red dots (C, D, E) indicate locations of SEM analyses of clay minerals. C) SEM analysis detect montmorillonite and carbon. D and E) SEM analysis detect illite with Mg peak and illite adjacent to OS 2 pyrite. Abbreviations: C = Carbon, I = Illite, M = Montmorillonite, OS2py = Ore-stage 2 pyrites, Qtz = Quartz, POSpy = Pre-ore-stage pyrite, RPPL = Reflected Plane Polarized Light, SEM BSE = Scanning Electron Microscope Back Scatter Electron.

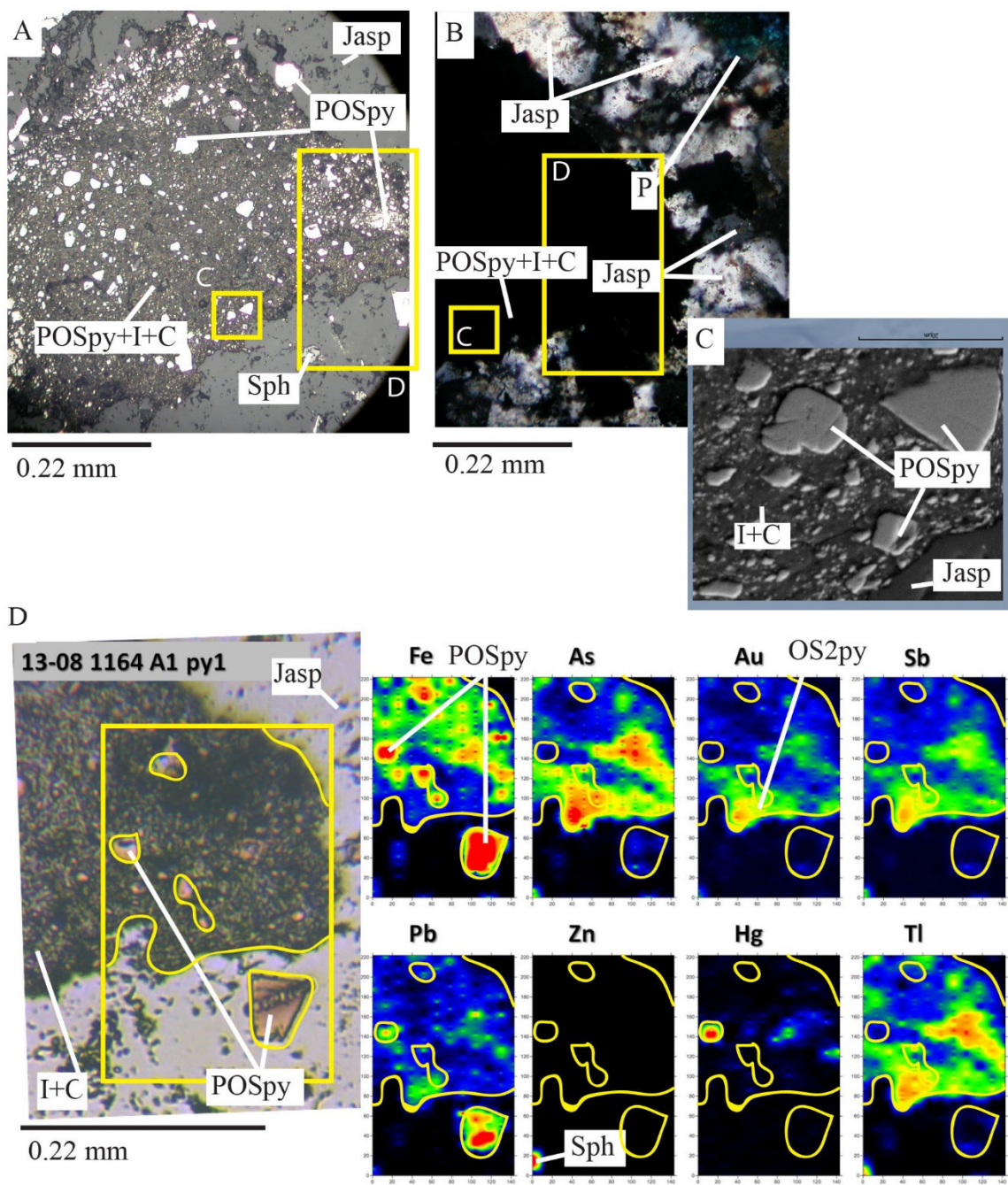


Figure 29. Trace element chemistry of OS 2 pyrite in Multi-lithic Breccia. A) Photomicrograph of 13-08 1164 (14.5 ppm Au) multi-lithic breccia, showing dissolution feature with jasperoid, illite plus carbon, and POS pyrite (RPPL). B) Photomicrograph of jasperoid and porosity around dissolution feature (TCPL). C) SEM BSE image of dissolution feature; POS pyrite (medium gray, high relief) with ore-stage alteration

minerals including jasperoid (dark gray, high relief), and illite plus carbon (dark gray, low relief matrix). D) Photomicrograph and LA-ICP-MS maps of pre-ore stage pyrite, ore-stage (OS) pyrite (RPPL w/ C). Abbreviations: C = Carbon, I = Illite, Jasp = Jasperoid, OS2py = Ore-stage 2 pyrite, POSpy = Pre-ore-stage pyrite, RPPL = Reflected Plane Polarized Light, RPPL w/C = Reflected Plane Polarized Light with carbon coating, Sph =Sphalerite, TCPL = Transmitted Cross Polarized Light.

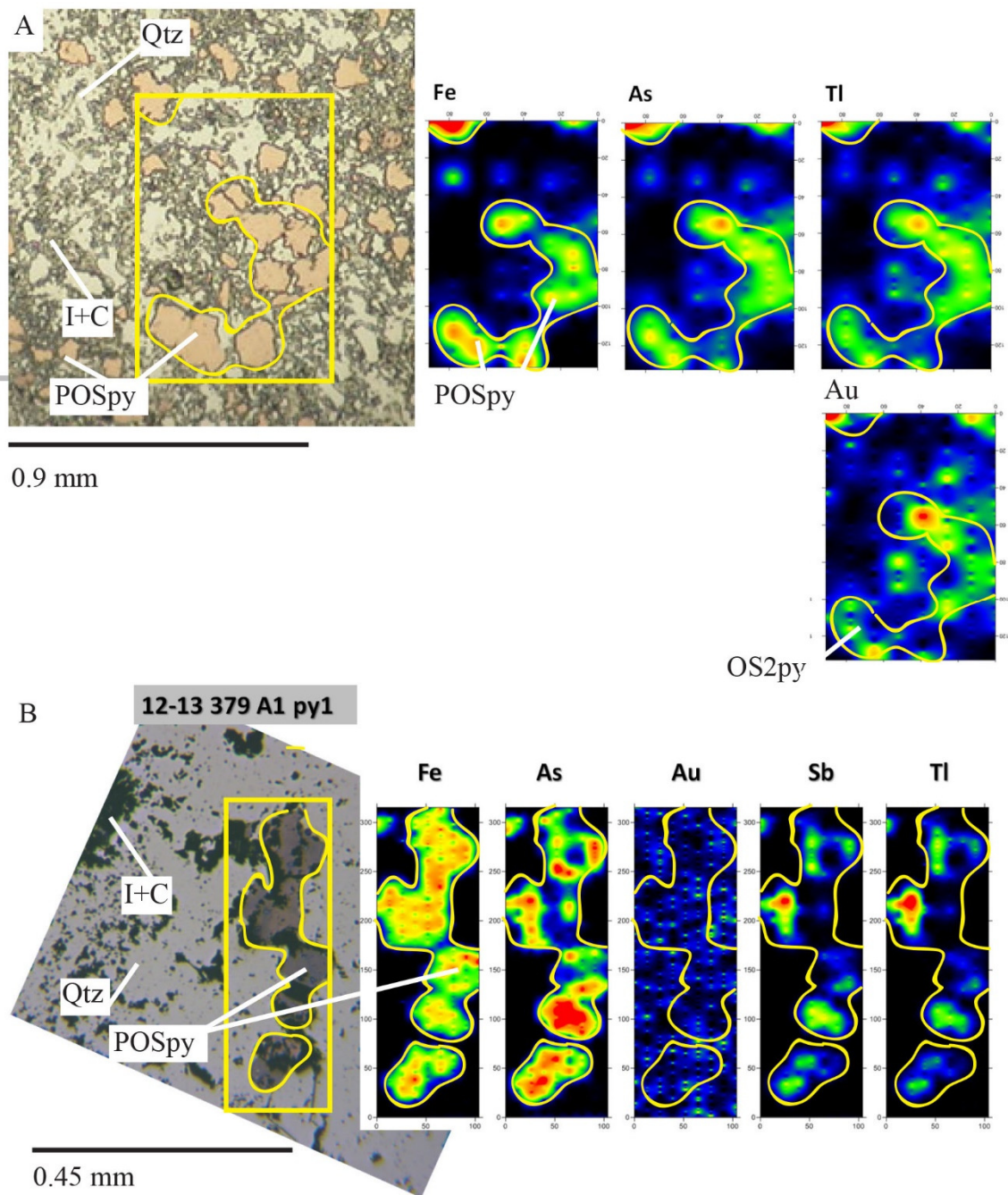


Figure 30. Spatial distribution of Au and Carlin-type pathfinder elements. A) Mississippian Webb mudstone, sample 12-01 992 (25.6 ppm Au), photomicrograph and LA-ICP-MS maps of POS anhedral pyrites (outlined in yellow) with Au-, As-, and Tl-bearing rims, illustrating that all CTGD pathfinder elements are not always present, (i.e. Hg and Sb were not detected), but As and Tl correlate well with Au (RPPL w/C). B) Mississippian Chainman Formation, sample 12-13 379 (1.365 ppm Au), photomicrograph and LA-ICP-MS maps of POS anhedral pyrites (outlined in yellow) with As, Sb, and Tl rims, but without Au, showing that CTGD pathfinder elements can be present when Au is below detection (RPPL w/C). Due to LA-ICP-MS maps poor resolution and spot size of

bearm, the As-, Sb-, and Tl-bearing rims do not appear rim shaped. Abbreviations: C = Carbon, I = Illite, OS2py = Ore-stage 2 pyrite, POSpy = Pre-ore-stage pyrite, Qtz = Quartz, RPPL w/C = Reflected Plane Polarized Light with carbon coating.

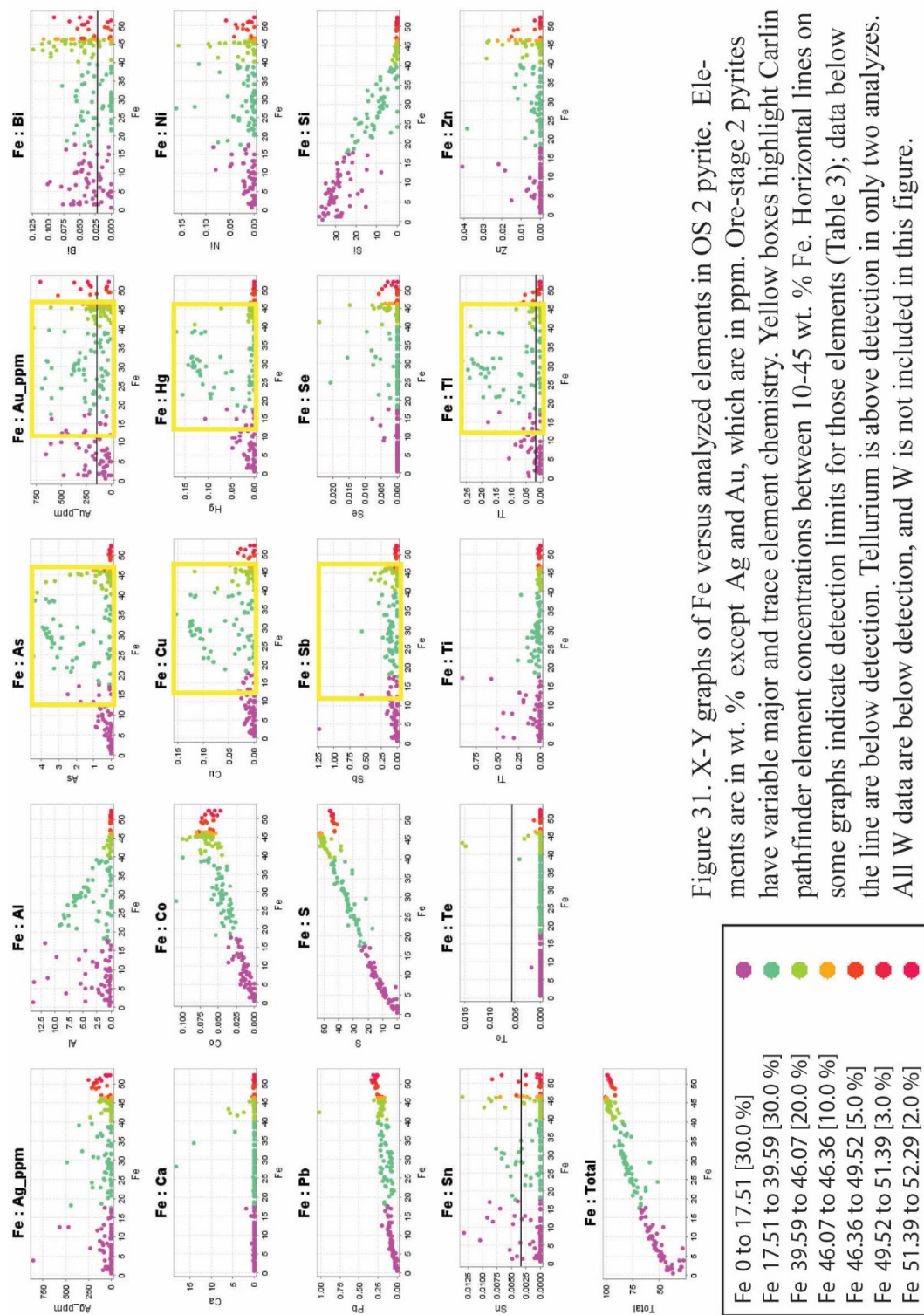


Figure 31. X-Y graphs of Fe versus analyzed elements in OS 2 pyrite. Elements are in wt. % except Ag and Au, which are in ppm. Ore-stage 2 pyrites have variable major and trace element chemistry. Yellow boxes highlight Carlin pathfinder element concentrations between 10-45 wt. % Fe. Horizontal lines on some graphs indicate detection limits for those elements (Table 3); data below the line are below detection. Tellurium is above detection in only two analyzes. All W data are below detection, and W is not included in this figure.

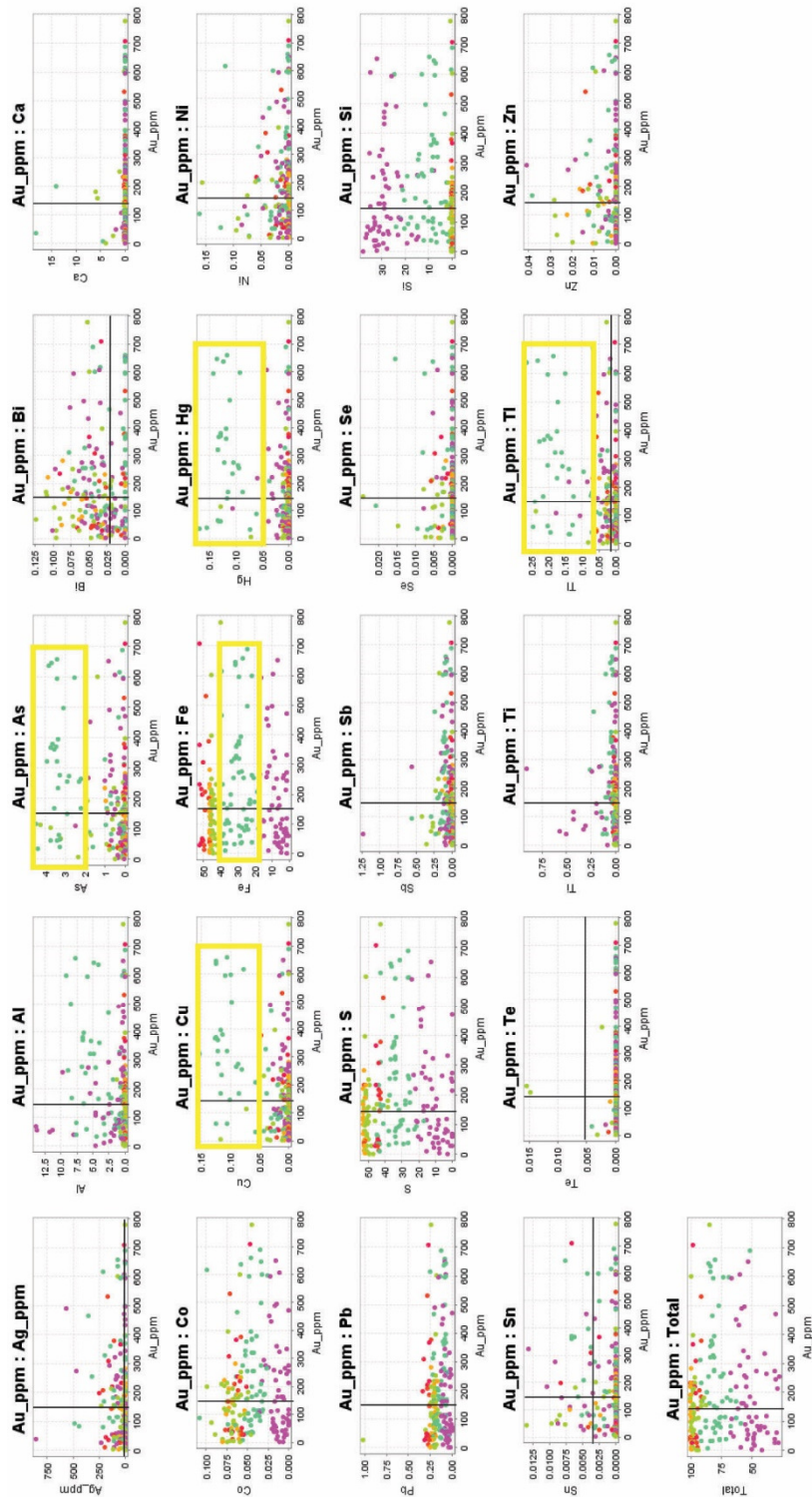


Figure 32. X-Y graphs of Au versus analyzed elements in OS 2 pyrite. Elements are in wt. % except Ag and Au, which are in ppm. Yellow boxes highlight Carlin pathfinder element concentrations between 10-45 wt. % Fe, and 0-700 ppm Au. Vertical lines show detection limits for gold, and horizontal lines indicate detection limits for elements on the x-axis; data below these lines are below detection. All W data are below detection, and are not included in this figure.

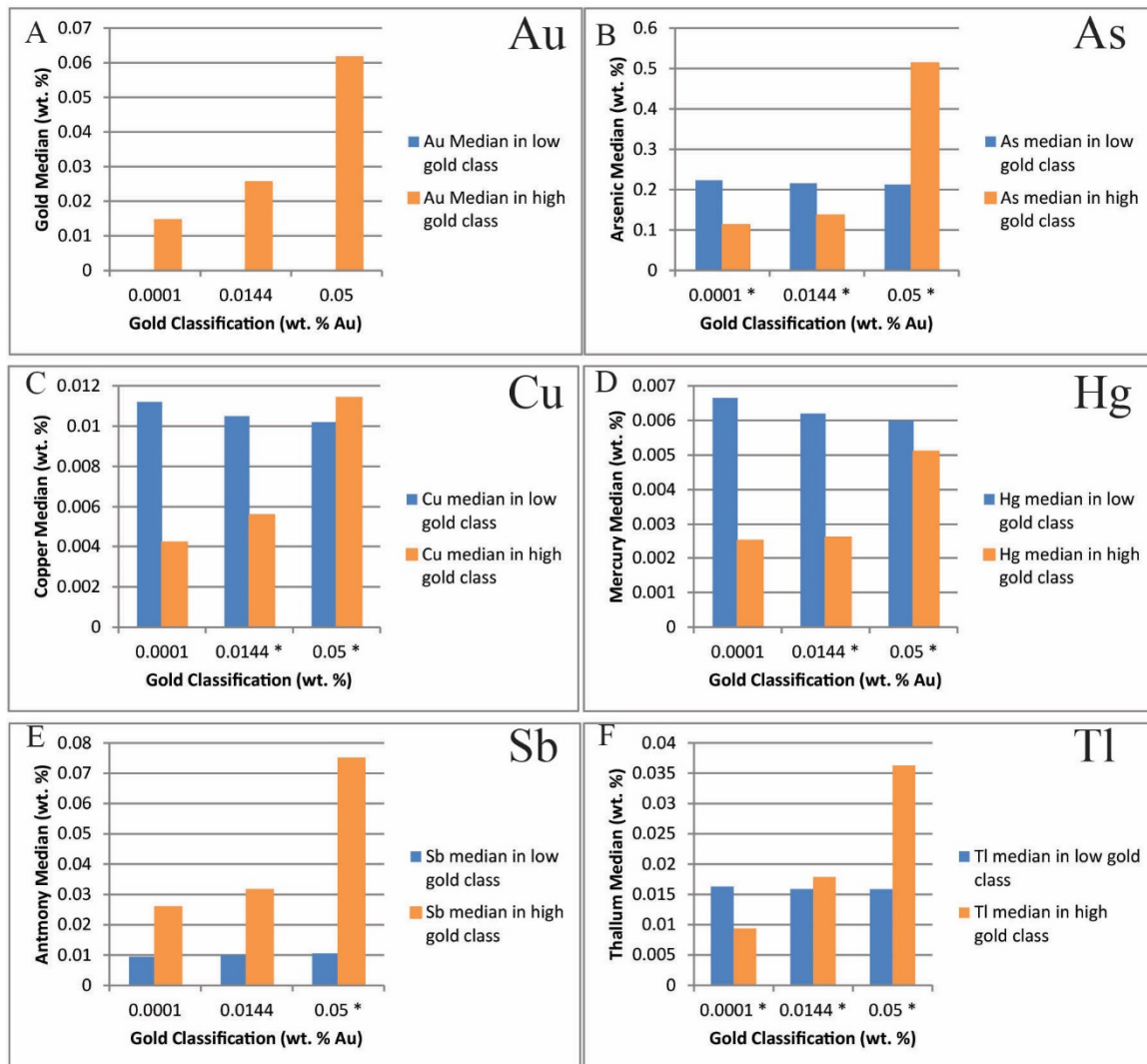


Figure 33. Mann-Whitney U-Test bar graphs of EPMA pyrite data for Au, As, Hg, Cu, Sb, and Tl. Bar graphs show progression of median values with increasing gold classification for Au and Carlin-type pathfinder elements A) Au, B) As, C) Cu, D) Hg, E) Sb, and F) Tl for each gold classification. Note that gold's median concentrations in the low gold class (blue) is 0.000 wt. % Au for all gold classifications. The (*) on the X-axis identifies gold classifications of the low and high gold classes are not significantly different, as determined by an asymptotic significant (2-tailed) value > 0.005 ; these values are not highlighted in blue in Table 14. Median values of the low and high gold classes identified as significantly different, as determined by an asymptotic significant (2-tailed) value < 0.005 , are highlighted in blue in Table 14.

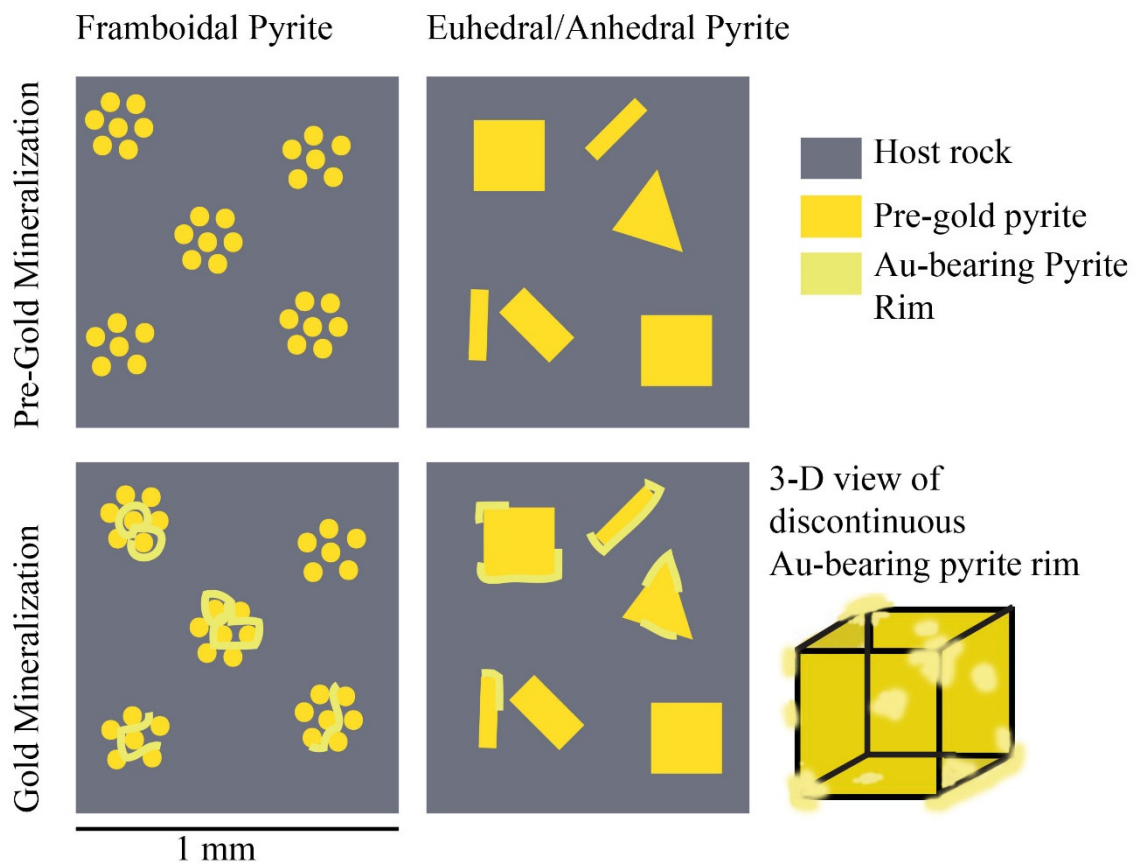


Figure 34. Cartoon of OS 2 pyrite on POS pyrite. This cartoon illustrates the discontinuous nature of the Au-bearing pyrite rims.

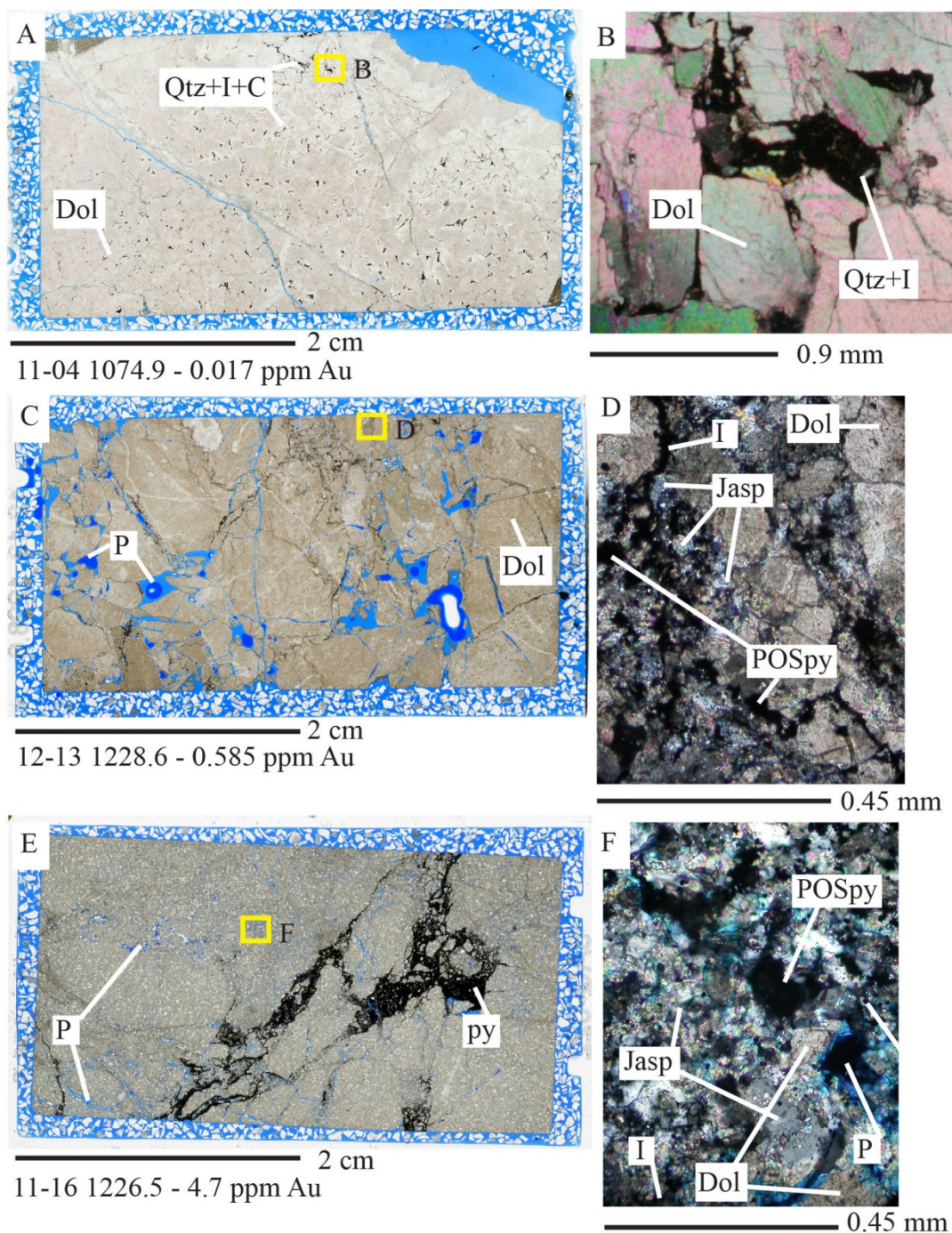


Figure 35. Devonian Devil's Gate Formation sample transect. A) Polished section 11-04 1074.9, Devil's Gate collapse breccia. B) Photomicrograph of illite, jasperoid, and carbon between dolomite crystals (TCPL). C) Polished section 12-13 1228.6, Devil's Gate collapse breccia; dolomite appears darker due to increased impurities in dolomite crystals. D) Photomicrograph shows changes in host rock from B including 1) increase in fractures containing illite, jasperoid, carbon, and POS pyrite, 2) increase in porosity, and 3) decrease in size of dolomite crystals (TCPL). E) Polished section 11-16 1226.5, Devil's Gate collapse breccia. F) Photomicrograph shows changes from D including 1)

increase in dolomite replacement by jasperoid, 2) increase in illite, jasperoid, carbon, and POS pyrite in fractures, and 3) increase in porosity (TCPL). Abbreviations: C = Carbon, Cc = Calcite, Dol, = Dolomite, I = Illite, Jasp = Jasperoid, P = porosity, POSpy = Pre-ore Stage pyrite, Py = Pyrite, Qtz = Quartz, TCPL =Transmitted Crossed Polarized Light.

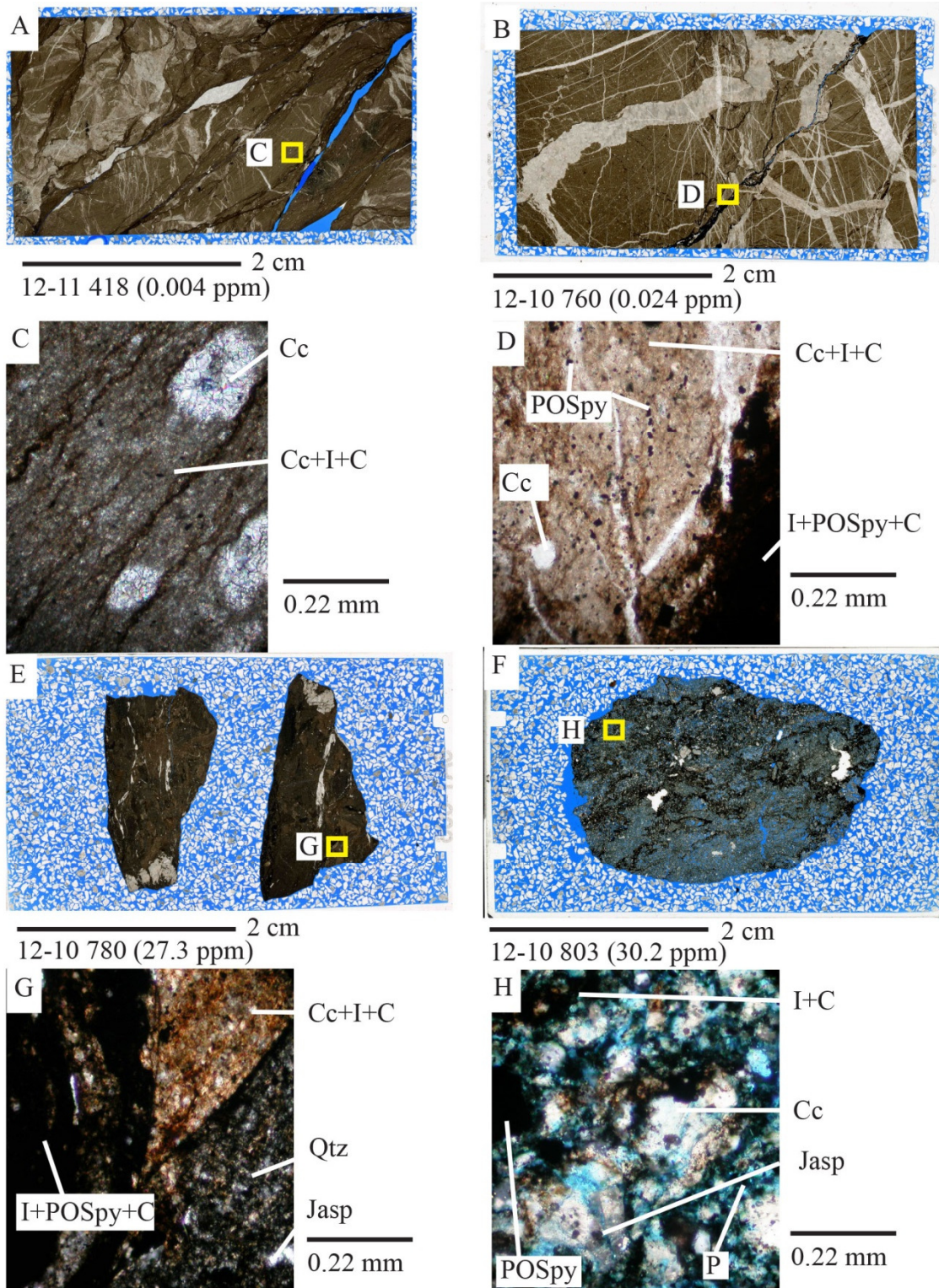


Figure 36. Mississippian Webb Formation micrite samples. A) Polished section 12-11 418, Webb micrite. B) Polished section 12-10 760, Webb micrite. C and D) Photomicrographs of Webb micrites that are composed of fine-grained calcite crystals within a calcite, illite, carbon, and POS pyrite matrix. The color of the illite is dependent

on carbon abundance within the rock (TCPL). E) Polished section 12-10 780, Webb micrite. F) Polished section 12-10 803, Webb micrite within a fault zone. G) Photomicrograph of brecciated Webb micrite, clasts are composed of calcite, illite, POS pyrite, and carbon, or calcite, illite, jasperoid, quartz, POS pyrite, and carbon (TCPL). H) Photomicrograph of jasperoid, illite, POS pyrite, and carbon matrix. Note increase in porosity indicated by blue epoxy (TCPL). Abbreviations: C = Carbon, Cc = Calcite, I = Illite, Jasp = Jasperoid, P = porosity, POSpy = Pre-ore Stage pyrite, Qtz = Quartz, TCPL = Transmitted Crossed Polarized Light.

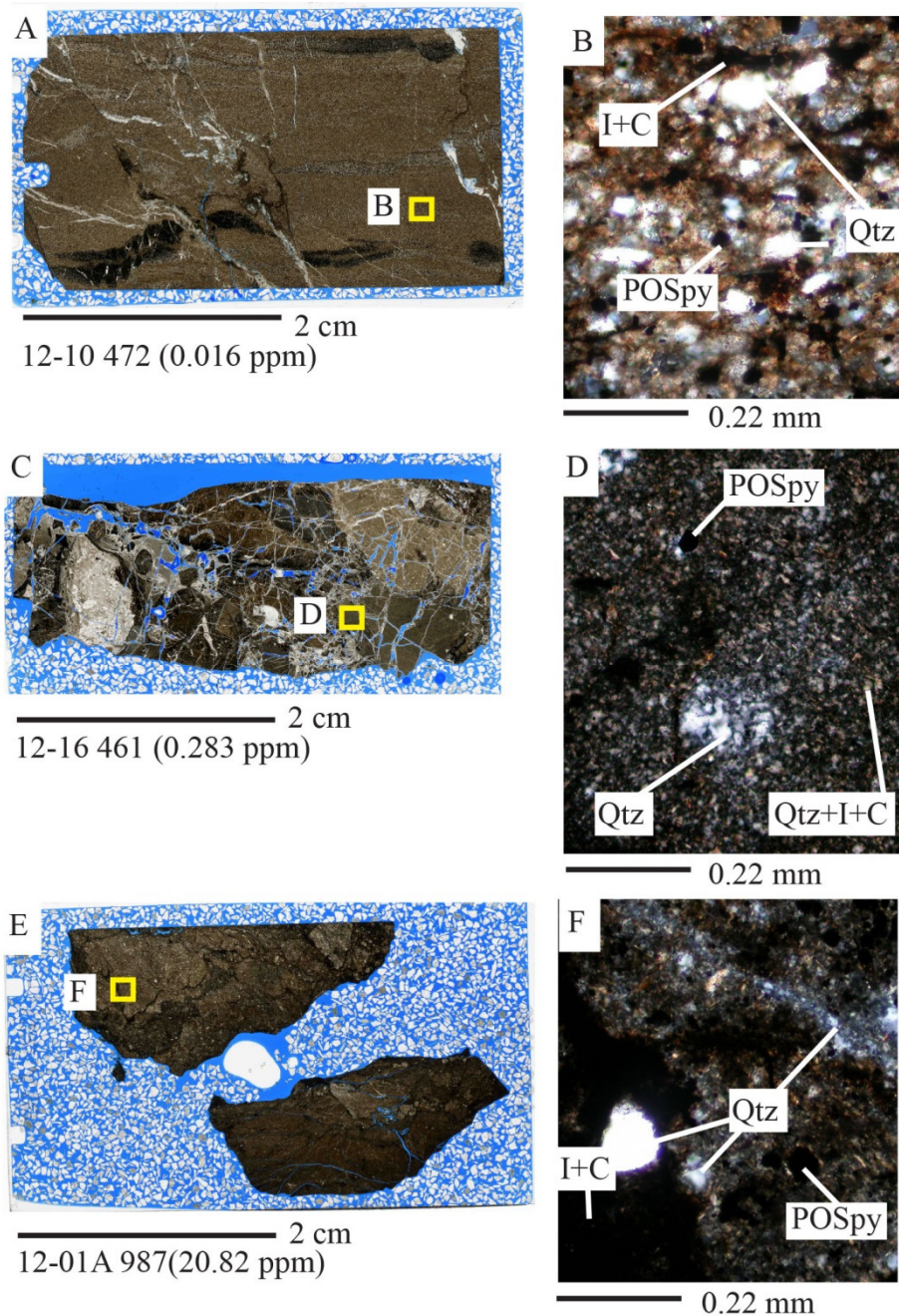


Figure 37. Mississippian Webb Formation mudstone samples. A) Polished section 12-10 472, Webb mudstone. B) Photomicrograph of Webb mudstones that are composed of detrital quartz grains within illite, carbon, POS pyrite, and minor montmorillonite (TCPL). C) Polished section 11-16 461 of Mississippian Webb mudstone breccia. D) Photomicrograph of Webb mudstone breccia showing an increase in secondary microcrystalline quartz in matrix and veins (TCPL). E) Polished section 12-01 987, Webb mudstone breccia. F) Photomicrograph showing an increase in secondary microcrystalline quartz in matrix and veins, and an increase in carbon and POS pyrite (TCPL). Abbreviations: C = Carbon, I = Illite, POSpy = Pre-ore Stage pyrite, Qtz = Quartz, TCPL = Transmitted Crossed Polarized Light.

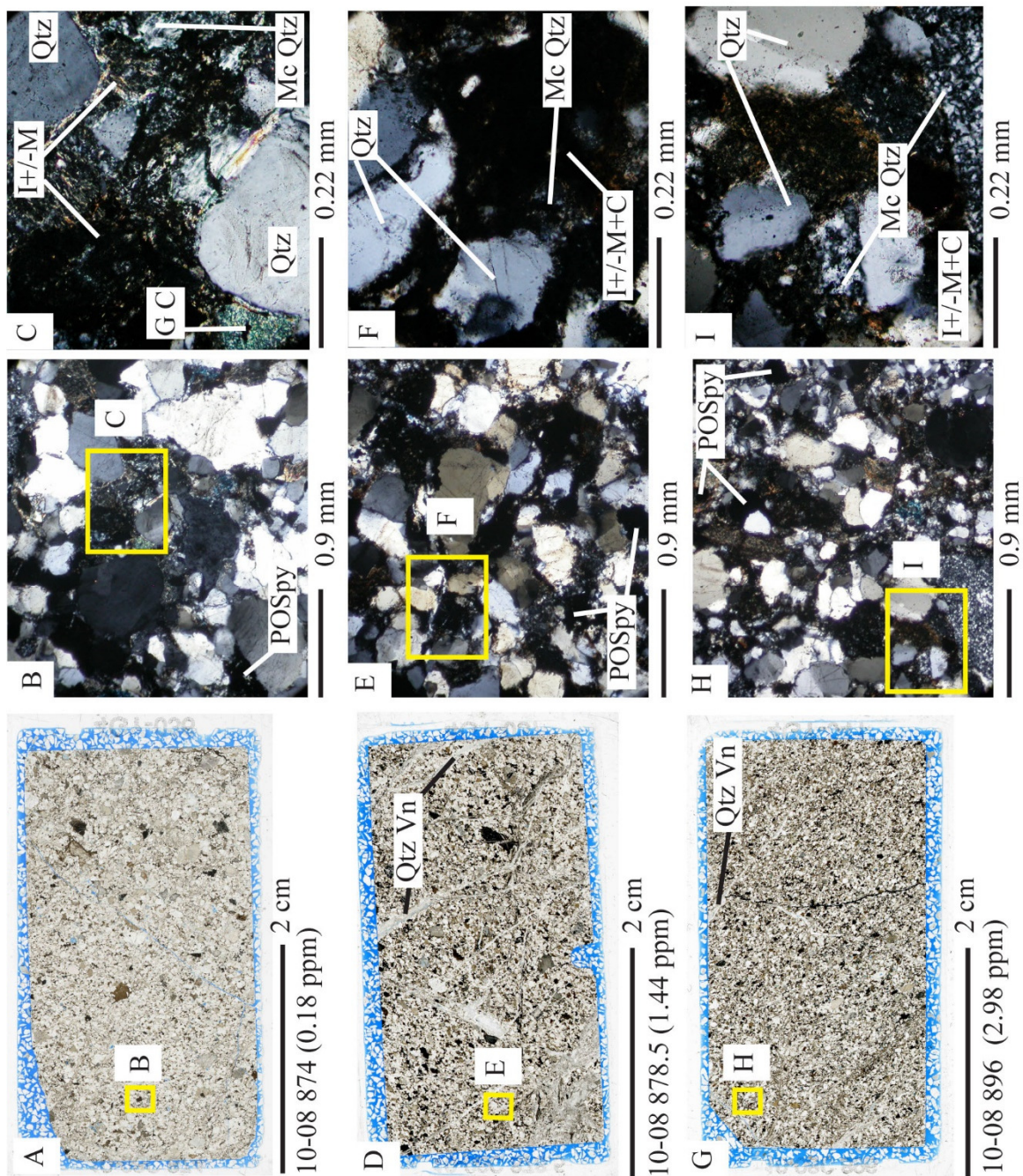


Figure 38. Mississippian Chainman Formation sandstone transect. A) Polished section 10-08 874, Chainman sandstone. B and C) Photomicrographs of Chainman sandstone composed of detrital quartz grains, green chert, apatite, and POS pyrite with illite, montmorillonite, and trace carbon between grains; trace recrystallized microcrystalline quartz (TCPL). D) Polished section 10-08 878.5, Chainman sandstone cross cut by quartz veins. E and F) Photomicrographs illustrate quartz grains, recrystallized microcrystalline quartz, pyrite, illite, and montmorillonite that increase with increasing grade. Illite and montmorillonite appear darker than illite and montmorillonite in B and C due to presence of carbon (TCPL). G) Polished section 10-08 896, Chainman sandstone cross cut by quartz veins. H and I) Photomicrographs illustrate quartz grains, recrystallized microcrystalline quartz, pyrite, illite, and montmorillonite are still present, but have not changed in abundance as compared to sample 10-08 878.5 (TCPL). Abbreviations: C = Carbon, GC = Green Chert, I = Illite, POSpy = pre-ore-stage pyrite, Qtz = Quartz grains, Qtz Vn = Quartz veins, Mc Qtz = Microcrystalline Quartz, TCPL = Transmitted Crossed Polarized Light.

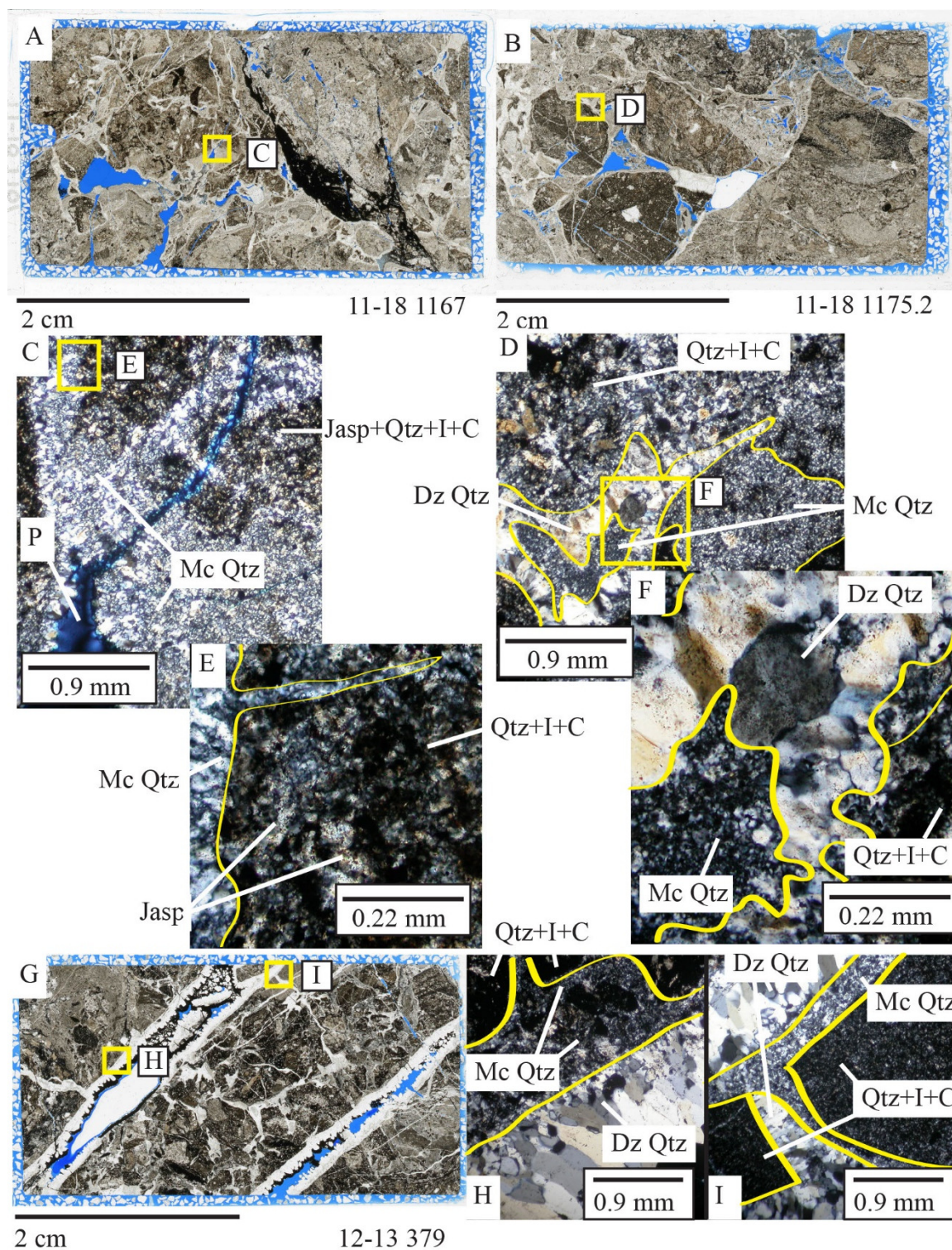


Figure 39. Late-ore-stage alteration minerals: quartz. A) Sample 11-18 1167 (1.91 ppm Au) and B) 11-18 1175.2 (1.715 ppm Au) of silicified multi-lithic breccia. C and E) Photomicrographs of microcrystalline quartz cross-cutting host rock (TCPL). D and F) Photomicrographs of drusy quartz conforming to and rimming primary host rock minerals, and microcrystalline quartz conforming to drusy quartz (TCPL). G) Sample 12-

13 379 (1.365 ppm Au) of multi-lithic breccia. H and I) Photomicrographs of microcrystalline quartz forming matrix and cementing host rocks clasts with drusy quartz that precipitated in open space. Microcrystalline quartz conforms to host rock, and drusy quartz conforms to microcrystalline quartz. Abbreviations: C = Carbon, Dz Qtz = Drusy Quartz, I = Illite, Jasp = Jasperoid, Mc Qtz = Microcrystalline Quartz, P = Porosity, TCPL = Transmitted Crossed Polarized Light.

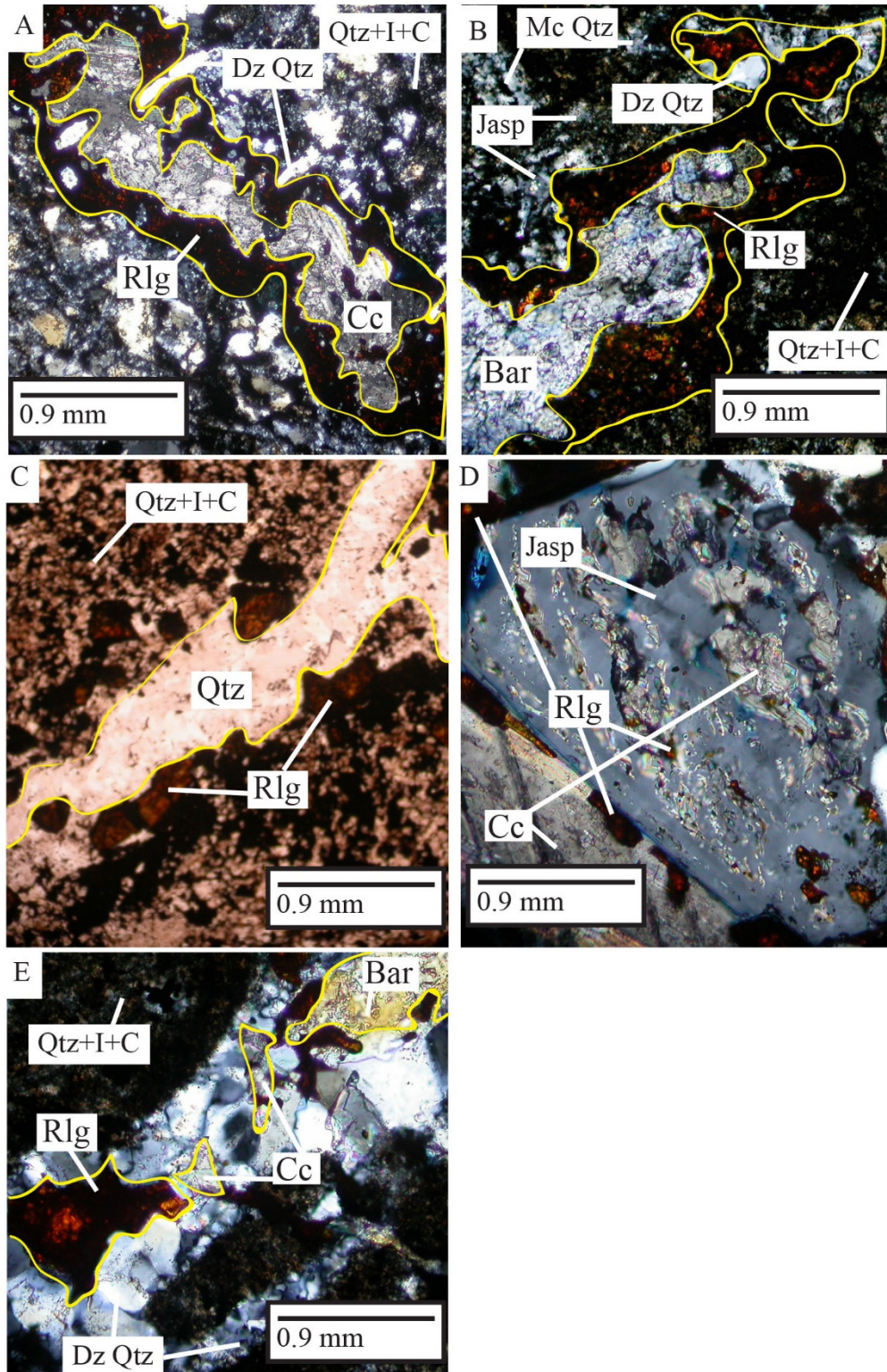


Figure 40. Late-ore stage and Post-ore-stage alteration minerals: realgar, coarsely crystalline calcite, and barite cross-cutting relationships. A and B) Sample 11-16 592 (14.65 ppm Au). A) Photomicrograph of cross-cutting relationships illustrates paragenetic relationships as follows from early to late: drusy quartz, realgar, and coarsely

crystalline calcite. Some quartz crystals exhibits jasperoid texture (TCPL). B) Photomicrograph of cross-cutting relationships shows the following paragenesis from early to late: drusy quartz rimming jasperoid, realgar, and barite (TCPL). C and D) Sample 13-08 1113.5 (13.9 ppm Au). C) Photomicrograph show a less common relationship of realgar rimming host rock with quartz conforming to realgar (TPPL). D) Photomicrograph of inclusions of realgar and calcite within quartz, suggests that timing of realgar and calcite and quartz overlapped (TCPL). E) Sample 12-01 985.5 (8.95 ppm Au), photomicrograph of isolated masses of realgar, calcite, and barite in quartz (TCPL). Textural relationships are ambiguous. Abbreviations: Bar = Barite, C = Carbon, Cc = Calcite, Dz Qtz = Drusy Quartz, I = Illite, Jasp = Jasperoid, Mc Qtz = Microcrystalline Quartz, P = porosity, Rlg = Realgar, TCPL = Transmitted Crossed Polarized Light, TPPL = Transmitted Plane Polarized Light

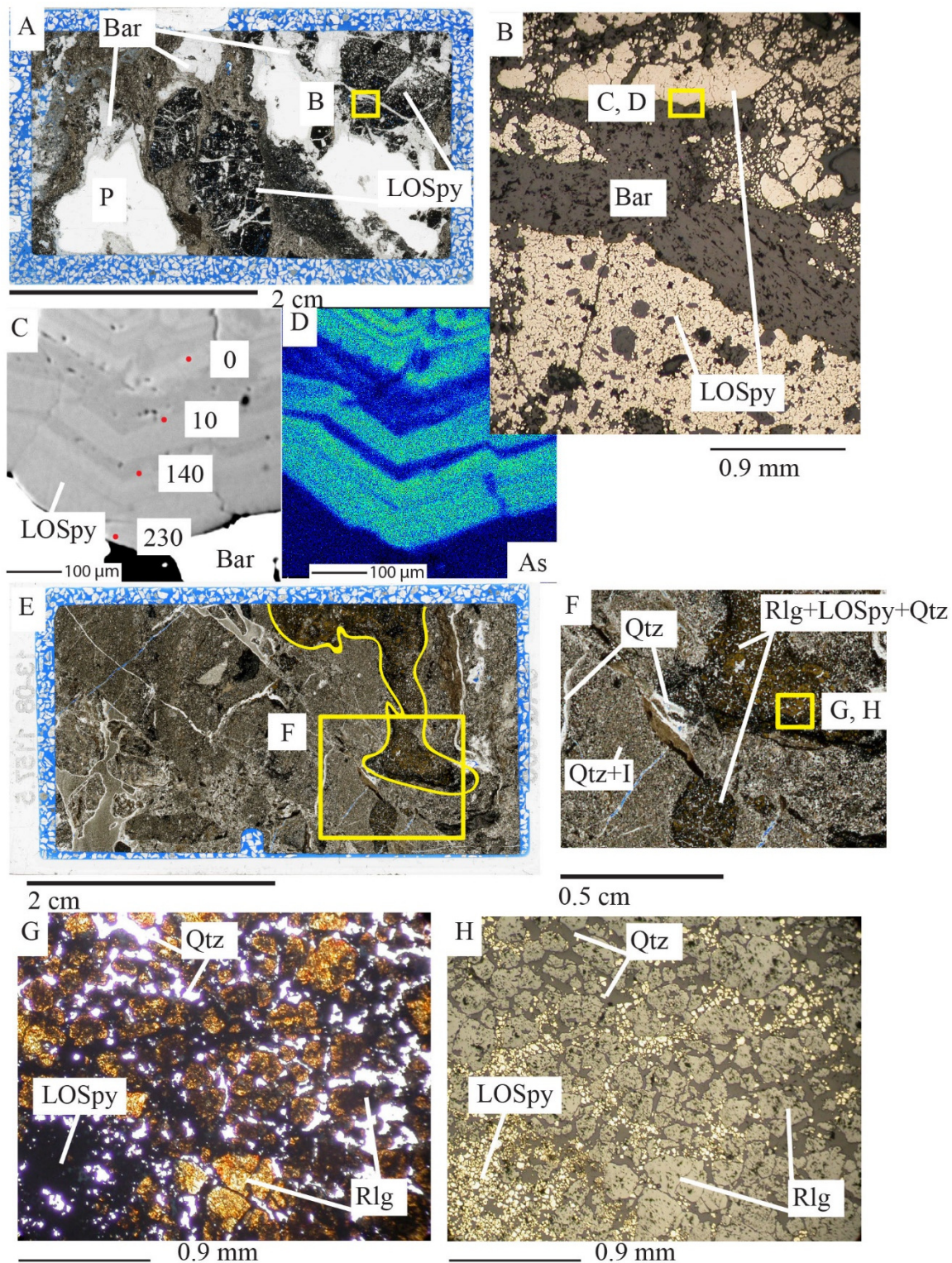


Figure 41. Late-ore-stage pyrite textures. A) Sample 11-18 453 (0.122 ppm Au) of LOS pyrite clasts within a massive sulfidized breccia cross cut by late-ore-stage barite. B) Photomicrograph of LOS pyrite shows growth direction into open space and later precipitation of late-ore-stage barite (RPPL). C, and D) BSE image and As map showing

As zoning in LOS pyrite. Red points in C, starting in bottom left show locations of EPMA points 2261-2264 (Table 8). The number indicates the concentration of gold in ppm. E) Sample 13-08 1157.5 (5.67 ppm Au) of multi-lithic breccia. Collapse feature outlined in yellow. F) Detail of collapse feature with realgar and LOS pyrite in late-ore stage quartz matrix. G and H) Paired photomicrograph images of realgar, LOS pyrite, and quartz within collapse feature (G- TPPL, H- RPPL). Abbreviations: Bar = Barite, I = Illite, LOSpy = Late-ore-stage pyrite, P = porosity, Qtz = Quartz, Rlg = Realgar, TPPL = Transmitted Plane Polarized Light, RPPL = Reflected Plane Polarized Light.

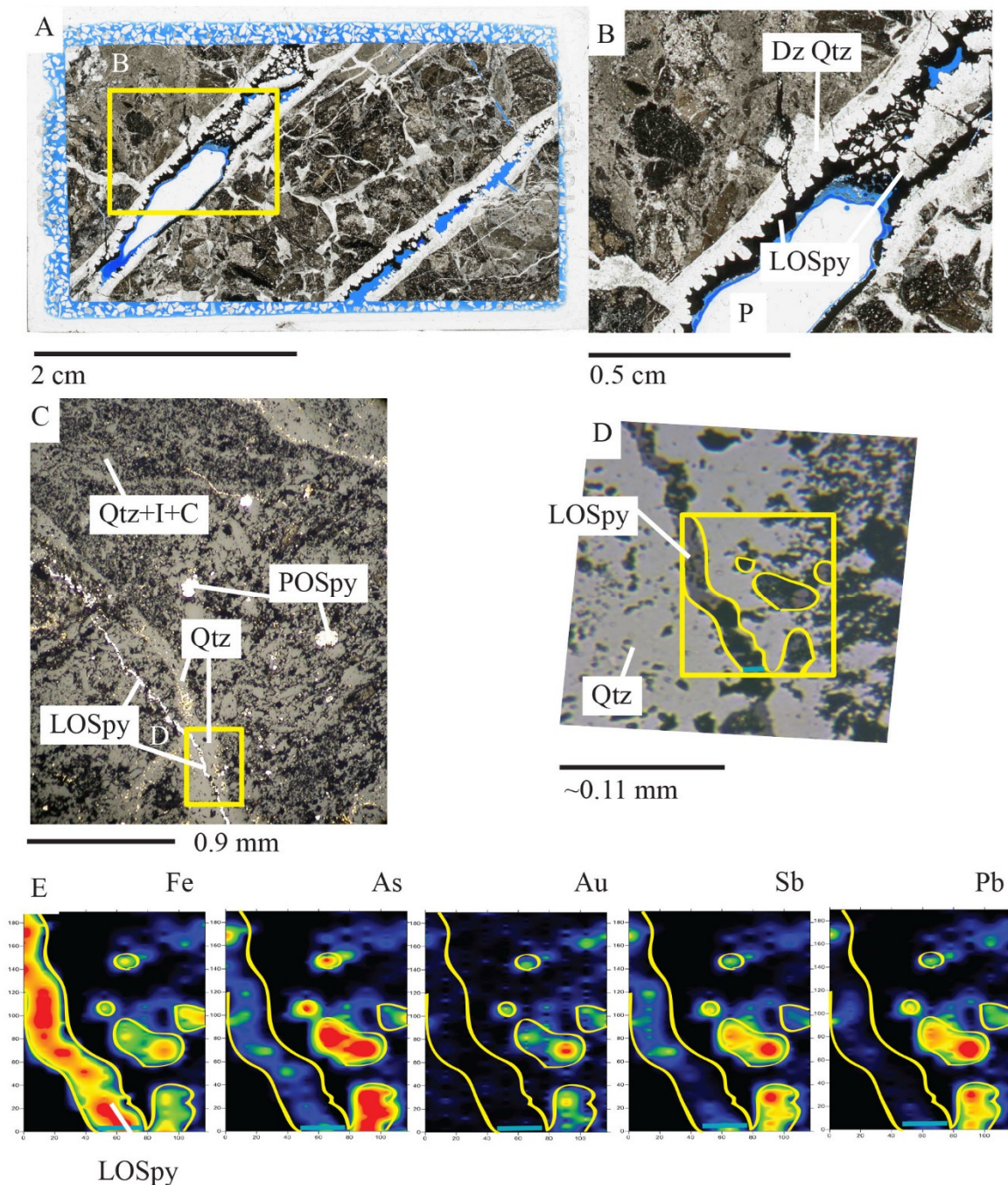


Figure 42. Late-ore-stage vein pyrite. A) Sample 12-13 379 (1.365 ppm Au) of multi-lithic breccia. B) Detail of LOS vein pyrite conforming to and cross cutting late-ore-stage drusy quartz. C) Photomicrograph of area analyzed by both EPMA and LA-ICP-MS showing LOS vein pyrite cross cutting both host rock and LOS quartz vein (RPPL). D) Yellow box outlines LA-ICP-MS map area, and LOS pyrite is outlined in yellow (D, E) (RPPL w/C). EPMA analysis transect of LOS vein (points 1133-1135 in Table #) indicated by light blue line in D and E. E) LA-ICP-MS maps of Fe, As, Au, Sb, and Pb of LOS pyrite, note no Au is associated with LOS vein pyrite, but As, Sb and Pb are detected. The POS anhedral pyrites on the right side of the image, however do contain

Au, As, Sb, and Pb. Abbreviations: C = Carbon, Dz Qtz = Drusy Quartz, I = Illite, Jasp = Jasperoid, LOSpy = Late-ore-stage pyrite, P = porosity, POSpy = Pre-ore-stage pyrite, RPPL = Reflected Plane Polarized Light, RPPL w/ C = Reflected Plane Polarized Light with carbon coating.

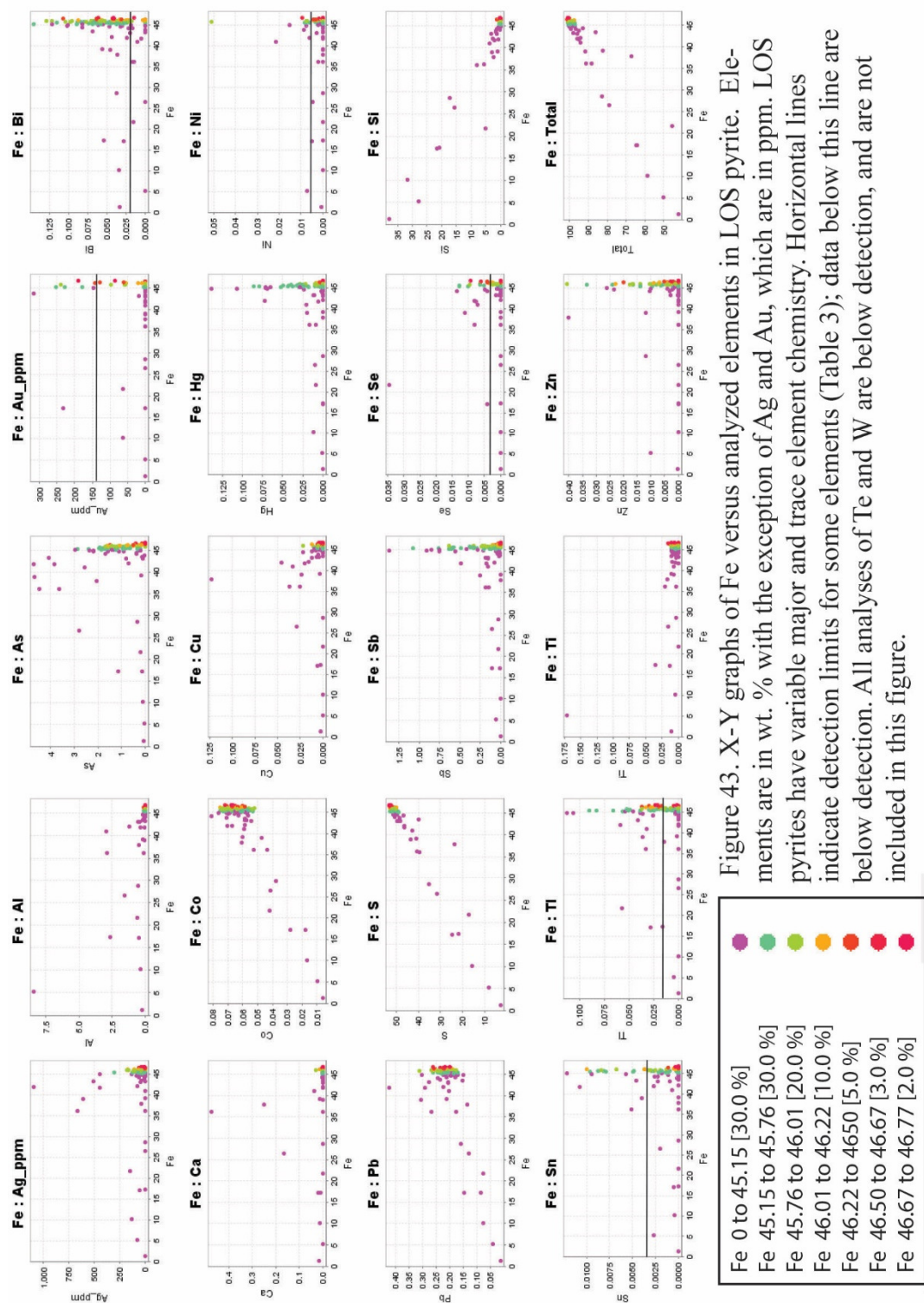


Figure 43. X-Y graphs of Fe versus analyzed elements in LOS pyrite. Elements are in wt. % with the exception of Ag and Au, which are in ppm. LOS pyrites have variable major and trace element chemistry. Horizontal lines indicate detection limits for some elements (Table 3); data below this line are below detection. All analyses of Te and W are below detection, and are not included in this figure.

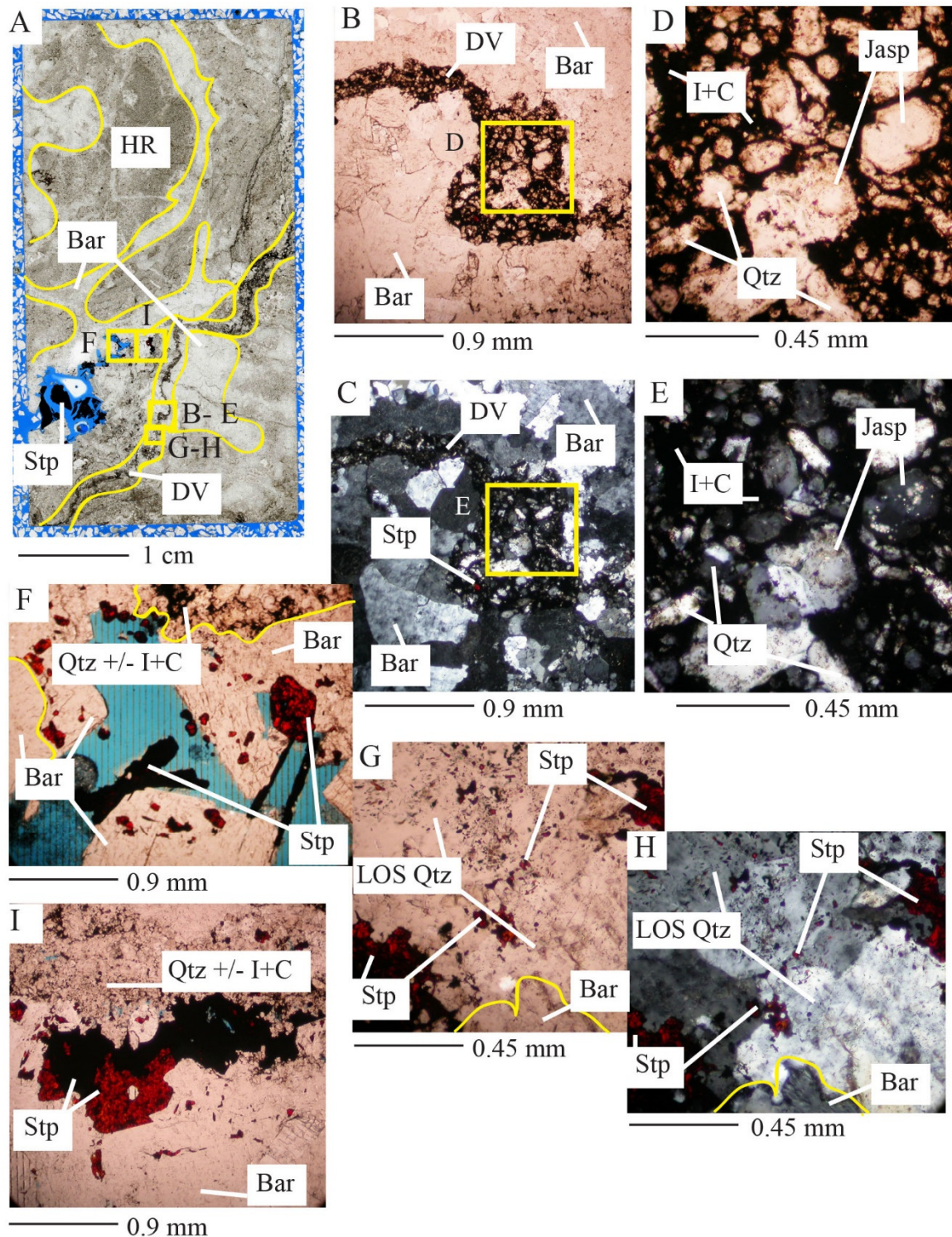


Figure 44. Post-ore-stage barite and stephanite. A) Sample 12-01 1226.5 (0.42 ppm Au, 876 ppm Ag) polished section; barite cross-cuts silty mudstone/sandstone breccia, and dissolution vein cross-cuts barite and host rock. B and C) Paired images of dissolution feature cross-cutting barite. Stephanite fragments occurs in dissolution feature (B – TPPL, C – TCPL). D and E) Paired images of ore-stage alteration minerals: quartz,

jasperoid, illite, and carbon in dissolution feature. Note that illite does not have high birefringence due to presence of carbon. (D – TPPL, E – TCPL). F) Photomicrograph showing barite conforms to host rock, this boundary is indicated by yellow line in top left corner of image. Stephanite conforms to barite, is intergrown with barite, or infills vugs within barite, indicated by yellow line in bottom right corner of image (TPPL). G and H) Paired images of stephanite intergrown with late-ore-stage quartz or infilling vugs within late-ore-stage quartz (G – TPPL, H – TCPL). I) Photomicrograph of stephanite infilling vug and conforming to barite and host rock (TPPL). Abbreviations: Bar = Barite, DV = Dissolution feature – Vein, C = Carbon, HR = Host Rock, I = Illite, Jasp = Jasperoid, Qtz = Quartz, LOS Qtz = Late-ore-stage Quartz, Stp = Stephanite, TCPL = Transmitted Crossed Polarized Light, TPPL = Transmitted Plane Polarized Light

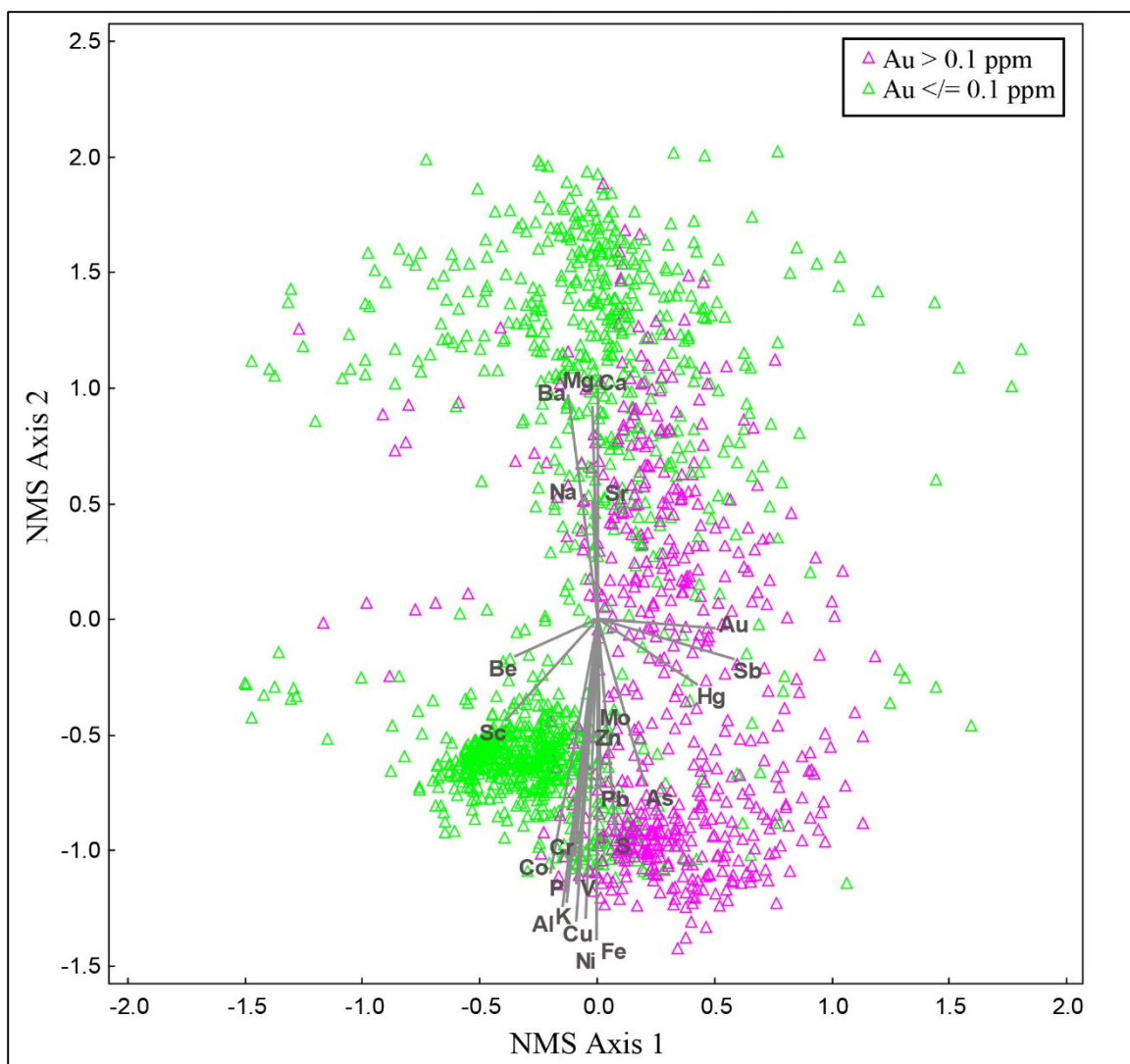


Figure 45. Non-metric multi-dimensional scaling model with 0.1 ppm Au classification. Randomized 1/3 of whole rock geochemistry data (N=1626) from drill holes selected in this study, show the distribution of two classes of Au relative to Axis 1 and 2 and other elements. Each element's r and r^2 value relative to Axis 1 and Axis 2 are listed in Table 25. (N = number of samples inputted in model).

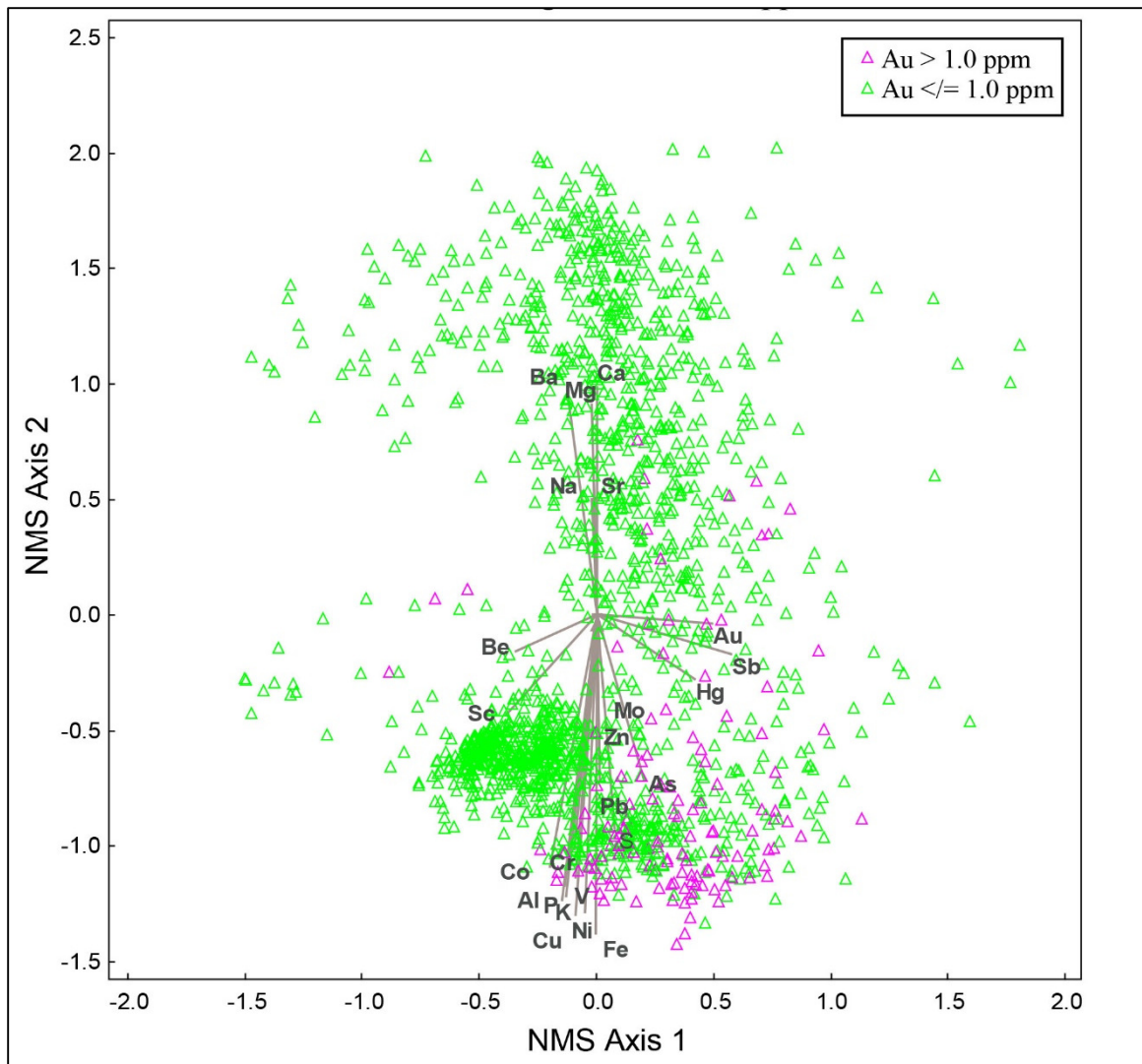


Figure 46. Non-metric multi-dimensional scaling model with 1.0 ppm Au classification. Randomized 1/3 of whole rock geochemistry data (N=1626) from drill holes selected in this study, show the distribution of two classes of Au relative to Axis 1 and 2 and other elements. Each element's r and r^2 value relative to Axis 1 and Axis 2 are listed in Table 25. (N = number of samples inputted in model).

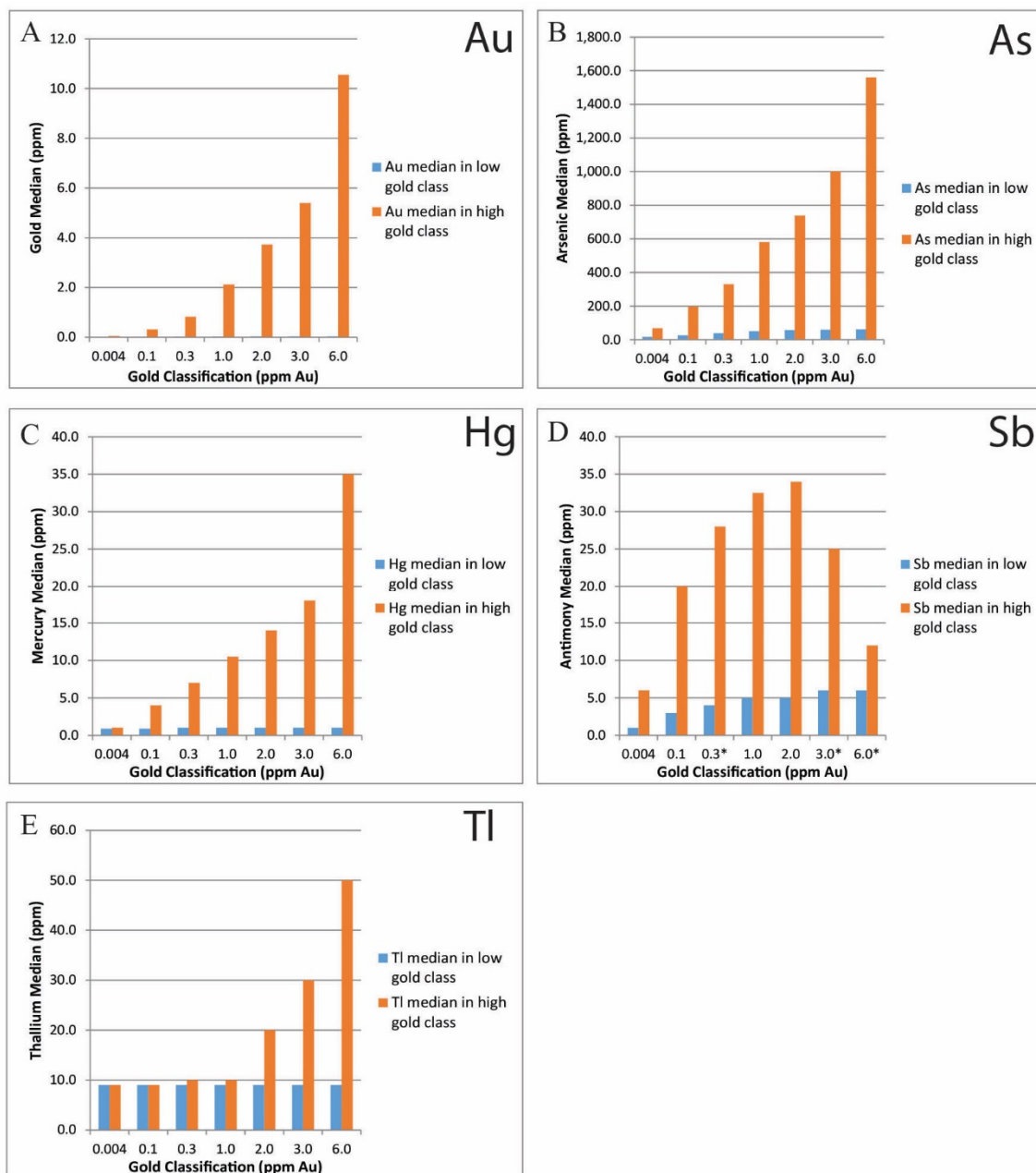


Figure 47. Mann-Whitney U-Test bar graphs of whole rock geochemistry data for Au, As, Hg, Sb, and Tl. The graphs show the progression of median values for the low and high classes with increasing gold classification for Carlin-type pathfinder elements A) Au, B) As, C) Hg, D) Sb, and E) Tl for each gold classification. Note that these elements have higher median values in the high gold class. Gold, As, and Hg exhibit an exponential increase with increasing gold classification. Tl increases at a 2.0 ppm Au classification, and Sb increases to its highest median at the 2.0 ppm gold classification and decreases after at higher classification. The (*) on the X-axis identifies gold classifications for which the median values of the low and high gold classes are not significantly different, as determined an asymptotic significant (2-tailed) value > 0.005; these values are not highlighted on Table 26. Gold classifications for which median values are significantly different are highlighted in blue on Table 26.

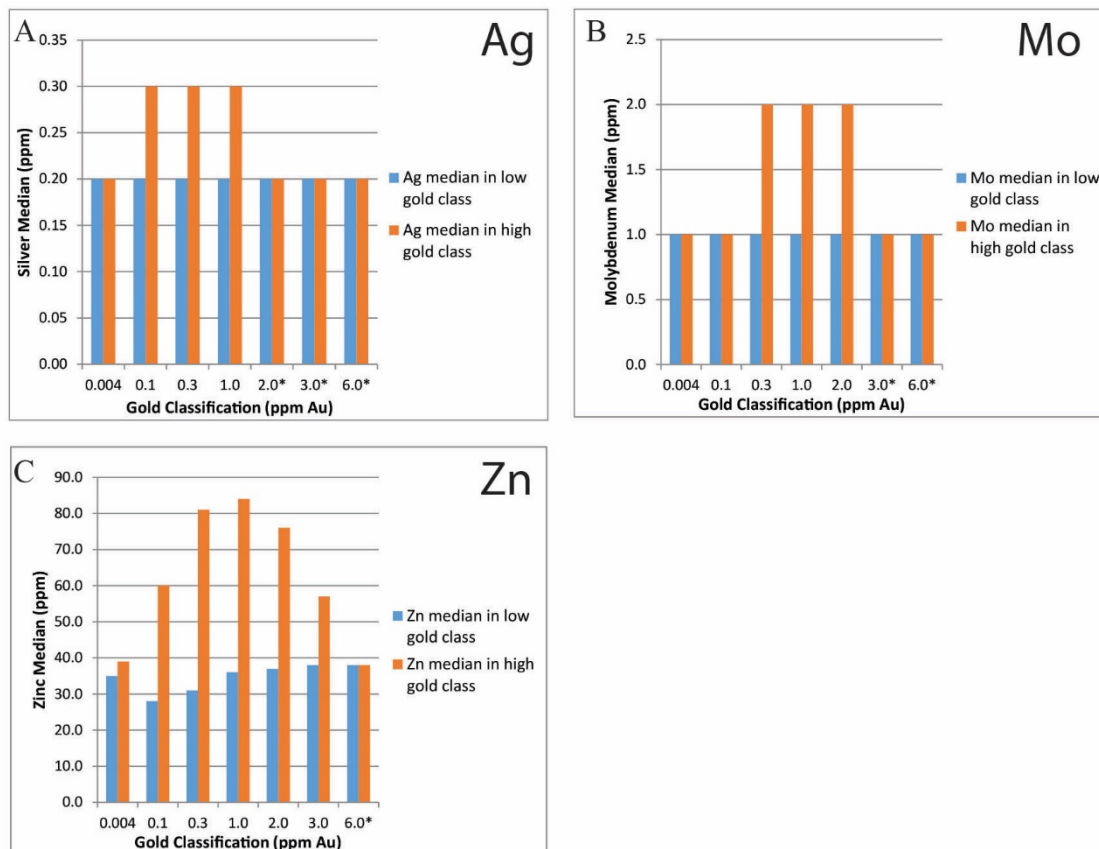


Figure 48. Mann-Whitney U-Test bar graphs of whole rock geochemistry data for Ag, Mo, and Zn. The graphs show median values for A) Ag, B) Mo, and C) Zn, for the low and high classes of each gold classification. Note that Ag, Mo, and Zn do not correlate with gold classification. The (*) on the X-axis identifies gold classifications for which the median values of the low and high gold classes are not significantly different, as determined an asymptotic significant (2-tailed) value > 0.005 ; these values are not highlighted on Table 26. Gold classifications for which median values are significantly different are highlighted in blue on Table 26.

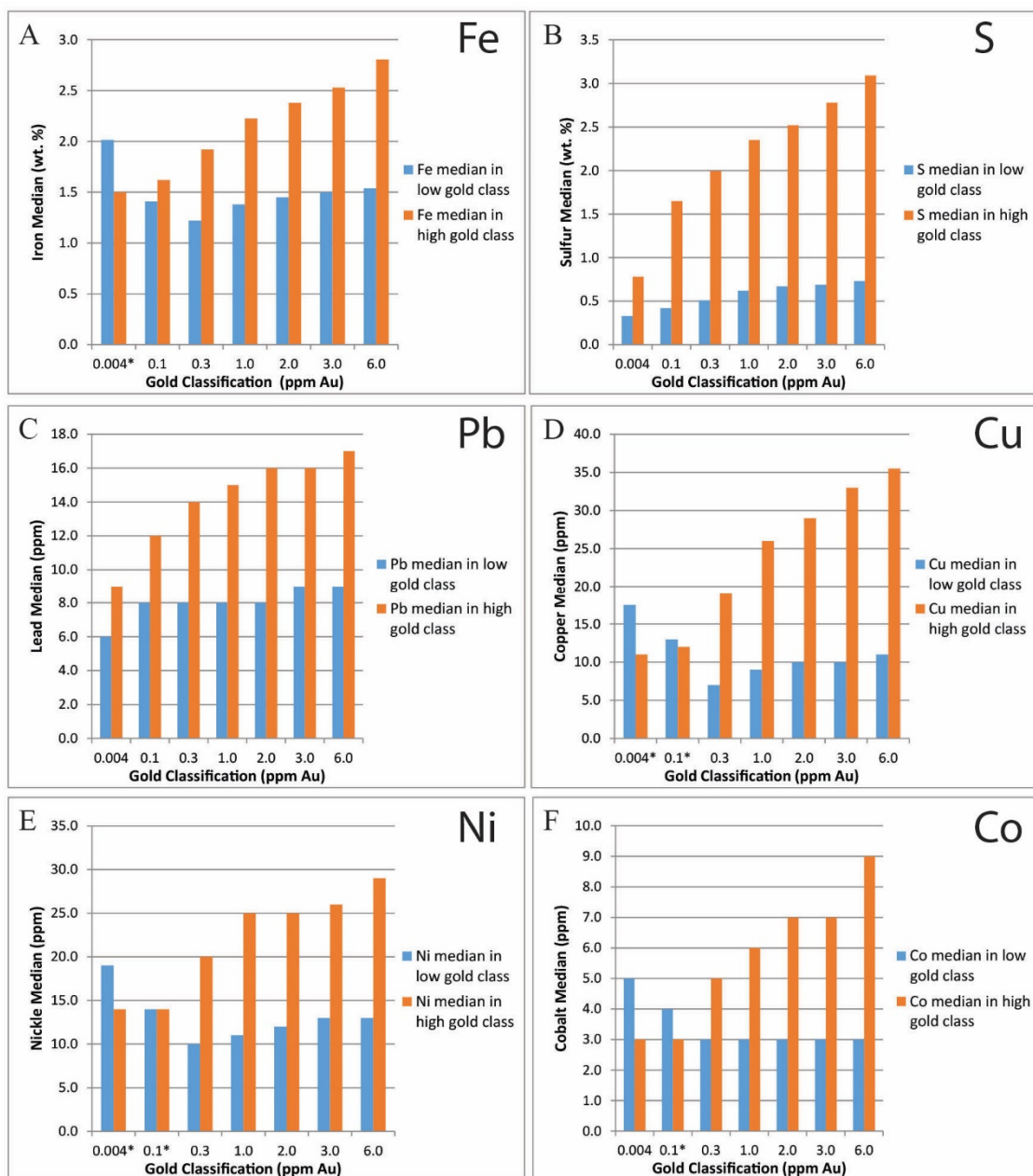


Figure 49. Mann-Whitney U-Test bar graphs of whole rock geochemistry data for Fe, S, Pb, Cu, Ni, and Co. The graphs show median values for A) Fe, B) S, C) Pb, D) Cu, E) Ni, and F) Co for the low and high classes of each gold classification. Note that these elements generally have higher median values in the high gold class. The (*) on the X-axis identifies gold classifications for which the median values of the low and high gold classes are not significantly different, as determined an asymptotic significant (2-tailed) value > 0.005; these values are not highlighted on Table 26. Gold classifications for which median values are significantly different are highlighted in blue on Table 26.

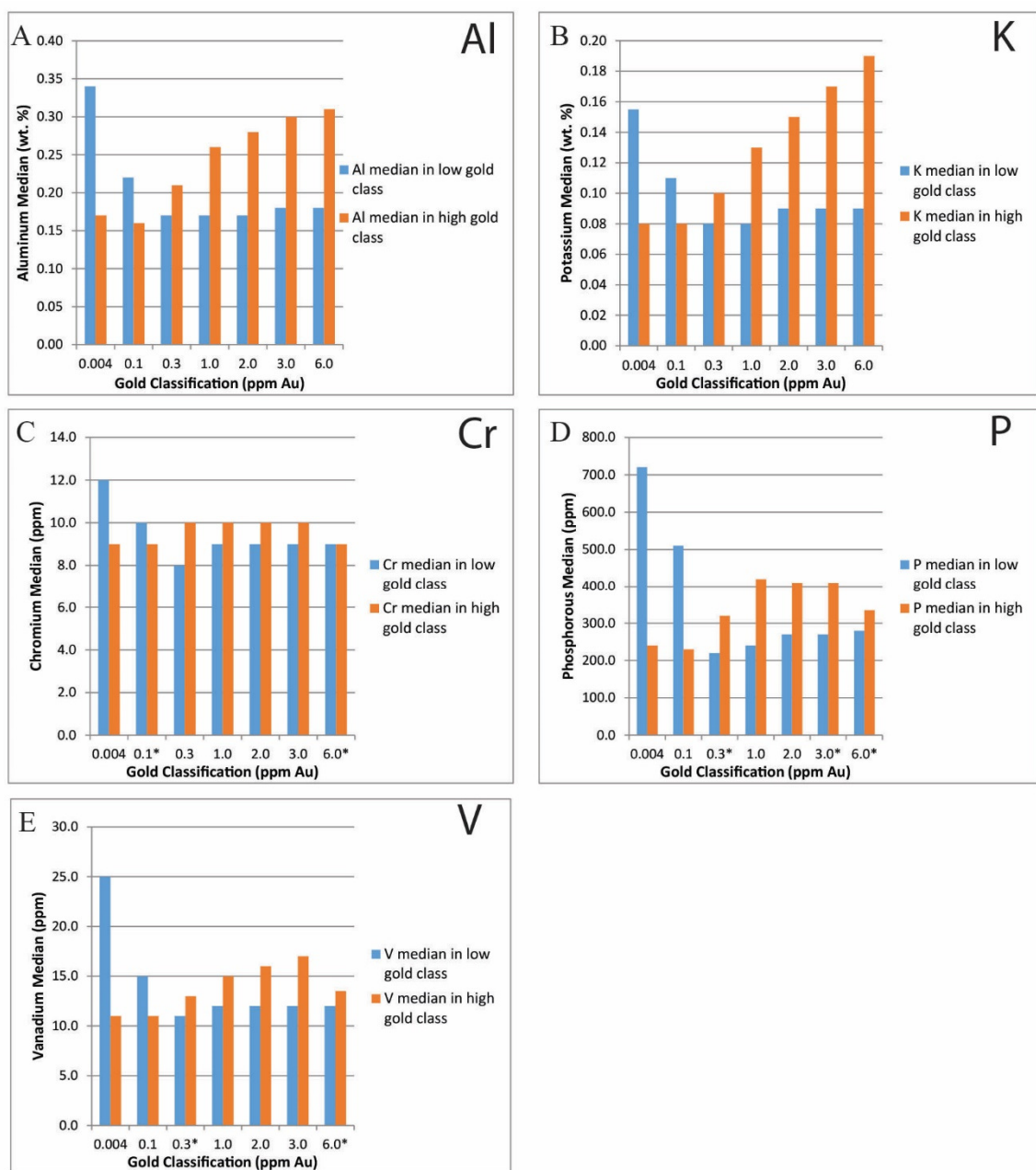


Figure 50. Mann-Whitney U-Test bar graphs of whole rock geochemistry data for Al, K, Cr, P, and V. The graphs show median values for A) Al, B) K, C) Cr, D) P, and E) V for the low and high classes of each gold classification. The (*) on the X-axis identifies gold classifications for which the median values of the low and high gold classes are not significantly different, as determined an asymptotic significant (2-tailed) value > 0.005 ; these values are not highlighted on Table 26. Gold classifications for which median values are significantly different are highlighted in blue on Table 26.

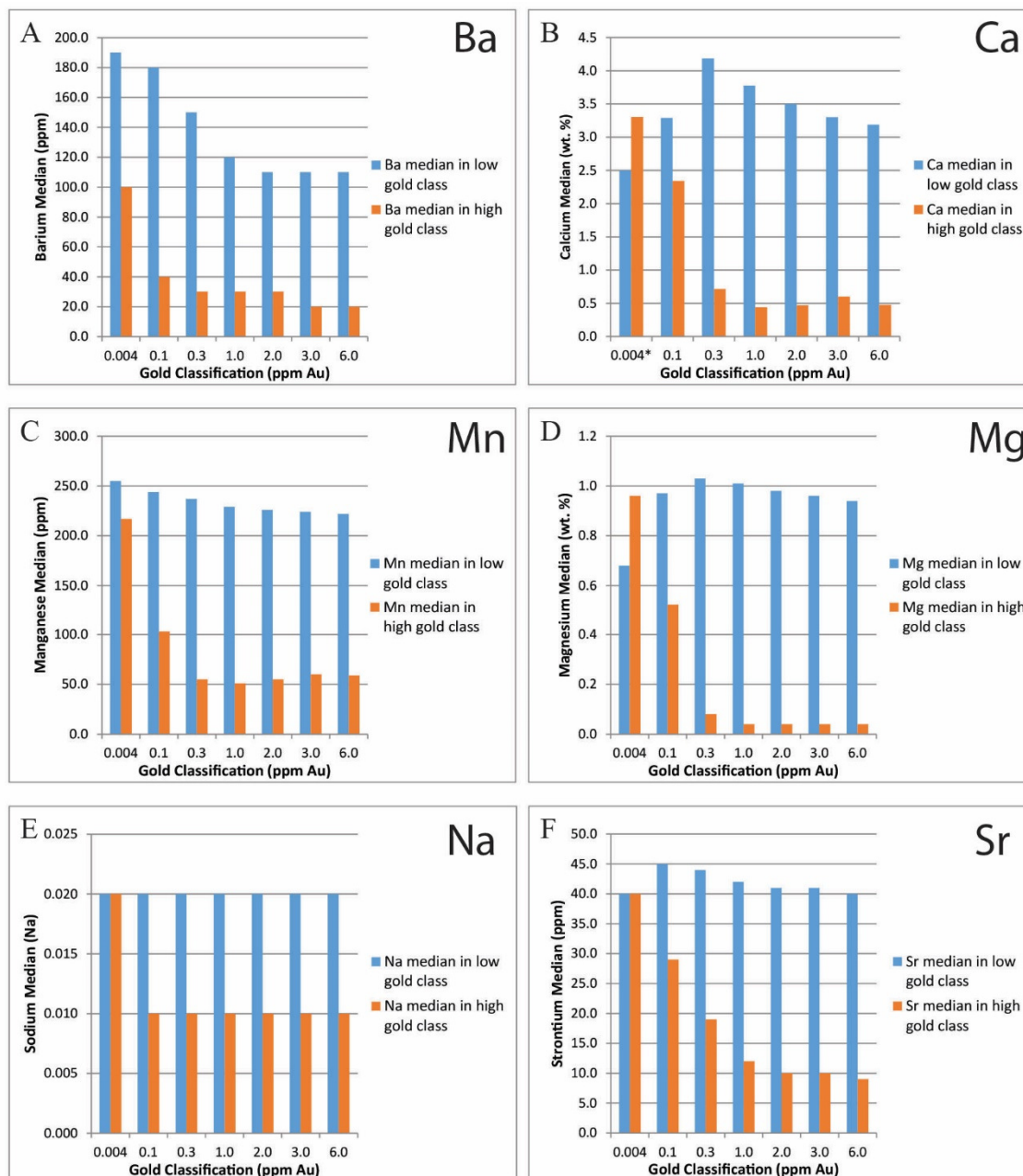


Figure 51. Mann-Whitney U-Test bar graphs of whole rock geochemistry data for Ba, Ca, Mn, Mg, Na, and Sr. The graphs show median values for A) Ba, B) Ca, C) Mn, D) Mg, E) Na, and F) Sr for the low and high classes of each gold classification. Note that these elements generally have higher median values in the lower gold class. The (*) on the X-axis identifies gold classifications for which the median values of the low and high gold classes are not significantly different, as determined an asymptotic significant (2-tailed) value > 0.005; these values are not highlighted on Table 26. Gold classifications for which median values are significantly different are highlighted in blue on Table 26.

APPENDIX C

SAMPLES COLLECTED

The four hundred and fifty nine samples collected for this study are listed here and were collected from fourteen drill holes at the North Bullion Carlin System. Sample names are the drill hole ID number and the footage at which the sample was collected, i.e. (12-01A 987), came from drill hole 12-01A at a depth of 987'. For each sample, this appendix lists the drill hole ID number, footage, and gold assay (gram/ton). For selected samples, an 'X' indicates that a polished section was made from the sample and identifies analytical techniques performed on each sample.

Hole ID #	Footage	Au Assay (g/ton)	Thin Section	SEM	EMPA	LA-ICP-MS	XRD bulk	Terra Spec	OA-ICOS
10-08	403	0.652							
10-08	407	0.975							
10-08	412	0.279							
10-08	416.9	0.079	X			X			
10-08	426	0.106							
10-08	496	0.009					X	X	
10-08	696	0.006							
10-08	703	0.042							
10-08	705.1	0.01							
10-08	807	>.005							
10-08	866	0.513							
10-08	874	0.18	X	X					
10-08	878.5	1.44	X		X	X			
10-08	882.1	1.635	x						
10-08	886	2.67	X						
10-08	891.9	2.75	X						
10-08	896	2.98	X	X			X		
10-08	898	2.98							
10-08	927	1.06							
10-08	943	1.79							
10-08	947.1	0.937							
10-08	952.1	0.764							
10-08	957.9	0.725							
10-08	972.9	0.866							
10-08	1049.9	0.324							
10-08	1117.5	0.227							
10-08	1123	1.33							
10-08	1127.1	2.07							
10-08	1131.9	2.6					X		
10-08	1152	2.2							
10-08	1156.9	1.455							X
10-08	1161	1.04							
10-08	1165.1	0.5							X
10-08	1211	1.73							X
10-08	1216	1.35							
10-08	1224.4	0.506							X

10-16	969	0.044							
10-16	970	0.044							X
10-16	972	0.241							
10-16	975	0.611							X
10-16	983	0.319							
10-16	986	0.251							
10-16	990.5	0.202							
10-16	997	0.042							
10-16	1001	0.026							
10-16	1009.5	0.009							X
10-16	1020.1	0.129							
10-16	1029	0.068							
10-16	1079.5	0.036							
10-16	1085	0.064							
10-16	1107	0.005							X
10-16	1110.9	0.036							
10-16	1117.5	0.005							X
10-16	1227	0.1879							
10-16	1234.5	0.065							
10-16	1261	0.027							
10-16	1334	0.4							X
10-16	1417.1	0.409							
10-16	1452.5	0.103							
10-16	1467	0.043							X
10-16	1468.5	0.043							X
11-03	651	0.969							
11-03	656	0.515							
11-03	677	0.587							
11-03	765.9	0.617					X		
11-03	768.5	0.402							
11-03	770.5	0.386					X		
11-03	829	0.459							
11-03	831	0.235							
11-03	836	0.196							
11-03	844	0.415							
11-03	868	0.55							
11-03	877.9	0.625							
11-03	882	0.713							
11-03	889.9	0.793							
11-03	930.1	0.283							

11-03	939.9	0.776							
11-03	956	1.085					X		
11-03	960.1	0.761							
11-03	978.4	.306	X	X					
11-03	978.6	2.01	X	X					
11-03	981	1.61							
11-03	1007.5	0.542							X
11-03	1013.5	0.899	X						
11-03	1019.5	1.105	X						
11-03	1023.5	4.11	x				X		
11-03	1033	3.75							
11-03	1057	4.12							
11-03	1061	3.59							
11-03	1067	0.659							
11-03	1089	1.075							
11-03	1094.9	0.651							
11-03	1103	1.025							
11-03	1121.1	0.28							
11-03	1188	0.699							
11-03	1194.5	1.505							
11-03	1197	0.999							
11-03	1214.5	0.298							
11-03	1222.5	0.286							
11-03	1263	0.778							
11-03	1290.1	0.284							
11-03	1335.1	0.125							
11-03	1369	0.184							
11-03	1372	0.235							X
11-03	1436	0.172							
11-03	1447.9	0.088							X
11-03	1450.5	0.24							X
11-03	1457	0.142					X		X
11-03	1539	0.111							X
11-03	1559	0.033							X
11-04	1003.5	0.011	X		X	X	X		
11-04	1059	0.034	X	X			X		
11-04	1074.9	0.017	X	X					X
11-04	1164	0.033							X
11-04	1187	0.056							X
11-04	1224	0.049							

11-04	1279	0.131							X
11-04	1285	0.075							
11-04	1294.5	0.027							X
11-04	1372	0.014							
11-04	1373	0.014							
11-04	1396	0.014							X
11-04	1467	0.017							X
11-04	1526.5	0.006	X		X	X	X		X
11-16	441	0.023							
11-16	454.5	0.005							X
11-16	459	0.011							
11-16	461	0.283	X		X	X			
11-16	559.8	0.742					X		
11-16	563	5.63							
11-16	589	6.83					X		
11-16	592	14.65	X				X		
11-16	595.1	0.338	X						X
11-16	607	3.1	X						
11-16	612	14.9	X						
11-16	617	9.31							
11-16	669	2.5							
11-16	673	7.4							
11-16	682	4.7	X	X					
11-16	877	0.012							
11-16	887	0.189							
11-16	1004.5	1.83							
11-16	1007.5	0.198							
11-16	1226.5	0.165	X		X				X
11-16	1243	0.135							
11-16	1332.5	0.401					X		
11-16	1430.5	0.881							X
11-16	1473.5	0.074							X
11-17	150.5	0.008							
11-17	222	0.008							
11-17	618	0.221							
11-17	662	0.37							
11-17	664	0.37							X
11-17	679	0.084							
11-17	707.5	0.093							

11-17	712	0.119							
11-17	716	0.246							
11-17	721	0.239							
11-17	725.5	0.103							
11-17	734	0.033							X
11-17	789.5	0.138							
11-17	833	5.48	X						
11-17	835.5	0.333							
11-17	1013	0.005							
11-17	1078	0.175							
11-17	1209.9	0.125							
11-17	1355.1	0.274							
11-17	1361	0.473							
11-17	1362	0.473							
11-17	1427	0.05							X
11-17	1518.5	0.184							
11-17	1529	0.055							
11-17	1537.1	0.3							X
11-17	1603	0.043							
11-17	1835.5	0.386							
11-17	1841	0.664							X
11-17	1845.1	0.438							
11-17	1864	0.101							X
11-17	1877	0.42							
11-17	1881	0.046							X
11-18	441	0.299							
11-18	453	0.122	X		X				
11-18	597.5-600	0.005							
11-18	872	0.02	X						
11-18	873	0.02							
11-18	1006.4	3.26							
11-18	1014	0.079							
11-18	1028	0.372							
11-18	1035.5	0.118							
11-18	1079	0.781							
11-18	1083.5	1.665							
11-18	1087	0.86							
11-18	1091.2	0.432							
11-18	1158	0.75	X						
11-18	1163.4	1.345	X	X					

11-18	1167	1.91	X						
11-18	1169	1.91							
11-18	1172.5	1.82							
11-18	1175.2	1.715	X						
11-18	1181	2.77	X						
11-18	1187	3.8							
11-18	1190.1	3.91	X	X					
11-18	1193	3.91							
11-18	1206	3.01							
11-18	1242	3.15							
11-18	1247.5	2.37							
11-18	1255.5	1.93							
11-18	1303	2.19							
11-18	1304.9	2.19							
11-18	1310.6	0.802							X
11-18	1317.5	0.549							X
11-18	1334.5	0.122							X
11-18	1338.5	0.205							
11-18	1652	0.046							X
11-18	1656.5	0.215							X
11-18	1674.9	0.101							
12-01	329.5	0.007							
12-01	373.5	< 0.005							
12-01	392.5	0.006							
12-01	498.4	0.004							
12-01	541	< 0.005	X						X
12-01	548	0.006							
12-01	556	0.022							
12-01	563	0.173							
12-01	569.9	0.547							
12-01	572	0.542							
12-01	577.1	0.394							
12-01	586	0.146	X						
12-01	629.9	0.246							
12-01	780	1.045							
12-01	840	0.418							
12-01	845.4	0.817							
12-01	876	1.67							
12-01	898	0.809							
12-01	911.5	1.745						X	

12-01	916	19.3						X	
12-01	924.1	6.85							
12-01	932	4.07							
12-01	938.5	12.85							
12-01	939.5	12.85							
12-01	943.5	11.45							
12-01	953	3.01							
12-01	970.9	2.53	X	X	X		X	X	X
12-01	974.9	11.55	X	X				X	
12-01	978	5.83	X						
12-01	985	8.96							
12-01	985.5	8.96	X	X					
12-01	986.1	20.8	X	X				X	
12-01	987	20.8	X	X	X	X	X		
12-01	992	25.6	X	X	X	X			
12-01	992b	25.6	X						
12-01	996.5	12.35							
12-01	1017.9	6.84	X						
12-01	1022	7.76	X				X		X
12-01	1026	15.65	X						
12-01	1026b	15.65	X		X	X			
12-01	1034.9	4.89							
12-01	1036	13.1							
12-01	1044	4.81							X
12-01	1048	3.35							
12-01	1051	2.41							X
12-01	1054.9	2.41							
12-01	1058	0.339							X
12-01	1067	0.48							
12-01	1105	3.52							
12-01	1131	1.04							
12-01	1141	3.26							
12-01	1150.2	2.57							
12-01	1157.4	1.905							
12-01	1158.5	6.2							
12-01	1159.7	1.435							
12-01	1171	0.881							
12-01	1176.5	1.735							
12-01	1182	3.71							
12-01	1185.5	4.68							
12-01	1223	0.852	X						

12-01	1226.5	0.42	X		X	X	X		
12-01	1229	0.42							
12-01	1230.1	0.423							
12-01	1233	0.962	X						
12-01	1246.9	0.834							
12-01	1249	1.22	X	X					
12-01	1254.9	1.86	X						
12-01	1258	0.915							
12-01	1262.5	0.586							
12-05	107	0							
12-05	331	0.007							
12-05	336.9	0.007							
12-05	388	0.015							
12-05	417	0.01							
12-05	511.1	0.01							
12-05	514	0.01							
12-05	528.5	0.012							
12-05	531	0.006							
12-05	567	0.014							
12-05	751.9	0.052							
12-05	755	0.026							
12-05	765.5	0.023							
12-05	770	0.016							
12-05	826	0.021							X
12-05	860	0.182							X
12-05	863.5	0.057							
12-05	919.9	1.41							
12-05	921.9	0.253					X		
12-05	925	0.141							
12-05	1042	0.294					X		X
12-05	1044	0.236							
12-05	1054	0.108							X
12-05	1076	0.235							X
12-05	1187.5	0.213							
12-05	1212	0.085							X
12-05	1285.1	0.048							
12-05	1399	0.042							
12-05	1406	0.18	X						
12-05	1408.5	1.005	X	X	X				
12-05	1466.9	0.475							

12-05	1508	0.232							
12-05	1518	0.094							
12-05	1627.1	0.27							
12-05	1651.9	0.115					X		X
12-05	1755	0.115							
12-05	1760.5	0.379							
12-05	1764	0.136							X
12-05	1810.1	1.1							X
12-05	1871	0.149							
12-05	1989	0.126					X		X
12-10	340	0.008					X		
12-10	353.1	0.199							
12-10	400	0.036							
12-10	405.1	0.042							
12-10	472.5	0.016	X						
12-10	482	0.03							
12-10	509.1	0.008							
12-10	525.9	0.006					X		X
12-10	528	0.021							
12-10	532	0.187	X						
12-10	580.5	0.098							
12-10	712	0.009	X				X	X	
12-10	716	4.41	X				X	X	
12-10	725	3.5							X
12-10	729	1.245							X
12-10	737.5	0.228							X
12-10	760	0.024	X		X	X			X
12-10	765	0.268							
12-10	768	13.4							
12-10	771	13.4	X						
12-10	776	16.2	X				X		
12-10	780	27.3	X						
12-10	800	3.44	X						
12-10	803	30.2	X	X	X	X	X	X	
12-10	803.2	30.2	X						
12-10	804.5	13.1	X						
12-10	825	3.53						X	
12-10	998	3.79							
12-10	1044	1.71					X		
12-10	1085	1.015							

12-10	1089	6.42							
12-10	1111.5	2.28							
12-10	1406.9	0.928							
12-10	1553.5	0.054							X
12-10	1555.9	0.226							X
12-10	1574	0.557							
12-10	1711	2.16							
12-10	1755	0.368					X		
12-10	1831	0.027							X
12-10	1949	0.038							
12-11	418	0.004	X						X
12-11	498	0.032	X						
12-11	573.1	0.186							
12-11	586.5	0.257					X		
12-11	634.9	0.076	X						
12-11	643	1.215							
12-11	647	7.75	X				X		
12-11	651.9	4.38							
12-11	774.5	0.004							
12-11	861	0.007							
12-11	1140.5	1.54							
12-11	1148.5	0.695					X		
12-11	1182	1.255							
12-11	1188	0.688							
12-11	1201	0.369							
12-11	1253.5	0.533							
12-11	1260.5	0.129							X
12-11	1325.1	0.181							
12-11	1329	0.952	X						X
12-11	1343.5	0.706					X		
12-11	1512.5	0.391							
12-11	1517.5	0.414							X
12-13	259	0.905							
12-13	351	0.367							
12-13	356	0.672							X
12-13	357.1	1.2							X
12-13	362.5	1.585							
12-13	365	1.585							X
12-13	378	1.365							

12-13	379	1.365	X		X	X			
12-13	386.5	1.175							
12-13	401	0.006							X
12-13	416	0.011							
12-13	428.5	0.008							
12-13	839.5	1.765							
12-13	842	0.996							
12-13	849.9	1.065							
12-13	852.5	0.677							
12-13	955	2.95							
12-13	959	0.905							
12-13	993.9	1.39							
12-13	1047.5	1.465	X				X		X
12-13	1070	0.375	X				X		X
12-13	1152	0.382	X				X		X
12-13	1228.6	0.585	X						X
12-13	1235	1.79							
12-13	1237.9	1.835							X
12-18	311	0.012							
12-18	376	0.01							
12-18	462.1	0.013							
12-18	471	0.008							
12-18	522	0.007							
12-18	561	0.04							
12-18	563.9	0.031							
12-18	640	0.025							
12-18	678.1	0.005						X	X
12-18	744	0.165							
12-18	806.9	0.241							
12-18	810.5	0.705							
12-18	907	3.43						X	X
12-18	909	0.068						X	X
12-18	969	0.468						X	
12-18	978	1.265							
12-18	989.1	1.46							
12-18	1021	0.694							
12-18	1023	1.295							
12-18	1116	0.293							
12-18	1121	0.234							
12-18	1159	0.256					X		

12-18	1190.5	0.034					X		X
12-18	1195.1	0.455							X
12-18	1234	0.173							
12-18	1317	0.028							
12-18	1392.5	0.082							
12-18	1406.5	0.11							
12-18	1476	0.154							
12-18	1580	0.301							X
12-18	1587	1.715							X
12-18	1640.1	0.253							
12-18	1649	0.019							
12-18	1746.5	0.025							
12-18	1832.9	0.007							X
12-18	1838	0.342							
12-18	1861	0.303							
12-18	1867.5	0.175							
12-18	2026	0.04							X
12-18	2143	0.083							
13-08	1087	0.186	X				X		
13-08	1101.5	3.79	X				X		
13-08	1108	10.1	X						
13-08	1113.5	13.9	X		X	X	X		X
13-08	1152.5	0.403	X		X	X	X		
13-08	1157.5	5.67	X		X				
13-08	1164	14.5	X	X	X	X	X		

APPENDIX D

DOCUMENTED MINERAL LOCATIONS

FOR POLISHED SECTIONS

Eighty-four samples were chosen for polished section and detailed optical petrography notes were taken for each. Sample names are the drill hole number and the footage at which the sample was collected, i.e. (12-01A 987), came from drill hole 12-01A and a footage of 987'. This appendix lists the Au (ppm) assay, Ag (ppm) assay where applicable, formation, host rock, and the minerals observed in each sample through optical petrography and other analytical methods. These minerals include dolomite (dol), calcite (cc), quartz (qtz), green chert (GC), illite (ill), montmorillonite (mon), apatite (ap), pre-ore stage pyrite (POS py), ore stage 1 pyrite (OS1 py), ore stage 2 pyrite (OS2 pyrite), late-ore stage quartz (LOS Qtz), late-ore stage pyrite (LOS py), late-ore stage realgar (LOS rgr), late-ore stage calcite (LOS cc), barite (bar), stephanite (stp), sphalerite (sph), rutile (rut), kaolinite (ka), halloysite (ha), and oxidation minerals such as hematite and goethite (ox). If samples have breccia textures (bx tex), they are indicated by a (Y). See Figures 8-9 for sample location in relation to E-W and N-S cross-sections.

Hole #	Footage	Au (ppm)	Ag ppm	Frm.	Host Rock	Dol	Cc	Qtz	G.C.
11-4	1003.5	0.011		Mc	Ss		X	X	X
11-4	1059	0.034		MLBX	Stms bxa			X	
11-4	1074.9	0.017		Ddg	Ls/Dol Bx	X			
11-4	1164	0.033		Ddg	Dol bxa	X	X		
11-4	1526.5	0.006		Dtc	Ccst	X		X	
12-01A	541	0.005		Mw	Mic-ls		X		
12-01A	586	0.146		Mw	Ms bxa			X	
12-01A	970.9	2.538		Mw	Mic- ms		X		
12-01A	974.9	11.557		Mw	Ms			X	
12-01A	978.9	5.830		Mw	Ms			X	
12-01A	985.5	8.951		Mw	Ms			X	
12-01A	986.1	20.816		Mw	Ms			X	
12-01A	987	20.800		Mw	Ms			X	
12-01A	992	25.583		Mw	Ms			X	
12-01A	992b	25.600		Mw	Ms			X	
12-01A	1017.9	6.824		Mw	MLbx			X	
12-01A	1022	7.750		Mw	MLbx		X		
12-01A	1026	15.638		Mw	Ms			X	
12-01A	1026b	15.650		Mw	Ms			X	
12-01A	1223	0.852	0.6	Mw	ss>ms				
12-01A	1226.5	0.420	876	Mw	ms>ss			X	
12-01A	1233	0.962	21.8	MLBX	ML bx			X	
12-01A	1254.9	1.860	64.5	MLBX	MI bx		X	X	
11-18	453	0.122		Mc	Mass sulf. Bx			X	
11-18	873.5	0.020		Mc				X	
11-18	1158	0.750		MLBX	Ss bx			X	
11-18	1163.4	1.345		MLBX	Ms bx			X	
11-18	1167	1.910		MLBX	Ms bx	X		X	
11-18	1175.2	1.715		MLBX	Ms bx			X	
11-18	1181	2.770		MLBX	Ms bx			X	
11-18	1190.1	3.910		MLBX	Ms bx			X	
12-05	1406	0.180		Ddg	Dol Bx	X		X	
12-05	1408.5	1.005		Tpd	Dacite			X	
10-08C	416.9	0.079		Mc	Ms sulf. bx			X	
10-08C	874	0.180		Mc	Ss			X	X
10-08C	878.5	1.440		Mc	Ss			X	
10-08C	882.1	1.635		Mc	Ss			X	
10-08C	886	2.670		Mc	Ss			X	

Hole #	Footage	Ill	Mon	Ap	Jasp	POS py	OS1 py	OS2 py	LOS Qtz	LOS py	LOS Rgr	Bar	LOS CC
11-4	1003.5	X	X			X							
11-4	1059	X				X							X
11-4	1074.9	X			X	X						X	X
11-4	1164	X			X	X							X
11-4	1526.5	X				X							
12-01A	541	X				X							X
12-01A	586	X				X			X	X		X	
12-01A	970.9	X			X	X							X
12-01A	974.9	X				X			X		X	X	
12-01A	978.9	X				X						X	
12-01A	985.5	X				X			X		X	X	X
12-01A	986.1	X				X			X		X	X	X
12-01A	987	X	X			X		X					
12-01A	992	X				X		X	X		X	X	
12-01A	992b	X				X		X			X	X	X
12-01A	1017.9	X			X	X			X		X		X
12-01A	1022	X			X	X					X		X
12-01A	1026	X				X		X					
12-01A	1026b	X			X	X		X	X		X	X	
12-01A	1223	X			X	X			X			X	
12-01A	1226.5	X			X	X		X				X	
12-01A	1233	X			X	X			X				
12-01A	1254.9	X			X	X			X			X	
11-18	453	X				X		X		X		X	
11-18	873.5	X				X							
11-18	1158	X				X		X				X	
11-18	1163.4	X				X						X	
11-18	1167	X			X	X			X	X	X	X	
11-18	1175.2	X			X	X			X			?	
11-18	1181	X				X			X			X	
11-18	1190.1	X				X			X				
12-05	1406				X	X							
12-05	1408.5	X		X			X	X				X	X
10-08C	416.9	X			X	X				X		X	
10-08C	874	X	X	X		X							
10-08C	878.5	X				X		X	X			X	X
10-08C	882.1	X				X			X			X	X
10-08C	886	X				X			X			X	

Hole #	Footage	Stp	Sph	Rut	Ka	Hal	Ox	Bx Tex
11-4	1003.5							N
11-4	1059							Y
11-4	1074.9							Y
11-4	1164							Y
11-4	1526.5							N
12-01A	541							N
12-01A	586							Y
12-01A	970.9							N
12-01A	974.9							N
12-01A	978.9							N
12-01A	985.5							N
12-01A	986.1							Y
12-01A	987							Y
12-01A	992							N
12-01A	992b							Y
12-01A	1017.9							Y
12-01A	1022							N
12-01A	1026							Y
12-01A	1026b							Y
12-01A	1223							Y
12-01A	1226.5	X						Y
12-01A	1233							Y
12-01A	1254.9							Y
11-18	453							Y
11-18	873.5							N
11-18	1158							Y
11-18	1163.4		X	X				Y
11-18	1167		X					Y
11-18	1175.2		X					Y
11-18	1181							Y
11-18	1190.1			X				Y
12-05	1406							Y
12-05	1408.5		X	X	X			N
10-08C	416.9							?
10-08C	874			X				N
10-08C	878.5							N
10-08C	882.1							N
10-08C	886							N

Hole #	Footage	Au (ppm)	Ag ppm	Frm.	Host Rock	Dol	Cc	Qtz	G.C.
10-08C	891.9	2.750		Mc	Ss			X	
10-08C	896	2.980		Mc	Ss			X	
10-08C	1117.5	0.227		Mc	ss			X	
10-08C	1123	1.330		MLBX	Ms bx		X	X	
10-08C	1131.9	2.600		MLBX	Ms bx		X	X	
10-08C	1156.9	1.455		MLBX	Ms bx	X	X	X	
10-08C	1161	1.040		Ddg	Dol bx	X			
11-03.	978.4	0.306			Dol bx			X	
11-03.	978.6	2.000			Dol bx			X	
11-03.	1013.5	2.010			Dol/Ms Bx		X		
11-03.	1019.5	1.105			Dol/Ms Bx			X	
11-03.	1023.5	4.110			Dol/Ms Bx			X	
12-13 (V)	379	1.365		Mc	ML bx			X	
12-13 (V)	1047.5	1.465		Mc	ss75 ms			X	
12-13 (V)	1070	0.375		MLBX	ls60 ss,ms			X	
12-13 (V)	1152	0.382		Ddg	Car>> msbxa	X	X		
12-13 (V)	1228.6	0.585		Ddg	ML bxa (car ar	X			
13-08.	1087	0.186		MLBX	MLBX			X	
13-08.	1101.5	3.790		MLBX	MLBX			X	
13-08.	1113.5	13.900		MLBX	MLBX			X	
13-08.	1152.5	0.403		MLBX	MLBX			X	
13-08.	1157.5	5.670		MLBX	MLBX			X	
13-08.	1164	14.500		MLBX	MLBX		X	X	
12-10.	472	0.016		Mw	ms			X	
12-10.	532	0.187		Mw	ML bxa			X	
12-10.	712	0.009		Mw	stms(65), ls		X		
12-10.	716	4.410		Mw	stms(65), ls		X	X	
12-10.	760	0.024		Mw	ls mic		X		
12-10.	771	13.400		Mw	Stms, ls			X	
12-10.	776	16.200		Mw	Stms, ls			X	
12-10.	780	27.300		Mw	Stms, ls		X	X	
12-10.	800	3.440		Mw	Mic		X		
12-10.	803	30.200		Mw	ML bxa		X		
12-10.	803.2	30.200		Mw	ML bxa			X	
12-10.	804.5	13.100		Mw	ML bxa			X	
11-17.	833	5.480		Mc	cong-ss			X	
11-16.	461	0.283		Mw	ms-jasp			X	
11-16.	592	14.650		Mw	ms			X	

Hole #	Footage	Ill	Mon	Ap	Jasp	POS py	OS1 py	OS2 py	LOS Qtz	LOS py	LOS Rgr	Bar	LOS CC
10-08C	891.9	X				X			X	X		X	
10-08C	896	X				X			X	X		X	
10-08C	1117.5	X				X			X	X			
10-08C	1123	X			X	X							
10-08C	1131.9	X			X	X			X				
10-08C	1156.9	X			X	X			X		X		
10-08C	1161	X			X	X			X			X	
11-03.	978.4	X				X			X			X	
11-03.	978.6	X			X	X			X			X	
11-03.	1013.5	X			X	X					X	X	
11-03.	1019.5	X				X			X				
11-03.	1023.5	X				X			X				
12-13 (V)	379	X				X		X	X	X		X	
12-13 (V)	1047.5	X				X							X
12-13 (V)	1070	X				X			X				X
12-13 (V)	1152	X			X	X							X
12-13 (V)	1228.6	X			X	X							
13-08.	1087	X				X			X	X			
13-08.	1101.5	X			X	X			X				X
13-08.	1113.5	X				X			X			X	X
13-08.	1152.5	X				X			X				
13-08.	1157.5	X				X			X	X	X		X
13-08.	1164	X			X	X			X		X	X	
12-10.	472	X				X						X	X
12-10.	532	X				X			X	X		X	
12-10.	712	X				X							X
12-10.	716	X				X							X
12-10.	760	X				X							X
12-10.	771	X			X	X			X			X	X
12-10.	776	X				X							X
12-10.	780	X			X	X						X	X
12-10.	800	X			X	X			X				
12-10.	803	X			X	X						X	X
12-10.	803.2	X			X	X			X				
12-10.	804.5	X			X	X			X			X	
11-17.	833	X			X	X						X	
11-16.	461	X				X			X			X	
11-16.	592	X			X	X			X		X	X	X

Hole #	Footage	Stp	Sph	Rut	Ka	Hal	Ox	Bx Tex
10-08C	891.9							N
10-08C	896							N
10-08C	1117.5							N
10-08C	1123							Y
10-08C	1131.9							Y
10-08C	1156.9							Y
10-08C	1161							Y
11-03.	978.4							Y
11-03.	978.6			X				Y
11-03.	1013.5		X				X	Y
11-03.	1019.5						X	Y
11-03.	1023.5							Y
12-13 (V)	379							Y
12-13 (V)	1047.5							N
12-13 (V)	1070							Y
12-13 (V)	1152							Y
12-13 (V)	1228.6							Y
13-08.	1087							Y
13-08.	1101.5						X	Y
13-08.	1113.5							Y
13-08.	1152.5							Y
13-08.	1157.5							Y
13-08.	1164		X					Y
12-10.	472							N
12-10.	532							Y
12-10.	712							Y
12-10.	716							N
12-10.	760							N
12-10.	771							N
12-10.	776							N
12-10.	780							Y
12-10.	800							Y
12-10.	803		X					Y
12-10.	803.2							Y
12-10.	804.5							Y
11-17.	833							Y
11-16.	461							Y
11-16.	592		X					N

Hole #	Footage	Au (ppm)	Ag ppm	Frm.	Host Rock	Dol	Cc	Qtz	G.C.
11-16.	595.1	0.338		Mw	ls		X	X	
11-16.	607	3.100		Mc	ss			X	X
11-16.	682	14.900	4.7	Mc	cong			X	X
11-16.	1226.5	0.165		Ddg	Dolo sulf bxa	X			
12-11.	418	0.004		Mw	mic		X		
12-11.	498	0.032		Mw	ms		X	X	
12-11.	634.9	0.076		Mw	MI bxa	X			
12-11.	1329	0.952		Ddg	dol	X			

Hole #	Footage	Ill	Mon	Ap	Jasp	POS py	OS1 py	OS2 py	LOS Qtz	LOS py	LOS Rgr	Bar	LOS CC
11-16.	595.1	X			X	X					X	X	X
11-16.	607	X				X					X	X	X
11-16.	682	X				X							X
11-16.	1226.5	X			X	X				X			
12-11.	418	X				X							X
12-11.	498	X				X			X				X
12-11.	634.9				X	X							
12-11.	1329	X			X	X						X	

Hole #	Footage	Stp	Sph	Rut	Ka	Hal	Ox	Bx Tex
11-16.	595.1							Y
11-16.	607							N
11-16.	682							N
11-16.	1226.5							Y
12-11.	418							N
12-11.	498							Y
12-11.	634.9							Y
12-11.	1329							Y

APPENDIX E

SEM DATA

Nineteen samples were analyzed using a JEOL-5600 scanning electron microscope (SEM) and semi-quantitative electron dispersive spectroscopy (EDS) analyses were collected using Link ISIS 3.2 software-INCA at the Electron Microanalysis and Imaging Laboratory at UNLV. Appendix E provides analyses results and images of processed maps shown in Appendix B.

Sample: 10-08 874 sample 1.1

Spectrum processing:

No peaks omitted

Processing option : All elements analyzed (Normalised)

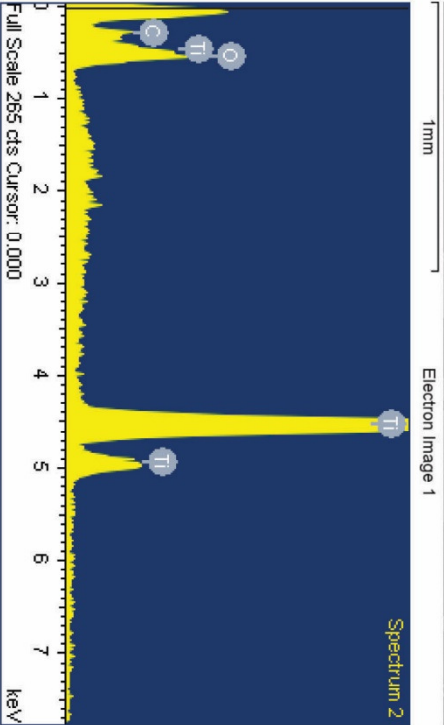
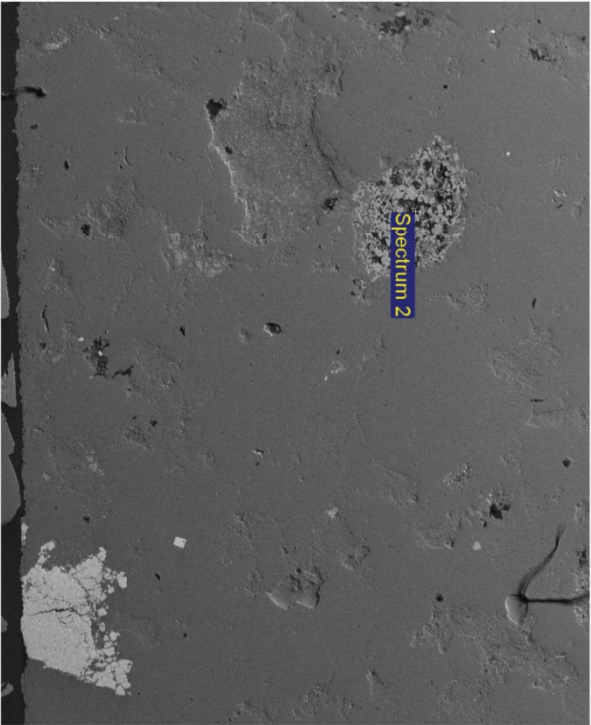
Number of iterations = 4

Standard:

C CaCO3 1-Jun-1999 12:00 AM
O SiO2 1-Jun-1999 12:00 AM
Ti Ti 1-Jun-1999 12:00 AM

Element	Weight%	Atomic%
C K	7.69	15.55
O K	37.23	56.51
Ti K	55.08	27.93
Totals	100.00	

Comment: Rutile



Project 1



Sample: 10-08 874 sample 1.2

Spectrum processing :

No peaks omitted

Processing option : All elements analyzed (Normalised)

Number of iterations = 5

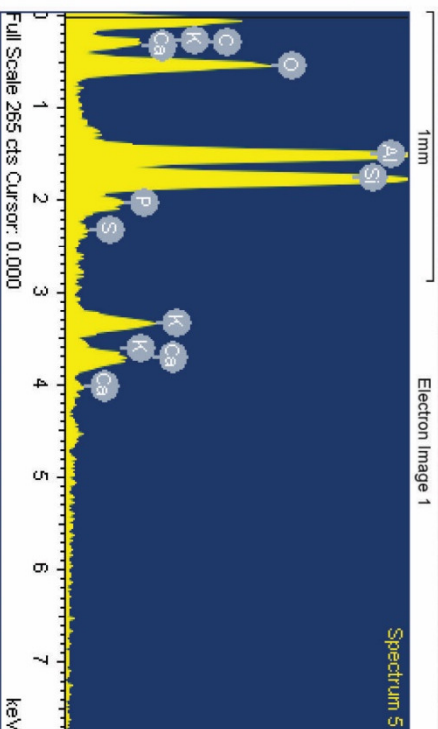
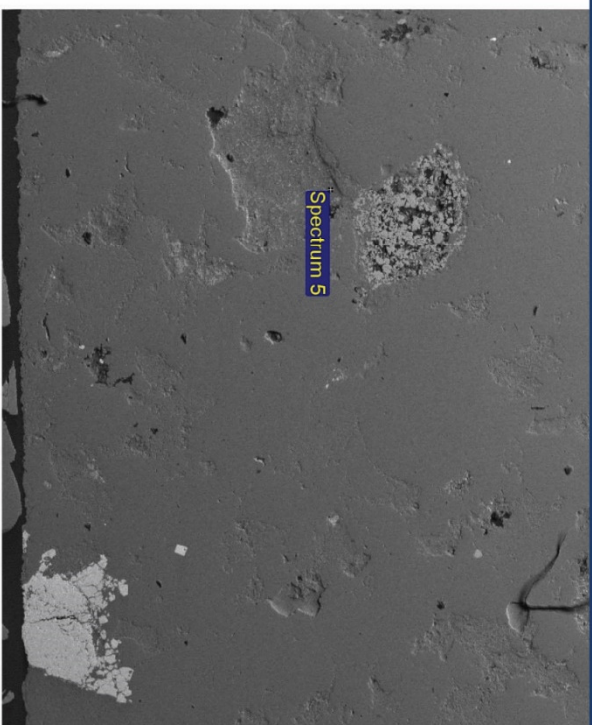
Standard :

C CaCO₃ 1-Jun-1999 12:00 AM
O SiO₂ 1-Jun-1999 12:00 AM
Al Al₂O₃ 1-Jun-1999 12:00 AM
Si SiO₂ 1-Jun-1999 12:00 AM
P Gap 1-Jun-1999 12:00 AM
S FeS₂ 1-Jun-1999 12:00 AM
K MAD-10 Feldspar 1-Jun-1999 12:00 AM
Ca Wollastonite 1-Jun-1999 12:00 AM

Element	Weight%	Atomic%
C K	34.15	47.44
O K	32.53	33.92
Al K	10.57	6.53
Si K	12.92	7.68
P K	2.03	1.09
S K	0.46	0.24
K K	4.15	1.77
Ca K	3.19	1.33

Totals 100.00

Comment: Clay, Apatite,



Project 1



Sample: 10-08 874 sample 1.3

Spectrum processing :

No peaks omitted

Processing option : All elements analyzed (Normalised)

Number of iterations = 5

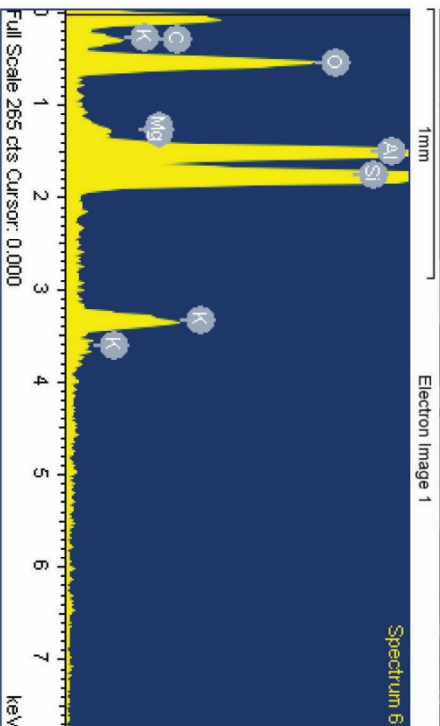
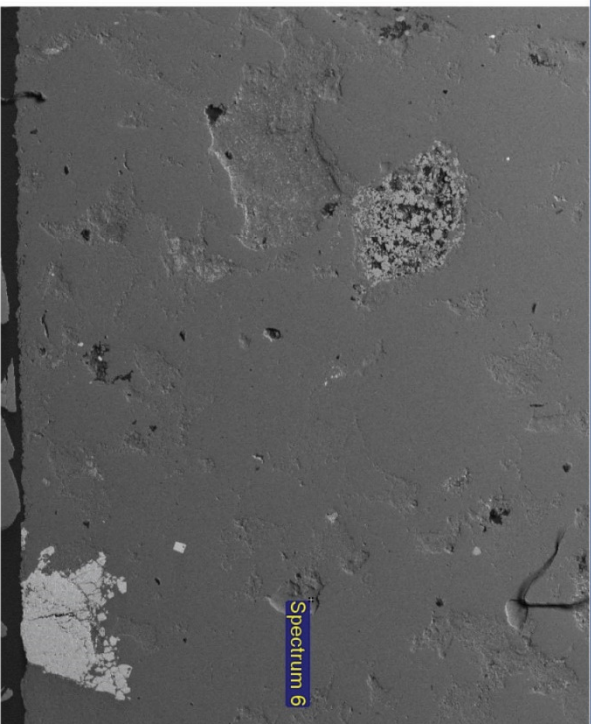
Standard :

C CaCO₃ 1-Jun-1999 12:00 AM
 O SiO₂ 1-Jun-1999 12:00 AM
 Mg MgO 1-Jun-1999 12:00 AM
 Al Al₂O₃ 1-Jun-1999 12:00 AM
 Si SiO₂ 1-Jun-1999 12:00 AM
 K MAD-10 Feldspar 1-Jun-1999 12:00 AM

Element	Weight%	Atomic%
C K	22.43	33.39
O K	37.30	41.68
Mg K	0.79	0.58
Al K	13.31	8.82
Si K	19.90	12.66
K K	6.27	2.87

Totals 100.00

Comment: Clay - Illite



Project 1



Sample: 11-04 1074.9 sample 1.1

Spectrum processing :

No peaks omitted

Processing option : All elements analyzed (Normalised)

Number of iterations = 5

Standard :

C CaCO₃ 1-Jun-1999 12:00 AM

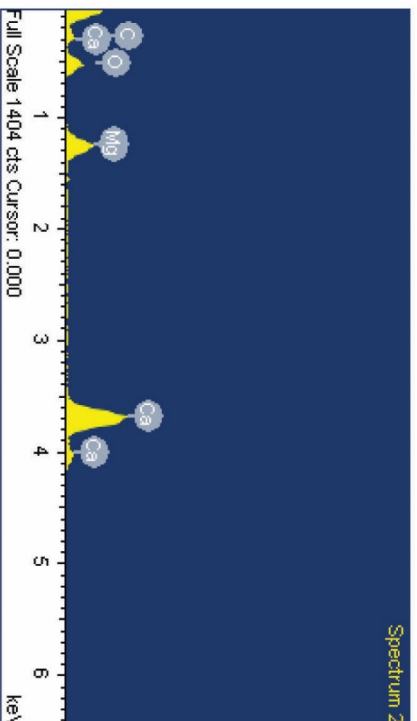
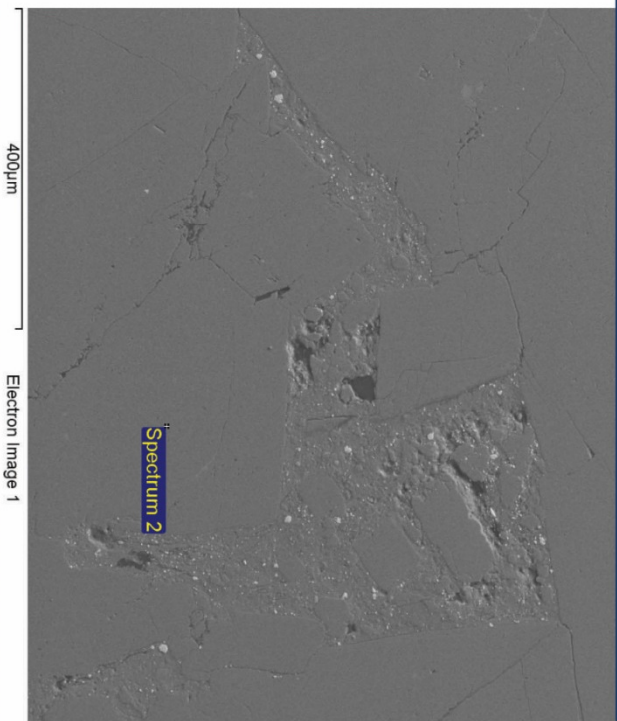
O SiO₂ 1-Jun-1999 12:00 AM

Mg MgO 1-Jun-1999 12:00 AM

Ca Wollastonite 1-Jun-1999 12:00 AM

Element	Weight%	Atomic%
C K	13.18	20.86
O K	48.29	57.38
Mg K	11.32	8.85
Ca K	27.21	12.90
Totals	100.00	

Comment: Dolomite



Project 1

Inca

Sample: 11-04 1074.9 sample 1.2

Spectrum processing :

No peaks omitted

Processing option : All elements analyzed (Normalised)

Number of iterations = 6

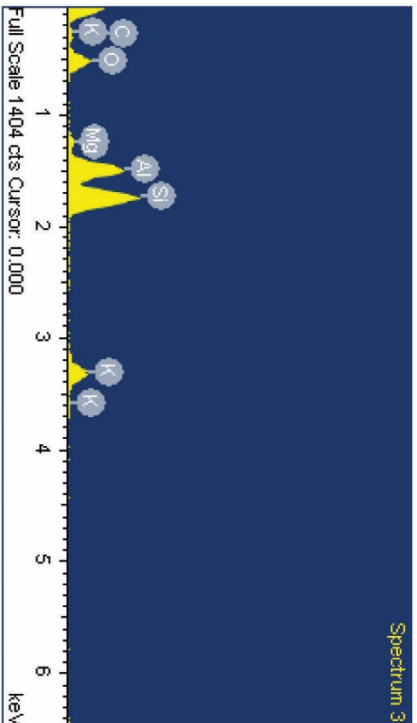
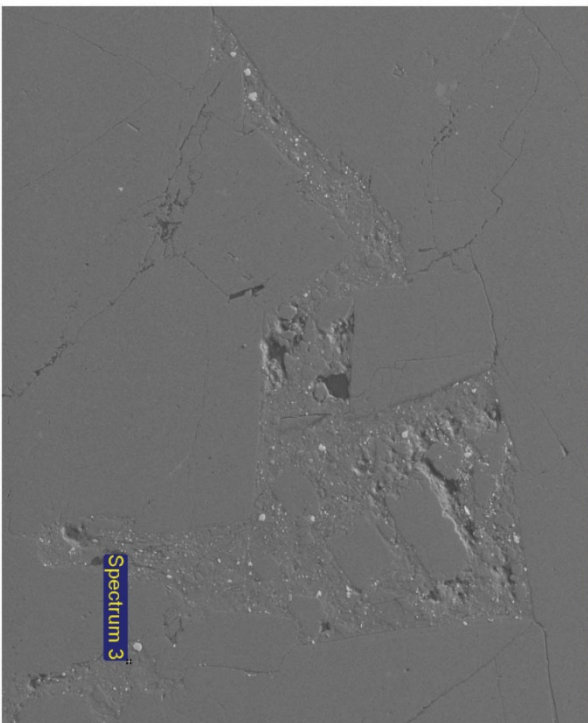
Standard :

C CaCO₃ 1-Jun-1999 12:00 AM
O SiO₂ 1-Jun-1999 12:00 AM
Mg MgO 1-Jun-1999 12:00 AM
Al Al₂O₃ 1-Jun-1999 12:00 AM
Si SiO₂ 1-Jun-1999 12:00 AM
K MAD-10 Feldspar 1-Jun-1999 12:00 AM

Element	Weight%	Atomic%
C K	28.28	40.24
O K	36.27	38.74
Mg K	1.46	1.03
Al K	11.46	7.26
Si K	16.87	10.26
K K	5.65	2.47

Totals 100.00

Comment: Clay - Illite



Project 1



Sample: 11-18 1163.4 sample 1.1

Spectrum processing :

No peaks omitted

Processing option : All elements analyzed (Normalised)

Number of iterations = 4

Standard :

C CaCO₃ 1-Jun-1999 12:00 AM

S FeS₂ 1-Jun-1999 12:00 AM

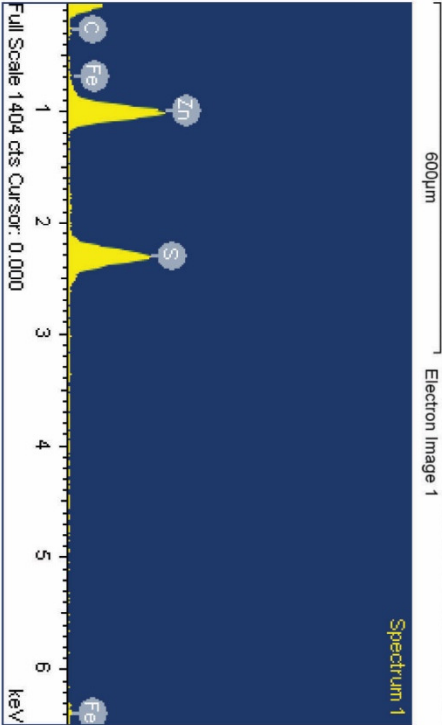
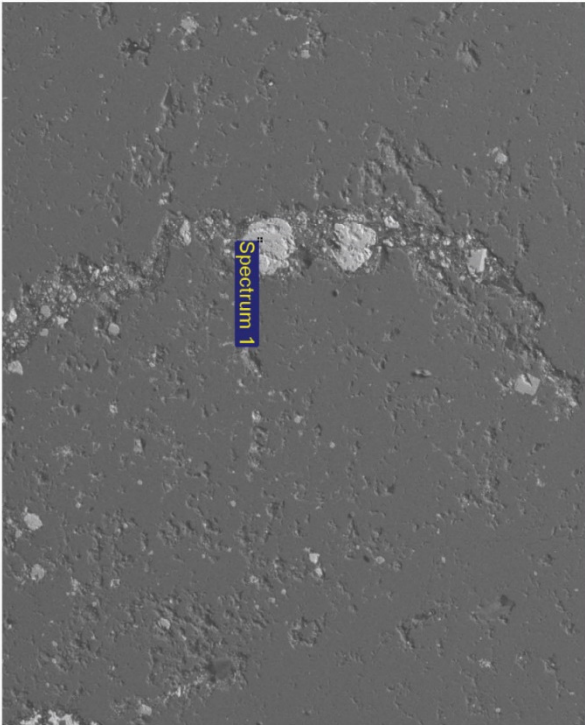
Fe Fe 1-Jun-1999 12:00 AM

Zn Zn 1-Jun-1999 12:00 AM

Element	Weight%	Atomic%
C K	23.09	54.91
S K	25.02	22.29
Fe K	1.70	0.87
Zn K	50.19	21.93

Totals 100.00

Comment: Sphalerite



Project 1



Sample: 11-18 1163.4 sample 1.2

Spectrum processing :

No peaks omitted

Processing option : All elements analyzed (Normalised)

Number of iterations = 7

Standard :

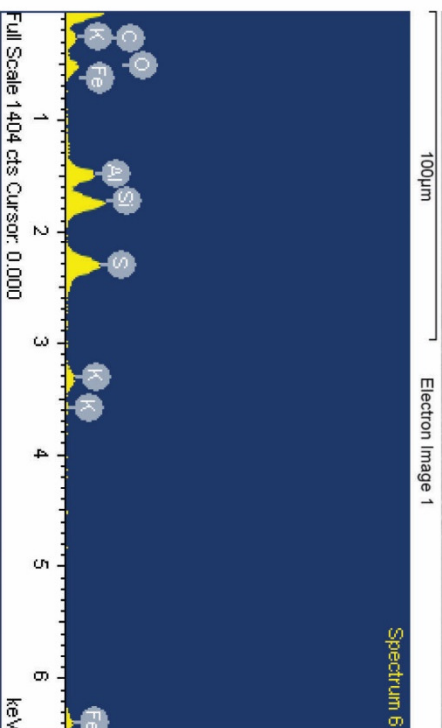
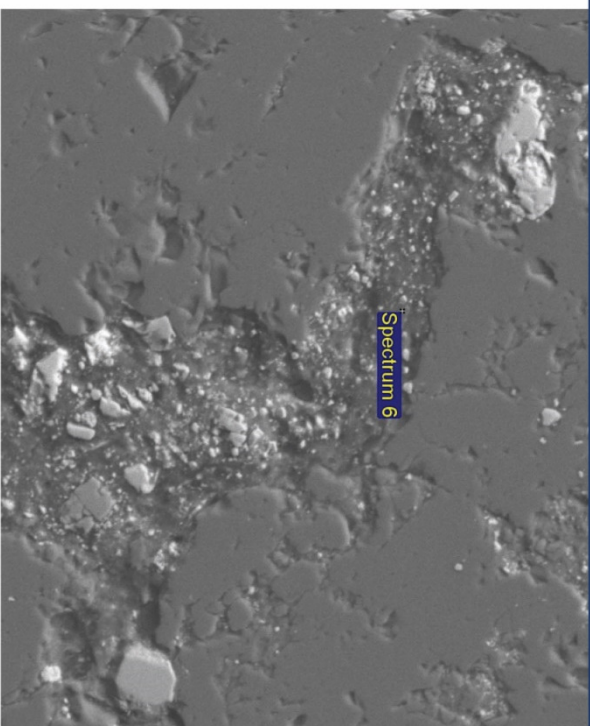
C CaCO₃ 1-Jun-1999 12:00 AM
O SiO₂ 1-Jun-1999 12:00 AM
Al Al₂O₃ 1-Jun-1999 12:00 AM
Si SiO₂ 1-Jun-1999 12:00 AM
S FeS₂ 1-Jun-1999 12:00 AM
K MAD-10 Feldspar 1-Jun-1999 12:00 AM
Fe Fe 1-Jun-1999 12:00 AM

Element	Weight%	Atomic%
---------	---------	---------

C K	43.23	58.71
O K	24.77	25.25
Al K	6.26	3.78
Si K	8.76	5.09
S K	8.66	4.41
K K	2.68	1.12
Fe K	5.66	1.65

Totals 100.00

Comment: Carbon, Clay, and minor Pyrite



Project 1



Sample: 11-18 1163.4 sample 1.3

Spectrum processing :

No peaks omitted

Processing option : All elements analyzed (Normalised)

Number of iterations = 4

Standard :

O SiO2 1-Jun-1999 12:00 AM

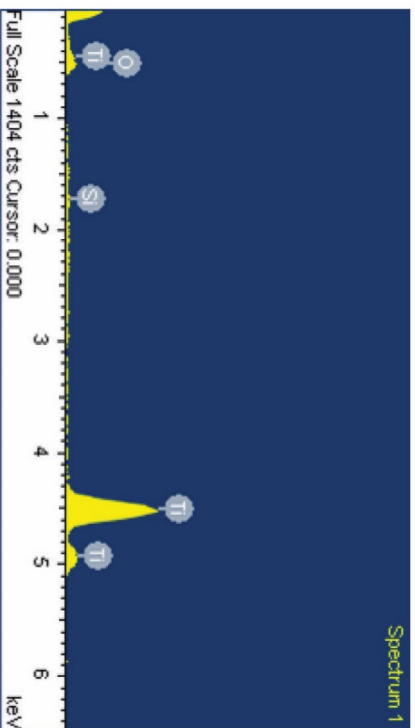
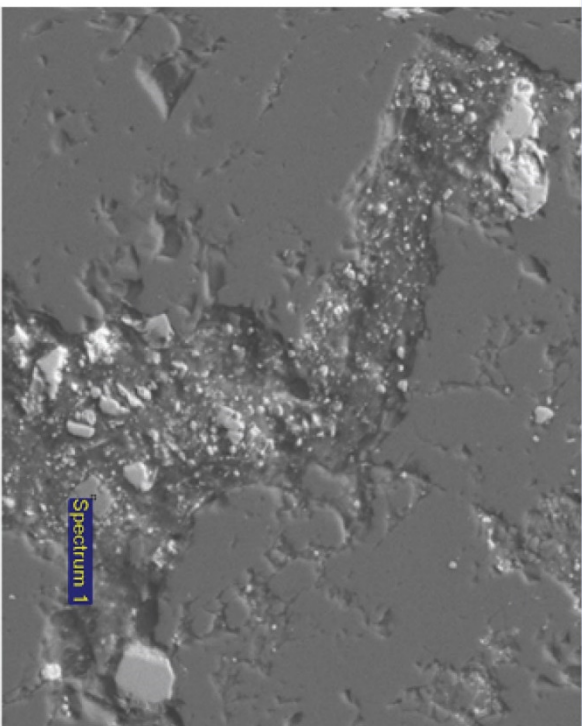
Si SiO2 1-Jun-1999 12:00 AM

Ti Ti 1-Jun-1999 12:00 AM

Element	Weight%	Atomic%
OK	42.43	68.60
Si K	0.84	0.77
Ti K	56.72	30.63

Totals 100.00

Comment: Rutile



Project 1



Sample: 12-01 987 sample 1.1

Spectrum processing :

No peaks omitted

Processing option : All elements analyzed (Normalised)

Number of iterations = 4

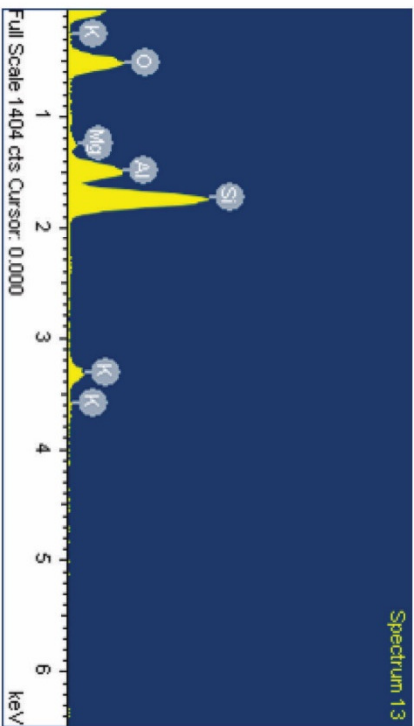
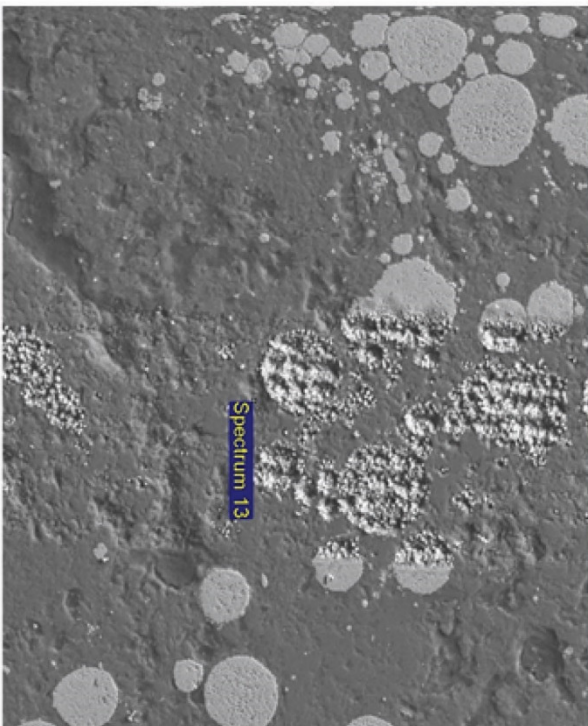
Standard :

O SiO2 1-Jun-1999 12:00 AM
Mg MgO 1-Jun-1999 12:00 AM
Al Al2O3 1-Jun-1999 12:00 AM
Si SiO2 1-Jun-1999 12:00 AM
K MAD-10 Feldspar 1-Jun-1999 12:00 AM

Element	Weight%	Atomic%
OK	52.52	66.27
Mg K	1.13	0.94
Al K	10.75	8.05
Si K	31.41	22.58
K K	4.19	2.16

Totals 100.00

Comment: Clay



Project 1



Sample: 13-08 1164 sample 1.1

Spectrum processing :

Peak possibly omitted : 4.515 keV

Processing option : All elements analyzed (Normalised)

Number of iterations = 5

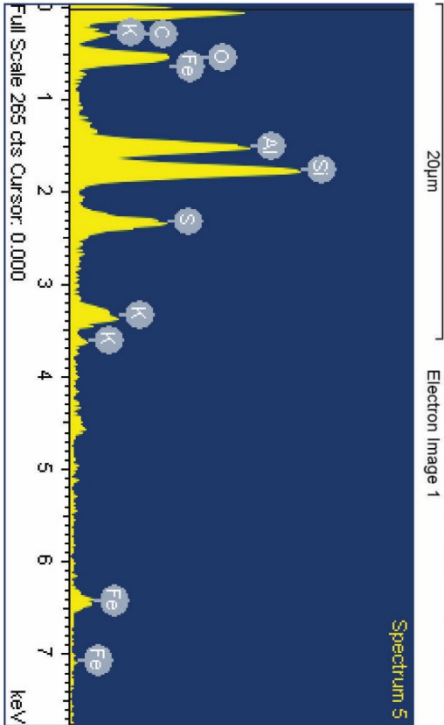
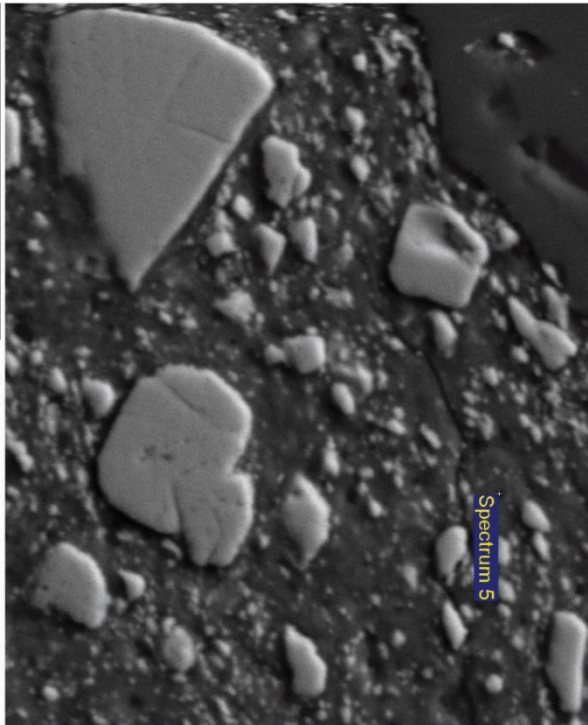
Standard :

C CaCO3 1-Jun-1999 12:00 AM
O SiO2 1-Jun-1999 12:00 AM
Al Al2O3 1-Jun-1999 12:00 AM
Si SiO2 1-Jun-1999 12:00 AM
S FeS2 1-Jun-1999 12:00 AM
K MAD-10 Feldspar 1-Jun-1999 12:00 AM
Fe Fe 1-Jun-1999 12:00 AM

Element	Weight%	Atomic%
C K	24.80	38.35
O K	30.71	35.66
Al K	10.10	6.95
Si K	15.72	10.40
S K	7.26	4.21
K K	4.54	2.15
Fe K	6.87	2.29

Totals 100.00

Comment: Clay and minor Pyrite



Project 1



Sample: 13-08 1164 sample 1.2

Spectrum processing :

No peaks omitted

Processing option : All elements analyzed (Normalised)

Number of iterations = 4

Standard :

C CaCO₃ 1-Jun-1999 12:00 AM

S FeS₂ 1-Jun-1999 12:00 AM

Zn Zn 1-Jun-1999 12:00 AM

Element	Weight%	Atomic%
---------	---------	---------

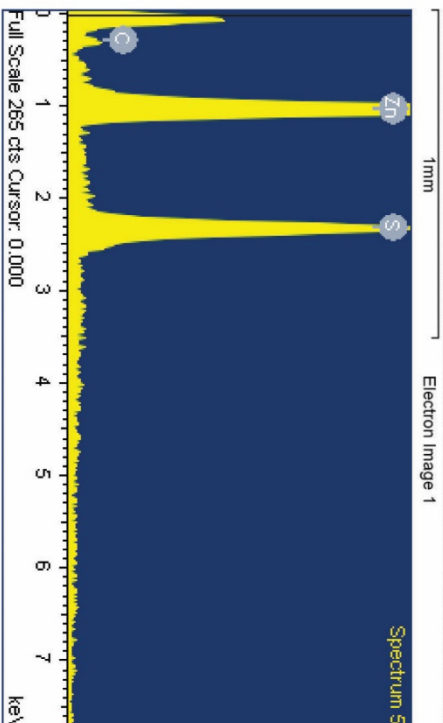
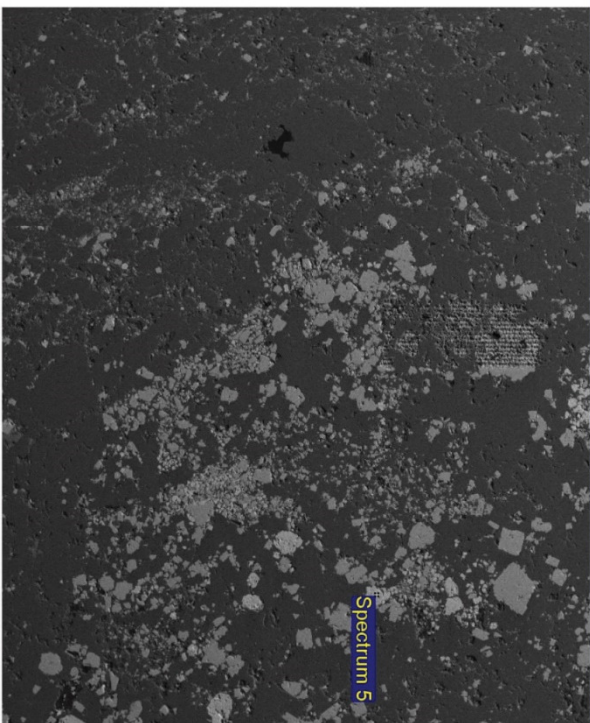
CK	22.73	54.61
----	-------	-------

SK	24.60	22.14
----	-------	-------

ZnK	52.67	23.25
-----	-------	-------

Totals	100.00	
--------	--------	--

Comment: Sphalerite



APPENDIX F

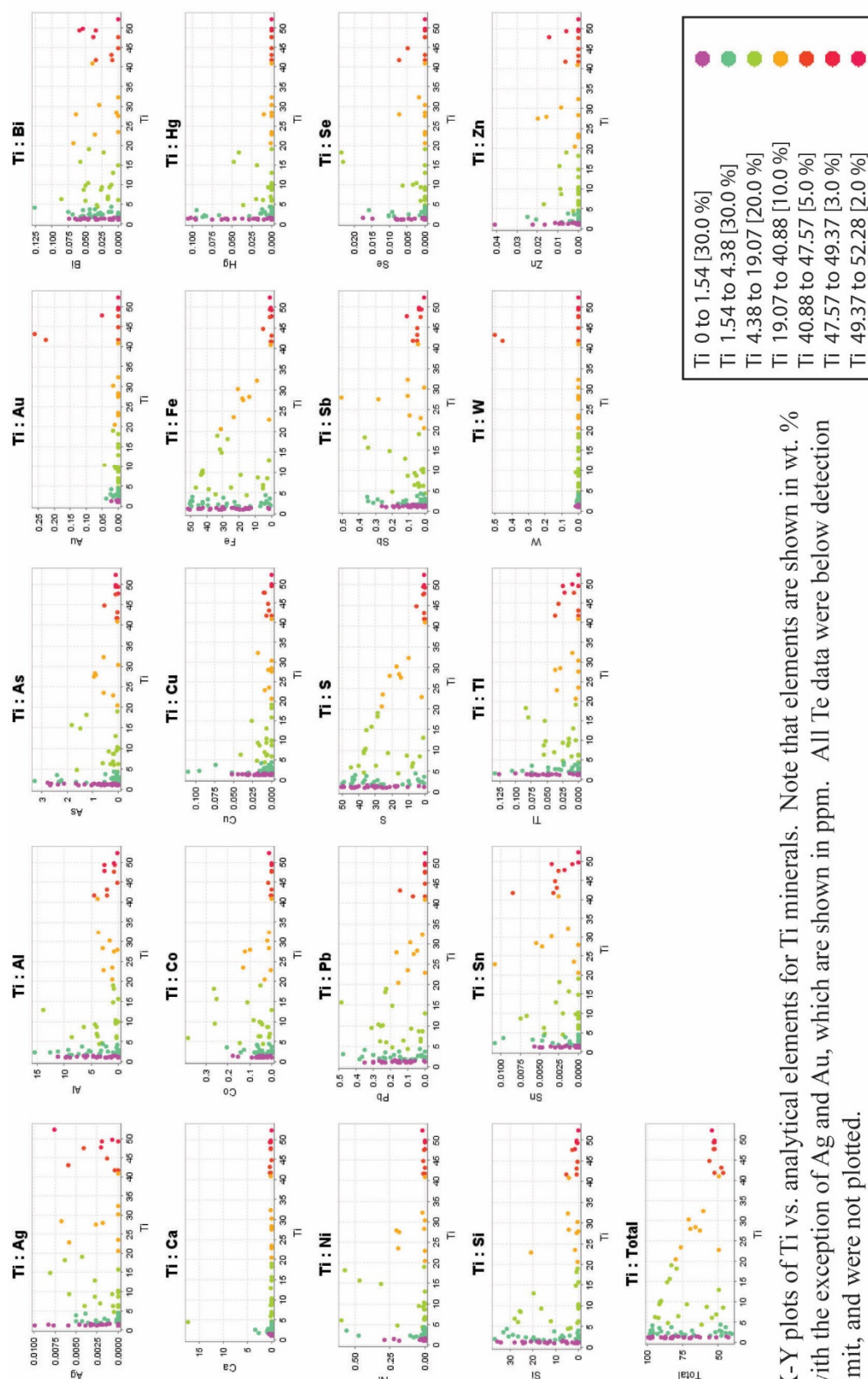
EPMA DATA

Nineteen samples were analyzed to quantify pyrite trace element data using a JEOL-8900 Electron Probe Microanalyzer (EPMA) at the University of Nevada, Las Vegas at the Electron Microanalysis and Imaging Laboratory (EMiL). The elements Ag, Al, As, Au, Bi, Ca, Co, Cu, Fe, Hg, Mo, Ni, Pb, S, Sb, Se, Si, Sn, Te, Ti, Tl, W, and Zn were measured. Trace elements were analyzed along line transects across primarily pyrite, with fewer analyses on stephanite, sphalerite, and rutile. Line transects are discussed in the Methods section of the thesis. The EPMA point name generally consists of the line # (ie. Line 2), the drill hole # (ie 11-04), the footage (ie. 1003), the area within the polished section (ie. A1), mineral analyzed and point number (ie. py1), and line transect # (ie Linetr1), yielding Line 2 11-04 1003 A1py1Linetr1. Some analysis names do not include the drill hole number in the name. Analysis point names of 987, 1026, or 992 are on samples from drill hole 12-01A, and analysis 803 is on a sample from drill hole 12-10.

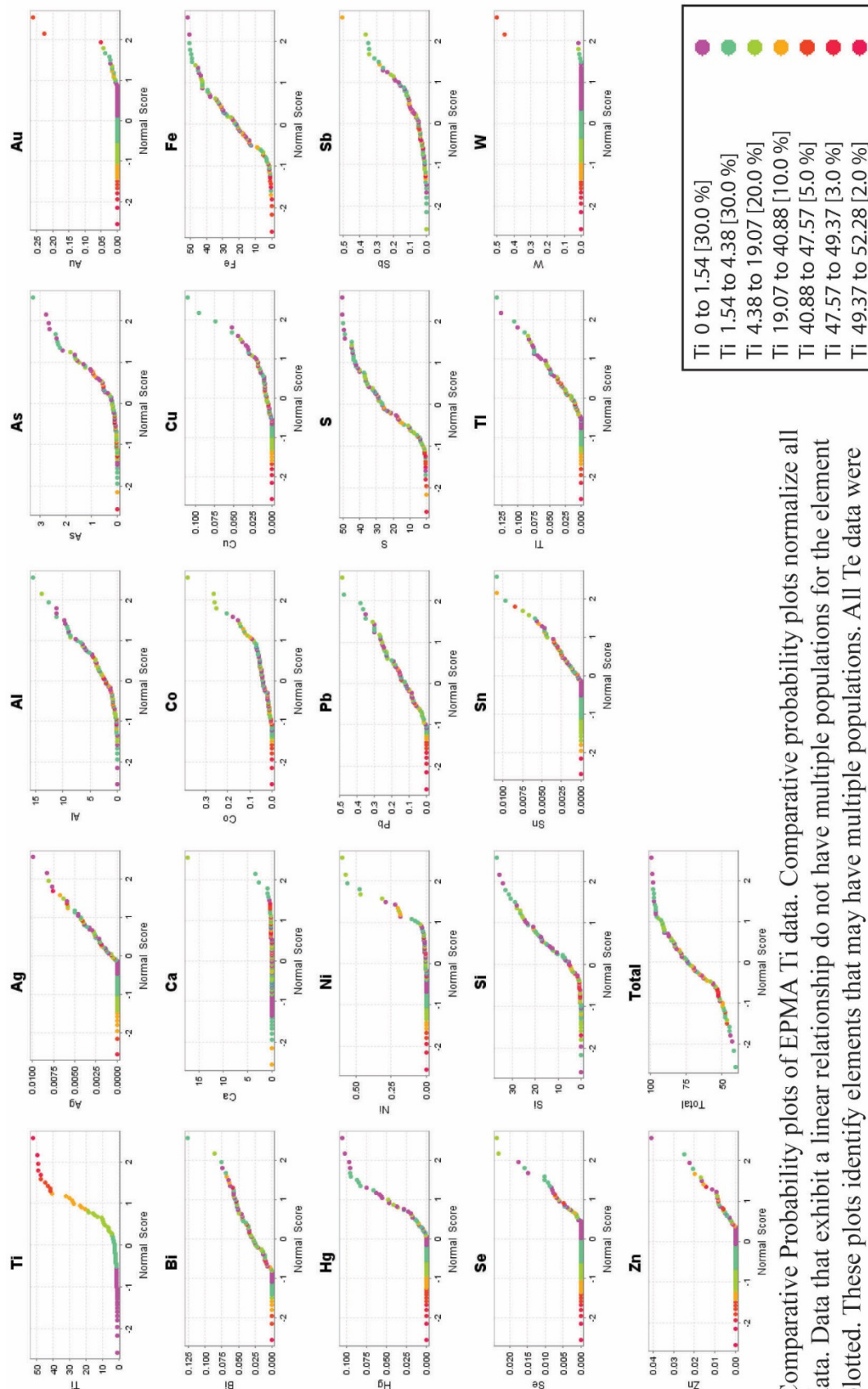
Several appendices provide data related to the EPMA results. Appendix F.1 provides EPMA Ti mineral data graphs. Appendix F.2 provides EPMA Zn mineral data graphs. Appendix F.3 provides the Catell's Scree Test for the EPMA pyrite data principle component analysis. Appendix F.4 provides EPMA POS pyrite data graphs and the Catell's Scree Test for the principle component analysis. Appendix F.5 provides EPMA OS 1 pyrite data graphs and the Catell's Scree Test for the principle component analysis. Appendix F.6 provides EPMA OS 2 pyrite data graphs and the Catell's Scree Test for the principle component analysis. Appendix F.7 provides EPMA gold points detected on

each pyrite type data graphs. Appendix F.8 provides EPMA LOS pyrite data graphs and the Catell's Scree Test for the principle component analysis. Appendix F.9 provides EPMA Stephanite maps, data graphs, and stephanite EPMA data table. Appendix F.10 EPMA data table is provided as a digital attachment.

Appendix F.1: EPMA Ti mineral maps and data plots

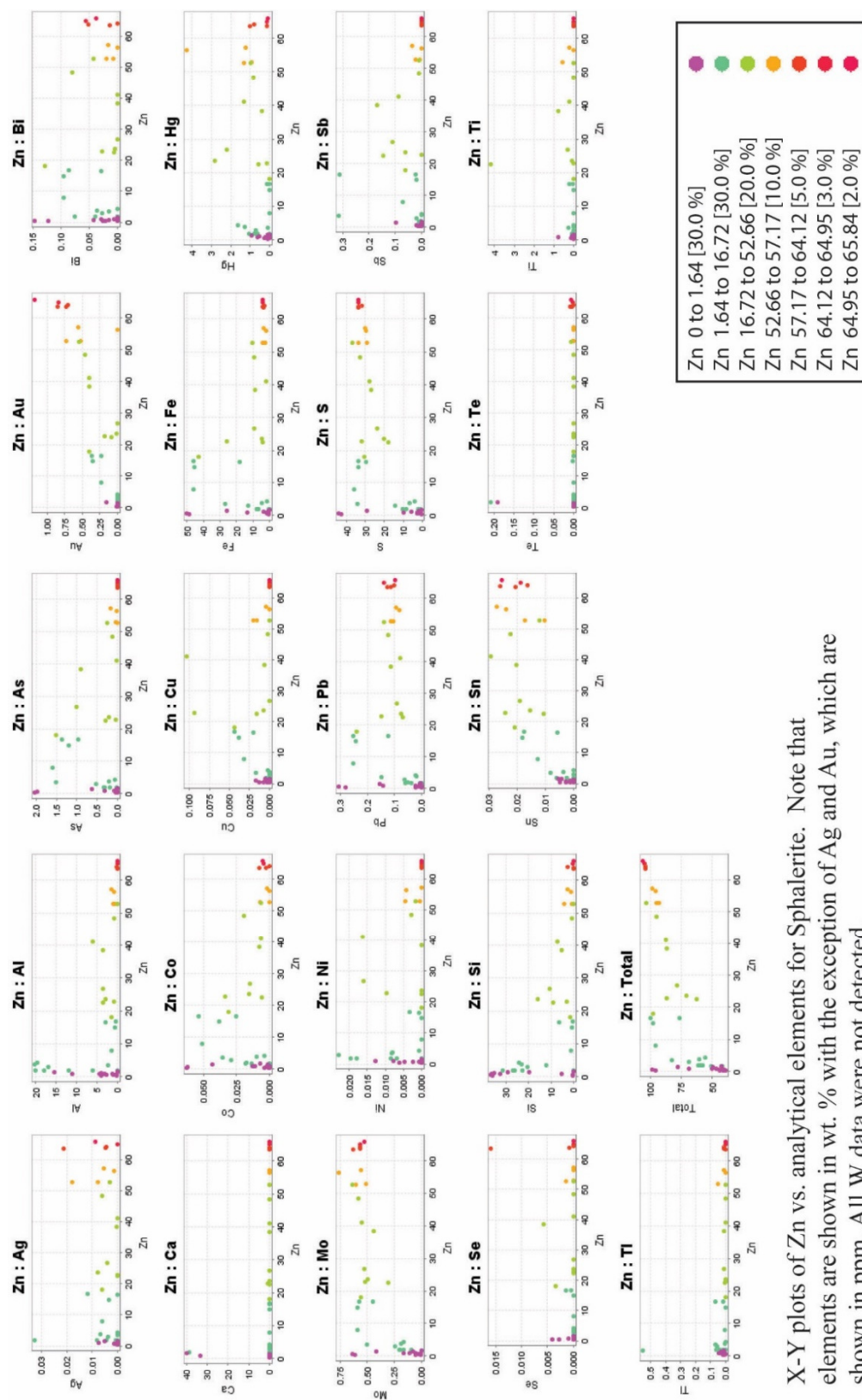


X-Y plots of Ti vs. analytical elements for Ti minerals. Note that elements are shown in wt. % with the exception of Ag and Au, which are shown in ppm. All Te data were below detection limit, and were not plotted.

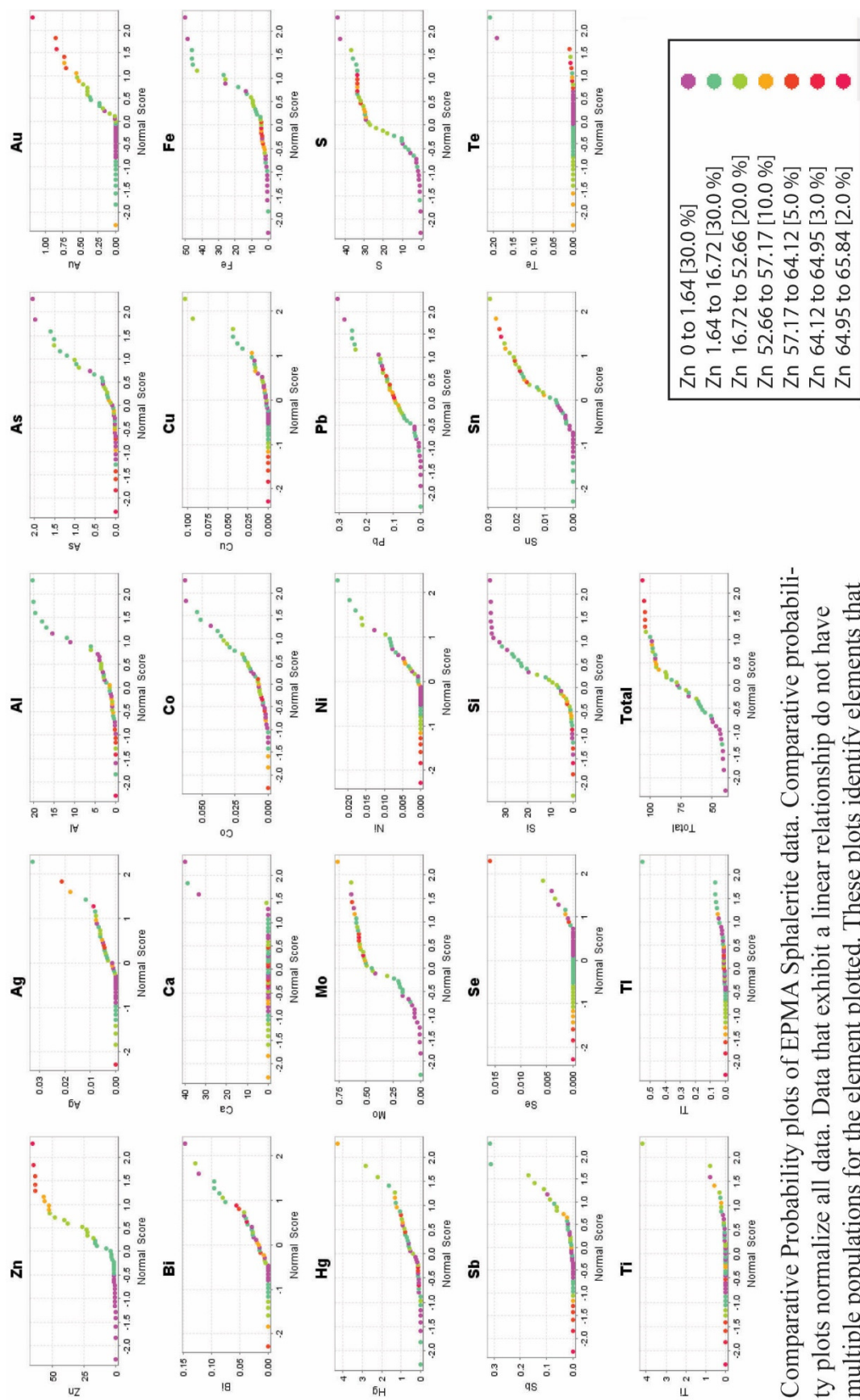


Comparative Probability plots of EPMA Ti data. Comparative probability plots normalize all data. Data that exhibit a linear relationship do not have multiple populations for the element plotted. These plots identify elements that may have multiple populations. All Te data were below detection limit, and were not plotted.

Appendix F.5: EPMA Zn mineral maps and data plots



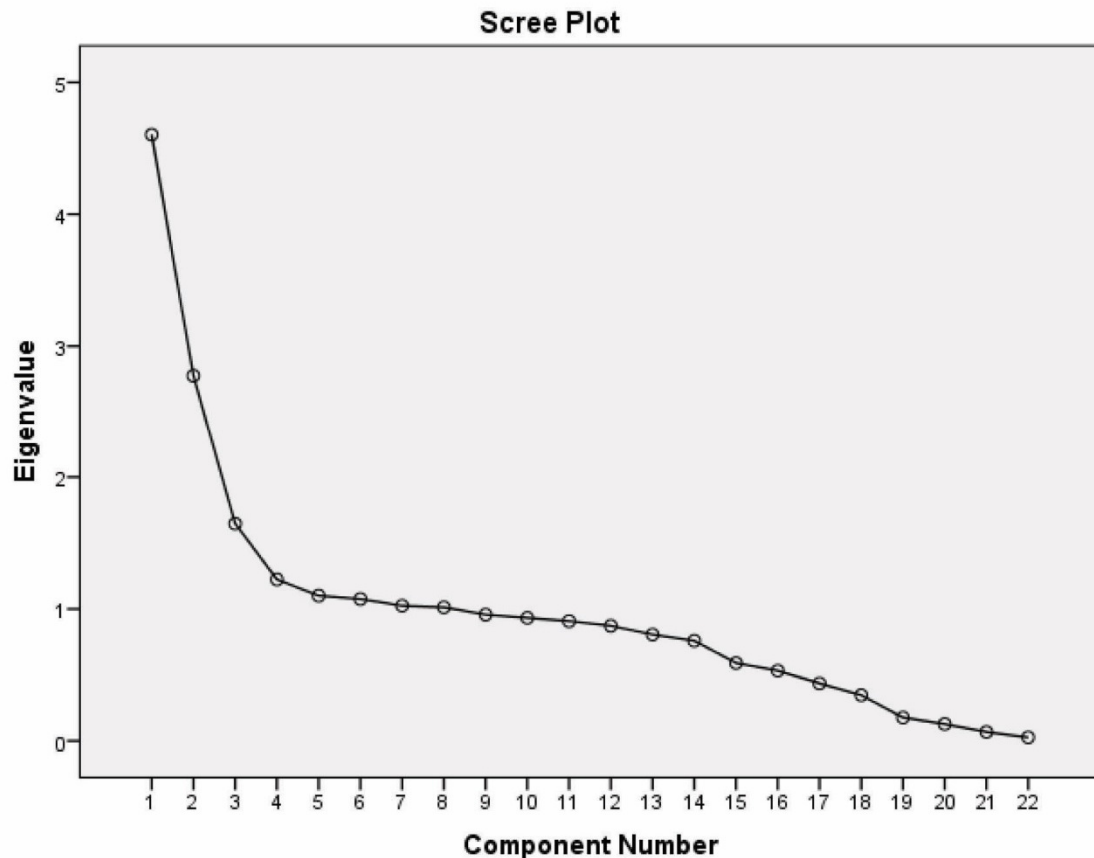
X-Y plots of Zn vs. analytical elements for Sphalerite. Note that elements are shown in wt. % with the exception of Ag and Au, which are shown in ppm. All W data were not detected.



Comparative Probability plots of EPMA Sphalerite data. Comparative probability plots normalize all data. Data that exhibit a linear relationship do not have multiple populations for the element plotted. These plots identify elements that may have multiple populations. All W data were not detected.

Appendix F.3: EPMA pyrite data Catell's Scree Test

Component	1	2	3	4	5	6	7	8
Total	4.604	2.776	1.647	1.224	1.100	1.075	1.024	1.012
Variance %	20.927	12.617	7.487	5.563	5.002	4.888	4.655	4.602
Cumulative %	20.927	33.544	41.031	46.595	51.597	56.485	61.140	65.742



The Catell's Scree Test for EPMA pyrite data involves plotting each of the initial eigenvalues ('Total') of the components. Components retained are above the "elbow" or where the curve changes direction and becomes flat. Components above the "elbow", "contribute the most to the explanation of the variance in the data set" (Pallent, 2007).

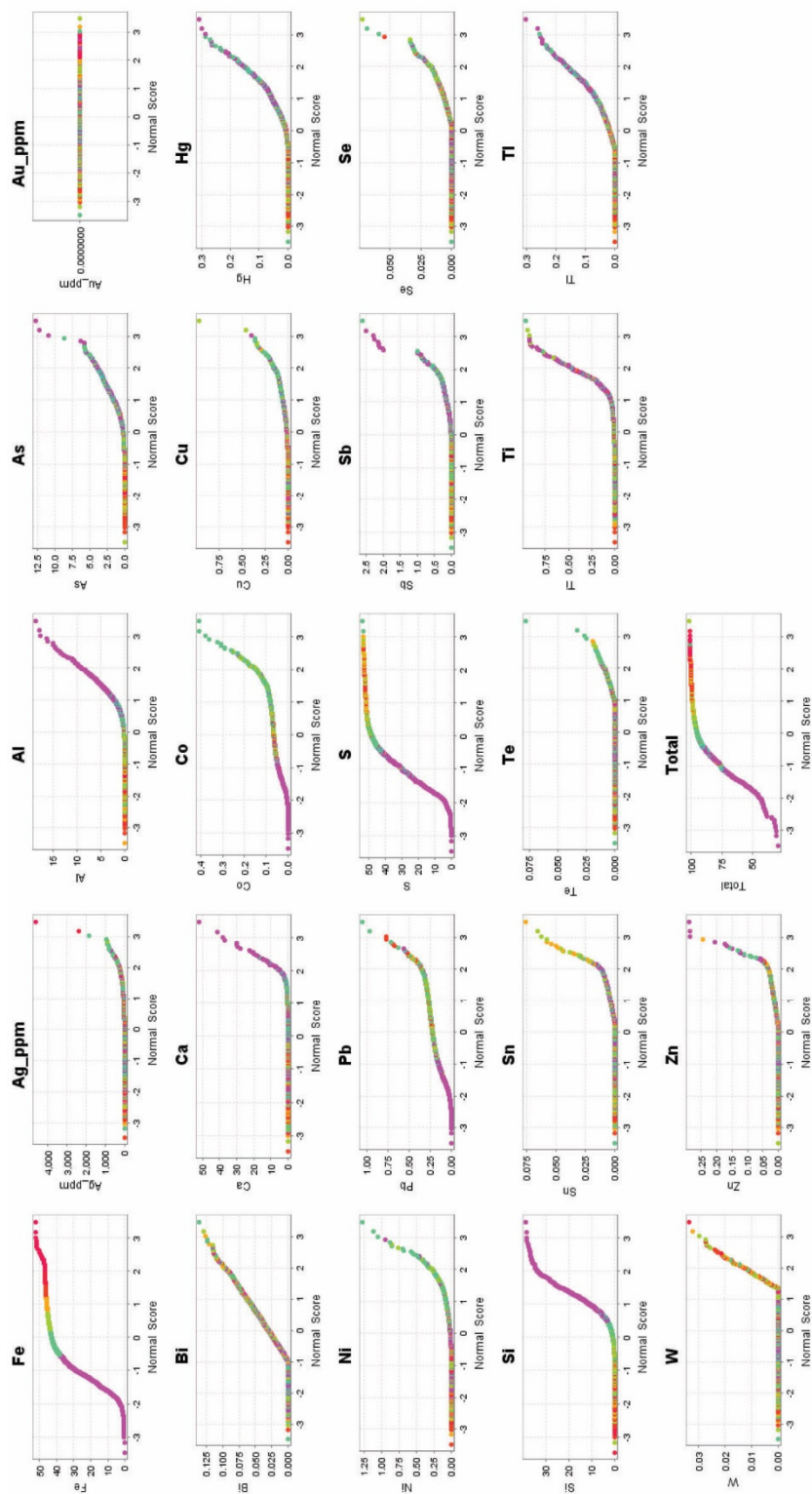
Appendix F.4: EPMA POS pyrite data plots

Comparative Normal Probability Plot for POS pyrites

A comparative normal probability plot of data points of all POS pyrites and OS 2 rims with no detectable gold collected along lines from host rocks through pyrite, assesses whether or not a data set departs from a normal distribution; illustrated by a straight line, and contains discrete populations within the data set, identified by changes in line slope for each element. The plots further indicate the weight percent at which the change in population occurs. A change of slope indicate if an element is being distributed differently from a normal distribution in a sample set or, for example, slope changes may indicate if an element is being distributed into different pyrite types. Since EPMA analytical line transects across host rock minerals, mineral boundaries, and POS pyrites, slope changes should be apparent and identify the two analyzed populations of POS pyrite and host rock. The POS pyrite comparative probability plot is shown in (Appendix F.4). Plots (Appendix F.4) for Fe, S, Si, and Al exhibit an S-shaped distribution, indicating the two populations that represent analyses of pyrite (red to green data points) and host rock (purple to green data points). Slope changes distinct from the S-shape could indicate additional analyzed populations within the POS pyrites.

Analytical results indicate multiple populations of POS pyrite, host rocks, a mixed phase of both pyrite and host rock, OS rims without detectable Au, and POS pyrites that have been partially oxidized. Comparative probability plots for each element are described and interpreted from left to right. Note how the color order of Fe and S is similar and how it's the inverse of color for Si, Al, and Ca. Iron slope changes represent the change from host rock to host rock/pyrite grain boundary to POS pyrite to partially

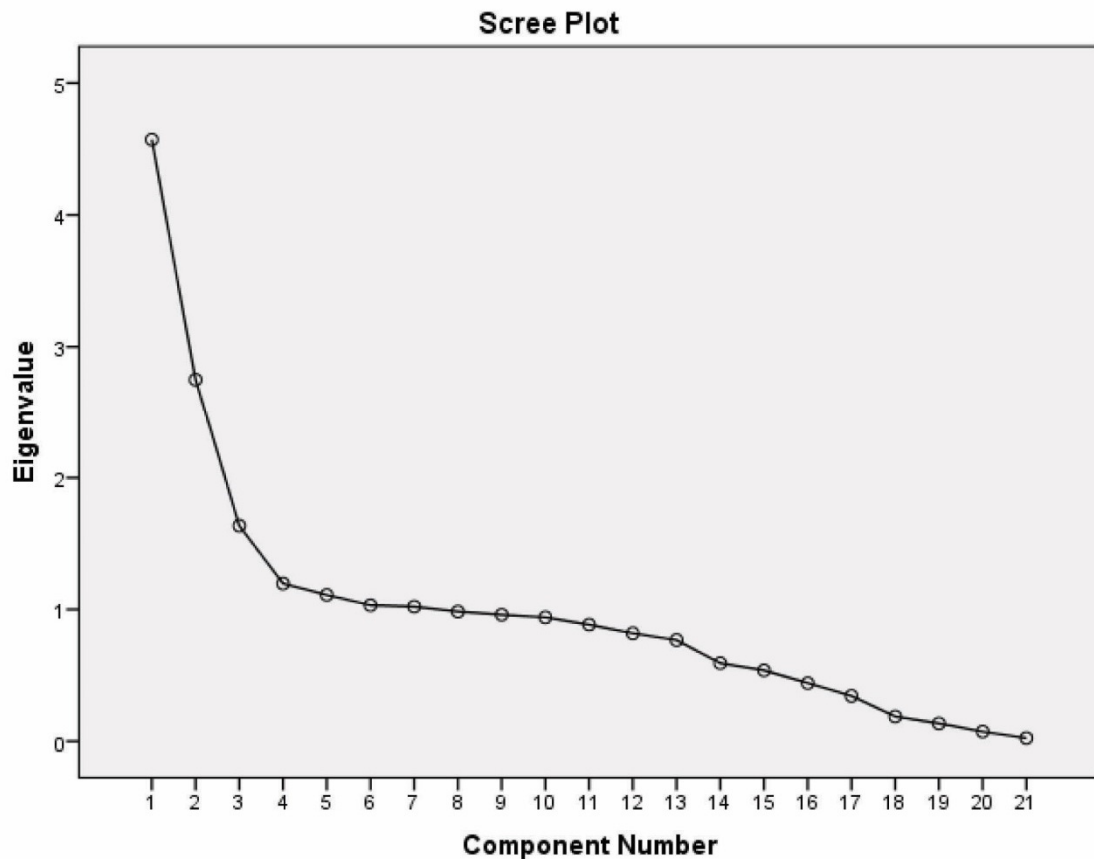
oxidized POS pyrites. Sulfur slope changes represent the change from host rock to host rock/pyrite grain boundary to POS pyrite. Silica and Al slope changes represent the change from POS pyrite to host rock/pyrite grain boundary to host rock. Calcium slope change represents change from POS pyrite to host rock. Cobalt slope changes represent the change from host rock to host rock/pyrite grain boundary to POS pyrite to POS pyrites elevated in Co which seem to be between 38.17 to 45.50 wt. % Fe (Appendix F.4). Lead slope changes represent the change from host rock to host rock/pyrite grain boundary to POS pyrite to POS pyrites elevated in Pb. Nickel slope changes are more difficult to interpret, and may represent host rock to POS pyrite to POS pyrites elevated in Ni which seem to be between 38.17 to 45.50 wt. % Fe (Appendix F.4). Carlin pathfinder elements As, Cu, Hg, Sb, and Tl have 3 to 4 slope changes. The slope change for As represents POS pyrite to OS rim with no detectable Au to other As phases, such as realgar. The first and second slope changes for Cu, Hg, Sb, and Tl represents not detected to detectable Cu, Hg, Sb, and Tl in POS or host rock to elevated Cu, Hg, Sb, and Tl in OS rims with no detectable Au. The other slope changes (3rd or 4th) for Cu, Hg, Sb, and Tl may represent other mineral phases or may still be OS rim with no detectable gold. Note that As, Hg, Sb, and Tl are generally elevated in the OS rim between 0- 43.92 wt. % Fe indicated by purple and teal dots. Copper is elevated between 38.17 to 45.50 wt. %, Fe and it is more difficult to distinguish if Cu is actually elevated in the OS rims or in POS pyrites. Silver and Sn slope changes appear to represent not detectable Ag and Sn to detectable Ag and Sn to elevated Ag and Sn. Silver is elevated between 38.17 to 47.05 wt. % and Sn is elevated between 43.92 to 46.22 wt. % Fe. Bismuth exhibits a normal distribution, unrelated to mineral populations.



Comparative Probability plots of EPMA POS pyrite data. Comparative probability plots normalize all data. Data that exhibit a linear relationship do not have multiple populations for the element plotted. These plots identify elements that may have multiple populations.

Principle Components Analysis POS Pyrites

Component	1	2	3	4	5	6	7
Total	4.571	2.751	1.635	1.196	1.110	1.032	1.022
Variance	21.768	13.098	7.788	5.698	5.284	4.914	4.864
Cumulative %	21.768	34.866	42.654	48.351	53.636	58.550	63.414



The Catell's Scree Test for POS pyrites involves plotting each of the initial eigenvalues ('Total') of the components. Components retained are above the "elbow" or where the curve changes direction and becomes flat. Components above the "elbow", "contribute the most to the explanation of the variance in the data set" (Pallent, 2007).

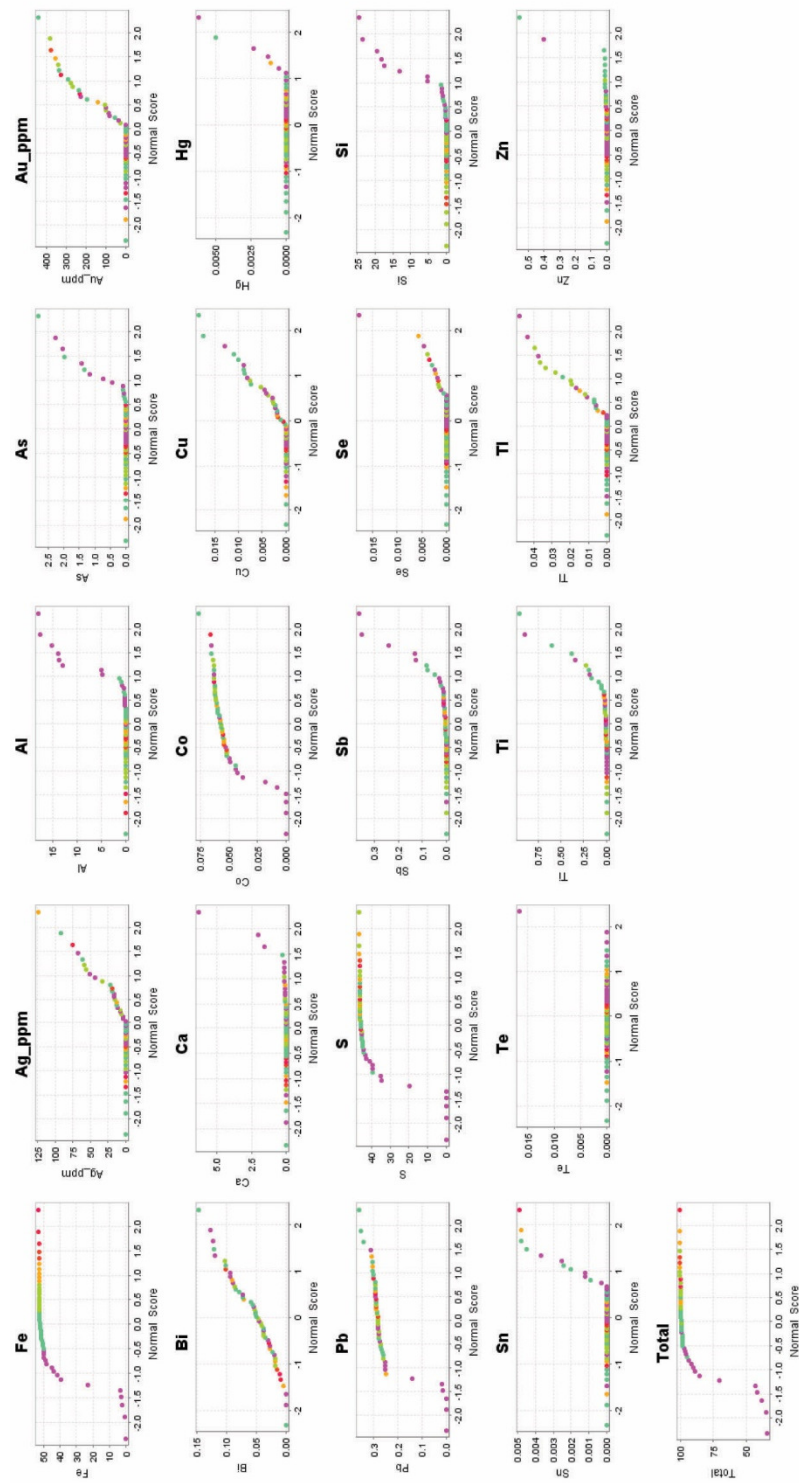
Appendix F.5: EPMA OS 1 pyrite data plots

Comparative Normal Probability Plots of Ore-stage 1 Pyrites

A comparative normal probability plot compares the distribution of the data set being evaluated against a normally distributed data set, illustrated by a straight line, or reveals the presence of discrete populations within the data set by exhibiting changes in line slope. The comparative normal probability plot of EPMA data for all OS 1 pyrites collected along lines from dacite across pyrite (Appendix F.5). Since EPMA analytical lines cross host rock minerals, grain boundaries, and OS 1 pyrites, slope changes should be apparent analyses of different minerals. Changes in slope are marked by black lines, but due to the small number of data points, there may be fewer slope changes than indicated. Plots for Fe, S, Si, and Al exhibit an S-shaped distribution, indicating the two populations present represent OS 1 pyrite and host rock.

Analytical results indicate multiple populations that include OS 1 pyrite, host rocks, and a mix of both pyrite and host rock. The comparative probability plots of all OS 1 pyrite data and slope changes (Appendix F.5) are a response to a change in minerals analyzed, and are described and interpreted from left to right. Note that the color order of Fe and S data points is similar and that it's the inverse of the color order for Si, Al, and Ca. Iron and S slope changes represent the change in analysis of host rock to host rock/pyrite crystal boundary to OS 1 pyrite. Silicon and Al slope changes represent mineralogy changes from OS 1 pyrite to host rock/pyrite crystal boundary to host rock. The Ca slope change represents a change from analysis of OS 1 pyrite to host rock. Cobalt and Pb slope changes represent the change from host rock to host rock/pyrite grain boundary to OS 1 pyrite. Gold may not have as many slope changes as suggested

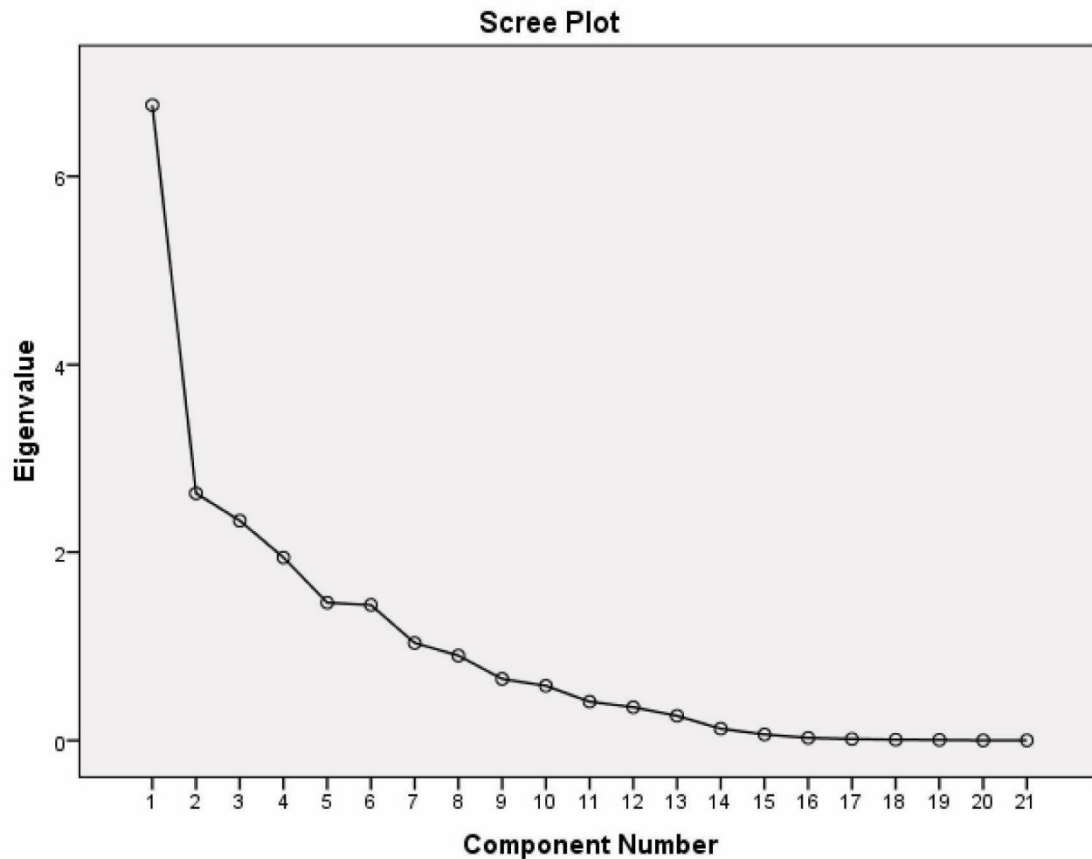
(Appendix F.5); however, the first slope change represents the change from undetected to detectable gold. Plots of Carlin pathfinder elements As, Hg, Sb, and Tl exhibit 1 to 2 slope changes each. The slope changes represent a change from undetected to detectable and elevated trace elements in OS 2 rims around OS 1 pyrites.



Comparative Probability plots of EPMA OS 1 pyrite data. Comparative probability plots normalize all data. Data that exhibit a linear relationship do not have multiple populations for the element plotted. These plots identify elements that may have multiple populations. All Ni and W data are below detection limit, and are not plotted.

Principle Components Analysis OS 1 Pyrites

Component	1	2	3	4	5	6	7
Total	6.756	2.624	2.333	1.942	1.463	1.438	1.035
Variance %	32.173	12.496	11.110	9.247	6.965	6.850	4.931
Cumulative %	32.173	44.669	55.779	65.026	71.991	78.841	83.771



The Catell's Scree Test for OS 1 pyrites involves plotting each of the initial eigenvalues ('Total') of the components. Components retained are above the "elbow" or where the curve changes direction and becomes flat. Components above the "elbow", "contribute the most to the explanation of the variance in the data set" (Pallent, 2007).

Appendix F.6: EPMA OS 2 pyrite data plots

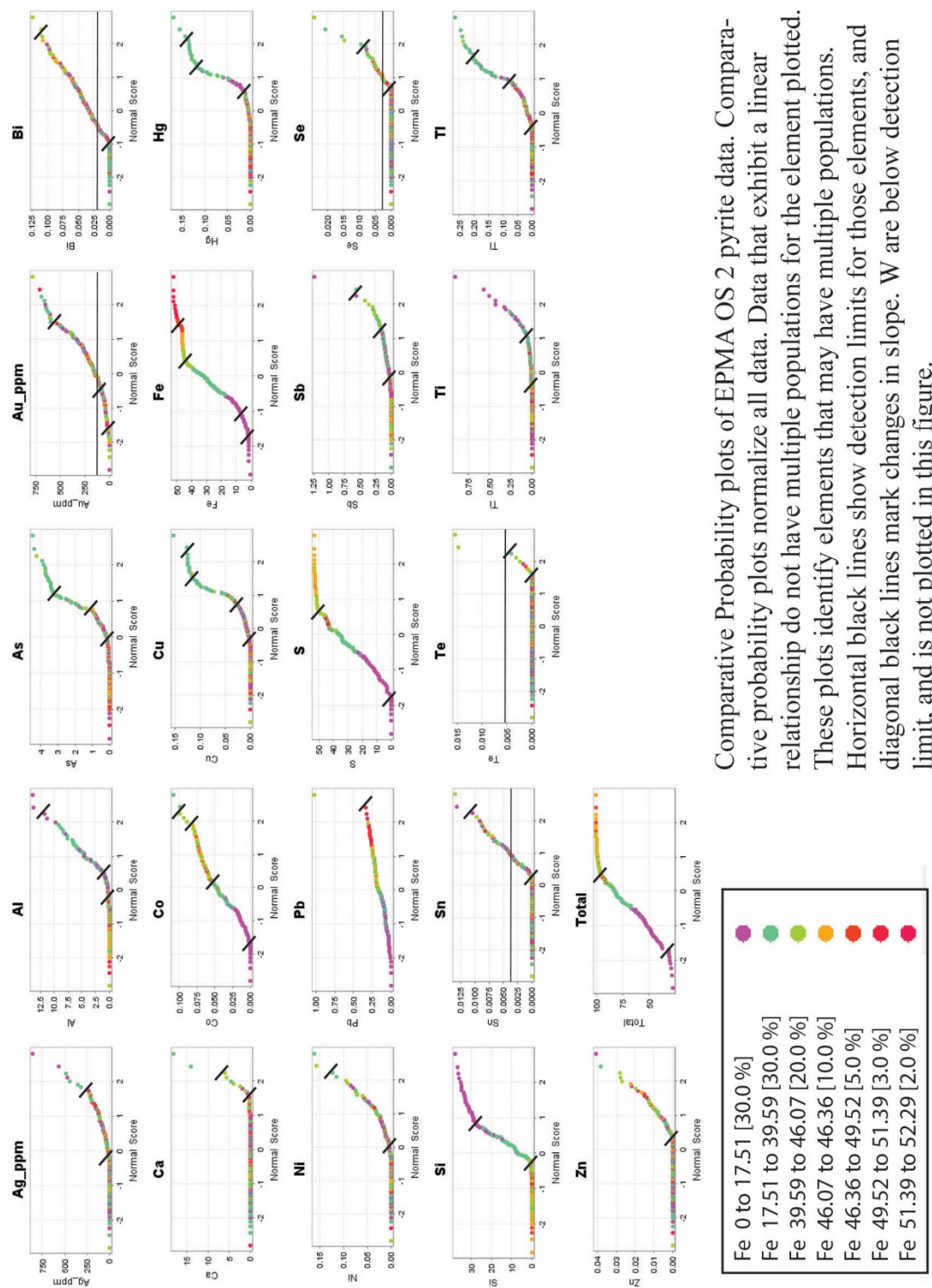
Comparative Probability Plots of Ore-Stage 2 Pyrite

A comparative normal probability plot compares the distribution of the data set being evaluated against a normally distributed data set. A comparative normal probability plot, assesses whether or not a data set departs from a normal distribution, illustrated by straight line, or contains discrete populations within the data set, identified by changes in line slope. The plots further indicate the weight percent at which the change in population occurs. A change of slope indicates an element is being distributed differently from a normal distribution in a sample set or, for example, indicates there are multiple types of pyrite distinguished by slope changes. Since EPMA analytical lines transect host rock minerals, mineral boundaries, and OS 2 and POS pyrites, slope changes should be apparent and identify analyzed populations of minerals including POS, OS 2, and host rock. Images for Fe, S, Si, and Al exhibit an S-shaped distribution (Appendix F.6), indicating two populations that represent analyses of pyrite (red to orange data points) and host rock (purple, blue, and green data points). Slope changes distinct from the S-shape could indicate additional analyzed populations within the OS 2 pyrites.

Interpretation

Analytical results indicate multiple populations of POS pyrite, host rocks, a mixed phase of both pyrite and host rock, and OS 2 pyrites. Comparative probability plots for each element are described and interpreted from left to right. The curve for Au exhibits three slope changes that represent the change from Au below detection limit to Au above detection limit (144 ppm) to 600 ppm Au, and elevated Au (600 to 800 ppm Au). Carlin pathfinder elements As, Cu, Hg, Sb, and Tl have 3 or 4 slope changes. The first slope

change for As, Cu, Hg, Sb, and Tl represents the first detection of these elements in pyrite, and the last slope change is where the majority of the data points are blue, which is where these elements are elevated in OS rims and Au is between 0 and 700 ppm. Other slope changes (2nd or 3rd) for As, Cu, Hg, Sb, and Tl may represent other mineral phases of other mineral phases that contain these elements or may still be OS rim with detectable gold. Note that where As, Cu, Hg, and Tl are elevated in the OS rim, Fe is generally between 21.98 to 45.03 wt. % Fe indicated by teal data points. Slope changes for Fe represent the change from analyses dominated by host rock to host rock/pyrite grain boundary to POS and OS 2 pyrite to partially oxidized POS pyrites. Slope changes for Si and Al represent the change from analyses dominated by POS pyrite to host rock/pyrite grain boundary to host rock. The Ca slope change represents a change from undetected Ca to Ca in analyses of the host rock/pyrite grain boundary. Cobalt slope changes represent the change from undetectable Co in host rock to detectable Co in host rock with some pyrite, to Co in pyrite as indicated by high Fe in red, orange, and green data points, to elevated Co at the host rock/pyrite grain boundary. Silver slope changes are at ~ 0, 250, and 500 ppm Ag, but these slope changes are not systematically related to Fe concentrations in the analyses; thus, the behavior of Ag is unclear. Bismuth, Ni, Pb, Se, Sn, Te, Ti, and Zn concentrations above detection exhibit few slope changes and tend to have linear trends, indicating normal distributions that have no correlation with Fe or Au.



Comparative Probability plots of EPMA OS 2 pyrite data. Comparative probability plots normalize all data. Data that exhibit a linear relationship do not have multiple populations for the element plotted. These plots identify elements that may have multiple populations. Horizontal black lines show detection limits for those elements, and diagonal black lines mark changes in slope. W are below detection limit, and is not plotted in this figure.

Non-metric Multi-dimensional Scaling Model of EPMA data

The non-metric multi-dimensional scaling model reduces a data set with multiple variables so that it can be viewed with the least number of ordination axes possible, and on an X-Y plot. Each variable and data point are plotted based on their R and R² value relative to each ordination axis. The R value is the measure of the linear correlation between two variables (Axis 1 or 2 and an element (X)); +1 indicates a 100% positive correlation, -1 indicates a 100% negative correlation, 0 indicates no correlation, and values in between indicate correlations that are less than 100% positive or negative. The values on non-metric multi-dimensional scaling X and Y axes (Appendix F.6 NMS graphs) are R values. The line lengths of the variables (elements) and their positions on the graph indicate the degree to which the variables (element's) correlate with the axis, and a longer line indicates a stronger correlation. Lines that cluster or group indicate variables (elements) that have similar behavior. Pink triangles represent data points that are less than or equal to gold classification, and green triangles are data points that are greater than the gold classification. Non-metric multi-dimensional scaling models were calculated for Au classifications of 1, 144, and 500 ppm Au for all EPMA pyrite data. The 144 non-metric multi-dimensional scaling R and R² values for each element analyzed are listed in (Appendix F.6 NMS table)

Au does not appear on any NMS model images (Appendix F.6 NMS graphs) for any gold classification, but results (Appendix F.6 NMS table) show that Au would plot at Axis 1: 0.185, Axis 2: 0.257, and Axis 3: 0.109, which means Au would plot in the same vector direction with As and Hg on the (Appendix F.6 NMS graphs).

NMS models for all Au classifications (Appendix F.6 NMS graphs) show that samples with Au > 1, 144, and 500 ppm, indicated by green triangles, do not cluster. The element line lengths and their positions on Figures 37, 41, and 44 (Appendix F.6 NMS graphs) show that the element clusters include: 1) Fe, S, Pb, Co, Mo, plus W, 2) Si plus Al, 3) As, Hg, plus Sb, and 4) Ca which doesn't cluster with other elements, but has a strong negative correlation to Axis 1 and a weak negative correlation to Axis 2, or a weak positive to Axis 3. The element line lengths and their positions on (Appendix F.6 NMS graphs) show: 1) weak clustering of Hg, As, Se, Ni, +/- Cu and 2) Sb and Ca show opposite behavior with Sb having a strong positive correlation to Axis 1 and Ca having a strong negative correlation to Axis 1. The element line lengths and their positions on the Axis 2 and 3 graph (Appendix F.6 NMS graphs) show that the element clusters include: 1) Fe, S, Pb, Co, Mo, plus W, 2) Si, Al, Ti, plus Sb, 3) As, Hg, Cu, Ni, plus Se, and 4) Bi which doesn't cluster with other elements, but has a weak positive correlation to Axis 2 and a weak negative correlation to Axis 3.

Interpretation

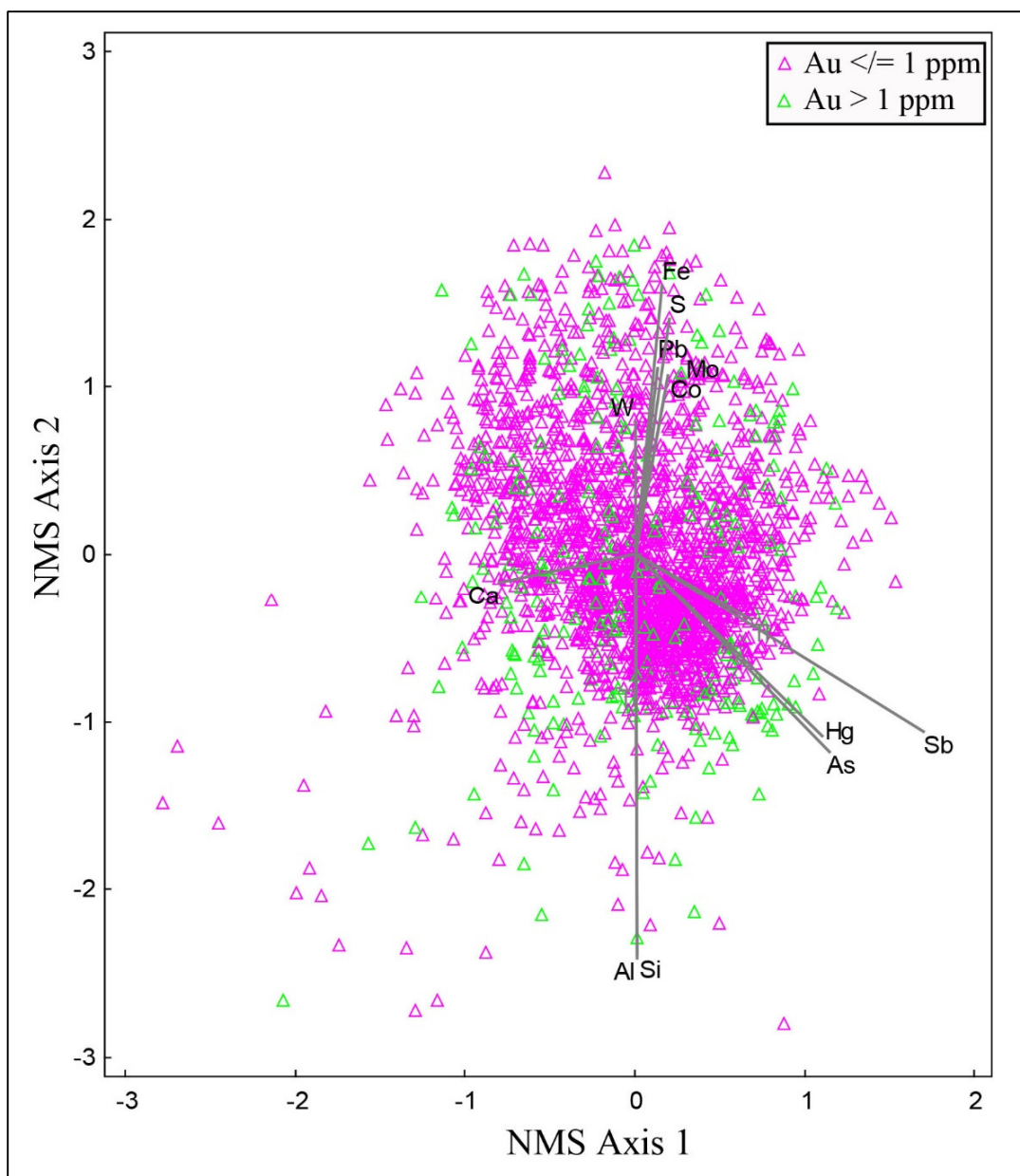
The non-metric multi-dimensional scaling model (Appendix F.6 NMS graphs) indicates that Au would plot with As and Hg. Iron, S, Pb, Co, Mo, and W, elements commonly in POS pyrites, show strong positive correlations to Axis 2 and no relation to Axis 1, and show strong negative correlation to Axis 3 and no relation to Axis 1 or 2. Silica and Al, elements commonly in host rocks, show strong negative correlation to Axis 2 and no relation to Axis 1. Si and Al show strong positive correlation to Axis 3, and no relation to Axis 2, and Sb and Ti share this relationship but have a weak positive correlation to Axis 3. Si and Al show strong positive correlation to Axis 3, and no

relation to Axis 1, and Ti share this relationship but have a weak positive correlation to Axis 3. As and Hg, Carlin-type pathfinder elements commonly in OS pyrite, show strong positive correlation to Axis 1 and strong negative correlation to Axis 2 with Sb, another Carlin-type pathfinder element. As and Hg show weak positive correlation to Axis 1, and weak negative to Axis 3, and weak positive to Axis 2 with Sb. As and Hg show weak positive correlation to Axis 3 and weak negative correlation to Axis 2 with Cu and Ni. Calcium commonly in carbonate host rocks does not plot with other elements in all plots. Ca show weak negative correlation with Axis 1 and 2, weak negative correlation with Axis 1 and no relation to Axis 2 or 3.

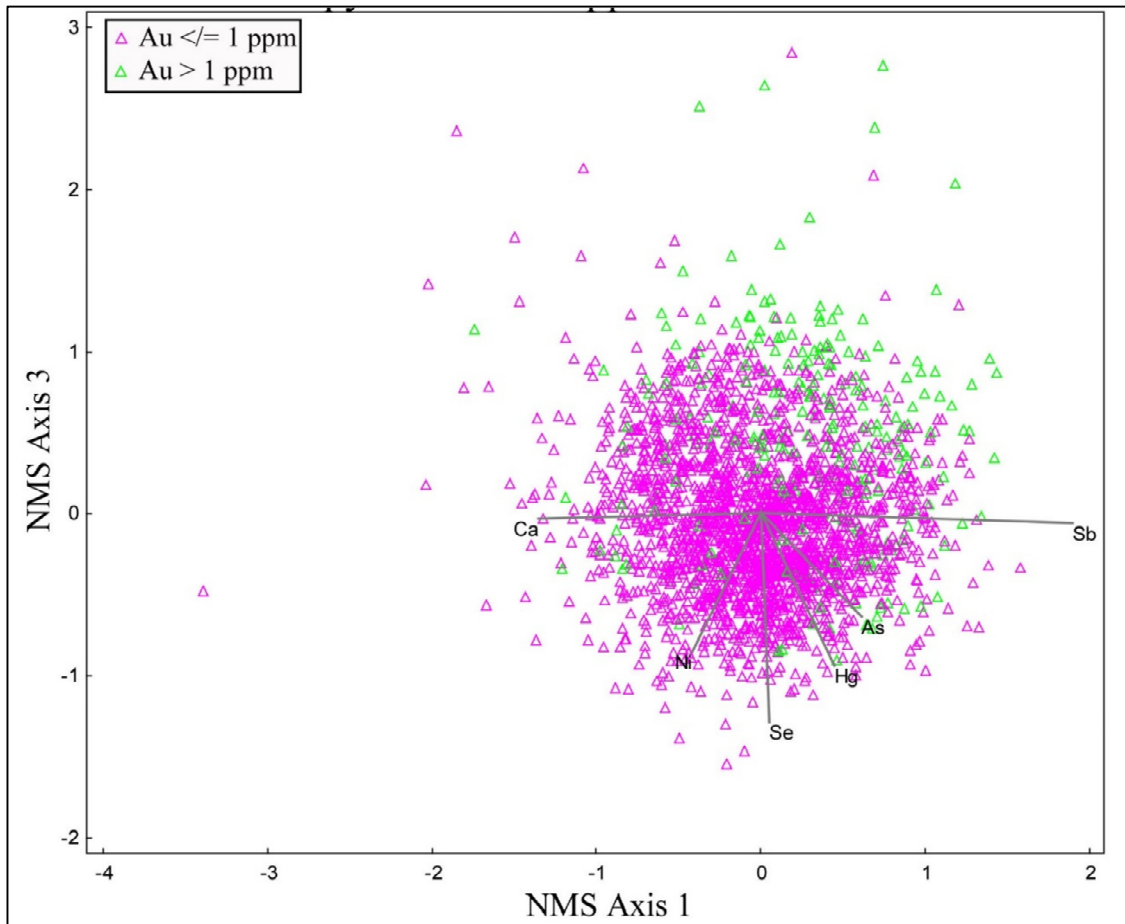
Non-metric Multi-dimensional Scaling Model Tale. Axis 1, 2, and 3 R, R2 values for 1, 144, and 500 ppm gold classification for all EPMA pyrite data

		Ag	Al	As	Au	Bi	Ca	Co	Cu	Fe	Hg	Ni	Mo
Axis 1	r	0.274	0.027	0.399	0.185	0.047	-0.59	0.029	-0.184	0.048	0.339	-0.329	0.054
	r ²	0.075	0.001	0.159	0.034	0.002	0.349	0.001	0.034	0.002	0.115	0.108	0.003
Axis 2	r	0.039	-0.248	-0.517	0.257	0.44	-0.144	-0.257	-0.457	-0.162	-0.593	-0.511	-0.225
	r ²	0.002	0.062	0.267	0.066	0.193	0.021	0.066	0.209	0.026	0.352	0.261	0.051
Axis 3	r	-0.096	0.776	0.497	0.109	-0.241	0.203	-0.549	0.294	-0.683	0.464	0.197	-0.57
	r ²	0.009	0.602	0.247	0.012	0.058	0.041	0.301	0.086	0.466	0.215	0.039	0.325

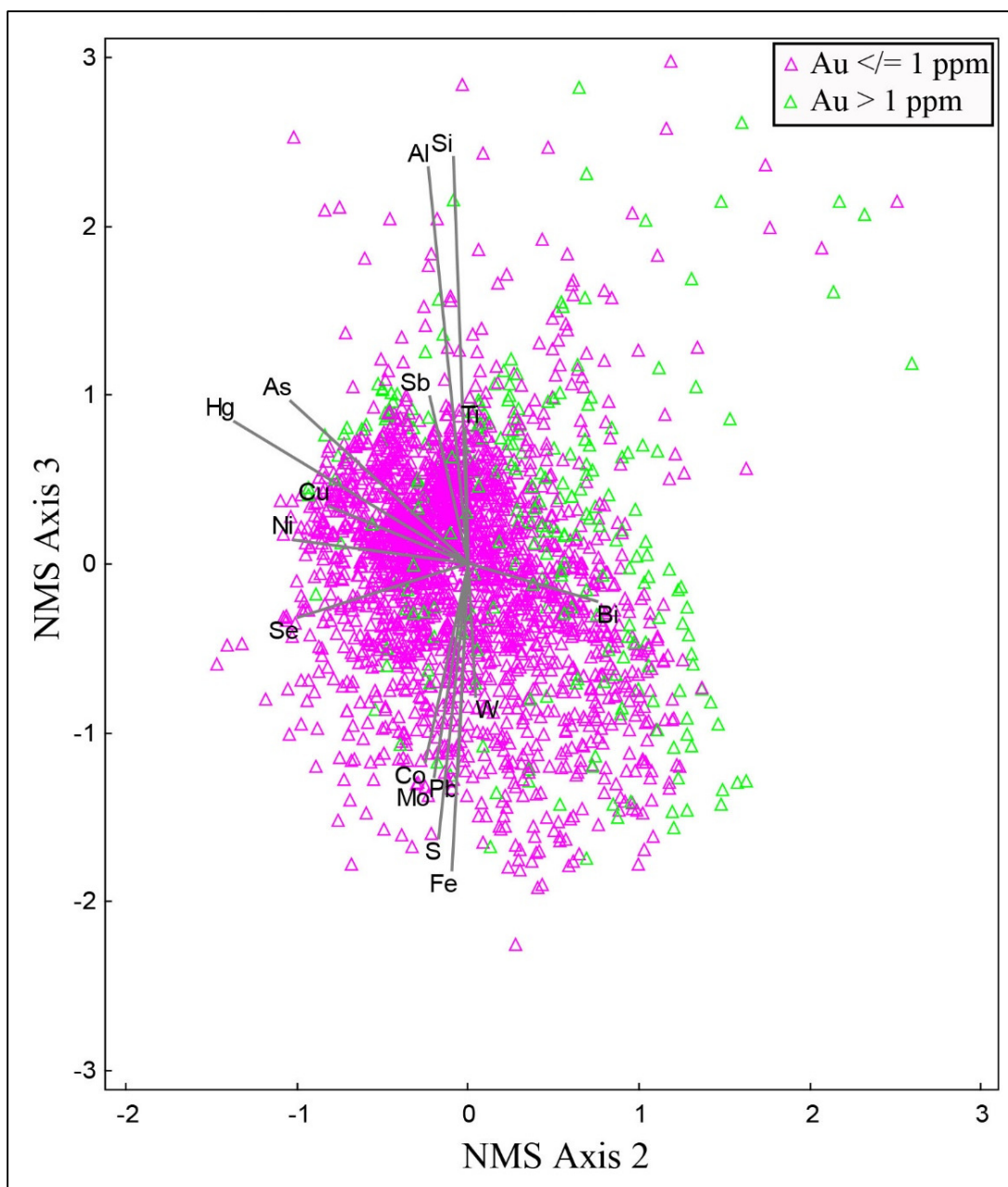
		Pb	S	Sb	Si	Se	Sn	Te	Ti	Tl	W	Zn
Axis 1	r	0.067	0.053	0.699	0.087	0.115	0.194	-0.210	-0.020	0.302	-0.004	-0.036
	r ²	0.004	0.003	0.489	0.008	0.013	0.038	0.044	0.000	0.091	0.000	0.001
Axis 2	r	-0.134	-0.217	-0.242	-0.151	-0.506	-0.038	-0.273	-0.066	-0.389	0.103	-0.032
	r ²	0.018	0.047	0.058	0.023	0.256	0.001	0.074	0.004	0.152	0.011	0.001
Axis 3	r	-0.567	-0.647	0.504	0.786	-0.289	0.139	-0.063	0.453	0.277	-0.450	-0.042
	r ²	0.321	0.418	0.254	0.618	0.083	0.019	0.004	0.205	0.077	0.202	0.002



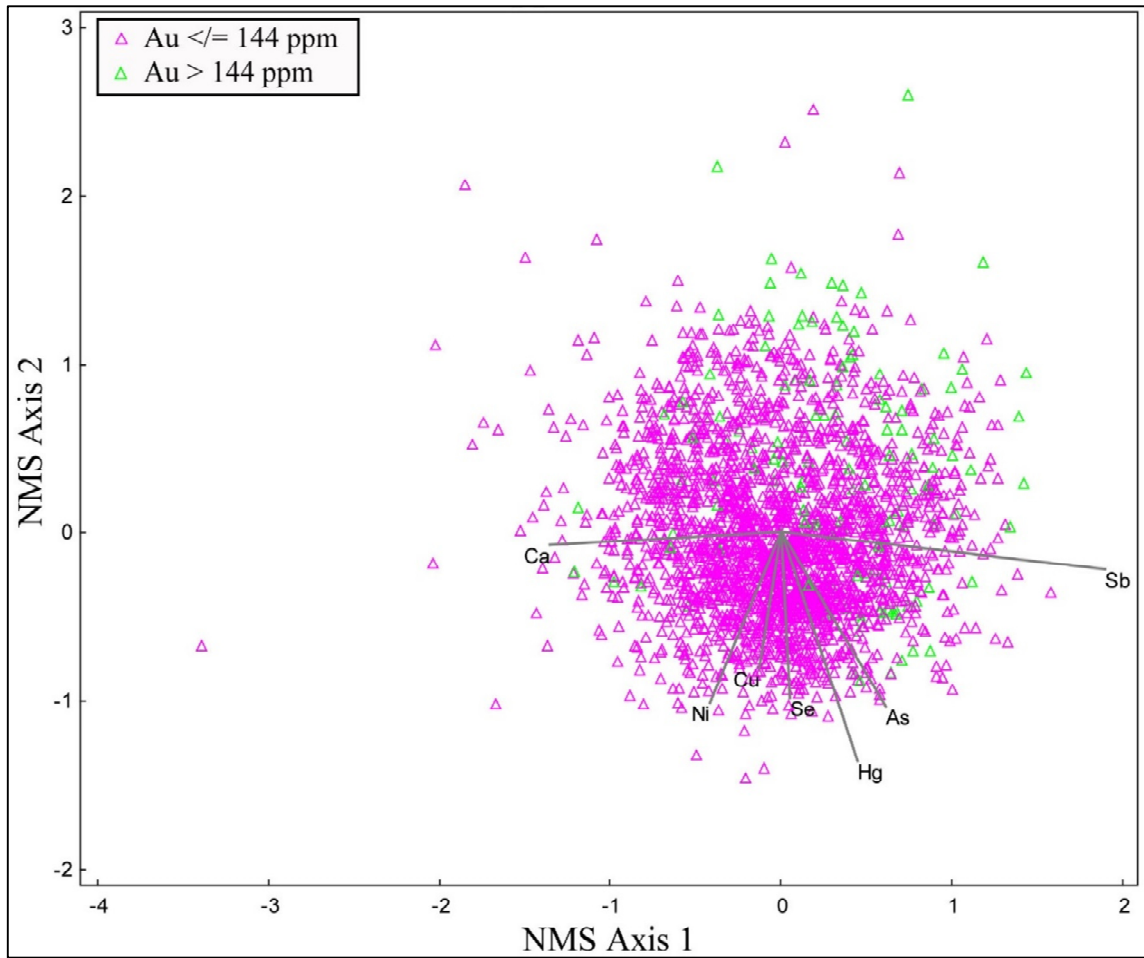
Non-metric multi-dimensional scaling model of Axis 1 and Axis 2 with 1 ppm Au classification with all EPMA pyrite. EPMA pyrite geochemistry data, show the distributions of two classes of Au relative to Axis 1 and 2 and other elements. Each element's r and r^2 value relative to Axis 1 and Axis 2 are listed in table.



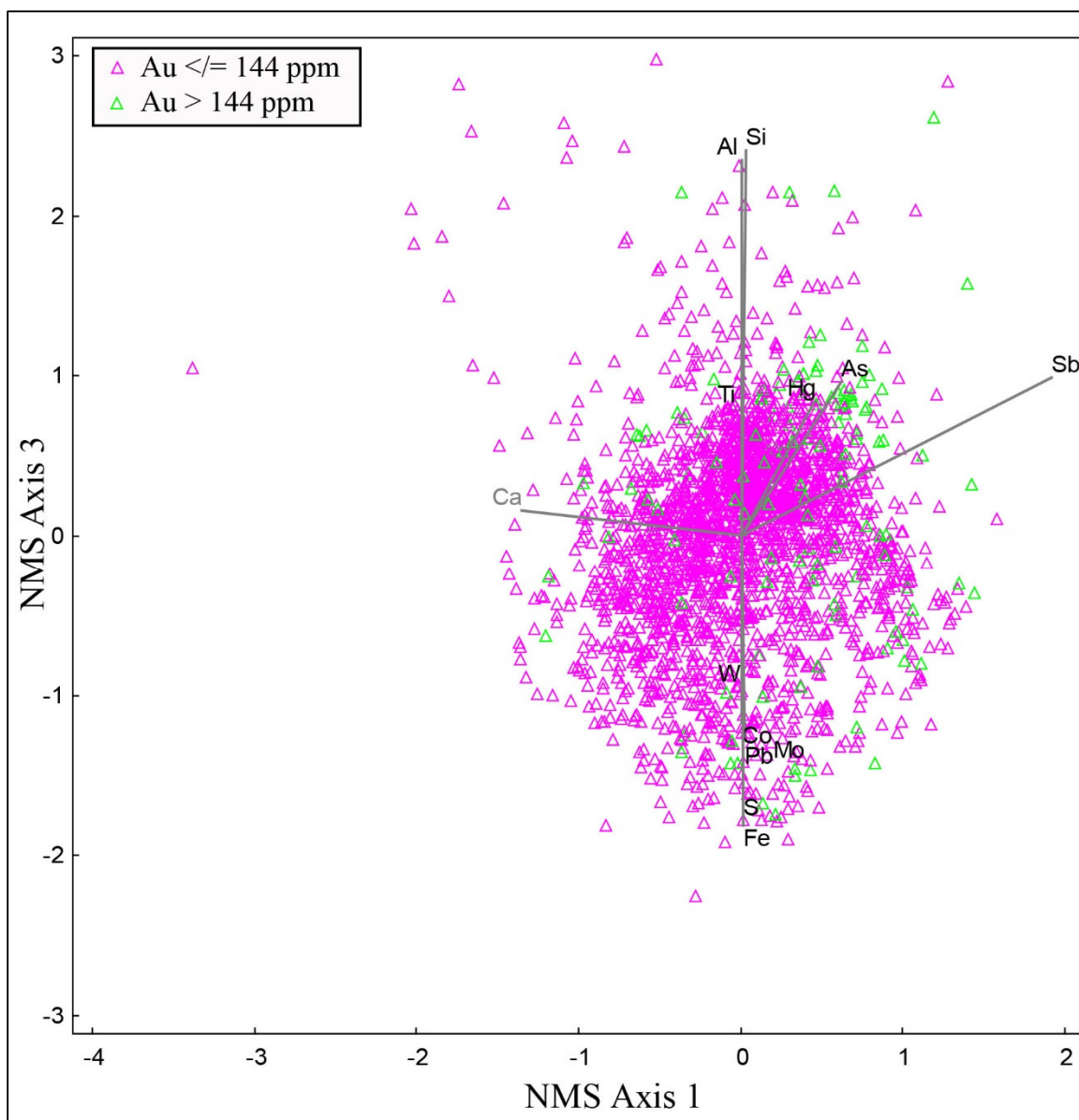
Non-metric multi-dimensional scaling model of Axis 1 and Axis 3 with 1 ppm Au classification with all EPMA pyrite. EPMA pyrite geochemistry data, show the distributions of two classes of Au relative to Axis 1 and 3 and other elements. Each element's r and r^2 value relative to Axis 1 and Axis 3 are listed in table.



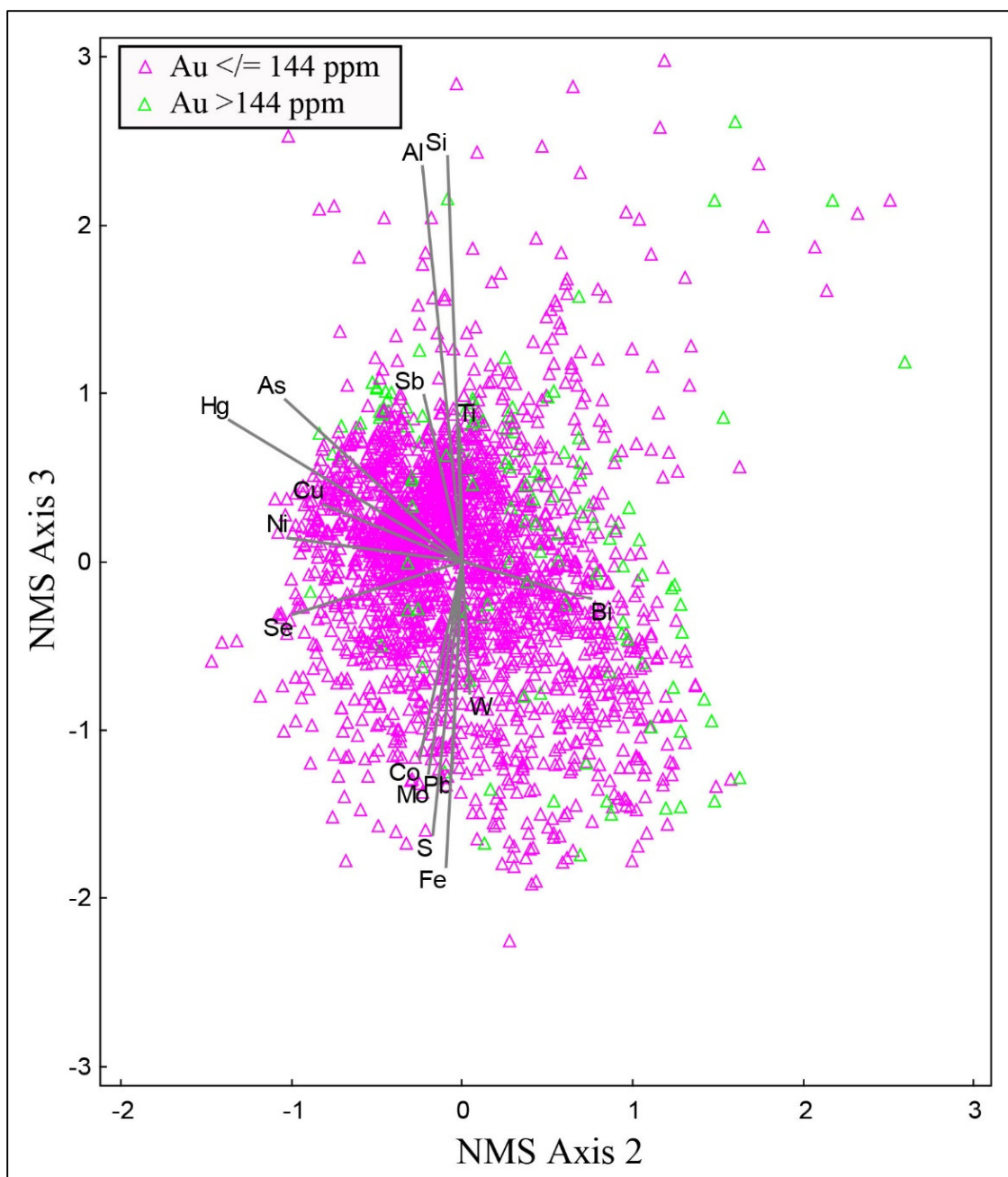
Non-metric multi-dimensional scaling model of Axis 2 and Axis 3 with 1 ppm Au classification with all EPMA pyrite. EPMA pyrite geochemistry data, show the distributions of two classes of Au relative to Axis 2 and 3 and other elements. Each element's r and r^2 value relative to Axis 2 and Axis 3 are listed in table.



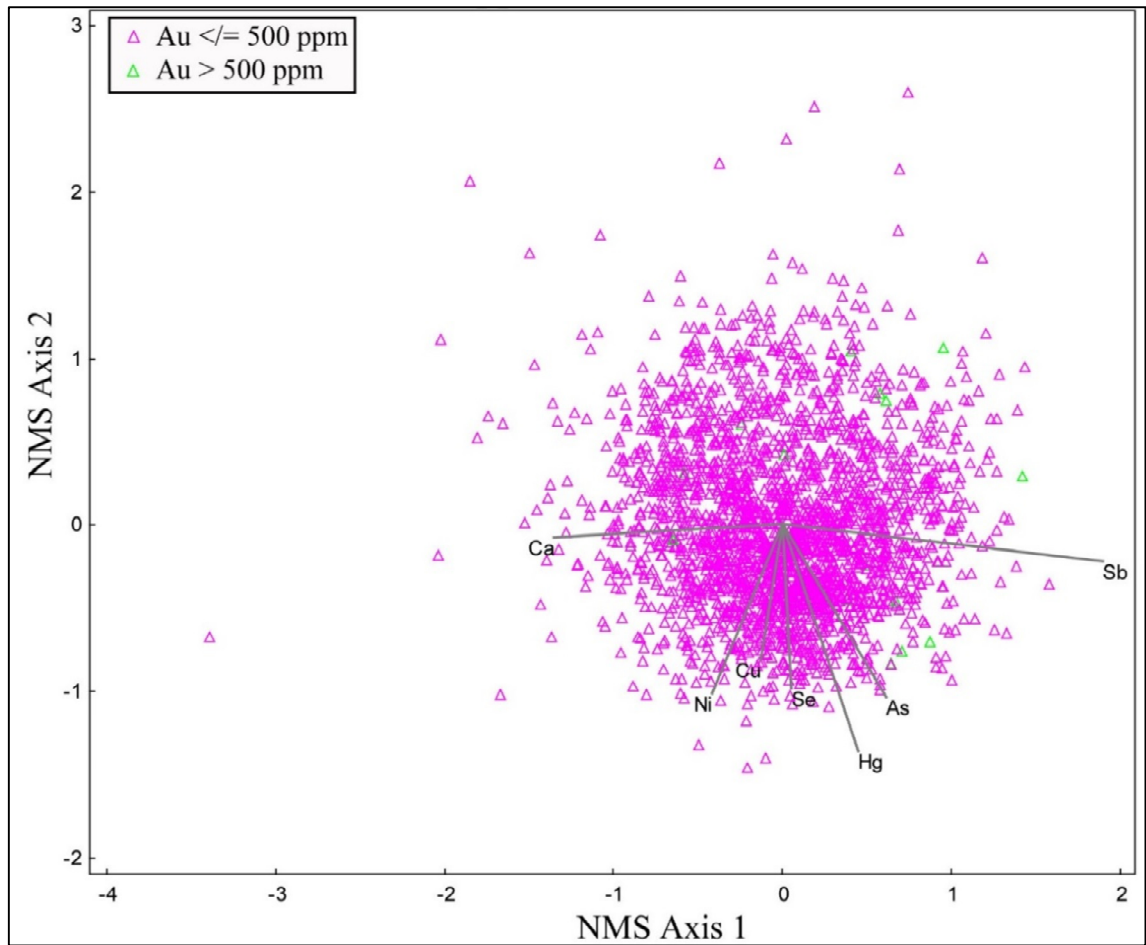
Non-metric multi-dimensional scaling model of Axis 1 and Axis 2 with 144 ppm Au classification with all EPMA pyrite. EPMA pyrite geochemistry data, show the distributions of two classes of Au relative to Axis 1 and 2 and other elements. Each element's r and r^2 value relative to Axis 1 and Axis 2 are listed in table.



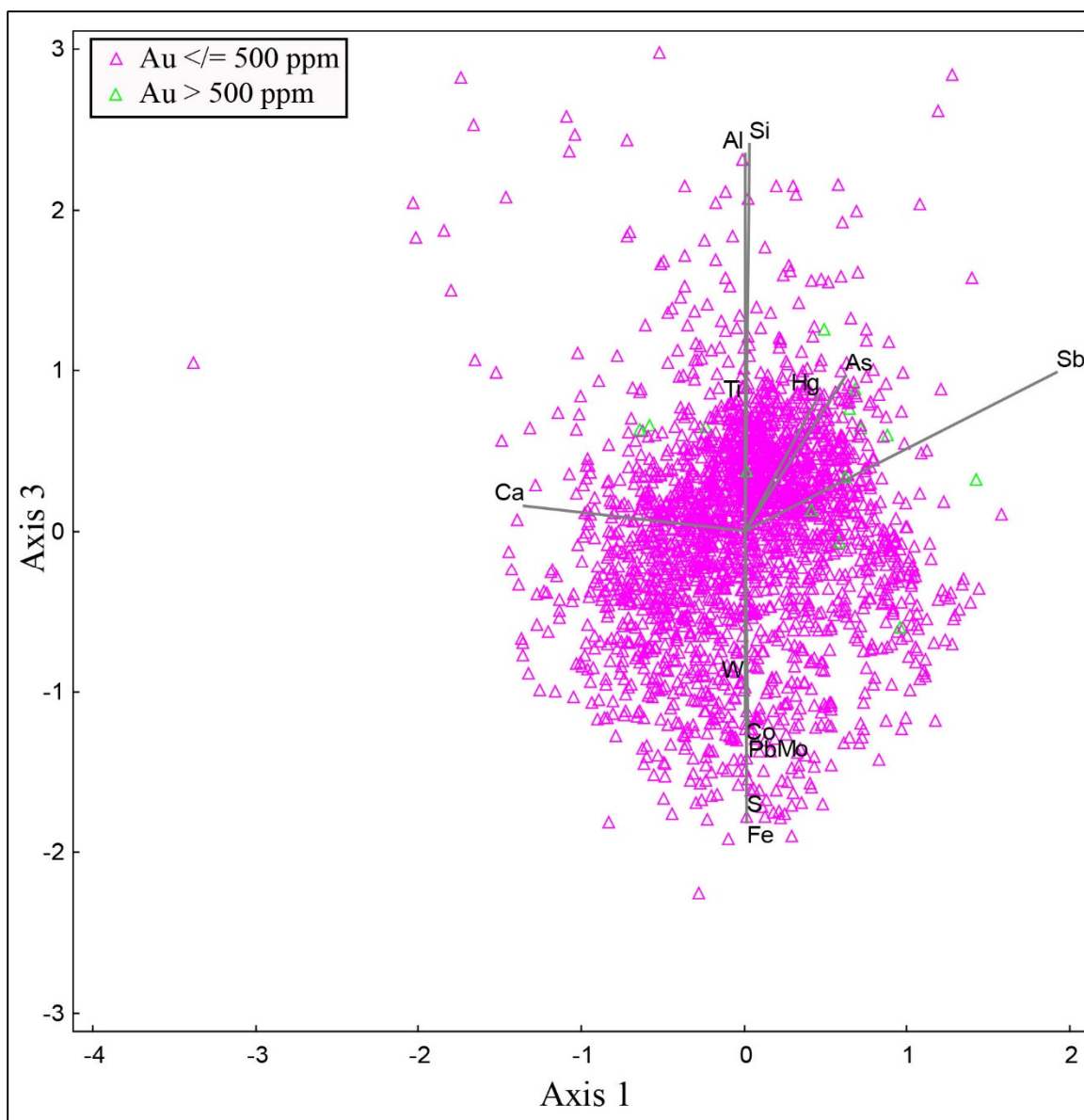
Non-metric multi-dimensional scaling model of Axis 1 and Axis 3 with 144 ppm Au classification with all EPMA pyrite. EPMA pyrite geochemistry data, show the distributions of two classes of Au relative to Axis 1 and 3 and other elements. Each element's r and r^2 value relative to Axis 1 and Axis 3 are listed in table.



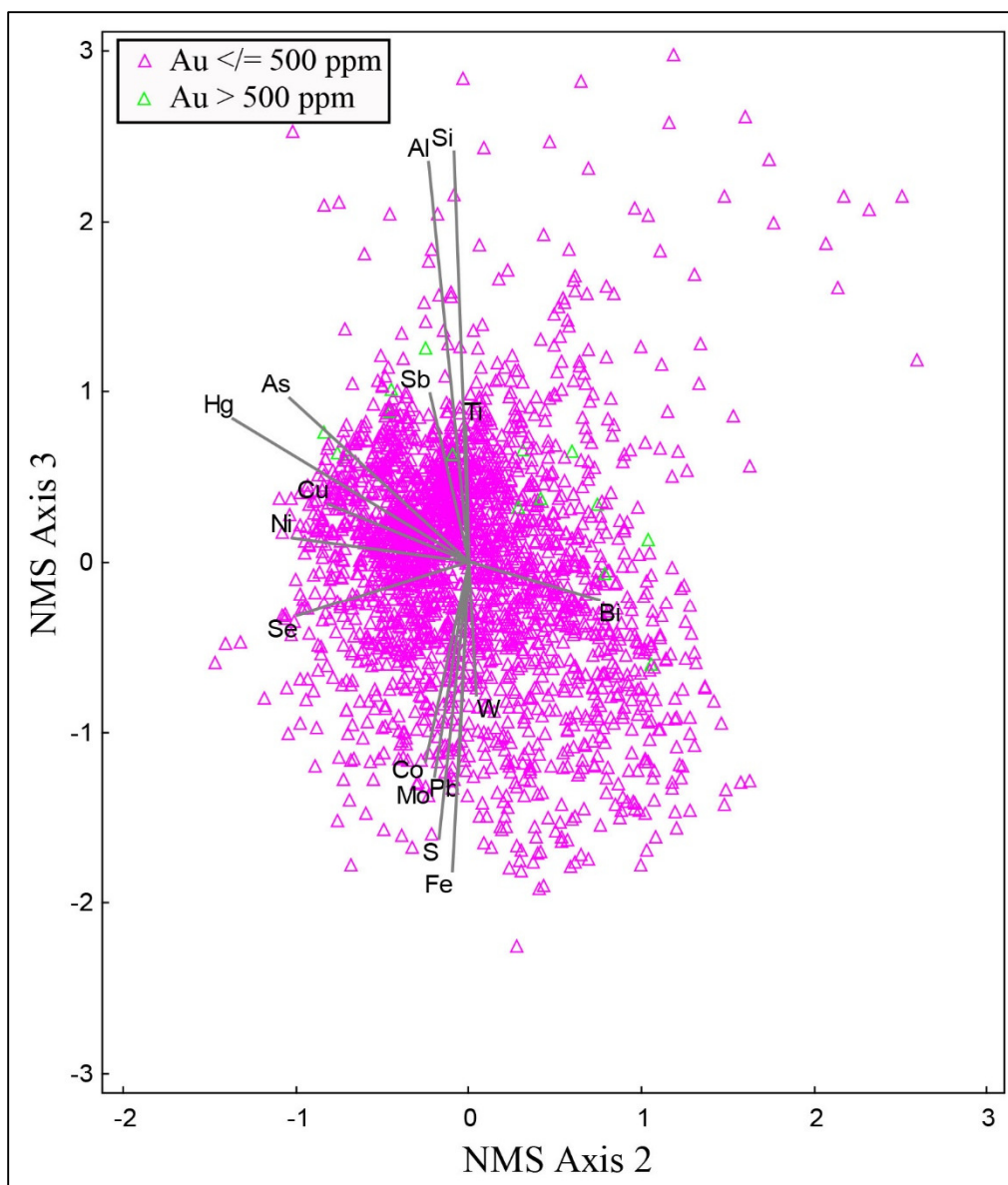
Non-metric multi-dimensional scaling model of Axis 2 and Axis 3 with 144 ppm Au classification with all EPMA pyrite. EPMA pyrite geochemistry data, show the distributions of two classes of Au relative to Axis 2 and 3 and other elements. Each element's r and r^2 value relative to Axis 2 and Axis 3 are listed in tabl.



Non-metric multi-dimensional scaling model of Axis 1 and Axis 2 with 500 ppm Au classification with all EPMA pyrite. EPMA pyrite geochemistry data, show the distributions of two classes of Au relative to Axis 1 and 2 and other elements. Each element's r and r^2 value relative to Axis 1 and Axis 2 are listed in table.



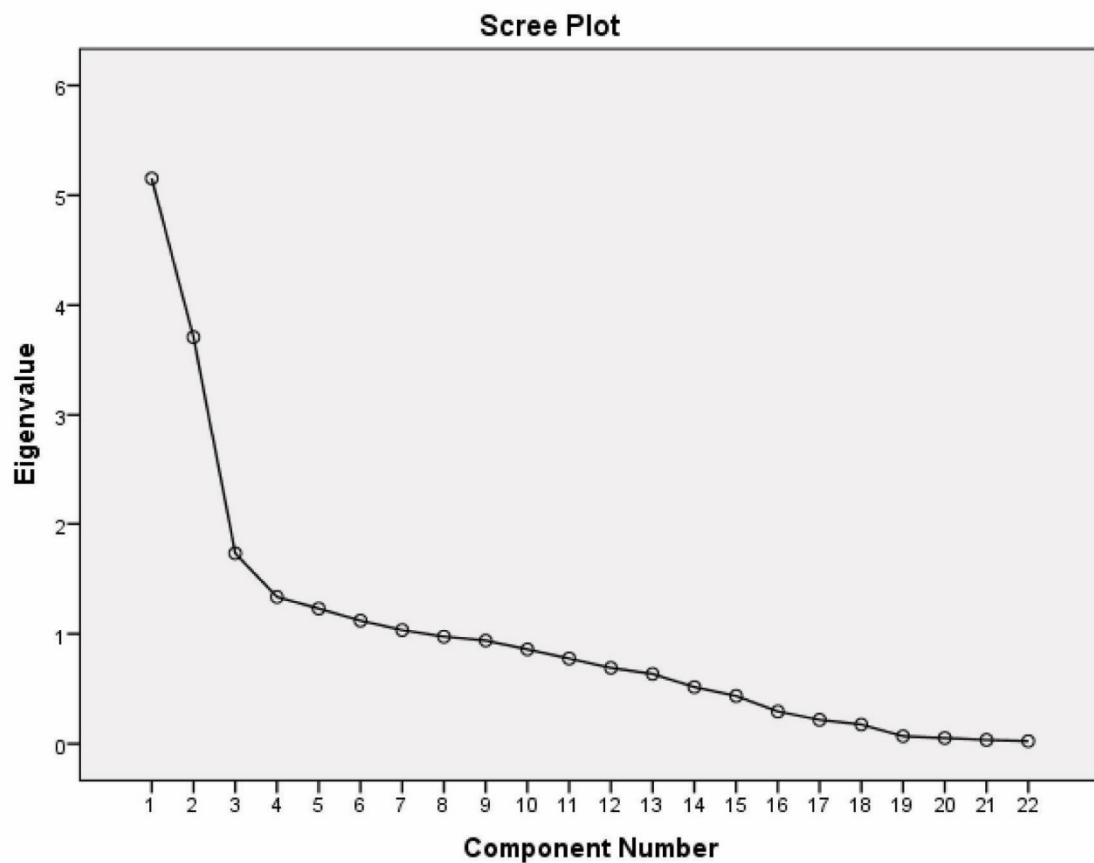
Non-metric multi-dimensional scaling model of Axis 1 and Axis 3 with 500 ppm Au classification with all EPMA pyrite. EPMA pyrite geochemistry data, show the distributions of two classes of Au relative to Axis 1 and 3 and other elements. Each element's r and r^2 value relative to Axis 1 and Axis 3 are listed in table.



Non-metric multi-dimensional scaling model of Axis 2 and Axis 3 with 500 ppm Au classification with all EPMA pyrite. EPMA pyrite geochemistry data, show the distributions of two classes of Au relative to Axis 2 and 3 and other elements. Each element's r and r^2 value relative to Axis 2 and Axis 3 are listed in table.

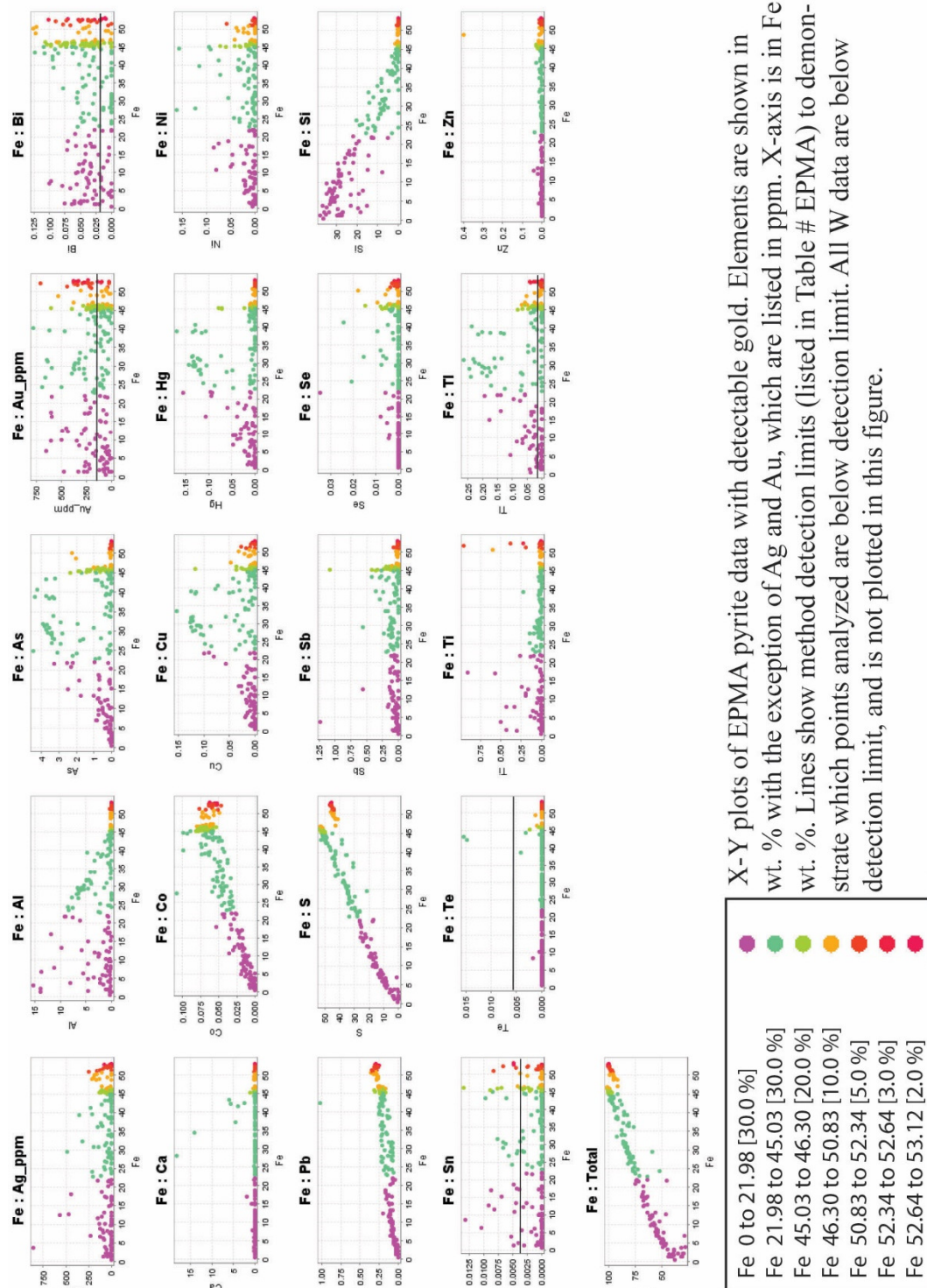
Principle Components Analysis OS 2 Pyrites

Component	1	2	3	4	5	6	7
Total	5.153	3.708	1.732	1.335	1.229	1.120	1.034
Variance %	23.425	16.854	7.874	6.069	5.588	5.090	4.700
Cumulative %	23.425	40.278	48.152	54.221	59.809	64.899	69.599

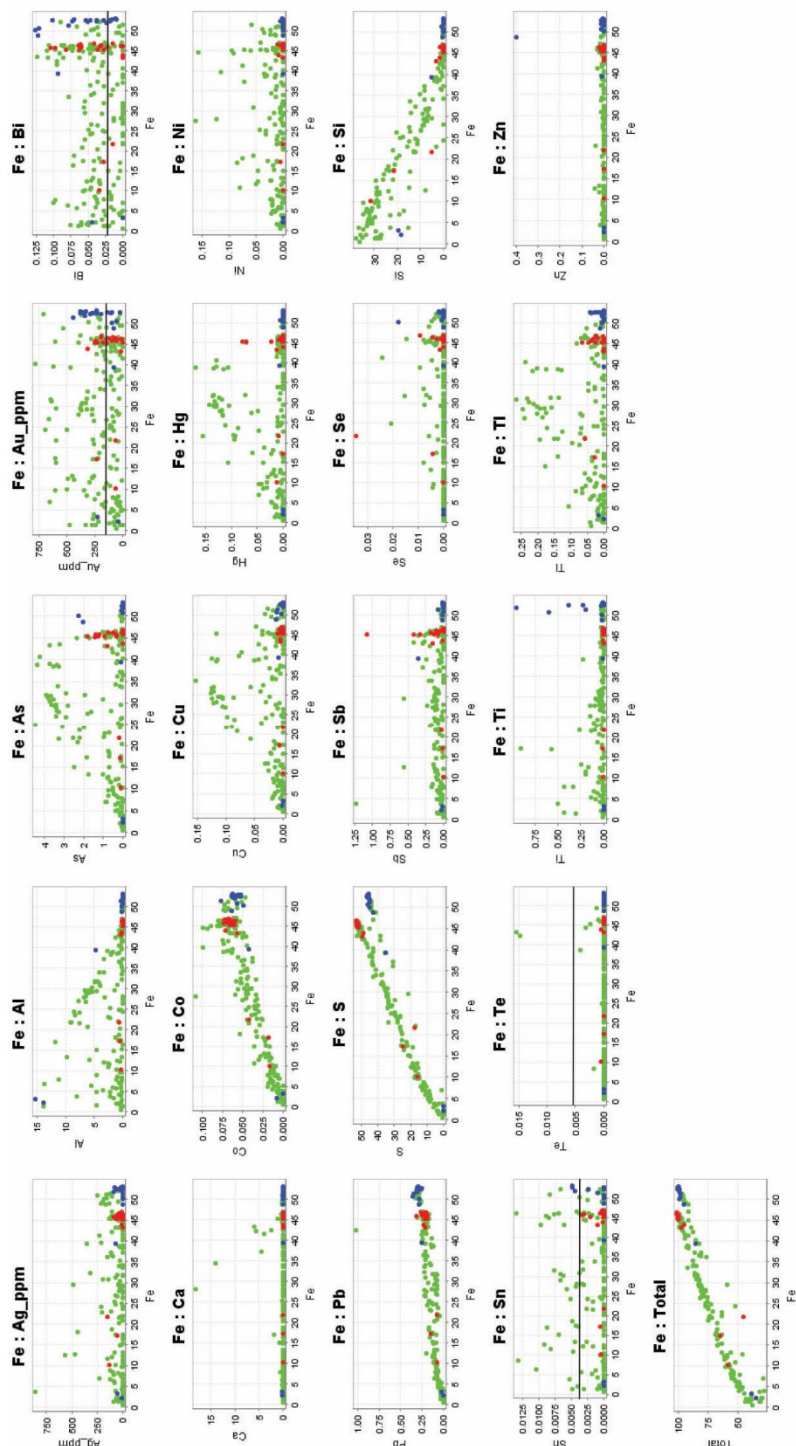


The Catell's Scree Test for OS 2 pyrites involves plotting each of the initial eigenvalues ('Total') of the components. Components retained are above the "elbow" or where the curve changes direction and becomes flat. Components above the "elbow", "contribute the most to the explanation of the variance in the data set" (Pallent, 2007).

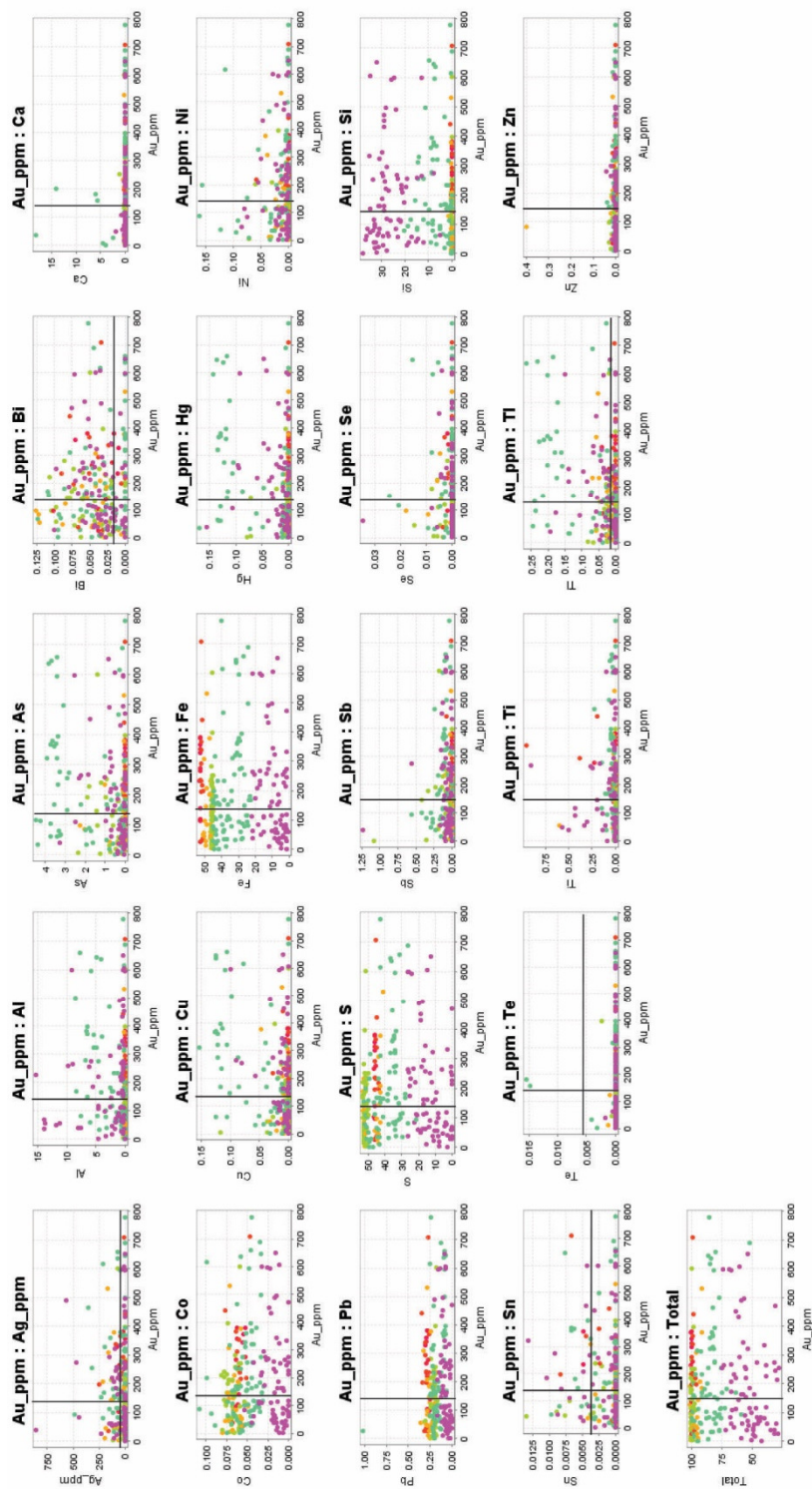
Appendix F.7: EPMA Gold points on each pyrite type plots



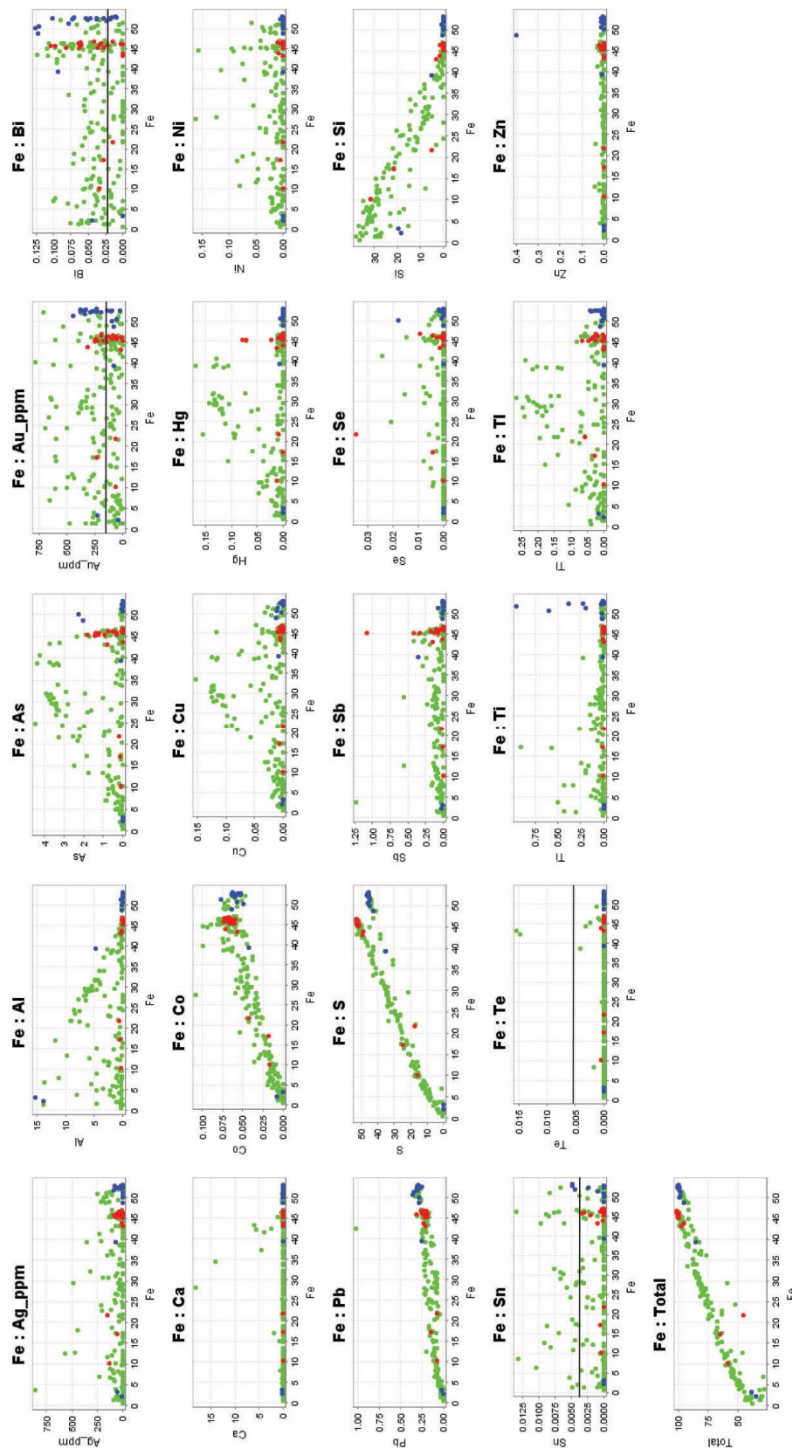
X-Y plots of EPMA pyrite data with detectable gold. Elements are shown in wt. % with the exception of Ag and Au, which are listed in Table # EPMA) to demonstrate which points analyzed are below detection limit. All W data are below detection limit, and is not plotted in this figure.



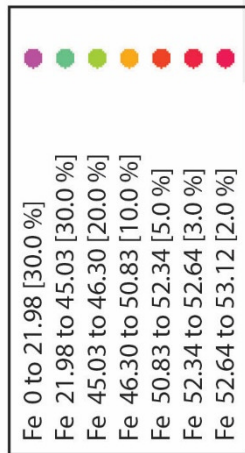
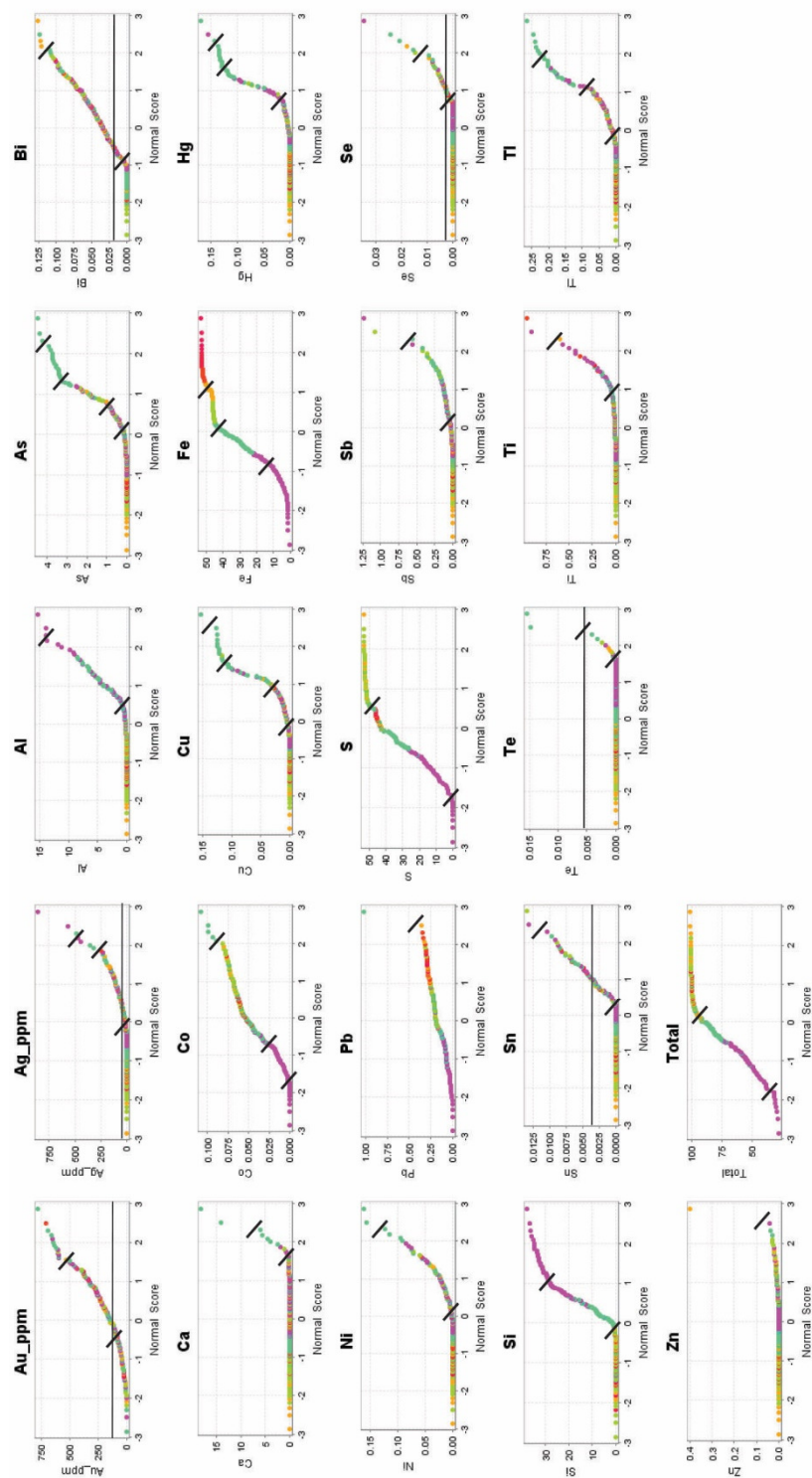
X-Y plots of EPMA pyrite data with detectable gold. Elements are shown in wt. % with the exception of Ag and Au, which are listed in ppm. X-axis is in Fe wt. %. Color illustrates which stage of pyrite (POS, OS 1, or LOS) gold analyses points were detected on. Lines show method detection limits (listed in Table # EPMA) to demonstrate which points analyzed are below detection limit. All W data are below detection limit, and is not plotted in this figure.



X-Y plots of EPMA pyrite data with detectable gold. Elements are shown in wt. % with the exception of Ag and Au, which are listed in Table # EPMA) to demonstrate which points analyzed are below detection limit. All W data are below detection limit, and is not plotted in this figure.



X-Y plots of EPMA pyrite data with detectable gold. Elements are shown in wt. % with the exception of Ag and Au, which are listed in ppm. X-axis is in Fe wt. %. Color illustrates which stage of pyrite (POS, OS 1, or LOS) gold analyses points were detected on. Lines show method detection limits (listed in Table # EPMA) to demonstrate which points analyzed are below detection limit. All W data are below detection limit, and is not plotted in this figure.



Comparative Probability plots of EPMA pyrite data with detectable gold.
 Comparative probability plots normalize all data. Data that exhibit a linear relationship do not have multiple populations for the element plotted. These plots identify elements that may have multiple populations. All W data are below detection limit, and are not plotted.

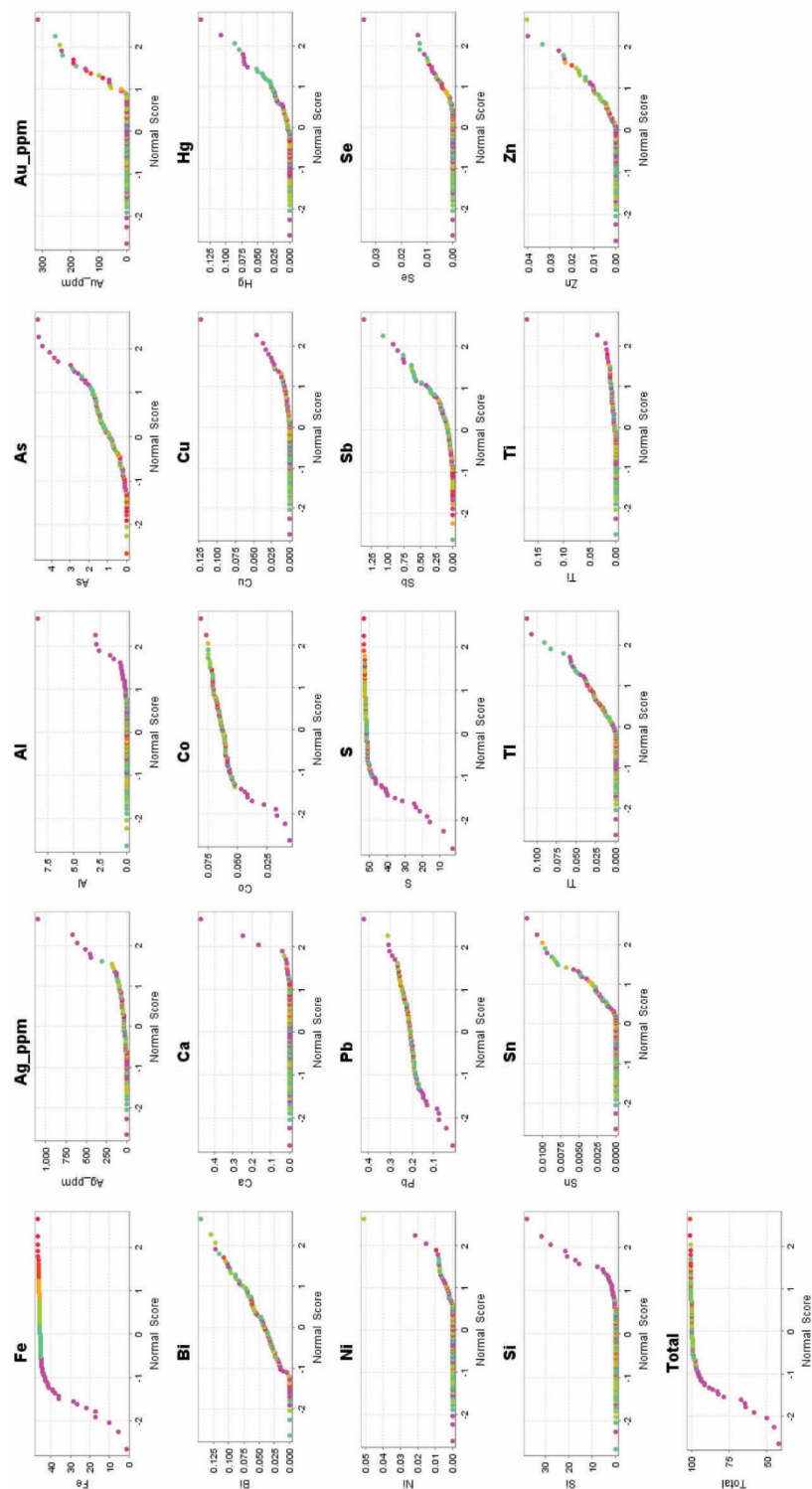
Appendix F.7: EPMA LOS pyrite data plots

Comparative Probability Plot of Late-ore-stage Pyrite

A comparative normal probability plot compares the distribution of the data set being evaluated against a normally distributed data set and assesses whether or not the data set departs from a normal distribution, illustrated by a straight line, or contains discrete populations within the data set identified by changes in slope. The LOS pyrite comparative probability plot (Appendix F.7). Images for Fe, S, Si, and Al exhibit an approximate S-shaped distribution (Appendix F.7), indicating two populations that represent analyses of pyrite (red to orange data points) and host rock (other colored data points). Slope changes distinct from the S-shape could indicate additional analyzed populations within the LOS pyrites.

In the following discussion, comparative probability plots for each element are described and interpreted from left to right across each graph. Analytical results indicate three populations of analyses that quantified elements in LOS pyrite shown by analytical points colored red, orange, green, and blue, host rocks shown by analytical points colored purple, or a mixture of both pyrite and host rock shown by analytical points colored by purple. Due to the small data set, there may be more black lines that indicate slope changes that is indicating elements are partitioning in different populations than is actually realistically accurate. Iron, S, Co, and Pb slope changes represent a change in analyzed minerals from host rock to host rock and pyrite grain boundary to LOS pyrite. Silica, Al and Ca slope changes represent the change from LOS pyrite to host rock and pyrite grain boundary to host rock. Gold slope changes represent the change from undetectable Au to detectable Au in LOS pyrite. Carlin pathfinder elements As, Cu, Hg,

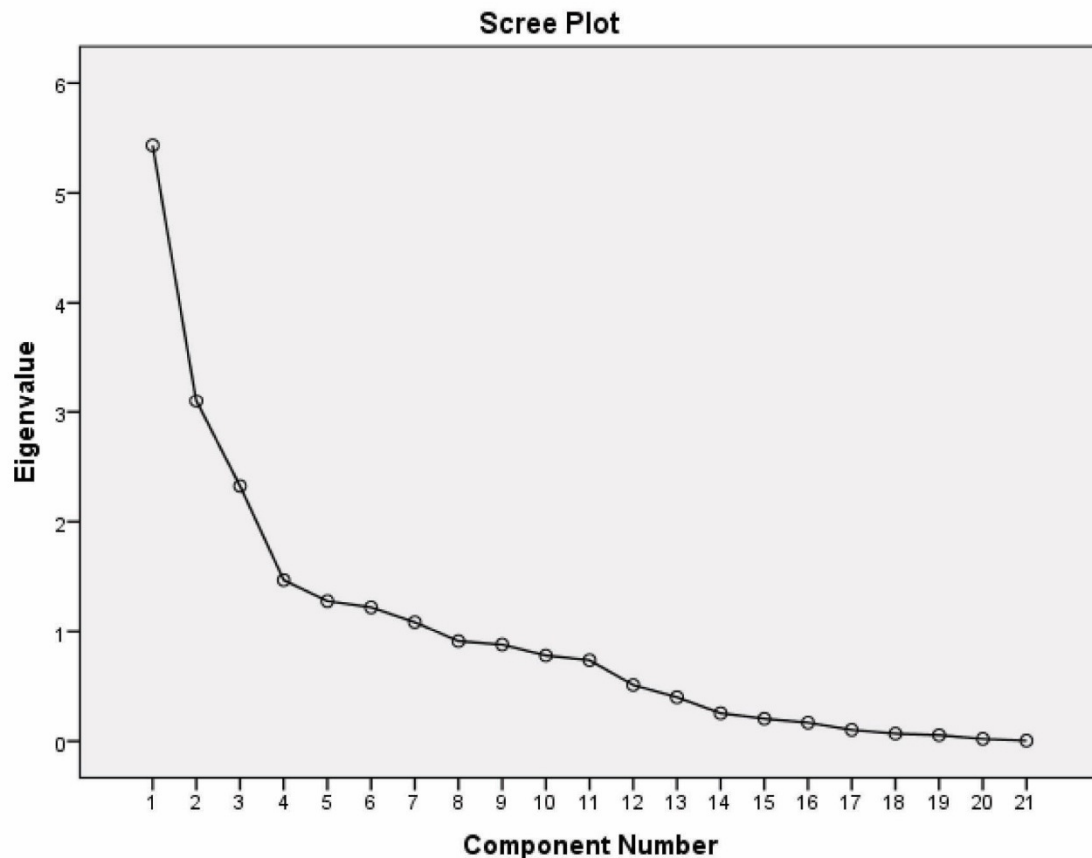
Sb, and Tl are more difficult to interpret and are roughly linear, but the first change in slope represents a change from undetected to detectable elements. Silver show three slope changes, and Ni shows three slope changes, but the reason for these slope changes is not understood.



Comparative Probability plots of EPMA LOS pyrite data. Comparative probability plots normalize all data. Data that exhibit a linear relationship do not have multiple populations for the element plotted. These plots identify elements that may have multiple populations. All Te and W data are below detection limit, and are not plotted in this figure.

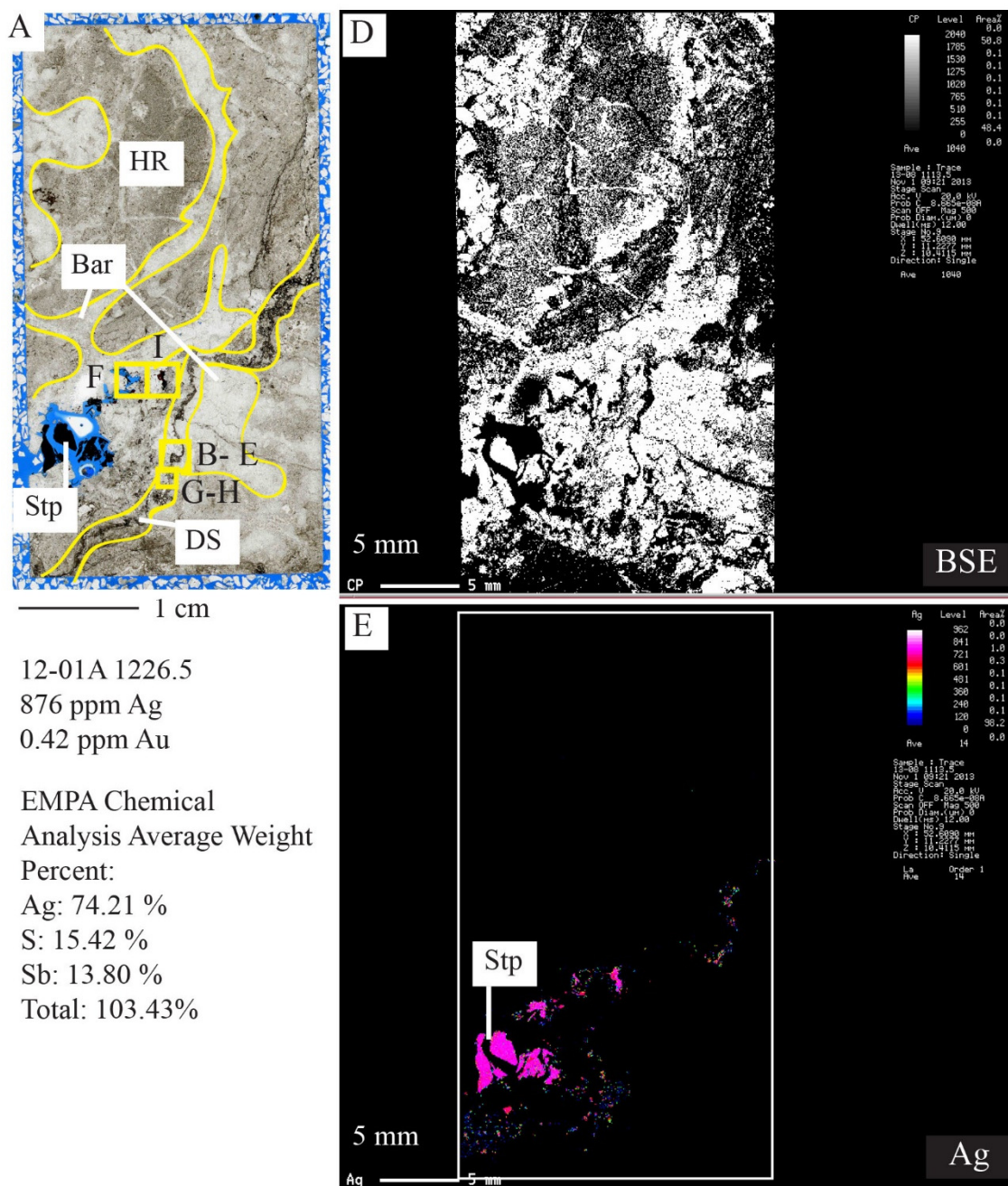
Principle Components Analysis LOS Pyrites

Component	1	2	3	4	5	6	7
Total	5.433	3.101	2.324	1.467	1.276	1.218	1.084
Variance	25.872	14.769	11.069	6.986	6.076	5.802	5.160
Cumulative %	25.872	40.641	51.709	58.695	64.771	70.572	75.733

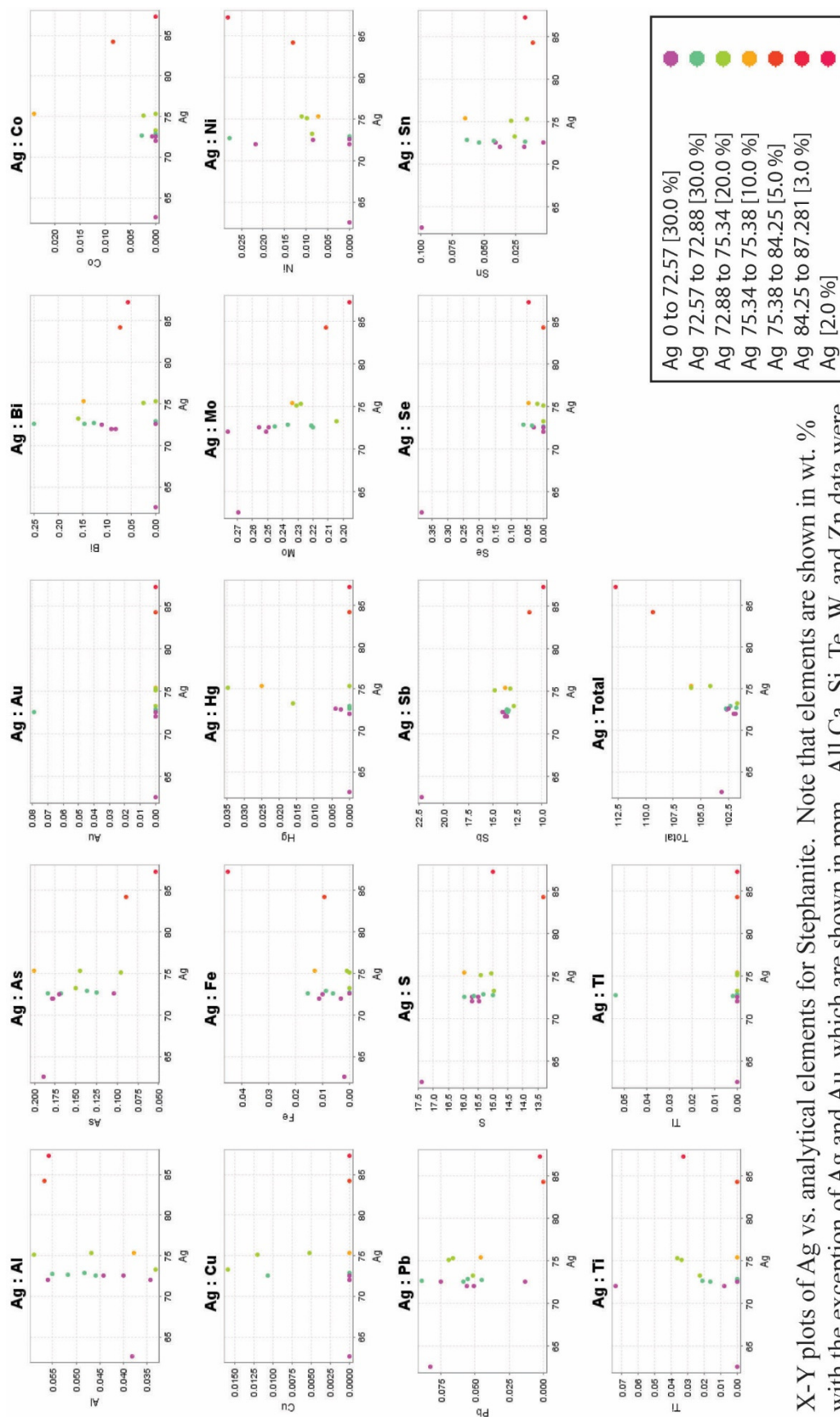


The Catell's Scree Test for LOS pyrites involves plotting each of the initial eigenvalues ('Total') of the components. Components retained are above the "elbow" or where the curve changes direction and becomes flat. Components above the "elbow", "contribute the most to the explanation of the variance in the data set" (Pallent, 2007).

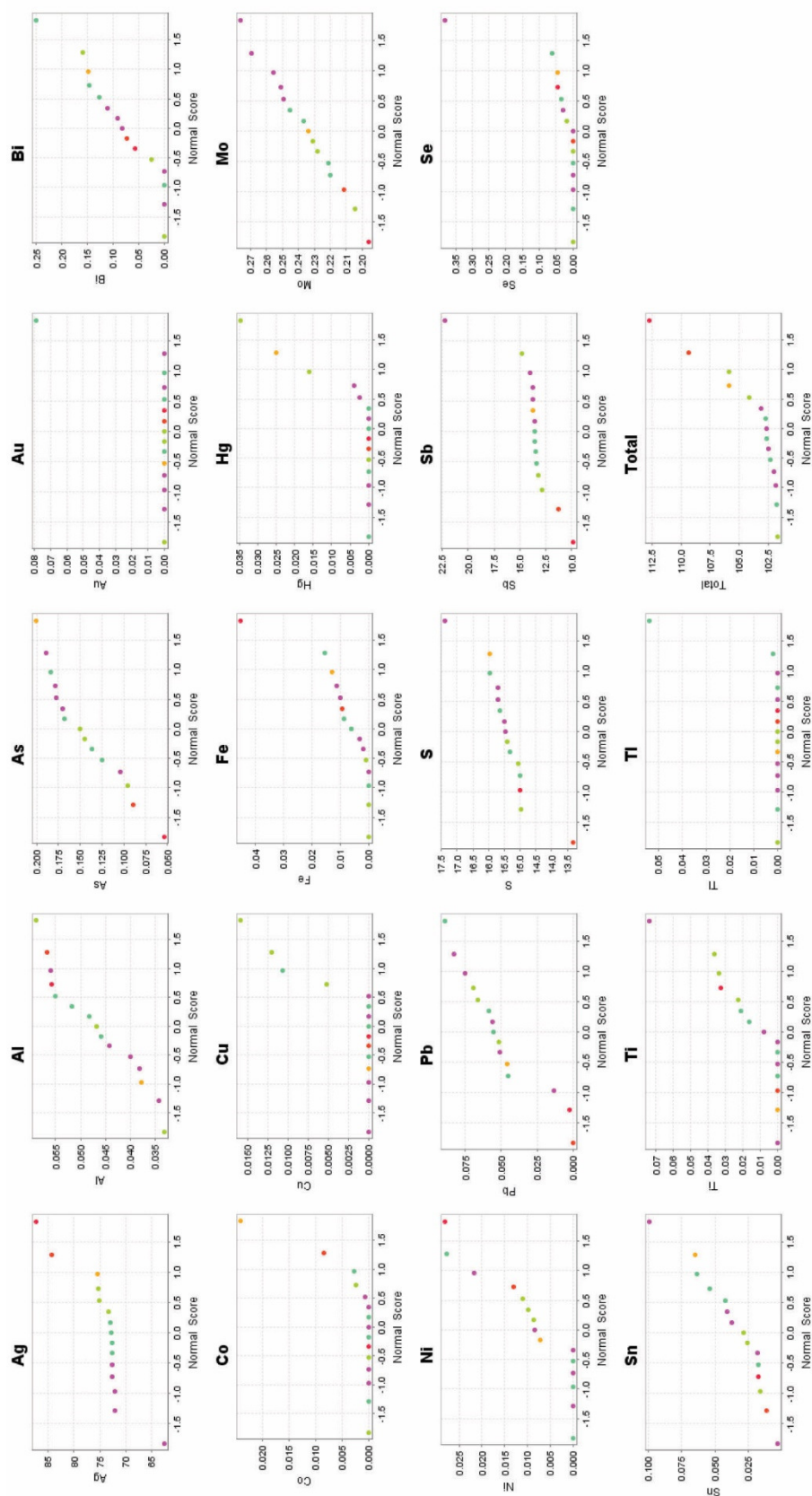
Appendix F.9: EPMA stephanite maps and data plots



Stephanite (Ag_5SbS) EPMA element maps. A) 12-01A 1226.5 thin section image, B and C) petrographic images of the mineral stephanite in thin section showing stephanite precipitating in vugs and dissolution veins on pre-ore barite and quartz, D) EPMA BSE map of thin section, bright white back scatter show distribution of pre-ore barite, E) EPMA Ag map showing the distribution of stephanite through the sample, F) EPMA Au map showing the distribution of Au in the sample. Average weight percent from EPMA analysis has a ratio of Ag: Sb: S consistent with the mineral stephanite. EPMA results are listed in table #.



X-Y plots of Ag vs. analytical elements for Stephanite. Note that elements are shown in wt. % with the exception of Ag and Au, which are shown in ppm. All Ca, Si, Te, W, and Zn data were not detected.



Comparative Probability plots of EPMA Stephanite data. Comparative probability plots normalize all data. Data that exhibit a linear relationship do not have multiple populations for the element plotted. These plots identify elements that may have multiple populations. All Ca, Si, Te, W, and Zn data were not detected.

No.	Comment	Se	Ag	Au	As	Hg	Tl	Si	Pb	Bi	Al	W
1715	12-01 1226.5 Agmin1	0.0000	73.2614	0.0000	0.1501	0.0161	0.0000	0.0000	0.0518	0.1596	0.0332	0.0000
1716	12-01 1226.5 Agmin pt2	0.0000	72.5771	0.0788	0.1682	0.0000	0.0000	0.0000	0.0583	0.1466	0.0459	0.0000
1717	12-01 1226.5 Agmin pt3	0.0000	72.0284	0.0000	0.1780	0.0000	0.0000	0.0000	0.0509	0.0823	0.0560	0.0000
1718	12-01 1226.5 Agmin pt4	0.0301	72.5454	0.0000	0.1705	0.0023	0.0000	0.0000	0.0132	0.1112	0.0442	0.0000
1719	12-01 1226.5 Agmin pt5	0.0000	72.0239	0.0000	0.1784	0.0000	0.0000	0.0000	0.0563	0.0912	0.0342	0.0000
1720	12-01 1226.5 Agmin pt6	0.0463	75.3837	0.0000	0.2004	0.0251	0.0000	0.0000	0.0459	0.1481	0.0378	0.0000
1721	12-01 1226.5 Agmin pt7	0.0000	72.6343	0.0000	0.1839	0.0000	0.0018	0.0000	0.0890	0.2502	0.0517	0.0000
1722	12-01 1226.5 Agmin pt8	0.0000	75.1600	0.0000	0.0957	0.0347	0.0000	0.0000	0.0691	0.0254	0.0589	0.0000
1723	12-01 1226.5 Agmin pt9	0.0175	75.3484	0.0000	0.1449	0.0000	0.0000	0.0000	0.0664	0.0000	0.0467	0.0000
1724	12-01 1226.5 Agmin pt10	0.0000	84.2542	0.0000	0.0893	0.0000	0.0000	0.0000	0.0000	0.0724	0.0567	0.0000
1725	12-01 1226.5 Agmin pt11	0.0446	87.2810	0.0000	0.0538	0.0000	0.0000	0.0000	0.0022	0.0560	0.0558	0.0000
1726	12-01 1226.5 Agmin pt12	0.0350	72.7280	0.0000	0.1247	0.0000	0.0536	0.0000	0.0450	0.1271	0.0550	0.0000
1727	12-01 1226.5 Agmin pt13	0.3806	62.5622	0.0000	0.1890	0.0000	0.0000	0.0000	0.0831	0.0000	0.0382	0.0000
1728	12-01 1226.5 Agmin pt14	0.0614	72.8842	0.0000	0.1366	0.0000	0.0000	0.0000	0.0551	0.0000	0.0482	0.0000
1729	12-01 1226.5 Agmin pt15	0.0000	72.5731	0.0000	0.1043	0.0040	0.0000	0.0000	0.0751	0.0000	0.0400	0.0000

No.	Cu	Zn	Te	Ni	Sb	Co	Sn	Ti	Mo	Fe	Ca	S	Total
1715	0.0159	0.0000	0.0000	0.0087	12.8755	0.0000	0.0256	0.0225	0.2043	0.0000	0.0000	14.9618	101.7865
1716	0.0107	0.0000	0.0000	0.0000	13.4584	0.0000	0.0538	0.0162	0.2201	0.0061	0.0000	15.9526	102.7928
1717	0.0000	0.0000	0.0000	0.0000	13.7853	0.0000	0.0179	0.0075	0.2508	0.0030	0.0000	15.4575	101.9176
1718	0.0000	0.0000	0.0000	0.0084	13.7392	0.0007	0.0411	0.0000	0.2558	0.0101	0.0000	15.7113	102.6835
1719	0.0000	0.0000	0.0000	0.0218	13.5483	0.0000	0.0373	0.0737	0.2761	0.0112	0.0000	15.7132	102.0656
1720	0.0000	0.0000	0.0000	0.0072	13.7242	0.0240	0.0647	0.0000	0.2335	0.0130	0.0000	15.9723	105.9262
1721	0.0000	0.0000	0.0000	0.0000	13.5478	0.0027	0.0176	0.0212	0.2453	0.0154	0.0000	15.6417	102.7026
1722	0.0120	0.0000	0.0000	0.0099	14.7866	0.0024	0.0287	0.0337	0.2310	0.0000	0.0000	15.4137	105.9618
1723	0.0052	0.0000	0.0000	0.0111	13.2467	0.0000	0.0157	0.0363	0.2281	0.0009	0.0000	15.0510	104.2189
1724	0.0000	0.0000	0.0000	0.0131	11.3048	0.0084	0.0115	0.0000	0.2115	0.0093	0.0000	13.3249	109.3561
1725	0.0000	0.0000	0.0000	0.0281	9.8876	0.0000	0.0174	0.0325	0.1960	0.0452	0.0000	15.0019	112.7021
1726	0.0000	0.0000	0.0000	0.0278	13.3921	0.0000	0.0423	0.0000	0.2210	0.0000	0.0000	15.0038	101.8554
1727	0.0000	0.0000	0.0000	0.0000	22.2106	0.0000	0.0990	0.0000	0.2692	0.0019	0.0000	17.3792	103.2130
1728	0.0000	0.0000	0.0000	0.0000	13.5312	0.0000	0.0634	0.0000	0.2366	0.0088	0.0000	15.3315	102.3570
1729	0.0000	0.0000	0.0000	0.0000	14.0207	0.0000	0.0032	0.0000	0.2491	0.0000	0.0000	15.5071	102.5766

Appendix F.10: EPMA data

See digital attachment for EPMA data.

APPENDIX G

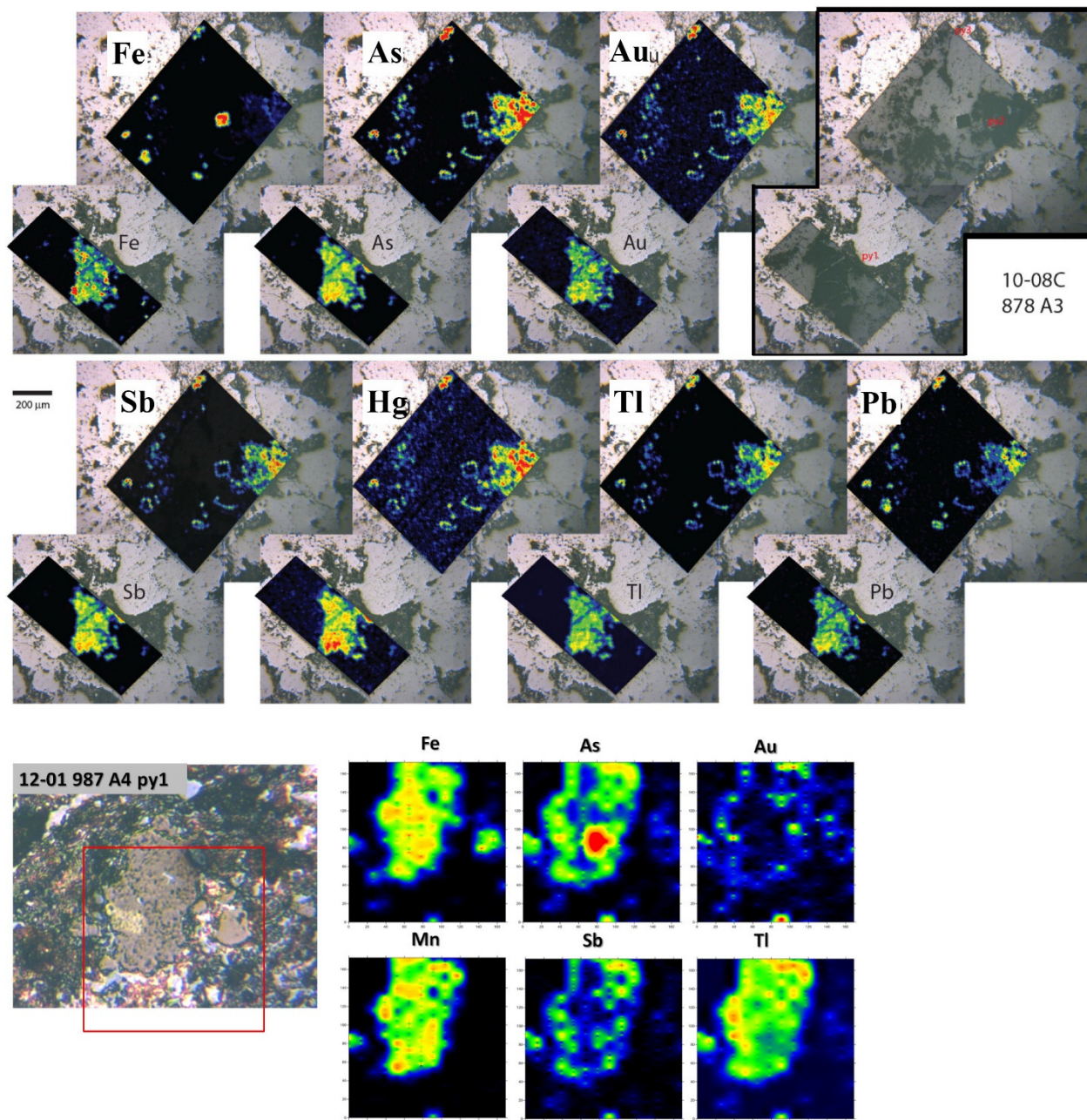
LA-ICP-MS DATA

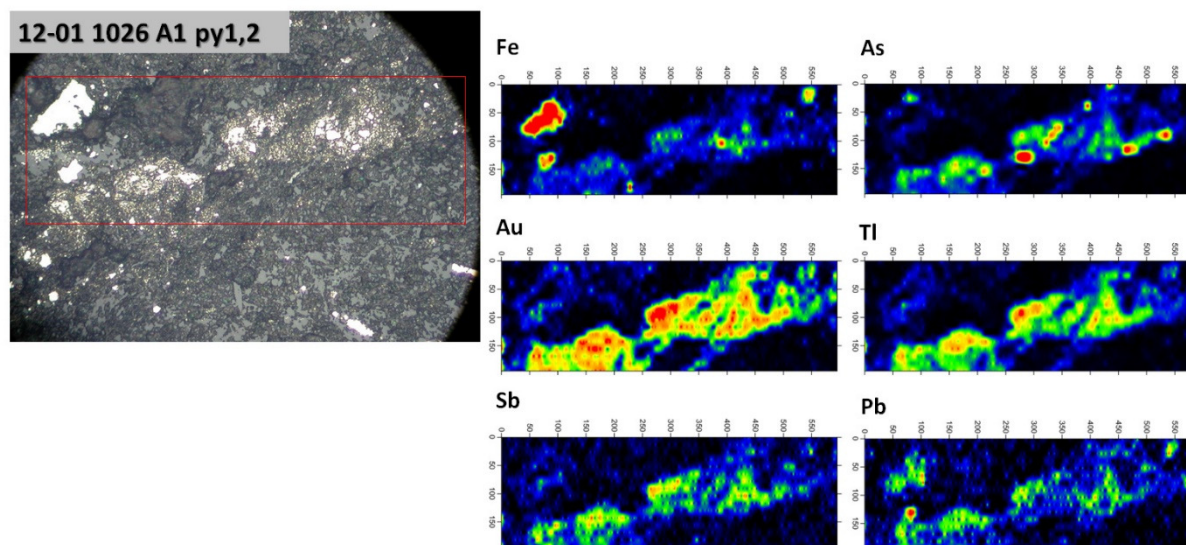
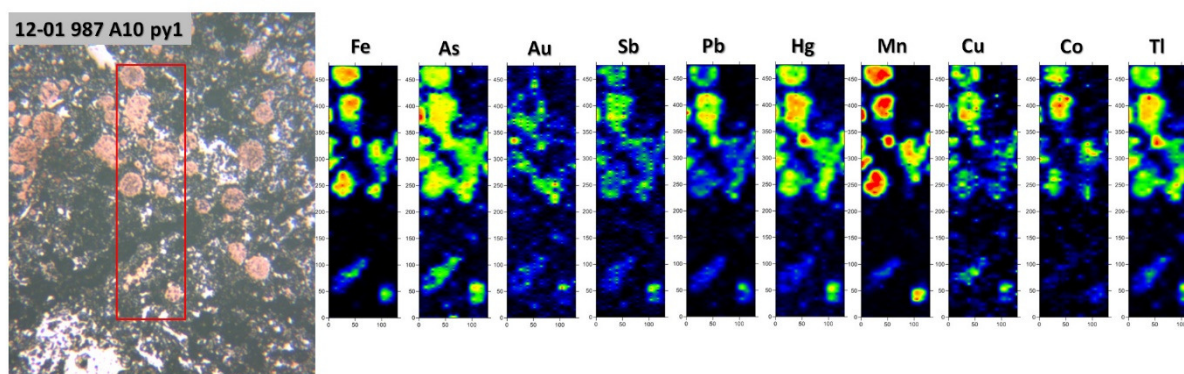
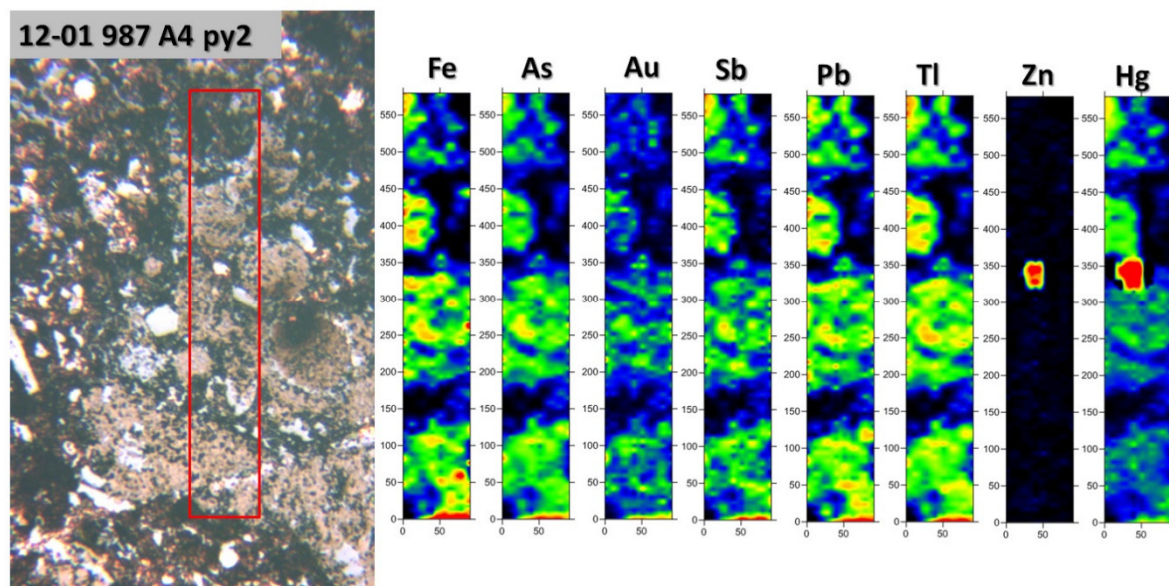
Eight samples were analyzed using laser ablation, inductively-coupled plasma, mass spectrometry (LA-ICP-MS) and processed at the United States Geological Survey laboratory in Denver, Colorado. LA-ICP-MS settings are provided in Table 4. Appendix G.1 provides analyzed polished section numbers, host rock, gold grade, target name, LA-ICP-MS map name, length of the map lines in μm , number of lines within the map, the line spacing between the lines in μm , and the spot size of the laser in μm . Appendix G.2 provides images of all processed maps.

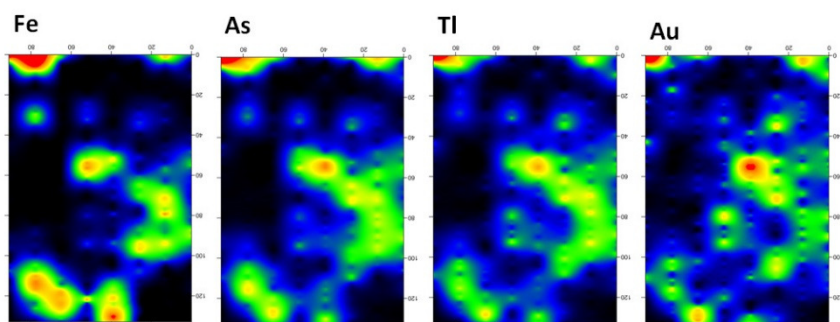
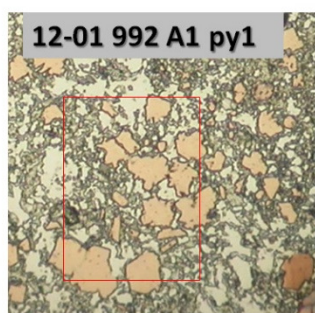
Appendix G.1

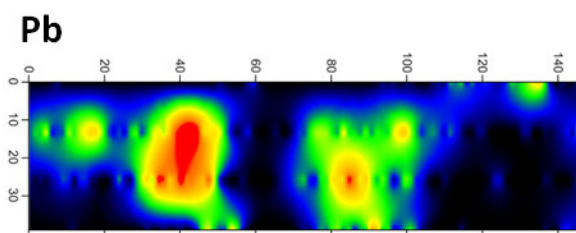
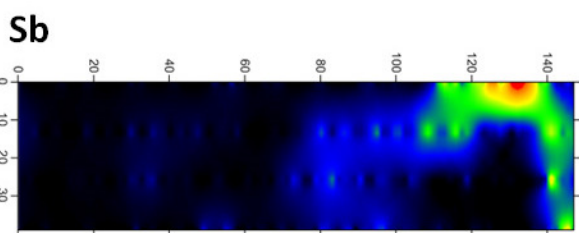
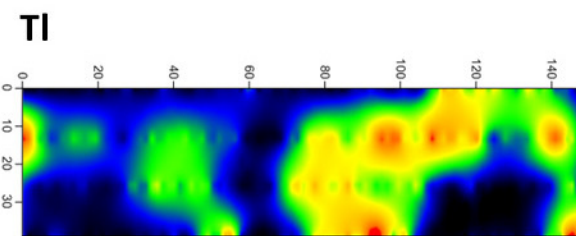
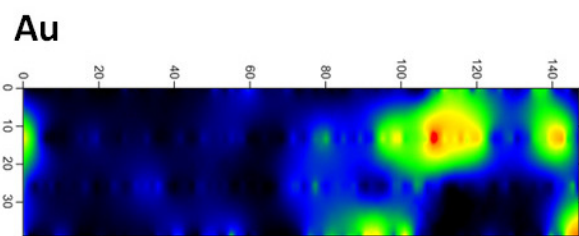
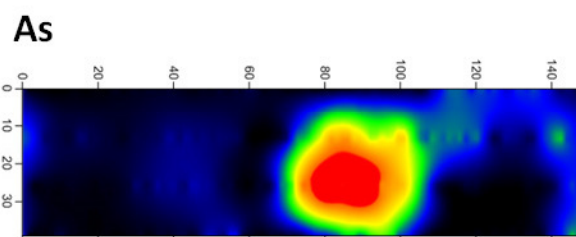
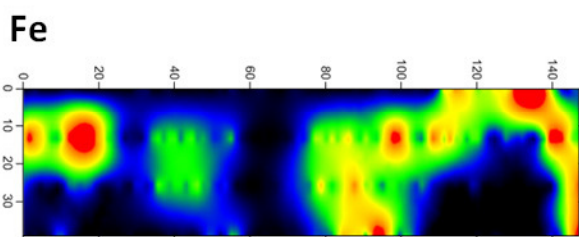
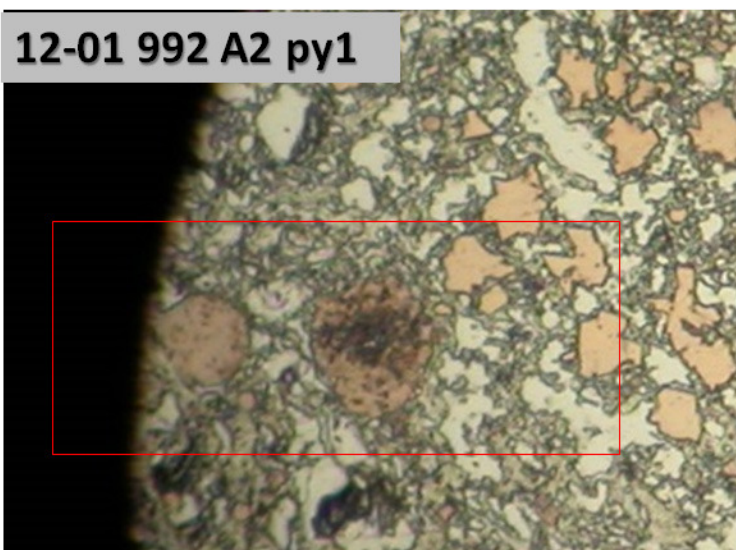
Thin Section	Host Rock	Gold (ppm)	Target	LAICPMS name	Line Length (um)	# of Lines	Line Spacing (um)	Spot size (um)
12-01A 987	Ms	20.8	A4py1	Map5	214	14	13	12
12-01A 987	Ms	20.8	A4py2	Map7	60	8	13	12
12-01A 987	Ms	20.8	A10Py1	Map 6	480	11	13	12
12-01A 992	Ms	25.7	A1py1	Map 22	140	8	13	12
12-01A 992	Ms	25.7	A2py1	Map 23	150	4	13	12
12-01A 992	Ms	25.7	A6py1	Map 24	425	9	13	12
12-01A 992	Ms	25.7	A8py1	Map 25	260	7	13	12
12-10 803	MLBxa	30.2	A7py2	Map 16	610	25	13	12
12-01A 1026B	Ms	15.65	A1py1 and 2	Map 21	600	21	13	12
13-08 1164	MLBxa	14.5	A1py1	Map 8	240	12	13	12
13-08 1164	MLBxa	14.5	A2py2	Map9	340	10	13	12
13-08 1113.5	Micrite	13.9	A1.2py1	Map 19	360	10	13	12
12-13 379	ML Bxa	1.365	A6py2	Map13	240	8	13	12
12-13 379	ML Bxa	1.365	A6py3	Map14	190	10	13	12
12-13 379	ML Bxa	1.365	A1py1	Map 10	240	7	13	12
10-08C 878.5	Ss	1.44	A3py1 and3	Map 26,27	1860	50	13	12

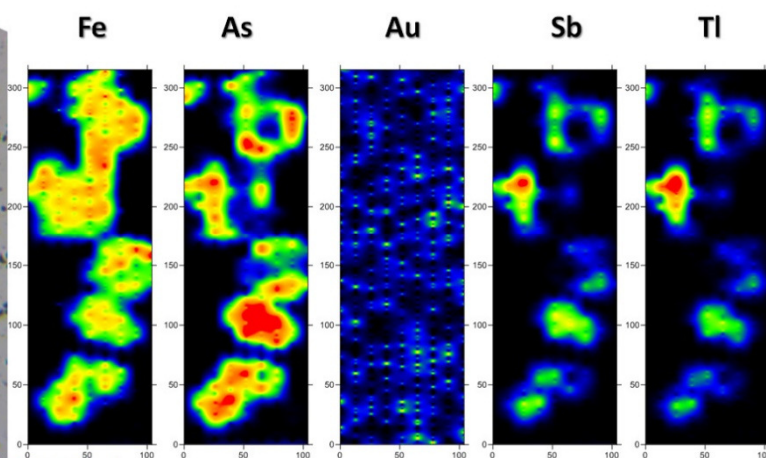
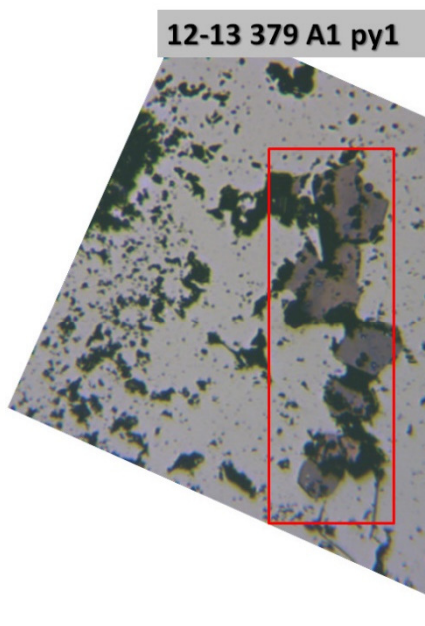
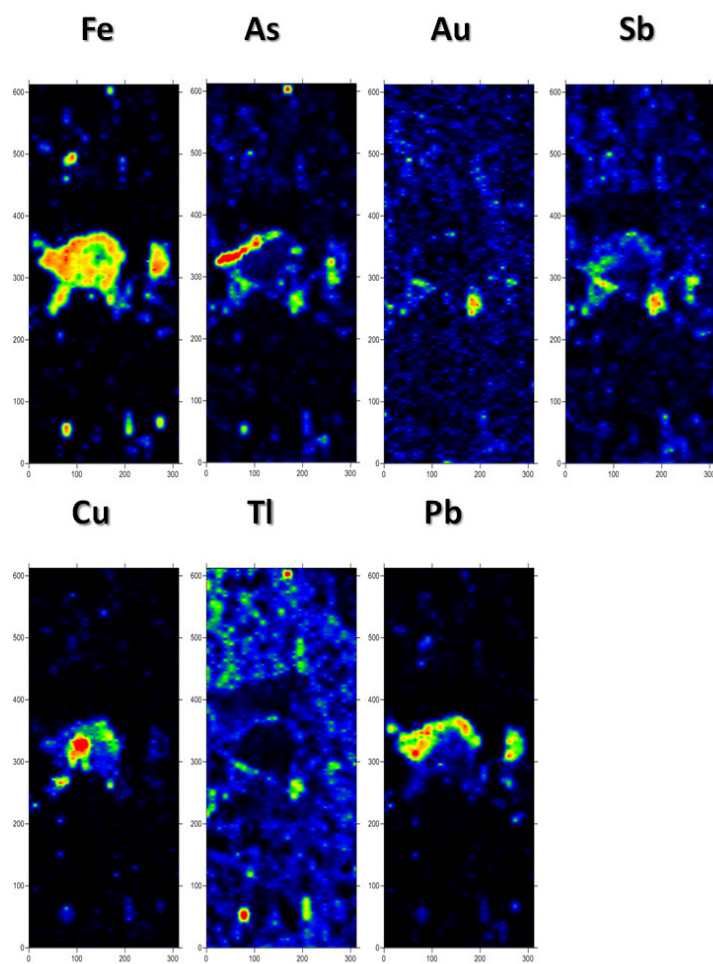
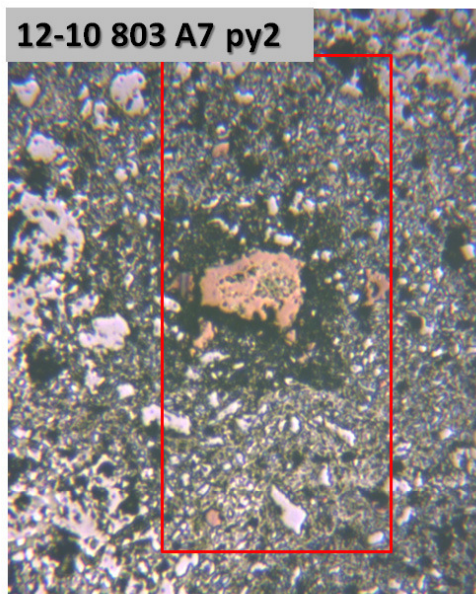
Appendix G.2

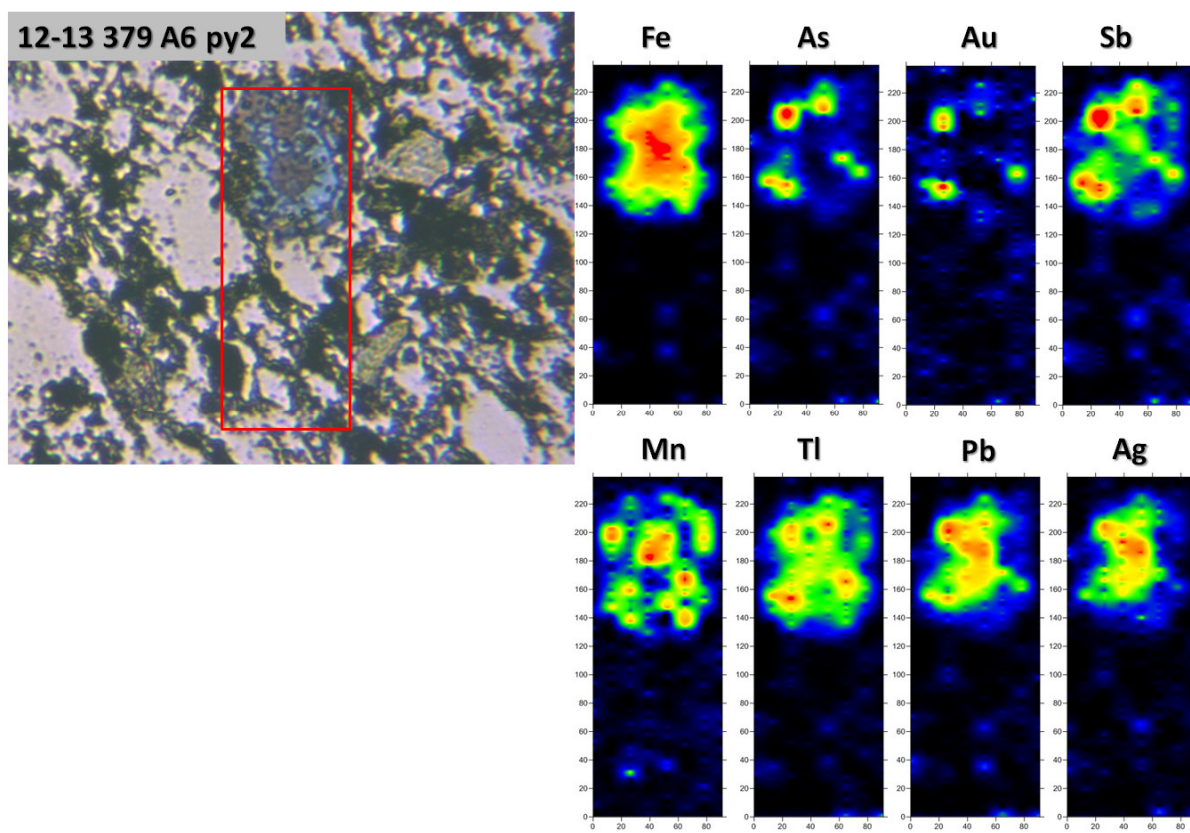


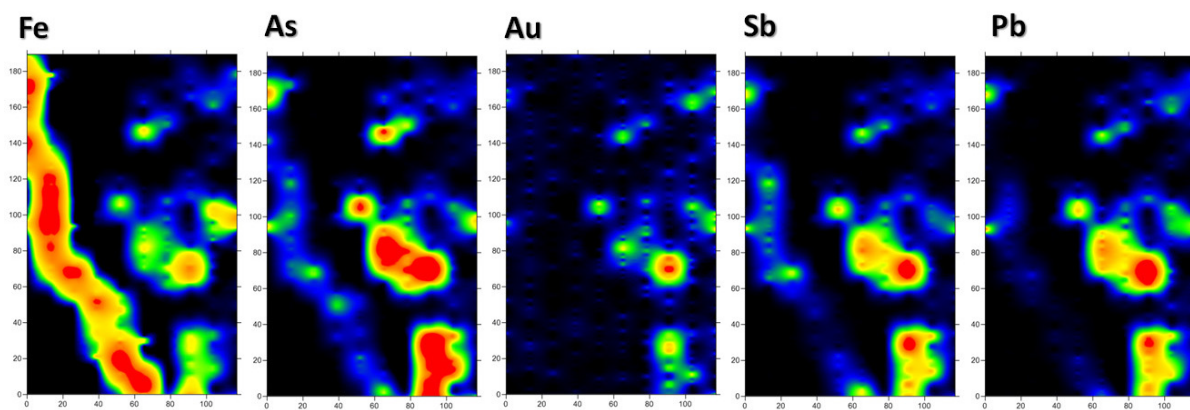
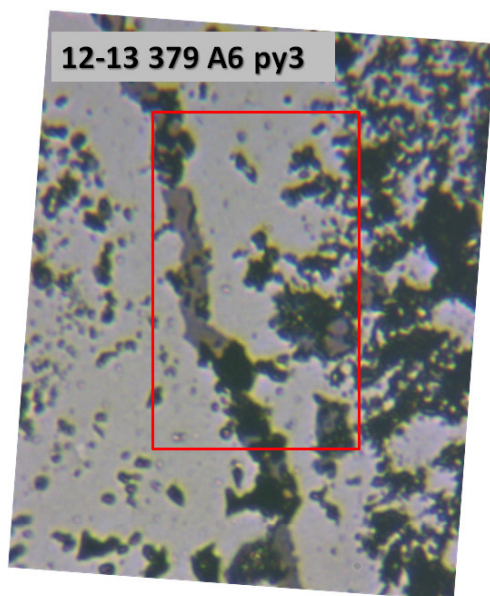


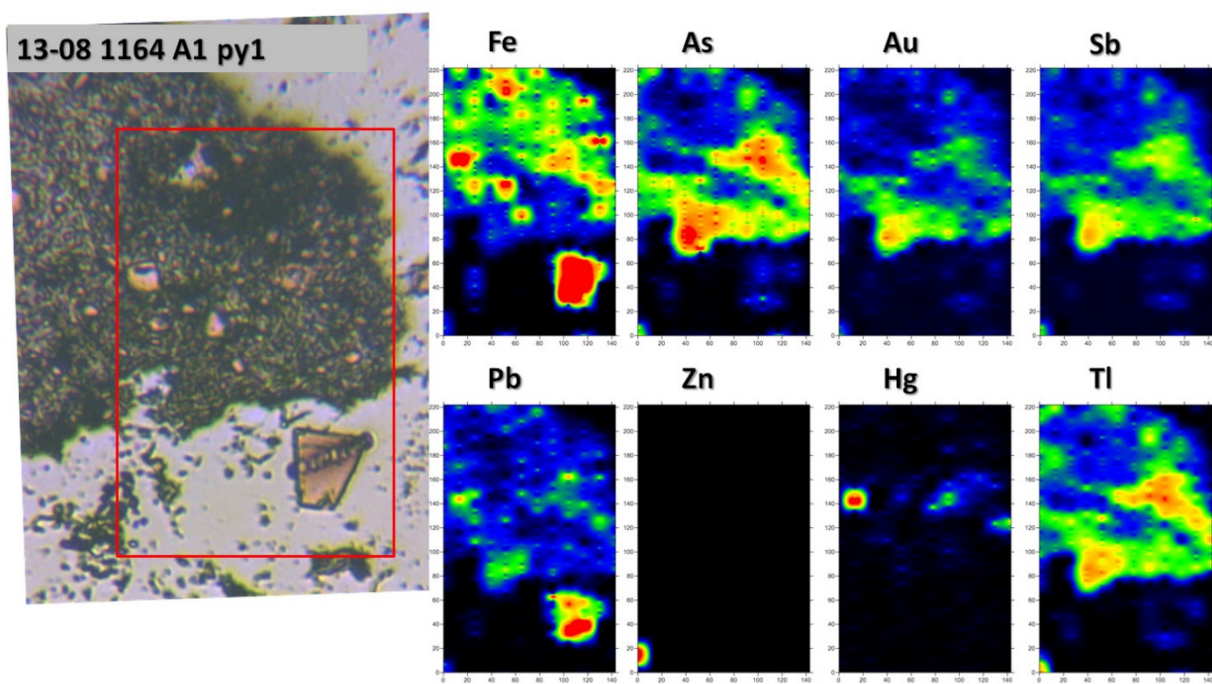


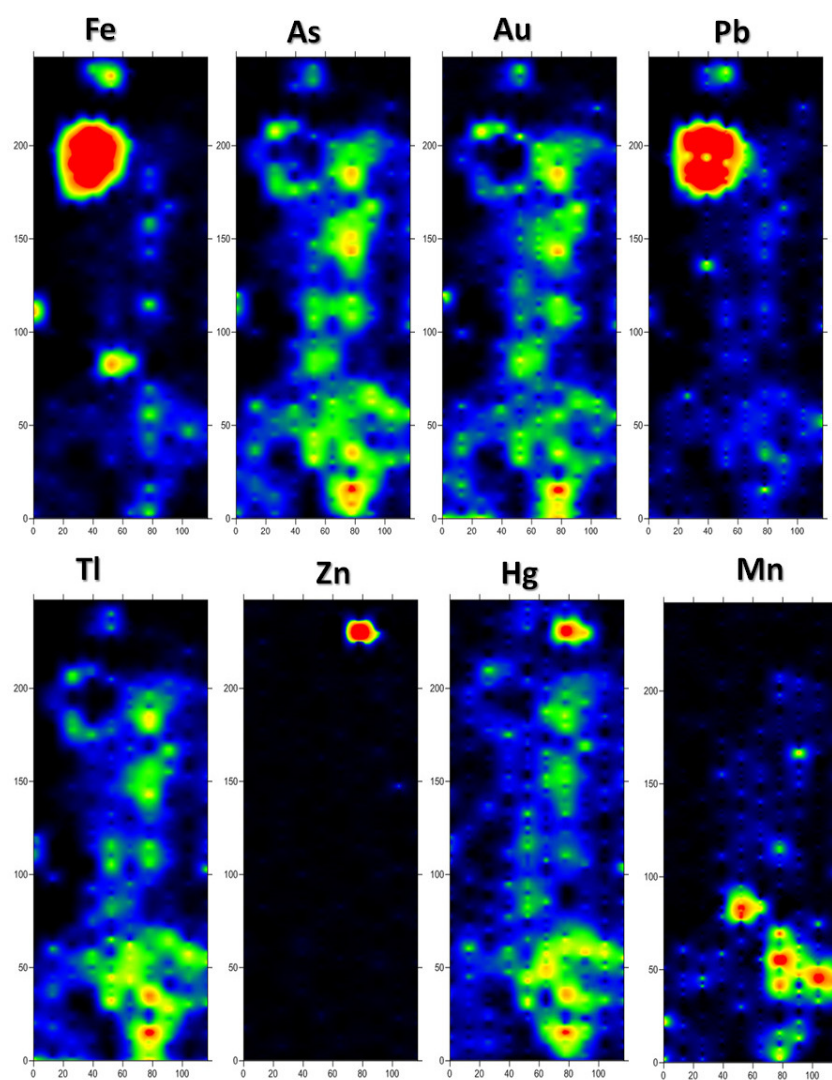
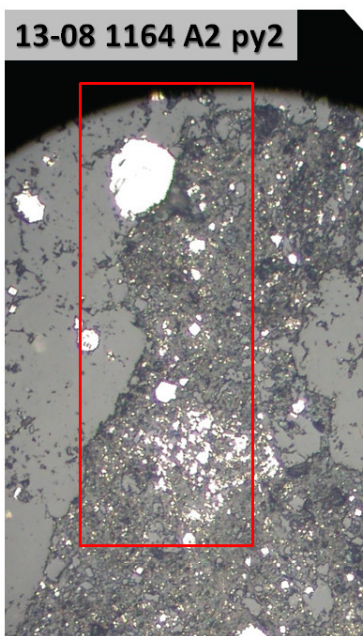


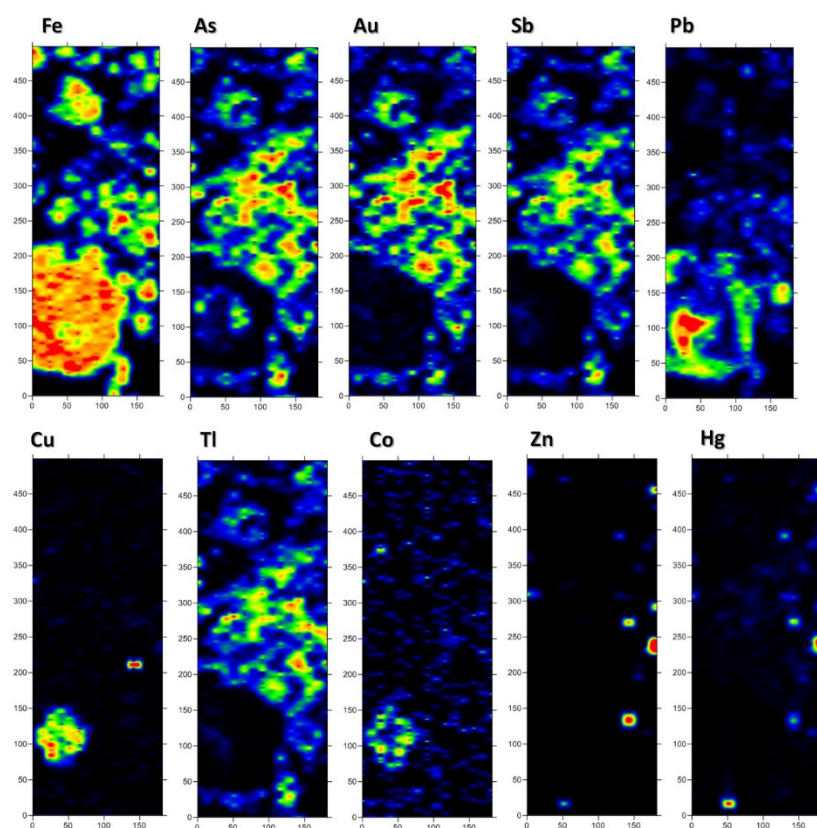
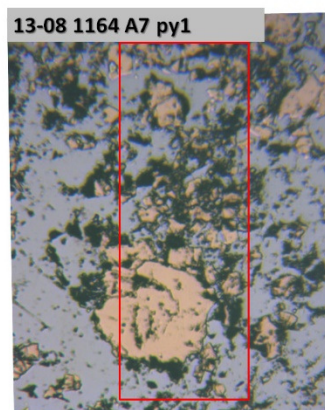












APPENDIX H

XRD DATA

Forty-five samples were crushed to a fine powder using a tungsten carbide shatter box and sieved at 250 mesh. Samples were analyzed using a PANalytical X'PERT Pro X-ray Diffraction Spectrometer at the UNLV XRD/XRF laboratory XRD settings are listed in Table 5. X'Pert Highscore Plus and Crystal Sleuth software were used to interpret the raw XRD patterns. Appendix H.1 lists the samples analyzed and provides drill hole #, footage, gold grade (ppm), lithology, sample weight without and with the 5 wt. % silica standard, and identifies samples that contain the silica standard. Appendix H.2 provides the reference intensity ratio (RIR) values for detected minerals, RIR reference code, and reference. RIR values are used to calculate the semi-quantitative weight percent of minerals analyzed within each sample. For some minerals such as dolomite, multiple RIR values were used. Appendix H.3 lists the samples, minerals detected and their calculated weight percent for each sample. Appendix H.4 displays the XRD patterns and the interpreted minerals present within each sample.

Appendix H.1: XRD Sample List

Hole ID #	Footage	Au (ppm)	Lithology Description	Sample Weight (g)	Weight with standard	STD %	STD
10-08C	496	0.009	ss bxa	0.9501	1.0001	5	y
10-08C	896	2.98	ss	0.9501	1.0001	5	y
10-08C	1131.9	2.6	mdst bxa	0.9501	1.0001	5	y
11-03.	765.9	0.617	stms(70) ss(30) bx	0.95	1	5	n
11-03.	770.5	0.386	Dol bx	0.95	1	5	n
11-03.	956	1.085	Jasp	0.95	1	5	n
11-03.	1023.5	4.11	Stms bxa	0.9501	1.0001	5	n
11-03.	1457	0.142	Dolo(Lmst) Bxa	0.95	1	5	n
11-4	1003.5	0.011	ss	0.95	1	5	y
11-4	1059	0.034	mdst Bxa	0.9501	1.0001	5	y
11-4.	1526.5	0.006	Dol/ Dol bxa	0.9501	1	4.99	n
11-16.	559.8	0.742	ss	0.95	1	5	n
11-16.	589	6.83	ss	0.95	1.0001	5.01	y
11-16.	592	14.65	mdst bxa	0.95	1.0001	5.01	y
11-16.	1332.5	0.401	sulf dolo bxa	0.95	1	5	n
12-01A	970.9	2.53	Mic>ms	0.95	1	5	y
12-01A	987	20.8	Ms	0.95	1.0001	5.01	y
12-01A	1022	7.76	LS, Ms (Tp)	0.9501	1.0001	5	y
12-01A	1226.5	0.42	ms>ss	0.95	1	5	n
12-05.	921.9	0.253	ss(90) ms(10)	0.9501	1.0001	5	n
12-05.	1042	0.294	Stmic	0.9501	1.0001	5	y
12-05.	1651.9	0.115	ML Bx (Dol>ms)	0.9501	1.0001	5	n
12-05.	1989	0.126	Dol Bx	0.9501	1.0001	5	n
12-10.	340	0.008	stms(70) ss(30)	0.9501	1.0001	5	n
12-10.	525.9	0.006	stmic(Tp)	0.95	1	5	y
12-10.	712	0.009	stms(65) ls(30) ss(5)	0.9501	1.0001	5	y

Hole ID #	Footage	Au (ppm)	Lithology Description	Sample Weight (g)	Weight with standard	STD %
12-10.	716	4.41	stms(65) ls(30) ss(5)	0.95	1	5
12-10.	776	16.2	stms, ls, ss	0.95	1	5
12-10.	803	30.2	ML bxa	0.9501	1.0001	5
12-10.	1044	1.71	ML bxa	0.95	1	5
12-10.	1755	0.368	ML bxa- Dol>>stms	0.9501	1.0001	5
12-11.	586.5	0.257	ML bxa	0.95	1	5
12-11.	647	7.75	stms (90) dol(10)	0.9501	1.0001	5
12-11.	1148.5	0.695	ss(70) ms(30)	0.95	1	5
12-11.	1343.5	0.706	Dol	0.9501	1.0001	5
12-13 (V)	1047.5	1.465	ss(75)ms(25)	0.95	1	5
12-13 (V)	1070	0.375	LS(60)ss(30)ms(10)	0.9501	1.0001	5
12-13 (V)	1152	0.382	Car>tr ms bxa	0.95	1	5
12-18.	1159	0.256	ML bxa	0.95	1.0001	5.01
12-18.	1190.5	0.034	Mic/ calc (ddg)	0.9501	1.0001	5
13-08.	1087	0.186	stms-ss	0.95	1	5
13-08.	1101.5	3.79	stms-ss	0.95	1	5
13-08.	1113.5	13.9	micrite	0.95	1	5
13-08.	1152.5	0.403	ML bxa	0.9501	1.0001	5
13-08.	1164	14.5	ML Bxa	0.95	1	5

Appendix H.2: RIR values and RIR references

Reference code:	Mineral:	RIR:
01-079-1910	Quartz	3.07
01-071-1680	Pyrite	0.89
01-080-0886	Kaolinite	1.08
01-078-1996	Kaolinite	1.12
01-075-0938	Kaolinite	1.05
01-076-0606	Aragonite	1.14
01-073-2361	Dolomite	2.47
01-084-1208	Dolomite	2.51
01-074-1022	Halloysite	1.37
01-083-1762	Calcite	3.25
01-083-0578	Calcite	3.21
01-086-0740	Hydroxylapatite	1.04
01-075-0589	Silicon	4.55

Quartz: **1910** - Calculated from ICSD using POWD-12++, (1997)

Hazen, R.M., Finger, L.W., Hemley, R.J., Mao, H.K., *Solid State Commun.*, **72**, 507, (1989)

Pyrite: **1680** - Calculated from ICSD using POWD-12++, (1997)

Bayliss, P., *Am. Mineral.*, **62**, 1168, (1977)

Kaolinite: **0886** - Calculated from ICSD using POWD-12++, (1997)

El-Sayed K., Heiba, Z.K., Abdel-Rahman, A.M., *Cryst. Res. Technol.*, **25**, 305, (1990)

Kaolinite: **1996** - Calculated from ICSD using POWD-12++, (1997)

Bish, D.L., Von Dreele, R.B., *Clays Clay Miner.*, **37**, 289, (1989)

Kaolinite: **0938** - Calculated from ICSD using POWD-12++

Gruner, W.J., *Z. Kristallogr., Kristallgeom., Kristallphys., Kristallchem.*, **83**, 75, (1932)

ARAG: **0606** - Calculated from ICSD using POWD-12++, (1997)

Dickens, B., Bowen, J.S., *J. Res. Natl. Bur. Stand., Sect. A*, **75**, 27, (1971)

Dolomite: **2361** - Calculated from ICSD using POWD-12++

Reeder, R.J., Markgraf, S.A., *Am. Mineral.*, **71**, 795, (1986)

Dolomite: **1208** - Calculated from ICSD using POWD-12++, (1997)

Miser, D.E., Swinnea, J.S., Steinfink, H., *Am. Mineral.*, **72**, 188, (1987)

Halloysite: **1022** - *Calculated from ICSD using POWD-12++*, (1997)

Mehmel, M., *Z. Kristallogr., Kristallgeom., Kristallphys., Kristallchem.*, **90**, 35, (1935)

Calcite: **1762** - *Calculated from ICSD using POWD-12++*, (1997)

Effenberger, H., Mereiter, K., Zemmann, J., *Z. Kristallogr.*, **156**, 233, (1981)

Calcite: **0578** - *Calculated from ICSD using POWD-12++*, (1997)

Wartchow, R., *Z. Kristallogr.*, **186**, 300, (1989)

Hydroxylapatite: **0740** - *Calculated from ICSD using POWD-12++*, (1997)

Tomita, K., Kawano, M., Shiraki, K., Otsuka, H., *J. Mineral. Petrol. Econ. Geol.*, **91**, 11, (1996)

Silicon standard: 0589 - *Calculated from ICSD using POWD-12++*, (1997)

Bond, W.L., Kaiser, W., *J. Phys. Chem. Solids*, **16**, 44, (1960)

Reference Intensity Ratio (RIR) is a general, instrument-independent constant for use in quantitative phase analysis by the X-ray powder diffraction internal standard method. When the reference standard is corundum, RIR is known as I/I_c (

Powder Diffraction / Volume 3 / Issue 02 / June 1988, pp 74-77

RIR - Measurement and Use in Quantitative XRD

Camden R. Hubbard^{a1} and Robert L. Snyder^{a2}

^{a1} Ceramics Division, National Bureau of Standards, Gaithersburg, Maryland 20899, U.S.A.

^{a2} New York State College of Ceramics, Alfred University, Alfred, New York 14802, U.S.A.

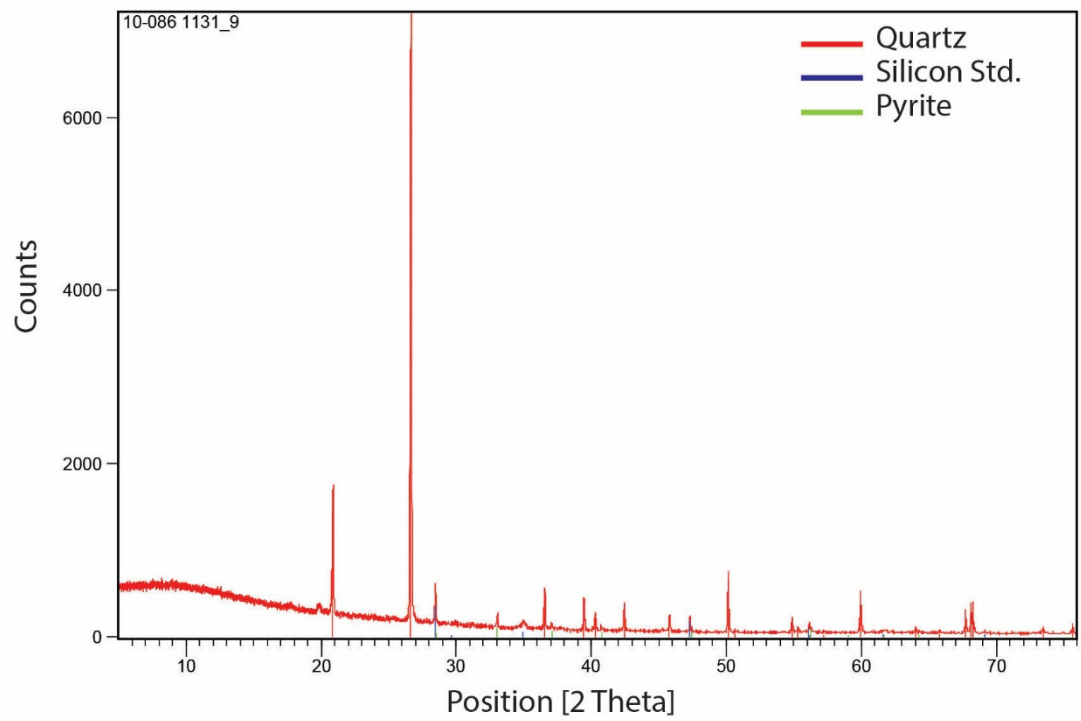
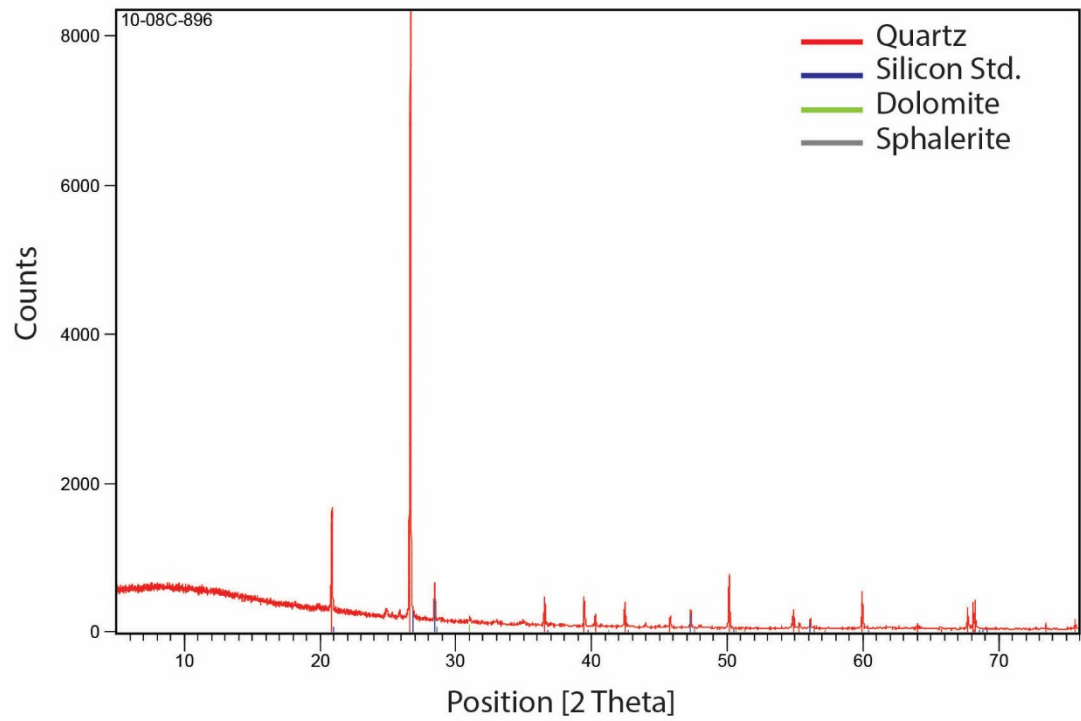
Appendix H.3: Data Summary Table

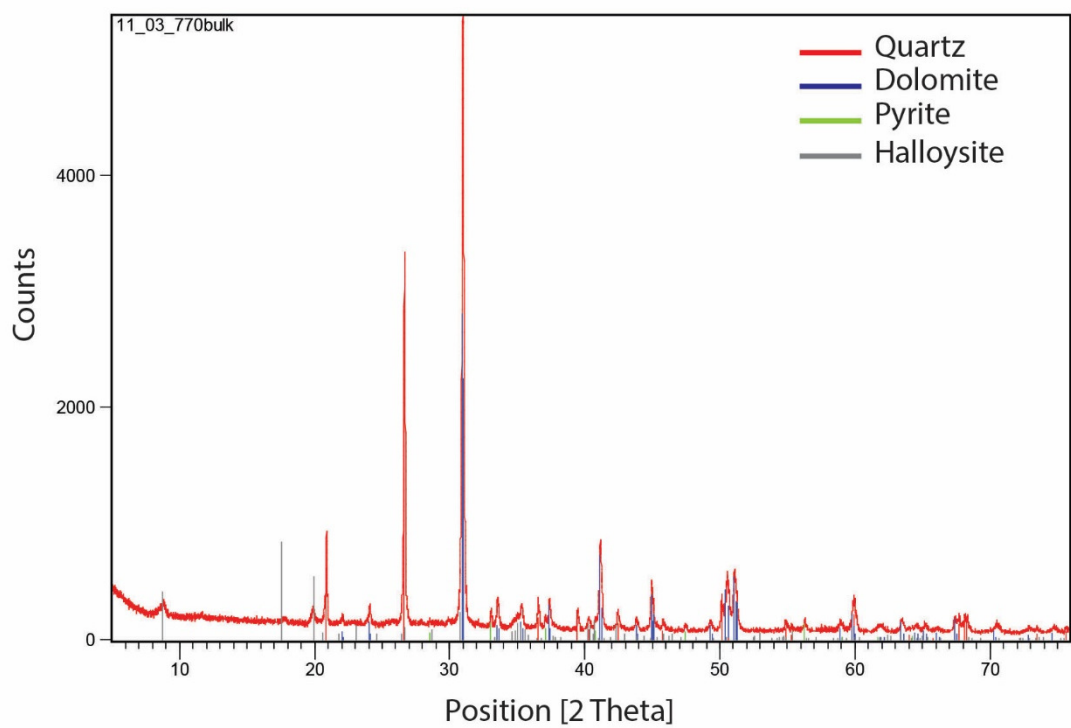
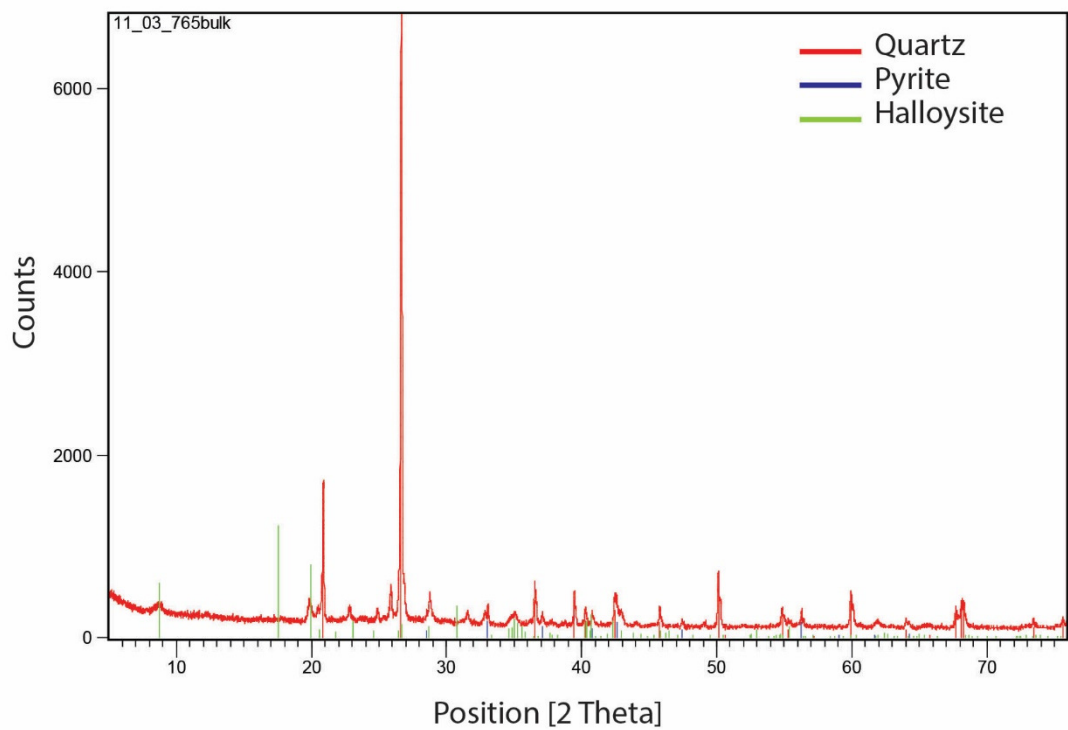
Hole ID #	Footage	STD (0589) wt. %	Qtz (1910) wt. %	Dol (2361) wt. %	Dol (1208) wt. %	Cc (1762) wt. %	Cc (0578) wt. %
10-08C	496		98		2		
10-08C	896	4	96	X			
10-08C	1132	3	92				
11-03.	765.9		64				
11-03.	770.5		33	40			
11-03.	956		82	12			
11-03.	1024		70				
11-03.	1457		62	33			
11-04.	1004	3	90	2			
11-04.	1059	3	86		6		3
11-04.	1527		1	85		15	
11-16.	559.8		90	3		3	
11-16.	589	4	87				4
11-16.	592	2	91				4
11-16.	1333		32	65			
12-01A	970.9	5	62	26			
12-01A	987	5	87			3	
12-01A	1022	9	13	3		75	
12-01A	1226		97				
12-05.	921.9		84			6	
12-05.	1042	5	23	62			6
12-05.	1651.9		21	79			
12-05.	1989			78			
12-10.	340		74		4		
12-10.	525.9	7	32				60
12-10.	712	6	52	6			30
12-10.	716	7	70		4	20	
12-10.	776	6	69				17
12-10.	803	5	73	17			
12-10.	1044	4	64				
12-10.	1755		26	39			
12-11.	586.5		76				
12-11.	647	5	85				
12-11.	1149		76				
12-11.	1344		19	81			
STD= Standard; Qtz= quartz; Dol= Dolomite; Cc= Calcite; Py= Pyrite; Kaol=kaolinite; Hall=Halloysite; Ara=Aragonite; Apa=Hydroxylapatite. X= indicates mineral present, but not calculated for wt. %.							

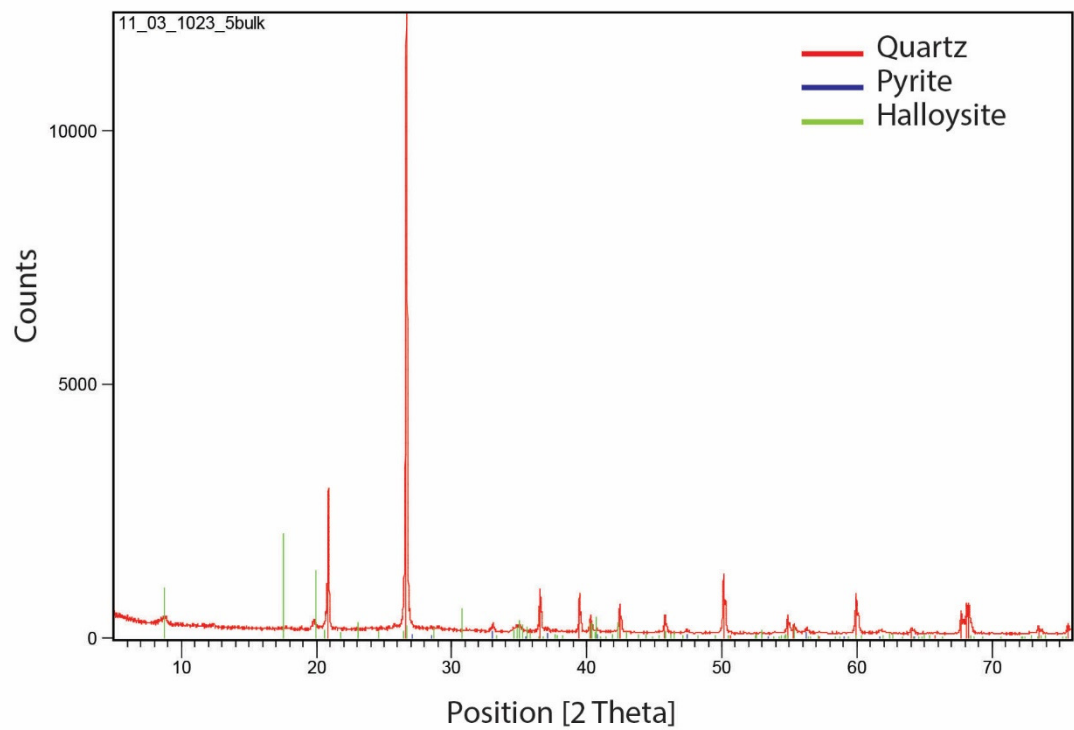
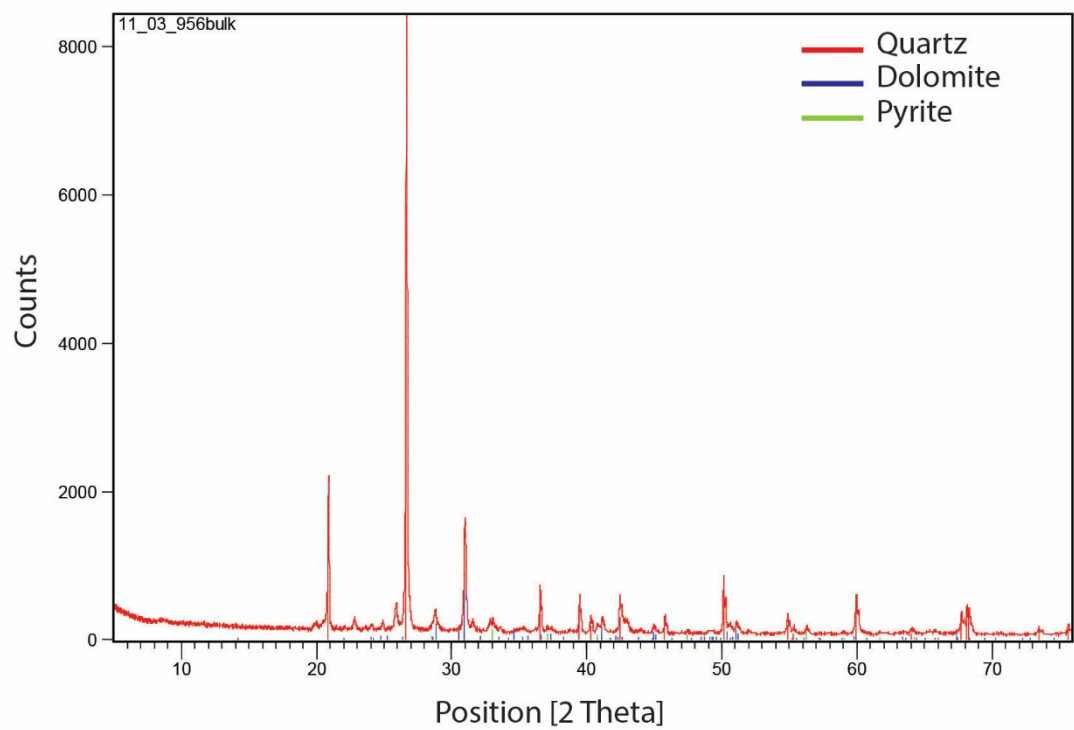
Hole ID #	Footage	Py (1680) wt. %	Kaol (0886) wt. %	Kaol (1996) wt. %	Kaol (0938) wt. %	Hall (1022) wt. %	Ara (0606) wt. %	Apa (0740) wt. %
10-08C	496							
10-08C	896							
10-08C	1132	4						
11-03.	765.9	7				29		
11-03.	770.5	6				22		
11-03.	956	6						
11-03.	1024	3				28		
11-03.	1457	5						
11-04.	1004	4						
11-04.	1059	3						
11-04.	1527							
11-16.	559.8	4						
11-16.	589	4						
11-16.	592	3						
11-16.	1333	3						
12-01A	970.9	6						
12-01A	987	6						
12-01A	1022							
12-01A	1226	3						
12-05.	921.9	3		6				
12-05.	1042	4						
12-05.	1651.9							
12-05.	1989	5						17
12-10.	340					22		
12-10.	525.9							
12-10.	712	6						
12-10.	716							
12-10.	776	8						
12-10.	803	6						
12-10.	1044	32						
12-10.	1755	6			9	20		
12-11.	586.5	24						
12-11.	647	9						
12-11.	1149	11	10				3	
12-11.	1344							
STD= Standard; Qtz= quartz; DoI= Dolomite; Cc= Calcite; Py= Pyrite; Kaol=kaolinite; Hall=Halloysite; Ara=Aragonite; Apa=Hydroxylapatite. X= indicates mineral present, but not calculated for wt. %.								

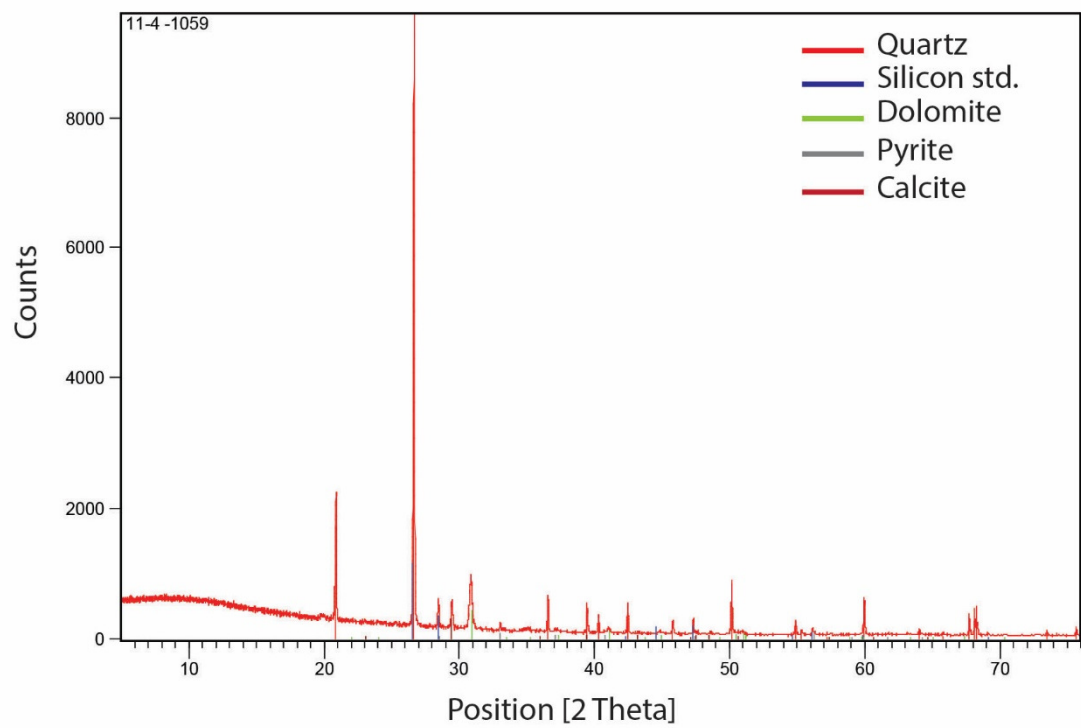
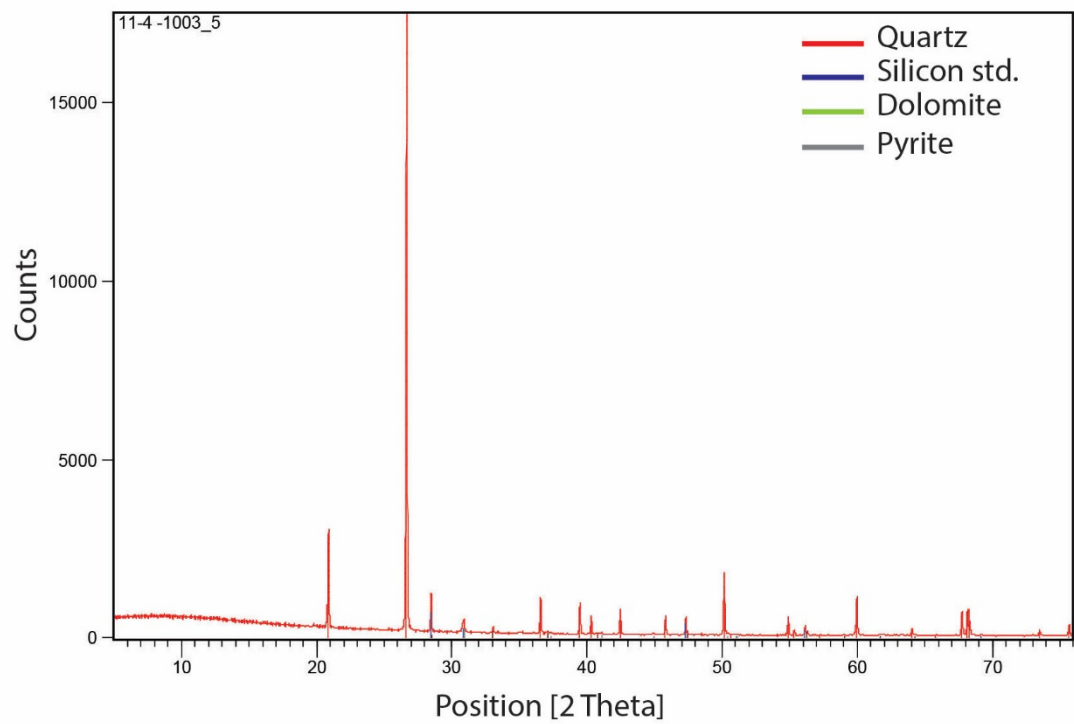
Hole ID #	Footage	STD (0589) wt. %	Qtz (1910) wt. %	Dol (2361) wt. %	Dol (1208) wt. %	Cc (1762) wt. %	Cc (0578) wt. %	
12-13.	1048		83			13		
12-13.	1070	3	93					
12-13.	1152		22			78		
12-18.	1159	3	60	28			3	
12-18.	1190.5	4	11		7		79	
13-08.	1087	7	93					
13-08.	1102	4	79				17	
13-08.	1114	5	89					
13-08.	1152.5	4	91		2			
13-08.	1164	5	77					
		Py (1680) wt. %	Kaol (0886) wt. %	Kaol (1996) wt. %	Kaol (0938) wt. %	Hall (1022) wt. %	Ara (0606) wt. %	Apa (0740) wt. %
12-13.	1048	4						
12-13.	1070	3						
12-13.	1152							
12-18.	1159	6						
12-18.	1191							
13-08.	1087							
13-08.	1102							
13-08.	1114	6						
13-08.	1153	4						
13-08.	1164	17						
STD= Standard; Qtz= quartz; Dol= Dolomite; Cc= Calcite; Py= Pyrite; Kaol=kaolinite; Hall=Halloysite; Ara=Aragonite; Apa=Hydroxylapatite. X= indicates mineral present, but not calculated for wt. %.								

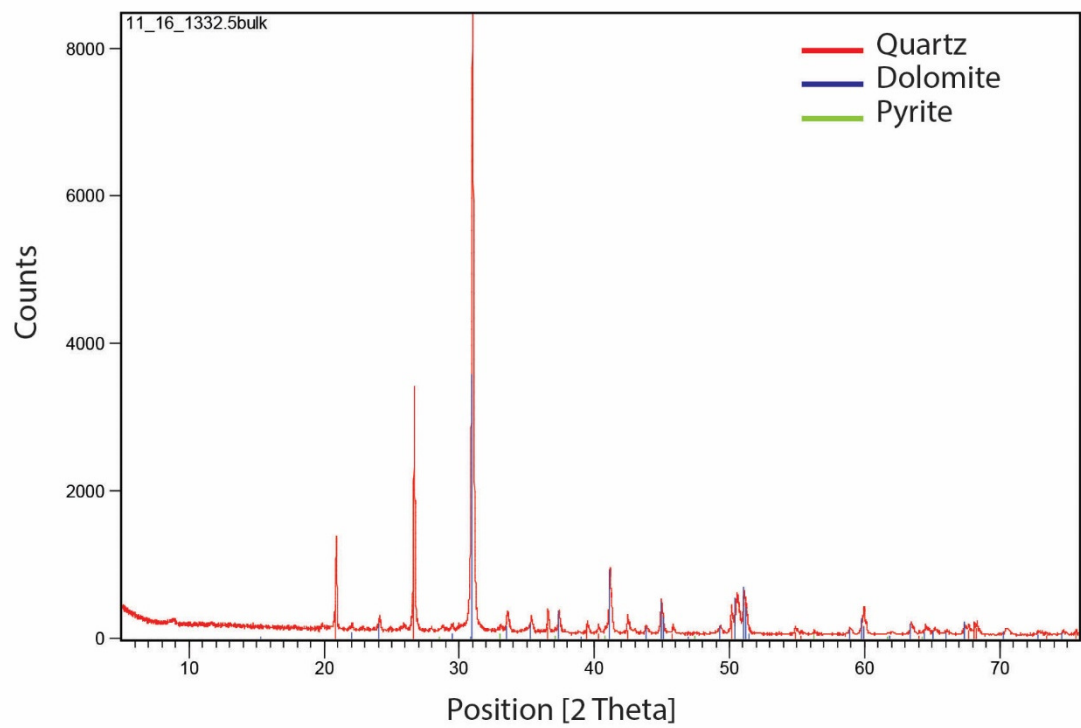
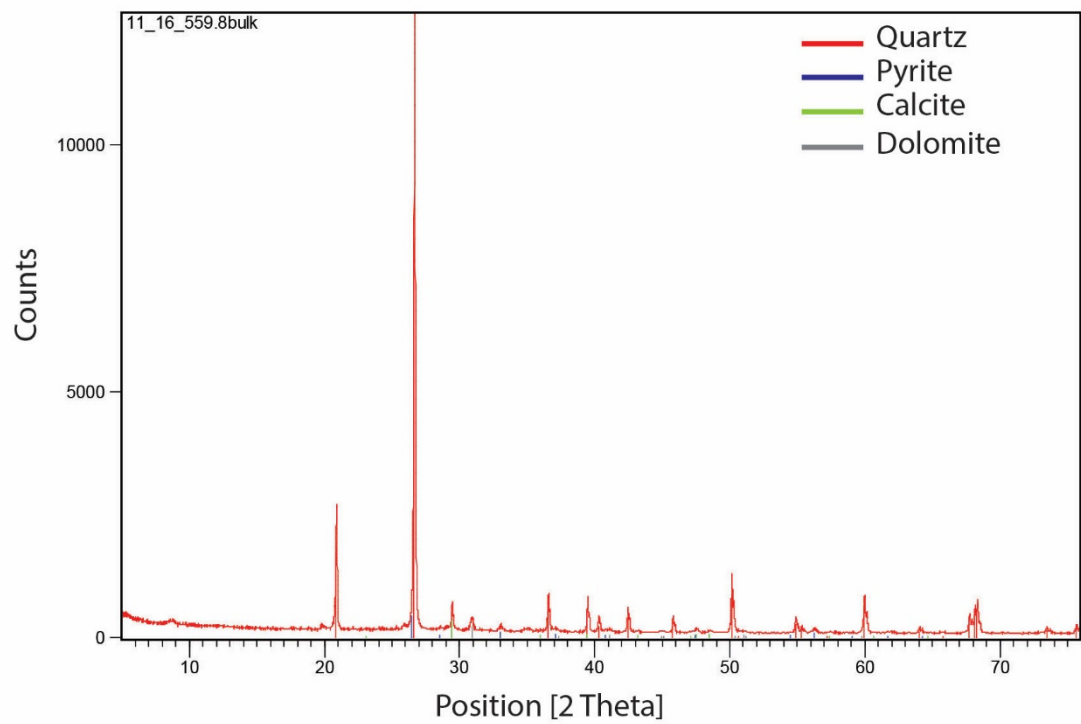
Appendix H.4: Data Figures

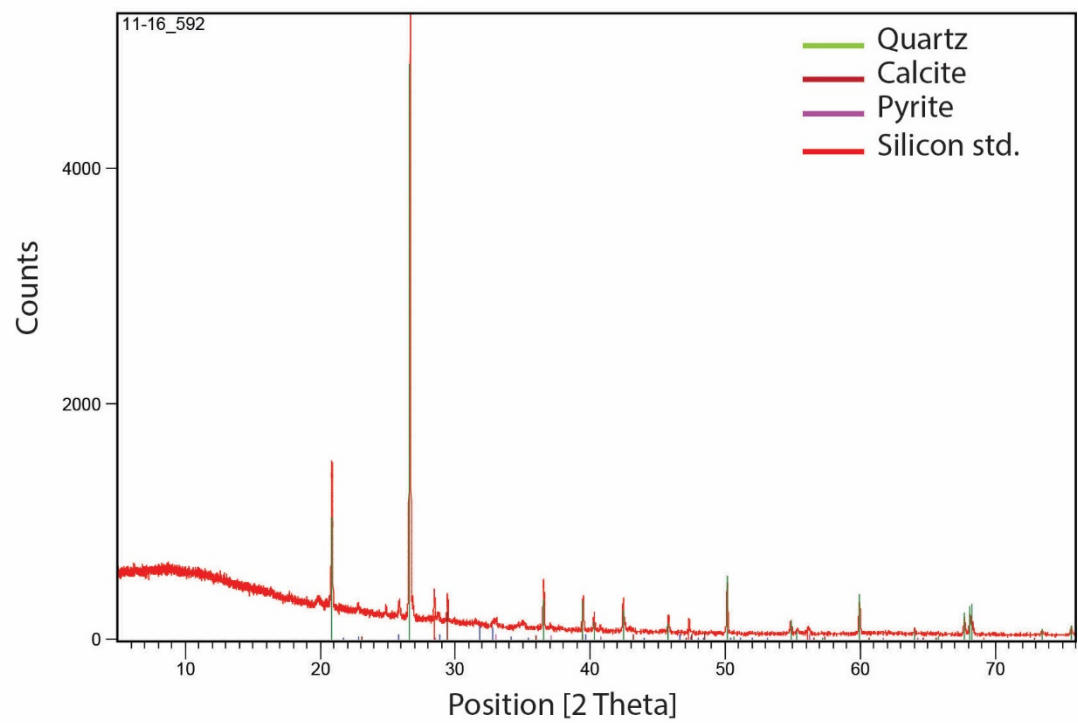
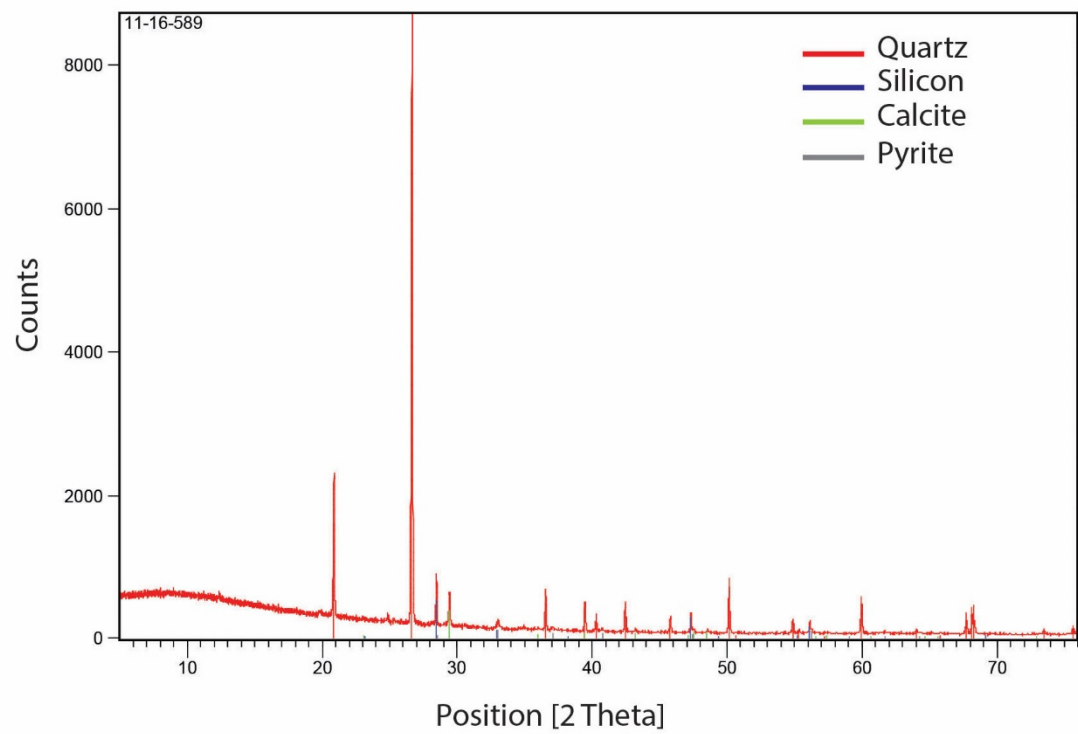


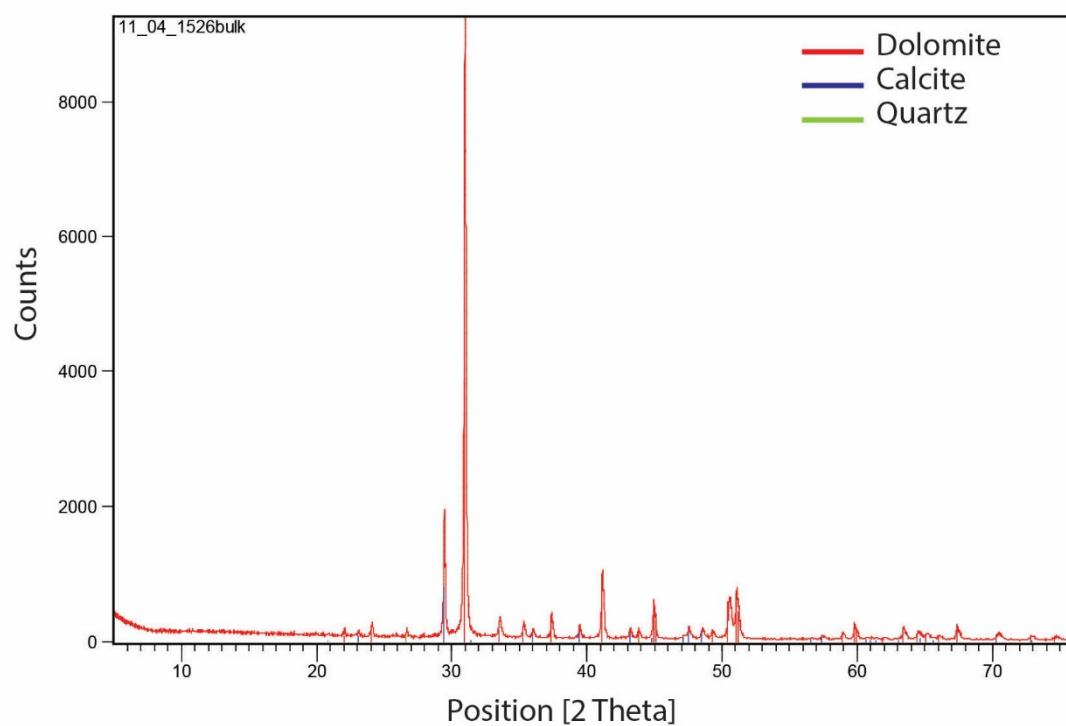
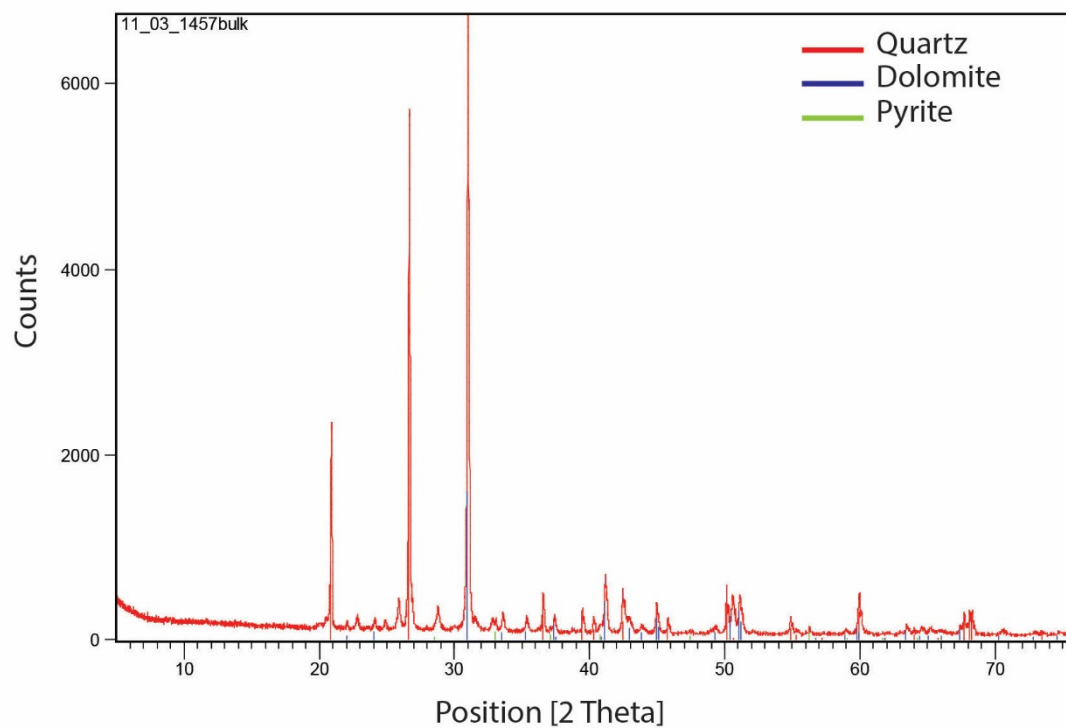


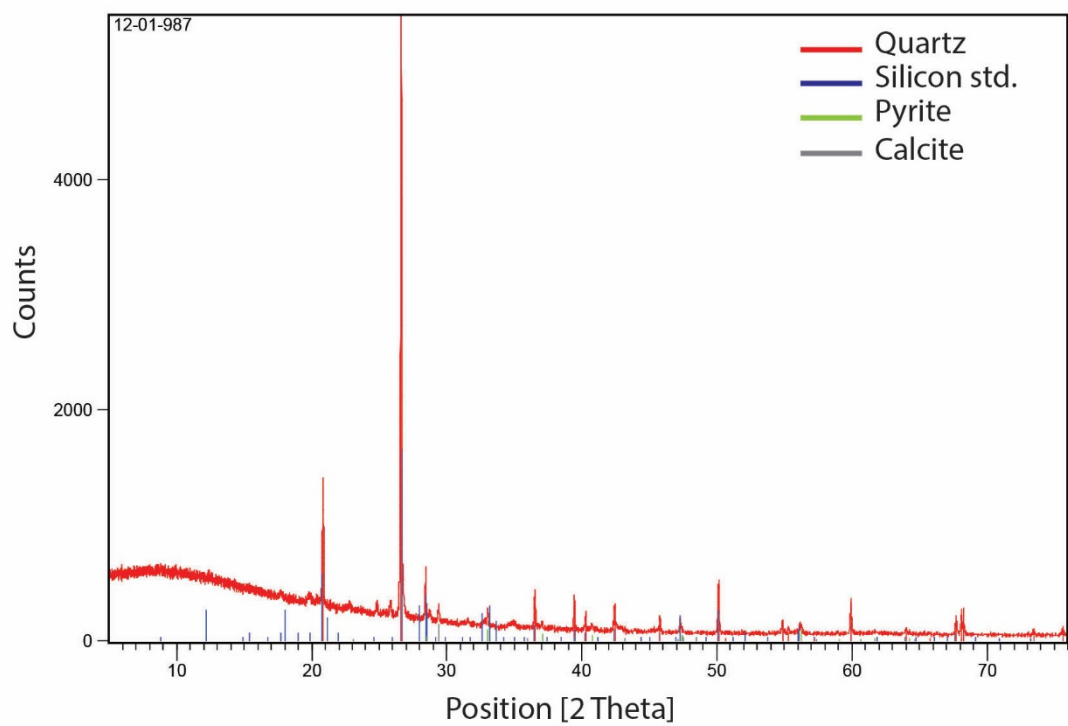
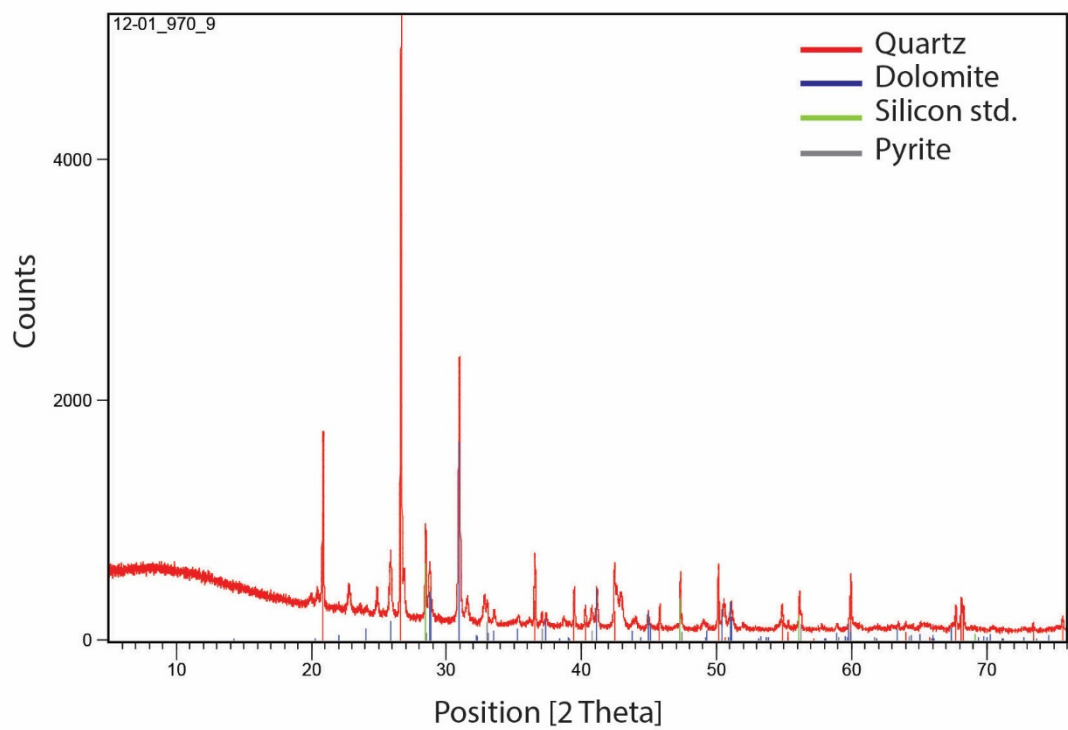


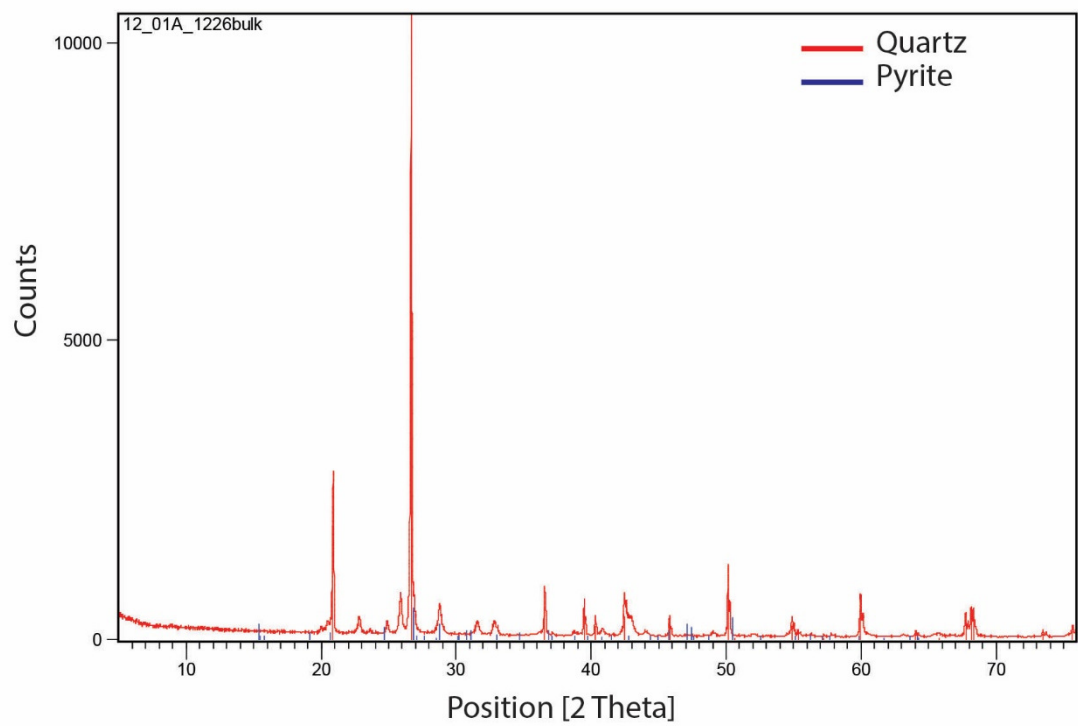
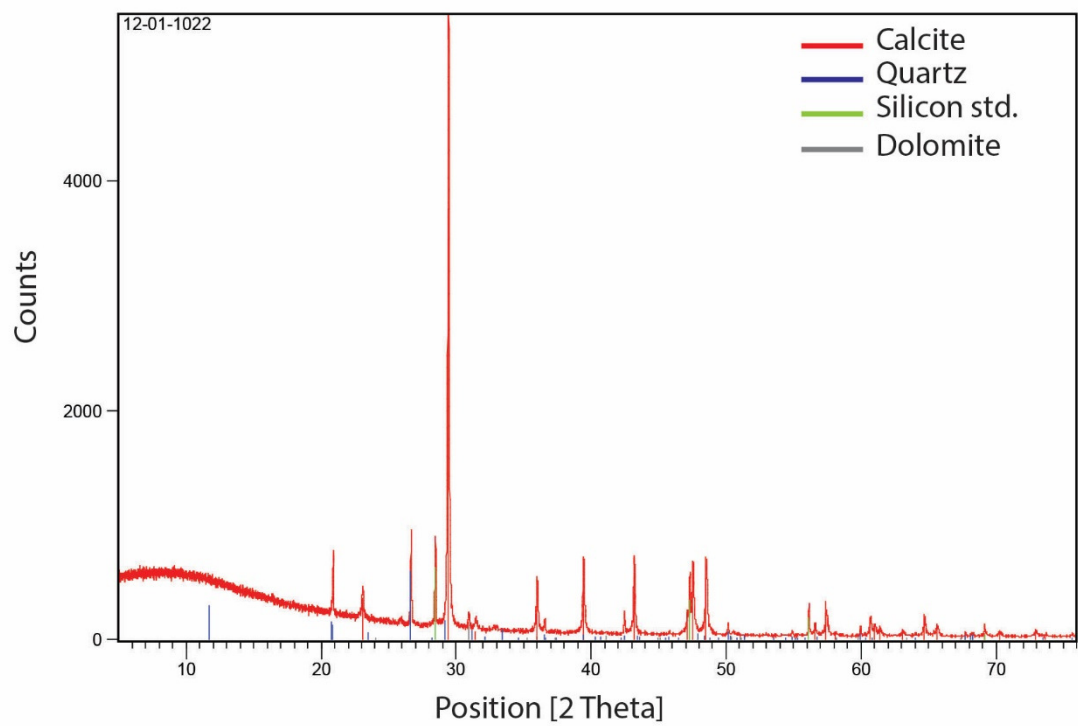


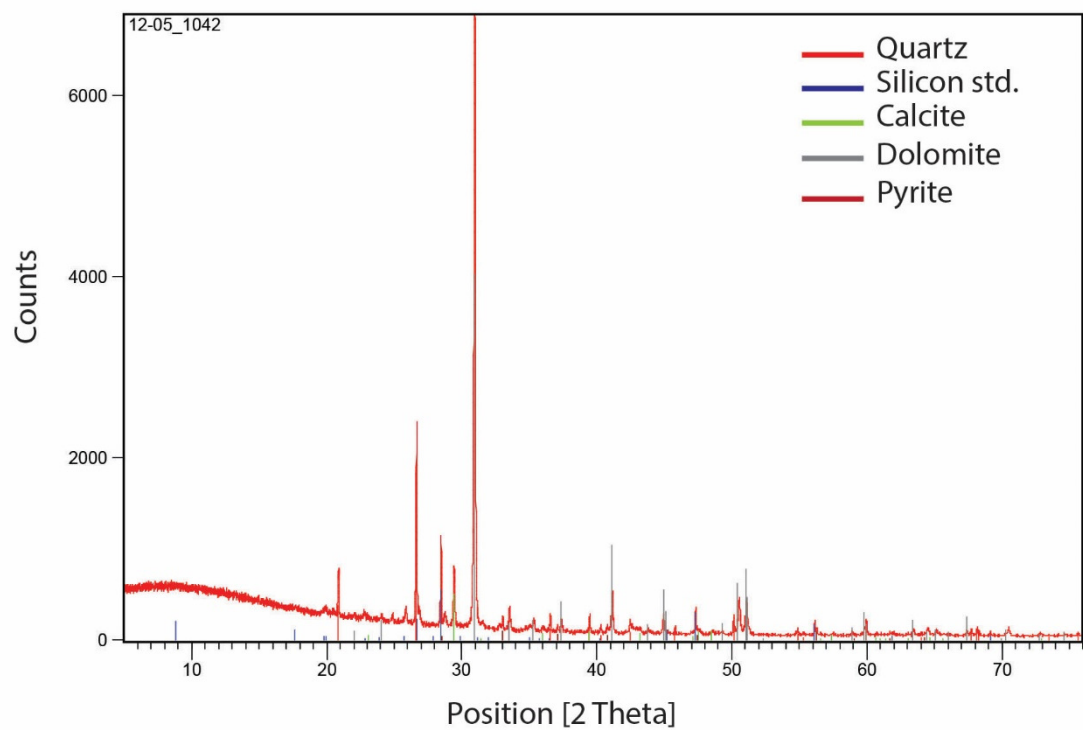
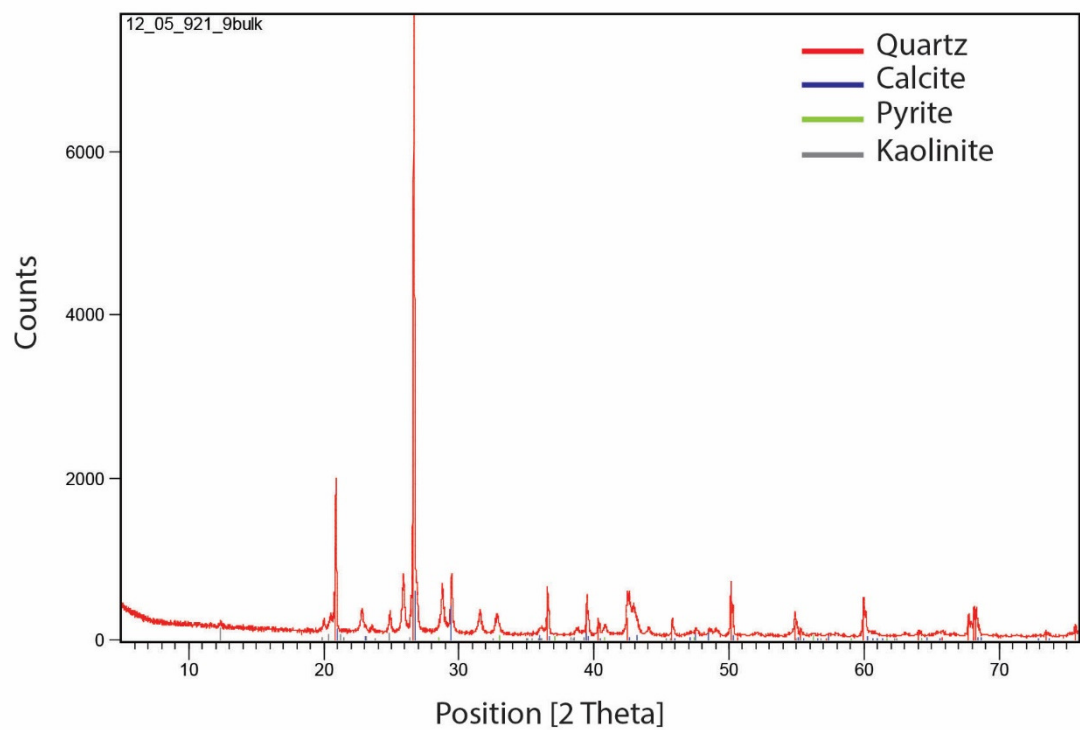


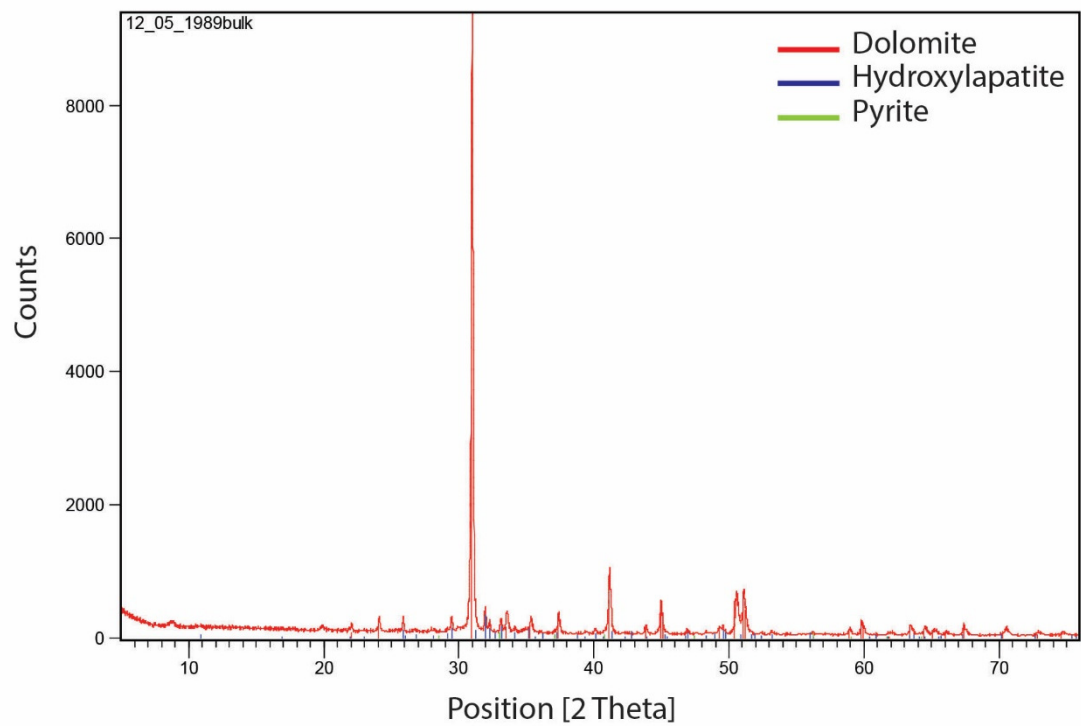
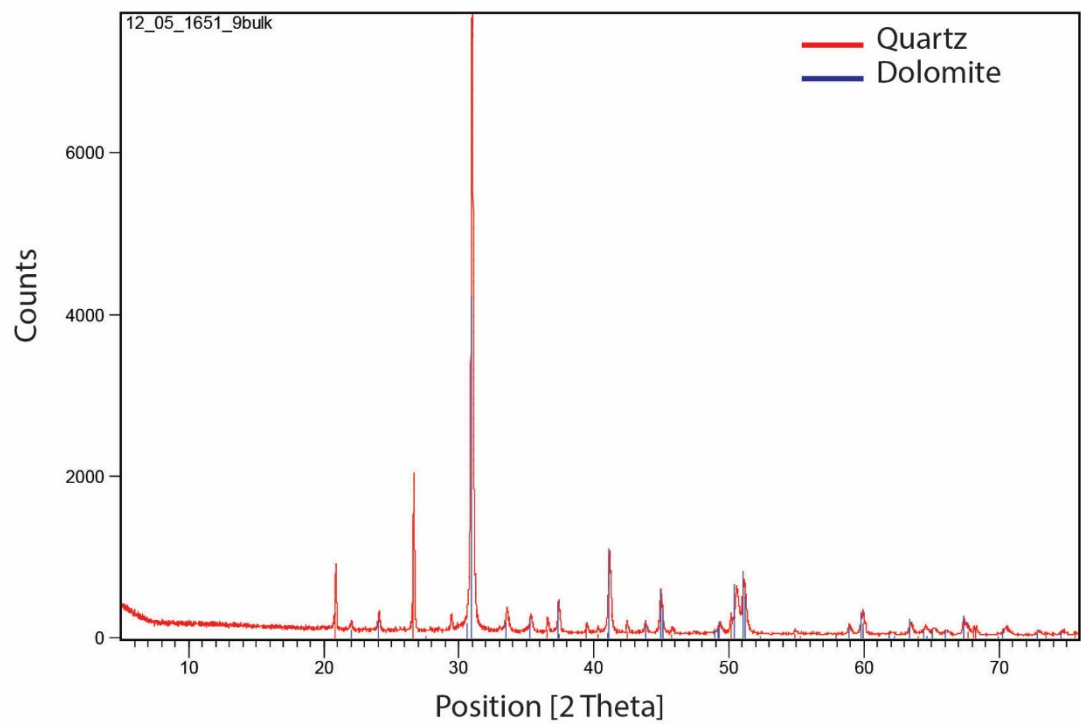


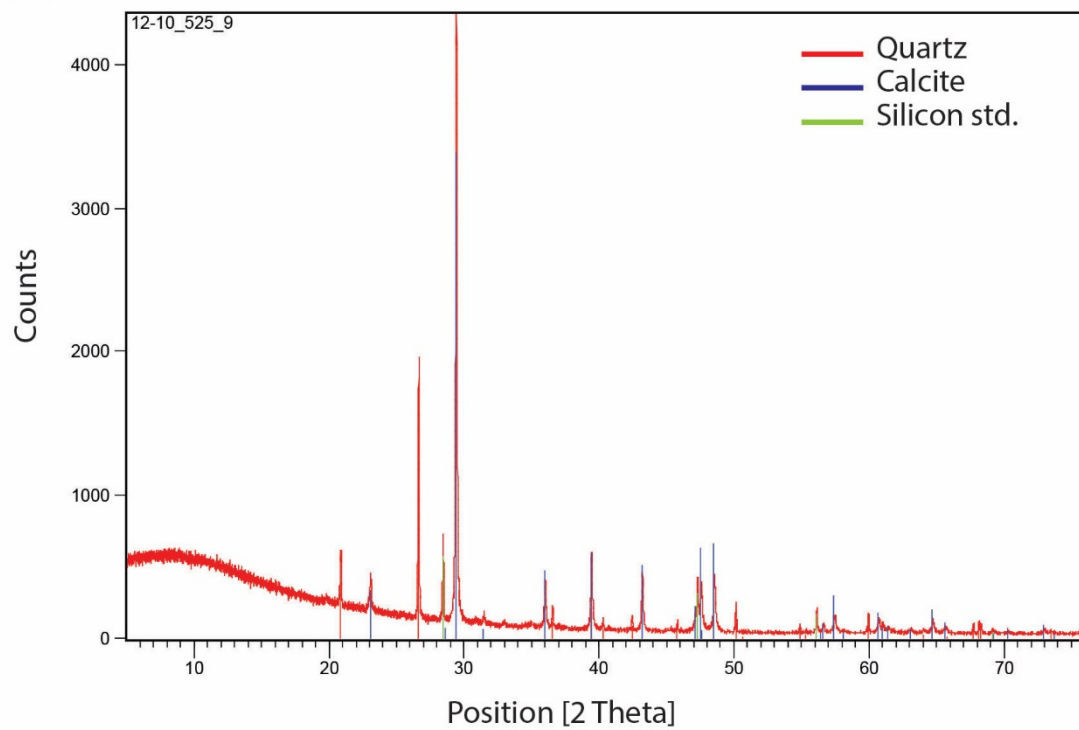
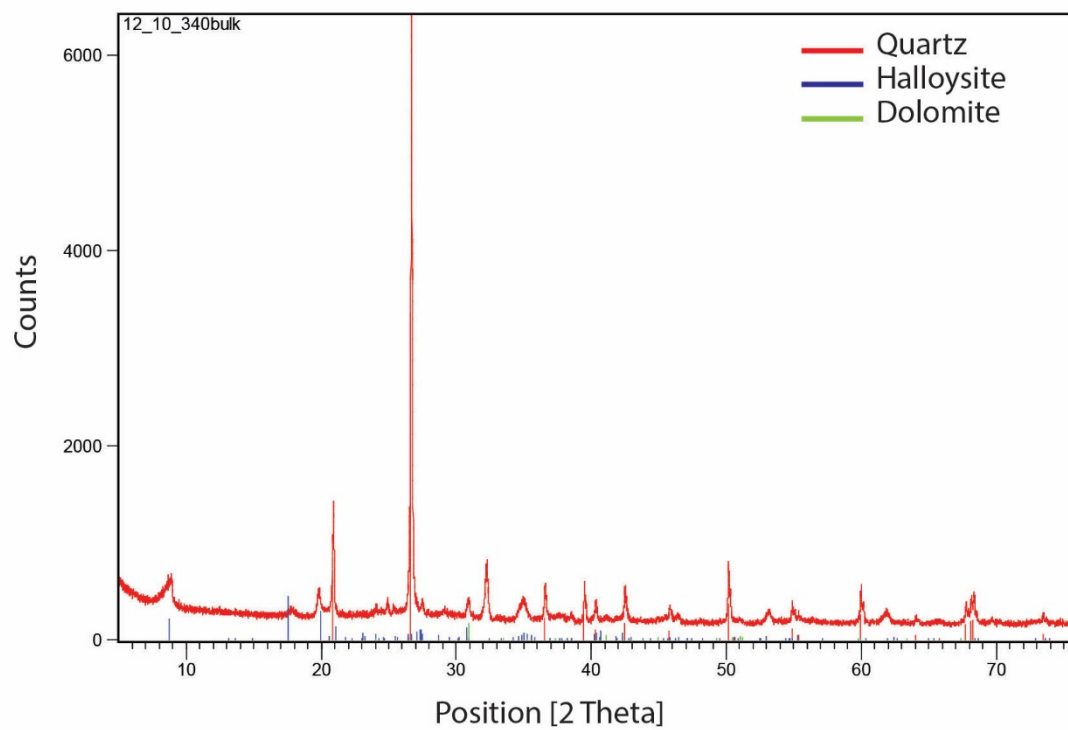


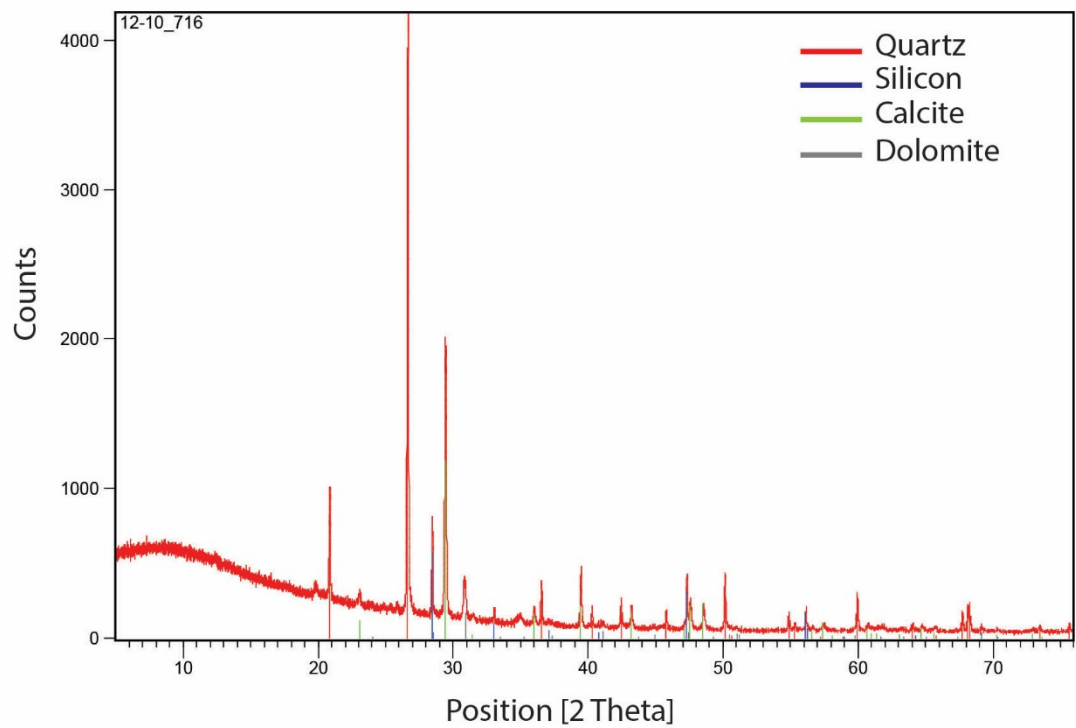
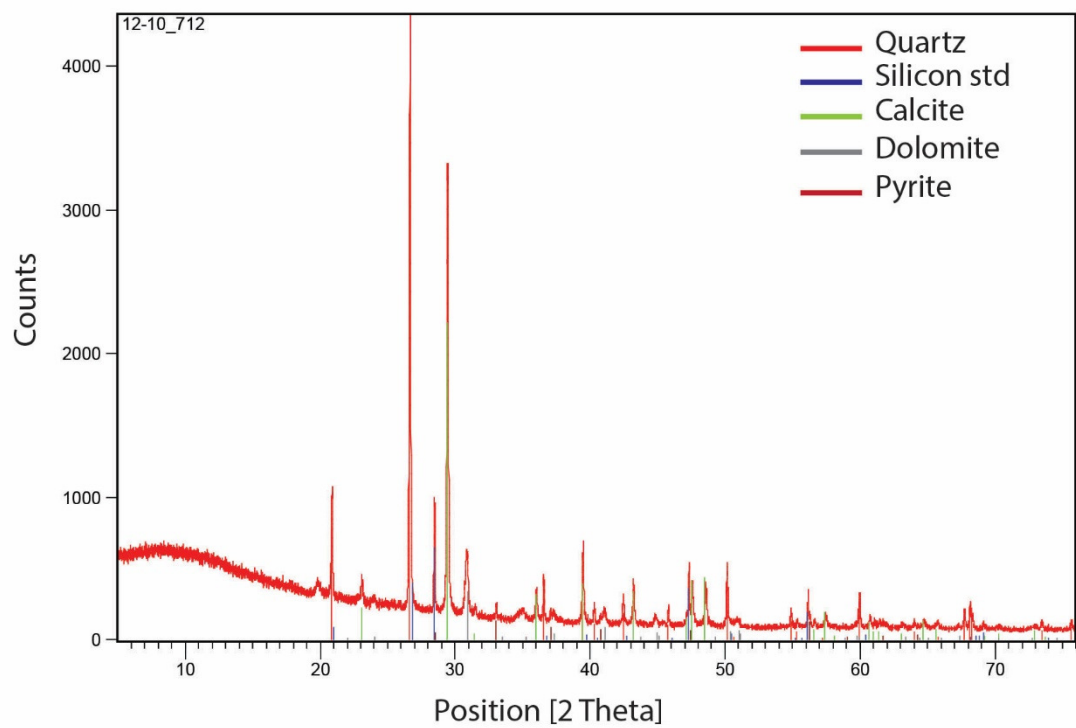


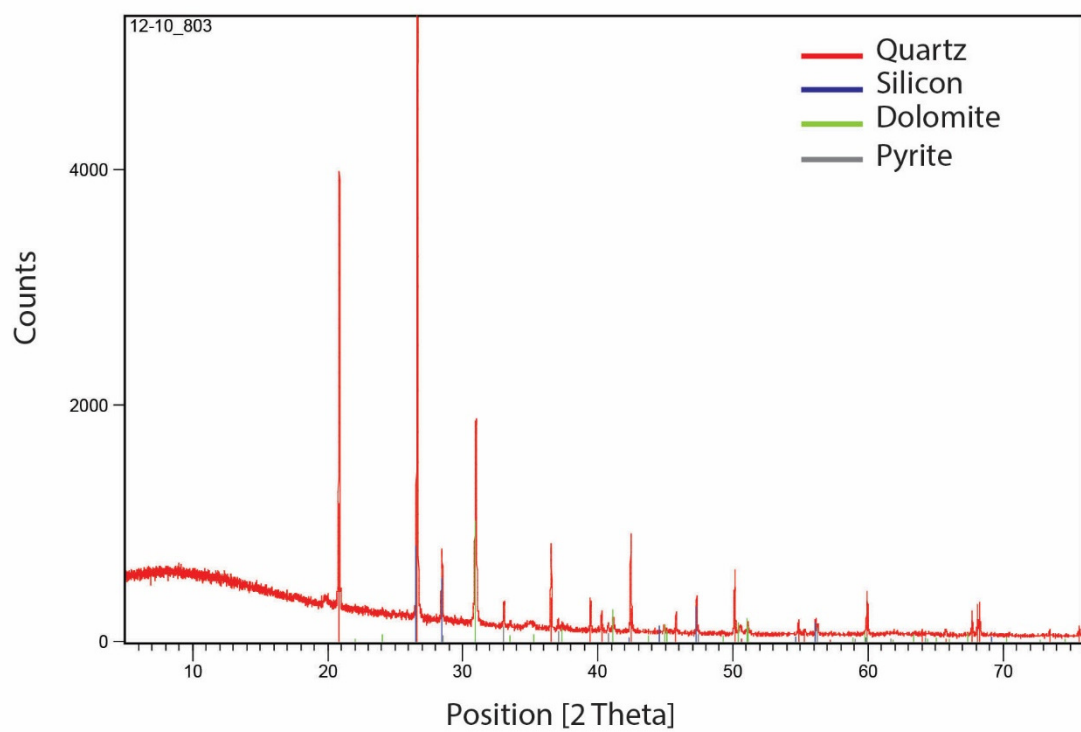
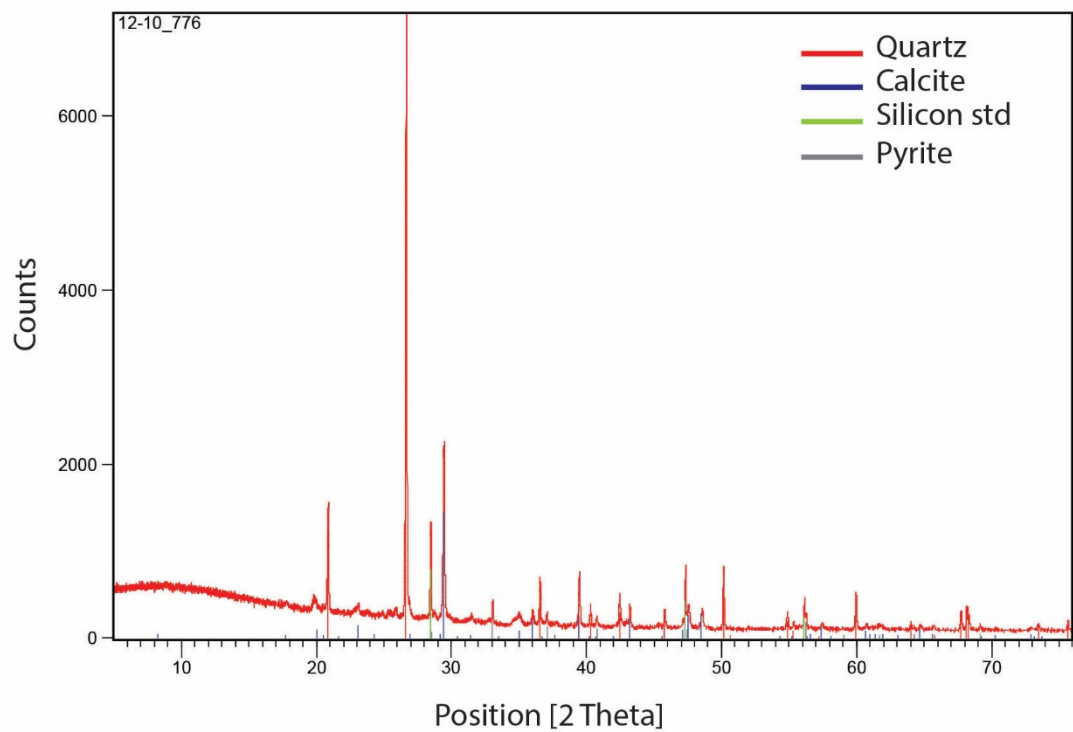


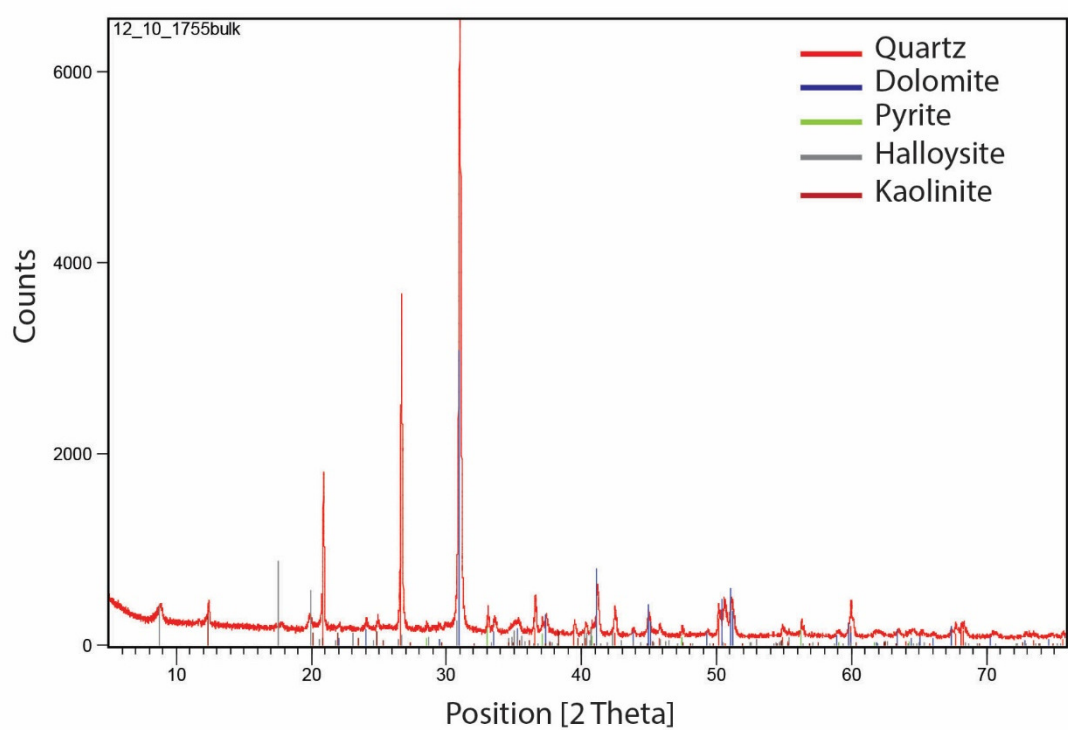
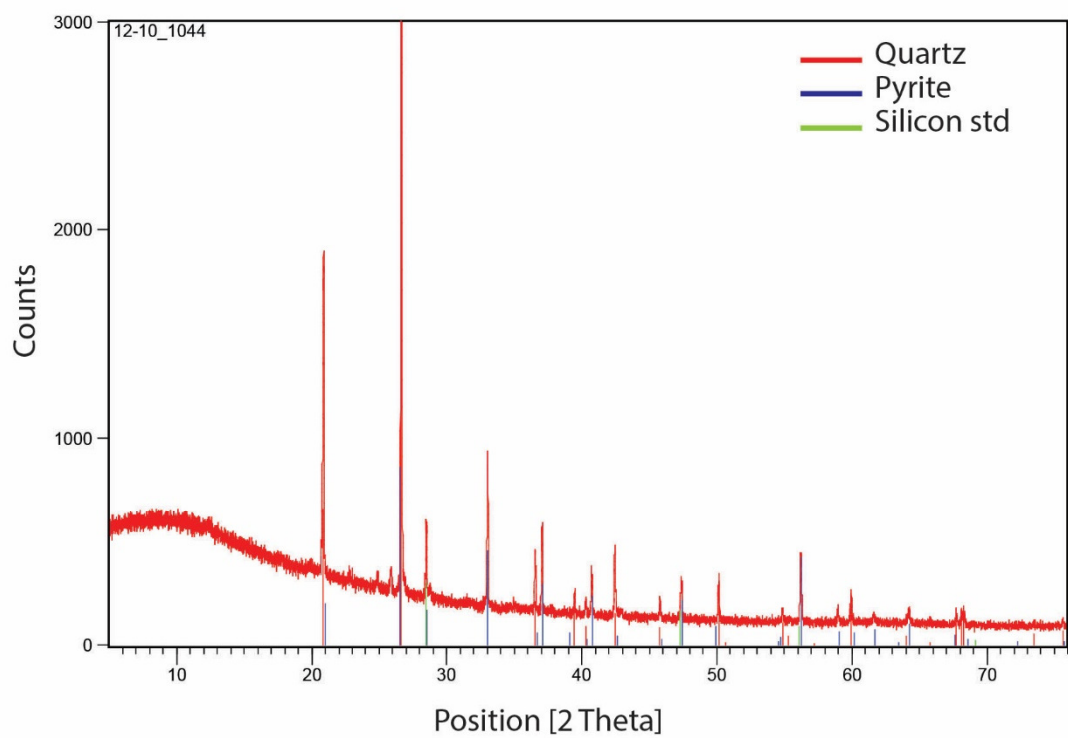


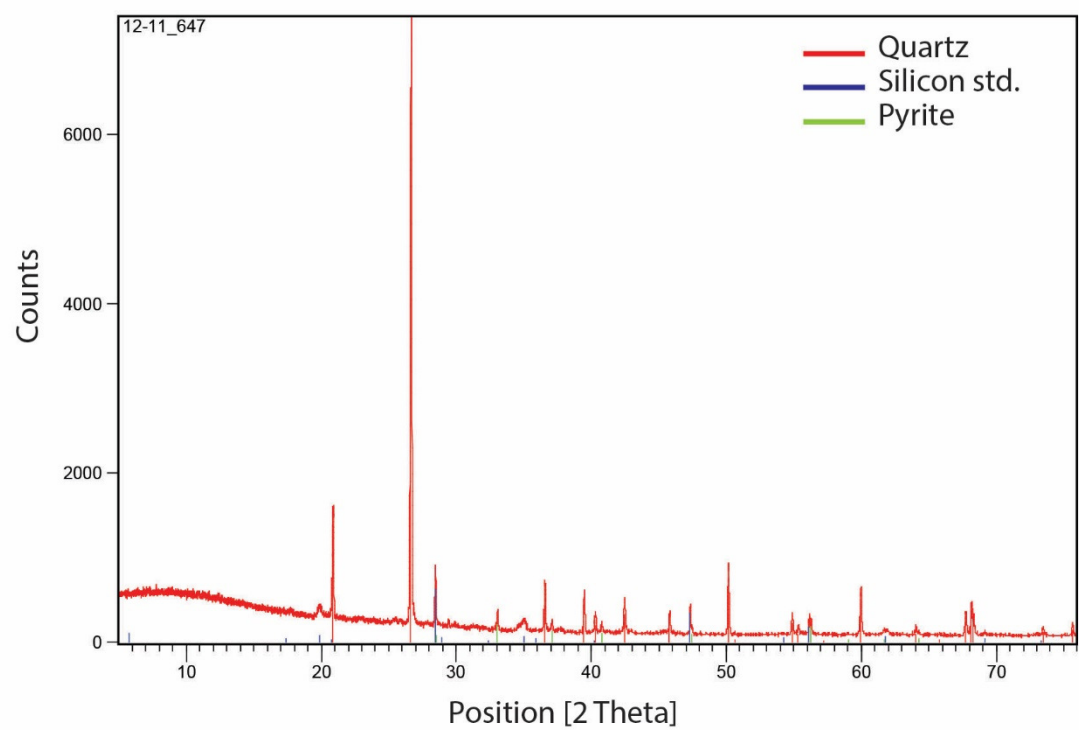
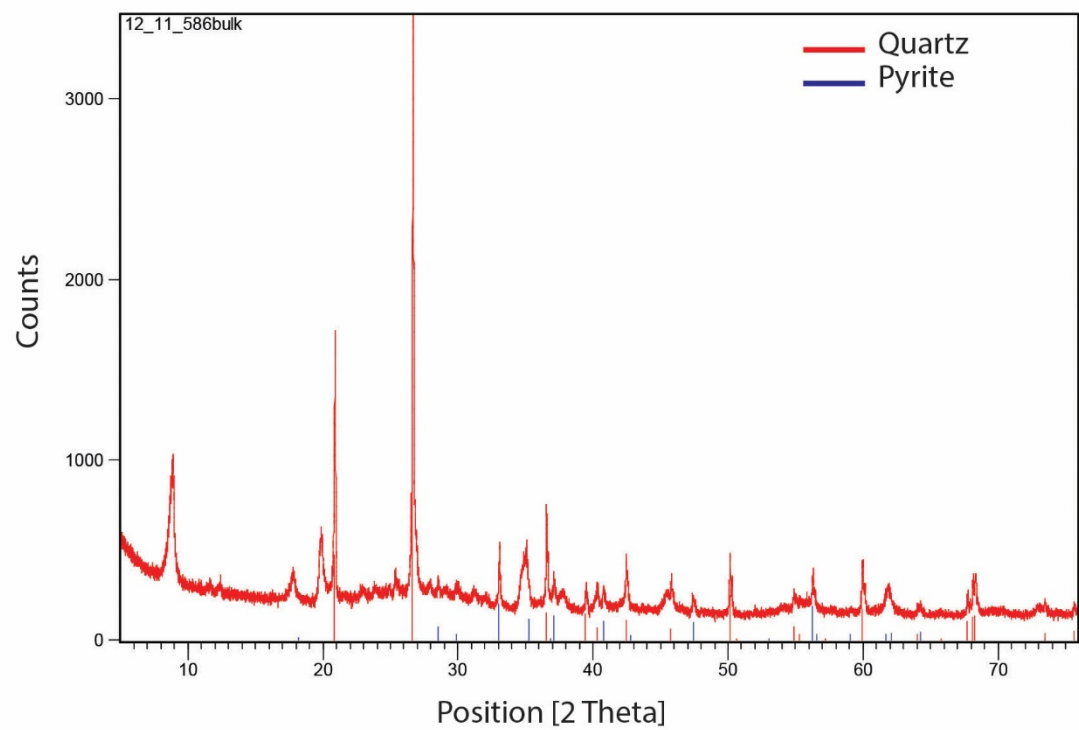


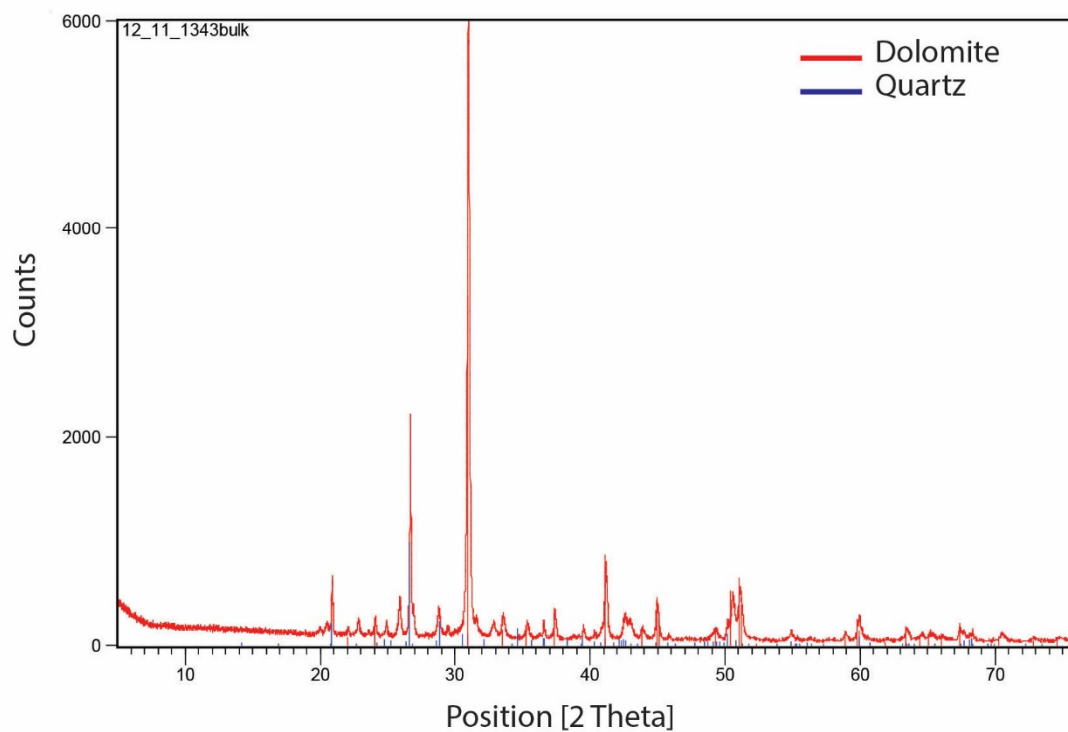
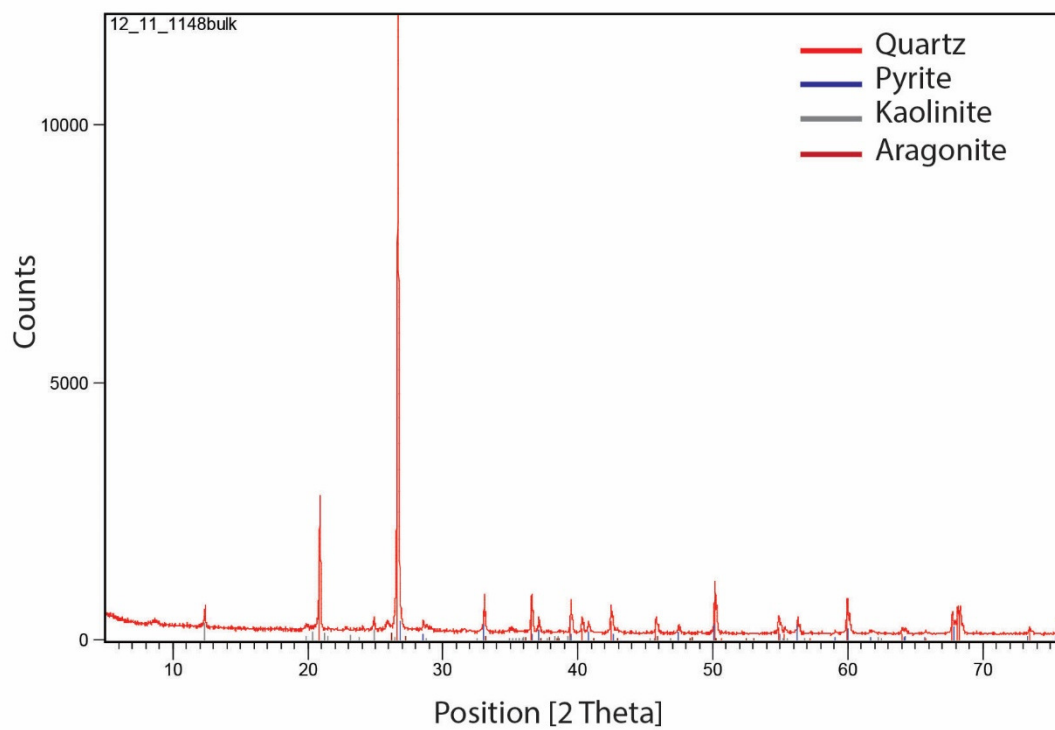


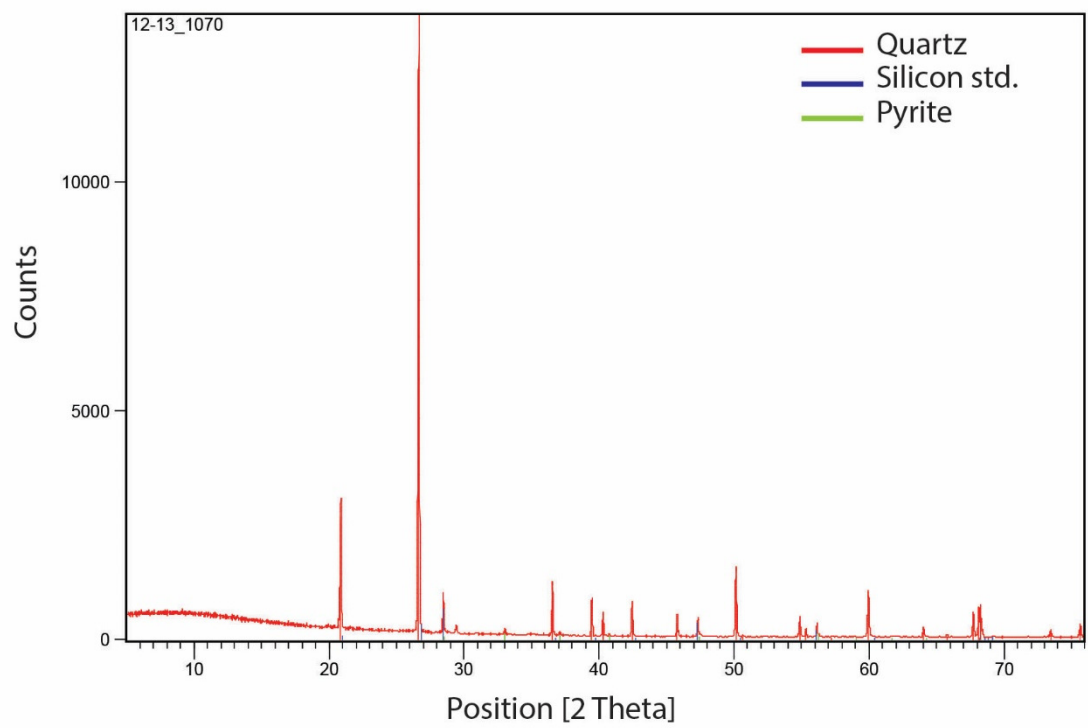
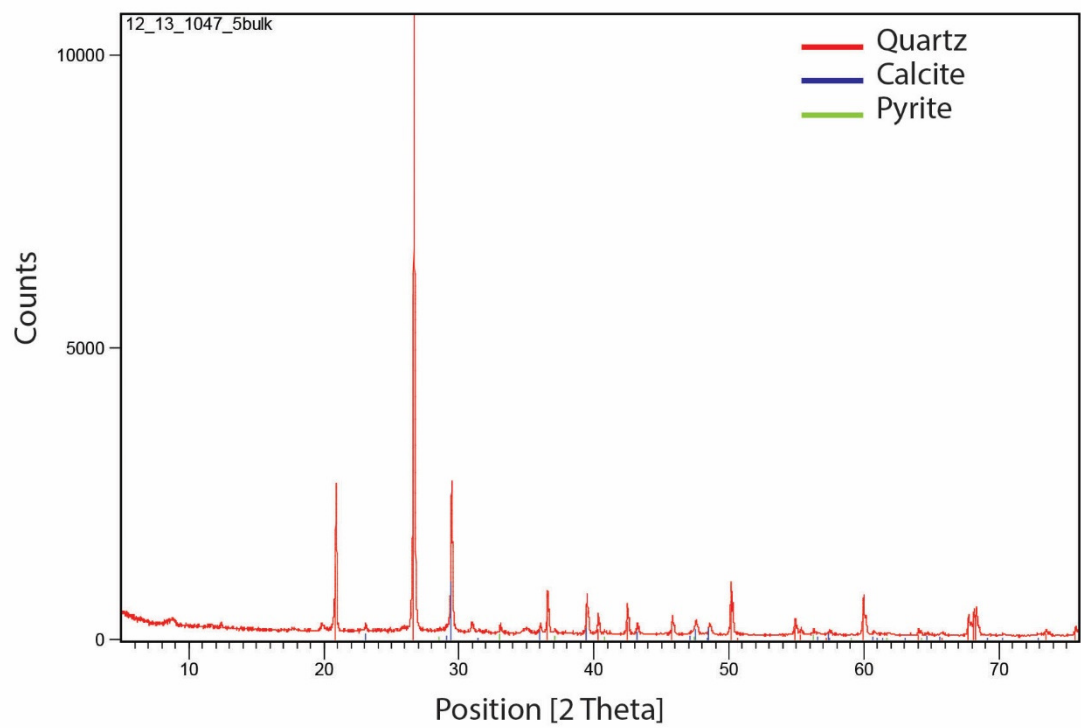


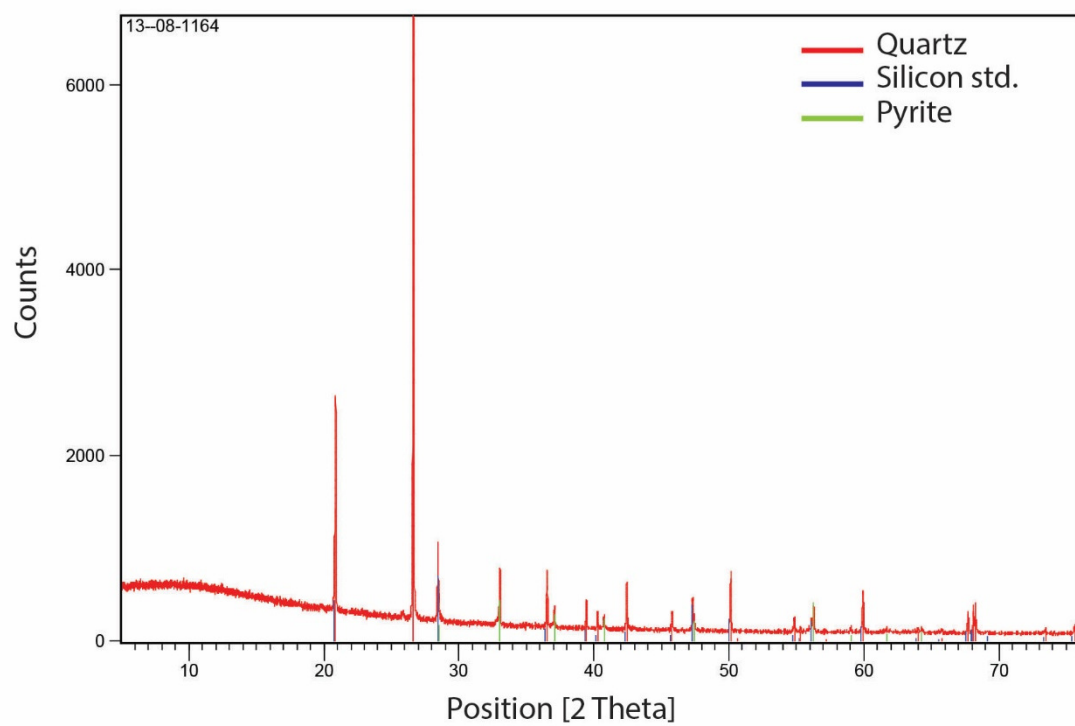
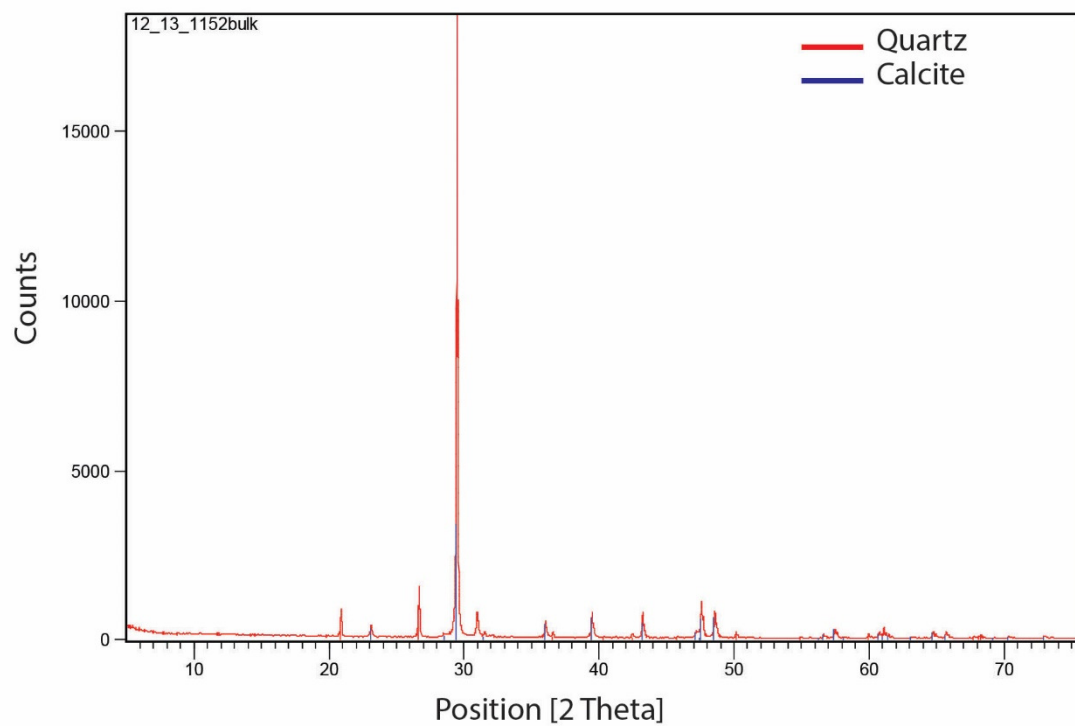


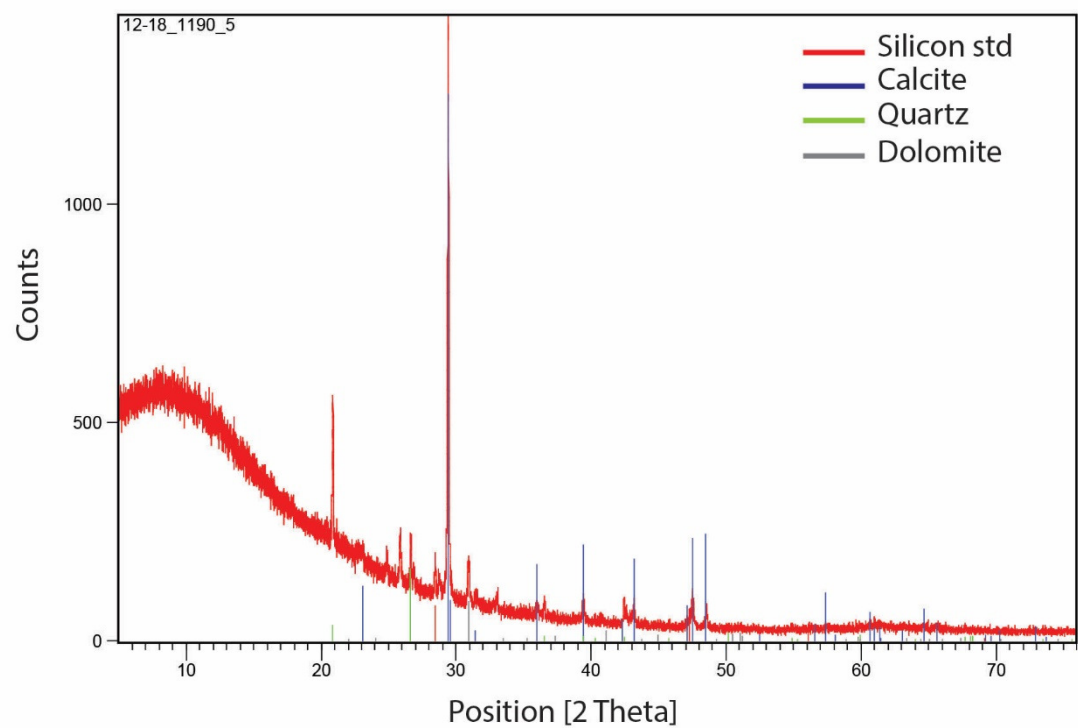
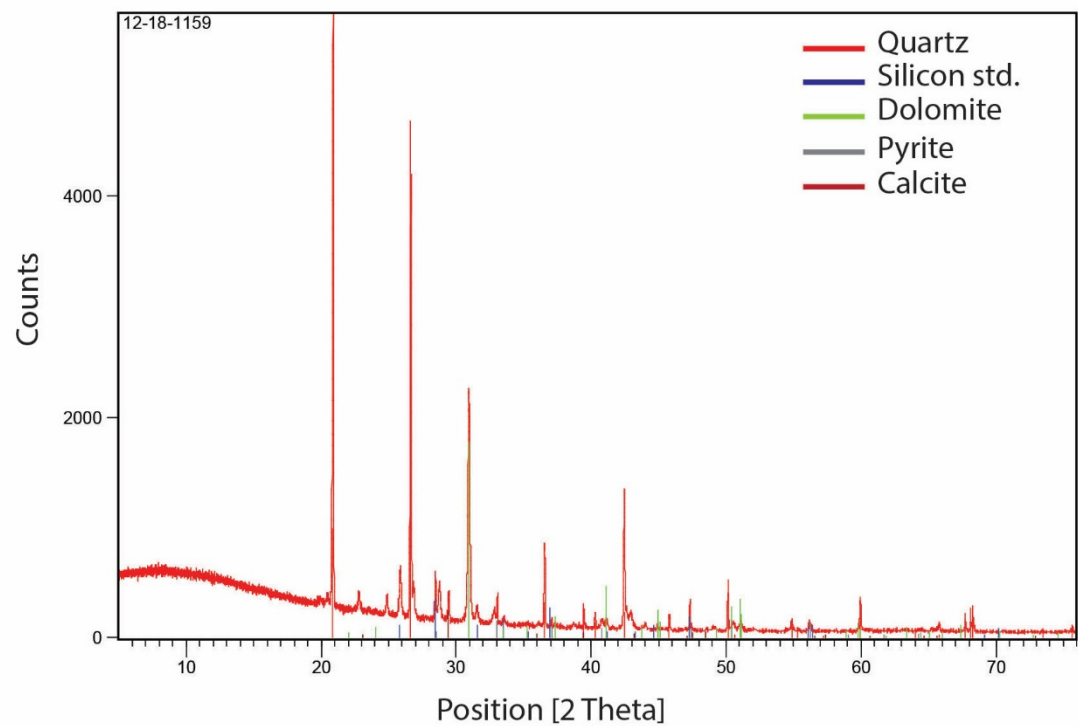


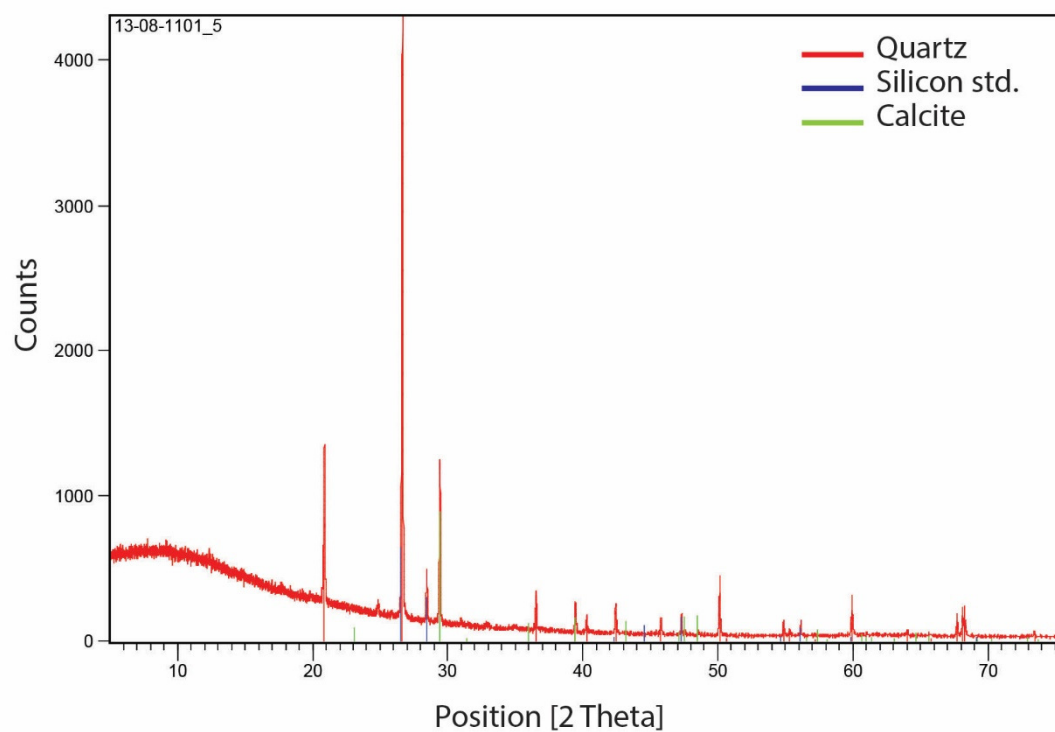
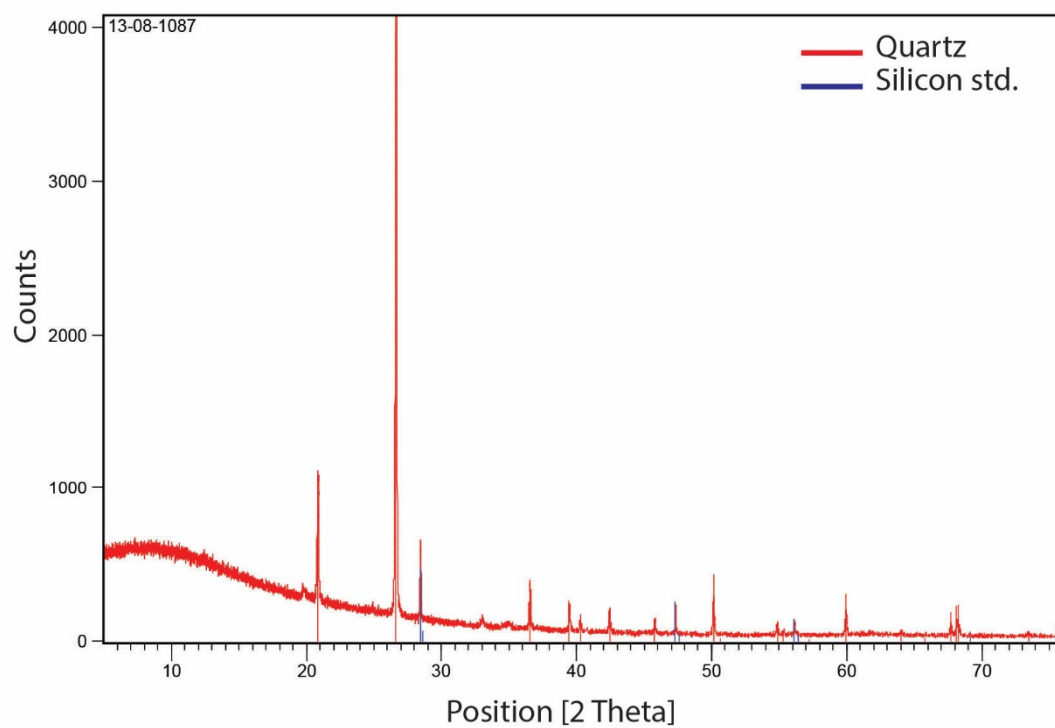


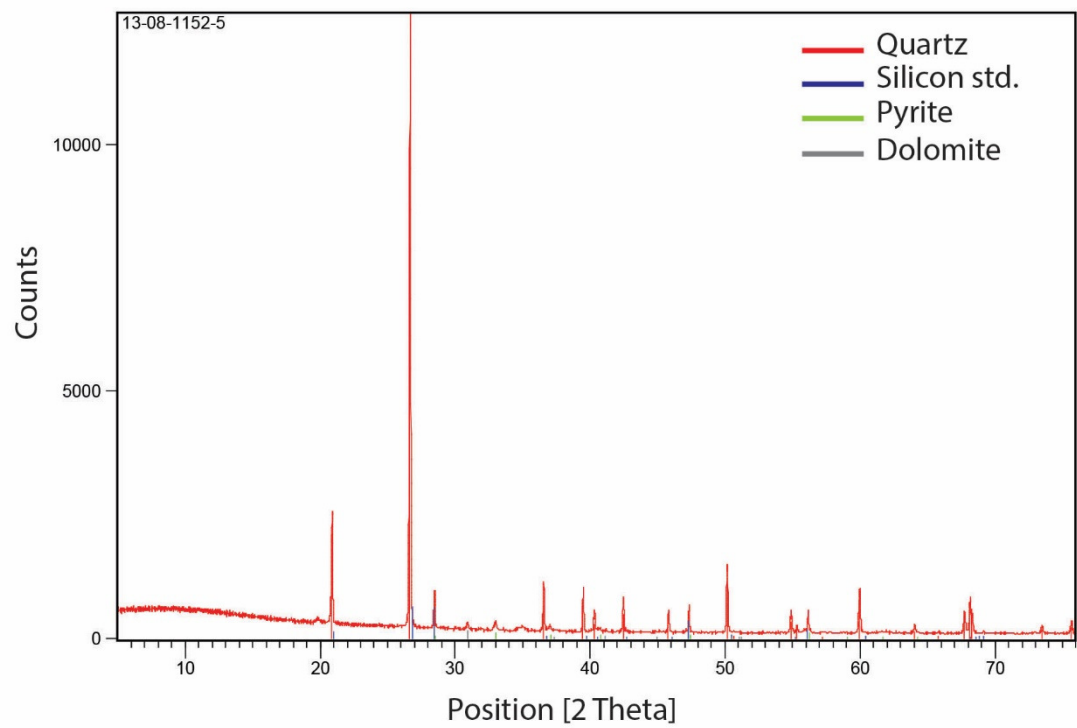
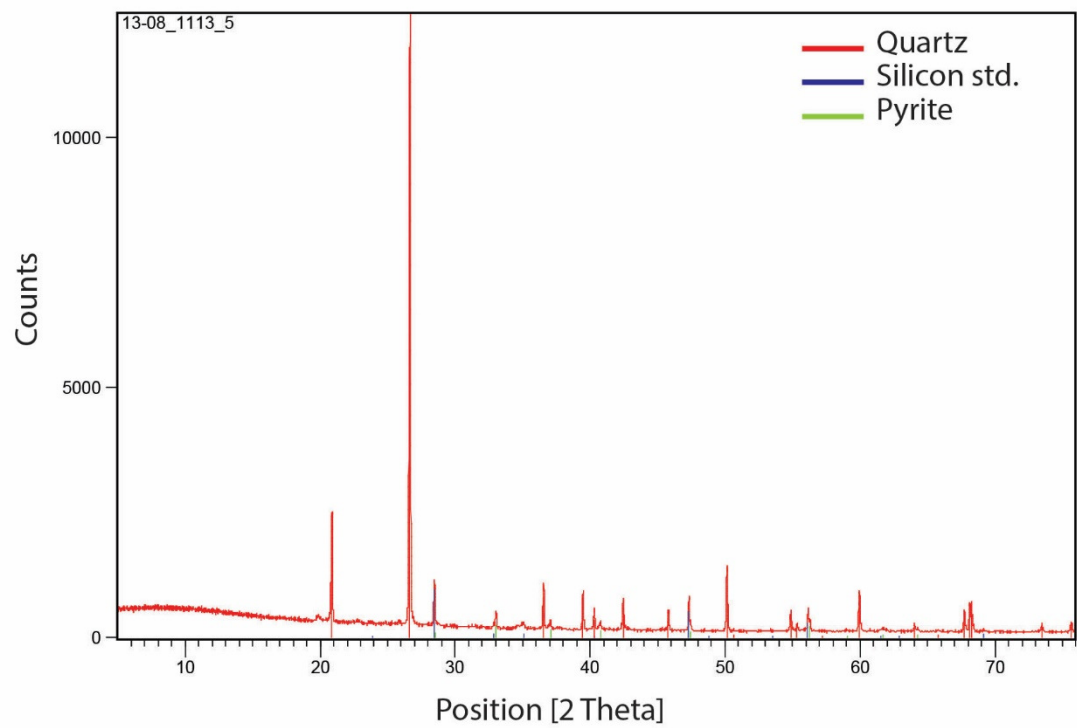


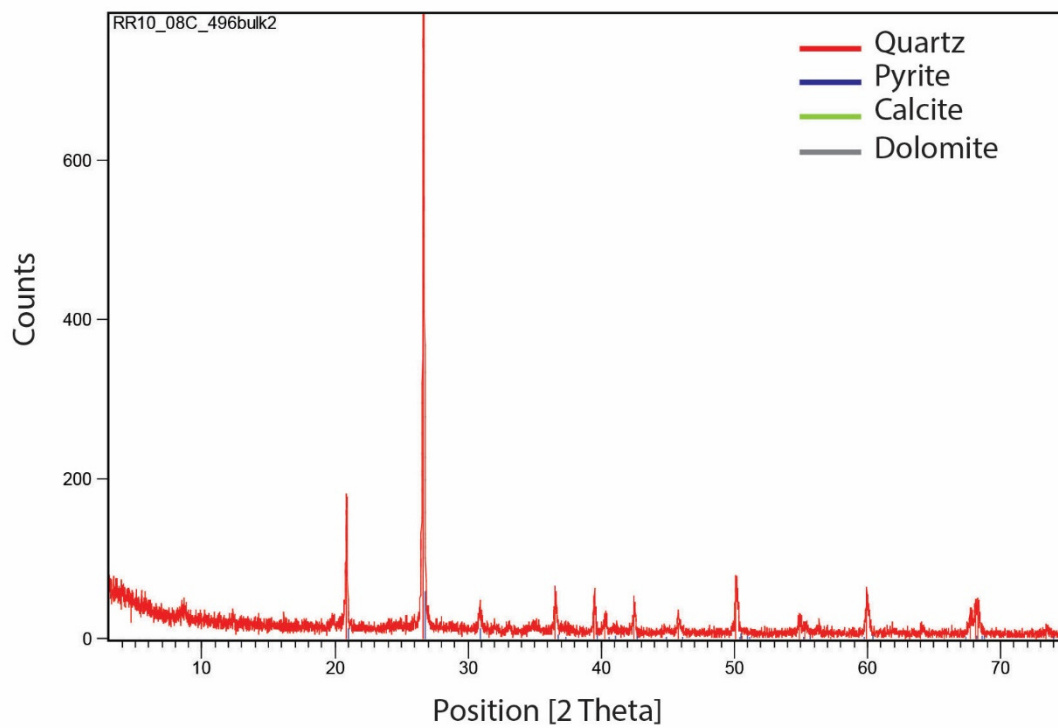












APPENDIX I

TERRASPEC DATA

Sixteen samples were analyzed by Paul Bowen, a geologic consultant in Las Vegas, using TerraSpec 4 Hi-Res Mineral Spectrometer to identify vein and clay minerals. This analytical technique identifies minerals based on the reflectivity of the mineral analyzed. Carlin-type gold deposit ore is commonly dark grey to black owing to the presence of carbon, causing problems with this technique as the analytical peaks can be poorly developed due to the low reflectivity of dark rock or to weakly crystalline clays. This appendix lists Terraspec analysis number, drill hole number, footage, gold grade, notes, interpreted minerals identified, and peaks identified. This technique did obtain matches, but identified clays that may or may not be present. Other techniques for clay identification are recommended for CTGD.

TerraSpec #	DDH #	Depth (ft)	Au (ppm)	Macroscopic	Profile
MN00000	12-18.	640	0.03	bk carb? Shiny surface wk powder on surface & frags	kaol>ill
MN00001	12-18.	678.1	> 0.005	wr bk solid ± cal ff	mont±hem?kaol
MN00002	12-18.	678.1	> 0.005	cal vn	cal
MN00003	12-18.	907	3.43	bk bx ± br & wh powder	ill/smc-mont±hem±sil
MN00004	12-18.	907	3.43	bk bx ± br & wh powder	ill?chl?hem
MN00005	12-18.	909	0.07	bk bx, falls apart easily	kaol>ill
MN00006	12-18.	969	0.47	bk mat mod gr frags	mont-sil
MN00007	12-18.	978	1.27	bk mat mod gr frags	mont-sil
MN00008	12-01A	911.5	1.75	bk powdery	mont-ill-sil±cal
MN00009	12-01A	916	19.30	bk powdery	mont-sil
MN00010	12-01A	970.9	2.54	bk solid ff	mont-ill-sil±cal
MN00011	12-01A	970.9	2.54	cal vn	cal
MN00012	12-01A	974.9	11.56	shiny bk surface	sil±bio
MN00013	12-01A	986.1	20.82	bk powdery bx	mont-sil
MN00014	10-08C	496	0.01	bk bx wh powdery fragil	kaol>ill
MN00015	10-08C	712	0.01	cal vn	cal
Analyzed by Paul Bowen					

Terra Spec #	1.3µm	1.4µm	1.8µm	1.9µm	2.0µm	2.1µm	2.2µm	2.3µm	Spectra
MN000000	1398	1417		1902		2168	2211	2383	Kaolfcmx-K8I2
MN000001		1402-1417		1910			2207	2344	MONTSD1f-CALCAZ1
MN000002		1417		1929	2000	2168		2308s-2340	CALCAZ1
MN000003		1413	1816	1946			2203		MONTSD1f-Sil9-IS67554f
MN000004	1398	1417		1910			2207	2328	ILLCHL2f-CHLAZ1-HemaNV1
MN000005	1382	1413		1910-1945		2183	2211	2398	Kaolfcmx-K8I2
MN000006		1445w		1945			2215		MONTJP13-SILINO8f
MN000007		1468w		1925			2211		SILINO9f-S9M1
MN000008		1409		1957			2203		S6M2I2-CalcCH1f-SILINO5f
MN000009		1405		1918			2207		MONTWY10f-SILFR4f
MN000010		1409		1976			2203		S6M2I2-CalcCH1f-SILINO5f
MN000011	1339	1417		1914				2301s-2336	CalCHf
MN000012							2219		SILINO8f-Biotite
MN000013		1413		1910w			2207		MONTWY10-SILFR4F
MN000014	1398	1417		1910-1945		2176s	2207		K8I2
MN000015		1413		1921	2000	2164	2293s	2340	CALCAZ1

TerraSpec #	DDH #	Depth (ft)	Au (ppm)	Macroscopic	Profile
MN00016	10-08C	712	0.01	bk wr - ± cal ff	mont-sil?ill
MN00017	10-08C	716	4.14	bk chips	mont-sil
MN00018	10-08C	803	30.20	bk powder	mont-sil
MN00019	10-08C	825	3.53	bk powder	mont-sil
Analyzed by Paul Bowen					

Terra Spec #	1.3µm	1.4µm	1.8µm	1.9µm	2.0µm	2.1µm	2.2µm	2.3µm	Spectra
MN00016		1413		1937			2211	2328	SS15-MONT JP 13-SILFR4f
MN00017		1405r		1902			2215		MONT JP 13-SILFR4f
MN00018		1402r		1914vw			2211		MONT JP 13-SILFR4f
MN00019		1402r		1910			2211		MONT JP 13-SILFR4f

** The 1.5, 1.6, 1.7, and 2.4 µm peaks are not listed; no peak present.

APPENDIX J

OFF AXIS - INTEGRATED OUTPUT CAVITY

SPECTROSCOPY DATA

One hundred samples were analyzed using Off Axis-Integrated Output Cavity Spectroscopy (OA-IOCS) at the University of British Columbia in Vancouver, Canada, to identify potential isotopic halos. Of the 100 samples analyzed only 68 samples produced results. Thirty-two samples did not produce results due to the low amount of carbonate material or presence of sulfur within sample, either because the sample was silicified, or because H_2S gas, which would interfere with results, was detected during the run. The 68 samples for which isotopic ratios were determined do not indicate whether or not an isotopic halo extends beyond the North Bullion Carlin System. Appendix J.1 lists the samples analyzed, their location, and a lithologic description. Appendix J.2 lists the samples analyzed and their carbon and oxygen isotope ratios. Appendix J.3 displays images of normalized oxygen isotope results from calcite veins, and parallel correlation and turkey box graphs of the oxygen isotope results relative to gold grade.

Additional sample analyses are necessary to clearly define an isotope halo, if one exists around the deposit. Sampling strategy should include several short transects with a large number of samples in order to clearly identify changes in oxygen isotopes along the sample transects related to variation in grade and lithology. Future analyses comprising a larger sample set are necessary to fully identify an isotope halo related to alteration and ore fluid pathways.

Appendix J.1 OA-IOCS: Sample Descriptions

Sample	UTM E	UTM N	Elevation (ft)	Lithology Description
10-08C 1156.9 rr	584916.228	4488728	5442.390391	Mudstone/ Limestone Bxa
10-08C 1224.4	584916.748	4488728	5377.418819	dolo Bxa
10-16 1009.5	585049.245	4488912	5481.034458	Ls Bxa
10-16 1107	585047.934	4488910	5381.348752	Ls Bxa
10-16 1117.5	585047.798	4488910	5371.381809	Ls Bxa
10-16 1334	585045.152	4488905	5157.099913	Ls Bxa- close to void ccfill
10-16 1467.5	585043.525	4488902	5022.538343	ls Bxa
10-16 1467.5r	585043.525	4488902	5022.538343	ls Bxa
11-03 1007.5	585063.156	4488709	5514.54849	Dolomite Bxa
11-03 1372	585060.141	4488698	5151.669768	Dolomitized Limestone Bxa
11-03 1447.9	585059.572	4488695	5077.029468	Dolomitized Limestone Bxa
11-03 1450.5	585059.538	4488695	5072.052655	Dolomitized Limestone Bxa
11-03 1559	585058.888	4488692	4967.564212	Dolomitized Limestone Bxa
11-04 1074.9	584607.38	4488690	5557.543406	Ls/Dol bxa
11-04 1164	584607.082	4488689	5467.6258	Dolo Bxa
11-04 1279	584606.623	4488687	5352.748747	Dolo Ls Bxa
11-04 1294.5	584606.531	4488687	5337.767824	Dolo Ls Bxa
11-04 1396	584605.97	4488686	5232.887155	Zebra dolomite

Sample	UTM E	UTM N	Elevation (ft)	Lithology Description
11-04 1467	584605.482	4488685	5162.987064	Dolo Bxa
11-04 1526.5	584604.965	4488684	5103.080451	Dolo
11-16 595.1	584929.706	4488612	6073.598024	Limestone
11-16 1226.5	584979.944	4488613	5465.571536	Dolo sulf bxa
11-16 1430.5	584995.404	4488613	5266.947467	Dolo Bxa
11-16 1473.5	584998.348	4488613	5228.132263	Zebra Dolo
11-17 734	585019.544	4488530	5904.181589	Sulf Dolo Bxa
11-17 1427	585064.468	4488544	5226.567698	Sulf Dolo Bxa
11-17 1537.1	585071.226	4488546	5119.072523	Sulf Dolo Bxa
11-17 1841	585088.578	4488553	4820.303217	Dolo Bxa
11-17 1864rr	585089.648	4488553	4800.678036	Dolo Bxa
11-17 1881	585090.709	4488554	4781.049507	Dolo Bxa
11-18 1317.5	584999.9	4488683	5345.791855	Ls/Ms Bxa?
11-18 1334.5	585001.213	4488683	5331.437632	Sulfitic Dolo Bxa?
11-18 1652	585029.705	4488679	5015.193104	Dolomite
12-05 826	585122.212	4488724	5716.89027	calcarenite
12-05 860	585124.619	4488724	5682.792823	calcarenite
12-05 1054	585137.542	4488724	5492.460973	Dolomite

Sample	UTM E	UTM N	Elevation (ft)	Lithology Description
12-05 1810.1	585183.122	4488725	4753.478043	Dolomite
12-05 1989	585192.967	4488725	4577.420839	Dolomite
12-10 525.9	584955.674	4488760	6089.615874	Silty Micrite
12-10 725	584984.22	4488757	5910.849409	Ls mic >clest
12-10 729rr	584984.915	4488757	5906.399538	Ls mic >clest
12-10 737.5	584985.609	4488757	5901.949667	Ls mic >clest
12-10 760	584989.08	4488757	5879.700313	Ls mic >clest
12-10 1553.5	585095.435	4488746	5168.5955	Micrite/calc-siltite
12-10 1555.9rr	585095.435	4488746	5168.5955	Micrite/calc-siltite
12-10 1831	585130.796	4488741	4915.591913	Dolomite
12-11 1260.5	584981.65	4488438	5573.995822	MultiLithic Bxa
12-11 1329	584987.39	4488439	5508.672762	Dolomite
12-11 1517.5	585002.565	4488440	5330.595007	Dolomite
12-13 1228.6rr	584792.76	4488586	5408.232366	calcarenite dolomite bxa
12-13 1237.9	584792.773	4488586	5401.732501	calcarenite dolomite bxa
12-18 678.1	584976.976	4488857	5924.569689	Micrite
12-18 1190.5	585047.061	4488854	5467.241484	mic/ calc-siltite
12-18 1195.1	585047.71	4488854	5462.717721	mic/ calc-siltite

Sample	UTM E	UTM N	Elevation (ft)	Lithology Description
12-18 1580 rr	585095.533	4488852	5115.5919	MultiLithic Bxa
12-18 1587	585096.721	4488852	5106.383445	MultiLithic Bxa
12-18 1832.9	585125.448	4488851	4880.272892	MultiLithic Bxa
12-18 2026	585147.206	4488850	4702.064277	MultiLithic Bxa
Vein Samples				
11-04 1187 vn	584606.97	4488689	5442.66017	calcite
11-04 1396vn	584605.97	4488686	5232.887155	calcite/dolomite
11-16 454.5 vn	584917.441	4488612	6212.900338	cc/dol?
12-01A 970.9vn	585018.075	4488658	5765.367757	Calcite
12-05 1042vn	585136.649	4488724	5506.150962	Calcite vn
12-10 525.9vn	584955.674	4488760	6089.615874	calcite
12-18 678.1 vn	584976.976	4488857	5924.569689	Calcite
12-18 1580 vn	585095.533	4488852	5115.5919	Calcite
12-18 2026 vnrr	585147.206	4488850	4702.064277	Calcite

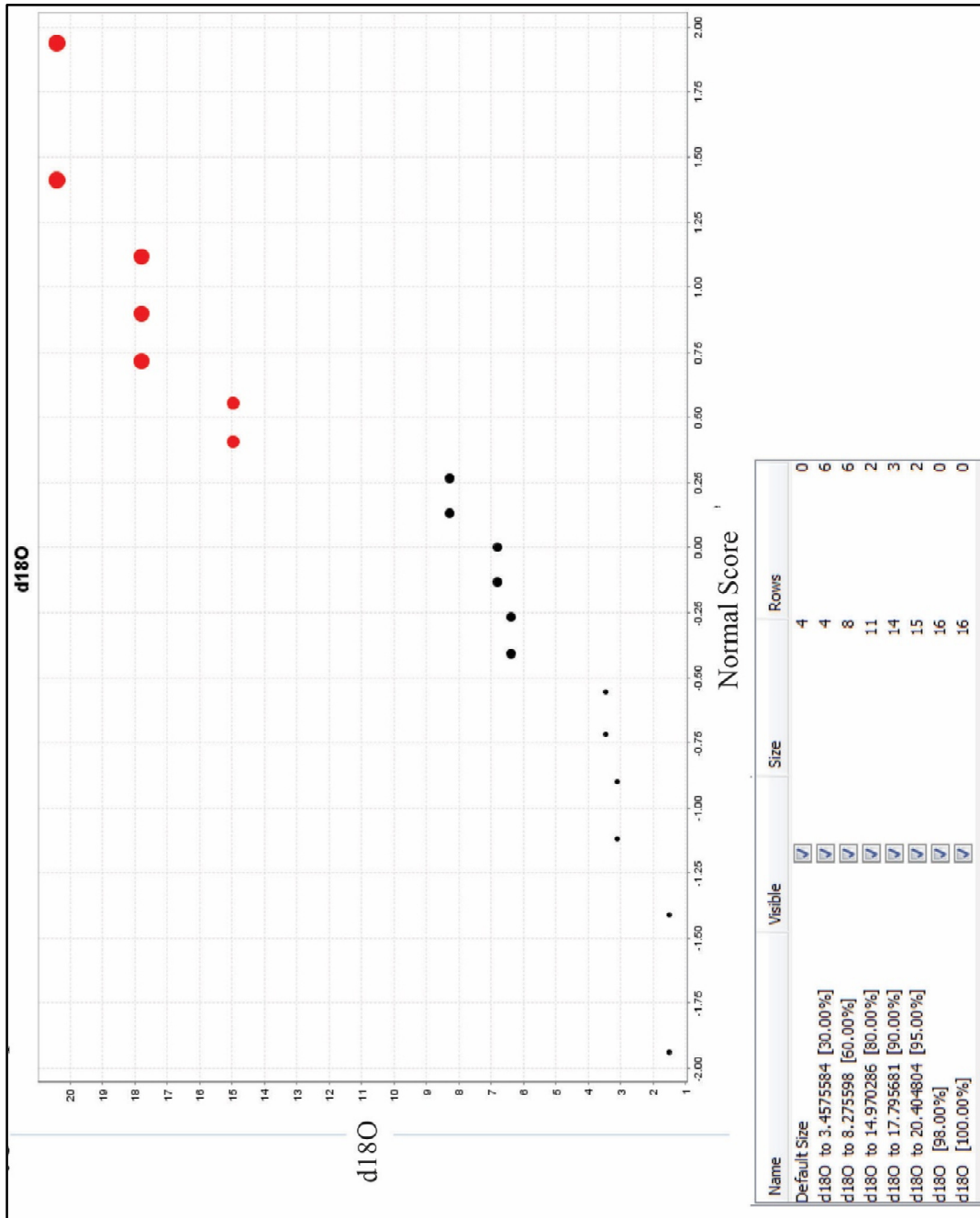
Appendix J.2 OA-IOCS: Results Table

Sample	Au Grade (ppm)	d18O	d13C
10-08C 1156.9 rr	1.455	15.85163	2.78
10-08C 1224.4	0.506	19.07023	1.37
10-16 1009.5	0.009	16.86149	1.41
10-16 1107	0.005	19.84125	0.82
10-16 1117.5	0.005	16.80922	0.54
10-16 1334	0.4	13.11279	1.37
10-16 1467.5	0.043	7.198358	2.32
10-16 1467.5r	0.043	15.76859	1.43
11-03 1007.5	0.542	15.95321	2.42
11-03 1372	0.235	17.17602	3.41
11-03 1447.9	0.088	23.69832	-0.99
11-03 1450.5	0.24	23.92527	-0.84
11-03 1559	0.033	18.9114	1.17
11-04 1074.9	0.017	19.28025	0.11
11-04 1164	0.033	23.23795	-0.25
11-04 1279	0.131	19.87765	1.38
11-04 1294.5	0.027	19.65903	-0.32
11-04 1396	0.014	22.20835	-0.48
11-04 1467	0.017	20.67588	-0.79
11-04 1526.5	0.006	10.32754	1.23
11-16 595.1	0.338	12.91512	1.69
11-16 1226.5	0.165	18.95617	1.6
11-16 1430.5	0.881	19.48898	1.42
11-16 1473.5	0.074	20.40057	0.36
11-17 734	0.033	25.34002	0.04
11-17 1427	0.05	21.90493	-0.11
11-17 1537.1	0.3	23.73703	0.24
11-17 1841	0.664	11.81938	2.34

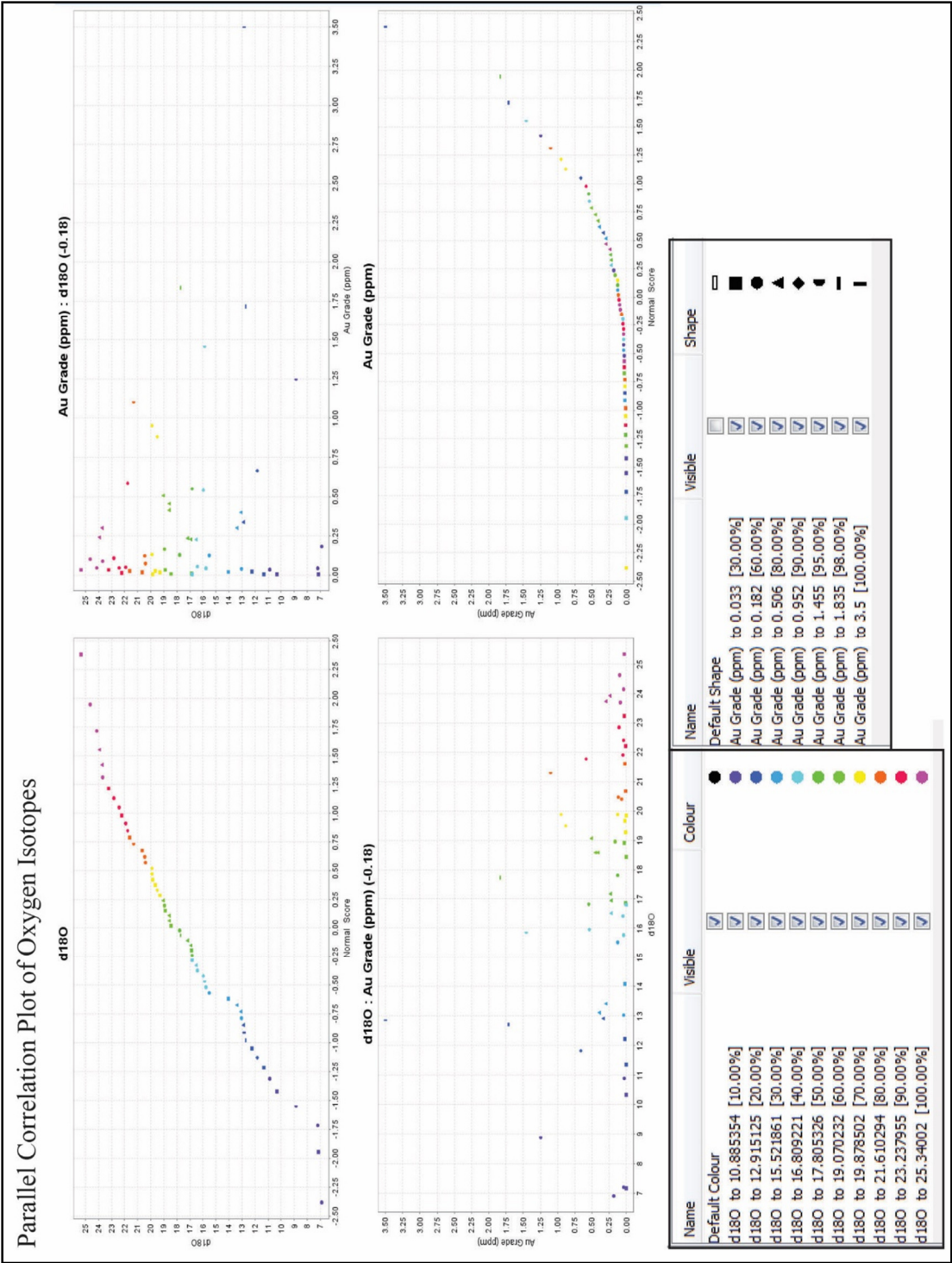
Sample	Au Grade (ppm)	d18O	d13C
11-17 1864rr	0.101	24.63046	-1.18
11-17 1881	0.046	24.14257	-0.15
11-18 1317.5	0.549	16.81862	0.57
11-18 1334.5	0.122	20.46778	0.78
11-18 1652	0.046	22.40767	-0.3
12-05 826	0.021	12.21846	1.57
12-05 860	0.182	6.905545	1.02
12-05 1054	0.108	22.84577	0.26
12-05 1810.1	1.1	21.29164	-0.34
12-05 1989	0.126	15.52186	0.29
12-10 525.9	0.006	7.161021	3.55
12-10 725	3.5	12.8585	3.97
12-10 729rr	1.245	8.870499	1.39
12-10 737.5	0.228	16.95331	3.95
12-10 760	0.02	14.07765	4.59
12-10 1553.5	0.054	16.41844	2.1
12-10 1555.9rr	0.226	16.51936	1.62
12-10 1831	0.027	21.61029	0.15
12-11 1260.5	0.129	17.80533	2.3
12-11 1329	0.952	19.8785	1.8
12-11 1517.5	0.414	18.58313	-0.33
12-13 1228.6rr	0.585	21.76941	0.77
12-13 1237.9	1.835	17.72357	1.32
12-18 678.1	0.005	11.35112	4.19
12-18 1190.5	0.034	10.88535	2.26
12-18 1195.1	0.455	18.58065	5.45
12-18 1580 rr	0.301	13.4137	0.23
12-18 1587	1.715	12.70451	0.34

Sample	Au Grade (ppm)	d18O	d13C
12-18 1832.9	0.007	18.42822	1.67
12-18 2026	0.04	13.02319	1.15
Vein Samples			
11-04 1187 vn	0.056	6.391226	0.27
11-04 1396vn	0.014	20.40481	0.17
11-16 454.5 vn	0.005	6.797545	3.05
12-01A 970.9vn	2.53772291	17.79568	1.49
12-05 1042vn	0.294	8.275598	0.66
12-10 525.9vn	0.006	1.51682	2.38
12-18 678.1 vn	0.005	3.115081	2.73
12-18 1580 vn	0.301	3.457558	0.49
12-18 2026 vnrr	0.04	14.97029	1.59

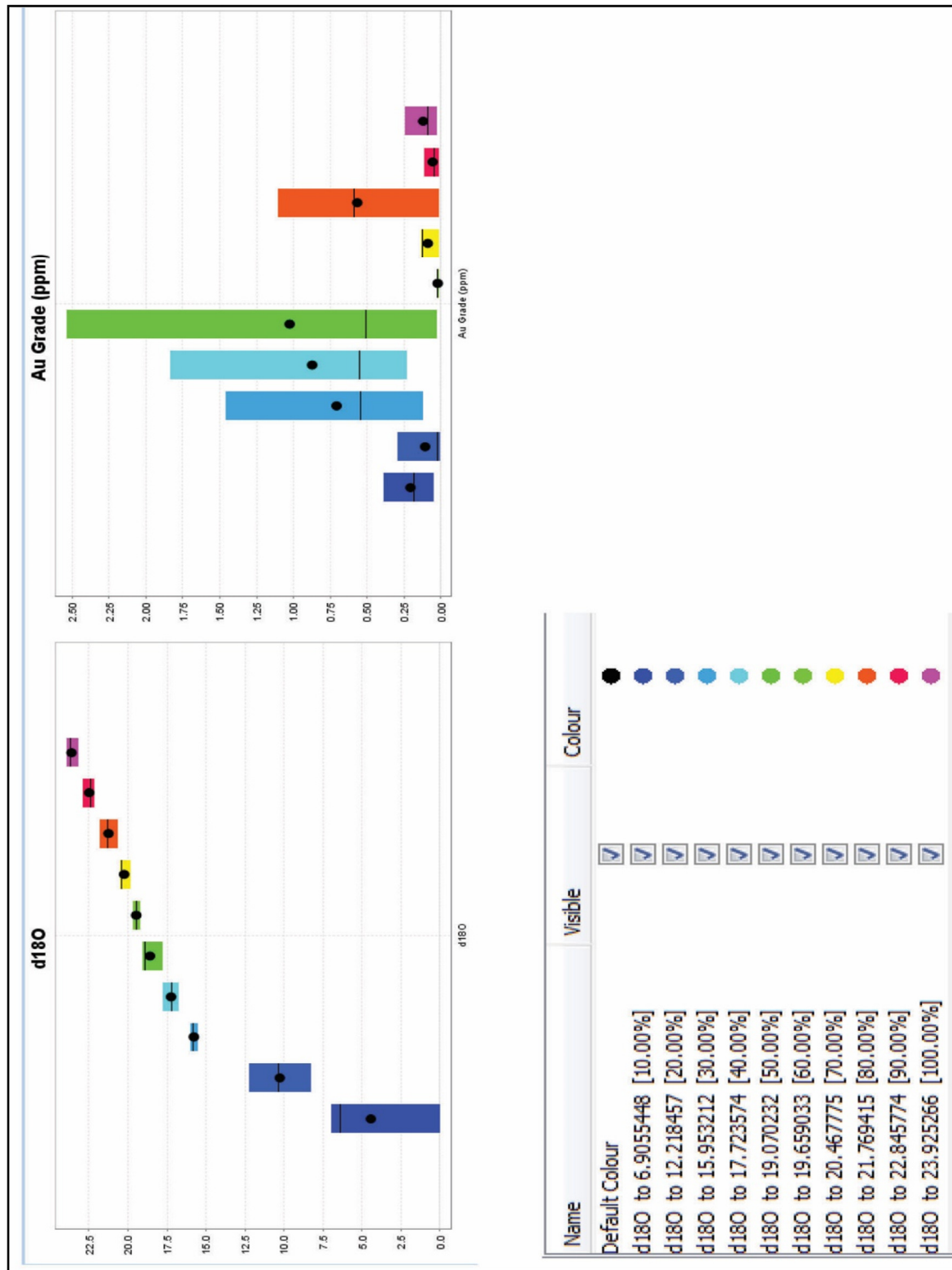
Appendix J.3 Images



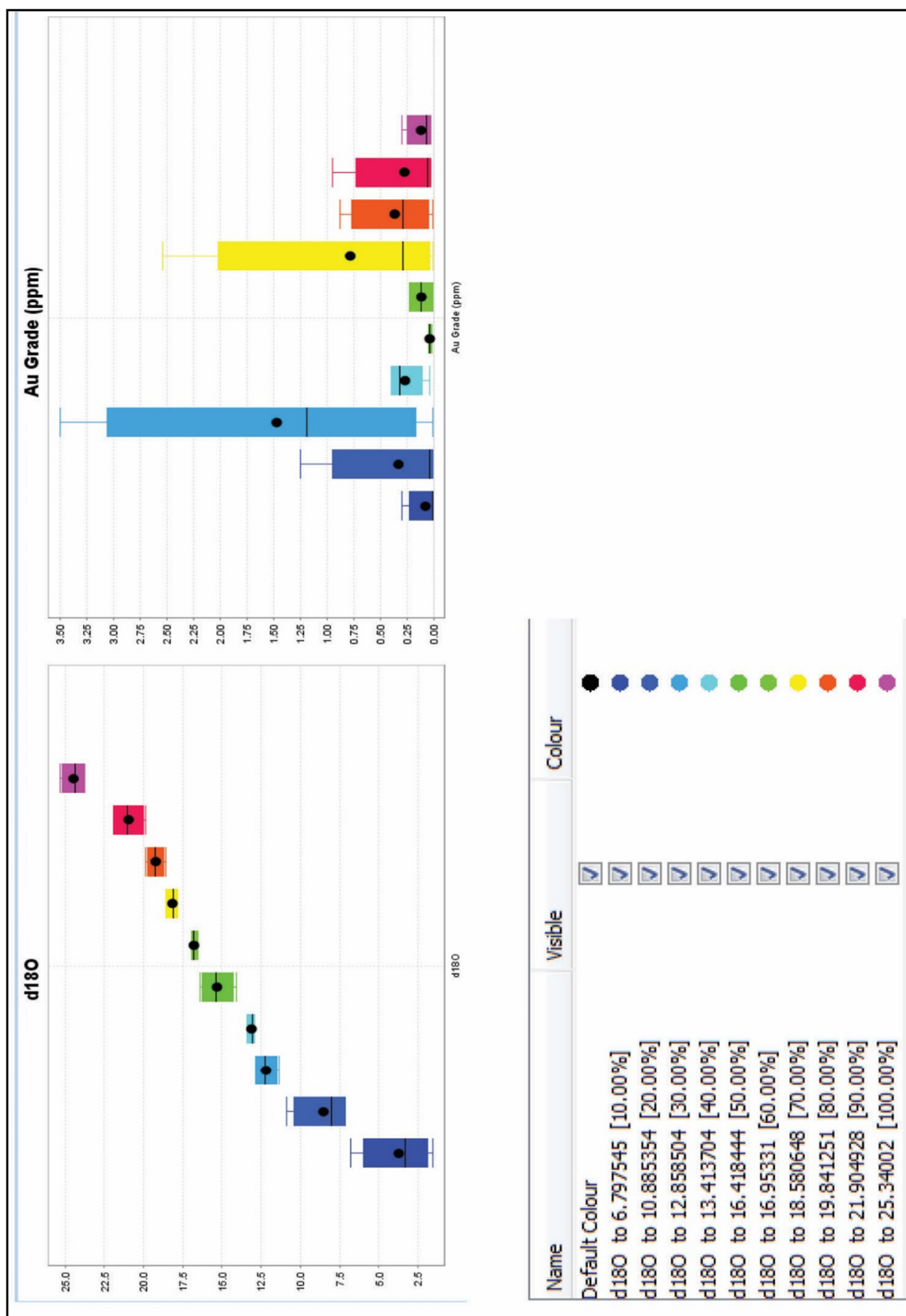
Normalized oxygen isotope data from calcite veins throughout the deposit. Calcite veins show two patterns, $\delta^{18}\text{O} = 14.97 - 20.40$, shown in red, and $\delta^{18}\text{O} = 1.51 - 8.27$ shown in black. Calcite veins with oxygen values ($\delta^{18}\text{O} = 14.97 - 20.40$) are similar to unaltered host rocks ($\delta^{18}\text{O} = \sim 20$) and are interpreted as diagenetic calcite veins related to the deposition to host rocks. Calcite veins with oxygen values ($\delta^{18}\text{O} = 1.51 - 8.27$) are interpreted as late-ore stage calcite veins.



Data from all carbonate samples analyzed.



Turkey Box Plots of oxygen isotope data from carbonate samples from the East-West transect. Samples with gold greater than 1 ppm have $\delta^{18}\text{O}$ values of 12.3 - 19.07 and 20.46 - 21.76.



Turkey Box Plots of oxygen isotope data from carbonate samples from the North- South transect. Samples with gold greater than 1 ppm have $\delta^{18}\text{O}$ values of 6.79 - 12.85 and 16.95 - 18.58.

REFERENCES

- de Almeida, C. M., Olivo, G. R., Chouinard, A., Weakly, C., & Poirier, G. (2010). Mineral paragenesis, alteration, and geochemistry of the two types of gold ore and the host rocks from the Carlin-type deposits in the southern part of the Goldstrike property, northern Nevada: Implications for sources of ore-forming elements, ore genesis, and mineral exploration. *Economic Geology*, 105(5), 971-1004.
- Barker, S. L., Dipple, G. M., Hickey, K. A., Lepore, W. A., & Vaughan, J. R. (2013). Applying stable isotopes to mineral exploration: teaching an old dog new tricks: *Economic Geology*, 108(1), 1-9.
- Blaxland, A.B. (1971). Occurrence of zinc in granitic biotite. *Mineralium Deposita*, 6, 313-320
- du Bray, E. A. (2007). Time, space, and composition relations among northern Nevada intrusive rocks and their metallogenic implications. *Geosphere*, 3(5), 381-405.
- Bowen, P., personal communication, December 19, 2013.
- Burchfiel, B.C., Royden, L.H. (1991). Antler Orogeny: A Mediterranean-type orogeny. *Geology*, 19, 66-69.
- Cail, T. and Cline, J.S. (2001). Alteration associated with gold mineralization at the Getchell Carlin-type gold deposit, Northern Nevada, USA. *Economic Geology*, 96, 1343-1359.
- Carlisle, D., Murphy, M. A., Nelson, C. A., & Winterer, E. L. (1957). Devonian stratigraphy of Sulphur Springs and Pinyon Ranges, Nevada. *AAPG Bulletin*, 41(10), 2175-2191.

- Clark, L. R. (2012). Ore and Gangue Mineral Paragenesis of the Cortez Hills Carlin-Type Gold Deposit, Nevada: Evidence for Coincident High-Grade Gold Deposition and Collapse Brecciation.
- Cline, J.S. (2001). Timing of gold and arsenic sulfide mineral deposition at the Getchell Carlin-type gold deposit, North Central Nevada. *Economic Geology*, 96, 75-90.
- Cline, J., Hofstra, A., Muntean, J., Tosdal, R., and Hickey, K. (2005). Carlin-type gold deposits in Nevada: Critical geologic characteristics and viable models, *in* Hedenquist, J.W., Thompson, J. F. H., Goldfarb, R. J., and Richards, J. P., eds., 100th Anniversary Volume. Littleton, CO: Society of Economic Geologists, p. 451-484.
- Cook, H.E., and Corboy, J.J. (2004). Great Basin Paleozoic Carbonate platform: Facies, facies transitions, depositional models, platform architecture, sequence stratigraphy, and predictive mineral host models. *USGS Open File report 2004*, 1078, 129.
- Crafford, A.E.J., and Grauch, V.J.S. (2002). Geologic and geophysical evidence for the influence of deep crustal structures on Paleozoic tectonics and the alignment of world class gold deposits, north central Nevada, USA. *Ore Geology Reviews*, 21, 157–184.
- Dickinson, W. (2004). Evolution of the North American Cordillera. *Annual Review Earth Planet Science*, 32, 13-45.
- Emsbo, P., Hutchinson, R. W., Hofstra, A. H., Volk, J. A., Bettles, K. H., Baschuk, G. J., & Johnson, C. A. (1999). Syngenetic Au on the Carlin trend: Implications for Carlin-type deposits. *Geology*, 27(1), 59-62.

- Gold Standard Ventures Corporation. (2012). Railroad. Retrieved October 25, 2012, from <http://goldstandardv.com/projects/railroad/>.
- Gold Standard Ventures Corporation. (2013). Railroad. Retrieved July 29, 2013, from <http://goldstandardv.com/projects/railroad/>.
- Gold Standard Ventures Corporation. (2014). Railroad. Retrieved December 12, 2014, from <http://goldstandardv.com/projects/railroad/>.
- Grauch, V. J. S., Rodriguez, B. D., and Wooden, J. L. (2003). Geophysical and isotopic constraints on crustal structure related to mineral trends in north-central Nevada and implications for tectonic history. *Economic Geology*, 98(2), 269-286.
- Groff, J.A., Heizler, M.T., McIntosh, W.C., and Norman, D.I. (1997). $^{40}\text{Ar}/^{39}\text{Ar}$ dating and mineral paragenesis for Carlin-type gold deposits along the Getchell Trend, Nevada: Evidence for Cretaceous and Tertiary gold mineralization. *Economic Geology*, 92, 601–622.
- Harp, M., personal communication, August 1, 2014.
- Henry, C.D., personal communication, August 1, 2014.
- Henry, C. D. (2014). Igneous Geology and Relation to Mineralization: Railroad-Bullion Area: Final Report to Gold Standard Ventures Corp. (unpublished), 1-24.
- Hofstra, A.H., and Cline, J.S. (2000). Characteristics and models for Carlin-type gold deposits: Vikre, P., Thompson, T.B., Bettles, K., Christensen, O., and Parratt, R. eds. *Society of Economic Geology Reviews*, 13, 163-220.
- Hofstra, A.H., Leventhal, J.S., Northrop, H.R., Landis, G.P., Rye, R.O., Birak, D.J., and Dahl, A.R. (1991). Genesis of sediment-hosted disseminated-gold deposits by fluid mixing and sulfidization: Chemical-reaction-path modeling of ore-

- depositional processes documented in the Jerritt Canyon district, Nevada.
Geology, 19, 36-40.
- Humphreys, E. (1995). Post Laramide removal of the Farallon slab, western United States. *Geology*, 23, 987-990.
- Humphreys, E. (2009). Relation of flat subduction to magmatism and deformation in the western United States. *Geological Society of America Memoirs*, 204, 85-98.
- Jackson, M., personal communication, July 17, 2014.
- Koenig, A.E., Rogers, R.R., and Trueman, C.N. (2009). Visualizing fossilization using laser ablation-inductively coupled plasma-mass spectrometry maps of trace elements in Late Cretaceous bones. *Geology*, 37, 511-514.
- Large, R. R., Halpin, J. A., Danyushevsky, L. V., Maslennikov, V. V., Bull, S. W., Long, J. A., and Calver, C. R. (2014). Trace element content of sedimentary pyrite as a new proxy for deep-time ocean–atmosphere evolution: *Earth and Planetary Science Letters*, 389, 209-220.
- Longo, A. A., Thompson, T. B., and Harlan J. B. (2002). Geologic Overview of the Rain Subdistrict, in: Gold Deposits of the Carlin Trend, edited by Tommy B. Thompson, Lewis Teal, and Richard O. Meeuwig. *Nevada Bureau of Mines and Geology Bulletin*, 111, 168-197.
- Mathewson, D.C. (1993). Rain folio, 1992 annual report: Newmont Exploration Ltd. Internal report, 27.
- Mathewson, D.C., Jones, M.E., and Beetler, J.L. (1994). Rain folio, 1993 annual report: Newmont Exploration Ltd. Internal report.

- Miller-Coleman, R. L., Dodsworth, J. A., Ross, C. A., Shock, E. L., Williams, A. J., Hartnett, H. E., and Hedlund, B. P. (2012). Korarchaeota diversity, biogeography, and abundance in Yellowstone and Great Basin hot springs and ecological niche modeling based on machine learning. *PLoS One*, 7(5).
- McCune, B., Grace, J. B., and Urban, D. L. (2002). *Analysis of ecological communities*. Gleneden Beach, OR: MjM Software Design.
- Mineral Data Publishing. (2001). Stephanite: stephanite mineral information and data. Retrieved October 10, 2014, from <http://www.mindat.org/min-3764.html>.
- Muntean, J. L., Cline, S.C., Simon, A.C., and Longo, A.A. (2011). Magmatic-hydrothermal origin of Nevada's Carlin-type gold deposits. *Nature Geoscience*, 4(2), 122-127.
- Nevada Bureau of Mines and Geology. (2010). The Nevada mineral industry 2010: Special Publication MI-2010. Reno, Nevada: Mackay School of Earth Sciences and Engineering, p. 151.
- Pallant, J. (2007). SPSS survival manual: A step-by-step guide to data analysis using SPSS version 15. Maidenhead, Berkshire, England: McGraw-Hill Education.
- Poole, F.G., Stewart, J.H., Palmer, A.R., Sandberg, C.A., Madrid, R.J., Ross, R.J., Hintze, L.F., Miller, M.M., and Wrucke, C.T. (1992). Latest Precambrian to latest Devonian time; development of a continental margin, in Burchfield, B.C., Lipman, P.W., and Zoback, M.L., eds., *The Cordilleran Orogen: Conterminous U.S.* Boulder, Colorado: Geological Society of America, *The Geology of North America*, G-3, 9-56.
- Ren, M., personal communication, December 3, 2014.

- Ressel, M. W. & Henry, C. D. (2006). Igneous geology of the Carlin trend, Nevada: Development of the Eocene plutonic complex and significance for Carlin-type gold deposits. *Economic Geology*, 101, 347-383.
- Roberts, R., Hotz, P., Gilluly, J., and Ferguson, H. (1958). Paleozoic rocks in north-central Nevada. *American Association of Petroleum Geologists Bulletin*, 42, 2813-2857.
- Saleeby, J.B., Hannah, J.L., and Varga, R.J. (1987). Isotopic age constraints of middle Paleozoic deformation in the northern Sierra Nevada, California. *Geology*, 15, 757-760.
- Sadlick, W. (1995). Stratigraphic subdivision of the Chainman Formation. Mississippian Source Rocks in the Antler Basin of Nevada and Associated Structural and Stratigraphic Traps. *Nevada Petroleum Society*, 3-44.
- Seedorff, E. (1991). Magmatism, extension, and ore deposits of Eocene to Holocene age in the Great Basin—Mutual effects and preliminary proposed genetic relationships: Geology and ore deposits of the Great Basin. Geological Society of Nevada, Symposium, Reno-Sparks, April 1990, Proceedings, 1, p. 133–178.
- Sillitoe, R. (2008). Major gold deposits of the North and South American Cordillera: Distribution, tectonomagmatic settings, and metallogenic considerations. *Economic Geology*, 103, 663-687.
- Smith, J.F., and Ketner, K.B. (1975). Stratigraphy of Paleozoic Rocks, Carlin-Piñon Range area, Nevada, U.S. Geological Survey Professional Paper 867-A.
- Smith, J.F., and Ketner, K.B. (1978). Geologic map of the Carlin-Piñon Range area, Elko and Eureka Counties, Nevada, U.S. Geological Survey Miscellaneous

Investigations Map MI-1028.

Solomon, B. J., McKee, E. H., and Andersen, D.A. (1979). Stratigraphy and depositional environments of Paleogene rocks near Elko, Nevada *in* Armentrout, J.M., Cole, M.R., and TerBest, Harry, Jr., eds., Cenozoic Paleogeography of the western United States: Pacific Coast Paleogeography Symposium, Society of Economic Paleontologists and Mineralogists, no. 3, Los Angeles, March 14, 1979, Pacific Section, p.75-88.

Sonder L.J. and Jones C.H. (1999). Western United States Extension: How the West was Widened. *Annual Review of Earth and Planetary Science*, 27, 417-462.

Tosdal, R.M., Wooden, J.L., and Kistler, R.W. (2000). Inheritance of Nevadan mineral belts from Neoproterozoic continental breakup, *in* Cluer, J.K., Price, J.G., Struhsacker, E.M., Hardyman, R.F., and Morris, C.L., eds., *Geology and Ore Deposits 2000. The Great Basin and Beyond*: Reno, Geological Society of Nevada Symposium, Proceedings, p. 451–466.

CURRICULUM VITAE

Graduate College
University of Nevada, Las Vegas

Melanie N. Newton
newtonm8@unlv.nevada.edu
Melanie.newton313@gmail.com

Education:

Graduate

Masters of Science in Geosciences

University of Nevada, Las Vegas, Department of Geoscience
Thesis Title: CHARACTERIZATION OF GOLD AND
RELATED MINERALIZATION OF GOLD AND RELATED
MINERALIZATION AT THE NORTH BULLION CARLIN
SYSTEM, RAILROAD PROJECT, A NEVADA CARLIN -
TYPE GOLD PROSPECT
Thesis Examination Committee:
Chairperson, Jean S. Cline, Ph. D.
Committee Member, Rodney Metcalf, Ph. D.
Committee Member, John Muntean, Ph. D.
Graduate Faculty Representative, Barbara Luke, Ph. D.
Anticipated Graduation: December 2015
Cumulative GPA: 3.86

Undergraduate

Bachelor of Science in Geology

Western Kentucky University, Bowling Green, Department of
Geography and Geology
Graduation: December 2011
Cumulative GPA: 3.92

Experience:

08/12 – Present

Graduate Assistant – **University of Nevada** – Las Vegas, NV
Research Assistant, Teaching Assistant; Thesis Project:
Characterization of Gold and Related Mineralization at the North
Bullion Fault Zone, Railroad Project, a Nevada Carlin-type Gold
Prospect.
Advisor: Jean Cline

- 03/15 – 07/15 Geologist – **ExxonMobil** – Houston, TX
 Conducted a regional study of intercontinental foreland basin.
 Responsibilities include creating well ties, interpret seismic horizons, generate structure maps, isopach maps, and determine migration pathways and play maps.
 Supervisor: Mark Richardson and John Reistroffer
- 06/14 – 08/14 Geologist – **Barrick Gold Corporation** – Elko, NV
 Interned with Barrick Gold Corporation at the Goldstrike Property, which is located on the North Carlin Trend. Skills learned include: Data transformation from ArcGIS to Vulcan, Vulcan 3-D modeling of lithologies and structures.
 Supervisor: Jim Byers and Gerry Griesel
- 06/13 – 08/13 Geologist – **Gold Standard Ventures Corporation** – Elko, NV
 Interned with Gold Standard Ventures Corp., a junior exploration company, that owned property south of the Carlin Trend, NV. Skills learned included: soil scoop sampling, rock chip sampling, core logging (Logged 1131 Ft.), and sample submitting. Other responsibilities included: Structural data entry.
 Supervisor: Dave Mathewson, Steven Koehler, and Mac Jackson
- 05/12 – 08/12 Geologist – **Denver Inclusion Analysis Laboratory** – Denver, CO
 Interned with the NAGT/ USGS 2012 summer internship program. Lab Analysis of fluid inclusions related to Henderson Porphyry Molybdenum deposit.
 Supervisor: Dr. Albert Hofstra
- 06/11 – 07/11 **REU: Evolution of the Precambrian Rocks of Yellowstone National Park**
 Observed field relations and described the lithologies involved in Yellowstone National Park. Collected, processed, and analyzed samples related to the Coulter Creek Campground, MT. Presentation of research of the Coulter Creek Campground, MT at the Rocky Mountain regional GSA meeting in May 2012.
 Supervisor: Dr. Dave Mogk, Dr. Darrell Henry, Dr. Paul Mueller, Dr. Dave Foster
- 05/12 – 06/12 **Illinois State University Field Course** – Wyoming, South Dakota
 Collected field data and mapped a total of seven projects for duration of six weeks.
 Instructors: Dr. Dave Malone, Dr. Mark Fisher, Dr. Andrew Wulff

- 08/10 – 12/10 Lab Analyst –**Advanced Materials Institute**– Bowling Green, KY

Analyzed industrial material samples. Tests include using: LECO AMA 254 advanced mercury analyzer, LECO SC-432 sulfur analyzer, LECO Carbon Hydrogen, and Nitrogen analyzer, LECO Model AC-350 calorimeter, Ion Chromatography, and LECO TGA-701 which measures ash and moisture content.
Supervisor: Dr. Aaron Celestian
- 06/10 – 08/10 Lab Analyst – **WATERS Lab** – Bowling Green, KY
Performed daily wet chemistry analysis on water samples. Tests include: total phosphorous, ammonium nitrogen, dissolved oxygen, biochemical oxygen demand, total organic carbon, total suspended/dissolved solids, oil and grease analysis, pH, specific gravity, total kjeldahl nitrogen, turbidity, atrazine, and gas chromatography mass spectrometry.
Supervisor: Mrs. Samantha J. Kramer
- 01/10 **Geology of the Bahamas Field Course** – San Salvador, Bahamas
Examined the geologic record of San Salvador Island by studying various locations that had outcrops of the Holocene and Pleistocene aged rocks. Conducted a cross section of Rice Bay in order to see the back and fore dune, beach and intertidal zone in relation to high and low tide. Collected, sorted, and compared sand, shells, and mud cores from various island locations
Instructor: Dr. Fred Siewers, and Dr. Lisa Parks

Professional Affiliations:

American Institute of Professional Geologists
Association for Mineral Exploration British Columbia
Geological Society of America
Geological Society of Nevada
Kentucky Academy of Science
Society of Economic Geologists
Society of Exploration Geophysicists

Professional Presentations:

Poster Presentation, 2014 SEG Conference, (Ore Characterization at the North Bullion Carlin-type Gold System, a New Prospect on the Carlin Trend, Nevada)

Poster Presentation, 2014 PACROFI Conference, (Fluid inclusion & stable isotopic evidence for extreme degassing of melt & condensation of brine in the Henderson porphyry Mo deposit)

Poster Presentation, UNLV Graduate College Conference 2014, (Characterization of Gold and Related Mineralization at the North Bullion Fault Zone, Railroad Project, a Nevada Carlin-type Gold Prospect)

Oral Presentation, UNLV 9th Annual Geosymposium 2014, (Characterization of Gold and Related Mineralization at the North Bullion Fault Zone, Railroad Project, a Nevada Carlin-type Gold Prospect)

Poster Presentation, Association for Mineral Exploration British Columbia 2014 Roundup, (Characterization of Gold and Related Mineralization at the North Bullion Fault Zone, Railroad Project, a Nevada Carlin-type Gold Prospect)

Poster Presentation, UNLV 8th Annual Geosymposium 2013, (Characterization of Gold and Related Mineralization at the North Bullion Fault Zone, Railroad Project, a Nevada Carlin-type Gold Prospect)

Poster Presentation, Meeting of the 2012 Rocky Mountain Regional GSA Meeting (Geology of Yellowstone National Park: Plutonic Rocks of the Cooke City Area, MT)

1st in 2010 Undergraduate Paper Presentation, Geology Division, of the 2010 Kentucky Academy of Science Annual Meeting (Characterization of the suite of Minerals from Dos Pobres, AZ)

Skills:

Acetate Peels Petrography	Adobe Illustrator
Adobe Photoshop	Electron Probe Microanalysis (EMPA)
ESRI ArcSoftware (GIS)	Field Mapping
Field Mapping	Fluid Inclusion Microthermometry
Franz- Magnetic Separator	Fusing XRF and Powder press disks
IOGAS	LA-ICP-MS
Making Thin Sections	Petrographic Microscope
Petrel	Powder X-Ray Diffraction (XRD) analysis
Raman Microscopy	SEM- Cathodluminescence
S-plus statistical software	Ur-Th-He method on ICP-MS
Vulcan 3-D Modeling	X-Ray Fractionation (XRF) Analysis

Industrial Material Analysis: LECO AMA 254 advanced mercury analyzer, LECO SC-432 sulfur analyzer, LECO Carbon Hydrogen, and Nitrogen analyzer,

LECO Model AC-350 calorimeter, Ion Chromatography, and LECO TGA-701 which measures ash and moisture content.

Water Chemistry Analysis: total phosphorous, ammonium nitrogen, dissolved oxygen, biochemical oxygen demand, total organic carbon, total suspended/dissolved solids, oil and grease analysis, pH, specific gravity, total kjeldahl nitrogen, turbidity, atrazine, and gas chromatography mass spectrometry.